

DYNAMICAL SYSTEMS

Mechatronics and Life Sciences

Editors

**J. AWREJCEWICZ
M. KAŹMIERCZAK
J. MROZOWSKI
P. OLEJNIK**



DYNAMICAL SYSTEMS

Mechatronics and Life Sciences

Editors

JAN AWREJCEWICZ, MAREK KAŻMIERCZAK
JERZY MROZOWSKI, PAWEŁ OLEJNIK

© Department of Automation, Biomechanics and Mechatronics
ISBN 978-83-7283-707-3
10.34658/9788372837073
<https://doi.org/10.34658/9788372837073>

Cover design: Marek Kaźmierczak
Technical editor: Marek Kaźmierczak

Printed by:
ARSA Druk i Reklama
90-270 Łódź, ul. Piotrkowska 4
tel./fax (042) 633 02 52
marta@arsa.net.pl
www.arsa.net.pl

PREFACE

This is the thirteen time when the conference “Dynamical Systems: Theory and Applications” gathers a numerous group of outstanding scientists and engineers, who deal with widely understood problems of dynamics met in daily life.

Organization of the conference would not have been possible without a great effort of the staff of the Department of Automation, Biomechanics and Mechatronics, as well as Committee of Mechanics of the Polish Academy of Sciences. The financial support has been given by the Polish Academy of Sciences.

It is a great pleasure that our invitation has been accepted by recording in the history of our conference number of people, including good colleagues and friends as well as a large group of researchers and scientists, who decided to participate in the conference for the first time. With proud and satisfaction we welcomed over **180** persons from **29** countries all over the world. They decided to share the results of their research and many years experiences in a discipline of dynamical systems by submitting many very interesting papers.

This year, the DSTA Conference Proceedings were split into three volumes entitled “Dynamical Systems” with respective subtitles: *Mathematical and numerical approaches*; *Mechatronics and life sciences* and vol. 3 *Control and stability*. Additionally there will be also published two volumes of Springer Proceedings in Mathematics and Statistics entitled “Dynamical Systems. Modelling” and “Dynamical Systems. Theoretical and Experimental Analysis”.

These books include the invited papers and regular papers dealing with the following topics:

- control in dynamical systems,
- stability of dynamical systems,
- asymptotic methods in nonlinear dynamics,
- mathematical approaches to dynamical systems,
- dynamics in life sciences and bioengineering,
- engineering systems and differential equations,
- original numerical methods of vibration analysis,
- bifurcations and chaos in dynamical systems,
- vibrations of lumped and continuous systems,
- non-smooth systems,
- other problems.

Proceedings of the 13th Conference „Dynamical Systems - Theory and Applications” summarize **164** and the Springer Proceedings summarize **60** best papers of university teachers and students, researchers and engineers from whole the world. The papers were chosen by the International Scientific Committee from **315** papers submitted to the conference. The reader thus obtains an overview of the recent developments of dynamical systems and can study the most progressive tendencies in this field of science.

Our previous experience shows that an extensive thematic scope comprising dynamical systems stimulates a wide exchange of opinions among researchers dealing with different branches of dynamics. We think that vivid discussions will influence positively the creativity and will result in effective solutions of many problems of dynamical systems in mechanics and physics, both in terms of theory and applications.

We do hope that DSTA 2015 will contribute to the same extent as all the previous conferences to establishing new and tightening the already existing relations and scientific and technological co-operation between both Polish and foreign institutions.

On behalf of both
Scientific and Organizing Committees

A handwritten signature in black ink, appearing to read 'Awrejcewicz', with a stylized flourish at the end.

Chairman

Professor Jan Awrejcewicz

CONTENTS

Igor V. Andrianov, Jan Awrejcewicz, Bernd Markert, Galina A. Starushenko <i>On the vibrations of a composite structure with hexagonal structure of a circular inclusions</i>	11
Jan Awrejcewicz, Paweł Olejnik <i>Identification of a nonlinear damping coefficient characteristics in the free decay test of a single pendulum with friction</i>	23
Henryk Bąkowski <i>An explanation of water acting on rails wear using finite elements method</i>	37
Laszlo Bencsik, Ambrus Zelei <i>A study on the effect of human running cadence based on the bouncing ball modell</i>	47
Yves Bergeon, Vaclav Krivanek, Jean Motsch, Alexandr Stefek <i>Optimization of accuracy on a low-cost 3D mapping system for indoor navigation</i>	57
Paweł Biesiacki, Jerzy Mrozowski, Jan Awrejcewicz <i>Study of dynamic forces in human upper limb in forward fall.....</i>	65
Andrzej Buchacz, Andrzej Baier, Krzysztof Herbuś, Michał Majzner, Piotr Ociepka <i>Investigations of motion of a freight wagon aimed to identify the forces acting on the side wall of the wagon</i>	77
Andrzej Buchacz, Damian Gałęziowski <i>Negative elements optimization and realization in synthesis of discrete mechatronic systems</i>	89
Vytautas Bučinskas, Andrius Dzedzickis, Nikolaj Šešok, Ernestas Šutinys, Igor Iljin, Artur Kazickij <i>Two-axis mechanical vibration harvester</i>	99
Radek Bulín, Michal Hajžman, Pavel Polach <i>Analysis of vibrations of a cable-pulley system using the absolute nodal coordinate formulation</i>	111
Andrzej Burghardt, Dariusz Szybicki, Piotr Gierlak, Krzysztof Kurc, Magdalena Muszyńska <i>Robotic automation of the turbo-propeller engine blade grinding process</i>	121
Anatoli Chigarev, Victor Polenov, Pavel Shirvel <i>Nonlinear dynamics of waves in inhomogeneous media with fractal structures</i>	131

Mariella Diaferio	
<i>On the dynamic response of suspended footbridges</i>	143
Fadi Dohnal, Athanasios Chasalevris	
<i>Inducing modal interaction during run-up of a magnetically supported rotor</i>	151
Peter Frankovský, František Trebuňa, Darina Hroncová, Alexander Gmitterko, Ján Kostka	
<i>Modelling of mechatronic systems using bond graphs</i>	163
Paweł Fritzkowski, Krzysztof Magnucki, Szymon Milecki	
<i>Nonlinear transverse vibrations of a beam under an axial load</i>	175
Jakub Gajek, Radosław Kępiński, Jan Awrejcewicz	
<i>Mathematical model of a multi-parameter oscillator based on a core-less three-phase linear motor with skewed coils</i>	185
Dariusz Grzelczyk, Bartosz Stańczyk, Jan Awrejcewicz	
<i>Power consumption analysis of different hexapod robot gaits</i>	197
Thomas H Hanley, Barry Gallacher, Harry Grigg	
<i>Towards the exploitation of local resonances for novel MEMS devices</i>	207
Andjelka Hedrih, Katica Hedrih (Stevanovic)	
<i>Deformation work of Zona Pelucida in process of fertilization</i>	217
Anna Jaskot, Bogdan Posiadała, Szczepan Śpiewak	
<i>Dynamics model of the four-wheeled mobile platform</i>	227
Jacek Jaworski, Olga Szlachetka	
<i>Free vibration of cantilever beams of various cross-section</i>	237
Stefan Kaczmarczyk	
<i>The dynamics of vertical transportation systems: from deep mine operations to the modern high-rise applications</i>	249
Radosław Kępiński, Jan Awrejcewicz, Jakub Gajek	
<i>Analysis of stepper motor dynamics using numerical methods</i>	261
Natalya Kizilova	
<i>Nonlinear inverted pendulum model with time delay control for postural sway in humans</i>	273
Shuangbao Li, Xiaoli Bian	
<i>The subharmonic Melnikov method for a class of planar piecewise-smooth systems</i>	283
Sebastian Lipa, Jerzy Mrozowski, Jan Awrejcewicz	
<i>Analysis of orbital strain and stress caused by multidirectional forces generated during a ball impact</i>	295

Jakub Lorencki, Stanisław Radkowski <i>Switched Reluctance Motor (SRM) mechanical faults and their identification in frequency domain</i>	305
Elif Cagda Kandemir Mazanoglu, Kemal Mazanoglu <i>Parametric study on implementation of viscous dampers for adjacent buildings</i>	313
Kemal Mazanoglu, Ali Ceylan <i>Rayleigh–Ritz natural frequency analyses for centrifugally stiffened functionally graded and tapered beams.....</i>	323
Kemal Mazanoglu, Elif Cagda Kandemir Mazanoglu <i>Anti-symmetric mode in-plane vibration analyses of several types of frame structures</i>	333
Arkadiusz Mężyk, Wojciech Klein, Tomasz Czapla, Gabriel Mura <i>Numerical simulation of suspension system for autonomous tracked hybrid vehicle</i>	343
Jakub Młyńczak, Rafał Burdzik, Ireneusz Celiński <i>Research on vibrations in the train driver's cab in the course of shunting activity</i>	353
Gabriel Mura, Marek Adamczyk, Michał Nocoń <i>Numerical simulation of mobility of miners rescue robot.....</i>	365
Milan Nad', Ladislav Rolník, Lenka Čičmancová <i>The effect of partially embedded inner reinforcing core on modal properties of the Euler-Bernouli beam structures</i>	377
Leonidas Paouris, Stephanos Theodossiades, Ramin Rahmani, Gregory Hunt <i>A hypoid gear pair tribo-dynamic model taking into account the rheological behavior of fully formulated gear lubricants</i>	389
Wiktor Parandyk, Jan Awrejcewicz <i>Numerical analysis of the pressure oscillations in the human circulatory based on nonlinear hydro-mechanical system</i>	407
Pavel Polach, Michal Hajžman, Miroslav Byrtus, Zbyněk Šika <i>Influence of the fibre spring-damper computational models in a mechanical system on the coincidence with the experimental measurement results</i>	419
Jacek Przybylski, Krzysztof Kuliński <i>The influence of piezoelectric actuation on the lateral oscillation of a beam with varying cross section</i>	431
Jarosław Rusin <i>Vibrations of a double-string complex system subjected to uniformly distributed moving forces</i>	443

Sergii Skurativskiy, Vjacheslav Danylenko <i>On the dynamics of solitary wave solutions supported by the model of mutually penetrating continua</i>	453
Alexandr Stefek, Vaclav Krivanek, Yves Bergeon, Jean Motsch <i>Simulation results of robot with differential drive moving on circular path</i>	461
Kamil Sybilski, Jerzy Małachowski <i>The influence of pretensioner characteristic of four-point fastening system on the disabled driver behavior during frontal crash</i>	471
Grażyna Sypniewska-Kamińska, Roman Starosta, Jan Awrejcewicz <i>Double pendulum colliding with a rough obstacle</i>	483
Gabriel Szymkiewicz, Olga Szymanowska, Donat Lewandowski, Jan Awrejcewicz <i>Hydraulic unit of rotation into linear motion conversion – design, model, construction and testing</i>	493
Maciej Trojnecki, Przemysław Dąbek <i>Modelling and studies of dynamics of a wheeled mobile robot during longitudinal motion on the soft ground</i>	503
Peter Varkonyi <i>Dynamics of rigid bodies with multiple frictional contacts: new faces of Painleve’s paradox</i>	519
Vsevolod Vladimirov, Sergii Skurativskiy <i>Solitary waves in one-dimensional pre-stressed lattice and its continual analog</i>	531
Damian Walczak, Łukasz Zieliński, Krzysztof Szczurowski, Stanisław Radkowski <i>Proposed methods of controlling dual fuel CI engine using CAN-BUS information</i>	543
Xiao Wang, Zhanming Qin <i>Nonlinear modal interactions in composite thin-walled beam structures with CAS lay-ups</i>	555
Jin Wei, Dengqing Cao, Yang Yang, Wenhui Huang <i>Global modal approach for nonlinear dynamical modeling of an L- shaped beam-mass structure</i>	567
Tomasz Węgrzyn, Jan Piwnik, Aleksander Borek, Wojciech Tarasiuk <i>Optimization of micro-jet dynamical systems cooling after steel welding</i>	579
Adam Wijata, Jan Awrejcewicz, Jan Matej, Michał Makowski <i>Mathematical model for two-dimensional dry friction modified by dither</i>	587

Wiktoria Wojnicz, Bartłomiej Zagrodny, Michał Ludwicki, Jan Awrejcewicz, Edmund Wittbrodt	
<i>Mathematical model of pennate muscle</i>	595
Nikolai Yaroshevich, Ivan Zabrodets, Tetiana Yaroshevich	
<i>Dynamics of vibrating machines with unbalanced drive in case of flat vibrations of bearing body</i>	609

**On the vibrations of a composite structure with
hexagonal structure of a circular inclusions
(VIB302-15)**

Igor V. Andrianov, Jan Awrejcewicz, Bernd Markert, Galina A. Starushenko

Abstract: One of the major advantages of homogenization is a possibility of the generalization of the obtained results. Namely, if a solution to the local problem is found, then without principal problems one may solve not only the analyzed problem, by also a series of related static and dynamic problems, including: linear, quasi-linear, the eigenvalue problems, etc. The mentioned approach has been applied to the eigenvalue problems regarding the perforated structures and periodically non-homogenous 2D constructions with a square mesh of inclusions. In this work we have used theory of averaging to solve the vibrations problem regarding stiffly clamped rectangular membrane with periodically located circular inclusions creating a hexagonal mesh. The relations governing eigenvalues (frequencies) and eigenfunctions have been derived. The derivation of analytical formulas governing membrane eigenforms and frequencies consists of three parts. In the first part the local problem regarding a cell (inclusion) of the composite is studied. Second part is focused on finding main terms of the averaged problem. The third part is aimed at an estimation of the first improvement term with respect to the membrane fundamental frequency.

1. Introduction

The problem of transition of waves in periodic structures consists of a wide spectrum of various questions having roots in different fields of physics and mathematics including mechanics of deformable solids, theory of electromagnetic vibrations and waves, electrotechnics, theory of vibrations, mechanics of composites, theory of crystals, etc.

The first background of the problem investigation has been introduced in 1686 by Newton [31], who studied 1D chain of oscillators while computing the second velocity. Beginning from 1727, a study of 1D chains of oscillators has been carried out by J. Bernoulli and next by his son D. Bernoulli, who in 1753 formulated the superposition principle i.e. any motion of the vibrating system can be presented as a superposition of its eigenvibrations.

Further development of 1D models of the wave transition in periodic structures is associated with the works of Cauchy, Rayleigh [34] and Kelvin [25]. In the years 1835-1836 Hamilton obtained remarkable results regarding the light transition in crystals [24]. A review of the state of the art of the development of theory of wave distributions in 1D chains of oscillators can be found in reference [16].

Among the fundamental works published in the middle of the previous century we mention monographs of Brillouin [14, 15] and Brillouin and Parodi, where not only the mathematical theory of 1 D chains is presented, but also systems with the cell of periodicity having a few degrees-of-freedom (DOFs) have been considered. In reference [16] the obtained results of investigations are generalized into 3D case and a solution to 3D wave equations is given. Chains of coupled particles have been considered by Ashcroft and Solid [8]. Born and Karman [12] have applied this concept of chains to model wave transitions in crystals from a point of view of solid mechanics. Idealization idea introduced through coupled chains of particles/masses has been also applied in other scientific disciplines like atomic and molecular dynamics in physics, in chemistry and biology as well as in mechanics for modeling rod and beam constructions with added particles, in quasi-periodic systems, etc. [see for, instance, 17, 19, 28, 29, 35].

In the series of publications [23, 30, 36, 37] the transition and localization of elastic waves in periodic composite materials have been studied.

On the other hand it is well known that the theory of averaging belongs to one of the effective mathematical tools for modeling physical processes of different kind in periodic non-homogenous structures [9, 10, 27]. One of the major advantages of the homogenization is a possibility of the generalization of the obtained results. Namely, if a solution to the local problem is found, then without principal problems one may solve not only the analyzed problem, but also a series of related static and dynamic problems, including: linear, quasi-linear, the eigenvalue problems, etc. The mentioned approach has been applied to the eigenvalue problems regarding the perforated structures and periodically non-homogenous 2D constructions with the square mesh of inclusions in references [4-7].

Application of the asymptotic homogenization [2, 3] is based on the procedure of multi-scale series and yields reliable solutions regarding long waves for the low frequencies level [1, 13,21]. The discussed approach has been applied in the linear case in references [1, 18, 20]. On the other hand, in references [11,22,33] the method of asymptotic homogenization has been applied in the case of large deformations with a successive linear distribution of the elastic wave.

In this work, based on the averaging theory and the multi-scale series, the analytical results regarding dynamic features of the membrane vibrations having periodically located circular inclusions in the form of a hexagonal mesh are obtained. In particular, relations yielding eigenfrequencies and the associated eigenfunctions including first improvement terms are derived.

2. Problem formulation in terms of averaging theory

We consider the eigenvalue problem of a vibrating rectangular membrane clamped along its contour treated as a composite structure with periodically located circled inclusions forming the hexagonal mesh (Figure 1).

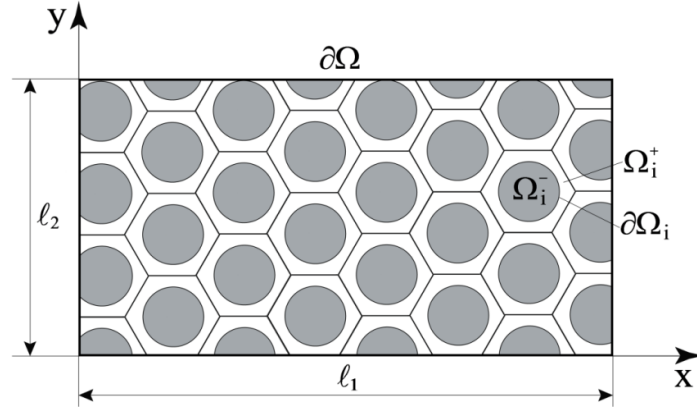


Figure 1. Composite material with hexagonal structure of inclusions

In the general case, the membrane eigenvalue problem can be formulated in the following form:

$$c^{+2} \left(\frac{\partial^2 u^+}{\partial x^2} + \frac{\partial^2 u^+}{\partial y^2} \right) = \frac{\partial^2 u^+}{\partial t^2} \quad \text{in } \Omega_i^+; \quad (1)$$

$$c^{-2} \left(\frac{\partial^2 u^-}{\partial x^2} + \frac{\partial^2 u^-}{\partial y^2} \right) = \frac{\partial^2 u^-}{\partial t^2} \quad \text{in } \Omega_i^-; \quad (2)$$

$$u^+ = u^-, \quad c^{+2} \frac{\partial u^+}{\partial n} = c^{-2} \frac{\partial u^-}{\partial n} \quad \text{on } \partial \Omega_i; \quad (3)$$

$$u^\pm = 0 \quad \text{on } \partial \Omega; \quad (4)$$

$$u^\pm = f^\pm(x, y), \quad \frac{\partial u^\pm}{\partial t} = F^\pm(x, y) \quad \text{for } t = 0, \quad (5)$$

where: u –transversal displacement of the membrane points; $c^2 = \frac{p}{\rho}$, p –stress inside the membrane, ρ –surface density; n –external normal to the inclusion contour.

Solution to the problem (1)-(5) is assumed to be as follows:

$$u^{\pm}(x, y, t) = u^{\pm}(x, y)e^{i\omega t}, \quad (6)$$

where ω –stands for a circular frequency.

Then, owing to (6) problem (1)-(3) can be transformed to the following form

$$\frac{\partial^2 u^+}{\partial x^2} + \frac{\partial^2 u^+}{\partial y^2} + \omega u^+ = 0 \text{ in } \Omega_i^+; \quad (7)$$

$$\lambda \left(\frac{\partial^2 u^-}{\partial x^2} + \frac{\partial^2 u^-}{\partial y^2} \right) + \omega u^- = 0 \text{ in } \Omega_i^-; \quad (8)$$

$$u^+ = u^-, \quad \frac{\partial u^+}{\partial n} = \lambda \frac{\partial u^-}{\partial n} \text{ on } \partial\Omega_i, \quad (9)$$

where: $\lambda = \frac{c^{-2}}{c^{+2}}; \quad \omega = \frac{\omega^2}{c^{+2}}.$

Following the theory of averaging [9, 10] and applying two-scale techniques [31] the solutions to the problem (7)-(9), (4) in the form of asymptotic series regarding a small parameter characterizing the structural period are assumed in the following form

$$u^{\pm} = u_0(x, y) + \varepsilon \left[u_{10}(x, y) + u_1^{\pm}(x, y, \xi, \eta) \right] + \varepsilon^2 \left[u_{20}(x, y) + u_2^{\pm}(x, y, \xi, \eta) \right] + \dots, \quad (10)$$

where: ξ, η stand for the fast variables, and $\xi = \frac{x}{\varepsilon}, \quad \eta = \frac{y}{\varepsilon}.$

The frequency is also presented in the form of the asymptotic series:

$$\omega = \omega_0 + \varepsilon \omega_1 + \varepsilon^2 \omega_2 + \dots \quad (11)$$

After splitting procedure regarding ε being applied to relations (7), (8), the following infinite recursive set of equations is obtained

$$\varepsilon^{-1}: \quad \begin{aligned} \frac{\partial^2 u_1^+}{\partial \xi^2} + \frac{\partial^2 u_1^+}{\partial \eta^2} &= 0; \\ \frac{\partial^2 u_1^-}{\partial \xi^2} + \frac{\partial^2 u_1^-}{\partial \eta^2} &= 0; \end{aligned} \quad (12)$$

$$\begin{aligned} \varepsilon^0 : \quad & \frac{\partial^2 u_0}{\partial x^2} + \frac{\partial^2 u_0}{\partial y^2} + 2 \frac{\partial^2 u_1^+}{\partial x \partial \xi} + 2 \frac{\partial^2 u_1^+}{\partial y \partial \eta} + \frac{\partial^2 u_2^+}{\partial \xi^2} + \frac{\partial^2 u_2^+}{\partial \eta^2} + \varpi_0 u_0 = 0; \\ & \lambda \left(\frac{\partial^2 u_0}{\partial x^2} + \frac{\partial^2 u_0}{\partial y^2} + 2 \frac{\partial^2 u_1^-}{\partial x \partial \xi} + 2 \frac{\partial^2 u_1^-}{\partial y \partial \eta} + \frac{\partial^2 u_2^-}{\partial \xi^2} + \frac{\partial^2 u_2^-}{\partial \eta^2} \right) + \varpi_0 u_0 = 0; \end{aligned} \quad (13)$$

$$\begin{aligned} \varepsilon : \quad & \frac{\partial^2 u_1^+}{\partial x^2} + \frac{\partial^2 u_1^+}{\partial y^2} + \frac{\partial^2 u_{10}}{\partial x^2} + \frac{\partial^2 u_{10}}{\partial y^2} + 2 \frac{\partial^2 u_2^+}{\partial x \partial \xi} + 2 \frac{\partial^2 u_2^+}{\partial y \partial \eta} + \frac{\partial^2 u_3^+}{\partial \xi^2} + \frac{\partial^2 u_3^+}{\partial \eta^2} + \\ & + \varpi_1 u_0 + \varpi_0 (u_1^+ + u_{10}) = 0; \\ & \lambda \left(\frac{\partial^2 u_1^-}{\partial x^2} + \frac{\partial^2 u_1^-}{\partial y^2} + \frac{\partial^2 u_{10}}{\partial x^2} + \frac{\partial^2 u_{10}}{\partial y^2} + 2 \frac{\partial^2 u_2^-}{\partial x \partial \xi} + 2 \frac{\partial^2 u_2^-}{\partial y \partial \eta} + \frac{\partial^2 u_3^-}{\partial \xi^2} + \frac{\partial^2 u_3^-}{\partial \eta^2} \right) + \\ & + \varpi_1 u_0 + \varpi_0 (u_1^- + u_{10}) = 0; \end{aligned} \quad (14)$$

The compatibility relations (9) takes the form:

$$\varepsilon^1 : \quad u_1^+ = u_1^-; \quad (15)$$

$$\varepsilon^2 : \quad u_2^+ = u_2^-; \quad (16)$$

$$\varepsilon^0 : \quad \frac{\partial u_1^+}{\partial \bar{n}} + \frac{\partial u_0}{\partial n} = \lambda \left(\frac{\partial u_1^-}{\partial \bar{n}} + \frac{\partial u_0}{\partial n} \right); \quad (17)$$

$$\varepsilon^1 : \quad \frac{\partial u_2^+}{\partial \bar{n}} + \frac{\partial u_1^+}{\partial n} + \frac{\partial u_{10}}{\partial n} = \lambda \left(\frac{\partial u_2^-}{\partial \bar{n}} + \frac{\partial u_1^-}{\partial n} + \frac{\partial u_{10}}{\partial n} \right), \quad (18)$$

where $\frac{\partial}{\partial \bar{n}}, \frac{\partial}{\partial n}$ are derivatives along the external normal to an inclusion contour regarding fast and slow variables, respectively:

$$\frac{\partial}{\partial \bar{n}} = \frac{\partial}{\partial \xi} \cos \alpha + \frac{\partial}{\partial \eta} \cos \beta, \quad (19)$$

$$\frac{\partial}{\partial n} = \frac{\partial}{\partial x} \cos \alpha + \frac{\partial}{\partial y} \cos \beta. \quad (20)$$

Therefore, the problem of finding a solution to the complex space governed by equations (7)–(9), (4) is split to a series of problems in the spaces of essentially simpler geometry in comparison to the input problem.

3. Derivation of analytical formulas governing membrane eigenforms and frequencies

Owing to the general procedure of the homogenization method a solution to the problem (7)–(9), (4) can be divided into three parts:

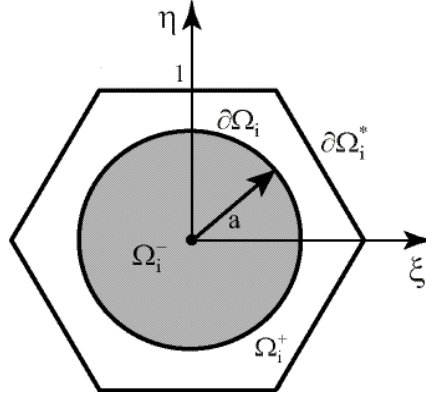


Figure 2. Characteristic structure of the composite cell: Ω_i^+ –matrix area; Ω_i^- –inclusion area.

(i) In the first part a solution to the local problem is defined [9, 10], i.e. we study a periodically repeated cell of the composite (see Figure 2):

$$\frac{\partial^2 u_1^+}{\partial \xi^2} + \frac{\partial^2 u_1^+}{\partial \eta^2} = 0 \text{ in } \Omega_i^+, \quad (21)$$

$$u_1^+ = u_1^-, \quad \frac{\partial u_1^+}{\partial \bar{n}} - \lambda \frac{\partial u_1^-}{\partial \bar{n}} = (\lambda - 1) \frac{\partial u_0}{\partial n} \text{ on } \partial\Omega_i, \quad (22)$$

$$u_1^+ = 0 \text{ on } \partial\Omega_i^*. \quad (23)$$

(ii) The second part is aimed at finding main parts of the eigenfunctions and frequencies of the averaged problems. The averaged equation is obtained through application of the following averaging operator

$$\tilde{\Phi}(x, y) = \frac{1}{|\Omega_i^*|} \left[\iint_{\Omega_i^+} \Phi^+(x, y, \xi, \eta) d\xi d\eta + \lambda \iint_{\Omega_i^-} \Phi^-(x, y, \xi, \eta) d\xi d\eta \right] \quad (24)$$

to relations (2.13), and the input problem takes the following form:

$$\bar{q} \left(\frac{\partial^2 u_0}{\partial x^2} + \frac{\partial^2 u_0}{\partial y^2} \right) + \frac{1}{|\Omega_i^*|} \left[\iint_{\Omega_i^+} \left(\frac{\partial^2 u_1^+}{\partial x \partial \xi} + \frac{\partial^2 u_1^+}{\partial y \partial \eta} \right) d\xi d\eta + \lambda \iint_{\Omega_i^-} \left(\frac{\partial^2 u_1^-}{\partial x \partial \xi} + \frac{\partial^2 u_1^-}{\partial y \partial \eta} \right) d\xi d\eta \right] + \varpi_0 u_0 = 0 \quad (25)$$

where $\Omega_i^* = \Omega_i^+ \cup \Omega_i^-$; $\bar{q} = \frac{|\Omega_i^+| + \lambda |\Omega_i^-|}{|\Omega_i^*|}$ –averaged parameter in the sense of Foight.

Taking into account the relations for u_1^+ , u_1^- which define the problem on the cell (21)–(23), the averaged problem can be transformed to the following one:

$$q_x \frac{\partial^2 u_0}{\partial x^2} + q_y \frac{\partial^2 u_0}{\partial y^2} + \bar{q} \varpi_0 u_0 = 0 \text{ in } \Omega^*, \quad (26)$$

$$u_0 = 0 \text{ on } \partial\Omega, \quad (27)$$

where: $\Omega^* : \begin{cases} 0 \leq x \leq \ell_1 \\ 0 \leq y \leq \ell_2 \end{cases}$ –smooth membrane space with the reduced characteristics; q_x , q_y –

averaged parameters of the following form:

$$q_x = \bar{q} + \frac{1}{|\Omega_i^*|} \left(\iint_{\Omega_i^+} \frac{\partial u_{1(1)}^+}{\partial \xi} d\xi d\eta + \lambda \iint_{\Omega_i^-} \frac{\partial u_{1(1)}^-}{\partial \xi} d\xi d\eta \right); \quad (28)$$

$$q_y = \bar{q} + \frac{1}{|\Omega_i^*|} \left(\iint_{\Omega_i^+} \frac{\partial u_{1(2)}^+}{\partial \eta} d\xi d\eta + \lambda \iint_{\Omega_i^-} \frac{\partial u_{1(2)}^-}{\partial \eta} d\xi d\eta \right), \quad (29)$$

where: $u_{1(i)}^\pm$ ($i=1, 2$) –are the solutions to the local problems (21)–(23), estimated with accuracy up to constant multipliers corresponding to the slow solution component:

$$u_1^\pm = u_{1(i)}^\pm(\xi, \eta) \frac{\partial u_0}{\partial x} + u_{1(2)}^\pm(\xi, \eta) \frac{\partial u_0}{\partial y}.$$

Solution to the eigenvalue problem (26), (27) in the smooth space of the rectangular membrane with reduced physical characteristics can be formulated in the following form

$$u_0 = \sum_{m=1}^{\infty} \sum_{n=1}^{\infty} S_{mn} \sin \frac{m\pi x}{\ell_1} \sin \frac{n\pi y}{\ell_2}, \quad (30)$$

$$\varpi_0 = \frac{\pi^2}{\bar{q}} \left(q_x \left(\frac{m}{\ell_1} \right)^2 + q_y \left(\frac{n}{\ell_2} \right)^2 \right), \quad (31)$$

where constants S_{mn} ($m, n = 1, 2, \dots$) are defined by the initial conditions (5).

(iii) The third part of our approach is focused on estimation of the first improvement term regarding the frequency ϖ_1 . This requires finding one more approximation to the function u^\pm , i.e. we need to find functions u_2^\pm as a solution to the following compatibility problem:

$$\frac{\partial^2 u_2^+}{\partial \xi^2} + \frac{\partial^2 u_2^+}{\partial \eta^2} = - \left(\frac{\partial^2 u_0}{\partial x^2} + \frac{\partial^2 u_0}{\partial y^2} + 2 \frac{\partial^2 u_1^+}{\partial x \partial \xi} + 2 \frac{\partial^2 u_1^+}{\partial y \partial \eta} \right) - \varpi_0 u_0 \text{ in } \Omega_i^+; \quad (32)$$

$$\lambda \left(\frac{\partial^2 u_2^-}{\partial \xi^2} + \frac{\partial^2 u_2^-}{\partial \eta^2} \right) = - \lambda \left(\frac{\partial^2 u_0}{\partial x^2} + \frac{\partial^2 u_0}{\partial y^2} + 2 \frac{\partial^2 u_1^-}{\partial x \partial \xi} + 2 \frac{\partial^2 u_1^-}{\partial y \partial \eta} \right) - \varpi_0 u_0 \text{ in } \Omega_i^-; \quad (33)$$

$$u_2^+ = u_2^-, \quad \frac{\partial u_2^+}{\partial \bar{n}} - \lambda \frac{\partial u_2^-}{\partial \bar{n}} = (\lambda - 1) \frac{\partial u_{10}}{\partial n} + \lambda \frac{\partial u_1^-}{\partial n} - \frac{\partial u_1^+}{\partial n} \text{ on } \partial \Omega_i; \quad (34)$$

$$u_2^+ = 0 \text{ on } \partial \Omega_i^*. \quad (35)$$

Observe that the structure of the problems regarding the first and second approximations of the cell is identical, and they differ only in the amount an even component, which does not play the principal role, i.e. it does not introduce an essential input to the averaging, and hence it can be omitted while estimating the frequency ϖ_1 [6,7].

Consequently, relations for the functions u_2^\pm , yielded by solving the problems (32)–(35), can be presented in the following general way:

$$u_2^\pm = u_1^\pm (u_0 \rightarrow u_{10}) + U_2^\pm (\xi, \eta),$$

where $U_2^\pm (-\xi, -\eta) = U_2^\pm (\xi, \eta)$.

Owing to the latter remark, the averaged problem of the second approximation is governed by the averaged equation obtained by application of the averaging operator (24) to relations (34):

$$q_x \frac{\partial^2 u_{10}}{\partial x^2} + q_y \frac{\partial^2 u_{10}}{\partial y^2} + \bar{q} (\varpi_0 u_{10} + \varpi_1 u_0) = 0 \text{ in } \Omega^*, \quad (36)$$

with the following boundary condition

$$u_{10} = -\tilde{u}_1 \text{ on } \partial\Omega, \quad (37)$$

where \tilde{u}_1 is the averaged part of the function $u_1^\pm(x, y, \xi, \eta)$.

It should be emphasized that the relation (36) includes two unknown functions: u_{10} – slow solution of the ε^1 order and the first improvement term to the frequency ϖ_1 . In order to find the frequency ϖ_1 we need to transform (36) applying the known scheme (see [26]). Namely, we multiply (30) by u_0 and next we integrate this equation by parts regarding the space Ω^* , which taking into account (26) and boundary condition (27) yields the following relation:

$$\varpi_1 \bar{q} \int_0^{\ell_1} \int_0^{\ell_2} u_0^2 dx dy - q_x \int_0^{\ell_2} \left. \frac{\partial u_0}{\partial x} u_{10} \right|_{x=0}^{x=\ell_1} dy - q_y \int_0^{\ell_1} \left. \frac{\partial u_0}{\partial y} u_{10} \right|_{y=0}^{y=\ell_2} dx = 0. \quad (38)$$

Therefore, if

$$u_{10} = -\tilde{u}_1 = 0 \text{ on } \partial\Omega,$$

then $\varpi_1 = 0$, and the series responsible for eigenfrequency begins with ϖ_2 , i.e. the term of order ε^2 .

In the case when u_{10} does not satisfy the boundary conditions on the external membrane contour, i.e. $u_{10} \neq 0$ on $\partial\Omega$, we get non-zero first improvement term regarding the eigenfrequency, which taking into account (38) has the following form:

$$\varpi_1 = \frac{q_x \int_0^{\ell_2} \phi(y) dy + q_y \int_0^{\ell_1} \phi(x) dx}{\bar{q} \int_0^{\ell_1} \int_0^{\ell_2} u_0^2 dx dy}, \quad (39)$$

where

$$\phi(y) = \frac{\partial u_0}{\partial x} u_{10} \Big|_{x=0}^{x=\ell_1}; \quad \varphi(x) = \frac{\partial u_0}{\partial y} u_{10} \Big|_{y=0}^{y=\ell_2}. \quad (40)$$

Subsequent term of the series (10), (11) can be found by analogous scheme and its estimation does not require principal difficulties.

4. Conclusions

The theory of averaging has been applied in order to solve the problem of vibrations of the rectangular membrane stiffly clamped along its contour, representing the composite structure with periodically located circular inclusions within the hexagonal mesh.

In the general case, the fundamental analytical relations of smooth components of the eigenfunctions and the eigenfrequencies (30), (31) as well as of their first fast oscillating terms (21)-(23), (39), (40) have been derived.

Practical realization of the proposed approach depends strongly on finding a solution of the problem regarding the cell, i.e. in a correct estimation of the averaged characteristics of the non-homogenous structure.

Depending on the values of the physical and geometric characteristics of the composite a solution to the local problem can be obtained either by an asymptotic series or by combined analytical-numerical approaches.

Acknowledgments

This work has been supported by the Polish National Science Centre, MAESTRO 2, No. 2012/04/A/ST8/00738.

References

- [1] Andrianov, I.V., Bolshakov, V.I., Danishevs'kyy, V.V. Weichert, D. Higher-order asymptotic homogenization and wave propagation in periodic composite materials. *Proceedings of the Royal Society of London* 464 (2008), 1181–1201.
- [2] Andrianov, I.V., Danishevs'kyy, V.V., Ryzhkov, O. I., Weichert, D. Dynamic homogenization and wave propagation in a nonlinear 1D composite material *Wave Motion* 50 (2013), 271–281.
- [3] Andrianov, I.V., Danishevs'kyy, V.V., Topol, H., Weichert, D. Homogenization of a 1D nonlinear dynamical problem for periodic composites *ZAMM-Journal of Applied Mathematics and Mechanics* 91 (2011), 523–534.
- [4] Andrianov, I.V., Starushenko, G.A. Asymptotic methods in the theory of perforated membranes of nonhomogeneous structure. *Engineering Transactions*. 43 (1995), 5–18.
- [5] Andrianov, I.V., Starushenko, G.A. Homogenization method for mechanical problems in multi-connected domain. *Problems of Mechanical Engineering* (1987) 48–54. (in Russian).

- [6] Andrianov, I.V., Starushenko, G.A. Solution of Dynamic Problem for Perforated Structures by the Method of Averaging. *Journal of Soviet Mathematics* 57 (1991), 3410–3412.
- [7] Andrianov, I.V., Starushenko, G.A. Using of homogenization method for investigation of perforated plates oscillations. *Journal of Soviet Mathematics* 65 (1995), 1503–1507.
- [8] Ashcroft, N.W., Mermin, D.N. *Solid state physics*. Thomson Learning, Toronto, 1976.
- [9] Bakhvalow, N.C., Panasenko G.P. *Averaging processes in periodic media*. Nauka, Moscow 1984. (in Russian)
- [10] Bensoussan A., Lions, J.L., Papanicolaou, G., *Asymptotic analysis for periodic structures*. North-Holland Publishing Company, Amsterdam, 1978.
- [11] Bertoldi, K., Boyce, M.C. Wave propagation and instabilities in monolithic and periodically structured elastomeric materials undergoing large deformations. *Physical Review B* 78 (2008), 184107
- [12] Born, M., von Kármán, T. On fluctuations in spatial grids. *Physikalische Zeitschrift* 13 (1912), 297-309
- [13] Boutin, C., Auriault, J.L. Rayleigh scattering in elastic composite materials. *European Journal of Mechanics B/Fluid* 31, 12 (1993), 1669-1689
- [14] Brillouin L., Über die fortpflanzung des liches in dispergieren den medien. *Annalen der Physik* 343, 10 (1914), 203-240.
- [15] Brillouin, L. *Wave propagation in periodic structures*. Dover Publications Inc, New York, 1953
- [16] Brillouin, L., Parodi, M., *Wave propagation in periodic structures*. Dunod Editeur, Paris, 1956 (In Russian)
- [17] Cao, W., Qi, W. Plane wave propagation in finite 2-2 composites. *Journal of Applied Physics* 78 (1995), 4627–4632.
- [18] Chen, W., Fish, J. A dispersive model for wave propagation in periodic heterogeneous media based on homogenization with multiple spatial and temporal scales. *Journal of Applied Mechanics* 68 (2001), 153–161.
- [19] Fang, X., Tang, J., Jordan, E., Murphy, K.D. Crack induced vibration localization in simplified bladed-disk structures. *Journal of Sound and Vibration* 291 (2006), 395–418.
- [20] Fish, J., Chen, W. Higher-order homogenization of initial / boundary-value problem. *Journal of Engineering Mechanics* 127 (2001), 1223–1230.
- [21] Fish, J., Chen, W. Space-time multiscale model for wave propagation in heterogeneous media. *Computer Methods in Applied Mechanics and Engineering* 193 (2004), 4837–4856.
- [22] Gei, M., Movchan, A.B., Bigoni, D. Band-gap shift and defect-induced annihilation in prestressed elastic structures. *Journal of Applied Physics* 105 (2009), 063507.
- [23] Golub, M.V., Zhang, C., Wang, Y.S. SH-wave propagation and scattering in periodically layered composites with a damaged layer. *Journal of Sound and Vibration* 331 (2012), 1829–1843.
- [24] Hamilton, W. R. *The Mathematical Papers of Sir William Rowan Hamilton. Vol. 2. Dynamics*. University Press, Cambridge, 1940.
- [25] Kelvin, W. T. *Popular Lectures and Addresses, Vol. 1*. Macmillan and Co., London, 1889
- [26] Collatz, L. *Eigenvalue problems*. Nauka, Moscow, 1968 (in Russian).

- [27] Lions, J.L. On some homogenisation problem, *ZAMM-Journal of Applied Mathematics and Mechanics* 62 (1982), 251-262.
- [28] Massimiliano, G. Wave propagation in quasiperiodic structures: stop / pass band distribution and prestress effects. *International Journal of Solids and Structures* 47 (2010), 3067–3075.
- [29] Mishuris, G.S., Movchan, A.B., Slepyan, L.I. Localised knife waves in a structured interface. *Journal of the Mechanics and Physics of Solids* 57 (2009), 1958-1979.
- [30] Movchan, A.B., Movchan, N.V., Haq, S. Localised vibration modes and stop bands for continuous and discrete periodic structures. *Materials Science and Engineering* 431 (2006), 175– 183.
- [31] Knife, A. *Methods disturbances*, Nauka, Moscow, 1976 (in Russian).
- [32] Newton I., *The mathematical principles of natural philosophy*. Dawsons of Pall Mall, London, 1968;
- [33] Parnell, W. J. Effective wave propagation in a pre-stressed nonlinear elastic composite bar. *IMA Journal of Applied Mathematics* 72 (2007), 223–244.
- [34] Rayleigh, L. On the maintenance of vibrations by forces of double frequency, and on the propagation of waves through a medium endowed with a periodic structure. *Philosophical Magazine* 24 (1887), 145–159.
- [35] Slepyan, L.I., Tsareva, O.V. Energy flux for zero group velocity of the current wave. *Soviet Physics-Doklady* 32 (1987) 522-526
- [36] Smyshlyaev, V.P. Propagation and localization of elastic waves in highly anisotropic periodic composites via two-scale homogenization. *Mechanics of Materials* 41 (2009), 434–447.
- [37] Yan, Z.Z., Zhang, C., Wang, Y.S. Analysis of wave propagation and localization in periodic/disordered layered composite structures by a mass-spring model. *Applied Physics Letters* 94 (2009), 161909.

Igor V. Andrianov, Professor: Institute of General Mechanics, RWTH Aachen University, Templergraben 64, D-52056, Aachen, Germany (igor.andrianov@gmail.com)

Jan Awrejcewicz, Professor: Technical University of Łódź, Department of Automation, Biomechanics and Mechatronics 1/15 Stefanowski St., PL-90-924, Łódź, Poland and Department of Vehicles, Warsaw University of Technology 84 Narbutta Street, 02-524 Warszawa, Poland (awrejcew@p.lodz.pl)

Bernd Markert, Professor: Institute of General Mechanics, RWTH Aachen University, Templergraben 64, Aachen 52062, Germany (markert@iam.rwth-aachen.de)

Galina A. Starushenko, Professor: Dnipropetrovs'k Regional Institute of State Management, of National Academy of State Management at the President of Ukraine, Gogolya 29, UA-49631, Dnipropetrovs'k, Ukraine (gs_gala-star@mail.ru)

Identification of a non-linear damping coefficient characteristics in the free decay test of a single pendulum with friction (VIB001-15)

Jan Awrejcewicz, Paweł Olejnik

Abstract: A pendulum in form of an equal arms angle body being a part of a two degrees-of-freedom mechanical system with friction is identified with respect to the observed influence of some resistance of its rotational motion in ball bearings. It is damped in a much more complex manner, what could be considered as a non-linear damping. There is supposed between others, that the effective non-linear damping characteristics depends on a few effects such as fluid friction caused by vibrations of the pendulum with two springs in the air, as well as unknown kinds of a frictional resistance existing in ball bearings. The model under investigation finds its real realization on a laboratory rig designed for experimental investigations of viscous and structural frictional effects. A transient response oscillations of the pendulum are described by the explicitly state-dependent free decay. A free decay test of the pendulum with the state-dependent non-linear parameters of damping and stiffness has been performed in this paper. It provided interesting observations that led to elaboration of a method of the overall damping coefficient identification. Effects of application of the proposed semi-empirical method of identification of the overall damping and stiffness coefficients have been illustrated and discussed.

1. Introduction

In the theory of waves the linear models are commonly applied to predict the performance of various engineering objects. In offshore engineering and naval architecture it is common practice to determine damping coefficients, both linear and non-linear, from free decay tests [10]. For example, in ocean engineering it is common practice to obtain damping coefficients of floating structures from free decay tests [1]. Authors of the paper present some work on the determination of non-linear damping coefficients for flap-type oscillating wave surge converters from free decay tests. Simulations of free decay tests in computational fluid dynamics are presented as well as their validation against experimental results is performed. Analysis of the obtained data reveals that linear quadratic-damping, as commonly used in time domain models, is not able to accurately model the occurring damping over the whole regime of rotation amplitudes. The authors concluded that a hyperbolic function is most suitable to express the instantaneous damping ratio over the rotation amplitude.

In the design process, it is essential to use accurate numerical simulation tools to predict the complex aero-hydro-servo-elastic response of a floating wind turbine [11]. Cited paper

focuses on the use of the open-water test data of the SWAY prototype wind turbine to calibrate a floating offshore wind turbine numerical model for future validation efforts. After turbine deployment and installation of the NREL instrumentation, five free decay tests were conducted on the SWAY prototype by displacing the system and allowing it to return to equilibrium. The inability to model frictional damping in the universal joints of the system contributes to discrepancies between measured and simulated results. The inability to model frictional damping in the universal joints in the tension rod became significant in affecting the overall motion of the system.

Presented examples and many problems in other measurements of damping [6–9] confirm the need of continuation of investigations on techniques related to identification of parameters of oscillating bodies, especially, when some difficult properties like viscous damping are necessary to determine [12–14].

Our paper is focused on identification of a non-linear damping coefficient characteristics during free vibrations of a single pendulum with friction [3].

The angle body – a single pendulum, a part of the 2-DoF mechanical system with friction shown in Fig. 1a is damped in a much more complex manner, what could be considered as a non-linear damping of some characteristics that is by assumption dependent on angular displacement and velocity of the pendulum rotating about the pivot point s (see Fig. 1).

One assumes in the research an existence of an effective non-linear damping characteristics, which could be dependent on system states affected by a few possible phenomena:

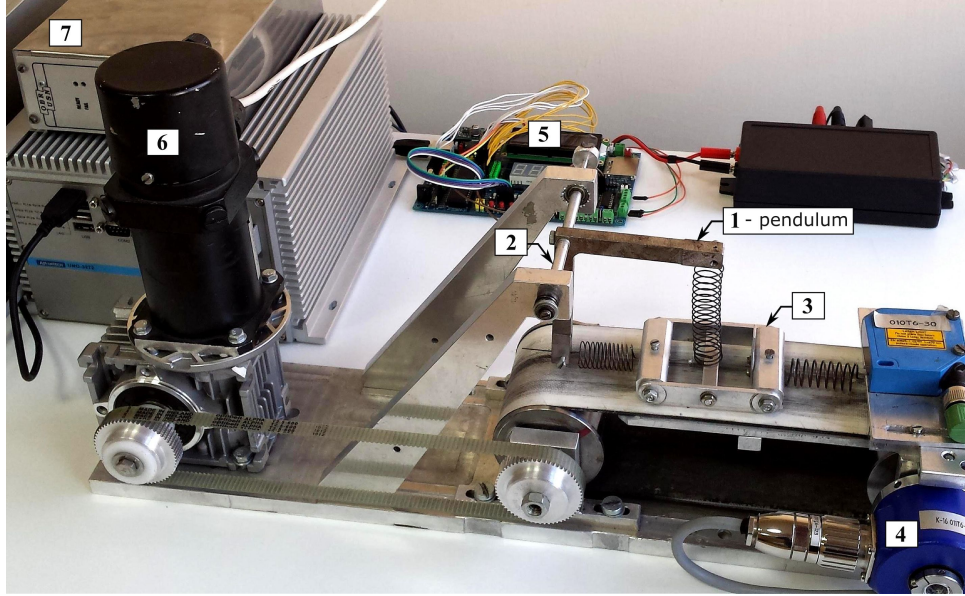
- fluid friction caused by vibrations of the pendulum 1 with two springs in the air (see Fig. 1a);
- unknown kinds of resistance existing in ball bearings, in which both ends of an aluminium shaft 2 are mounted to allow rotation of the pendulum about the joint s .

It is likely a hypothesis, but there will be proved in a free decay test an existence of a non-linear explicitly state-dependent characteristics of damping and stiffness of the pendulum.

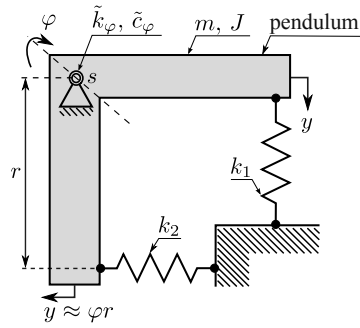
To get knowledge about the true characteristics of both parameters, the block 3 (see in Fig. 1a) has been stopped and a transient response (see Fig. 2) of pendulum 1 in the free decay test was analysed using some parameter identification method presented below.

Originally, self-excited vibrations of the block 3 sliding on the moving belt cause some irregularly forced response of the pendulum [15]. The pendulum 1 is coupled with the block by means of two springs, and therefore, it changes the normal and tangent contact forces in the frictional connection created by the stick-slip contact of the block sliding on the moving belt. A precise mathematical description of dynamical behaviour of the the single

pendulum 1 is very important in the context of identification of the static as well as kinematic characteristics of a frictional contact in the block-on-belt model [16].



a) experimental stand



b) a physical model of single pendulum

Figure 1. Picture of the experimental stand (a) for measurement of friction characteristics with the particular physical model (b): 1 – the pendulum under investigation, 2 – an aluminium shaft rotating in ball bearings fixed in the frame, 3 – the block sliding on the belt (temporarily stopped in the experiment), 4 – incremental encoder, 5 – a microcontroller for data acquisition, 6 – a direct current motor with gear, 7 – a direct current motor driver.

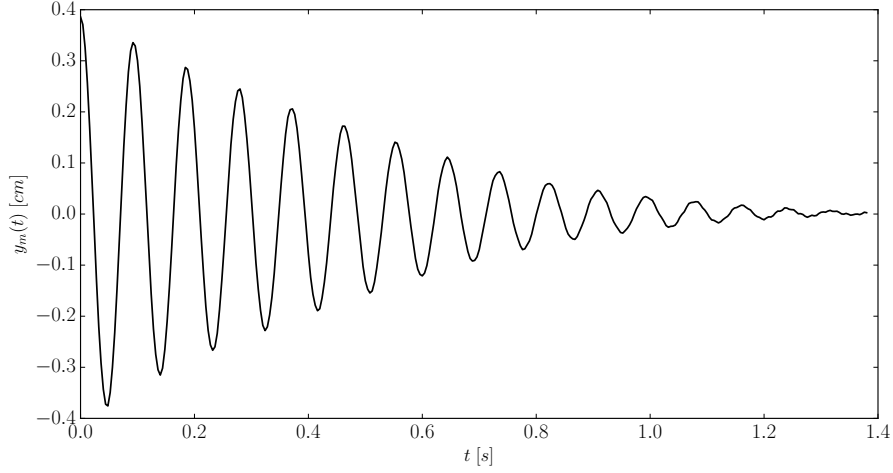


Figure 2. Time history of a transient response of the pendulum in the free decay test. The time series $y_m(t)$ has been acquired from measurements on the laboratory rig (see Fig. 1).

2. A semi-empirical method of estimation of the non-linear characteristics of overall damping and stiffness

It would be interesting to check if the damping and stiffness coefficients of the investigated free decay oscillations are constant.

At small enough angles of rotation, the starting equation in our research follows

$$m\ddot{y} + c\dot{y} + ky = 0, \quad \text{for } y \approx \varphi r \text{ and } \varphi < \pi/36, \quad (1)$$

where: y [m] is the linear displacement of the pendulum, φ [rad] – angle of rotation, a virtual mass $m = J/r^2$ [kg], mass moment of inertia $J = 2.4423 \cdot 10^{-4}$ [kg·m²], arm length $r = 0.078$ [m], unknown overall damping $c \rightarrow \tilde{c}_\varphi(t)$ [N·s/m], unknown overall stiffness $k \rightarrow \tilde{k}_\varphi(t) + k_1 + k_2 = \tilde{k}_\varphi(t) + 145.82$ [N/m], where: k_1, k_2 – constant stiffness coefficients estimated from static characteristics of both elastic elements (linear springs), $\tilde{k}_\varphi(t)$ – unknown implicitly state-dependent function of stiffness of the rotational connection (see the joint s in Fig. 1b), which is created by the ball bearings and the pendulum mounted in the bearings, $\tilde{c}_\varphi(t)$ – unknown implicitly state-dependent function of overall coefficient of damping in both symmetrically situated rotational joints.

Equation (1) can be represented in a classic form of a non-forced traditionally damped harmonic oscillator

$$\ddot{y} + \frac{\omega}{Q}\dot{y} + \omega^2 y = 0, \quad (2)$$

where the damping component at \dot{y} is written in canonical form by means of a quality factor Q – a dimensionless parameter of strength of viscous friction in motion of the pendulum [1].

Our oscillator has small mass and is fairly small damped, so factor Q is defined by $2\pi E/|\Delta E|$, where E is the energy of oscillation, ΔE is the energy loss per cycle of the oscillation because of dissipation [17]. The dissipation is expressed either in terms of the dimensionless quality factor or by a damping ratio δ , which has the dimension of frequency.

Then, by a definition [17]

$$2\delta\dot{y} = \frac{\omega}{Q}\dot{y}. \quad (3)$$

Applying in Eq. (3) the definition of period $T = 2\pi/\omega$ between time instances of every two adjacent turning point amplitudes A_i and A_{i+1} , one finds, that constant logarithmic decrement of damping, called the damping ratio δ is given by

$$\delta = \frac{1}{T} \ln \frac{A_i}{A_{i+1}} = \frac{\pi}{Q}.$$

If we check the successive period durations of the free decay oscillations shown in Fig. 2, then all points are irregularly distributed as shown in Fig. 5. Therefore, some usage of any constant damping ratio of the real free response of our single pendulum is not well justified. In consequence, constant damping ratio δ is to be substituted by $\tilde{\delta}(t)$, which will exhibit a non-linear characteristics dependent on time going in the free decay test.

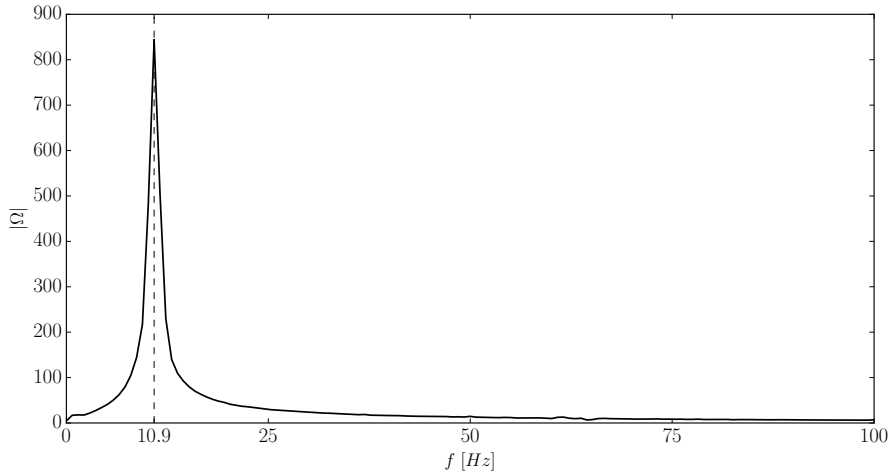


Figure 3. A discrete FFT of a time series $y_m(t)$ of the pendulum's linear displacement acquired from the measurement of angle φ on the experimental stand. One dominant frequency is found as marked by the dashed line.

Analysing in Fig. 3 the frequency spectrum of vibrations from the experimental time series $y_m(t)$ of our single pendulum, one observes, that the body vibrates with the dominant frequency $f_F \approx 10.9$ [Hz] corresponding to $\omega_F \approx 68.45$ [rad/s].

Let us now select two adjacent turning point amplitudes separated by one period T of motion, i.e.: $A_1 = 0.421$, $A_2 = 0.371$ [cm].

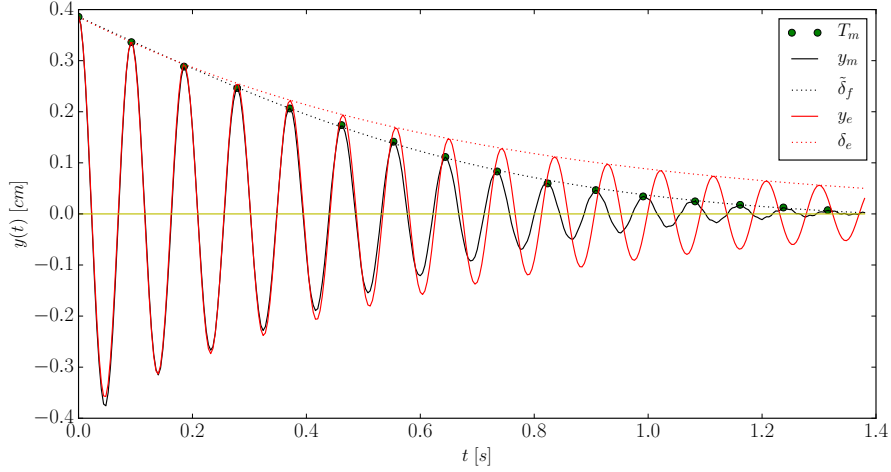


Figure 4. A comparison of two time histories confirming discrepancy between the experimental trajectory $y_m(t)$ and correspondingly the analytical solution $y_e(t)$.

Then, let us calculate the angular frequency ω with respect to the period T related to the time elapsed between two successive measurements of peak amplitudes A_1 and A_2 . We get constant angular frequency, period of oscillations and a damping ratio as below:

$$\omega = \frac{2\pi}{T} = 67.630 \text{ [rad/s]}, \quad T = t_{A_2} - t_{A_1} = 0.093 \text{ [s]}, \quad \delta = \frac{1}{T} \ln \frac{A_1}{A_2} = 1.481 \text{ [1/s]}.$$

Comparable values of both angular frequencies, i.e. $\omega \approx \omega_F$ are confirmed, so after that simple calculus the exact transient response $y_e(t)$ [cm] of the oscillator with exponential decay

$$\delta_e(t) = A_1 \exp(-\delta t), \tag{4}$$

and constant angular frequency ω takes the analytical form

$$y_e(t) = \delta_e(t) \cos(\omega t) = A_1 \exp(-\delta t) \cos(\omega t) = 0.421 \exp(-1.481t) \cos(67.63t). \tag{5}$$

The solution $y_e(t)$ given in Eq. (5) is drawn in Fig. 4 using a red line.

We see in Fig. 4, that the obtained estimate solution $y_e(t)$ bounded by the line of the exponential decay $\delta_e(t)$ passing through turning point amplitudes of the solution, does not coincide with the experimental trajectory $y_m(t)$ (black line) representing the measurement.

Drawing a conclusion, the estimated parameters of the investigated transient response given by Eq. (5) are not valid at each successive constant period T . Therefore, the highest inaccuracy in the coverage of both compared time trajectories is visible at the end of the pendulum's free decay oscillations, i.e. at final time $t_k = 1.4$ [s], when $y_e(t)$ should much closely tend to zero.

The procedure of searching for the new approximating function $\tilde{\delta}_f(t)$ – a state-dependent polynomial decay, which replaces the standard exponential decay with a constant damping ratio, as well as for an approximation of $\tilde{\omega}(t)$, resulting from $\tilde{T}(t)$ is proposed below. Tilde over the symbols make them distinguishable from constants ω , T and function $\delta_e(t)$.

2.1. Estimation of a polynomial decay $\tilde{\delta}_f$ of oscillations

The polynomial decay is an important function in context of the initiated dynamical analysis and the frictional phenomena observed on a stick-slip contact surface of the block-on-belt model investigated on the experimental stand. Moreover, it has significant influence on evaluation of damping properties of the pendulum vibrating at significant velocity variations as observed during experiments [2, 4, 5, 18].

The quality factor introduced in Eq. (2) is expressed by [17]

$$Q(t) = \frac{\pi}{\tilde{T}(t) \left(a_1 \tilde{\delta}_f(t) + a_2 + \frac{a_3}{\tilde{\delta}_f(t)} \right)}. \quad (6)$$

We obtain the first sought approximation in a form of the polynomial decay (see black dotted line in Fig. 4 and 8)

$$\tilde{\delta}_f(t) = \frac{a_2(p(t) - 1) + r(p(t) + 1)}{2a_1(1 - p(t))}, \quad (7)$$

where: $\tilde{\delta}_f(t)$ is the polynomial decay of oscillations, $p(t) = \frac{2a_1A_1+a_2-r}{2a_1A_1+a_2+r} \exp(-rt)$, $r = \sqrt{a_2^2 - 4a_1a_3}$, and $a_1 = -3.45$, $a_2 = 2.52$, $a_3 = 0.05$ are numerically estimated.

2.2. Estimation of variable angular frequency $\tilde{\omega}$

Now, we search for an estimation of the second system parameter that is directly connected with the unknown variable stiffness coefficient, i.e. $\tilde{\omega}$ – the implicitly state-dependent angular frequency of motion.

As it is shown in Fig. 5, the polynomial function $\tilde{T}(t)$ of period instances can be obtained from a continuous approximation of measurement points $T_m(i) = t_{A(i)} - t_{A(i+1)}$

for $i = 0 \dots 16$ with the use of the following polynomial of third degree

$$\tilde{T}(t) = \gamma_3 t^3 + \gamma_2 t^2 + \gamma_1 t + \gamma_0 \quad \text{for } \bar{\gamma}_{(3\dots 0)} = [-2, 28, -147, 9385] \times 10^{-5}. \quad (8)$$

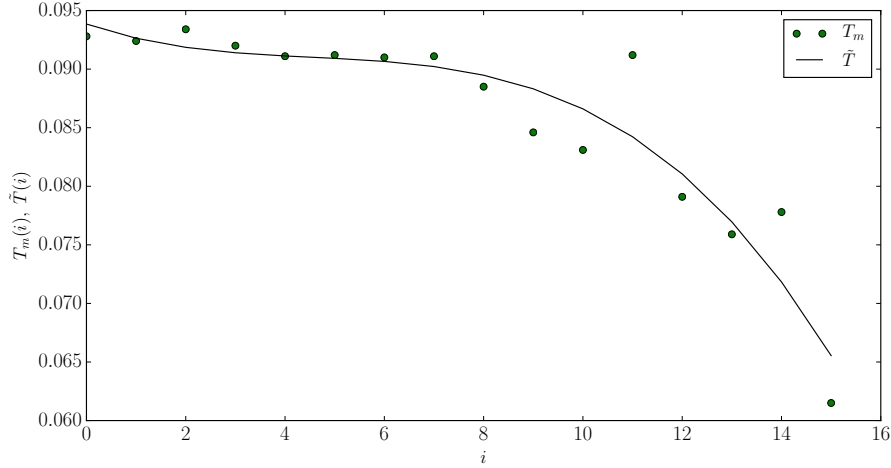


Figure 5. Non-smooth distribution of periods $T_m(i)$ (green circles) calculated between time $t_{A(i)}$ and $t_{A(i+1)}$ of appearance of the successive peak amplitudes $A(i)$ and $A(i+1)$ of oscillations in the experimentally acquired series $y_m(t)$ versus i -th cycle number. Third degree polynomial approximation $\tilde{T}(t)$ of the distribution is matched by solid line.

We have observed that fitting of the trajectory $y_m(t)$ at its final stage for $t \in [1.2, 1.4]$ [s] regarded to small-amplitude vibrations of the pendulum could be more precise. Therefore, the free response's approximation was checked for a replacement of the polynomial approximation $\tilde{\omega}(t)$ by a logarithmic one $\tilde{\omega}_l(t)$ (see Fig. 6), that reads

$$\tilde{\omega}_l(t) = b_1 \tilde{\omega}(t) + b_2 \log \tilde{\omega}(t) + b_3 \quad \text{for } \bar{b}_{(1\dots 3)} = [2.57, 0.13, 93] \times 10^{-3}. \quad (9)$$

Figure 6 illustrates a time-dependent function $\tilde{\omega}(t)$ that results from the polynomial approximation $\tilde{T}(t)$ given by Eq. (8) with its logarithmic fit $\tilde{\omega}_l(t)$ for the purpose of improvement of the stage of small-amplitude vibrations of the pendulum. After checking the resulting effectiveness of approximations $\tilde{\omega}(t)$ and $\tilde{\omega}_l(t)$, the first one has been selected.

If $\tilde{\delta}_f(t)$ given by Eq. (7) states for the desired approximation of turning point amplitudes of free decay oscillations of the analysed pendulum, then using the obtained polynomial approximation (8) an implicitly state-dependent angular frequency reads

$$\tilde{\omega}(t) = \frac{2\pi}{\tilde{T}(t)} \quad \text{for } t \in [0, t_k]. \quad (10)$$

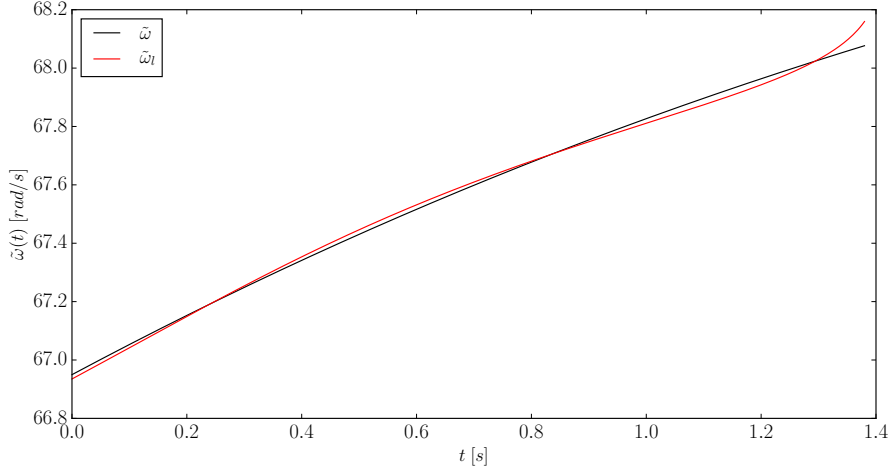


Figure 6. A polynomial approximation of the angular frequency $\tilde{\omega}(t)$ (black line) and its logarithmic fit $\tilde{\omega}_l(t)$ (red line).

2.3. Estimation of implicitly state-dependent parameters of the pendulum

This section takes into account the obtained estimates (6) and (10) to provide definitions of parameters for the investigated dynamical system.

Comparison of terms at state variables y and \dot{y} in Eq. (1) divided by m and in Eq. (2) yields:

$$\frac{\tilde{c}_\varphi(t)}{m} = \frac{\tilde{\omega}(t)}{Q(t)} \quad \text{and} \quad \frac{\tilde{k}(t)}{m} = \tilde{\omega}^2(t),$$

and after rearrangement:

$$\tilde{c}_\varphi(t) = \frac{m\tilde{\omega}(t)}{Q(t)} \quad \text{and} \quad \tilde{k}(t) = m\tilde{\omega}^2(t). \quad (11)$$

The non-linear functions of system parameters, i.e. the variable damping coefficient $\tilde{c}_\varphi(t)$ and variable stiffness coefficient $\tilde{k}(t)$ have been drawn in Fig. 7. These parameters are denoted as functions of time, but it is only valid for the time going in the free decay test. Therefore, the parameters will be implicitly state-dependent when one will need to apply them in the simulation of dynamics of full mechanical system shown in Fig. 1 composed of the block-on-belt subsystem and the identified pendulum forced by motion of the block.

It is worth reminding that by obtaining the stiffness coefficient $\tilde{k}(t)$ in Eq. (11) we have identified the overall stiffness of the pendulum (see Sec. 2) that includes constant components k_1 and k_2 of springs. Unknown at the beginning the state-dependent stiffness $\tilde{k}_\varphi(t)$ of the rotational connection of the pendulum at point s (see Fig. 1b) is found $\tilde{k}_\varphi(t) = \tilde{k}(t) - k_1 - k_2$.

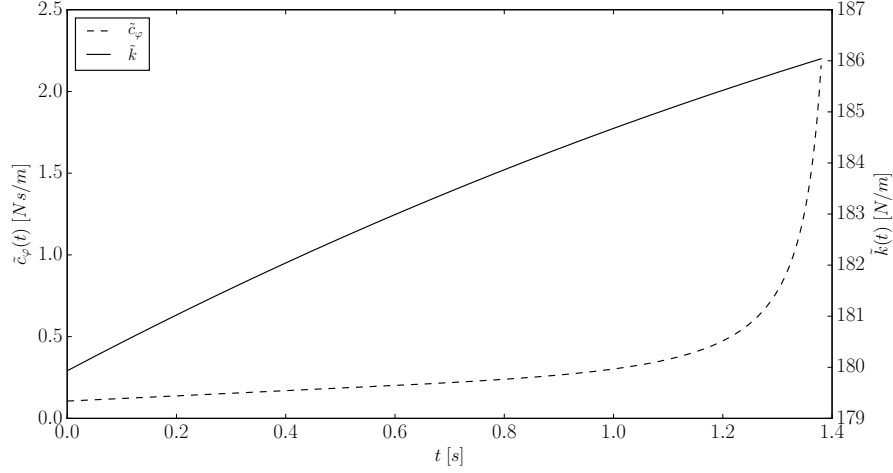


Figure 7. Non-linear functions of system parameters: a) the variable damping coefficient $\tilde{c}_\varphi(t)$ (dashed line), b) the variable stiffness coefficient $\tilde{k}(t)$ (solid line).

3. Numerical verification of the non-linear approximations of parameters of the pendulum

First case. Verification of accurateness of the analytical formula (see blue line in Fig. 8)

$$y_f(t) = \tilde{\delta}_f(t) \cos(w_1 \tilde{\omega}(t)t), \quad (12)$$

where: $\tilde{\delta}_f(t)$ is defined by expression (7), $\tilde{\omega}(t)$ is defined by (10), and $w_1 = 1.02$ is a non-dimensional fitting parameter of angular frequency.

Second case. The identified non-linear approximations (7) and (10), respectively for $\tilde{\delta}_f(t)$ and $\tilde{\omega}(t)$, are put into a numerical model of the analysed single pendulum to check accurateness of the numerical solution $y_s(t)$ in comparison to measurement $y_m(t)$.

A state-space representation of the single pendulum dynamics described by one second order differential equation (2) is as follows:

$$\begin{aligned} \dot{y}_1(t) &= y_2(t), \\ \dot{y}_2(t) &= -\frac{\tilde{\omega}(t)}{Q(t)} y_2(t) - w_2^2 \tilde{\omega}^2(t) y_1(t). \end{aligned} \quad (13)$$

Solving numerically system (13) we obtain a numerical solution $y_s(t) = y_1(t)$ – a linear displacement of the pendulum matched in Fig. 8 by red line. Also here, a non-dimensional fitting parameter of angular frequency $w_2 = 1.029$ is applied in the numerical model to obtain the computed time history $y_s(t)$ better fit to the experimental counterpart $y_m(t)$.

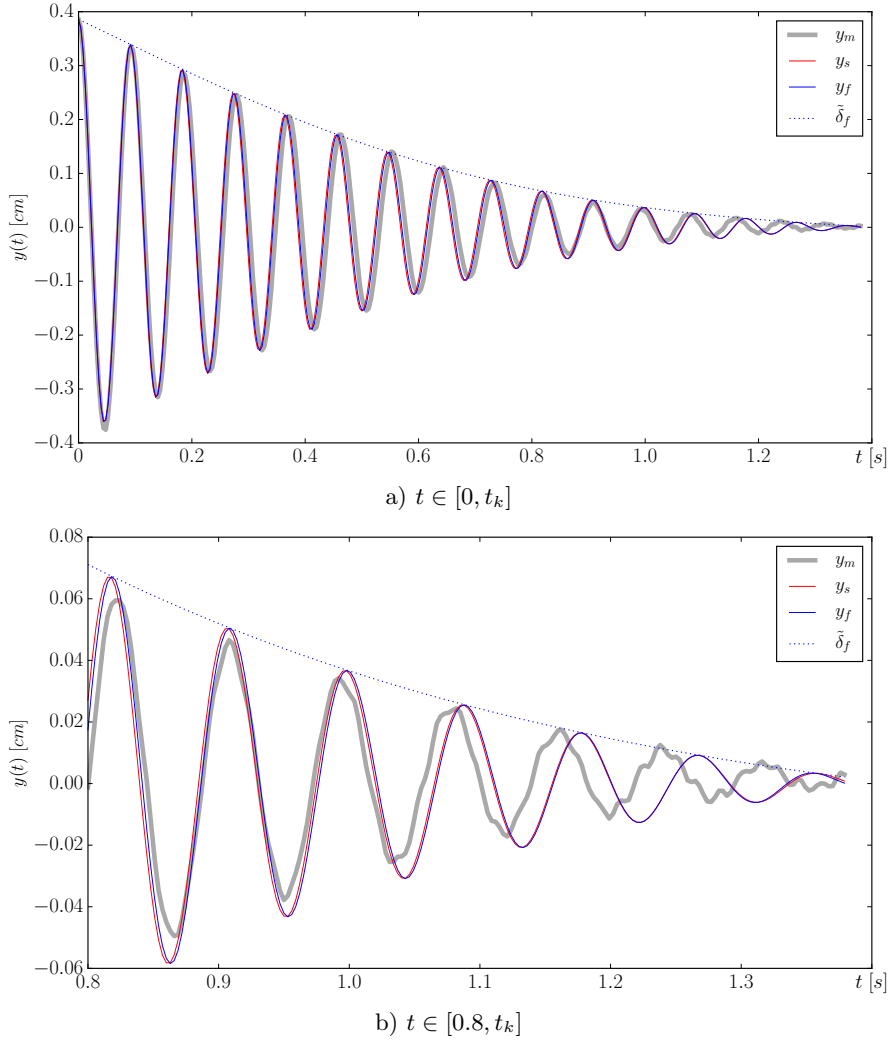


Figure 8. Time histories of a transient response of the pendulum in the free decay test: $y_m(t)$ – measurement (thick grey line), $y_s(t)$ – numerical solution (red line), $y_f(t)$ – analytical solution (blue line) that takes into account the identified parameters of the pendulum.

Third case. Average displacement of the pendulum in i -th period of oscillations of the time trajectories $y(t)$ visible in Fig. 8 can be taken into account in the qualitative assessment of the obtained approximations.

The average displacements $\bar{y}(i)$ in i -th cycle period have been computed numerically for the three time series $y_m(t)$, $y_s(t)$ and $y_f(t)$ by means of the formula (bar over the symbol

denotes the average value)

$$\bar{y}(i) = \frac{1}{\tilde{T}(i)} \int_0^{\tilde{T}(i)} y(t) dt \quad \text{for } i = 1 \dots 16 \text{ and } y = \{y_m, y_s, y_f\}. \quad (14)$$

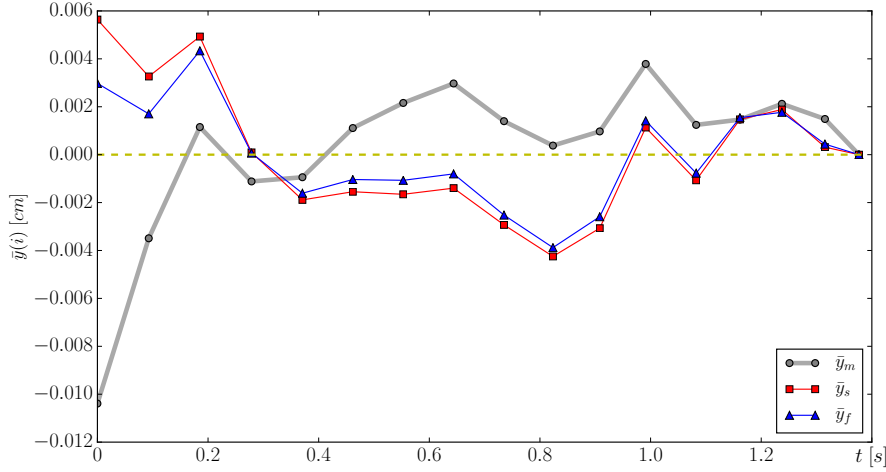


Figure 9. Average displacements of the pendulum in i -th cycle period of oscillations for the measurement $y_m(t)$ in relation to the approximates $y_s(t)$ and $y_f(t)$.

If we take a look at series $\bar{y}_s(i)$ and $\bar{y}_f(i)$ drawn in Fig. 9, then interchangeably, an average of $\bar{y}_s(i)$ is closer to $\bar{y}_m(i)$, but sometimes an average of $\bar{y}_f(i)$. As it is seen, our measurement series $y_m(t)$ is irregular in the duration of each time period of its oscillations. One would find the best result of our identification if $\bar{y}_s(i)$ or $\bar{y}_f(i)$ could as much as possible coincide with $\bar{y}_m(i)$. Hereby, a qualitative method of assessment of the presented identification a single pendulum's parameters has been proposed.

4. Conclusions

The high degree of coverage of trajectories $y_m(t)$ and $y_f(t)$ presented in Fig. 8 proves, that the two system parameters such as damping c and stiffness k introduced at the beginning in Eq. 1 have to be made dependent on the pendulum's state variables. For that requirement, the two implicitly state-dependent parameters $\tilde{c}_\varphi(t)$ and $\tilde{k}(t)$ are proposed.

The non-linear function of $\tilde{c}_\varphi(t)$ drawn in Fig. 7 has an important property. Up to about 1 second of the free decay response, damping of the pendulum depends almost linearly on time. In rough approximation it can be assumed as constant. In Fig. 4, the moment of time points to the turning point amplitude of about 0.05 [cm]. One can use the linear piece

of function $\tilde{c}_\varphi(t)$ while the oscillator's angular velocity is high enough. When the vibration body exhibits an irregular dynamics by reaching low velocity regimes of motion, then the whole non-linear characteristics visible in Fig. 7 has to be used.

The identified parameters of irregularly damped single pendulum's motion have significant influence on dynamics of the entire dynamical system, which also includes the block-on-belt model. For the practical use of the identified functions of both system parameters, it is necessary to use a transition from the phase space of the free decay to the phase space of full system dynamics including self-excited vibrations of the block on the moving belt. It will regard to much deeper analysis supported by a dedicated numerical methods and will be presented by the authors in further extension of the work.

Acknowledgements

The work has been supported by the Polish National Science Centre, MAESTRO 2, No. 2012/04/A/ST8/00738.

References

- [1] ASMUTH, H., SMITT, P., ELSAESSER, B., AND HENRY, A. *Determination of non-linear damping coefficients of bottom-hinged oscillating wave surge converters using numerical free decay tests*. Proceedings of the 1st International Conference on Renewable Energies Offshore, Lisbon, Portugal, 24-26 November 2014. Taylor & Francis Group, London, 2015, pp. 507–513.
- [2] AWREJCEWICZ, J., AND OLEJNIK, P. Numerical and experimental investigations of simple non-linear system modelling a girling duo-servo brake mechanism. In *Proceedings of Design Engineering Technical Conferences and Computers and Information in Engineering Conference of ASME* (Chicago (Illinois) USA, September 2-6 2003), no. DETC2003/VIB-48479, ASME, pp. 1–7.
- [3] AWREJCEWICZ, J., AND OLEJNIK, P. Stick-slip dynamics of a two-degree-of-freedom system. *Int. J. Bifurcation Chaos* 13, 4 (2003), 843–861.
- [4] AWREJCEWICZ, J., AND OLEJNIK, P. Sliding solutions of a simple two degrees-of-freedom dynamical system with friction. In *Proceedings of 5th EUROMECH Nonlinear Dynamics Conference* (Eindhoven, The Netherlands, August 7-12 2005), pp. 277–282.
- [5] AWREJCEWICZ, J., AND OLEJNIK, P. Occurrence of stick-slip phenomenon. *J. Theoret. Appl. Mech.* 45, 1 (2007), 33–40.
- [6] BUTTERWORTH, J., LEE, J., AND DAVIDSON, B. Experimental determination of modal damping from full scale testing. In *13th World Conference on Earthquake Engineering* (Vancouver, B.C., Canada, August 1-6 2004).
- [7] CRUCIAT, R., AND GHINDEA, C. Experimental determination of damping characteristics of structures. *Mathematical Modelling in Civil Engineering* 4 (2012), 51–59.

- [8] DUDA, K., MAGALAS, M., MAJEWSKI, M., AND ZIELISKI, T. Dft-based estimation of damped oscillation parameters in low-frequency mechanical spectroscopy. *IEEE Trans. Instrum. Meas.* 60, 11 (2011), 3608–3618.
- [9] ERET, P., AND MESKELL, C. A practical approach to parameter identification for a lightly damped, weakly nonlinear system. *J. Sound Vibration* 310, 2008 (2008), 829–844.
- [10] FALTINSEN, O. *Hydrodynamics of High-Speed Marine Vehicles*. Cambridge University Press, 2010.
- [11] KOH, J., ROBERTSON, A., JONKMAN, J., DRISCOLL, F., AND NG, E. Building and calibration of a fast model of the sway prototype floating wind turbine. In *International Conference on Renewable Energy Research and Applications* (Madrid, Spain, October 20-23 2013), National Renewable Energy Laboratory, pp. 1–7.
- [12] MESKELL, C. A decrement method for quantifying nonlinear and linear damping parameters. *J. Sound Vibration* 296, 2006 (2006), 643–649.
- [13] MESKELL, C. A decrement method for quantifying nonlinear and linear damping in multidegree of freedom systems. *International Scholarly Research Network, ISRN Mechanical Engineering*, 659484 (2011), 1–7.
- [14] MOTTERSHEAD, J., AND STANWAY, R. Identification of nth-power velocity damping. *J. Sound Vibration* 105, 1986 (1986), 309–319.
- [15] OLEJNIK, P., AND AWREJCEWICZ, J. Application of hnon method in numerical estimation of the stickslip transitions existing in filippov-type discontinuous dynamical systems with dry friction. *Nonlinear Dynamics* 73, 1 (2013), 723–736.
- [16] OLEJNIK, P., AWREJCEWICZ, J., AND FECKAN, M. An approximation method for the numerical solution of planar discontinuous dynamical systems with stick-slip friction. *Applied Mathematical Sciences* 8, 145 (2014), 7213–7238.
- [17] PETERS, R. *Damping Theory*. Vibration Damping, Control, and Design. Taylor & Francis Group, London, 2007, ch. 2, pp. 1–65.
- [18] PILIPCHUK, V., OLEJNIK, P., AND AWREJCEWICZ, J. Transient friction-induced vibrations in a 2-dof model of brakes. *Journal of Sound and Vibration* 344, 2015 (2015), 297–312.

Jan Awrejcewicz, Professor: Lodz University of Technology, Department of Automation, Biomechanics and Mechatronics, 1/15 Stefanowski Str., 90-924 Lodz, Poland (jan.awrejcewicz@p.lodz.pl).

Paweł Olejnik, Ph.D. D.Sc. (Assistant Professor): Lodz University of Technology, Department of Automation, Biomechanics and Mechatronics, 1/15 Stefanowski Str., 90-924 Lodz, Poland (pawel.olejnik@p.lodz.pl). The author gave a presentation of this paper during one of the conference sessions.

**An explanation of water acting on rails wear
using finite elements method
(NON054-15)**

Henryk Bąkowski

Abstract: The article presents, in a complex way, the impact of most essential operational factors upon tribological properties such as the wear and friction coefficient being the main cause of fatigue-contact wear in the rolling-sliding contact both in the presence and absence of water. Operational curves have been elaborated to predict the character and intensity of the wear in various operational conditions. Obtained the wear debris from rolling-sliding contact provided to creation the models 3D of the real contact with defects. However, the performed laboratory research on an Amsler testing stand in the rolling- sliding contact of the roller-roller system made it possible to determine the mechanism and intensity of the wear taking into consideration railway stock, road profile and some constraints along railway tracks i.e. load, skid and speed as well as weather conditions. The paper attempts at explaining the wear mechanisms of wheel-rail in laboratory test with the Finite Elements Method (FEM). Numerical analysis allow to determine local stress values which are essential for understanding the wear mechanisms of the analyzed contact. The obtained results of operational investigations prove that cracks and spallings of the micro and macro scale appear in areas with maximum stress and deformation. On the basis of the conducted simulation tests, FEM was found to be the right tool used to identify the areas of special wear hazard. This seems crucial for the improvement of safety of rail vehicles.

1. Introduction

The wear of wheel-rail couple is an extremely complex and difficult process to analyze. Continuous change and the presence of diverse factors over the short period of time make the wear difficult to interpret. However, the performed laboratory research on an Amsler testing stand in the rolling- sliding contact of the roller-roller system made it possible to determine the mechanism and intensity of the wear taking into consideration railway stock, road profile and some constraints along railway tracks i.e. load, skid and speed as well as weather conditions. The so far carried out researches have been run in a sectional procedure, investigating the impact of skid, selected stresses or speed upon the wear of rolling-sliding contact and rolling contact fatigue which do not permit complex analysis to be performed. Moreover, the effect of railway stock type, different values of skids with most frequently found road profile or speeds depending on the introduced constraints or purpose have not been taken into consideration. The article [1] provides the description of the

research which aim at determining the values of axial and tangent forces as well as presents the results of tribological tests on the railway wheel. The values of contact stresses in the presented article are convergent with the results featured in the paper (645-882 MPa) [2]. Papers [2,3] feature the description of laboratory tests performed in dry contact at the skid values of 2.5-25% or 0.06% at the assumed value of speed of 500 rpm. The tests with the presence of lubricating medium have been described in papers [4,9] where the skid was appropriately reflected for the operational conditions (0.5-5%). However, the authors did not do any tribological research with the effect of rotational speed to be taken into account since the constant value of 400 rpm had been suggested beforehand. More extreme conditions were suggested by the authors of the paper [4,5] where the speed ranged between 160-300 km/h at the load of 16000-25000 N. Lower speed results in greater depth of plastic strains than it is observed in case of higher speed. Thorough analysis of load impact prove that fatigue cracks occur at lower load values (16000 N) whereas longer cracks have a tendency to develop at higher speed which pose a real risk since crosswise cracks propagation might appear.

1.1. The effect of water

Another fundamental operational factor which changes the mechanism and intensity of the wear is undoubtedly the presence of lubricating medium in a wheel-rail couple [6]. The research on a real object have been described where the presence of lubricating medium (oil) resulted in twofold decrease in mass decrement. Unfortunately, rainwater impact has been disregarded here.

According to official statistics the presence of water upon the rails surface in Poland lasts 130 days (April to October) which means the annual rainfall ranges between 500-700 mm i.e. 500-700 liters per m² [8]. In the overwhelming part of Europe (Table 1) annual rainfall amounts to 300-800 mm (300-800 liters per m²).

Table 1. Annual rainfall in Europe [4]

The value of precipitation, mm	Europe		
	Mountainous areas	Coast	Lowland areas
	1000-2000	3000-4000	400-600

More attention should be focused on the presence of water from melted snow upon the rolling surface of rails in winter season. Thus the number of days when water stays upon the rail surface increases which significantly effects tribological properties of wheel-rail contact (see figure 1).

Water accumulated upon the rail rolling surface penetrates cracks and pores and in consequence increasing the length of subsurface fracture [6,7]. The most dangerous case is observed when cracks propagate not on the surface but deep into the material (see figure 2).

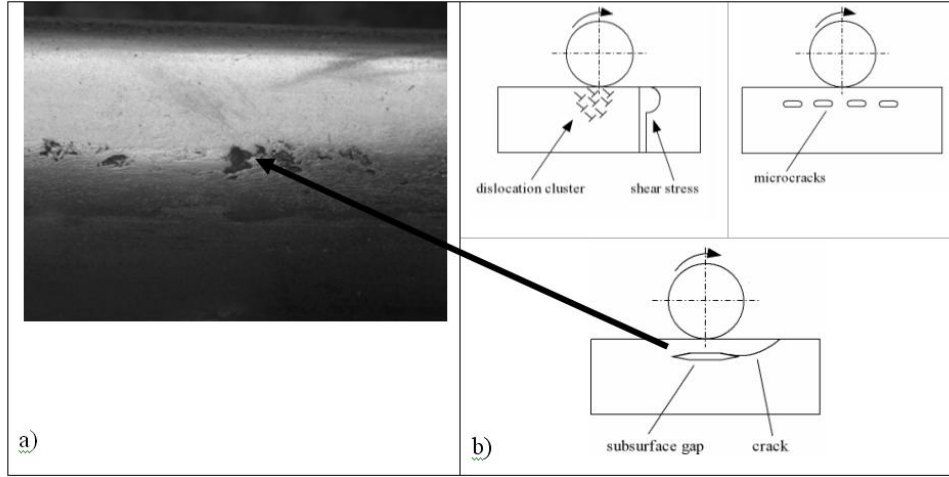


Figure 1. Delamination character of the wear: a) rolling surface of a rail, b) wear model according to Suh's flakes wear theory [10]

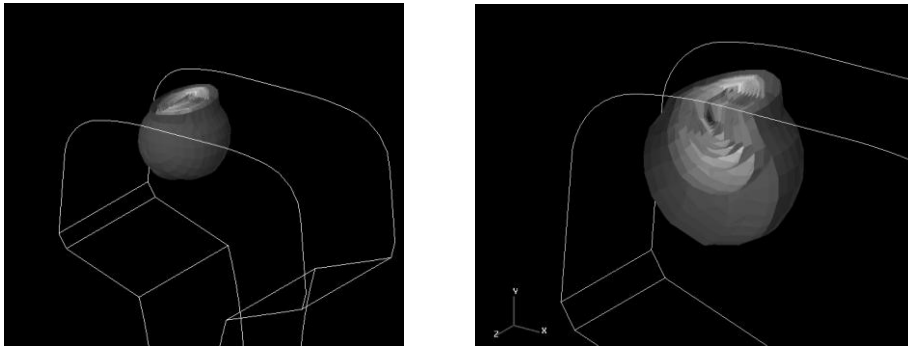


Figure 2. The 3D distribution of stresses in the rail

2. Experimental details

2.1. Test apparatus

The studies have been performed in a rolling-sliding contact in the conditions of dry friction and the presence of water. Amsler testing stand with a roller-roller friction center, where both the specimen and specimen-counter were of a roller shape, was used (see figure 3a). As the result of rotational motion the rollers, sharing the same contact area, generated the phenomena of surface fatigue or abrasive-adhesive wear of the material (depending on the values of operational factors). Friction coefficient was measured with tensometric force transducer mounted in the bottom part of the arm loaded with weights. Fig. 3b shows the scheme for friction force calculation.

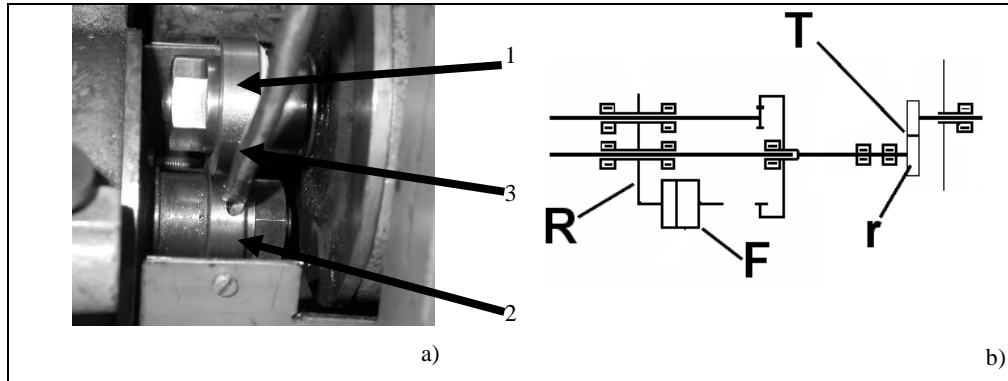


Figure 3. Friction center (a) action of forces in a rollin-sliding contact on Amsler stand, scheme mashine (b): 1- specimen, 2 - specimen-counter, 3 – water pipe

Friction force T was determined on the basis of formula (1) resulting from the condition of equilibrium of flat converging forces:

$$T \cdot r = F \cdot R \Rightarrow T = \frac{F \cdot R}{r} \quad (1)$$

where:

T – friction force, N

F – countervailing force of friction force N

r –radius of specimen-counter, m

R – arm of force F , m

Laboratory investigations performed reflected the most significant operational factors present in a real object which effect the durability of wheel-rail contact. In real conditions the minimum wheel load upon the rail occurs during the ride of an empty freight train, whereas the ride of a fully loaded freight train corresponds to the maximum wheel load i.e. 20000N/wheel and 100000N/wheel. The minimum sliding value ($\gamma = 0.3\%$) occurs at the ride of a train along the straight section of the railway track, whereas the maximum value ($\gamma = 5\%$) along a curve with a slope and/or elevation. The third parameter is speed and two values were analyzed: ca. 40 km/h and over 100 km/h. All values are the regulations and provisions in force at Polish Railway. Laboratory investigations were performed both in dry and lubricated contact on Amsler stand in roller-roller system. The measurement of mass decrement of the tested specimens was run in cycles but the values of friction coefficient were registered constantly. Laboratory tests feature one peculiarity which is the fact that monitoring the impact of one selected factor is possible here. This cannot be done in real conditions. These all data allowed to carry out a simulation using Finite Elements Method.

3. Results and discussion

To carry out simulation studies for Finite Elements Method was to perform experimental tests to determine the tribological properties (eg. coefficient of friction). This allowed the knowledge of wear mechanisms operating in the contact area by carrying out simulation studies.

3.1. Test wear

Figure 4 present the impact of operational conditions upon the wear and friction coefficient. Laboratory tests aimed at reflecting the impact of operational conditions upon the intensity and mechanism of wear in relation to diverse operational conditions.

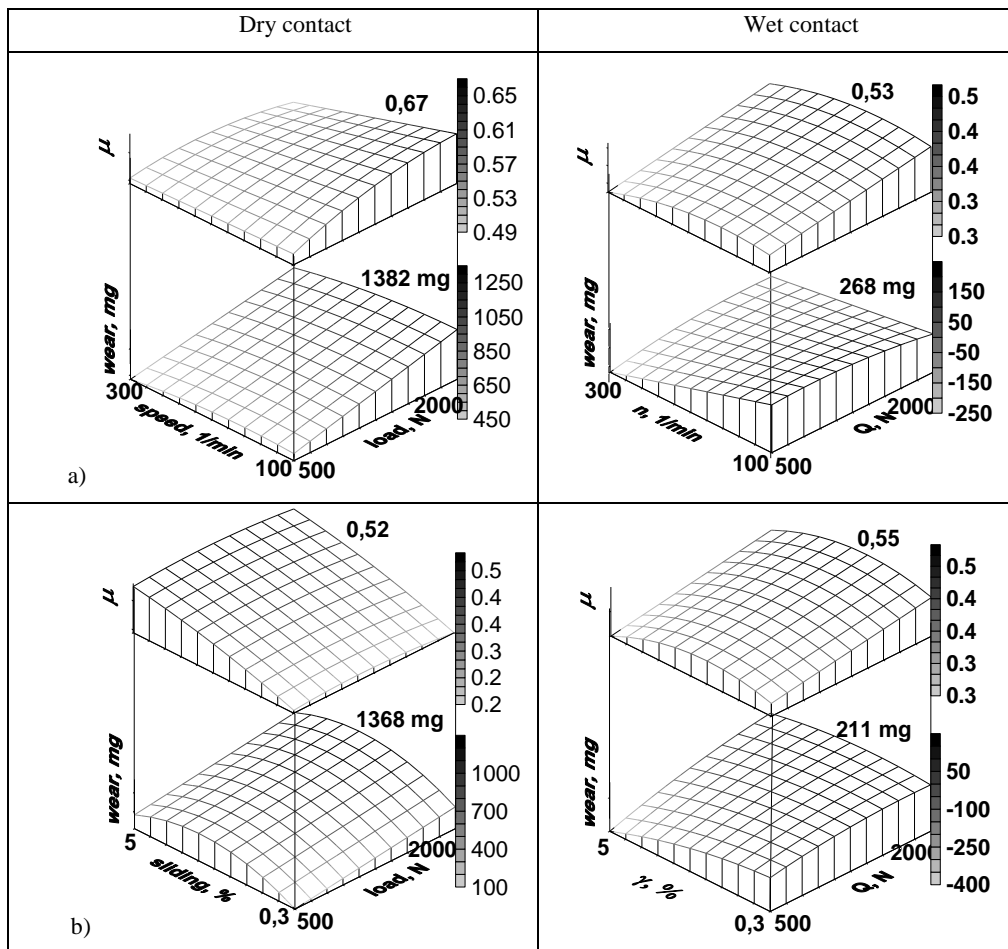


Figure 4. The relation of mass decrement and friction coefficient in a rolling-sliding contact following the tribological test versus skid and speed of the train ride : a) on the curve, b) at the speed of maximum

On the figure 4a observed high value of wear in the contact wet reflecting a train passenger or cargo unloaded at a low coefficient of friction. Under such conditions, the intensity of wear is not too large and may lead to the phenomenon of surface fatigue running surface.

The ride of a fully loaded freight and passenger train in the straight section and on the curve in the wet contact can lead to the intensification of wear. With increasing value of the wear of the train load is slightly reduced, but it increases the coefficient of friction and does not damage the appearance of RCF at the running surface. With the increase the speed reduces the wear value in dry and wet contacts, is dictated by the formation of a hydrodynamic lubrication. Effect of speed on wear mechanism is significant, because it changes the intensity wear.

The most alarming signals come in tribological research, reflects a train passenger or freight straight length at the maximum speed (see figure 4b). Wear value is close to the maximum wear. This can lead to the appearance of fatigue damage on the surface friction.

3.2. Surface layers

After the tribological tests had been performed upon the specimens, they were again subjected to microscopic studies in order to explain the essence of wear mechanism and to examine discrepancies between the dry and wet contact. Figure 5 presents the illustrative surfaces after tribological test was performed. Discrepancies in the wear process upon the friction surface were observed and show the change in wear mechanism with the same operational parameters i.e. load, skid and speed. Cracks which occur in wet contact lead to the development of ragged flakes protruding upwards. The phenomenon of wear pitting reflected in the form of wear products being torn off the friction surface does not occur in a dry contact (see figure 5a,b,c).

Friction surface in a wet contact features the roughness and numerous crevices which might also be penetrated by water leading to further propagation of cracks as the result of closing the liquid inside. Water pressure is so high that it causes crack propagation which results in large craters developing upon the surface (see figure 5d).

On the figure 6 presented wear mechanism occurring in wheel-rail contact. The wear mechanism in the presence of water occur under the influence of the propagation of fatigue cracks as a result of action space fluid. This process is closely related to the so-called, the effect of closing the fluid in the gap, resulting in a crack of the contact area comes to closing the gap present in the fluid. Closing of the liquid occurs as a result of contact between the edge of the gap influenced by the forced contact. At the time of closing the gap between the edge of the parted walls located below the edge of the fluid which has entered the gap from the outer contact surface. When closing the gap inside of it, there is a high pressure fluid which acts on the wall of the gap, causing to increase of crack.

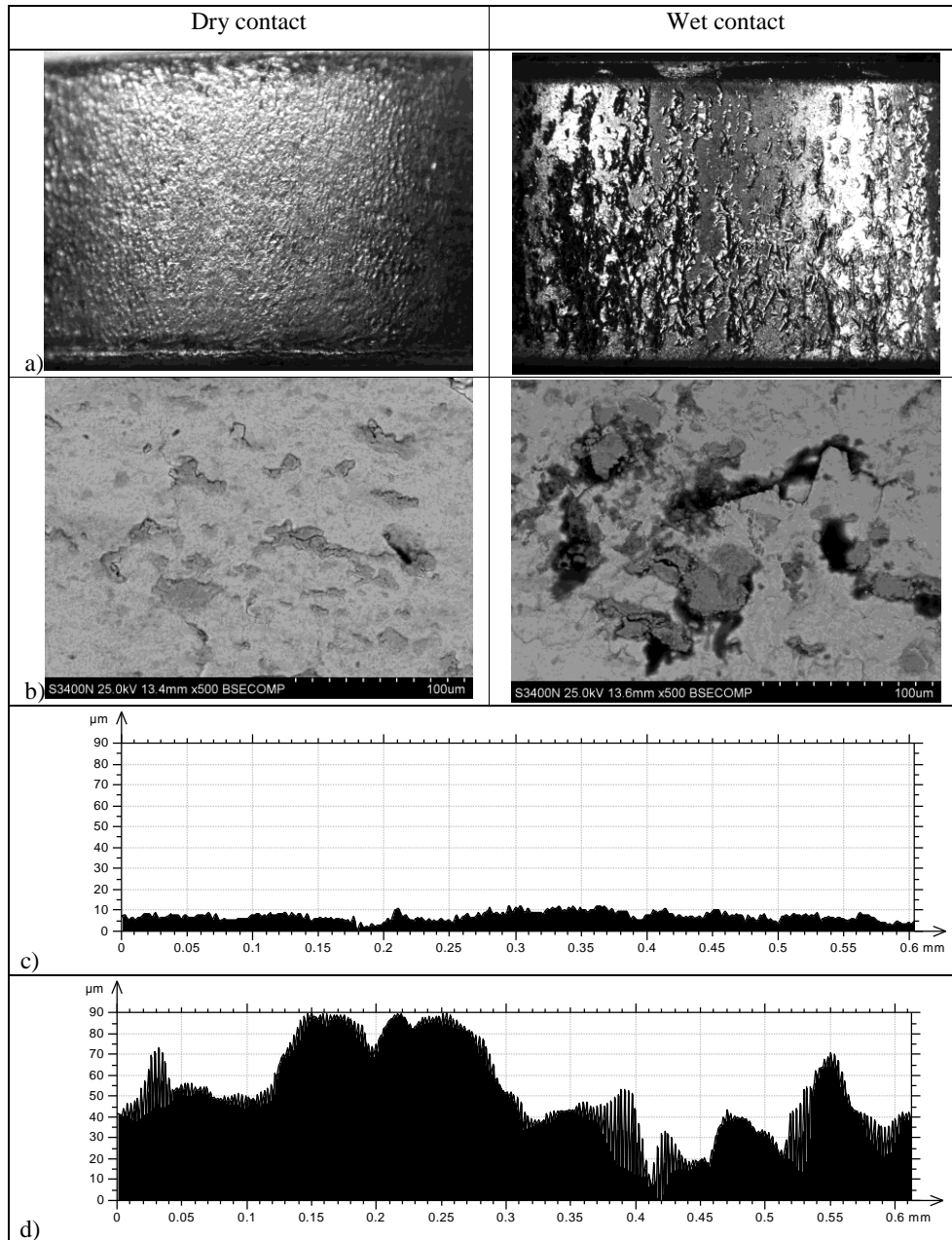


Figure 5. Friction surface of specimens made of rail steel after rubbing: a) stereomicroscope, b) SEM microscope, c) surface topography in a dry contact, d) surface topography in a wet contact

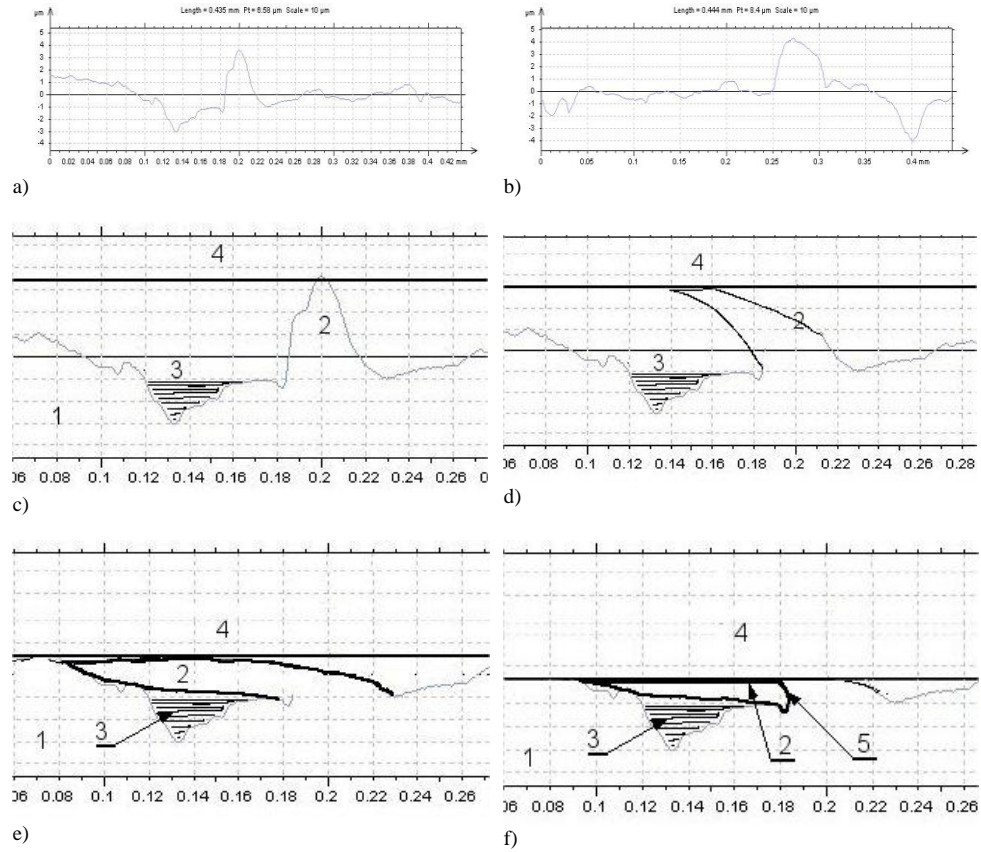


Figure 6. The wear mechanism in rolling-sliding contact in the presence of a liquid represented by the surface analysis: 1 - railway rail 2 – roughness, 3 - liquid reservoir, 4 - railway wheel

3.3. Simulation test

Simulation tests were performed by the Method of Finite Elements in rolling-sliding contact. The designed geometrical models were equipped with a crack identical to the one which occurs during operation. In order to compare the distribution and values of stresses/strains, the studies in dry and wet contact were carried out (see figure 7). The presence of water decreases the value of stresses but it also make them accumulate at the tip of a crack which might result in crosswise fracture in consequence leading to rail braking at the defined operational conditions which enhance the fatigue wear.

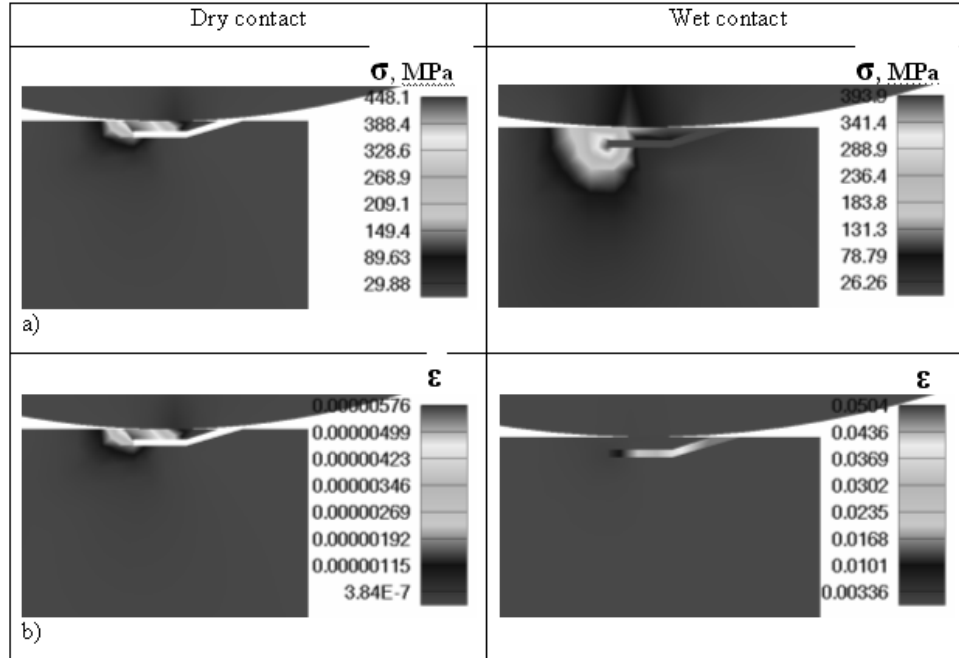


Figure 7. Distribution of reduced stresses according to von Mises (a) and strains (b)

4. Conclusions

On the basis of the performed tribological, metallographic and profilographometric tests the following was found:

- destruction of the surface layer in rolling-sliding contact takes the form of the delamination wear mechanism in the form of the flake wear debris,
- in a dry contact, directly proportional correlation between the wear and friction coefficient is found which results in the increased wear intensity or change of wear mechanism,
- in a wet contact, inversely proportional correlation between the wear and friction coefficient is found which results in RFC damages upon the rolling surface,
- in a wet contact during the train ride along a straight section, the wear mechanism changes for maximum speed and load values which might lead to contact fatigue damages (RCF rolling contact fatigue),
- for minimum speed, the wear is much more threatening (real possibility of fatigue wear) than in case of higher speed due to lubricating film which appears,
- tearing off wear debris have a shape and size appropriate to the material and operational factors influencing to the process of the formation and propagation cracks,

- size and shape wear debris are a reflection of the surface layer states. By means of an efficient system for the collection and identification of the wear debris and friction surface condition can successfully monitor the status of the technical system,
- it is advisable to monitor the execution of state of mobile device surface layer of the diagnostic criteria proposed in this work. Additional studies using the above device is a rapid, non-invasive and inexpensive solution complementary ultrasonic and magnetic allow to make the right decisions about the technical condition of the object.

References

- [1] Xuesong J., Xinbiao Xiao, Zefeng Wen, JunGuo, MinhaoZhu: *An investigation into the effect of train curving on wear and contact stresses of wheel and rail*. Tribology International, 42 (2009), pp. 475–490.
- [2] Zakharov S., Zharov I.: *Simulation of mutual wheel/rail wear*. Wear 253 (2002), pp. 100–106.
- [3] Donzella G., Faccoli M., Mazz A., Petrogalli C., Roberti R.: *Progressive damage assessment in the near-surface layer of railway wheel–rail couple under cyclic contact*. Wear 271 (2011), pp. 408–416.
- [4] Zhong W., Hu J.J., Shen P., Wang C.Y., Lius Q.Y.: *Experimental investigation between rolling contact fatigue and wear of high-speed and heavy-haul railway and selection of rail material*. Wear 271 (2011), pp. 2485– 2493.
- [5] Francisco C., Hernández R., Demasc N.G., Gonzalesa K., Andreas A. Polycarpouc: *Correlation between laboratory ball-on-disk and full-scale rail performance tests*. Wear 270 (2011), pp. 479–491.
- [6] Matsudaa H., Satohb Y., Kanematsub Y., Iwafuchib K.: *On-site investigation and analysis of flaking damage leading to rail break*. Wear 271 (2011), pp. 168–173.
- [7] Stocka R., Pippanb R.: *RCF and wear in theory and practice—The influence of rail grade on wear and RCF*. Wear 271 (2011), pp. 125–133.
- [8] Garnier B. J.: *Basics of climatology*. IMGW, Warszawa, 1996.
- [9] Gallardo-Hernandez E.A., Lewis R.: *Twin disc assessment of wheel/rail adhesion*. Wear 265 (2008), pp. 1309–1316.
- [10] Fleming J. R., Suh N. P.: *Mechanics of crack propagation in delamination wear*. Wear, 44 (1977), pp. 39-56.

Henryk Bąkowski, Ph.D.: Silesian University of Technology, Faculty of Transport, Krasińskiego Street 8, 40-019, Katowice Poland (henryk.bakowski@polsl.pl, henryk.bakowski@gmail.com). The author gave a presentation of this paper during one of the conference sessions.

A study on the effect of human running cadence based on the bouncing ball model

(LIF099-15)

László Bencsik, Ambrus Zelei

Abstract: Running is a very popular sport on professional and especially on hobby level. Professional athletes improve their body motion carefully, while hobby runners usually do not focus on the energy efficient and injury preventing running form. The running form is characterized by some fundamental parameters, like step size, stride frequency and strike pattern besides many other kinematic parameters. Much information can be found on the internet and in magazines about the correct running form, although these information are not based on scientific investigation in most of the cases. The main reason is that the running has a quite complex dynamics with many parameters leading to highly complex mechanical models. Thus it is hard to accomplish quantitative investigations that provides useful and practical conclusion. Although the running form characteristics can be investigated by pure mechanical calculations if a proper model exists. We propose a simple bouncing ball model to prove that runners should choose relatively high stride frequency. Cadence should be always kept around 180 steps/min according to the experience, while running speed should be modified by varying the stride length. We show that higher stride frequency implies lower risk of injury and energy efficiency. The model based estimations are supported by a large sample measurement data.

1. Introduction

Many works like [2, 23] contribute to the thorough understanding of bipedal locomotion, human walking and running. Several approaches have been developed which try to realize the healthy, injury preventing, energy efficient and natural way of running in practice [16–18]. Many papers study the effect of foot strike pattern and footwear experimentally [1, 7, 10, 13, 15, 19, 25].

A lot of complex high degree of freedom (DoF) mechanical models exist, which are suitable for motion capturing, dynamic and kinematic analysis of the human body and running motion carefully. However these investigations are hard to use for prediction regarding the effect of a parameter modification. A simplified dynamical model can be more predictive than a very complex model with large number of parameters. Starting from the most complex models, e.g. [21] towards the simplest ones, we can mention some low DoF segmental models [15, 26, 27] and some spring legged models [20, 24], besides many other examples.

Increasing the complexity of the model, the number of parameters can grow exponentially. The most fundamental parameters, with which the running form can be characterised, are the running speed, step size, stride frequency and strike pattern besides many other kinematic parameters. Many articles study the effect of cadence c , which is considered to be one of the most important parameters, when running form is analysed [4, 5, 9, 14, 22]. This work also focuses on *stride frequency* which is also common to call *cadence*.

At a certain speed, an infinitely many variations of stride length and stride frequency can be chosen. The experiments explained in [4] showed that the optimal cadence, when the oxygen uptake (the indicator of physical loading of the body) is minimal, and the freely chosen convenient cadence are not the same for everyone.

In this paper we show by means of a simple dynamic model that cadence has a direct effect on energy efficiency and impact intensity. The estimations are based on the bouncing ball model. The bouncing ball model itself is validated by measurements.

2. The bouncing ball model

In order to achieve the minimally complex model, the mass of the body can be shrunk into one point mass when it is in flight phase. The model is valid if external forces, like aerodynamic forces are neglected. The parabolic path of the CoM during flight phase is depicted in figure 1. The motion of the centre of gravity (CoG) in flying phase is described

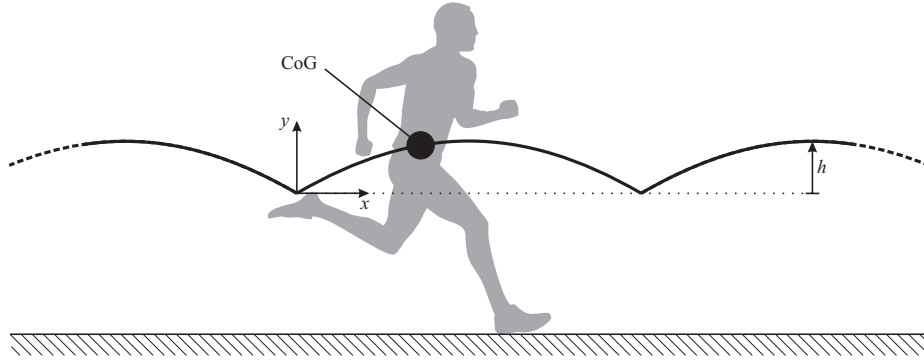


Figure 1. Idealized path of a runner's CoG.

by a parabolic curve:

$$x(t) = x_0 + \dot{x}_0 t, \tag{1}$$

$$y(t) = y_0 + \dot{y}_0 t - \frac{g}{2} t^2, \tag{2}$$

where x_0 and y_0 are the initial position coordinates and \dot{x}_0 and \dot{y}_0 are the initial velocity components represented in a Cartesian system, depicted in figure 1.

The time period T_f of the flight phase can be expressed based on time derivative of equation (2). The vertical velocity is zero, when the CoG is on the top of the parabola at $t = T_f/2$, so that we can write:

$$0 = \dot{y}_0 - g \frac{T_f}{2}. \quad (3)$$

Besides, we can apply the principle of conservation of mechanical energy in vertical direction, from which it is easy to determine the initial vertical velocity magnitude as the function of the height h of the parabolic path.

$$\dot{y}_0 = \sqrt{2gh}. \quad (4)$$

Combining equations (3) and (4) we obtain the height h of the parabola as a function of the flying phase time period:

$$h = \frac{1}{8}gT_f^2. \quad (5)$$

Equation (5) clearly shows that the height of the parabolic path is a function of the time period of each step hence it is a parameter of cadence.

The total time period T [s] of one step is in direct relation with cadence c which possesses [steps/min] unit:

$$T = \frac{60}{C}, \quad (6)$$

and the time period T_f of the flying phase and cadence has the relation:

$$T_f = \frac{60}{C}r_f, \quad (7)$$

where $r_f = T_f/T$ is the ratio of the flying phase time duration. Its typical value is in the range $r_f = 0.4...0.7$. In this work we assumed $r_f = 0.6$ airborne phase ratio. The path in the flying phase is depicted in figure 2 in case of different cadence values.

3. Measurements

In order to prove the validity of the bouncing ball model we accomplished an experiment, when the motion of 41 runners was video-captured. Every investigated person was hobby runner in the age from 15 to 50 and from both sex. The measured people were told to run a distance of 5km with a convenient speed on an open air running track. Their motion was recorded on a 3m long distance by a high resolution video camera after the first 4 km. The speed of the camera was 50 frames/s and the resolution was set to 1920×1080 pixels.

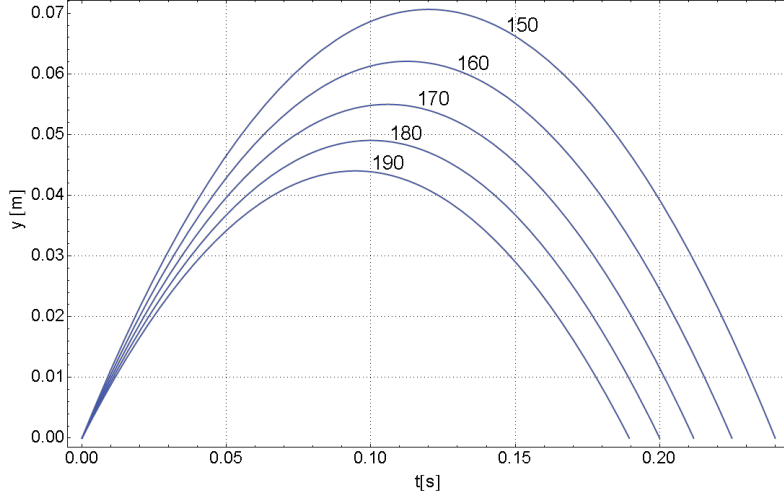


Figure 2. Parabolic path of CoG during flying phase in different cadence values (150...190).

The foot landing position and the vertical elevation A of the head was registered based on the video frames. The vertical displacement A of the head gives an acceptable estimation of the vertical displacement of the CoG of the body, however reference [8] provides a comparison of methodologies and the results of a large scale data experiment which aims to measure the vertical displacement of runners. Besides, the characteristic time durations, like stride period T , and flight phase duration T_f was determined based on the frame indices. The velocity of each person was determined based on the time duration that was needed to complete a 2.5m predefined distance. The parameters listed in table 1 were determined in case of each runner: horizontal speed v_x , stride length s , cadence c and vertical displacement A .

4. Validation of the model and discussion of the results

In order to validate the model, the measured data was plotted in figure 3 in which the theoretical height h of the parabolic path as a function of cadence c is shown by solid line. The measured values are depicted by dots, while the a curve fitted on the measurement data is plotted by a dashed curve. Qualitatively good coherence can be observed between the measured data and the theoretical curve, however the quantitative data have 20% error in average. The average of the measured displacement is larger than the theoretically predicted value. The possible reason is the further vertical displacement in reality when the leg is grounded. For the investigation of this phenomena many researches are available, e.g. [20,24].

The relation between the parabola height h and the vertical velocity component $v_y^- = \dot{y}_0$ right before the impact is given by (4). It is shown by [12] and [6] that the impact forces

Table 1. Measured data of 41 people: running speed v_x , stride length s , cadence c , vertical displacement A

no.	v_x km/h	s m	c 1/min	A mm
1	16.1	1.45	176	65
2	13.6	1.3	167	80
3	9.4	0.9	171	52
4	9.2	0.9	176	76
5	9.8	0.975	167	74
6	9.4	0.875	188	70
7	9.8	0.96	167	66
8	9.4	0.91	171	74
9	11.0	1.125	158	93
10	8.8	0.975	150	88
11	13.6	1.3	171	91
12	10.6	1.11	162	96
13	7.5	0.725	171	63
14	9.6	0.901	171	40
15	10.2	0.975	176	59
16	9.7	0.99	162	86
17	6.8	0.725	150	56
18	6.8	0.725	150	44
19	13.8	1.375	167	91
20	9.8	0.88	171	85
21	9.8	1.08	150	92

no.	v_x km/h	s m	c 1/min	A mm
22	12.3	1.27	167	76
23	8.0	0.8	171	52
24	8.8	0.97	150	76
25	8.3	0.845	162	73
26	8.2	0.945	146	104
27	10.6	0.95	182	46
28	9.4	1.05	146	85
29	9.5	1.0	158	65
30	7.3	0.725	167	38
31	10.3	0.925	182	55
32	9.8	1.075	150	107
33	7.5	0.835	150	70
34	9.6	0.995	178	64
35	11.5	1.105	171	69
36	9.7	0.99	162	85
37	8.0	0.79	171	66
38	10.6	0.995	176	44
39	11.4	1.08	176	68
40	12.9	1.23	171	87
41	7.6	0.855	150	70

correlates with the kinetic energy content which is absorbed due to the foot impact. It is called *constrained motion space kinetic energy* (CMSKE) in the literature. CMSKE is directly proportional to the impulse of the contact reaction force and also to the peak reaction force [11, 12]. The related effective mass concept for foot impact is introduced in [3] for a one DoF model. The cited studies showed that foot strike intensity can be characterised by the CMSKE which depends on the pre-impact configuration and velocity and the effective mass matrix. All in all, the lower the vertical velocity is, the smaller the impact intensity is.

Since, the vertical direction motion is constrained by the ground in the bouncing ball model, CMSKE is calculated from the vertical velocity component only:

$$E_c = \frac{1}{2}m\dot{y}_0^2. \quad (8)$$

We substitute equation (4) into (8) which provides the relation between the pre-impact velocity and the height of the parabolic path. We obtain the following *linear relation* between

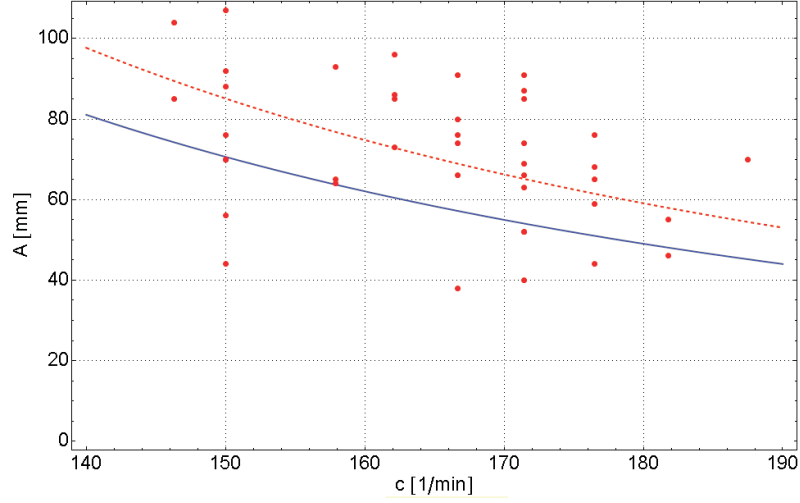


Figure 3. Height h of the parabolic path as the function of cadence is plotted by solid line. The measurement data for the vertical displacement A is depicted by dots. The dashed line shows the curve fitted to the measurement data.

CMSKE (E_c) and parabola height:

$$E_c = mgh. \quad (9)$$

Equation (9) shows that all of the potential energy of level h is absorbed by the constraint that arises when the foot touches the ground at the end of the flight phase. The main message is that the impact intensity is in linear relation with the vertical displacement of the body. The vertical displacement values A on figure 3 are directly proportional with the impact intensity, that can be characterised by the impulse I_F of the vertical component of the contact force:

$$A = \gamma I_{Fy}, \quad (10)$$

where γ is a scale factor. The the impulse of the contact force is obtained by integrating it on the time duration of the impact:

$$I_{Fy} = \int F_y. \quad (11)$$

Figure 3 shows that infinitely high stride frequency and zero stride length should be chosen theoretically in order to reach minimal energy cost and impact intensity. It is obvious, that it is not feasible in reality. The optimal stride frequency is limited by the muscular activity that depends on the stretch-shortening cycle of the muscles, which is not included

by the model. Nevertheless, the model predicts correctly, that higher cadence should be kept in order to achieve better energy efficiency and lower risk of impact induced injury.

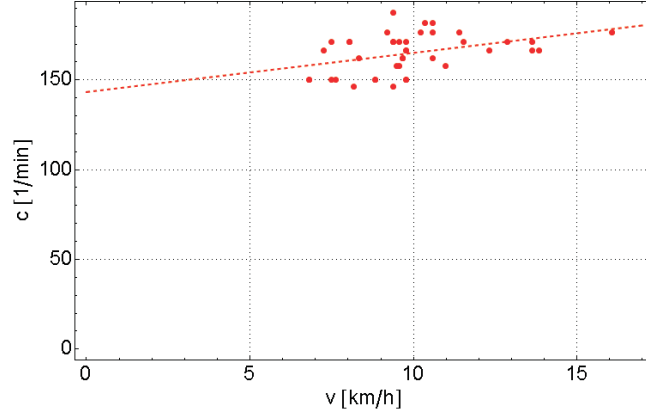


Figure 4. Running speed (v_x) versus cadence (c): measured data and the best fit line.

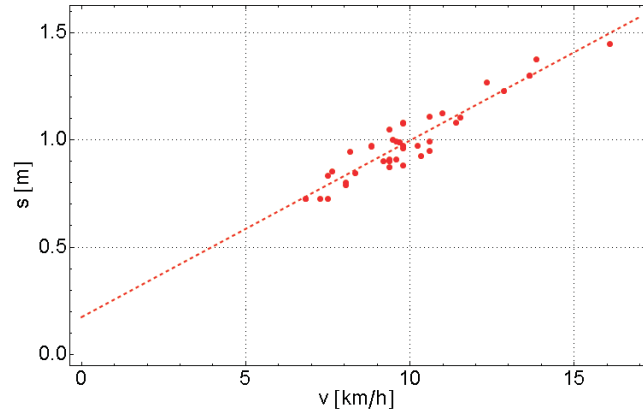


Figure 5. Running speed (v_x) stride length (s): measured data and the best fit line.

As a secondary result shown by figures 4 and 5 the measurements confirmed that people tend to chose a larger stride length and they do not change the cadence, when they are running in different speed. So in case of the examined people, the running speed is set by changing the stride length and not the cadence. The dashed line shows a line fitted on the measured values.

5. Conclusions

The bouncing ball model was proposed and large scale experimental data was collected in order to validate the model. It is experimentally confirmed that the bouncing ball model is the minimally complex dynamic model when cadence and its effect on ground impact intensity and energy efficiency of running are studied. According to the model, the vertical displacement is directly proportional to the impact intensity, characterized by the impulse of the ground-foot contact force. We showed by means of a very simple dynamical model that stride frequency has a direct effect on energy efficiency of human running and impact intensity when foot collides with the ground. The model verified that higher cadence is preferable, when energy efficiency and injury preventing running form is developed.

Acknowledgments

This research has been supported by the Hungarian Scientific Research Fund, Hungary (Project Identifier: PD 108691) and by the MTA-BME Research Group on Dynamics of Machines and Vehicles. These supports are gratefully acknowledged.

References

- [1] AHN, A., BRAYTON, C., BHATIA, T., AND MARTIN, P. Muscle activity and kinematics of forefoot and rearfoot strike runners. *Journal of Sport and Health Science* 3, 2 (2014), 102–112. doi:10.1016/j.jshs.2014.03.007.
- [2] BLAJER, W., AND SCHIEHLEN, W. Walking without impacts as a motion/force control problem. *Journal of dynamic systems, measurement, and control* 114, 4 (1992), 660–665.
- [3] CHI, K. J., AND SCHMITT, D. Mechanical energy and effective foot mass during impact loading of walking and running. *Journal of Biomechanics* 38 (2005), 1387–1395.
- [4] DUVERNEY-GUICHARD, E., AND HOECKE, J. V. The effect of stride frequency variation on oxygen uptake and muscular activity in running. *Journal of Biomechanics* 27, 6 (1994), 661–661. Abstract of the XIVth ISB congress, doi:10.1016/0021-9290(94)90963-6.
- [5] FARLEY, C. T., AND GONZÁLEZ, O. Leg stiffness and stride frequency in human running. *Journal of Biomechanics* 29, 2 (1996), 181–186. doi:10.1016/0021-9290(95)00029-1.
- [6] FONT-LLAGUNES, J. M., PAMIES-VILA, R., AND KÖVECSES, J. Configuration-dependent performance indicators for the analysis of foot impact in running gait. In *ECCOMAS, Multibody Dynamics 2013, Book of Abstracts*.
- [7] GRUBERA, A. H., BOYERA, K. A., DERRICKB, T. R., AND HAMILLA, J. Impact shock frequency components and attenuation in rearfoot and forefoot running. *Journal of Sport and Health Science* 3, 2 (2014), 113–121. doi:10.1016/j.jshs.2014.03.004.

- [8] GULLSTRAND, L., HALVORSEN, K., TINMARK, F., ERIKSSON, M., AND NILSSON, J. Measurements of vertical displacement in running, a methodological comparison. *Gait & Posture* 30, 1 (2009), 71–75. doi:10.1016/j.gaitpost.2009.03.001.
- [9] HAMILL, J., DERRICK, T. R., AND HOLT, K. G. Shock attenuation and stride frequency during running. *Human Movement Science* 14, 1 (1995), 45–60. doi:10.1016/0167-9457(95)00004-C.
- [10] JUNGERS, W. L. Barefoot running strikes back. *Nature, Biomechanics* 463, 7280 (2010), 433–434.
- [11] KÖVECSES, J., AND FONT-LLAGUNES, J. M. An eigenvalue problem for the analysis of variable topology mechanical systems. *ASME Journal of Computational and Nonlinear Dynamics* 4, 3 (2009), 9 pages. doi:10.1115/1.3124784.
- [12] KÖVECSES, J., AND KOVÁCS, L. Foot impact in different modes of running: mechanisms and energy transfer. *Procedia IUTAM 2* (Symposium on Human Body Dynamics, 2011), 101–108.
- [13] LARSON, P. Comparison of foot strike patterns of barefoot and minimally shod runners in a recreational road race. *Journal of Sport and Health Science* 3, 2 (2014), 137–142. doi:10.1016/j.jshs.2014.03.003.
- [14] LI, L., VAN DEN BOGERT, E. C. H., CALDWELL, G. E., VAN EMMERIK, R. E. A., AND HAMILL, J. Coordination patterns of walking and running at similar speed and stride frequency. *Human Movement Science* 18, 1 (1999), 67–85. doi:10.1016/S0167-9457(98)00034-7.
- [15] LIEBERMAN, D. E., VENKADESAN, M., WERBEL, W. A., DAOUD, A. I., D’ANDREA, S., DAVIS, I. S., MANG’ENI, R. O., AND PITSILADIS, Y. Foot strike patterns and collision forces in habitually barefoot versus shod runners. *Nature, Biomechanics* 463, 7280 (2010), 531–535.
- [16] CHI RUNNING OFFICIAL HOMEPAGE. www.chirunning.com, 2015. last accessed: Aug. 2015.
- [17] NATURAL RUNNING CENTER OFFICIAL HOMEPAGE. www.naturalrunningcenter.com, 2015. last accessed: Aug. 2015.
- [18] NEWTON RUNNING OFFICIAL HOMEPAGE. www.newtonrunning.com, 2015. last accessed: Aug. 2015.
- [19] MEREDITH, K., CASTLE, B., HINES, D., OELKERS, N., PETERS, J., REYES, N., CONTI, C., POLLARD, C., AND WITZKE, K. Peak impact ground reaction force during barefoot and shod running. *International Journal of Exercise Science: Conference Proceedings* 8, 3 (2015). article 13.
- [20] MERKER, A., KAISER, D., AND HERMANN, M. Numerical bifurcation analysis of the bipedal spring-mass model. *Physica D: Nonlinear Phenomena* 291, 15 (2015), 21–30.

- [21] MOMBAUR, K., OLIVIER, A.-H., AND CRÉTUAL, A. Forward and inverse optimal control of bipedal running. *Modeling, Simulation and Optimization of Bipedal Walking* 18 (2008), 165–179. Volume 18 of the series Cognitive Systems Monographs.
- [22] MORIN, J., SAMOZINO, P., ZAMEZIATI, K., AND BELLI, A. Effects of altered stride frequency and contact time on leg-spring behavior in human running. *Journal of Biomechanics* 40, 15 (2007), 3341–3348. doi:10.1016/j.jbiomech.2007.05.001.
- [23] NOVACHEK, T. F. The biomechanics of running. *Gait and Posture* 7 (1998), 77–95.
- [24] SRINIVASAN, M., AND HOLMES, P. How well can spring-mass-like telescoping leg models fit multi-pedal sagittal-plane locomotion data? *Journal of Theoretical Biology* 255, 1 (2008), 1–7. doi:10.1016/j.jtbi.2008.06.034.
- [25] WIT, B. D., CLERCQ, D. D., AND AERTS, P. Biomechanical analysis of the stance phase during barefoot and shod running. *Journal of Biomechanics* 33 (2000), 269–278.
- [26] ZELEI, A., BENCSIK, L., KOVÁCS, L. L., AND STÉPÁN, G. Energy efficient walking and running - impact dynamics based on varying geometric constraints. In *12th Conference on Dynamical Systems Theory and Applications* (Lodz, Poland, 2-5, December 2013), pp. 259–270.
- [27] ZELEI, A., BENCSIK, L., KOVÁCS, L. L., AND STÉPÁN, G. Impact models for walking and running systems - angular moment conservation versus varying geometric constraints. In *ECCOMAS Multibody Dynamics 2013, Book of Abstracts* (Zagreb, Croatia, 1-4 July 2013), Z. Terze, Ed., pp. 47–48. ISBN: 978-953-7738-21-1.

László Bencsik, M.Sc. (Ph.D. student): Department of Applied Mechanics, Budapest University of Technology and Economics, H-1111, Muegyetem rkp. 3., Budapest, Hungary (bencsik@mm.bme.hu).

Ambrus Zelei, Ph.D.: MTA-BME Research Group on Dynamics of Machines and Vehicles, H-1111, Muegyetem rkp. 3., Budapest, Hungary (zelei@mm.bme.hu). The author gave a presentation of this paper during one of the conference sessions.

**Optimization of accuracy on a low-cost 3D mapping
system for indoor navigation
(MTR200-15)**

Yves Bergeon, Václav Křivánek, Jean Motsch and Alexandr Štefek

Abstract: This paper focuses on the possibility for a robot to retrieve its position relatively to a previous map created in a preliminary pass. To be able to find a position of a robot, the common solution is to use costly sensors (mostly lasers) to recalibrate the position evaluated by low cost onboard sensors (in order to deal with drifts of the low cost sensors). Our work evaluates the possibility to use a low cost 3D sensor (Microsoft Kinect or Asus Xtion) in an unknown environment, creating a 3D map in a first pass and using this map to estimate the position of the robot. This paper describes the tools used and presents some optimizations to improve accuracy.

1. Introduction

Nowadays, robots begin to be widely used and near future will see newer robots for new usages, especially at home for supplying old people in their daily tasks. One of the challenges about such robots is the ability for them to know where they are in rooms (in a flat or inside a house). To get its position, robot should use a map of every room. On the other hand, to get a low cost robot, the map can't be furnished for each house by the manufacturer. The robot needs to be able to build its own map alone or under the supervision of an operator the first time the robot discovers the house. Then, after this first operation to create the map, low cost sensors are commonly used on robots to compute its position. This process is not straightforward as it looks like. Several artefacts make it difficult to achieve a high degree of accuracy: odometry on wheels lost position if robot slips on the floor, accelerometer or gyroscope sensor drifts over time due to a double integration to get position from acceleration. Even if these sensors were perfect, in a house, the robot can be hurt by an opening door or a walking pet.

Such problems are already known, especially in industrial plants. When autonomous robots move in an industrial environment, different kinds of low cost sensors are onboard (odometry, inertial measurement unit, infrared and ultrasounds sensors) but also lasers which allow to recalibrate the position each time the robot comes near specific targets, dispatched in strategic locations along the moves of the robot. The main drawback of this method is that an analysis had to be done beforehand to find these strategic locations.

Robots for security application face the same problems. To inspect buildings, robots can be brought by people to inspect a specific place. In this case, the robots have to find their correct position to be able to inspect the different rooms with the programmed algorithm which define the different moves.

For such problems, we developed an entire system to be able to build the map of the different rooms (using autonomous moves or supervised creation of the map) and we evaluate in practice the accuracy of our localization. We also identify some drawbacks of our method and optimize the system to improve accuracy after examination of preliminary results.

2. Architecture of the system

We focus on using open solutions and relying only on non-free tools to evaluate the accuracy of our system. The robot chosen is originally based on the RDS Reference Platform from Microsoft (Parallax Eddie Robot). This platform was created to be integrated with Microsoft Robotics Development Studio [RDS], at that time a complete integrated development system for robots. Unfortunately, RDS has been discontinued. As a consequence, we moved to a different system: Robot Operating System, aka ROS. ROS is a meta-operating system which can work on top of Ubuntu Linux system (its primary development), Android system and Microsoft Windows partially. ROS was developed at its debut by Willow Garage and is now maintained by the Open Source Robotics Foundation (OSRF) and by many contributors around the world. The simulator maintained by OSRF was used in last DARPA challenge.

ROS allows to use packages coming from different sources and to communicate from one package to another one using asynchronous messages (publisher/subscriber system) or services provided by other packages. This quite loose coupling eases the use of packages from different sources, like a package provided by a manufacturer, another one developed by a free contributor, and your own package. Currently, more than 1900 packages are available for ROS on its indigo version.¹

For our robot, whose structure is not far from the *turtlebot* robot from Willow Garage, we used a modified package for the *turtlebot* to be able to get our robot moving, to control its moves and to avoid obstacles.

¹ <http://www.ros.org/debbuild/indigo.html>



Figure 1. Microsoft Reference Development Platform (left) and Turtlebot 2 from Willow Garage² (right)

We are looking for more than to move the robot in the different rooms of a building, but we also want to be able to create a map of the different rooms as the robot is moving. For this, we use a low-cost RGBD Camera (Microsoft Kinect for Xbox 360) that doesn't use a laser, but only infrared sensors to measure depth.



Figure 2. Microsoft Kinect for Xbox360

The building of such a 3D Map is performed using the RGBDSLAM package developed by Freiburg University. This package performs localization and mapping simultaneously. We developed a strategy of moves for our robot to be able to compute a 3D Map. Reflecting the Kinect sensor own limitations, our map is restraint to an angular view of 78° about the z -axis.. This building of a global map is based on the fusion of successive RGB images, using points of interest in the images (found by SIFT [3] or SURF). We also need to get the depth of each of these points of interest to create a 3D map.

² <https://www.willowgarage.com/turtlebot>

Our first implementation of such this architecture was used to move the robot allowing the creation of the map of 2 rooms in 3D. The strategy of moving is not covered by this article. The result of the creation of the map of these 2 rooms is provided in figure 3 in 3D and in figure 4 in 2D.

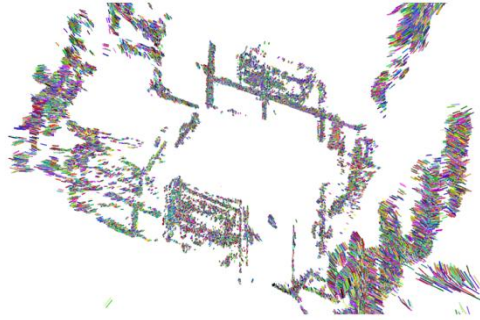


Figure 3. Creation of the 3D Map in RGBDSLAM in the first room

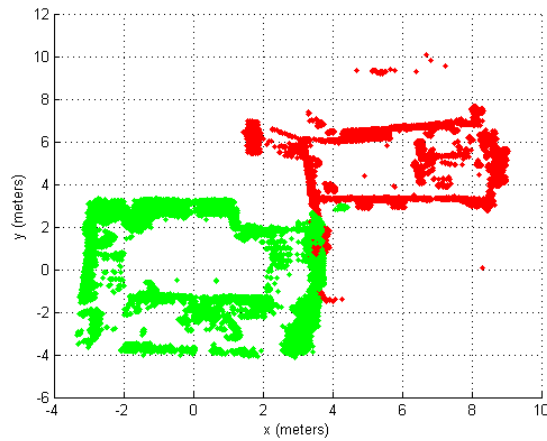


Figure 4. Map of the 2 rooms in 2D

As you can see on the map in 2D on figure 4, it seems that walls are not well detected as large lines for these walls are found. In fact, the artefacts are created by shelves that are against the walls and get detected. They look like some walls. We can conclude that the walls are indeed well detected.

3. Development of localization

After the first pass of creation of the map, we want to be able to localize the robot with respect to the map stored. To do this, we stored all the points of interest detected during the creation of the map. Each point of interest is defined as a quasi-unique key-point including x, y, z coordinates and a local description. The descriptor associated is a collection of 128 double values computed from gradient in the vicinity of this point (see figure 5).

```
%YAML:1.0
Feature_Locations:
- { x:1.9235734939575195e+00, y:9.1164451837539673e-01,
    z:8.4125488996505737e-01 }
Feature_Descriptors: !!opencv-matrix
  rows: 394
  cols: 128
  dt: f
  data: [ 2.83587305e-03, 2.81927316e-03, 6.62827045e-02,
          2.08859712e-01, 1.70482565e-02, 6.17182814e-03, 3.56298918e-03,
          1.79634208e-03, 6.66413130e-03, 5.77429961e-03, 1.11864410e-01,...
```

Figure 5. Descriptor of key-point in YAML format provided by RGBDSLAM.

When we put the robot on the floor, we choose to get only one picture to detect few points of interest and to compare them with points stored during the creation of the map. To evaluate if a new key-point is similar to one stored in the map, we need to evaluate for each new point the closest key-point in the map and to reject points too far. This is performed using the method developed in [4]. Of course, the more points you get, the more computations you have to perform. The process may be costly both for time and energy.

4. Results and optimization

The first results of this work were published in [1] with an average of accuracy of 60 cm. To improve accuracy, we optimized some points of our algorithm. This optimization is done offline on another computer, compared to the mapping that is performed using an onboard computer.

The first problem is due to descriptor provided for SIFT points. In specific cases, some values of descriptor are not determined and RGBDSLAM provide NaN (Not a Number) in place of values. This affects our algorithm because some false key-points are detected which influence the precision of the position. In our new algorithm, all of the SIFT points that contain NaN were removed from the points detected in the new picture.

The second aspect we optimize is about the range of detection. Even if Microsoft doesn't provide accuracy data about his Kinect sensor (in term of volume of detection), this sensor was developed to be used in a range from 2m to 4.5m. We therefore remove all key points outside this range for the new picture.

Figure 6 presents the position of the robot (black triangle) without optimization, figure 7 with optimization and figure 8 shows the comparison with real position.

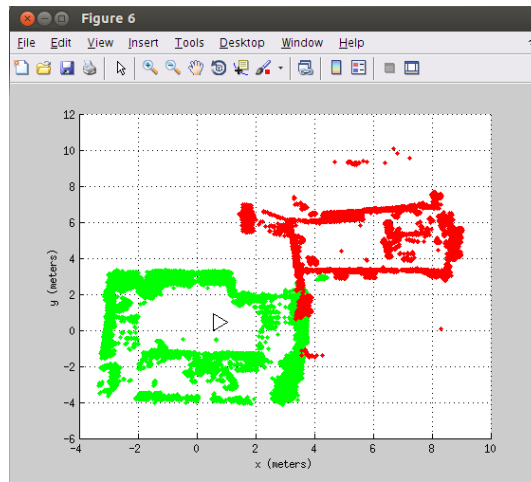


Figure 6. Position of the robot detected (triangle) without optimization

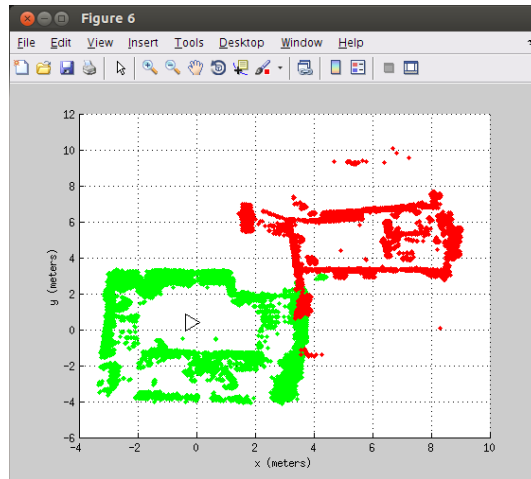


Figure 7. Position of the robot detected (triangle) with optimization

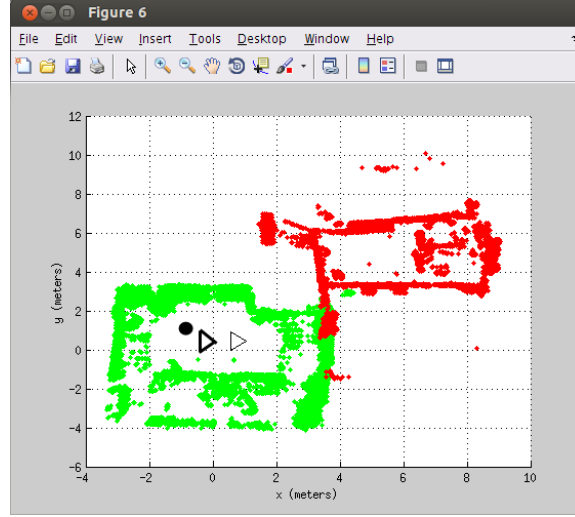


Figure 8. Position of the robot without optimization (light triangle), with optimization (strong triangle) and black circle for the real position.

As expected, the accuracy of detection is better with optimization. This comes at a reduction of the number of key-points detected. For example, without optimization, 450 points were detected. In our tests, we have generally one fourth of the initial key-points that are kept. In some cases, as for larger room, depending of position and orientation of the Kinect sensor, we get only a few key-points.

One further comment is about the nature of the key-points detected. The key points detected on the last picture are not always the ones detected in the initial map. It depends heavily on luminance, position and orientation of the robot and even occlusions. With optimization, we observe that some case of no common key-points appeared. To be able to get more matching points, we can increase the distance of the matching comparison. As the method used [4] offer, we can modify a parameter to accept matching of farthest points. This ensures more key-points that can be matched but also induces a higher probability of wrong matching. In that case, there is a trade-off to find between accuracy and matching key-points detection.

5. Conclusions

In this paper, we presented the architecture of our 3D mapping system and the approach we chose. At this time, we are able to create a 3D Map and to localize the robot in the room. We added a refinement step to our algorithm to detect the position of the robot in the room. These optimizations allow getting a better accuracy at a price of rejecting many key-points detected, and in some cases no detection is possible. The result of increasing the number of matched key-points doesn't look like a good solution, because the effect on accuracy is not easy to assess.

The future work will focus on using multiple views with the robot on the floor. The first idea will be to take pictures using only rotation of the robot to see if this improves detection of key-points and to check if accuracy is improved.

The other point we had to work on is the CPU consumption. Detecting SIFT points and showing in 3D the result with RGBDSLAM is a heavy task that is relatively slow. We have to improve this part and to implement all part of our algorithm of detection directly onboard on the robot.

References

- [1] Bergeon, Y.; Hadda, I.; Krivanek, V.; Motsch, J. and Štefek, A. Low Cost 3D Mapping for Indoor Navigation, ICMT2015, IEEE Brno., ISBN 978-80-7231-976-3
- [2] Y. Bergeon, Calculation of the Distance Covered by a robot thanks to Image Analysis with a two-robot team, Proceedings of ICMT'11 – International Conference on Military Technologies, Brno, University of Defence, 2011, pp 849-854
- [3] D.G. Lowe, "Object recognition from local scale-invariant features", IEEE Proc. 7th Int. Conf. Computer Vision (ICCV'99), Kerkyra, Greece, Sep 1999, pp 1150-1157
- [4] I. Hadda, J. Knani, "Global mapping and localization for mobile robots using stereo vision", Systems, Signals & Devices (SSD), 2013 10th International Multi-Conference, pp 1 - 6
- [5] Á. Llamazares, E. J. Molinos, M. Ocaña, L. M. Bergasa, N. Hernández, F. Herranz, "3D Map Building Using a 2D Laser Scanner", *Computer Aided Systems Theory – EUROCAST 2011*, Lecture Notes in Computer Science Volume 6928, 2012, pp 412-419
- [6] Felix Endres, Juergen Hess, Nikolas Engelhard, Juergen Sturm, Daniel Cremers, Wolfram Burgard, "An Evaluation of the RGB-D SLAM System, *Proc. of the IEEE International Conference on Robotics and Automation (ICRA)*, May 2012, St. Paul, Minnesota, USA
- [7] Bourdonnaye, A.; Doskočil, R.; Křivánek, V.; Štefek, A.. Practical Experience with Distance Measurement Based on the Single Visual Camera. *Advances in Military Technology*, 2012, vol. 8, no. 1, p. 51-58. ISSN 1802-2308.

Yves Bergeon, Ph.D. D.Sc: Schools Saint-Cyr Coëtquidan 56381 GUER Cedex, France (yves.bergeon@st-cyr.terre-net.defense.gouv.fr). The author gave a presentation of this paper during one of the conference sessions.

Václav Křivánek, Ph.D.: University of Defence, Faculty of Military Technology, Kournicova 65, Brno, Czech Republic (vaclav.krivanek@unob.cz)

Jean Motsch, Ph.D.: Schools of Saint-Cyr Coëtquidan 56381 GUER Cedex, France (jean.motsch@st-cyr.terre-net.defense.gouv.fr)

Alexandr Štefek, Ph.D. D.Sc: University of Defence, Faculty of Military Technology, Kournicova 65, Brno, Czech Republic (alexandr.stefek@unob.cz)

Study of dynamic forces in human upper limb in forward fall (LIF281-15)

Paweł Biesiacki, Jerzy Mrozowski, Jan Awrejcewicz

Abstract: Knowledge of dynamic forces acting on the upper limb is useful, and sometimes even necessary, in its treatment and rehabilitation after injuries, during prostheses designing, as well as in optimization of the sports training process. In this work an attempt to determine the quantity of the inertia forces generated in forward fall has been undertaken. For this purpose a simplified mechanical model of the human body biokinematic chain has been prepared. Geometric data and mass of each element have been taken from anthropometric atlas for the Polish population. Kinematic data necessary to perform the analysis was calculated using fundamental laws of Mechanics. In this way accelerations of the selected points necessary for the determination of inertia forces acting on the individual links of the model were yielded. For validation of the obtained results a numerical model was constructed using SimMechanic module of the Matlab Simulink software. It made possible to compare the results obtained in both simulation methods. To make joints model more realistic a values of the viscous friction were assumed.

1. Introduction

Approximately 90% of all fractures of the distal radius, humeral neck and supracondylar region of the elbow are caused by the forward fall onto the outstretched hand [1]. The mechanism of joint interaction, the forces distribution within the joint and the contributory effects of elbow joint disorders must be fully understood in order to prevent and minimize those injuries.

Chiu and Robinovitch [2] applied a two-degrees-of-freedom (2-DOF) lumped-parameter mathematical model for simulations of a fall on the outstretched hand with full elbow extension. Their model analysis suggested that fall from a height greater than 0.6 m carry significant risks of wrist fractures. The effect of elbow flexion at the moment of impact was investigated by Chou et al [3]. were considered elbow loads for models between elbows full flexion and full extension during a forward fall. The results of valgus-varus elbow analysis showed that shear force for the elbow full flexion model is 68% lower than in the case of the elbow full extension. Investigations of the ground reaction forces during forward fall showed that the first peak force value is reduced during an elbow flexion movement, while the impact peak force is postponed to the second peak force. From this follows conclusion that the elbow flexion movement may reduce the risk of injury during a forward fall. An experimental model for elbow load during a simulated one-armed fall arrest for three different forearm axially rotated postures and the relationship between the elbow flexion angle and different axially rotated postures were investigated in [4]. The results indicated that a fall on the

outstretched hand with externally rotated forearm should be avoided in order to reduce excessive valgus-varus shear force on the elbow joint.

A 2-DOF impact model of bimanual forward fall arrests, basing on *in vivo* data of experimental falls, was constructed [5]. Its validation was confirmed by response simulation with separate experimental data. Results of its analysis indicated that the rapid arm movement towards the ground alone could be a major risk factor for fall-related injuries and that prolongation of the impact time through decreasing relative velocity between hand and ground allows to decrease the ground reaction force. In the study [6] authors investigated a stress contribution in the human upper limb during forward fall on the outreached hands. The results indicated that less risk of the fracture is supination position of the forearm.

Dynamic models of human movement help researchers identify key forces, movements, and movement patterns that should be measured. It was found that the muscle function depends strongly on both shoulder and elbow joints position. Using Lagrange' a method an at-home resistance training upper limb exoskeleton was designed with a 3DOF shoulder joint and a 1DOF elbow joint to allow both single and multiple joints upper limb movements in different planes [7]. The contribution of individual muscles motion of the glenohumeral joint during abduction and the examination of the effect of elbow flexion on shoulder muscle function was investigated by Ackland and Pandy [8].

The fall simulation studies have investigated the biomechanical analysis on elbow extension and elbow flexion models. However, there is very little information about dynamical forces acting on the upper limb. Thus, the present study performs an numerical investigations to evaluate the torque in each joint during forward fall. The numerical results may provide useful insights into potential reduced risk of injuries during forward fall.

2. Methods

Computer modeling is an effective tool to accelerate and improve the design of new mechanical system. Matlab and Simulink module are appropriate tools for creating computer model. To investigate the velocities and accelerations of the mass center of gravity (CG_i) of each parts of the proposed simplified model of the human body developed was the mathematical model by.

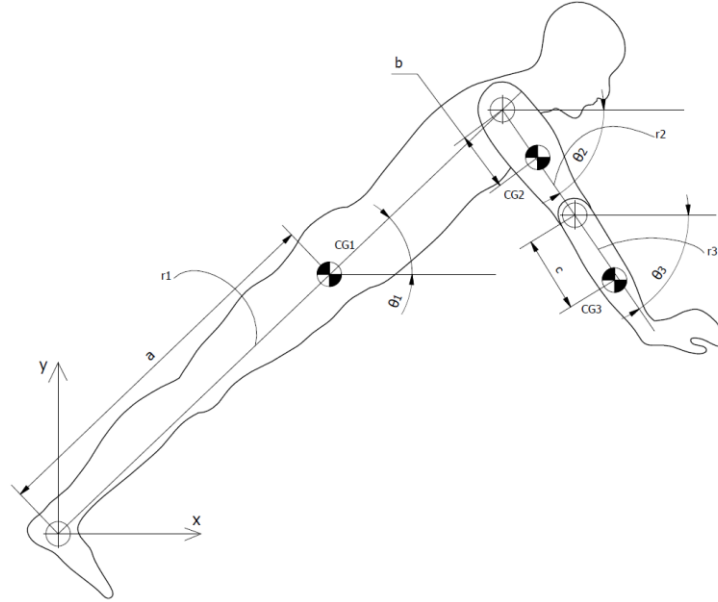


Figure 1. Mathematical model of human body

Human body was modeled as a three parts system including: torso with legs (link1 - dimension r_1), arm (link2 - dimension r_2) and forearm with hand (link3 - dimension r_3). Each part is represented as a rigid link with length proportions and mass distribution corresponding to the Polish population. The dynamic equations of such a mechanical system were derived using energy method. Lagrangian L of this system is defined as:

$$L(q, \dot{q}) = T(q, \dot{q}) - V(q) \quad (1)$$

where T is the total kinetic energy and V is the total potential energy of the system, q and \dot{q} are the generalized coordinates and generalized velocities of the system, respectively. The equation of motion is given by:

$$\frac{d}{dt} \left(\frac{\partial L}{\partial \dot{q}} \right) - \frac{\partial L}{\partial q} = - \frac{\partial \Delta}{\partial \dot{q}} \quad (2)$$

where $\Delta(q, \dot{q})$ is the dissipation function.

A three links system has three degrees of freedom (3-DOF), and hence three generalized coordinates are needed to describe it in arbitrary configuration. The generalized coordinates are θ_n , where $n=1,2,3$.

In formulation of the dynamic equations the following designations were used:

- r_i - length of i^{th} body part, where $i = 1,2,3$,
- CG_i – locations of the center of gravity of i^{th} link, where $i = 1,2,3$,
- a – distance from joint 1 to CG_2 ,
- b - distance from joint 2 to CG_2 ,
- c - distance from joint 3 to CG_3 ,
- m_i – mass of i^{th} body part, where $i = 1,2,3$,
- I_i – moment of inertia of i^{th} link about CG_i , where $i = 1,2,3$,
- k_i - friction factor of i^{th} link, where $i = 1,2,3$.

The position vectors for the center of mass for parts 1, 2 and 3 with respect to the fixed coordinate system are as follows:

- torso with legs

$$\vec{r}_{CG1} = a \cos \theta_1 i + a \sin \theta_1 j, \quad (3)$$

- arm

$$\vec{r}_{CG2} = (r_1 \cos \theta_1 + b \cos \theta_2) i + (r_1 \sin \theta_1 + b \sin \theta_2) j, \quad (4)$$

- forearm with hand

$$\begin{aligned} \vec{r}_{CG3} = & (r_1 \cos \theta_1 + r_2 \cos \theta_2 + c \cos \theta_3) i + \\ & + (r_1 \sin \theta_1 + r_2 \sin \theta_2 + c \sin \theta_3) j \end{aligned} \quad (5)$$

Differentiation of the equations (3), (4), (5) gives the velocities of the CG_i :

- torso with legs

$$\dot{\vec{r}}_{CG1} = -a(\sin \theta_1 \dot{\theta}_1) i + a(\cos \theta_1 \dot{\theta}_1) j, \quad (6)$$

- arm

$$\dot{\vec{r}}_{CG2} = (-r_2 \sin \theta_1 \dot{\theta}_2 - b \sin \theta_2 \dot{\theta}_2) i + (r_1 \cos \theta_1 \dot{\theta}_2 + b \cos \theta_2 \dot{\theta}_2) j, \quad (7)$$

- forearm with hand:

$$\begin{aligned} \dot{\vec{r}}_{CG3} = & (-r_2 \sin \theta_1 \dot{\theta}_1 - r_2 \sin \theta_1 \dot{\theta}_2 - c \sin \theta_3 \dot{\theta}_3) i + \\ & + (r_1 \cos \theta_1 \dot{\theta}_1 + r_2 \sin \theta_2 \dot{\theta}_2 + c \sin \theta_3 \dot{\theta}_3) j \end{aligned} \quad (8)$$

The total kinetic energy of the whole system is given by:

$$T(q, \dot{q}) = \frac{1}{2} (m_1 v_1^2 + m_2 v_2^2 + m_3 v_3^2) + I_1 \dot{\theta}_1 + I_2 \dot{\theta}_2 + I_3 \dot{\theta}_3 \quad (9)$$

Where v_1, v_2, v_3 are the absolute velocities of CG_1, CG_2 and CG_3 , respectively. They was found by solving the equations (4), (5), (6). After simplification we have:

$$v_1 = \sqrt{a^2 \dot{\theta}_1^2} \quad (10)$$

$$v_2 = \sqrt{r_1^2 \dot{\theta}_1^2 + b^2 \dot{\theta}_2^2 + 2r_1 b \dot{\theta}_1 \dot{\theta}_2 \cos(\theta_2 - \theta_1)} \quad (11)$$

$$v_3 = \sqrt{r_1^2 \dot{\theta}_1^2 + r_2^2 \dot{\theta}_2^2 + c^2 \dot{\theta}_3^2 + 2r_1 r_2 \dot{\theta}_1 \dot{\theta}_2 \cos(\theta_2 - \theta_1) + 2r_1 c \dot{\theta}_1 \dot{\theta}_3 \cos(\theta_1 + \theta_3) + 2r_2 c \dot{\theta}_2 \dot{\theta}_3 \cos(\theta_2 + \theta_3)} \quad (12)$$

Substituting equations (10), (11), (12) into equation (9) we get following equation for the total kinetic energy of the system:

$$\begin{aligned} T(q, \dot{q}) = & \frac{1}{2}(m_1 a^2 + m_2 r_1^2 + m_3 r_1^2 + I_1) \dot{\theta}_1^2 + \frac{1}{2}(m_2 b^2 + m_3 r_2^2 + I_2) \dot{\theta}_2^2 + \frac{1}{2}(m_3 c^2 + I_3) \dot{\theta}_3^2 + \\ & + r_1 (m_2 b + m_3 r_2) \cos(\theta_2 - \theta_1) \dot{\theta}_1 \dot{\theta}_2 + \\ & + m_3 r_1 c \cos(\theta_1 + \theta_3) \dot{\theta}_1 \dot{\theta}_3 + m_3 r_2 c \cos(\theta_2 + \theta_3) \dot{\theta}_2 \dot{\theta}_3 \end{aligned} \quad (13)$$

Potential energy of the system is expressed by the following formula:

$$V(q) = m_1 g h_{CG1} + m_2 g h_{CG2} + m_3 g h_{CG3}, \quad (14)$$

where $h_{CGi}, i=1,2,3$ is the height of center of gravity of i^{th} link. The respective values are as follows:

$$h_{CG1} = a \sin \theta_1 \quad (15)$$

$$h_{CG2} = r_1 \sin \theta_1 + b \sin \theta_2 \quad (16)$$

$$h_{CG3} = r_1 \sin \theta_1 + r_2 \sin \theta_2 + c \sin \theta_3 \quad (17)$$

Substituting equations (15), (16), (17) into equation (14), we obtained the total potential energy of the system as:

$$V(q) = (m_1 a + m_2 r_1 + m_3 r_1) g \sin \theta_1 + (m_2 b + m_3 r_2) g \sin \theta_2 + m_3 g c \sin \theta_3 \quad (18)$$

The Lagrangian of the system has the form:

$$L(q, \dot{q}) = T(q, \dot{q}) - V(q) \quad (19)$$

Substituting equations (13) and (18) into equation (19) we get

$$L(q, \dot{q}) = \frac{1}{2}(m_1 a^2 + m_2 r_1^2 + m_3 r_3^2 + I_1) \dot{\theta}_1^2 + \frac{1}{2}(m_2 b^2 + m_3 r_2^2 + I_2) \dot{\theta}_2^2 + \frac{1}{2}(m_3 c^2 + I_3) \dot{\theta}_3^2 + r_1(m_2 b + m_3 r_2) \cos(\theta_2 - \theta_1) \dot{\theta}_2 \dot{\theta}_3 +$$
(20)

$$m_3 r_1 c \cos(\theta_1 + \theta_3) \dot{\theta}_1 \dot{\theta}_3 + m_3 r_2 c \cos(\theta_2 + \theta_3) \dot{\theta}_2 \dot{\theta}_3 - (m_1 a + m_2 r_1 + m_3 r_1) g \sin \theta_1 - (m_2 b + m_3 r_2) g \sin \theta_2 - m_3 g c \sin \theta_3$$

To find the dynamic equations of the system we have to compute partial derivatives of the Lagrangian (20):

$$\frac{\partial L}{\partial \theta_1} = r_1(m_2 b + m_3 r_2) \sin(\theta_2 - \theta_1) \dot{\theta}_1 \dot{\theta}_2 -$$
(21)

$$+ m_3 r_1 c \sin(\theta_1 + \theta_3) \dot{\theta}_1 \dot{\theta}_3 - (m_1 a + m_2 r_1 + m_3 r_1) g \cos \theta_1$$

$$\frac{\partial L}{\partial \theta_2} = -r_1(m_2 b + m_3 r_2) \sin(\theta_2 - \theta_1) \dot{\theta}_1 \dot{\theta}_2 -$$
(22)

$$+ m_3 r_2 c \sin(\theta_2 + \theta_3) \dot{\theta}_2 \dot{\theta}_3 - (m_2 b + m_3 r_2) g \cos \theta_2$$

$$\frac{\partial L}{\partial \theta_3} = -m_3 r_1 c \sin(\theta_1 + \theta_3) \dot{\theta}_1 \dot{\theta}_3 - m_3 r_2 c \sin(\theta_2 + \theta_3) \dot{\theta}_2 \dot{\theta}_3 - m_3 g c \cos \theta_3$$
(23)

$$\frac{\partial L}{\partial \dot{\theta}_1} = (m_1 a^2 + m_2 r_1^2 + m_3 r_1^2 + I_1) \dot{\theta}_1 +$$
(24)

$$+ r_1(m_2 b + m_3 r_2) \cos(\theta_2 - \theta_1) \dot{\theta}_2 + m_3 r_1 c \cos(\theta_1 + \theta_3) \dot{\theta}_3$$

$$\frac{\partial L}{\partial \dot{\theta}_2} = (m_2 b^2 + m_3 r_2^2 + I_2) \dot{\theta}_2 + r_1(m_2 b + m_3 r_2) \cos(\theta_2 - \theta_1) \dot{\theta}_2 +$$
(25)

$$+ m_3 r_2 c \cos(\theta_2 + \theta_3) \dot{\theta}_3$$

$$\frac{\partial L}{\partial \dot{\theta}_3} = (m_3 c^2 + I_3) \dot{\theta}_3 + m_3 r_1 c \cos(\theta_1 + \theta_3) \dot{\theta}_1 + m_3 r_2 c \cos(\theta_2 + \theta_3) \dot{\theta}_2$$
(26)

$$\frac{d}{dt} \left(\frac{\partial L}{\partial \dot{\theta}_1} \right) = (m_1 a^2 + m_2 r_1^2 + m_3 r_1^2 + I_1) \ddot{\theta}_1 + r_1(m_2 b + m_3 r_2) \cos(\theta_2 - \theta_1) \ddot{\theta}_2 - r_1(m_2 b + m_3 r_2) \sin(\theta_2 - \theta_1) (\dot{\theta}_2 - \dot{\theta}_1) \dot{\theta}_2 + m_3 r_1 c \cos(\theta_1 + \theta_3) \ddot{\theta}_3 - m_3 r_1 c \sin(\theta_1 + \theta_3) (\dot{\theta}_1 + \dot{\theta}_3) \dot{\theta}_3$$
(27)

$$\begin{aligned} \frac{d}{dt} \left(\frac{\partial L}{\partial \dot{\theta}_2} \right) &= (m_2 b + m_3 r_2^2 + I_2) \ddot{\theta}_1 + r_1 (m_2 b + m_3 r_2) \cos(\theta_2 - \theta_1) \ddot{\theta}_2 \\ &\quad - r_1 (m_2 b + m_3 r_2) \sin(\theta_2 - \theta_1) (\dot{\theta}_2 - \dot{\theta}_1) \dot{\theta}_1 + m_3 r_2 \cos(\theta_2 + \theta_3) \ddot{\theta}_3 \\ &\quad - m_3 r_2 c \sin(\theta_2 + \theta_3) (\dot{\theta}_2 + \dot{\theta}_3) \dot{\theta}_3 \end{aligned} \quad (28)$$

$$\begin{aligned} \frac{d}{dt} \left(\frac{\partial L}{\partial \dot{\theta}_3} \right) &= (m_3 c^2 + I_3) \ddot{\theta}_3 + m_3 r_1 c \cos(\theta_1 + \theta_3) \ddot{\theta}_1 \\ &\quad - m_3 r_1 c \sin(\theta_1 + \theta_3) (\dot{\theta}_1 + \dot{\theta}_3) \dot{\theta}_1 + m_3 r_2 c \cos(\theta_2 + \theta_3) \ddot{\theta}_2 \\ &\quad - m_3 r_2 c \sin(\theta_2 + \theta_3) (\dot{\theta}_2 + \dot{\theta}_3) \dot{\theta}_2 \end{aligned} \quad (29)$$

Assuming that the dissipation of the system comes from friction in the joints, we get the following relation:

$$\Delta(\dot{q}) = \frac{1}{2} [k_1 \dot{\theta}_1^2 + k_2 (\dot{\theta}_2^2 - \dot{\theta}_1^2) + k_3 (\dot{\theta}_3^2 - \dot{\theta}_2^2)] \quad (30)$$

Partial differentiation of the equation (30) yields:

$$\frac{\partial \Delta}{\partial \dot{\theta}_1} = (k_1 + k_2) \dot{\theta}_1 - k_2 \dot{\theta}_2 \quad (31)$$

$$\frac{\partial \Delta}{\partial \dot{\theta}_2} = (k_2 + k_3) \dot{\theta}_2 - k_2 \dot{\theta}_1 - k_3 \dot{\theta}_3 \quad (32)$$

$$\frac{\partial \Delta}{\partial \dot{\theta}_3} = k_3 (\dot{\theta}_3 - \dot{\theta}_2) \quad (33)$$

Substituting equations (21)-(33) into equation (2), one gets the following dynamic equations of three parts human body model:

$$\begin{aligned} &(m_1 a^2 + m_2 r_1^2 + m_3 r_1^2 + I_1) \ddot{\theta}_1 + r_1 (m_2 b + m_3 r_2) \cos(\theta_2 - \theta_1) \ddot{\theta}_2 \\ &\quad + m_3 r_1 c \cos(\theta_1 + \theta_3) \ddot{\theta}_3 - r_1 (m_2 b + m_3 r_2) \sin(\theta_2 - \theta_1) \dot{\theta}_2 \\ &\quad - m_3 r_1 c \sin(\theta_1 + \theta_3) \dot{\theta}_3^2 + (m_1 a + m_2 r_1 + m_3 r_1) g \cos \theta_1 = -(k_1 + k_2) \dot{\theta}_1 - k_2 \dot{\theta}_2 \end{aligned} \quad (34)$$

$$\begin{aligned} &(m_2 b^2 + m_3 r_2^2 + I_2) \ddot{\theta}_2 + r_1 (m_2 b + m_3 r_2) \cos(\theta_2 - \theta_1) \ddot{\theta}_1 \\ &\quad + r_1 (m_2 b + m_3 r_2) \sin(\theta_2 - \theta_1) \dot{\theta}_1 + \\ &\quad m_3 r_2 c \cos(\theta_2 + \theta_3) \ddot{\theta}_3 - m_3 r_2 c \sin(\theta_2 + \theta_3) \dot{\theta}_3^2 + \\ &\quad + (m_2 b + m_3 r_2) g \cos \theta_2 = -(k_2 + k_3) \dot{\theta}_2 + k_2 \dot{\theta}_1 + k_3 \dot{\theta}_3 \end{aligned} \quad (35)$$

$$\begin{aligned} &(m_3 c^2 + I_3) \ddot{\theta}_3 + m_3 r_1 c \cos(\theta_1 + \theta_3) \ddot{\theta}_1 \\ &\quad - m_3 r_1 c \sin(\theta_1 + \theta_3) \dot{\theta}_1^2 + m_3 r_2 c \cos(\theta_2 + \theta_3) \ddot{\theta}_2 \\ &\quad - m_3 r_2 c \sin(\theta_2 + \theta_3) \dot{\theta}_2^2 + m_3 g c \cos \theta_3 = -k_3 (\dot{\theta}_3 - \dot{\theta}_2) \end{aligned} \quad (36)$$

Figure 2 presents the Simulink diagram used to solve the equations (34), (35) and (36). The results obtained in this way was validated using Simmechanic module of Matlab (Figure 3).

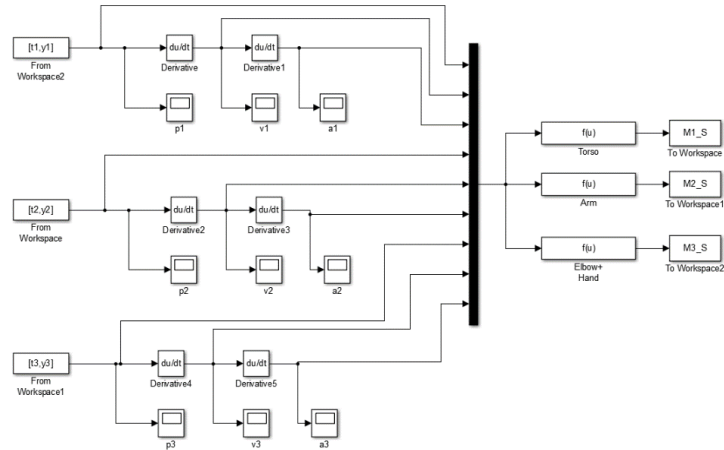


Figure 2. Simulink diagram used to simulate the dynamical system.

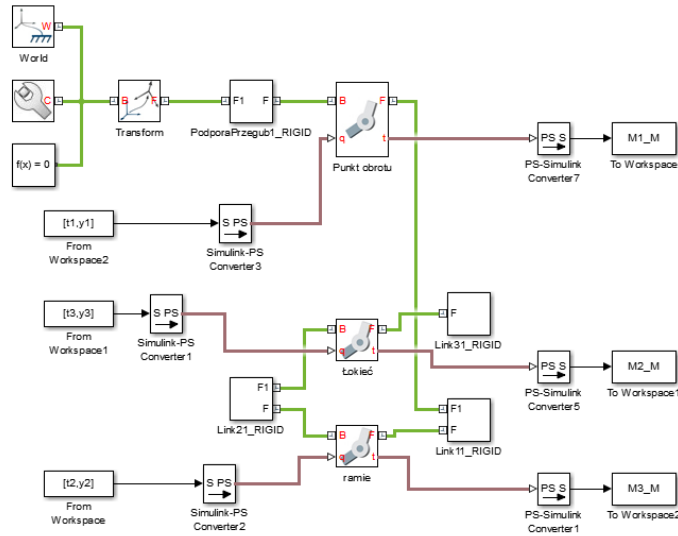


Figure 3. Simmechanic diagram used to simulate the dynamical system.

3. Results

A *sine* function has been used as an input for calculation of the angular position of each link at the time. The sine input function is presented in Figure 4. Each joint is actuated individually with the sine function as an angular displacement about rotational axis z_i , where $i=1,2,3$. Continuous line (y1) represents angular position of link 1 (torso with legs), dotted-dashed line (y2) denotes angular position of link 2 (arm), and fine dashed line (y3) shows angular position of link 3 (forearm with hand).

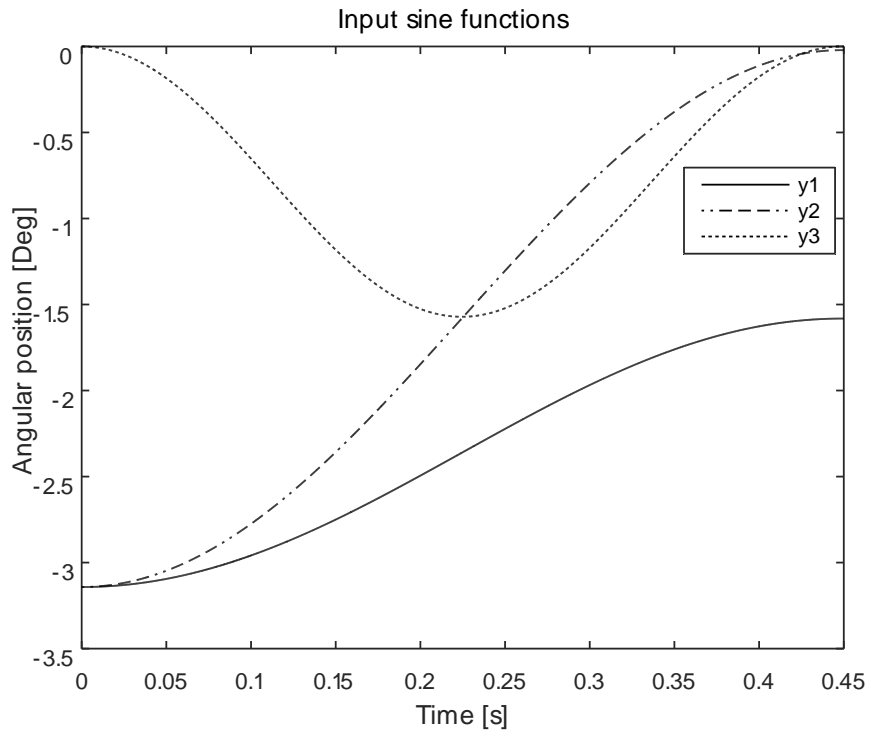


Figure 4. Angular input function.

The figure above shows the simulated movement of the torso with legs, where ankle, shoulder and elbow joints are actuated. The functions were chosen in order to reflect the movement of the human body during the forward fall. The simulation time corresponds to the movement of the body without external forces, only under the action of the force of gravity.

Table 1. Model parameters of the simulated system.

		Body parts		
		Torso with legs	Arm	Forearm with hands
Parameters	r_i [m]	1.80	0.3	0.4
	a [m]	0.861	-	-
	b [m]	-	0.15	-
	c [m]	-	-	0.2
	m_i [kg]	66	2.4	1.9
	I_i [kg m ²]	21.564	0.015	0.017
	k_i	0.01	0.01	0.01

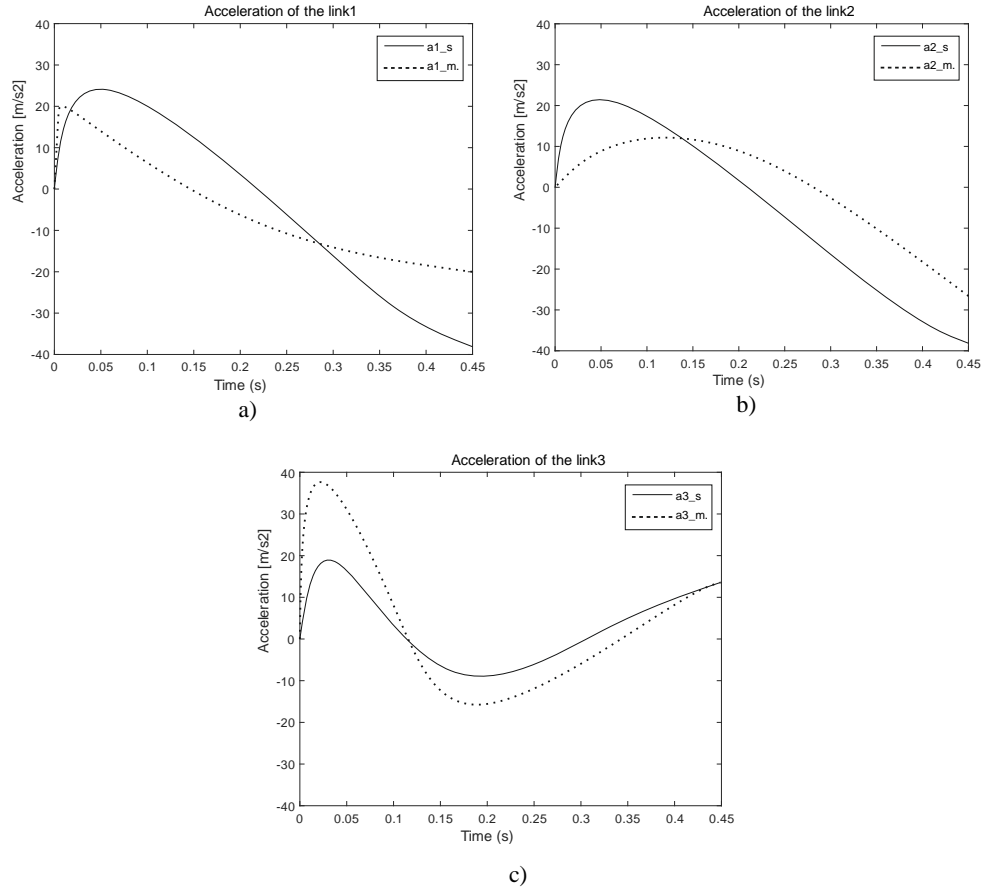


Figure 5. Accelerations of the links' centers of gravity: a) torso with legs, b) shoulder, c) forearm with hands.

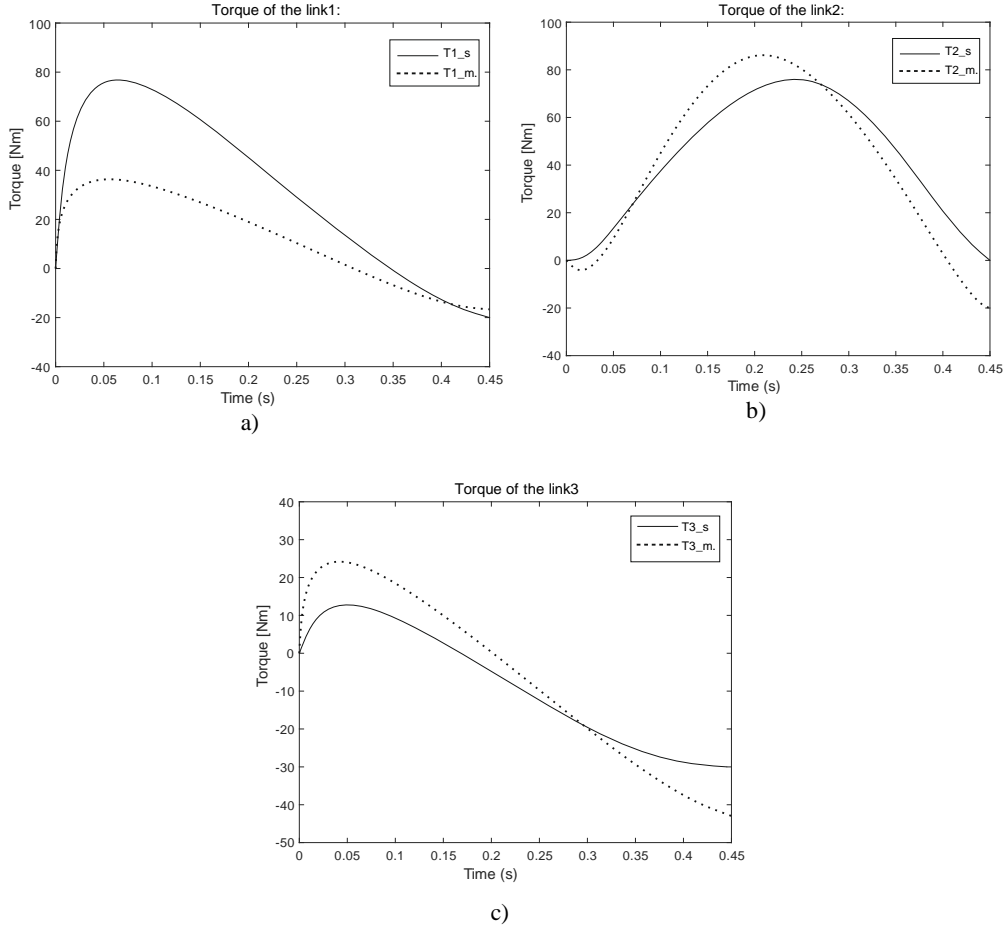


Figure 6. Torques applied to the links: a) torso with legs, b) shoulder, c) forearm with hands.

The diagrams on the figures 5 and 6 present accelerations and torques, respectively. Figures 5a and 6a refer to CG_1 of torso with legs body part, figures 5b and 6b to CG_2 of arm, figures 5c and 6c to CG_3 of forearm. The subscripts m and s occurring in diagrams' description denote values obtained using Simulink and Simmechanic programs, respectively.

4. Conclusions

Modelling of the upper limb is important for better understanding of the relationship between different kinds of motion parameters and generated internal forces. The proposed model, although very simplified, gives some insight on the possible human dynamic behavior under the influence of

various forces acting on a man, during his locomotion, for example. The model discussed in this study was built to identify the problems arising from modelling in general and the issues concerning the forward dynamics simulation. In the results of the forward model, it could be seen that the initial conditions are of extreme importance. The aim of this research was to develop a dynamic model of the human upper limb and to evaluate this model by adopting an appropriate motion analysis system to verify hypotheses of the established motion during forward fall and to determine the torque in each joint of the upper limb for further verification studies.

Comparison of the results of the motion simulation during forward fall, obtained using both Simulink and Simmechanic methods, showed good consistency. The little discrepancies in the results may be due to minor differences in the geometric model built in Simmechanic and its mathematical description.

References

- [1] Melton, L. J. Chao, E.Y.S., Lane, J. Biomechanical aspects of fractures. In. Riggs, B.L., Melton, L.J. (Eds.), *Osteoporosis, Etiology, Diagnosis, and Management*. Raven Press, New York, 1998, 111-131.
 - [2] Chiu, J., Robinovitch, S. N., Prediction of upper extremity impact forces during falls on the outstretched hand. *Journal of Biomechanics* 31(12), 1998, 1169-1176.
 - [3] Chou, P.H., Chou, Y.L., Lin, C.J., Su, F.C., Lou, S.Z., Lin, C.F., Huang, Effect of elbow flexion on upper extremity impact forces during a fall. *Clinical of Biomechanics* 16 (10), 2001, 888-894.
 - [4] Chou, P.H., Lou S.Z., Chen H.Ch., Chiu Ch.F., Chou Y.L., Effect of various forearm axially rotated postures on elbow load and elbow flexion angle in one-armed arrest of forward fall. *Clinical of Biomechanics* 24, 2009, 632-636.
 - [5] Kim, K.J., Ashton-Miller, J.A., Segmental dynamics of forward fall arrest: A system identification approach. *Clinical Biomechanics* 24, 2009, 348-354.
 - [6] Biesiacki, P., Mrozowski J., Awrejcewicz J., *Dynamic Systems-Applications*. TUL, Lodz, 2013, 229-240.
 - [7] Wu T.M., Chen D.Z., Dynamic Analysis and Preliminary Evaluation of a Spring-Loaded Upper Limb Exoskeleton for Resistance Training with Overload Prevention. *Journal of Mechanics* 29, 2013, 35-44.
 - [8] Yu J., Ackland D.C., Pandy M.G., Shoulder muscle function depends on elbow joint position: An illustration of dynamic coupling in the upper limb. *Journal of Biomechanics* 44, 2011, 1859-1868.
- Paweł Biesiacki, M.Sc. (Ph.D. student): Lodz University of Technology, Department of Automation, Biomechanics and Mechatronics, Stefanowskiego 1/15, 90-537, Lodz, Poland, the author gave a presentation of this paper during one of the conference sessions (800045@edu.p.lodz.pl).
- Jerzy Mrozowski, Ph.D., D.Sc.: Lodz University of Technology, Department of Automation, Biomechanics and Mechatronics, Stefanowskiego 1/15, 90-537, Lodz, Poland (jmrozow@p.lodz.pl).
- Jan Awrejcewicz, Professor: Lodz University of Technology, Department of Automation, Biomechanics and Mechatronics, Stefanowskiego 1/15, 90-537, Lodz, Poland (jan.awrejcewicz@p.lodz.pl).

**Investigation of motion of a freight wagon aimed to
identify the forces acting on the side wall of the wagon
(VIB235-15)**

Andrzej Buchacz, Andrzej Baier, Krzysztof Herbuś, Michał Majzner, Piotr Ociepka

Abstract: In the work is considered the modification of the cargo space of a freight wagon of the 418V type. On the basis of the conducted inspection of the state of plating of freight wagons, carried out under the project number PBS2/A6/17/2013 realized as a part of the Applied Research Program, funded by the National Research and Development Centre, it is possible to state that the main causes of damage and therefore repairing of wagon plating are chemical interactions of the carried material and the wagon body as well as mechanical damages. The introduced structural change consists in the use of composite panels which should protect the steel plating of a wagon body. Therefore, it is necessary to carry out a series of studies to check, among others, the strength parameters of the adopted constructional solution. For this purpose it is necessary to determine the maximal value of the force, derived from transported freight, which acts on the side walls of a wagon. In the work is presented a series of tests related to motion analysis of a freight wagon of the 418V type. The aim of numerical analysis was to determine the maximal permitted speed at which the car does not go off the rails. These tests were performed using the “Motion Simulation” module of the software of the CAD/CAE/CAM class Siemens PLM NX. It has been created a model prepared for motion simulation, in which have been defined joints necessary for the proper mapping of the wagon motion on a track way. The cycle of numerical tests was preceded by determination of the expected value of the permitted speed limit. This allowed narrowing the range of numerical investigations.

1. Introduction

The introduction of various modifications in constructional solutions of the existing technical means, which aim is to improve their chosen properties, requires every time additional tests. In this study is considered the technical mean, which is a dumping freight wagon of the 418V type (Fig. 1). The main components of the analyzed system are: wagon box (1) mounted on the frame, two-axle bogies (2), the axes with mounted wheels (3) and a track (4), after which moves the considered wagon. Plating of the wagon box is constantly exposed to chemical interaction related to the harsh environment of the transported cargo and to mechanical influences associated mainly with the wrong process of loading and unloading of the wagon [1]. The mentioned groups of interactions could adversely affect the length of the life cycle of the wagon. Eliminating or reducing the listed interactions should allow to

extend the time of operation of the wagons, as well as reducing the costs of repairs. In the research project, realized by the team of investigators, is considered the idea of utilization the composite panels to cover the interior of the plating of the wagon box. The introduction to the wagon construction these changes forces conducting a series of strength tests regarding the modified system components. For this type of researches is necessary to know the maximal force with which the carried load acts on objects entered into the system. The analyzed force reaches its maximal value at the time when the freight wagon is moving, at the maximal permitted value of the speed, on the arc-shaped raceway. Therefore it was attempted to determine the maximal speed of movement of the wagon on the raceway in the form of an arc.

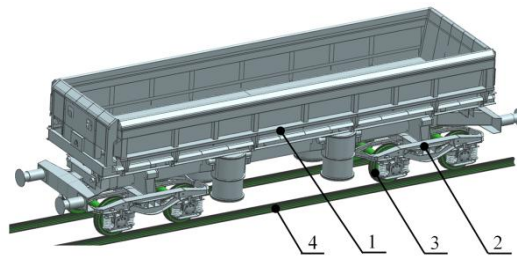


Figure 1. Object subjected to virtual investigations (freight wagon of the 418V type)

The considered object of investigations has the following characteristics: the length of 12,54 [m], width of 3.08 [m], height of 3.2 [m], wagon weight 27 000 [kg], loading capacity 31 [m³] payload 52 000 [kg].

2. Analysis of motion of the freight wagon

The first step of investigations of the freight wagon was to create a model prepared for motion simulation. For this purpose was used the “Motion Simulation” module of the system of the CAD / CAE / CAM class (Siemens PLM NX) [2,3]. The model, prepared to motion simulation, was created on the basis of a solid model, which imitates the geometrical form of the 418V dumping, freight wagon. The model preparation consisted of defining: the objects of the “link” type (representing the geometrical form of particular components of the wagon); the objects of the “joint” type (specifying possible ways of movement mating between objects of the “link” type by receiving a certain number of degrees of freedom); objects of the “connectors” type (defining the nature of the contact between the wheels of the wagon and the rails). During creating the model, prepared for motion simulation, the following assumptions were made:

- all objects of the “link” type are perfectly rigid - they do not undergo a deformation,
- geometric objects, being a part of a single object of the “link” type, do not change its position in relation to other objects belonging to the same object of the “link” type,

- assumed model of the track maps its ideal state of the geometric form without deformation resulting from the manufacturing process and exploitation,
- model of the track including its tilt,
- wagon moves independently on the track, without regarding the contact with other wagons or a locomotive,
- part of the track, which is a straight line, is designated to accelerate the wagon to the required speed value,
- main motion analysis is carried out on the part of the track in the form of an arc.

In the first developed model it was created 8 objects of the “link” type, 7 objects of the “joint” type and 16 objects of the “connectors” type. The first model, prepared to the motion simulation, contains the following groups of objects (Fig. 3). Objects of the “link” type:

- L_Wagon – representing the geometrical form of the wagon box, with a frame and all elements which, during the movement, do not change their position relative to each other,
- L_Tor – representing the geometrical form of the track on which moves the investigated wagon,
- L_Os_WP_1, L_Os_WP_2, L_Os_WT_3, L_Os_WT_4 – representing the geometrical form of particular axles with wheels,
- L_Wozek_P, L_Wozek_T – representing the geometrical form of two-axle bogies 25TNa.

Objects of the „joint” type:

- J_Fix (fixed type) – defining the behavior of the L_Tor object by limiting him 6 degrees of freedom (restrain),
- J_Os_1_P, J_Os_2_P, J_Os_3_T, J_Os_4_T (revolute type) – defining the possible move between the objects L_Os_WP_1, L_Os_WP_2 and L_Wozek_P and L_Os_WT_3, L_Os_WT_4 as well as L_Wozek_T by limiting three degrees of freedom associated with object translation and two degrees of freedom associated with object rotation (it provides the rotation of the bogie axis together with wheels in relation to the body of the bogie),
- J_Wozek_P-Wagon, J_Wozek_T-Wagon (revolute type) – defining the possible move between the objects L_Wozek_P, L_Wozek_T and L_Wagon (it provides the rotational move of bogies in relation to the wagon box).

Objects of the „connectors” type:

- G_Prosta_Koloi-osj – $i=1..8, j=1..4$ (3D contact type) – defining the nature of the 3D contact between the objects L_Os_WP_1, L_Os_WP_2, L_Os_WT_3, L_Os_WT_4 and L_Tor on a straight part of the track,
- G_Luk_Koloi-osj – $i=1..8, j=1..4$ (3D contact type) – defining the nature of the 3D contact between the objects L_Os_WP_1, L_Os_WP_2, L_Os_WT_3, L_Os_WT_4 and L_Tor on the section of track in the form of an arc.

In order to introduce the extortion in the analyzed system it was defined the object of the „driver” type, which was linked with the J_Os_1_P object of the „joint” type. This link allowed to apply the extortion force in the form of the angular velocity of the front axle of the wagon, on which are mounted wheels. Forced in this way rotational movement of the bogie axle, through the use of the objects of the 3D contact type between the track and wheels of the wagon, and the objects of the revolute type between the axles of the bogie and its body as well as the bogie body and the wagon box, is transferred into the linear movement of the whole wagon. The extortion, introduced to the system, is defined as follows (Fig. 2):

$$STEP(time, t_0, \omega_0, t_1, \omega_1), \quad (1)$$

where:

t_0 – the beginning of the time interval in which the rotational speed of the L_Os_WP_1 object reach the value ω_0 ,

t_1 – the end of the time interval in which the rotational speed of the L_Os_WP_1 object reach the value ω_1 .

Between the value of the rotational speed ω related with the L_Os_WP_1 object and the value of the linear speed V of a moving wagon is the following relationship:

$$V = \omega \cdot r, \quad (2)$$

where: r – the radius of the L_Os_WP_1 object in the place of a contact with the L_Tor object.

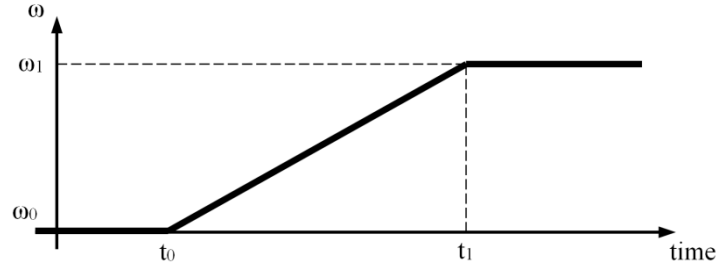


Figure 2. Graphical representation of the utilized extortion

To map the behavior of the wagon running on a trackway were created the objects of the 3D contact type. These objects characterize the way of mating between the wheels, included in the objects L_Os_WP_1, L_Os_WP_2, L_Os_WT_3, L_Os_WT_4 and rails belonging to the L_Tor object. It was assumed that the wheels with axles and rails are made of steel with the following basic parameters: density $7.8 \cdot 10^{-6}$ [kg/mm³], Young's modulus 210 000 [N/mm²], Poissons ratio 0.3. On the basis of the documentation it was assumed that the created contact will be characterized by the

following parameters: stiffness (k) 100000 [N/mm], stiffness exponent (m) 1.5, material damping (c_{max}) 50 [N*s/mm], penetration depth (g) 0.1 [mm], stiction velocity 0.1 [mm/s], friction velocity 10 [mm/s], static coefficient of friction 0.3, dynamic coefficient of friction 0.25. Basing on the presented parameters the model of 3D contact calculates the contact normal force (F_n). Normal force of the contact is expressed as the following relationship:

$$F_n = F_{ns} + F_{nd}, \quad (3)$$

$$F_{ns} = k \cdot g^m, \quad (4)$$

$$F_{nd} = c \cdot \frac{dg}{dt}, \quad (5)$$

$$c = STEP(g, 0, 0, g_{max}, c_{max}), \quad (6)$$

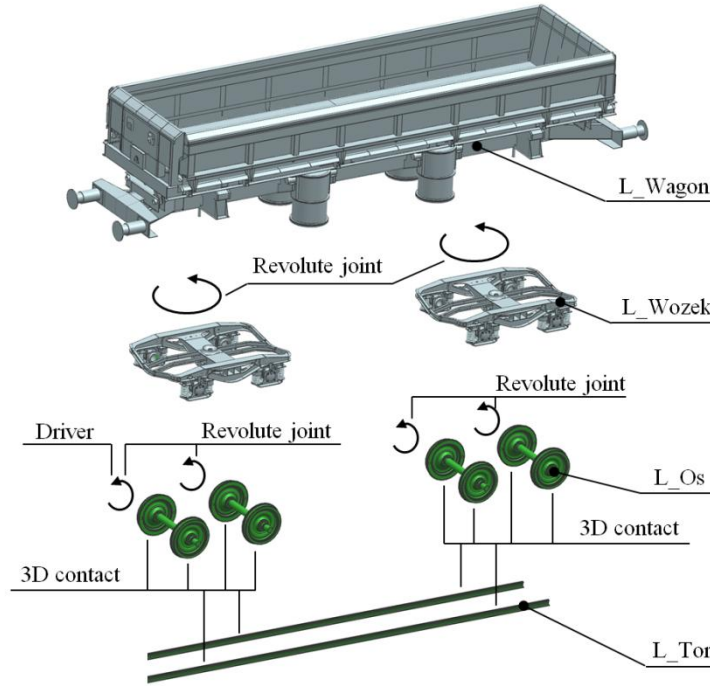


Figure 3. Model prepared for the motion simulation

In order to accelerate the wagon to the required speed it should be created a straight section of the track with the length of 200 [m] (Fig. 4). The length of the acceleration part of the track is resulted from the assumption that the tested object moves independently along a track-way, wherein is only driven the front axle of the wagon (to the desired speed and then it is kept constant value during the

motion on the arc-shaped raceway) according to the expression 1. Due to the occurrence of the slip between the wagon wheels and the rail, in the start-up phase, it was increased the static coefficient of friction and dynamic coefficient of friction to the value that guarantees the target speed in the assumed period of time. It should be noted that these coefficients were changed only on the straight part of the track, and the move on the most dangerous part of the railway in the form of an arc took place in accordance with the previously adopted values of the parameters of the o 3D contact object.

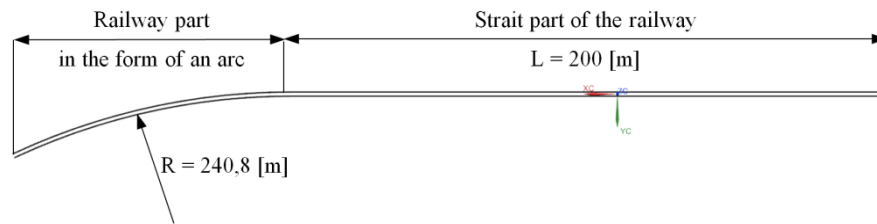


Figure 4. Graphical representation of the railway

Firstly it was realized the analysis of the movement of such elaborated model, without taking into account the carried load. The simulations were performed taking into account the motion parameters listed in Table 1.

Table 1. The list of values of parameters related with the extortion (wagon without the cargo)

V [km/h]	t_0 [s]	t_1 [s]	ω_0 [°/s]	ω_1 [°/s]	Simulation result
70	0	15	0	2422	Without derailment
80	0	15	0	2768	Without derailment
90	0	15	0	3114	Without derailment
95	0	15	0	3287	Without derailment
100	0	15	0	3460	Derailment

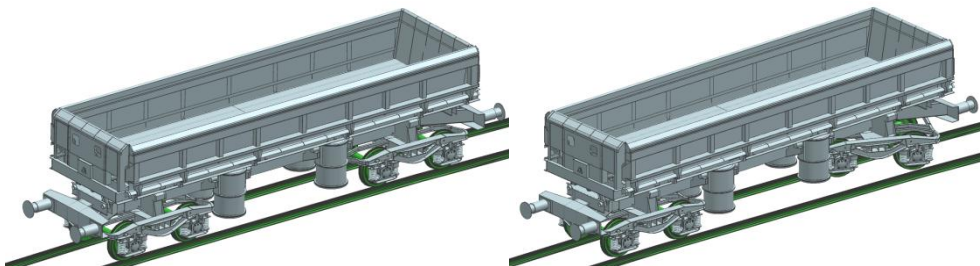


Figure 5. Exemplar results of the movement simulations of the wagon without the carried cargo:

a) without derailment, (b) the wagon derailment

Then it was analyzed the wagon model with the carried cargo. For this purpose the object L_Wagon has been modified and it was introduced the body with a volume corresponding to the volume of the cargo space, equal to 31 [m³]. It was assumed that the wagon is transported gravel with an average density of 1 650 [kg/m³]. It was obtained the value close to the maximal capacity of the wagon of 52 000 [kg]. For the model taking into account the carried load also was conducted a series of simulations, with regard to the parameters in Table 2.

Table. 2. The list of values of parameters related with the extortion (wagon with the cargo)

V [km/h]	t ₀ [s]	t ₁ [s]	ω ₀ [°/s]	ω ₁ [°/s]	Simulation result
70	0	15	0	2422	Without derailment
75	0	15	0	2595	Without derailment
77	0	15	0	2665	Without derailment
78	0	15	0	2768	Derailment

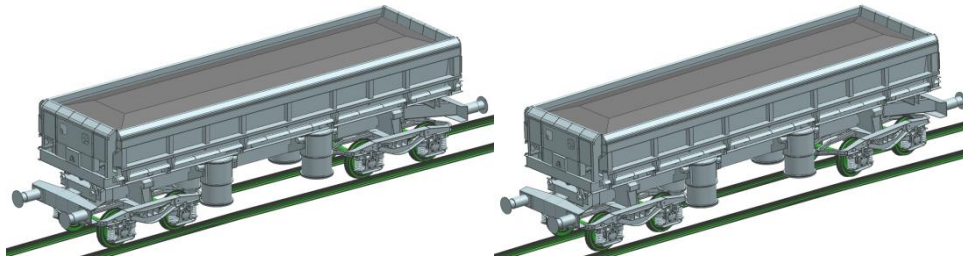


Figure 6. Exemplar results of the movement simulations of the wagon with the carried cargo:
a) without derailment, (b) the wagon derailment

The obtained results of the analysis, on the basis of visual evaluation of derailling of the wagon, let to eliminate the ranges of speed values above which explicitly comes to wagon derailment from the track. However, with regard to the positive results of the simulation it should be examined the level of safety of the wagon movement on the track in the form of an arc. Accordingly, in the work is assumed that in the cases in which there has been no explicit derailment, it should be calculated the index of derailment danger, shown in [4,5]. The authors of these works suggest that the safety of wagon movement on the track is dependent on the relationship of forces F_y/F_z (Fig. 7). Where F_y force is described as a lateral, guiding one and the F_z force is described as the force of a vertical pressure of a wheel on the rail. Due to the geometry of the rail head and existing components of friction forces between the wheel and the rail head, it is assumed that the movement of the wagon along the track is safe if the ratio $F_y/F_z < 0.78$. Whereas this value is exceeded, it should be checked the vertical displacement of the wagon wheel, which should not be greater than 5 [mm].

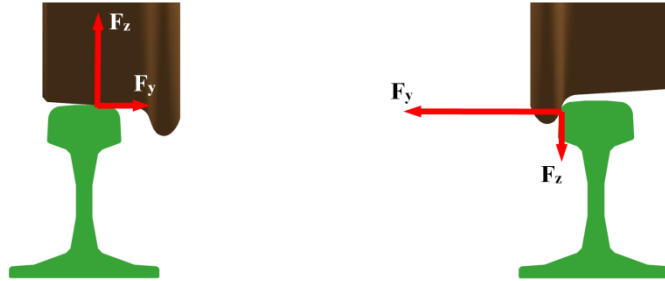


Figure 7. Graphical representation of the guiding force F_y and the force of vertical pressure of the wheel on the rail F_z : (a) safety case, (b) danger case [comp. 4]

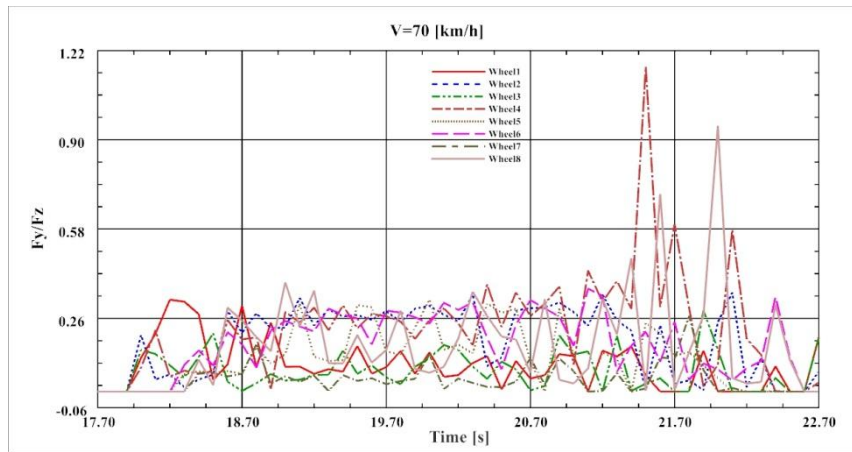


Figure 8. Values of the derailment index of the wagon at the speed equal to 70 [km/h]

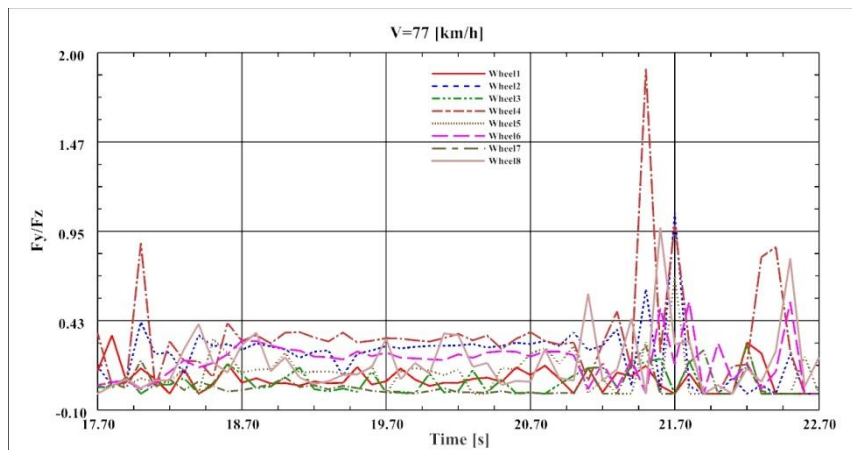


Figure 9. Values of the derailment index of the wagon at the speed equal to 77 [km/h]

Due to the considered, in this work, the area of the problem the more interesting object of investigations is the wagon carrying the cargo. Figure 7 and 8 show diagrams which present the derailment index for the wagon with the transported load. In both presented cases, the value of this index is greater than the limit value. It could be seen that in the case of a wagon moving at the speed of 70 [km/h], the maximal value of the index is 1.2 and relates to wheel4 moving on the outer rail on the arc (wheel1,3,5,7 - the wheels moving on the internal rail, wheel2, 4,6,8 - the wheels moving on the outer rail). When the speed increased to 77 [km/h] maximal value of the ratio has increased to approx. 1.9 and relates to the same wheel. In the next step the displacement characteristics of the axle with wheel4 was examined. Fig. 10 shows that the characteristics of the wheel4 is within the range of the allowable displacement in the vertical axis (value referred to the reference value equal to 634 [mm] in the absolute coordinate system).

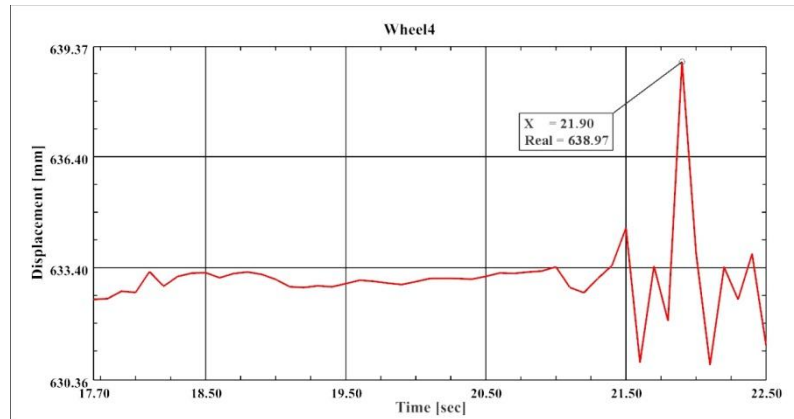


Figure 10. Displacement of the wheel4 in the vertical axis during the wagon movement on the arc at the speed equal to 77 [km/h]

On the basis of the two criteria it could be assumed that the maximal safe speed value at which moves the investigated wagon with the cargo, on the arc-shaped track, is 77 [km/h]. It should be noted however that in the case of analyzing the movement of a wagon moving at high velocities, besides to the phenomenon of climbing the wagon wheel on the rail head is also dangerous the phenomenon of detachment of the wheels of the wagon moving on the inner rail due to the occurrence of a centrifugal force. Therefore, in the work it was decided to examine the course of the value of the force F_z pressing the wagon to the rail. If the value of this force is equal to zero then the vertical movement of the wheels should be checked. In Figure 11 it could be seen that at approximately 22 second of the movement the force F_z is equal to zero. This means that the wheels wheel1,3,5,7 of the traveling wagon completely detached from the rail. This is illustrated in Fig. 12. The maximal displacement of the wheel in the vertical axis amounted to 25 [mm].

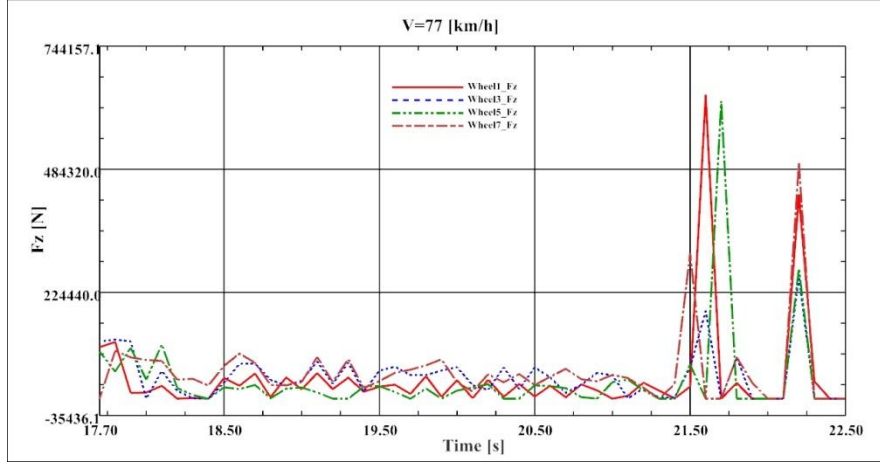


Figure 11. Course of variability of the pressing force F_z

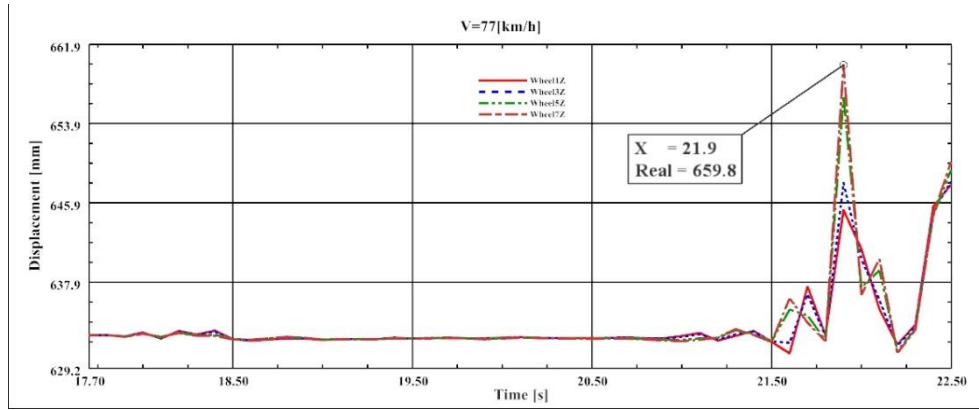


Figure 12. Vertical displacement of the wagon wheels

3. Modification of the model prepared for motion simulation

The next phase of the work included operations aimed at the detailing of the virtual model of the wagon movement on the trackway. For this purpose, the model prepared for motion simulation was complemented with the elastic elements. The introduced change forced also the remodeling of the same model. In the analyzed model was adopted an elastic element with a line characteristics:

$$F_s = k \cdot (x_1(t) - x_2(t)), \quad (7)$$

where: k – stiffness $1 \cdot 10^8 [\text{N/m}]$, $x_1(t)$, $x_2(t)$ – displacements of the ends of the spring as a function of time.

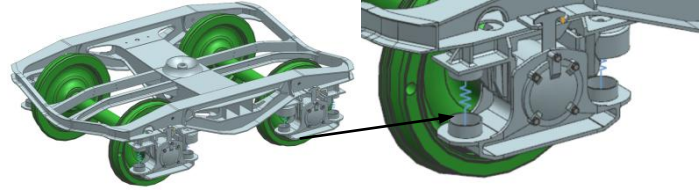


Figure 13. Introduction of elastic elements to the virtual model

For the modified wagon model, a cycle of motion simulation has been carried. Simulations were conducted in accordance with the previously described procedure for the speed values equal to 70 [km/h] - no derailment, 75 [km/h] - no derailment, 77 [km/h] - no derailment, 80 [km/h] - wagon derailment. Subsequently, the value of the wagon derailment index, at the maximal speed equal to 77 [km/h], has been determined. In the described case, the maximal value of the index amounted to 7. Accordingly, it was verified the vertical displacement of wheels which run on the outer rail. All values of vertical displacements of these wheels does not exceed the value of 5 [mm]. Then it was verified the variation of the pressing force F_z and the vertical displacements of all wheels. On the basis of Fig. 14 it could be concluded that the maximal vertical displacement of the wheels was 8 [mm] with respect to the initial displacement equal to 634 [mm] in the absolute coordinate system.

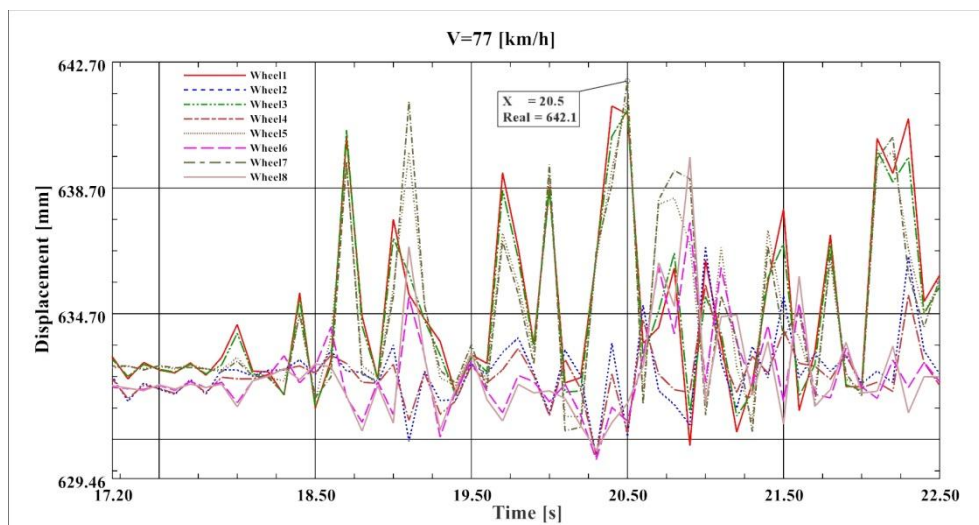


Figure 14. Vertical displacements of wagon wheels (detailed model)

4. Conclusions

As the result of conducted investigations was obtained the value of the safe speed movement of a wagon transported a cargo on the trackway equal to 77 [km/h]. The simplification, used in the work,

in the form of the lack of a trackway slope allows assume that the adopted model provides a margin of the safe speeds. As the result of model detailing it was obtained the model with lower values of vertical displacements of the wagon wheels, at the same speed of movement of the wagon on the track in the form of an arc. In order to obtain a proper fit of operation of the virtual model to the real object the research aimed at identifying the real object properties should be continued.

Acknowledgments

The work was carried out under the project number PBS2/A6/17/2013 realized as a part of the Applied Research Program, funded by the National Research and Development Centre.

References

- [1] Buchacz A., Baier A., Świder J., Jamroziak K., Majzner M., Żółkiewski S., Wróbel A.: Experimental Tests of Chosen Fibre-metal Laminates. Monograph 374. Silesian University of Technology Press, Gliwice 2012. ISBN 978-83-7335-936-9.
- [2] Gwiazda A., Herbuś K., Kost G., Ociepka P., Motion analysis of mechatronic equipment considering the example of the Stewart platform, Solid State Phenomena 220/221 (2015) 479-484..
- [3] Banaś W., Gwiazda A., Herbuś K., Kost G., Ociepka P., Reclik D., Analysis of the dynamic properties of the mechatronic integrator of control procedures of the vehicle driven by persons with disabilities, Solid State Phenomena 220/221 (2015) 3-8.
- [4] Matej, J.: Symulacyjna metoda oceny poziomu zagrożenia wykołaceniem wagonu towarowego na torze prostym. Przegląd Mechaniczny, Nr 1/2011, s. 20-25 (in Polish).
- [5] Dusza M., Zboiński K. Dokładne wyznaczanie prędkości krytycznej modelu pojazdu szynowego – porównanie metod. Czasopismo Techniczne. Mechanika, 109(14), str. 71-80, 2012 (in Polish).

Andrzej Buchacz, Professor: The Silesian University of Technology, The Faculty of Mechanical Engineering, The Institute of Engineering Processes Automation and Integrated Manufacturing Systems, 18A Konarskiego Street, 44-100 Gliwice, Poland (*andrzej.buchacz@polsl.pl*). The author gave a presentation of this paper during one of the conference sessions.

Andrzej Baier, Professor: The Silesian University of Technology, The Faculty of Mechanical Engineering, The Institute of Engineering Processes Automation and Integrated Manufacturing Systems, 18A Konarskiego Street, 44-100 Gliwice, Poland (*andrzej.baier@polsl.pl*).

Krzysztof Herbuś, Ph.D.: The Silesian University of Technology, The Faculty of Mechanical Engineering, The Institute of Engineering Processes Automation and Integrated Manufacturing Systems, 18A Konarskiego Street, 44-100 Gliwice, Poland (*krzysztof.herbus@polsl.pl*).

Michał Majzner, M.Sc. (Ph.D. student): The Silesian University of Technology, The Faculty of Mechanical Engineering, The Institute of Engineering Processes Automation and Integrated Manufacturing Systems, 18A Konarskiego Street, 44-100 Gliwice, Poland (*michal.majzner@polsl.pl*).

Piotr Ociepka, Ph.D.: The Silesian University of Technology, The Faculty of Mechanical Engineering, The Institute of Engineering Processes Automation and Integrated Manufacturing Systems, 18A Konarskiego Street, 44-100 Gliwice, Poland (*piotr.ociepka@polsl.pl*).

Negative elements optimization and realization in synthesis of discrete mechatronic systems (VIB151-15)

Andrzej Buchacz, Damian Gałęziowski

Abstract: In the paper, authors the known problem of vibration control, have studied in case of elements which can exhibits negative values and are applied to mechatronic discrete systems. Structures have been combined from piezo actuators, connected electric networks and mechanical discrete models. Depending on the phase of the synthesis process, chosen damping configuration of the piezo with the electric network, negative elements have been identified and described. Subsequently with the study on selection of corresponding negative stiffness and damping, presented in the graph form, optimal values for the systems can be read. Additionally, as the result limits and constrains in physical application and realization can be determined. The study has been done based on two degrees of freedom replacement model of cascade system.

1. Introduction

In general, the technological development results in the automation and robotisation of several different processes and productions in various kinds of industrial branches. Nowadays, all engineering works depends on the design that should correspond as much as possible to the real models. With help of the surrounding digitization, computer aided modeling, calculations, and smart materials, it's possible to determine new and consistently cheapest solutions for known physical problems. The unwanted effect of vibration which is related mainly with machines, devices creation, work or their usage in divers conditions, is also one of the most important problems. That is due to the influence for the durability, maintenance and costs it can generate. This means an optimization in the parameters of modeled systems, in the assumed simplification level, will lead to calculable benefits and advantages in the reality. As a consequence it will lead to the optimization of the costs in the fabrication and production of the proper goods.

In the paper, authors the shortly introduced problem of vibration control, have studied in case of elements that can exhibits negative values and have applied them to mechatronic systems that have to comply with given requirements in form of the resonant and antiresonant frequencies. These systems have been combined from piezoelectric stack actuators, electric external networks, mechanical discrete models and have been synthesized [1]. The usage of piezoelectric materials for vibration control is commonly known [2, 3]. With the semi-active damping method that utilize the negative

capacitance elements it's possible to improve damping performances of vibrating systems [3-5]. Following achievements [1, 3-5] authors investigated the possibilities of determination and usage of parameters that will lead to negative value elements in the considered structures, what has been introduced in [6]. Negative stiffness [7], or damping elements, which can be obtained from dimensionless transformation and retransformation of mechanical replacement models are leading to negative capacitance and resistance elements in considered final mechatronic structures.

The work extends and continues the works done in Gliwice Research Centre related with designing, analysis and synthesis of various types of mechanical and mechatronic vibration systems [1, 2, 6]. Based on last world-wide studies and achievements connected with negative value elements the work is giving a new approach to the problem of synthesis, going out of known frames. Negative capacitance [3-5], negative resistance [8, 9] connected within specific circuits might be new interesting solutions in vibration isolation area. Applying these achievements to the synthesis issue, it's possible to shorten design time for the new systems that should work under specific and required conditions and widen the field of practical application in vibration control area.

2. Negative elements in mechatronic discrete systems

Considered mechatronic systems in each case are excited by the force $F(t)$ and contain: mechanical part, piezo stack actuator connected to external electric network. Elements that can obtain negative values in these systems during solving the reverse task, have been introduced by the authors in [6]:

- in mechanical replacement model: stiffness and damping,
- in final mechatronic structure: negative capacitance and resistance.

All of them depends on the structure type, complexity of the system (number of degrees of freedom - DOF, piezo elements) and selected synthesis method. What is important, the ones related to mechanical replacement models, are used indirectly. This is connected with the algorithm of synthesis [6], that contains transformation to dimensionless model and retransformation to final mechatronic structure phases.

3. Key parameters identification and study

Due to complexity of the problem, the study has been done based on the cascade discrete mechanical replacement model with 2 DOF, received from distribution of the dynamical characteristics function $U(s)$ into continuous fractions, fig 1. The slowness function $U(s)$, has been written as:

$$U(s) = H \frac{d_l s^l + d_{l-2} s^{l-2} + \dots + d_0}{c_k s^k + c_{k-2} s^{k-2} + \dots + c_1 s}, \quad (1)$$

where: l – odd degree of numerator, k – degree of denominator, $l - k = 1$, H – any positive real number.

Dynamical equation of the systems, and further analysis is done in dimensionless time τ :

$$\tau = \omega_{1,2} t. \quad (2)$$

To transform the electric parameters that comes from piezo element characteristics from non-dimensional model to final mechatronic one, piezoelectric equation are used:

$$\sigma = K_E s - e E, \quad (3)$$

$$D = e s + \varepsilon_s E, \quad (4)$$

where: σ – mechanical stress, K_E – Young Modulus, s – mechanical strain, D – electrical displacement, ε_s – electrical permittivity, E – electrical field, e – piezoelectric constant.

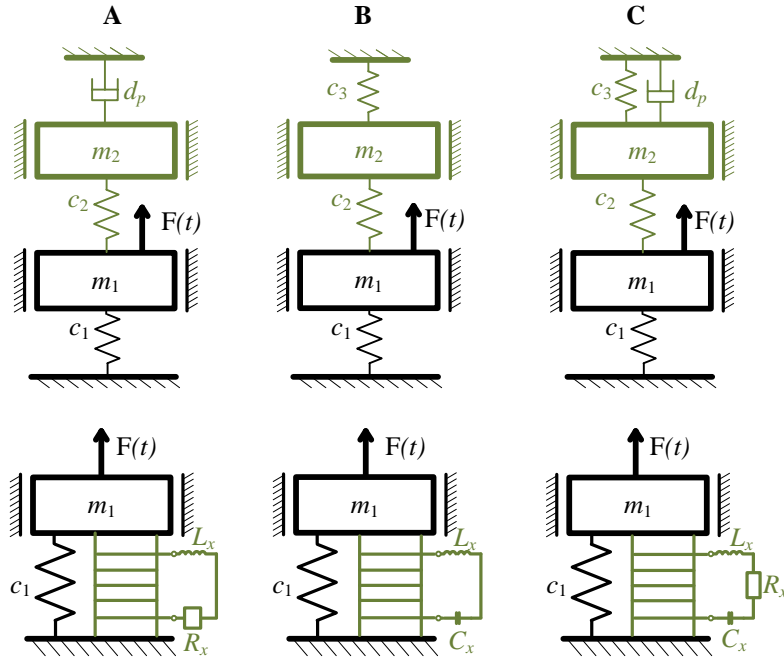


Figure 1. Mechanical replacement models with 2 DOF and their final mechatronic structures with piezo stack actuators

Synthesis process, while receiving the mechanical replacement model has been algorithmized. Key parameter during the distribution, is the stiffness c_1 which is the first element obtained from solving the reverse task.

This value impacts on the rest of the elements inside the mechanical replacement model and indirectly for connection of piezo with electric circuit. Following of (1), in general selection range of c_1 , is defined as:

$$\left(0, H \frac{d_0}{c_1}\right). \quad (5)$$

From the other side, parameters related with applied piezo stack actuator, has been limited to the capacitance C_{ps} . That is needed to calculate the values of corresponding elements in the connected external circuits: LRn , LCn , $LRCn$ (symbol n in written configuration types refers to negative values inside the network). The influence of the selection of both parameters that are leading to the optimal values and application constrains has been shown in next subsections.

3.1. LRn configuration

To obtain system represented in the fig. 1A, stiffness c_1 has to be equal to the upper limit (5). That generates in total the system with two inertial and stiffness elements in the mechanical replacement model. Here damping element d_p normally should be taken according equations:

$$d_p = 2hm_2, 0 < h < |\omega_{\min}|, |\omega_{\min}| \neq 0. \quad (6)$$

However to receive it negative, it has to be treated separately and the value of parameter h has to be taken out of the limits (6) and should be below the 0. That is generate after transformation and retransformation negative value of resistance R_x , which existence and usage in vibration damping was shown in [8, 9].

The impact of selection of d_p out of defined frames (6) for the resistance in the LR configuration R_{xLR} of considered systems has been presented in the fig 2.

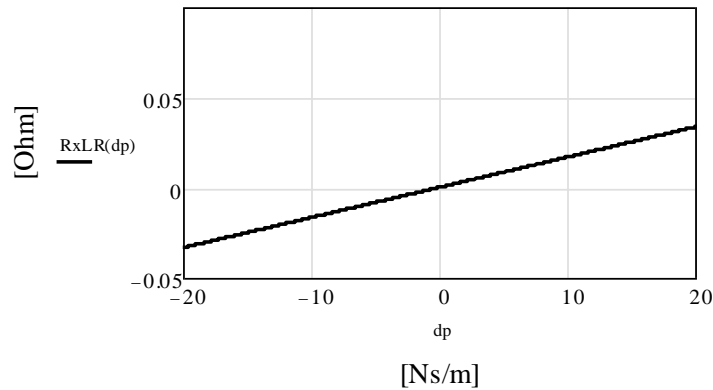


Figure 2. Resistance R_{xLR} in the electric circuit in the function of damping d_p

The capacitance C_{ps} of the piezo can get only positive values. This is related with the fact that this value is connected with applied stack actuator. However in the fig. 3 it has been shown the influence of C_{ps} for the values of the resistance R_x , written as:

$$R_x = \frac{d_p}{C_{ps}c_2}, \quad (7)$$

with positive and negative values of damping d_p in the mechanical replacement model.

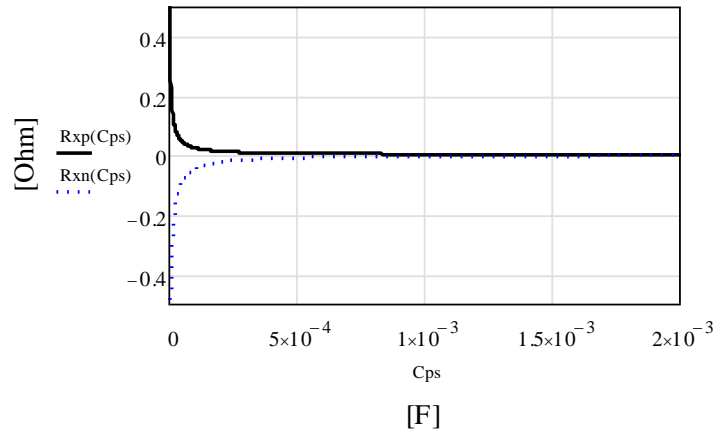


Figure 3. Resistance in the electric circuit in the function of damping, for: the positive value of d_p – R_{xp} , and negative value – R_{xn}

3.2. LCn configuration

The LCn , is one of the semi-active damping configuration of the system. Here the selection of c_1 , determines all parameters in mechanical replacement model and what is the most important impacts on appearance of additional c_3 stiffness in the system. Taking the value of c_1 out of required range (5), it's possible to determine negative values of stiffness c_3 , that with the stiffness c_2 determine the dimensionless parameter δ , which directly impacts on capacitance C_x in the external electric network:

$$\delta = \frac{c_3}{c_2}, \quad (8)$$

$$C_x = \frac{C_{ps}}{\delta}. \quad (9)$$

In the fig. 4 the impact of selection of c_1 to c_2 and c_3 stiffness has been highlighted. Then in the figure 5, behavior of the capacitance C_x .

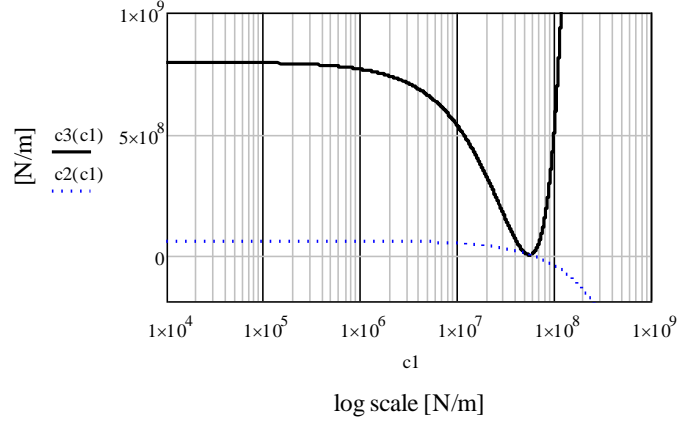


Figure 4. The influence of selection of c_1 to c_2 and c_3 stiffness

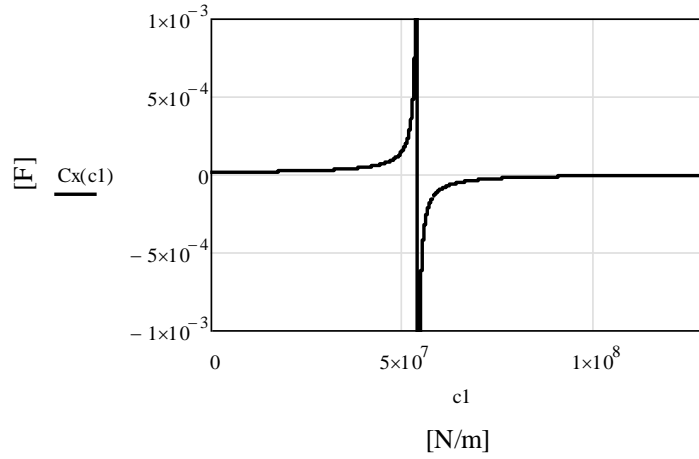


Figure 5. Capacitance C_x in the function of c_1 stiffness

In case of LCn system, selection of the c_1 , impacts also on inertial element m_2 . That's making indirect influence on external inductance L_x . To check that impact, following parameter λ is defined in the system as:

$$\lambda = \frac{\omega_1^2}{\omega_2^2}. \quad (10)$$

Based on (10), dynamical equations of the mechanical replacement model and transformations done according (2-4), the inductance L_x in electric network is written as:

$$L_x = \frac{\lambda}{C_{ps}\omega_l^2}. \quad (11)$$

Final dependence of the inductance L_x with constant C_{ps} , from selection of c_1 has been presented in the figure 6.

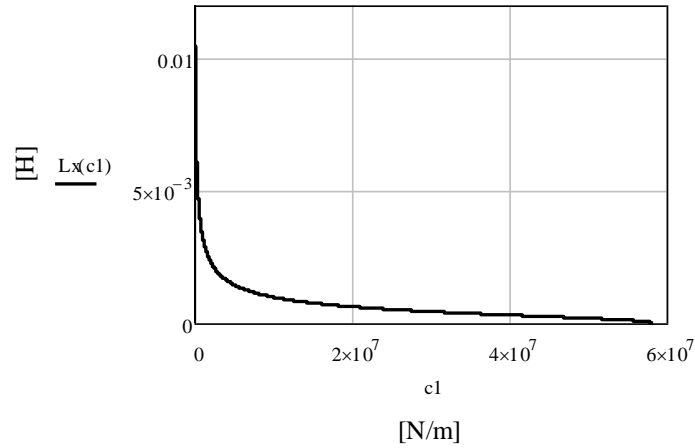


Figure 6. Dependence of L_x , from selection of the stiffness c_1

Increasing the value of capacitance C_{ps} with the selection of piezo type actuator, referring to the equation (11) is causing the decrease of the value of L_x in the system.

3.3. *LRCn* configuration

Relations between inductance L_x , capacitance C_x and the selection of c_1 , in case of the system *LRCn* are equal to *LCn* configuration. The difference is coming from additional damping element, which as opposed to *LRn* system is proportional to stiffness element:

$$d_p = \chi c_3, 0 < \chi < \frac{2}{\omega_{\max}}, \omega_{\max} \neq 0. \quad (12)$$

Therefore influence of c_1 to the external resistance R_x has been investigated and shown in the figure 7. The value is calculated following equation (7). Dependence of stiffness c_2 from c_1 is the same as in the figure 4.

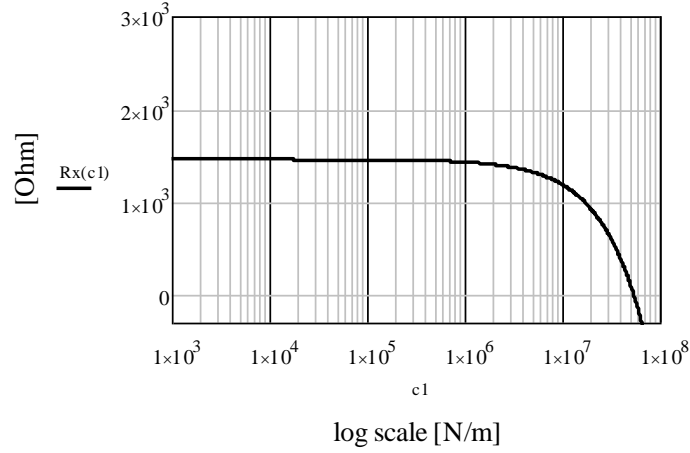


Figure 7. Resistance R_x in the external electric network in the function of c_1

4. Discussion for physical realization

From physical realization side, during synthesis of considered systems, and the first phase of creation of mechanical replacement model, selection of c_1 is the most important. As in case of LRn configuration it do not have the influence on the parameters of the systems, in case of LCn and $LRCn$ it has to be taken into consideration while designing of structures that has to comply with given resonant and antiresonant frequencies. However there are some constrains that comes from synthesis process. Taking the value out of required range (5) results in negative value of stiffness c_3 . Nonetheless this is realizable with the piezostack actuator connection with LCn or $LRCn$ system, as it is transformed to circuit with negative capacitance proposed in [3-5]. Taking the value too much from defined range out of upper limit (5), is causing the value of c_3 gets again positive value, but c_2 receives in the same time negative value, figure 8. That's out of defined frames of considered systems, which means systems with negative stiffness c_2 are not possible to be synthesized.

Another issue has been identified as damping, or resistance in LRn or $LRCn$ system. As in case of LRn , the value of damping has to be lower than zero from the definition, in case of $LRCn$ it can be as well but this is not a must. With the selection of c_1 , the value of d_p can be adjusted to negative value (figure 9) and used in the structure. The damping performance in each circumscribe case can be tuned or adjusted by the designer needs according presented elements, parameters related and their values.

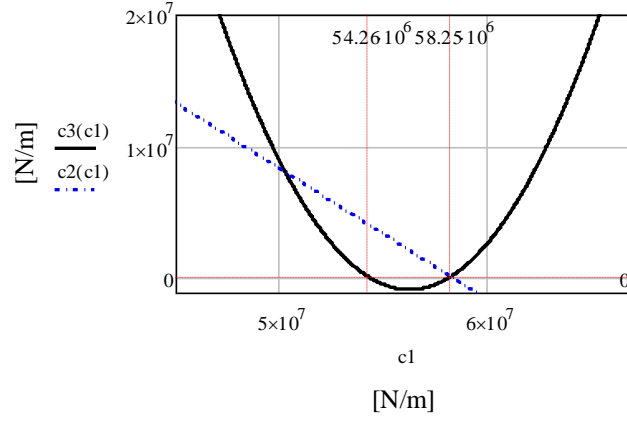


Figure 8. Limits in the selection of c_1 for c_2 and c_3

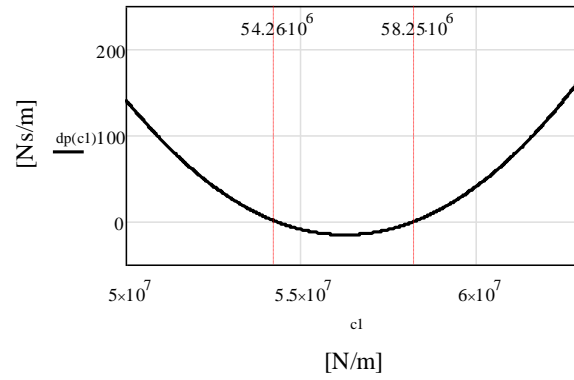


Figure 9. Damping d_p in the function of c_1

5. Conclusions

In the paper the negative elements and related most important parameters, to find optimal values while designing of mechatronic discrete vibrating systems, have been studied and presented. Physical realization constrains and range of the limits for described parameters following shown graphs can be read. The paper is the verification and extension of latest achievements related with synthesis of considered systems and usage of piezo and negative elements in vibration control. It is planned to study the problem in further works focusing for stability conditions, and do the investigation of usage directly the novel negative resistance isolators in vibration control.

Acknowledgments

This work has been conducted as a part of research project PBS2/A6/17/2013 supported by the National Centre for Research and Development in 2013-2016.

References

- [1] Białas K., Buchacz A., Gałęziowski D. Modelowanie dyskretnych układów mechatronicznych ze względu na funkcję tłumienia. *Modelowanie Inżynierskie*, 2013, t. 16, nr 47, 31-35.
- [2] Buchacz A., Płaczek M. Damping of mechanical vibrations using piezoelements, including influence of connection layer's properties on the dynamic characteristic. *Solid State Phenomena*, 2009, 147-149; 869-875.
- [3] Neubaer M., Oleskiewicz R., Popp K., Krzyzynski T. Optimization of damping and absorbing performance of shunted piezo elements utilizing negative capacitance, *Journal of sound and vibration*, 2006, Vol. 298, No 1-2, 84-107.
- [4] Fukada M., Date K., Kimura and others. Sound Isolation by Piezoelectric Polymer Films Connected to Negative Capacitance Circuits, *IEEE Transactions on Dielectrics and Electrical Insulation*, April 2004, Vol. 11, No. 2, 328-333.
- [5] Han X., Neubauer M., Wallaschek J. Improved piezoelectric switch shunt dumping technique using negative capacitance, *Journal of Sound and Vibration*, Volume 332, Issue 1, 2013, 7-16.
- [6] Buchacz A., Gałęziowski D. Designing of discrete mechatronic vibrating systems with negative value parameters, *Mechanical Systems and Signal Processing*, 2015, doi:10.1016/j.ymssp.2015.02.003.
- [7] Kashdan L., Conner Seepersad C., Haberman M., Wilson P.S. Design, fabrication, and evaluation of negative stiffness elements using SLS, *Rapid Prototyping Journal* 2012:18 Iss: 3, 194-200.
- [8] Yan B., Zhang X., Niu H. Design and test of a novel isolator with negative resistance electromagnetic shunt damping, *Smart Materials and Structures*, Vol. 21, No 3., 2012, ID035003.
- [9] Zhao J., Tang J. Amplifying damage signature in periodic structures using enhanced piezoelectric networking with negative resistance elements, *Journal of Intelligent Material Systems and Structures*, 2013, Vol. 24, No 13, 1613-1625.

Andrzej Buchacz, Professor PhD, DSc, Eng: Silesian University of Technology, Institute of Engineering Processes Automation and Integrated Manufacturing Systems, The Faculty of Mechanical Engineering, Konarskiego 18a Street, 44-100 Gliwice, Poland, (andrzej.buchacz@polsl.pl).

Damian Gałęziowski, PhD, Eng: Silesian University of Technology, Institute of Engineering Processes Automation and Integrated Manufacturing Systems, The Faculty of Mechanical Engineering, Konarskiego 18a Street, 44-100 Gliwice, Poland, (damian.galeziowski@gmail.com). The author gave a presentation of this paper during one of the conference sessions.

Two-axis mechanical vibration harvester (VIB176-15)

Vytautas Bučinskas, Andrius Dzedzickis, Nikolaj Šešok,
Ernestas Šutinys, Igor Iljin, Artur Kazickij

Abstract: Powering of various sensors and data transmitter in remote environment requires power supply from batteries or installed power lines. In case of autonomic devices this became technologically inconvenient and raises maintenance costs. Ability of utilize mechanical vibration for small-scale power generation is known, but there are many cases, when such devices are not available due to characteristics of vibration. Applications like railroad cargo wagon, having no electrical equipment, there is an excellent example of application of vibration harvester. Usually harvesters, used in industry, are tuned to certain frequency and serve as source of power for many sensor powering applications. In case of chaotic vibrations, especially low frequency chaotic vibration, taking place in the space, requires special solution. This paper proposes solution of two-axis harvester, operating as mechatronic system with two mechanical and two electrical degrees of freedom. Research of such harvester is done theoretically and experimentally. Theoretical research was performed using Simulink model, build for all 4 degrees of freedom in different physical domains using original methodology. Experimental research performed on special test piece, excited by dynamic vibrator, using real vibration data from wagon frame accelerations in the trip. Paper presents results of the research and comparison between theoretical and experimental research. Finally, conclusion on research and obtained results are drawn.

1. Introduction

Harvesting of mechanical energy there is well known and widely used process in small energy applications. It is necessary to state that mostly these devices are efficient in harmonic vibration cases and they are tuned to single frequency. Non-tuned harvesters still are under research and harvesting of energy from chaotic vibrations still is a challenge [1].

In XXI century technologies such as MEMS, MS and wireless systems, monitoring and supporting systems are increasingly penetrating to human's life. All these technologies requires source of energy, which typically are batteries of different kind. Significant amount of different batteries in these devices requires monitoring and change of these batteries on time. In order to make systems more reliable and free from taking care of these sources of energy, there are possible to use mechanical energy for fulfilling of such small energy needs [1-4].

Energy harvesting systems are known in nowadays life. They can supply energy in places where conventional batteries is inconvenient to use of one or another reason. Mechanical energy is widely

available in real life. Structural vibration of road from traffic, bridge vibration can be easily harvested and used for mili- and microwatt energy supply. Human body also generates certain amount of mechanical energy. For example, if one considers large networks of low powered sensors (such as those, which may be attached to a bridge as part of a structural health monitoring system) then one can envisage a scenario where energy harvesters are used to transfer the vibration energy of the bridge into electrical energy for the sensors. This would alleviate the need for batteries, which, in this scenario, would be difficult to replace. Low energy consumption devices are requested in the market and will be more requested in the future [2-6].

This paper is dedicated to some aspects of building wagon frame generated mechanical energy harvester, based on electromagnetic induction effect. Wagon frame motion has low frequency (<20 Hz) and chaotic directions. Classic vibration harvesters with low resonance frequency will have big mass and size, so there exist mechanical problem to build a sensitive dynamic system, consisting from high-frequency energy transforming systems and sensitive to low frequency mechanical system. In order to create a harvester system is necessary to research dynamical properties of such system. Research here is performed in few steps using dynamic and mathematical model of the system. Use of such model allows finding values of the system stiffness, damping ratio, which will allow maximize amount of generated power from railway wagon vibrations.

This paper is an attempt to create system for railway wagon sensor power feeding device, which can give autonomy for sensors and other information transmitting devices.

2. Theoretical research

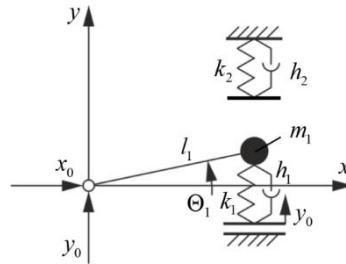


Figure 1. The horizontal pendulum revolves freely around suspension point.

The pendulum revolves freely around suspension point, which is excitation aroused by coordinates x_0 and y_0 (see figure 1). At a time, when the pendulum touches the lower spring, the system get kinematic excitation y_0 from the spring in vertical direction. The movements of the pendulum are described by coordinate θ_1 .

The coordinates of the pendulum concentrated mass:

$$x_1 = x_0 + l_1 \cdot \cos \theta_1; \quad y_1 = y_0 + l_1 \cdot \sin \theta_1. \quad (1)$$

The systems kinematic energy is:

$$T = \frac{1}{2} (m_1 \dot{x}_1^2 + m_1 \dot{y}_1^2) \quad (2)$$

Considering that x_0 , y_0 and θ_1 is function of time:

$$\dot{x}_1 = \dot{x}_0 - l_1 \dot{\theta}_1 \cdot \sin \theta_1; \quad \dot{y}_1 = \dot{y}_0 + l_1 \dot{\theta}_1 \cdot \cos \theta_1. \quad (3)$$

In this way, the kinematic energy expression, which is applied to any state of the system:

$$T = \frac{1}{2} m_1 (\dot{x}_0 - l_1 \dot{\theta}_1 \cdot \sin \theta_1)^2 + \frac{1}{2} m_1 (\dot{y}_0 + l_1 \dot{\theta}_1 \cdot \cos \theta_1)^2. \quad (4)$$

The Lagrange equation of second type created for each state of the system is:

$$\frac{d}{dt} \left(\frac{\partial T}{\partial \dot{\theta}_1} \right) - \frac{\partial T}{\partial \theta_1} + \frac{\partial \phi}{\partial \theta_1} + \frac{\partial \Pi}{\partial \theta_1} = 0. \quad (5)$$

There are three state of the object in question:

- 1) The horizontal pendulum lying on the bottom affixed springs (see figure 2):

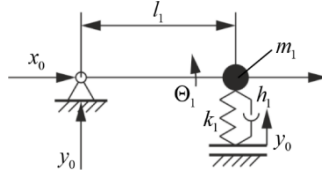


Figure 2. The horizontal pendulum in the lower position.

In this case, the potential energy is:

$$\Pi = m_1 g y_1 + \frac{1}{2} k_1 \Delta_{11}^2; \quad \Delta_{11} = l_1 \cdot \theta_1 - y_0 \quad (6)$$

Dissipation function is:

$$\phi = \frac{1}{2} r_1 \dot{\theta}_1^2 + \frac{1}{2} h_1 \dot{\Delta}_{11}^2; \quad \dot{\Delta}_{11} = l_1 \cdot \dot{\theta}_1 - \dot{y}_0 \quad (7)$$

In this case, the equation corresponds to this condition:

$$m_1 l_1^2 \ddot{\theta}_1 - m_1 l_1 \ddot{x}_0 \cdot \sin \theta_1 + m_1 l_1 \ddot{y}_0 \cdot \cos \theta_1 + (r_1 + h_1 l_1^2) \dot{\theta}_1 + m_1 g l_1 \cdot \cos \theta_1 + k_1 l_1^2 \theta_1 = . \quad (8)$$

$$= k_1 l_1 y_0 + h_1 l_1 \dot{y}_0$$

Or taking into consideration that $\sin\theta_I=\theta_I$; $\cos\theta_I=1$.

$$m_1 l_1^2 \ddot{\theta}_1 - m_1 l_1 \ddot{x}_0 \theta_1 + m_1 l_1 \ddot{y}_0 + (r_1 + h_1 l_1^2) \cdot \dot{\theta}_1 + m_1 g l_1 + k_1 l_1^2 \theta_1 = k_1 l_1 y_0 + h_1 l_1 \dot{y}_0. \quad (9)$$

2) Horizontal pendulum raised up from the rest position, as shown in figure 3:

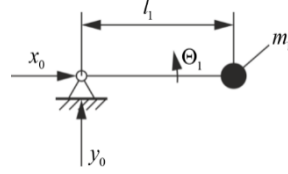


Figure 3. The horizontal pendulum intermediate position.

In this case, the potential energy is:

$$\Pi = m_1 g y_1 \quad (10)$$

Dissipation function is:

$$\phi = \frac{1}{2} r_1 \dot{\theta}_1^2 \quad (11)$$

This state of taking $\sin\theta_I=\theta_I$; $\cos\theta_I=1$ corresponds to equation:

$$m_1 l_1^2 \ddot{\theta}_1 - m_1 l_1 \ddot{x}_0 \theta_1 + m_1 l_1 \ddot{y}_0 + r_1 \dot{\theta}_1 + m_1 g l_1 = 0 \quad (12)$$

3) Horizontal pendulum raised to the top for some reason and it compresses on the top the protective spring (see figure 4).

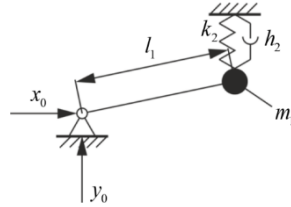


Figure 4. The horizontal pendulum in the top position.

The potential energy is:

$$\Pi = m_1 g y_1 + \frac{1}{2} k_2 \Delta_{12}^2; \Delta_{12} = l_1 \theta_1 \quad (13)$$

Dissipation function is:

$$\phi = \frac{1}{2} r_1 \dot{\theta}_1^2 + \frac{1}{2} h_2 \dot{\Delta}_{12}^2; \dot{\Delta}_{12} = l_1 \dot{\theta}_1 \quad (14)$$

Corresponding to the equation:

$$m_1 l_1^2 \ddot{\theta}_1 - m_1 l_1 \ddot{x}_0 \theta_1 + m_1 l_1 \ddot{y}_0 + (r_1 + h_2 l_1^2) \dot{\theta}_1 + m_1 g l_1 + k_2 l_1^2 \theta_1 = 0 \quad (15)$$

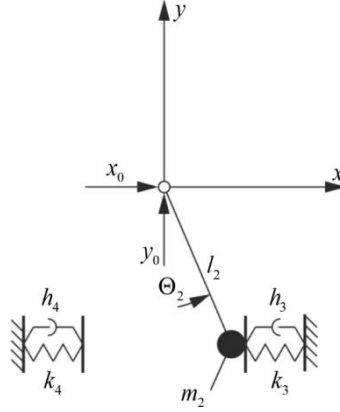


Figure 5. The vertical pendulum revolves freely around suspension point.

The pendulum revolves freely around suspension point, which transmits excitation along coordinates x_0 and y_0 (see figure 5). The movement of the pendulum describes the coordinate θ_2 .

The vertical pendulum additionally has two springs on the left and on the right, whose function - to prevent the pendulum to rotate too much. (The pendulum is applicable structural limitations).

It is three condition of systems:

- 1) – Pendulum is in contact with a spring on the right side;
- 2) – Pendulum isn't in contact with a spring;
- 3) – Pendulum is in contact with a spring on the left side.

The coordinates of the pendulum concentrated mass:

$$x_2 = x_0 + l_2 \cdot \sin \theta_2; y_2 = y_0 - l_2 \cdot \cos \theta_2 \quad (16)$$

The systems kinematic energy is:

$$T = \frac{1}{2} (m_2 \dot{x}_2^2 + m_2 \dot{y}_2^2) \quad (17)$$

Considering that x_0 , y_0 and θ_2 is function of time:

$$\dot{x}_2 = \dot{x}_0 + l_2 \dot{\theta}_2 \cdot \cos \theta_2; \dot{y}_2 = \dot{y}_0 + l_2 \dot{\theta}_2 \cdot \sin \theta_2 \quad (18)$$

Then kinematic energy expression any state of the system is:

$$T = \frac{1}{2} m_2 (\dot{x}_0 + l_2 \dot{\theta}_2 \cdot \cos \theta_2)^2 + \frac{1}{2} m_2 (\dot{y}_0 + l_2 \dot{\theta}_2 \cdot \sin \theta_2)^2 \quad (19)$$

The Lagrange equation of second type created for each state of the system is:

$$\frac{d}{dt} \left(\frac{\partial T}{\partial \dot{\theta}_2} \right) - \frac{\partial T}{\partial \theta_2} + \frac{\partial \phi}{\partial \dot{\theta}_2} + \frac{\partial \Pi}{\partial \theta_2} = 0 \quad (20)$$

1 condition

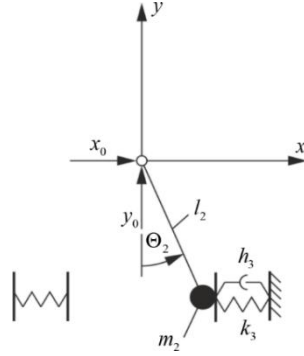


Figure 6. The vertical pendulum is in contact with a spring on the right side.

Then vertical pendulum is in contact with a spring on the right side (see figure 6), the equation of potential energy is:

$$\Pi = m_2 g y_2 + \frac{1}{2} k_3 \Delta_{21}^2 \quad (21)$$

Where $y_2 = y_0 - l_2 \cos \theta_2$; $\Delta_{21} = l_2 \theta_2$.

$$\Pi = m_2 g y_0 - m_2 g l_2 \cdot \cos \theta_2 + \frac{1}{2} k_3 (l_2 \theta_2)^2 \quad (22)$$

Dissipation function is:

$$\phi = \frac{1}{2} r_2 \dot{\theta}_2^2 + \frac{1}{2} h_3 \dot{\Delta}_{21}^2 \quad (23)$$

Where $\dot{\Delta}_{21} = l_2 \dot{\theta}_2$.

$$\phi = \frac{1}{2} r_2 \dot{\theta}_2^2 + \frac{1}{2} h_3 (l_2 \dot{\theta}_2)^2 \quad (24)$$

Corresponding to the equation:

$$m_2 l_2 \ddot{\theta}_2 \cdot \cos \theta_2 + m_2 l_2 \ddot{\theta}_2 \cdot \sin \theta_2 + m_2 l_2^2 \ddot{\theta}_2 + m_2 g l_2 \cdot \sin \theta_2 + r_2 \dot{\theta}_2 + h_3 l_2^2 \dot{\theta}_2 + k_3 l_2^2 \theta_2 = 0 \quad (25)$$

or taking everywhere $\sin \theta_2 = \theta_2$; $\cos \theta_2 = 1$:

$$m_2 l_2 \ddot{x}_0 + m_2 l_2 \ddot{y}_0 \theta_2 + m_2 l_2^2 \ddot{\theta}_2 + m_2 g l_2 \theta_2 + r_2 \dot{\theta}_2 + h_3 l_2^2 \dot{\theta}_2 + k_3 l_2^2 \theta_2 = 0. \quad (26)$$

2 condition

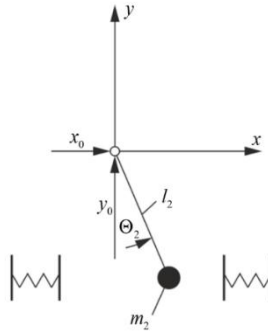


Figure 7. The vertical pendulum is not in contact with a spring.

Then vertical pendulum is not in contact with a spring (see figure 7), the equation of potential energy is:

$$\Pi = m_2 g y_2 = m_2 g y_0 - m_2 g l_2 \cdot \cos \theta_2 \quad (27)$$

Dissipation function is:

$$\phi = \frac{1}{2} r_2 \dot{\theta}_2^2 \quad (28)$$

This state of taking $\sin \theta_2 = \theta_2$; $\cos \theta_2 = 1$ corresponds to equation:

$$m_2 l_2 \ddot{x}_0 + m_2 l_2 \ddot{y}_0 \theta_2 + m_2 l_2^2 \ddot{\theta}_2 + m_2 g l_2 \theta_2 + r_2 \dot{\theta}_2 = 0 \quad (29)$$

3 condition

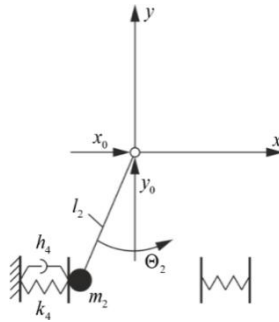


Figure 8. The vertical pendulum is in contact with a spring on the left side.

Then vertical pendulum is in contact with a spring on the left side (see figure 8), the equation of potential energy is:

$$\Pi = m_2 g y_2 + \frac{1}{2} k_4 \Delta_{22}^2 \quad (30)$$

Where $\Delta_{22} = l_2 \theta_2$.

$$\Pi = m_2 g y_0 - m_2 g l_2 \cdot \cos \theta_2 + \frac{1}{2} k_4 (l_2 \theta_2)^2 \quad (31)$$

Dissipation function is:

$$\phi = \frac{1}{2} r_2 \dot{\theta}_2^2 + \frac{1}{2} h_4 \dot{\Delta}_{22}^2 \quad (32)$$

Where $\dot{\Delta}_{22} = l_2 \dot{\theta}_2$.

Corresponding to the equation:

$$m_2 l_2 \ddot{x}_0 \cdot \cos \theta_2 + m_2 l_2 \ddot{y}_0 \cdot \sin \theta_2 + m_2 l_2^2 \ddot{\theta}_2 + m_2 g l_2 \cdot \sin \theta_2 + r_2 \dot{\theta}_2 + h_4 l_2^2 \dot{\theta}_2 + k_4 l_2^2 \theta_2 = 0 \quad (33)$$

or taking everywhere $\sin \theta_2 = \theta_2$; $\cos \theta_2 = 1$:

$$m_2 l_2 \ddot{x}_0 + m_2 l_2 \ddot{y}_0 \theta_2 + m_2 l_2^2 \ddot{\theta}_2 + m_2 g l_2 \theta_2 + r_2 \dot{\theta}_2 + h_4 l_2^2 \dot{\theta}_2 + k_4 l_2^2 \theta_2 = 0. \quad (34)$$

The horizontal pendulum transition conditions from one state to another.

The starting position of the pendulum is horizontal (see figure 2). The mass of pendulum m_1 lying on the spring (k_1 , h_1). Whereas the lower spring (k_1 , h_1) bottom induction operates in a known oscillation y_0 , is switching to another condition (the horizontal pendulum intermediate position see figure 3) consider the condition (the lower spring not compressed and in which case it is disable with):

$$L_1 \cdot \theta_1 - y_0 > 0.$$

The transition to another condition (the pendulum rise to achieve and presses the spring (k_2 , h_2) see figure 4) consider the condition:

$$\theta_1 > \theta_{1\max}$$

It is assumed that $\theta_{1\max} = 10^\circ$.

The vertical pendulum slides mode condition during oscillation from one state to another.

The starting position of the pendulum is vertical. The main condition: the pendulum oscillate between springs k_3 , h_3 and k_4 , h_4 but not touch them (see figure 7).

If pendulum moves in direction of coordinate θ_2 and oscillation angle is bigger than θ_{2max} , spring is compressed k_3 , h_3 (see figure 6). In this why condition of changing state is:

$$\theta_2 > \theta_{2max}$$

When pendulum moves in direction opposite to coordinate θ_2 and pendulum reaches spring k_4 , h_4 (see figure 8), condition of changing system state is:

$$\theta_2 < \theta_{2max}$$

Accredited, that $\theta_{2max}=10^\circ$; $\theta_{2max}=-10^\circ$.

Equations are solved using methodology described in [7]. Equations are rewritten in operational form after that in virtual MatLab environment is created SIMULINK model. In both system states excitation coordinates is x_0 , y_0 .

The system of horizontal pendulum is described by coordinate θ_1 . Pendulum oscillation speed is $\dot{\theta}_1$ kinetic energy of horizontal pendulum is T_1 :

$$T_1 = \frac{m_1 \cdot L_1^2 \cdot \dot{\theta}_1^2}{2}. \quad (35)$$

System of vertical pendulum is described by coordinate θ_2 . Oscillation speed is $\dot{\theta}_2$ kinetic energy of vertical pendulum T_2 :

$$T_2 = \frac{m_2 \cdot L_2^2 \cdot \dot{\theta}_2^2}{2}. \quad (36)$$

Simplified schematic of energy harvester with horizontal pendulum and harvester with vertical pendulum is presented in figures 9 and 10.

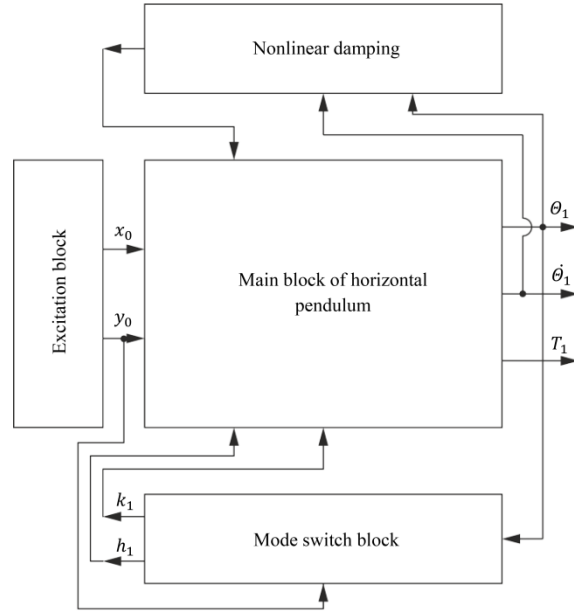


Figure 9. The simplified block diagram of horizontal vibration harvester.

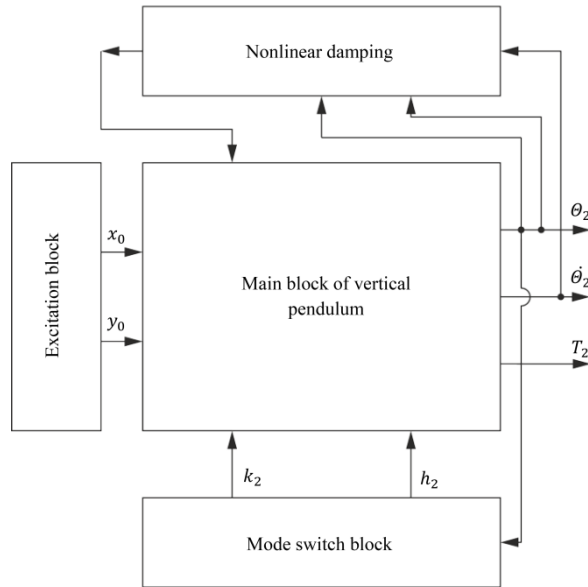


Figure 10. The simplified block diagram of vertical vibration harvester.

Electromagnet, which is used in our system, creates nonlinear coefficients of resistance. $r_1 = f(\theta_1; \dot{\theta}_1)$ and $r_2 = f(\theta_2; \dot{\theta}_2)$. In simplified diagrams this coefficients are represented by nonlinear damping blocks.

3. Results of research

In order to determine optimal parameters of pendulum it was decided to change oscillating mass m and coefficient of stiffness k . For the experiment were randomly selected free different masses ($m_1=0,040\text{kg}$; $m_2=0,030\text{kg}$; $m_3=0,020\text{kg}$) and free coefficients of stiffness ($k_1=5000\text{kg}$; $k_2=10000\text{kg}$; $k_3=20000\text{kg}$). Using different masses and coefficients of stiffness were created 9 combinations for calculations: m_1k_1 ; m_2k_1 ; m_3k_1 ; m_1k_2 ; m_2k_2 ; m_3k_2 ; m_1k_3 ; m_2k_3 ; m_3k_3 . The Bests result are obtained solving combination m_1k_3 , this results are represented in figures 11 and 12.

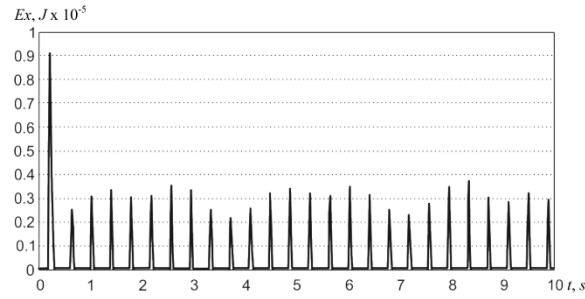


Figure 11. Dependency of kinetic energy in respect to time.

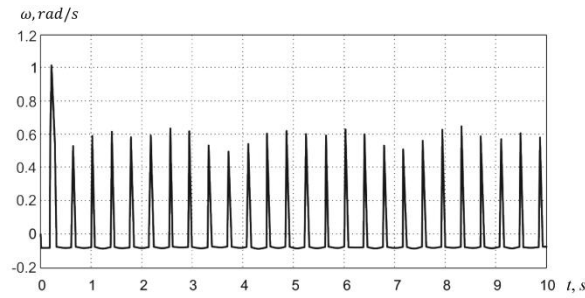


Figure 12. The horizontal pendulum angular velocity dependence of time.

4. Conclusions

Performed theoretical research and modelling of horizontal and vertical pendulum of two axis harvester behavior from kinematic excitation brings interesting and useful results. These pendulums can be excited from movement of real transport mean suspension parts, railroad wagon bogie frame,

for example. Such pendulum system can realize movement of wagon for energy harvesting in efficient way. Given results allows drawing these conclusions:

- system efficiently excited from existing movement of railway wagon frame and bogie;
- amplitudes of excitation allows to harvest few miliwatts of electrical energy on coil;
- proposed model is useful for such system analysis and definition of parameters.

References

- [1] Paradiso, J.A. 2005. Energy scavenging for mobile and wireless electronics. *Technology Media Laboratory* 4, 1 (2011), p. 312–318.
- [2] Kazickij, A., Bučinskas, V., Šutinys, E. The research of stiffness characteristics of active elements of harvester. *Electrical, Electronic and Information Sciences (eStream)* (2015), 1–4.
- [3] Kazickij, A., Bučinskas, V., Šešok, N., Iljin, I., Subačius, R., Bureika, G., Dzedzickis, A. Research on implementation of harvester on the cargo wagon. *Transport problems* (2015), 247–256.
- [4] Roundy, S., Wright P.K., Rabaey J. A study of low level vibrations as a power source for wireless sensor nodes. *Computer Communications* 26 (2003), 1131–1144.
- [5] Bučinskas, V., Šutinys, E., Augustaitis, V.K. Experimental research of steel rope integrity problem. *Journal of vibroengineering* 13, 2 (2011), p. 312–318.
- [6] Lourier, A.I. Analytical mechanics. State publishing house of physical-mathematical literature. Moscow, 1961, 824 p. (in Russian).
- [7] Augustaitis, V.K., Gichan, V., Sheshok, N., Iljin, I. Computer-aided generation of equations and structural diagrams for simulation of linear stationary mechanical dynamic systems. *Mechanika* 17, (2011), 255–263.

Vytautas Bučinskas, Professor: Vilnius gediminas technical university, Basanaviciaus 28, LT03224, Vilnius, LITHUANIA (vytautas.bucinskas@vgtu.lt), the author presented this work at the conference.

Andrius Dzedzickis, M.Sc. (Ph.D. student): Vilnius gediminas technical university, Basanaviciaus 28, LT03224, Vilnius, LITHUANIA (andrius.dzedzickis@vgtu.lt).

Nikolaj Šešok, Associate Professor: Vilnius gediminas technical university, Basanaviciaus 28, LT03224, Vilnius, LITHUANIA (nikolaj.sesok@vgtu.lt).

Ernestas Šutinys, Associate Professor: Vilnius gediminas technical university, Basanaviciaus 28, LT03224, Vilnius, LITHUANIA (ernestas.sutinys@vgtu.lt).

Igor Iljin, Associate Professor: Vilnius gediminas technical university, Basanaviciaus 28, LT03224, Vilnius, LITHUANIA (igor.iljin@vgtu.lt).

Artur Kazickij, B.A. (M.Sc. student): Vilnius gediminas technical university, Basanaviciaus 28, LT03224, Vilnius, LITHUANIA (artur.kazickij@vgtu.lt).

Analysis of vibrations of a cable-pulley system using the absolute nodal coordinate formulation

(VIB086-15)

Radek Bulín, Michal Hajžman, Pavel Polach

Abstract: Cable vibrations can have an important effect on the motion of a whole mechanical system and therefore it is reasonable to investigate the dynamic behaviour of such systems including these structural parts. This paper deals with the application of the absolute nodal coordinate formulation (ANCF) used for the modelling of a system composed of a cable, a pulley, a motor with prescribed motion and another rigid body, which is driven by the motor with the cable. The ANCF was chosen as a suitable approach that can allow to consider detailed interaction of a cable and a pulley with its nonlinear behaviour. The ANCF uses absolute positions of nodes (reference vectors) and slopes (reference vector derivations) as the set of nodal coordinates. An in-house modelling tool in the MATLAB system was created based on the proposed modelling methodology and the vibrations of the cable during the motion of the whole system was studied with respect to different parameters. The calculated results were compared with the measured results during real experiments.

1. Introduction

There exist various machines and mechanisms, which are composed of the cables or wires as driving elements. The motion control of such mechanical systems can be affected by undesirable vibration of the flexible cable elements. Therefore, detailed modelling of such systems is an actual problem in nonlinear dynamics.

Ways of the cable modelling can be divided into several groups based on complexity. The simplest way how to incorporate cables in the equations of motion of a mechanism is the force representation of a cable (e.g. [5]), where the inertia of cables is negligible with respect to the other parts. The cable is represented by the force dependent on the cable deformation and its stiffness and damping properties. A more accurate approach is based on the representation of the cable by a point-mass model (e.g. [6]). In order to represent also bending behaviour of cables their discretization using the finite segment method [10] or so called rigid finite elements [11] is possible. Other more complex approaches can utilize nonlinear 3D finite elements [3] or can employ elements based on the absolute nodal coordinate formulation (ANCF) [10].

This paper deals with the application of the ANCF used for the modelling of a system composed of a cable, a pulley, a motor with prescribed motion and another rigid body, which is driven by the motor with the cable. An in-house modelling tool in the MATLAB system was created based on the proposed modelling methodology and the vibrations of the cable during the motion of the whole system was studied with respect to different parameters. The calculated results were compared with the measured results during real experiments.

2. ANCF cable model

A planar ANCF beam element of length l with two nodes (see figure 1) will be briefly introduced in this section. Global position $\mathbf{r} = [r_x, r_y]^T$ of an arbitrary beam point determined by parameter p can be written as

$$\mathbf{r}(p) = \mathbf{S}(p)\mathbf{e}, \quad \mathbf{e} = [e_1 \ e_2 \ \dots \ e_8]^T, \quad (1)$$

where $\mathbf{S} \in \mathbb{R}^{2,8}$ is a global shape function matrix, \mathbf{e} is a vector of element nodal coordinates and $p \in (0, l)$ is a parameter of a curve.

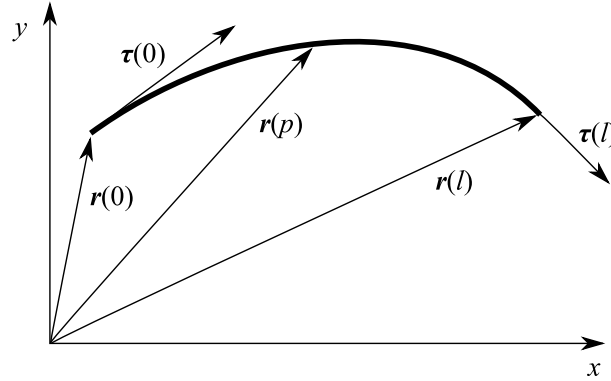


Figure 1. ANCF planar beam.

Standard procedures (e.g. the Lagrange equations or the principle of virtual work) can be used in order to derive a mathematical model of the planar ANCF beam element. Kinetic energy of the element with material density ρ is

$$E_k = \frac{1}{2} \int_0^l \rho A \dot{\mathbf{r}}^T \dot{\mathbf{r}} dp = \frac{1}{2} \dot{\mathbf{e}}^T \int_0^l \rho A \mathbf{S}^T \mathbf{S} dp \dot{\mathbf{e}} = \frac{1}{2} \dot{\mathbf{e}}^T \mathbf{M}_e \dot{\mathbf{e}}, \quad (2)$$

where \mathbf{M}_e is the element mass matrix.

Strain energy E_p of the element is used for the derivation of elastic forces in the ANCF beam model and the form of an adopted elasticity model determines the complexity of

the whole model. In [1], there are several approaches, which employ the separation of the strain energy of longitudinal deformation E_{pl} and the strain energy of transverse (bending) deformation E_{pt} as

$$E_p = E_{pl} + E_{pt} = \frac{1}{2} \int_0^l EA \varepsilon^2 dp + \int_0^l EI \kappa^2 dp, \quad (3)$$

where E is Young modulus, A is the area of the cross-section and I is the second moment of the area about a transverse axis. The possible models are then classified according to the expressions for longitudinal strain ε and curvature κ . General expressions for these quantities are

$$\varepsilon = \frac{1}{2}(\mathbf{r}'^T \mathbf{r}' - 1), \quad \kappa = \left| \frac{d^2 \mathbf{r}}{ds^2} \right|, \quad (4)$$

where s is the parameter of a curve. Berzeri and Shabana [1] introduced several suitable models for both longitudinal and transverse elastic forces, whereas the formulation denoted L2T2 is employed in this paper in order to investigate the cable-pulley interaction.

The whole model of the ANCF planar beam element [1] is of the form

$$\mathbf{M}_e \ddot{\mathbf{e}} + \mathbf{K}_e(\mathbf{e})\mathbf{e} = \mathbf{Q}_{ek} \quad (5)$$

and is characterized by constant mass matrix \mathbf{M}_e , strongly nonlinear stiffness matrix $\mathbf{K}_e(\mathbf{e})$ derived using the strain energy and by vector of external forces \mathbf{Q}_{ek} . The assembling of a discretized flexible body (i.e. fibre, cable) model is straightforward and can be extended by a suitable model of viscous forces.

3. Contact forces between a cable and a pulley

The presented cable model can be combined with the models of other bodies. The pulley is modelled as a rigid body with one degree of freedom (rotation), the fibre is modelled as a deformable body and it is discretized using the ANCF method to n elements. During the interaction of these two bodies, the contact forces arise not only in element nodes and the contact forces are distributed along the length of the contact arc. Therefore k points, which correspond with the Gauss-Legendre integration points, are determined on each element ($k = 5$ was used in this work). The contact forces are then evaluated for each of these point. Let us have element e ($e = 1, \dots, n$) and point i ($i = 1, \dots, k$). In each time step, the contact variables for each cable point are determined. The normal and friction forces can be evaluated and then a Gauss-Legendre quadrature is used to obtain the vector of generalized contact forces.

3.1. Contact kinematics

Few contact variables, which are used in contact force models, are introduced. When each cable contact point i interacts with the pulley for the first time, new stiction point i_{st} is defined on the pulley. The initial position of stiction point i_{st} is the same as the position of contact point i . During the simulation, the position of these two points is not equal, because contact point i is rigidly attached to the cable and stiction point i_{st} moves with the pulley. The position of the contact and stiction point can be defined by angles α_i and $\alpha_{i,st}$, respectively. Then the radial penetration δ_{ei} is defined as

$$\delta_{ei} = R - |\mathbf{r}_i - \mathbf{r}_0|, \quad (6)$$

where R is the pulley radius, \mathbf{r}_i is the position of contact point i of the cable (defined in equation (1)) and \mathbf{r}_0 is the absolute position of the pulley center. The tangential displacement of the contact point with respect to the stiction point is defined as

$$s_{ei} = R(\alpha_i - \alpha_{i,st}). \quad (7)$$

Penetration velocity $\dot{\delta}_{ei}$ and tangential velocity \dot{s}_{ei} are

$$\dot{\delta}_{ei} = -\dot{\mathbf{r}}_i^T \mathbf{n} \quad \dot{s}_{ei} = -\dot{\mathbf{r}}_i^T \mathbf{t} - R\omega, \quad (8)$$

where \mathbf{n} and \mathbf{t} are normal and tangent vectors to the pulley surface at the contact point.

3.2. Normal contact force model

The well-known normal contact force formula was introduced by Hertz [2]. This model is based on the theory of elasticity and describes a force between two perfectly flexible solids with frictionless surfaces. The Hertz law can be expressed as

$$F_{Nei} = K\delta_{ei}^n, \quad (9)$$

where K is the contact stiffness and n is the positive exponent, which reflects the shape of contact bodies. This basic contact force model does not consider the dissipation of energy during contact, therefore more complex models were developed. Hunt-Crossley's model of the normal contact force [2]

$$F_{Nei} = K\delta_{ei}^n(1 + D\dot{\delta}_{ei}), \quad (10)$$

where D is the damping factor, was proposed as a more complex modelling approach. It is based on a simple dissipation model, where the damping coefficient is dependent on the penetration. The resultant normal contact force vector is defined as $\mathbf{F}_{Nei} = F_{Nei}\mathbf{n}$.

3.3. Friction force model

The friction forces must be also added to the interaction model. At first, friction force model based on Threlfall model [2] were tested. It is formed by equation

$$F_{Tei} = c_f F_N \left(1 - e^{-3(\dot{s}_{ei}/v_r)} \right), \quad (11)$$

where c_f is a friction coefficient, v_r is a small characteristic relative tangential velocity. This friction model is easy to implement, but it does not describe the stiction phenomenon very well. Better stiction friction model can be found in [7]. This model uses two separate tangential force models, one for stiction force and one for sliding force and was tested in this paper. The resultant friction contact force vector is defined as $\mathbf{F}_{Tei} = F_{Tei} \mathbf{t}$.

4. Whole multibody model

The cable model can be combined with the models of other flexible or rigid bodies and with the model of kinematic joints. Due to the usage of absolute displacements as nodal coordinates it is easy to define the kinematic constraint equations such as revolute or translational joints. The constraints between the chosen coordinates can be written using the vector notation

$$\Phi(\mathbf{q}, t) = \mathbf{0} \quad (12)$$

and for the use in equations of motion it must be differentiated to obtain the Jacobian matrix

$$\Phi_q = \frac{\partial \Phi}{\partial \mathbf{q}} = \left[\frac{\partial \Phi_i}{\partial q_j} \right], \quad i = 1, 2, \dots, m, \quad j = 1, 2, \dots, n, \quad (13)$$

where m is the number of constraints and n is the number of dependent coordinates. After the introduction of vector of Lagrange multipliers $\boldsymbol{\lambda}$ the whole system of equations, which fully describe the problem of the coupled system of flexible and rigid bodies, can be written in the matrix form

$$\begin{bmatrix} \mathbf{M} & \Phi_q^T \\ \Phi_q & \mathbf{0} \end{bmatrix} \begin{bmatrix} \ddot{\mathbf{q}} \\ -\boldsymbol{\lambda} \end{bmatrix} = \begin{bmatrix} \mathbf{g}(\mathbf{q}, \dot{\mathbf{q}}, t) \\ \boldsymbol{\gamma}(\mathbf{q}, \dot{\mathbf{q}}, t) \end{bmatrix} = \begin{bmatrix} \mathbf{Q}_k - \mathbf{B}(\dot{\mathbf{q}}, \mathbf{q})\dot{\mathbf{q}} - \mathbf{K}(\mathbf{q})\mathbf{q} \\ \boldsymbol{\gamma}(\mathbf{q}, \dot{\mathbf{q}}, t) \end{bmatrix}. \quad (14)$$

Generally, vector $\mathbf{g}(\mathbf{q}, \dot{\mathbf{q}}, t)$ contains the sum of all generalized, potential and dissipative forces and appropriate other derivatives of a kinetic energy, while vector $\boldsymbol{\gamma}(\mathbf{q}, \dot{\mathbf{q}}, t)$ follows from the differentiation of the constraint equations (see [10]). The approaches to the numerical solution of equation (14) used practically in this paper are summarized in [4].

5. Application

Experimental measurements focused on the investigation of the fibre behaviour were performed on an assembled weigh-fibre-pulley-drive mechanical system (see figure 2), which was described e.g. in [8, 9]. A carbon fibre with a silicone coating is driven with one drive and it is led over a pulley. The fibre length is 1.82 meters (fibre weight is 4.95 grams), the pulley diameter is 80 millimetres. At the drive the fibre is fixed on a force gauge. In the other end of the fibre there is a prism-shaped steel weight (weight of 5.035 kilograms in this case), which moves in a prismatic linkage on an inclined plane. Drive excitation signals can be of a rectangular, a trapezoidal and a quasi-sinusoidal shape and there is a possibility of variation of a signal rate. The amplitudes of the drive displacements are up to 90 millimetres. In the case presented in this paper the weight position angle α is 30 degrees and the pulley-fibre angle φ is 150 degrees and it is changing during the motion.

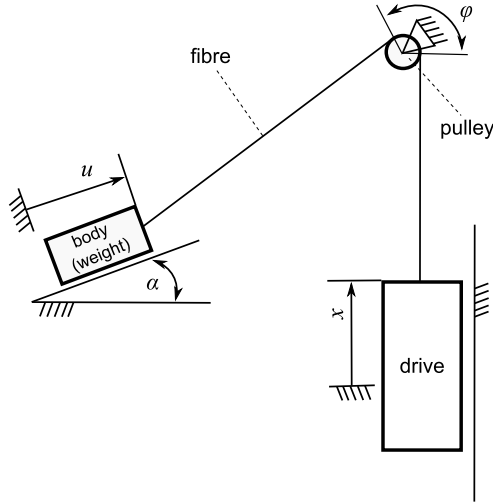


Figure 2. Scheme of the testing mechanical system composed of a drive, a pulley, a weight and a cable.

The particular signal defining the motion of the drive is in figure 3 together with the measured position of the weight with respect to time. The measured motion of the drive served as an input signal (kinematic excitation) for the numerical simulations. Chosen calculated dynamic response of the weight using complex cable-pulley interaction based on ANCF beam elements is shown in figure 4.

In order to study the complex behaviour of the cable during the motion, figure 5 shows

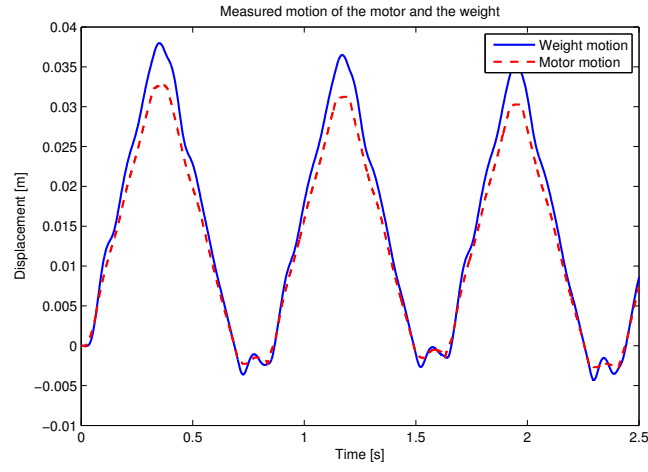


Figure 3. Measured motion of the drive and the weight during the experiment.

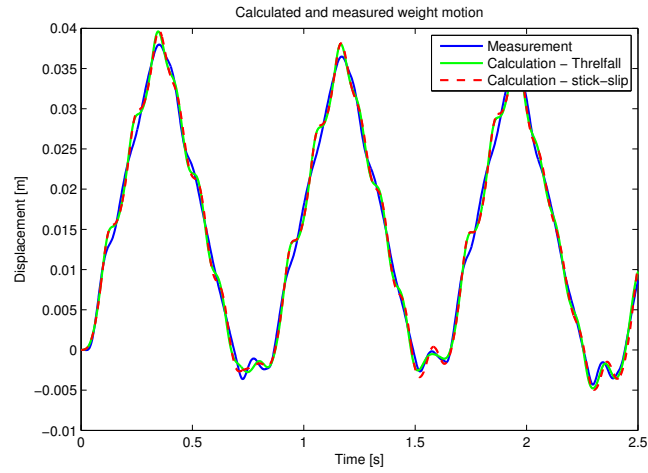


Figure 4. Measured and calculated motion of the weight for two different friction models.

time history of the transversal motion of the chosen node between the pulley and the drive. This motion characterized transversal vibration of the cable which could be the problem during the motion control of accurate mechanisms. Such character of the motion can be seen also in figure 6, where the real trajectory of one chosen node between the pulley and the weight is shown for two different friction models. Interesting information can be obtained

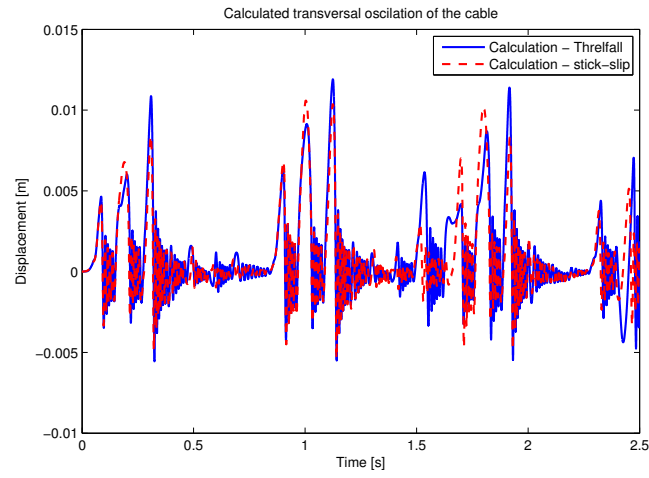


Figure 5. Calculated transversal vibration in a chosen node of the cable between the pulley and the drive.

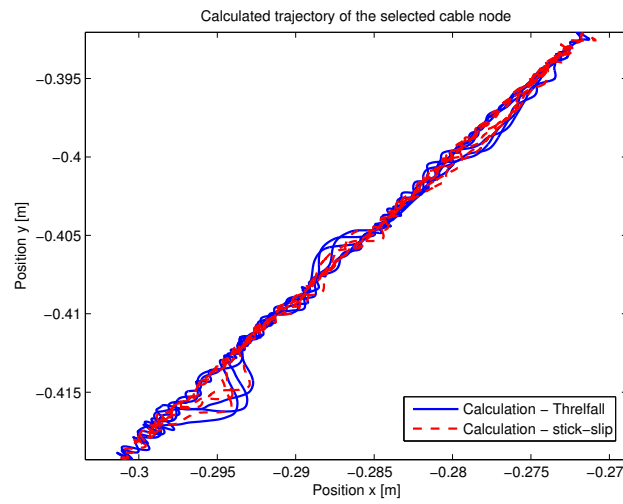


Figure 6. Calculated trajectory of a chosen node of the cable between the pulley and the weight.

also from the parametric studies combined with state space plots for the motion of chosen nodes (figure 7).

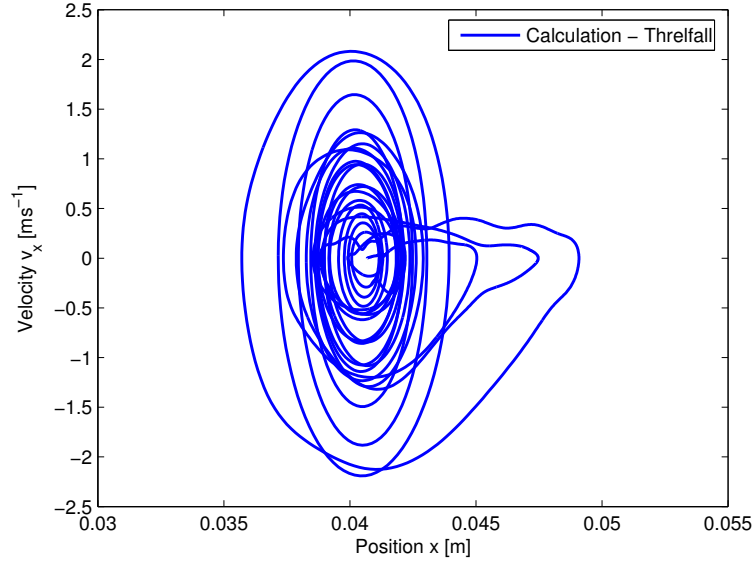


Figure 7. State space trajectory of a chosen node of the cable.

6. Conclusions

The beam based on the absolute nodal coordinate formulation was used for the modelling of cables, which could interact with pulleys or sheaves and demonstrate interesting nonlinear behaviour. The cable-pulley interaction was studied by the weight-fibre-pulley-drive system with prescribed kinematic excitation of the drive. Similar problem was also addressed e.g. in [7] but the contribution of this paper is in the comparison with experimental results measured on the real mechanical system and the focus on the transversal vibration.

Acknowledgments

The authors have been supported by project No. 15-20134S of the Czech Science Foundation entitled “Multi-level Light Mechanisms with Active Structures”. The first author was supported by the project LO1506 of the Czech Ministry of Education, Youth and Sports.

References

- [1] BERZERI, M., AND SHABANA, A. Development of simple models for elastic forces in the absolute nodal co-ordinate formulation. *Journal of Sound and Vibration* 235 (2000), 539–565.
- [2] FLORES, P., AMBRÓSIO, J., CLARO, J., AND LANKARANI, H. Influence of the contact-impact force model on the dynamic response of multi-body systems. *Proceedings of the*

IMechE, Part K: J. Multi-body Dynamics 220, 1 (2006), 21–34.

- [3] FREIRE, A., AND NEGRÃO, J. Nonlinear dynamics of highly flexible partially collapsed structures. *C.A. Mota Soares et al. (Eds.) Proceedings of III European Conference on Computational Mechanics, Solids, Structures and Coupled Problems in Engineering* (2006).
- [4] HAJŽMAN, M., AND POLACH, P. Application of stabilization techniques in the dynamic analysis of multibody systems. *Applied and Computational Mechanics* 1, 2 (2007), 479–488.
- [5] HAJŽMAN, M., AND POLACH, P. Modelling of cables for application in cable-based manipulators design. *J.-C. Samin, P. Fisette (Eds.) Proceedings ECCOMAS Thematic Conference Multibody Dynamics* (2011).
- [6] KAMMAN, J., AND HUSTON, R. Multibody dynamics modeling of variable length cable systems. *Multibody System Dynamics* 5 (2001), 211–221.
- [7] LUGRÍS, U., ESCALONA, J., DOPICO, D., AND CUADRADO, J. Efficient and accurate simulation of the rope-sheave interaction in weight-lifting machines. *Proceedings of the Institution of Mechanical Engineers, Part K: Journal of Multi-body Dynamics* 225, 4 (2011), 331–343.
- [8] POLACH, P., HAJŽMAN, M., VÁCLAVÍK, J., ŠIKA, Z., AND SVATOŠ, P. Model parameters influence of a simple mechanical system with fibre and pulley with respect to experimental measurements. *Z. Terze, M. Vrdoljak (Eds.) Proceedings of ECCOMAS Thematic Conference Multibody Dynamics* (2013).
- [9] POLACH, P., HAJŽMAN, M., VÁCLAVÍK, J., ŠIKA, Z., AND VALÁŠEK, M. Investigation of a laboratory mechanical system with fibre and pulley. *International Journal of Dynamics and Control* 3, 1 (2015), 78–86.
- [10] SHABANA, A. Flexible multibody dynamics: Review of past and recent developments. *Multibody System Dynamics* 1 (1997), 189–222.
- [11] WITTBRODT, E., ADAMIEC-WÓJCIK, I., AND WOJCIECH, S. *Dynamics of Flexible Multibody Systems. Rigid Finite Element Method*. Springer, Berlin, 2006.

Radek Bulín, Ing. (Ph.D. student): European Centre of Excellence, NTIS - New Technologies for Information Society, Faculty of Applied Sciences, University of West Bohemia, Univerzitni 8, 306 14 Pilsen, Czech Republic (rbulin@ntis.zcu.cz). The author gave a presentation of this paper during one of the conference sessions.

Michal Hajžman, Ing., Ph.D.: European Centre of Excellence, NTIS - New Technologies for Information Society, Faculty of Applied Sciences, University of West Bohemia, Univerzitni 8, 306 14 Pilsen, Czech Republic (mhajzman@kme.zcu.cz).

Pavel Polach, Ing., Dr.: European Centre of Excellence, NTIS - New Technologies for Information Society, Faculty of Applied Sciences, University of West Bohemia, Univerzitni 8, 306 14 Pilsen, Czech Republic (ppolach@ntis.zcu.cz).

Robotic automation of the turbo-propeller engine blade grinding process (MTR091-15)

Andrzej Burghardt, Dariusz Szybicki, Piotr Gierlak, Krzysztof Kurc,
Magdalena Muszyńska

Abstract: This paper proposes a robotic automation system for the grinding of turbo-propeller engine compressor vanes. This proprietary conceptual solution includes a data acquisition system (a robotic 3D scanner), a neural control system and a robot which executes the grinding process using force control. The proposed solution has been verified on real-life components.

1. Introduction

The continuous development of a sensory and actuation system allows the extension of the useful range of robotic systems into new areas of technology. The development of industrial robotics focuses mainly on applications that require a high level of process-robot interaction. This includes the blade or vane grinding process, where varying allowances must be removed. The key driver behind this development (with the minimization of human labor costs aside) is to improve the levels of safety and repeatability of product manufacture.

The available references provide noteworthy works from two companies: AV&R Automation of Canada and JOT Automation of Finland. Moreover, the issue of blade and vane grinding and polishing by a Yamaha robot is considered in [2]. An interesting approach to the problem is demonstrated with an extensive ABB robotic station in [3]. The results of investigations into the aspects of force distribution, tool wearability and allowance removal during robotic processing are discussed in [4, 5]. The technology-related topics are largely confidential corporate information; hence the number of works published on this matter is very low.

2. Genesis of the problem

Blades, vanes or airfoils are components of turbine engines, installed therein in cascades. The airfoil form allows conversion of the energy of the passing fluid into mechanical energy. In reverse applications of that solution, the airfoils allow conversion of mechanical energy into the kinetic energy of the passing medium, as used in compressors, for example. The main users of currently manufactured blades and vanes are the aerospace and power engineering sectors. There are a number of blade airfoil manufacturing technologies: from the most advanced, such as single-crystal casting, through CNC machining to electrochemical machining, a technique which has been used for decades.

Electrochemical airfoil forming is economically viable; however, the technology is sensitive to a number of factors that affect the processing parameters, e.g. temperature, electrical current value, gap clearance, etc. The resulting unique airfoils require a manual grinding process, which must be undertaken for every single piece produced, culminating in final polishing.

The solution presented herein has been delivered for, on request of and in cooperation with Pratt & Whitney Rzeszów. It is a proposal for the automation of the blade/vane airfoil grinding process. Airfoil grinding is a repetitive and tiresome process which demands high manual skills, and thus it is fit for robotization or automation. Moreover, the solution discussed herein will markedly improve occupational hygiene and safety in the work environment, while reducing the number of defects by improving the finished product quality through elimination of the human factor (stress, fatigue and other errors) from the process.

3. Process robotization

A blade from the Pratt & Whitney PT6 engine was selected as an example of the type requiring the grinding process to be performed with robotic automation.

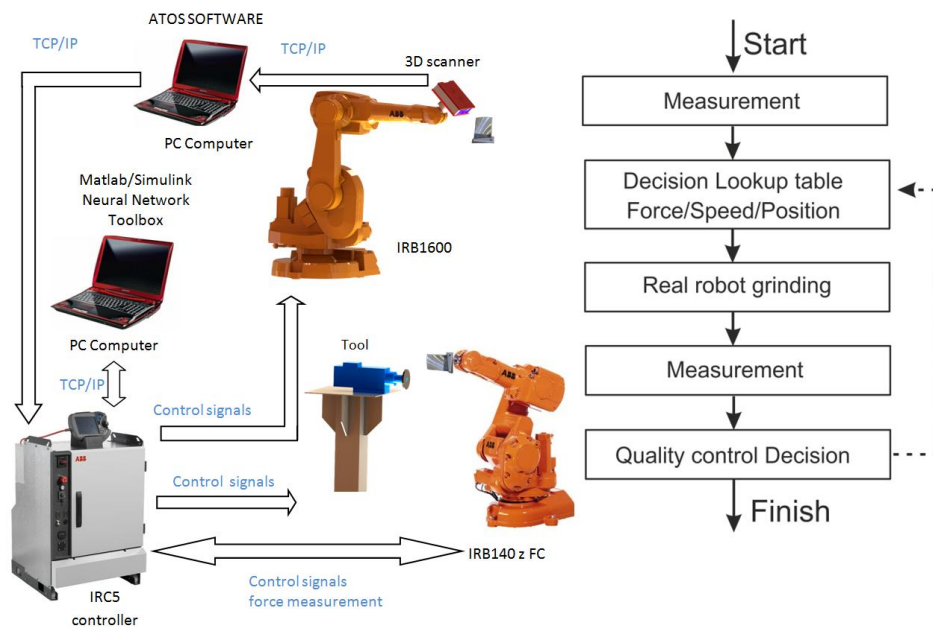


Figure 1. Diagram of the robotic processing station.

The proposed robotic station will comprise an IRB 140 robot for processed component handling, a grinding tool, and an IRB 1600 robot with a 3D scanning head. The measurement system cooperates with the ATOS Professional software to exchange data with the robot controller (IRC5) over the TCP/IP protocol. The RobotWare robotic controller software assures control over both robots, and also features a force control functionality.

The processing parameter (pressure force) variable is determined by a neural network. Based on a set of data produced from a number of test trials, the FVRL neural network makes decisions depending on the information fed back from the measurement system. The final force value, determined by the neural network, is transmitted to the IRC5 controller.

The proposed robotic processing station, as shown in Fig. 1, was used in a study into the feasibility of automating the process of grinding turbine-prop engine blades.

3.1. Data acquisition system

The proposed robotic system enabled acquisition of measurement data representing the processed shape established by 3D scanning (Fig. 2).

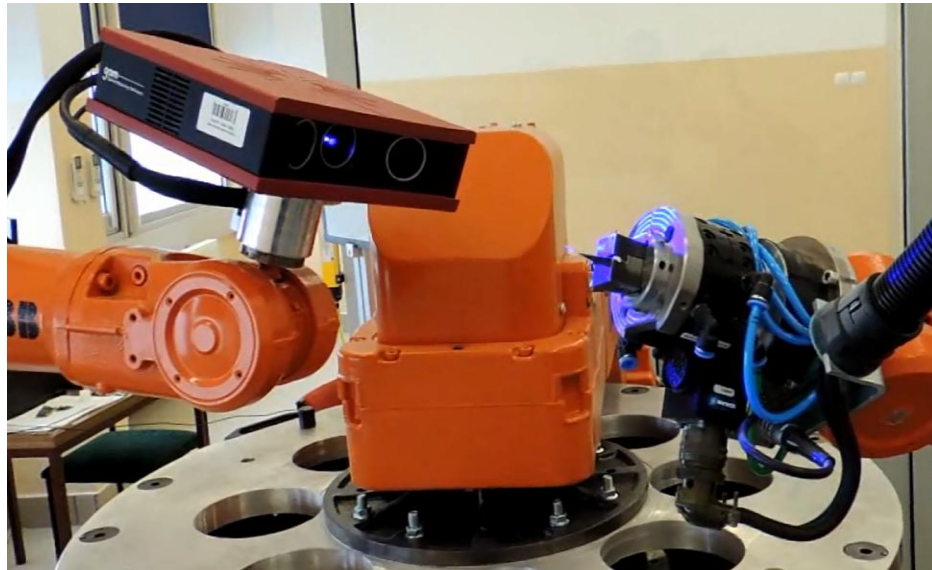


Figure 2. The measurement process.

The scanned 3D model is compared with a CAD master model to provide measurable information. The data thus provided is then exported to Matlab/Simulink. The measurement process uses an extension of the ATOS software, Professional Blade, which is intended for the measurement inspection of all types of blades.

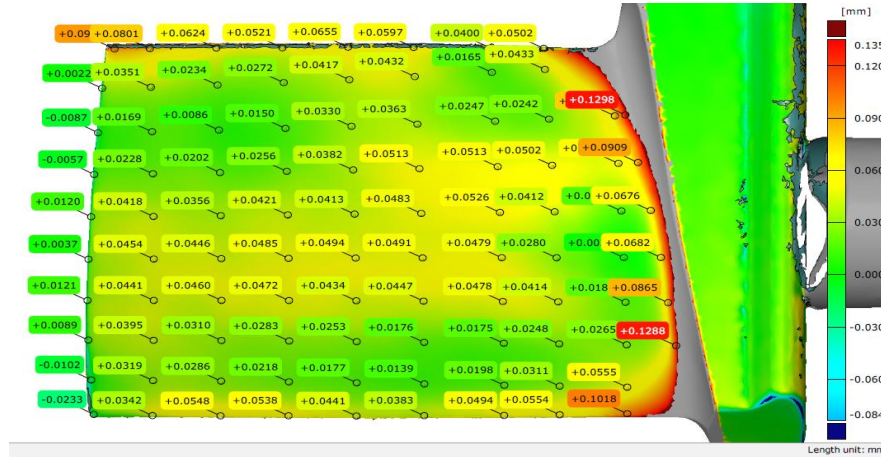


Figure 3. Image of measurements in progress.

The measurement system allowed 80 points to be produced (Fig. 3), representing the relationship of force to the amount of removed material.

3.2. Neural process controller

The neural controller for the blade grinding process was built in Matlab with the use of the Neural Network Toolbox library feature. A feed-forward network was applied to approximate the relationship between tool pressure and material allowance, with learning occurring via an error backpropagation algorithm [1]. A programming tool was developed for the study that allowed testing of the quality of the network approximation in relation to the following parameters: number of hidden network layers, number of neurons in hidden layers, neuron activation functions, teaching parameters, etc. Tests were carried out by changing the number of hidden layers from 1 to 3 and the number of neurons per layer from 3 to 30, while three types of neuron activation functions were investigated: linear, unipolar sigmoid and bipolar sigmoid. Based on the results, a network was chosen having two hidden layers and nine neurons in each hidden layer. The hidden layers featured unipolar sigmoid functions for neuron activation, whereas the output layer had linear activation functions. The weights for the neural network were learned using an algorithm based on the Levenberg-Marquardt optimization method.

The teaching data were provided from the experimental measurements. The blade suction face had 80 evenly spaced points, positioned at the intersection of the lines shown in Fig. 4, where the geometrical features were measured in order to determine the material allowance. Next, the same surface was machined at a predefined tool pressure force, followed by another measurement of the surface geometry. The experimental procedure allowed the relationship to be established between the removed material layer and the tool pressure force.

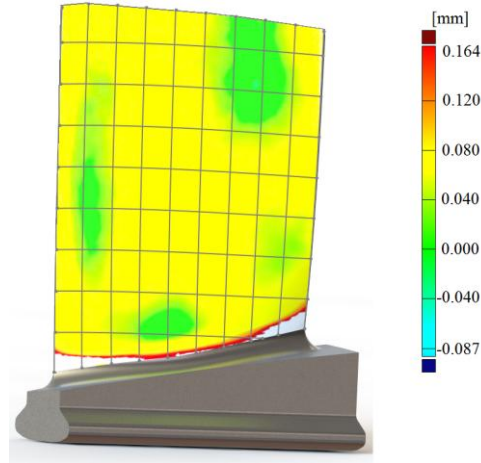


Figure 4. Material allowance on the blade suction face.

The neural process controller was designed to learn the studied problem in reverse: the controller generated the tool pressure force values at each of the 80 measurement points at a known value of allowance for each of these locations. The input and output layer structures of the neural network was related to the measurement data structure; hence the neural network had 80 inputs and 80 outputs (see Fig. 5), equal to the number of measurement points.

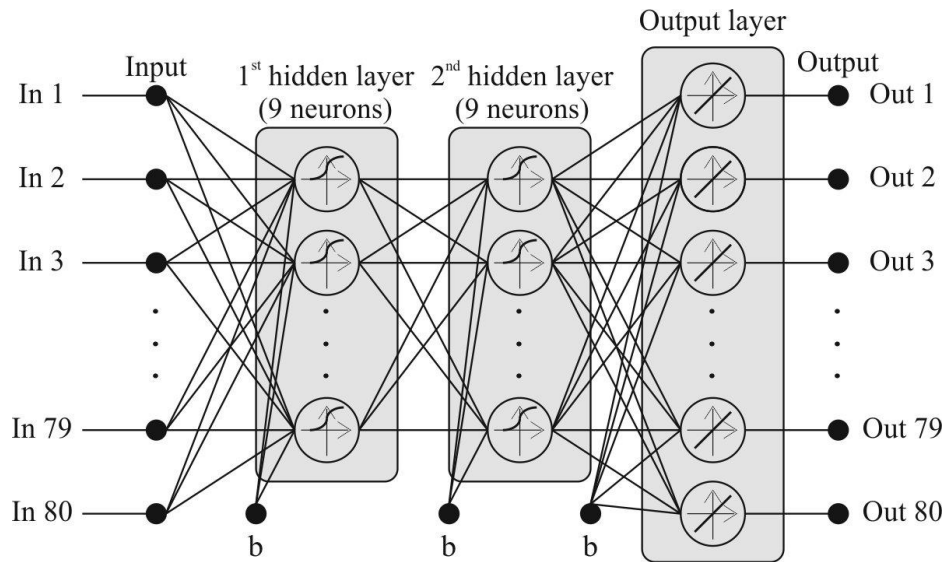


Figure 5. Neural network structure.

The network input data vector contained the material allowance values for the 80 measurement points, and the input data was standardized at an interval of [0-1]. The structure of the neural network means that the material allowance value at any defined point affected the value of the force generated at that same point as well as the pressure force values at other points. The advantage of this solution was that the generated pressure force would not change rapidly between adjacent points. This was considered important in order to achieve streamlined (smooth) machining. Moreover, it made the process control system less sensitive to potential measurement errors.

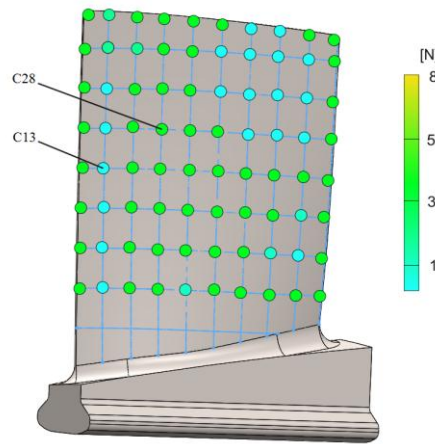


Figure 6. Graphical presentation of the tool pressure forces required to remove the material allowance at the individual measurement points.

Fig. 6 gives a graphic representation of the values of pressure force at the individual measurement points as generated by the neural process controller for the blade shown in Fig. 4.

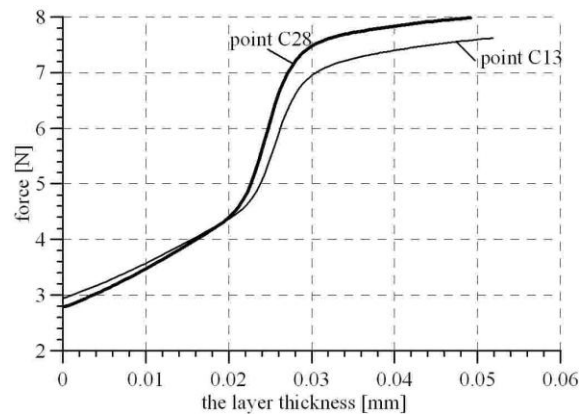


Figure 7. Relationship between pressure force and allowance at selected measurement points, as generated by the neural process controller.

It is evident that where larger allowances occurred the generated pressure forces was higher than at the points with a lower allowance. The exact dependences between tool pressure force and material addition at measurement points C13 and C28 are shown in Fig. 7. The magnitudes of the relationships were developed by the neural controller for the grinding process. The dependences were similar in nature at the other measurement points.

The values of applied pressure forces were in the range 2.5-8 N. The applied tool pressure forces were never below 2 N, which is the lowest limit of effective force control in the robot control system. On the other hand, pressure forces above 8 N would result in overheating of the cutting tool surface, which was considered unacceptable.

3.3. Force controlled robot

The traditional approach to robotic processing of material involves the execution of preprogrammed motion trajectories. In reality, there are a number of technological processes (e.g. casting or electrochemical machining) that warrant the production of intermediates with an accuracy tolerance high enough to require adapting the robot motion trajectory to suit the varying airfoil form. One of the tools able to solve this problem is force control, where the robot controlled motions are adjusted according to feedback from force sensors.

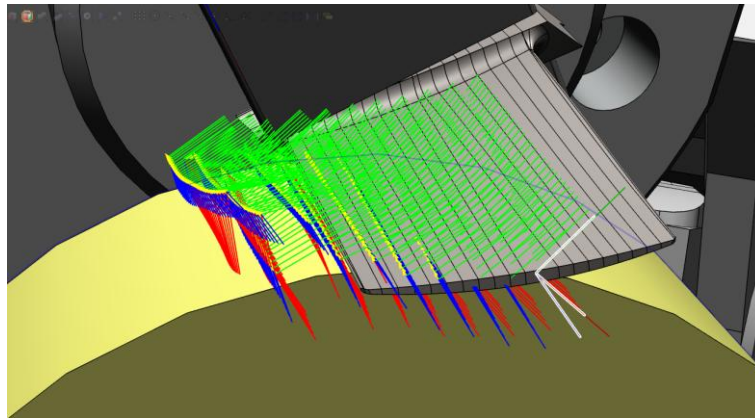


Figure 8. View of robot paths, RobotStudio software.

The solution proposed here applies the FC pressure functionality. Based on a number of test runs, a solution was proposed that consisted of a fixed tool and a moving reference system for the work object, attached to the robot arm. The IRC5 controller software of the robot, the program, and the pre-set motion trajectories were developed in RobotStudio (Fig.8).

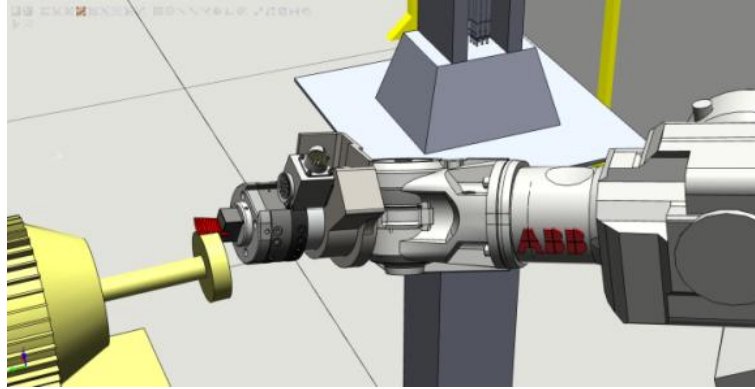


Figure 9. Simulation of a station, RobotStudio software.

An advantage of the proposed approach is the reduced impact of disturbances from electrochemical machining spindles. With the rotating tool installed on a robotic arm, a force sensor records the force value and its disturbance (Fig. 9). In order to eliminate the latter, low-pass filtering values are selected for each individual solution. The filtered measurement signal of the force values in three axes operated with an electrochemical spindle mounted on a robotic arm is shown in Fig. 10. The measurements were recorded at a preset stabilization of the force at 5 N using the ABB Test Signal Viewer software.

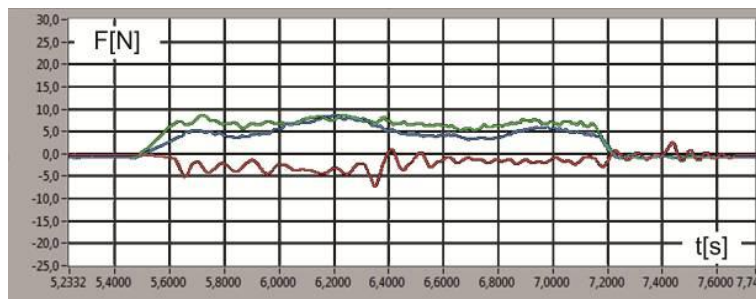


Figure 10. Measurement values from the three axes.

The force control approach allows the system to be protected from the effects of long-term wear of the tool, and the adaptation of the motion trajectory to minor variables on the component form.

4. Verification

The present study concerned the grinding of a blade suction surface. The robotic processing station is shown in Fig. 11. The blade before and after grinding is shown in Fig. 12. The measurement report for pre and post grinding is shown in Fig. 13, respectively.

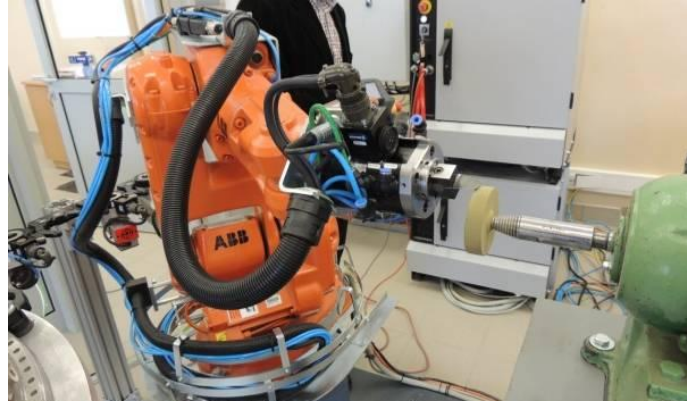


Figure 11. Robotically automated processing station.

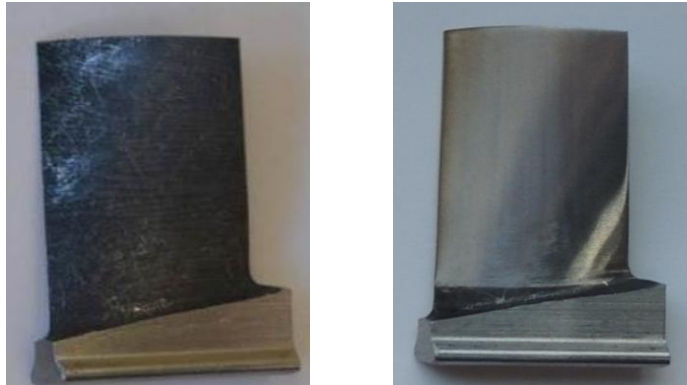


Figure 12. View of a blade before and after grinding.

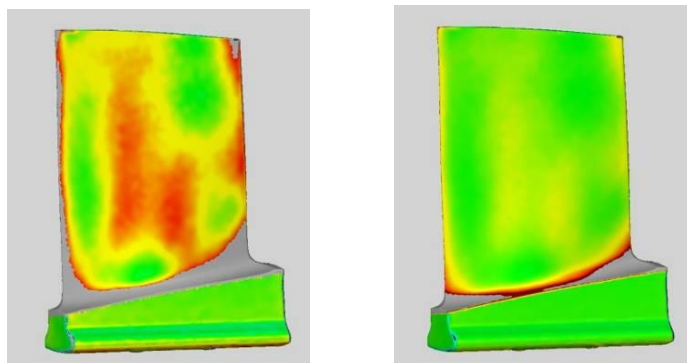


Figure 13. Measurement report before and after grinding.

The present study demonstrated that the grinding process could be completed within the preset manufacturing tolerance ranges.

5. Conclusions

The employment of generalizing properties in an artificial neural network has allowed the generation of information that enables the tool to component contact force to be managed in a way that assures grinding to the predefined specifications. The present solution is still at the laboratory stage; further development work will focus on automation of the solution by integrating the network algorithms within the robot controller instead of using a separate PC workstation.

References

- [1] Hagan, M.T., Demuth, H.B., Beale, M.H. *Neural Network Design*, PWS Publishing, Boston, 1996.
- [2] Huang H, Gong Z M, Chen X Q, et al.: *Smart robotic system for 3D profile turbine vane airfoil repair*. The International Journal of Advanced Manufacturing Technology 21(4), (2003), p.275-283.
- [3] Ren X, Kuhlenkotter B, Muller H. *Simulation and verification of belt grinding with industrial robots*. Machine Tools & Manufacture 46 (7-8), (2006), p.708-716.
- [4] Sun Y Q, Giblin D J, Kazerounian K. *Accurate robotic belt grinding of workpieces with complex geometry using relative calibration techniques*. Robotics and Computer-Integrated Manufacturing 25(1), (2009), p.204-210.
- [5] Zhang X, Kuhlenkotter B, Kneupner K. *An efficient method for solving the Signorini problem in the simulation of free-form surfaces produced by belt grinding*. Machine Tools & Manufacture 45(6), (2005), p.641-648.

Piotr Gierlak, Ph.D.: Rzeszow University of Technology, Department of Applied Mechanics and Robotics, al. Powstańców Warszawy 12, 35-959 Rzeszów, Poland (pgierlak@prz.edu.pl).

Andrzej Burghardt, Ph.D. D.Sc. (Assistant Professor): Rzeszow University of Technology, Department of Applied Mechanics and Robotics, al. Powstańców Warszawy 12, 35-959 Rzeszów, Poland (andrzejb@prz.edu.pl). The author gave a presentation of this paper during one of the conference sessions.

Dariusz Szybicki, Ph.D.: Rzeszow University of Technology, Department of Applied Mechanics and Robotics, al. Powstańców Warszawy 12, 35-959 Rzeszów, Poland (dszybicki@prz.edu.pl).

Magdalena Muszyńska, Ph.D.: Rzeszow University of Technology, Department of Applied Mechanics and Robotics, al. Powstańców Warszawy 12, 35-959 Rzeszów, Poland (magdaw@prz.edu.pl).

Krzysztof Kurc, Ph.D.: Rzeszow University of Technology, Department of Applied Mechanics and Robotics, al. Powstańców Warszawy 12, 35-959 Rzeszów, Poland (kkurc@prz.edu.pl).

**Nonlinear dynamics of waves in inhomogeneous media with
fractal structures
(NON244-15)**

Anatoli Chigarev, Victor Polenov, Pavel Shirvel

Abstract: The wave propagation in an elastic inhomogeneous medium with mechanical parameters which are functions of the spatial coordinates is considered. It is assumed that the pore sizes or the including sizes are small compared with the distance at which the kinematic and geometrical characteristics of the motion change significantly. Generally, the mathematical models in the theory of wave propagation are continuous, linear and smooth. Natural media are generally rough and discontinuous. It is possible to determine the fractal dimension, which characterizes in fact the irregularity of the real media. It is known that the fractal dimension exceeds the Euclidean dimensions. An wave in an inhomogeneous medium is understood as an isolated surface, which the stresses and rates of displacement are discontinuous. The Fermat's principle allows to construct ray trajectories, the principle of Huygens allows to construct wave fronts. An acoustical energy in continuous media in accordance with Fermat's principle and principle of Huygens propagates along ray tubes and locates at a surface front of the wave. In the paper is considered the modification of the Fermat's principle for wave propagation in the media with fractal structure. In this case the differential equations for the ray trajectories have the order which is equal to the dimension of the medium. Mathematical simulation of the deterministic chaos for the behavior of the energy flux lines in the frame of nonlinear dynamics of rays in the inhomogeneous medium is considered.

1. Introduction

The model of elastic stratified medium widely is applied in seismology geotechnique [1-4]. In the case, if a medium constitutes from discrete layers, then it is necessary to solve the boundary problem for each layer. It is enough a laborious investigation [5]. The dynamic equations for inhomogeneous media are the differential equations with variable coefficients. As is known for solving of these equations have not general analytical methods. The most famous methods which are applied for solving of differential dynamical equations for inhomogeneous media are a ray method [6] and method of effective medium [7]. For some time past a hypoplastic model is applied for an investigation of seismic wave propagation in a soil [8, 9]. The model of hypoplastic medium allows to describe many effects which are observed in granular soils. We consider a successive application of

effective medium method and of ray method in order to receive of approximate analytical solutions for description of shear wave propagation in stratified layer, which lies on a half space.

How it is known a real soil is inhomogeneous, it being knows that usually it is stratified in a depth. We take the model of effective medium which has the same macroscopic properties as real inhomogeneous medium. The effective model can be received on a basic of experimental results in the form of phenomenological theory or on a basic of theoretical accounts. We take as effective model a hypoplastic medium [8, 9], which describes a medium with initial stresses increased in depth linearly. It is correct if a thickness $l_i (i = 1, 2, \dots, n)$ of each layer is comparatively less than a thickness L of a great layer ($l_i \ll L$).

For a solving of constitutive phenomenological equations we apply a ray method. An application of this method is correct if a wave length λ (or a width of a wave packet) is less than a variation scale of effective properties. It is mean that macroscopic properties change monotonically in a depth.

1.1. Formulation of problem

The layer of stratified granule medium lies on the surface $x_1 \geq x_{10}$ (Fig. 1). A thickness of the layer is L . At $t = 0$ the plane $x_1 = x_{10}$ (the surface S_0) the velocity begins to move with the velocity $\vartheta = \vartheta(x_{10}, t)$ in the directions x_2 . Then there is the plane shear wave which propagates in the direction x_1 . At first we consider a propagation of energy in any layer.

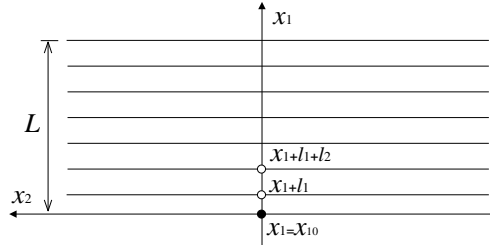


Figure 1. The stratified layer L which lies on halfspace $x < x_{10}$.

2. Shear wave propagation in stratified granular layer with effective hypoplastic properties

Let a layer of a thickness L be on a half space $x_1 \leq x_{10}$. The layer L constitutive from some layers of thicknesses $l_i (i = 1, 2, \dots, n)$, it being know that $l_i \ll L$, ($i = 1, 2, \dots, n$). For example it may be an interchange of layers of sand and clay (Fig. 1).

Let a shear wave be to incidences on a plane boundary $x_1 = x_{10}$ and is propagated from the half space $x_1 < x_{10}$. If we want to solve the problem exactly we must set boundary conditions (or connected conditions) and describe wave propagation for each layer. There are very unwieldy expressions especially for multiple scattered waves.

A method of effective medium allows to obtain a solution of this problem [7]. Applied an averaging method (method of homogenization or energy continuation) we obtain a phenomenological model of inhomogeneous medium [7].

Suppose that macroscopic (effective) conditions of layer medium are described of the equations of a hypoplastic medium [8, 9].

In general case the equations of wave propagation in hypoplastic medium have the form [6, 7]

$$\text{Div} T + \rho^* \bar{f} = \frac{d\rho \bar{\mathfrak{G}}}{dt}, \quad (1)$$

where \bar{f} is a mass force vector, $\rho \bar{\mathfrak{G}}$ is a vector of quantity of motion, $\bar{\mathfrak{G}}$ is a rate vector, $\rho^* = \frac{\rho_l e + \rho_s}{1+e}$ is effective (average) density, ρ_l and ρ_s are densities of liquid and hard fraction in a soil respectively, T is a tensor of effective (total) stresses in an inhomogeneous medium, e is a pore quantity.

The kinetic equations we write in the form of constitutive equations of a hypoplasticity [8, 9]

$$\overset{\circ}{T} = H(T, D, e), \quad (2)$$

where $\overset{\circ}{T}$ is Jaunman's derivative time.

$$\overset{\circ}{T} = \dot{T} - T\omega - \omega T, \quad (3)$$

in (3) \dot{T} is material derivative time, D and ω are a tensor of rate and a spin tensor respectively.

$$D_{ij} = \frac{1}{2} \left(\frac{\partial \mathfrak{G}_i}{\partial x_j} + \frac{\partial \mathfrak{G}_j}{\partial x_i} \right), \quad \omega_{ij} = \frac{1}{2} \left(\frac{\partial \mathfrak{G}_i}{\partial x_j} - \frac{\partial \mathfrak{G}_j}{\partial x_i} \right). \quad (4)$$

A density ρ^* satisfies the equation of continuity

$$\frac{d\rho^*}{dt} + \text{div}(\rho^* \bar{\mathfrak{G}}) = 0, \quad (5)$$

and pore quantity e satisfies the equation

$$\dot{e} = (1+e) \text{tr} D. \quad (6)$$

We represent the each field value $T_{ij}(\bar{x}, t)$, $\vartheta_i(\bar{x}_i, t)$, $\bar{u}_i(\bar{x}, t)$, $\rho(\bar{x}, t)$, $e(\bar{x}, t)$ which describes a dynamical state in hypoplastic medium in the form of the sum

$$T = T^\circ + \tilde{T}, \quad \bar{\vartheta} = \bar{\vartheta}^\circ + \tilde{\vartheta}, \quad \bar{u} = \bar{u}^\circ + \tilde{u}, \quad \rho^* = \rho^\circ + \tilde{\rho}, \quad e^* = e^\circ + \tilde{e},$$

where T° , $\bar{\vartheta}^\circ$, \bar{u}° , ρ° , e° describe initial state and \tilde{T} , $\tilde{\vartheta}$, \tilde{u} , $\tilde{\rho}$, \tilde{e} describe disturbances.

The initial stresses $T^\circ(x, t)$ satisfies to the equations of equilibrium

$$\text{Div} T^\circ - \text{grad } \bar{P}_l^\circ + \rho \bar{f} = 0, \quad (7)$$

then the equations for disturbances have the form

$$\text{Div} T - \text{grad } P_l = \frac{d\rho \vartheta}{dt}, \quad (8)$$

Here and in the future the sign \sim we do not write.

Let Eq. (2) be the form

$$\dot{T} = L(T, e)D + N(T, e) \| D \| \quad (9)$$

$$L_{ijkl} = \frac{f_b f_e}{\text{tr}(\hat{T}^2)} [F^2 \delta_{ik} \delta_{jl} + a^2 \hat{T}_{ij} \hat{T}_{kl}], \quad L_{ij} = \frac{f_b f_e f_\alpha a F}{\text{tr}(\hat{T}^2)} [\hat{T}_{ij} + \hat{T}_{ij}^*], \quad \hat{T}_{ij} = \frac{T_{ij}}{\text{tr} T},$$

$$\hat{T}_{ij}^* = \hat{T}_{ij} - \frac{1}{3} \delta_{ij}, \quad a = \sqrt{\frac{3}{8}} \frac{3 - \sin \varphi_c}{\sin \varphi_c},$$

The equation for disturbances follows from Eq. (4) for case when \hat{T}_{ij}^* is not enough

$$\dot{T} = L(T^\circ, e)D + N(T^\circ, e) \| D \|. \quad (10)$$

Therefore the Eqs. (1), (3), (5) describe a disturbance propagation in hypoplastic medium.

3. Shear wave propagation in effective hypoplastic medium

Set initial and boundary conditions on plane $x_1 = x_{10}$ in the form

$$\vartheta_2(x_1, t)|_{t=0} = \vartheta_2(x_1, 0), \quad \vartheta_2(x_1, t)|_{x_1=x_{10}} = \vartheta_2(x_{10}, t), \quad (11)$$

$$T_{12}(x_1, t)|_{t=0} = T_{12}(x_1, 0), \quad T_{12}(x_1, t)|_{x_1=x_{10}} = T_{12}(x_{10}, t). \quad (12)$$

The motion equation Eq. (3) in this case has the form

$$\frac{\partial T_{11}}{\partial x_1} - \frac{\partial P_l}{\partial x_1} = 0, \quad \frac{\partial T_{12}}{\partial x_1} - \rho \frac{\partial \vartheta_2}{\partial x_1} = 0, \quad (13)$$

and the definition Eqs. (10) we write in the form [5, 7].

$$\begin{aligned}\frac{\partial T_{11}}{\partial t} - K_1 \frac{\partial \vartheta_2}{\partial x_1} - K_2 \left| \frac{\partial \vartheta_2}{\partial x_1} \right| &= 0, \quad \frac{\partial T_{12}}{\partial t} - K_3 \frac{\partial \vartheta_2}{\partial x_1} - K_4 \left| \frac{\partial \vartheta_2}{\partial x_1} \right| = 0, \\ \frac{\partial T_{22}}{\partial t} - K_5 \frac{\partial \vartheta_2}{\partial x_1} - K_6 \left| \frac{\partial \vartheta_2}{\partial x_1} \right| &= 0, \quad \frac{\partial T_{33}}{\partial t} - K_7 \frac{\partial \vartheta_2}{\partial x_1} - K_8 \left| \frac{\partial \vartheta_2}{\partial x_1} \right| = 0.\end{aligned}\tag{14}$$

The coefficients K_i we write analogous [6, 7] in the form

$$\begin{aligned}K_1 &= -T_{12}^\circ + h_2 \widehat{T}_{12}^\circ \widehat{T}_{11}^\circ, & K_2 &= \sqrt{2} h_3 (\widehat{T}_{11}^\circ - 1/6), \\ K_3 &= 1/3 [T_{11}^\circ - T_{22}^\circ] + h_1/2 + h_2 (\widehat{T}_{12}^\circ)^2, & K_4 &= \sqrt{2} h_3 \widehat{T}_{12}^\circ, \\ K_5 &= T_{12}^\circ + h_2 \widehat{T}_{12}^\circ \widehat{T}_{22}^\circ, & K_6 &= \sqrt{2} h_3 (\widehat{T}_{22}^\circ - 1/6), \\ K_7 &= h_2 \widehat{T}_{12}^\circ \widehat{T}_{33}^\circ, & K_8 &= \sqrt{2} h_3 (\widehat{T}_{33}^\circ - 1/6),\end{aligned}\tag{15}$$

$$\widehat{T}_{12}^\circ = \frac{T_{ij}^\circ}{tr(T_{ij}^\circ)}.\tag{16}$$

Suppose that for an initial state it has place the condition $T_{12}^\circ(x_1) = 0$.

Then the coefficients K_1, K_4, K_5, K_7 vanish and we obtain from Eqs. (13-16):

$$\begin{aligned}\frac{\partial T_{11}}{\partial x_1} - K_2 \left| \frac{\partial \vartheta_2}{\partial x_1} \right| &= 0, \quad \frac{\partial T_{12}}{\partial t} - K_3 \frac{\partial \vartheta_2}{\partial x_1} = 0, \\ \frac{\partial T_{22}}{\partial t} - K_6 \left| \frac{\partial \vartheta_2}{\partial x_1} \right| &= 0, \quad \frac{\partial T_{33}}{\partial t} - K_8 \left| \frac{\partial \vartheta_2}{\partial x_1} \right| = 0.\end{aligned}\tag{17}$$

where

$$\begin{aligned}K_2 &= \sqrt{2} h_3 (\widehat{T}_{11}^\circ - 1/6), \\ K_3 &= 1/3 [T_{11}^\circ - T_{22}^\circ] + h_1/2, \\ K_6 &= \sqrt{2} h_3 (\widehat{T}_{22}^\circ - 1/6), \\ K_8 &= \sqrt{2} h_3 (\widehat{T}_{33}^\circ - 1/6),\end{aligned}\tag{18}$$

Combined Eq. (13), Eq. (16) we obtain the equations for wave disturbance propagation in the layer with effective properties

$$\frac{\partial}{\partial t} \left(\rho(x_1) \frac{\partial \vartheta_2}{\partial t} \right) - \frac{\partial}{\partial x_1} \left(K_3(x_1) \frac{\partial \vartheta_2}{\partial x_1} \right) = 0,\tag{19}$$

$$\frac{1}{K_3(x_1)} \frac{\partial^2 T_{12}}{\partial t^2} = \frac{\partial}{\partial x_1} \left(\frac{1}{\rho(x_1)} \frac{\partial T_{12}}{\partial x_1} \right) = 0.\tag{20}$$

4. Solving of equations of shear wave propagation in layer

The differential equations Eqs. (19),(20) have variable coefficients. It does not exist of general analytical methods for a solving of similar equations. The ray method is the most effective among different asymptotic methods for solving of differential equations with variable coefficients [6].

For nonstationary waves an application of this method is correctly, if a wave length λ is more less than a variable of a scale of effective layer parameters. It has place if an inhomogeneity of a layer changes in a depth monotonic.

It is know that usually a stiffness of a layer changes local nonmonotonic in a depth, but effective stiffness is monotonic function of spatial coordinate in a depth.

Let in the equations Eq. (19), Eq. (20) be the coefficients $K_i(x_1), \rho(x_1)$ are effective parameters of medium and a scale of variable K_i, ρ is more greater than a wave length. An effective approximation gives us principal estimation of wave field values caused of integral (average) conditions of real medium.

Write the solution of the equations Eq. (19), Eq. (20) in the form

$$\vartheta_2(x_1, t) = \sum_{n=0}^{\infty} \vartheta_2^{(n)}(x_1) f_n(t - \psi(x_1)), \quad (21)$$

$$T_{12}(x_1, t) = \sum_{n=0}^{\infty} T_{12}^{(n)}(x_1) f_n(t - \psi(x_1)), \quad (22)$$

$$\frac{\partial f_n(\xi)}{\partial \xi} = f_{n-1}(\xi), \quad (23)$$

where $\psi(x_1)$ is eiconal, $\vartheta_2^{(n)}(x_1), T_{12}^{(n)}(x_1)$ are unknown quantities.

If $f_n(t - \psi(x_1)) = \frac{[t - \psi(x_1)]^n}{n!}$ then ray series Eq. (21), Eq. (22) have form

$$\vartheta_2^{(n)}(x_1, t) = \sum_{n=0}^{\infty} \vartheta_2^{(n)}(x_1) \frac{[t - \psi(x_1)]^n}{n!} \quad (24)$$

$$T_{12}^{(n)}(x_1, t) = \sum_{n=0}^{\infty} T_{12}^{(n)}(x_1) \frac{[t - \psi(x_1)]^n}{n!} \quad (25)$$

If f_0 is Heaviside function $H(\tau)$ then f_n has form

$$f_n = \frac{[t - \psi(x_1)]^n}{n!} H(t - \psi(x_1)). \quad (26)$$

Let initial impulse be an impulse function $f_0(t)$ in the form

$$f_0(t) = J_0(t, \tau) = \begin{cases} 0, & t < 0 \\ 1, & 0 \leq t \leq \tau, \\ 0, & \tau < t \end{cases} \quad (27)$$

where the function $J_0(t, \tau)$ is expressed with a helping of Heaviside function

$$J_0(t, \tau) = H_0(t) - H_0(t - \tau). \quad (28)$$

The boundary conditions by $x_1 = x_{10}$ have the form

$$\begin{aligned} g_2^{(0)}(x_{10}, t) &= g_2^{(0)}(x_{10}) J_0(t, \tau) \\ T_{12}^{(0)}(x_{10}, t) &= T_{12}^{(0)}(x_{10}) J_0(t, \tau) \end{aligned} \quad (29)$$

The wave which comes in the point x_1 is described with a registration in the formulas

$$\begin{aligned} g_2^{(0)}(x_1, t) &= g_2^{(0)}(x_{10}) \sqrt[4]{\frac{K_3(x_{10})\rho(x_{10})}{K_3(x_1)\rho(x_1)}} J_0\left(t - \tau - \int_{x_{10}}^{x_1} \frac{dx_1}{C_S(x_1)}\right) \\ T_{12}^{(0)}(x_1, t) &= T_{12}^{(0)}(x_{10}) \sqrt[4]{\frac{K_3(x_{10})\rho(x_{10})}{K_3(x_1)\rho(x_1)}} J_0\left(t - \tau - \int_{x_{10}}^{x_1} \frac{dx_1}{C_S(x_1)}\right) \end{aligned} \quad (30)$$

The conditions allow to obtain a variation of wave profile. With a registration Eq. (29), Eq. (30) we have

$$\begin{aligned} J_0(t_1, \tau) &= \sqrt[4]{\frac{K_3(x_0)\rho(x_0)}{K_3(x)\rho(x)}} J_0\left(t - \tau - \int_{x_{10}}^{x_1} \frac{dx_1}{C_S(x_1)}\right) \text{ for } g_2^{(0)} \\ J_0(t_1, \tau) &= \sqrt[4]{\frac{K_3(x)\rho(x)}{K_3(x_0)\rho(x_0)}} J_0\left(t - \tau - \int_{x_{10}}^{x_1} \frac{dx_1}{C_S(x_1)}\right) \text{ for } T_{12}^{(0)} \end{aligned} \quad (31)$$

Integrated on t the left part of (31) from O up to $\tau(x_1)$ we obtain

$$\tau_g = \tau_{1g} \sqrt[4]{\frac{K_3(x_1)\rho(x_1)}{K_3(x_{10})\rho(x_{10})}}, \quad (32)$$

$$\tau_T = \tau_{1T} \sqrt[4]{\frac{K_3(x_{10})\rho(x_{10})}{K_3(x_1)\rho(x_1)}}. \quad (33)$$

From Eq. (4.31), Eq. (33) it follows that if $\sqrt[4]{\frac{K_3(x_1)\rho(x_1)}{K_3(x_{10})\rho(x_{10})}} < 1$ then a wave profile takes place a

compression. Therefore the rate displacement wave has the compression and the shear stress wave has the decompression (Fig. 2).

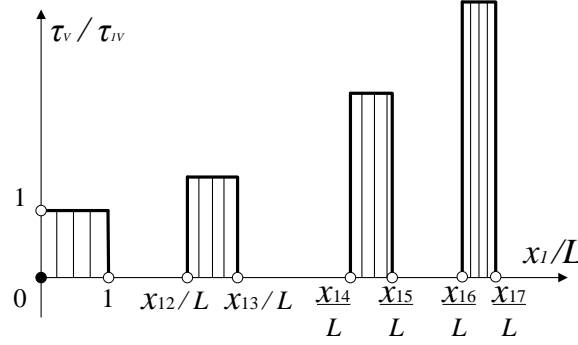


Figure 2. The results of shear stress wave's decompression.

Consider a propagation of shear wave which has triangular profile. In this case we can calculate analogous to rectangular impulse. The results of these calculations are presented schematically on Fig. 3.

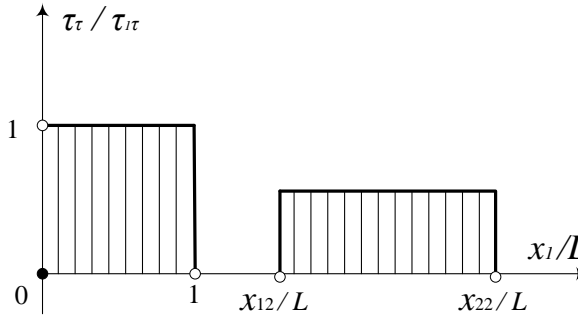


Figure 3. The schematically results of propagation of shear wave which has triangular profile.

5. Oblique wave incidence on boundary of layer

Consider the oblique wave incidence on the boundary $x_1 = x_{10}$ from the half space $x_1 < x_{10}$. In this case the rays will be curve lines which satisfy to the equations [17].

$$\frac{d\bar{x}}{ds} = \bar{\tau}, \quad \frac{d(n\bar{\tau})}{ds} = \text{grad}n, \quad \frac{d\psi}{ds} = n, \quad (34)$$

where $\vec{\tau}$ is a tangential vector to ray trajectory, n is a refraction coefficient, s is a length along a ray.

For the systems of differential equations we set boundary conditions on initial surface

$$\vec{x} = \vec{x}_0, \quad \vec{\tau} = \dot{\vec{x}} = \dot{\vec{x}}_0, \quad \psi = \psi_0, \quad (35)$$

for $S = S_0$ ($x_1 = x_{10}$).

If ray trajectory is found so surface (eiconal) ψ is calculated along a ray accordingly do formula

$$\psi(\vec{x}_1) = \int_{M_0}^{M_1} \frac{ds}{C(\vec{x}_1)} = \int_{M_0}^{M_1} n(\vec{x}_1) ds \quad [7,8,17,18]. \text{ Ray trajectories are orthogonal to surface } \psi(\vec{x}_1) = \text{const}.$$

Consider the Eq. (34) in plane $x_1 O x_2$

$$\frac{d(n \sin \theta)}{dS} = \frac{\partial n}{\partial x_1} = 0, \quad (36)$$

The equation for ray trajectory has the form [17]

$$\frac{dx_2}{dx_1} = \tan \theta = \frac{\sin \theta_0}{\sqrt{n^2 - \sin^2 \theta_0}}. \quad (37)$$

Set L be 500 m then we have

$$n^2 = \sqrt{\frac{500}{500 - x_1}}, \quad (38)$$

where $n(x_1, x_2) = C_0 / C_S(x_1, x_2)$ is a refraction coefficient.

The behavior of rays for different angles between an axis x_1 and rays is depicted on Fig. 4. How

it follows from Eqs. (37,38) $dn/dx_1 > 0$, then ray trajectories which have the angle $\theta_0 < \frac{\pi}{2}$ become

bent and drew near to the vertical. Therefore the wave front, which incidences on the free surface $x_{10} + L$, is parallel to plane $x_1 = x_{10} + L$ and a refraction wave is plane, too.

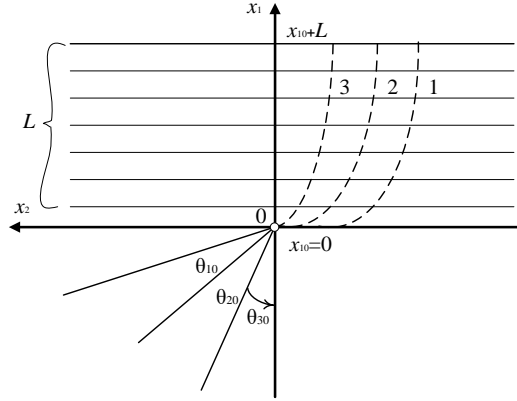


Figure 4. The schematically behavior of rays for different angles between an axis x_1 and rays.

6. Conclusions

A combined application of effective medium method and of ray method allows to solve the problems of wave propagation in a stratified medium. A model of a hypoplastic medium is applied in the capacity of an effective medium. This approach is correct if thickness l_i of each layer is more less then L ($l_i < L, i = 1, 2, \dots, n$). An application of ray method is correct if $\lambda \ll L$, where λ is wave length. The most best approaching has place for $l_i < \lambda$.

The acoustical approach describes wave propagation in effective layer for condition $T_{ij} \ll T_{ij}^0$, where T_{ij}^0 is an initial stress state, T_{ij} is disturbance stress state which propagates in the form of shear wave in a direction of free surface.

A wave, reflected from a free surface, propagates in the direction $-x_1$ and is summed from a direct and a reflective wave. From the energy conservation law it follows that an amplitude of a direct wave decreases and amplitude of a reflective wave accumulates and increases in the direction of a free surface.

References

- [1] Kennet, B.L., Kerry, N.I. *Seismic waves in a stratified half space*, Geophys. J. R. astr. Soc., **57**, 557–583, (1979).
- [2] Delph, T.J., Herrman, G. and Kanl, R.K. *Harmonic wave propagation in periodically layered infinite elastic body: amplitude strain*, Trans. ASME, Appl. Mech., **45**(2), 343–349, (1978).

- [3] Delph, T.J., Herrmann, G. and Kaul, R.K. *Harmonic Wave Propagation in a Periodically Layered, Infinite Elastic Body: Plane Strain, Numerical Results*, New York: American Society of Mechanical Engineers, Journal of Applied Mechanics, **47**(3), (1980).
- [4] Brekhovskikh, L. M. *Waves in Layered Media*, Academic Press, (1980).
- [5] Rossikhin, Yu. A., Shitikova, M.V. Ray method for solving dynamic problems connected with the propagation of wave surfaces of strong and weak discontinuities, *Appl. Mech. Reviews*, **48**(1), 1–39, (1995).
- [6] Chigarev, A.V. *Stochastic and regular dynamics of heterogeneous environments* [Russian translation], Minsk: UE “Tehnoprint”, (2000).
- [7] Polenov, V.S., Chigarev, A.V. *Wave propagation in a fluid-saturated inhomogeneous porous medium*, *J. Appl. Math. and Mech.*, **7**(4), 193–203, (2010).
- [8] Osinov, V.A., Gudehus, G. *Dynamics of Hypoplastic Materials: Theory and Numerical Implementation*, In: *Deformation and Failure of Granular and Porous Continua*, N. Kirchler, K. Hutter eds., *Lecture Notes in Applied Mechanics*, Springer, Berlin, (2003).
- [9] Kolarov, D., Baltov, A. and Boncheva, N. *Mechanics of Plastic Media* [Russian translation], Mir Publ., Moscow, (1979).
- [10] Sedov, L.I. *Mechanics of continuous media* [Russian translation], Moscow: Science, 1, (1979).
- [11] Brown, Dm. N. *Physics of strong motions excited by earthquakes. Seismic Risk and Engineering Decisions*, Elsevier, Amsterdam – Oxford – New York, 129–161, (1976).
- [12] Kanamori, H. (Ed.) *Earthquake Seismology: Treatise on Geophysics*, Elsevier, (2009).
- [13] Barkan, D. D. *Dynamics of bases and foundations*, New York, McGraw Hill, (1962).
- [14] Cravtsov, Jn. A., Orlov, Jn. I. *Geometrical optics of inhomogeneous media* [Russian translation], M. Science, (1980).
- [15] Vinogradova, M. B.; Rudenko, O. V.; Sukhorukov, A. P. *Theory of waves: textbook for physics qualifications in higher education* [Russian translation], Moscow: Nauka, (1990).
- [16] Babkin, G. I., Klyatskin, V. I. Invariant imbedding method for wave problems, *Wave Motion*, **4**(2), 195–207, 1982.
- [17] Klyatskin, V. I. *The Imbedding Method in Wave Propagation Theory* [Russian translation], Moscow: Nauka, (1986).
- [18] Klyatskin, V. I. *Dynamics of Stochastic Systems*, Elsevier Science, (2005).

Chigarev Anatoli Vlasovich, Professor, Head of Theoretical Mechanics Department, Belarusian National Technical University, Minsk, Belarus (Chigarev@rambler.ru). The author gave a presentation of this paper during one of the conference sessions.

Polenov, Victor Sidorovich, Professor, Professor of Mathematics Department, Voronezh State University, Voronezh, Russia (Polenov.vrn@mail.ru)

Shirvel Pavel Ivanovich, Ph.D. in Physical and Mathematics Sciences, Associate Professor of Department "Theoretical Mechanics", Belarusian National Technical University, Minsk, Belarus (Pavel.Shirvel@yandex.ru)

On the dynamic response of suspended footbridges (VIB139-15)

Mariella Diaferio

Abstract: Several Authors have underlined the possible activation of large amplitude oscillations of suspended footbridges due to the nonlinear behavior of the hangers, which act as linear elastic springs in tension and do not react in compression. In fact, in particular conditions the pedestrian- induced loads and/or the wind actions may cause oscillations that, in some parts of the footbridge span, achieve amplitude higher than the initial deformation of the hangers due to dead loads; in these cases such hangers slack and, consequently, the stiffness of the footbridge decreases. Thus the footbridge may undergo to unexpected large amplitude oscillations that the usually utilized models cannot predict, as they assume a bilateral behavior for the suspended system. Here, the response of suspended footbridges is evaluated introducing a continuous model that is obtained adopting the nonlinear equivalent regularization technique proposed for suspended bridges. The solution of the aforementioned continuous model is evaluated in closed form by means of perturbation methods. The dynamic analysis shows the possibility of the coexistence of multiple solutions, some of which are characterized by high amplitude. In order to identify the conditions for the activation of such phenomena, the evaluated responses are plotted for different values of the mechanical parameters of the examined structure and of the considered actions.

1. Introduction

Starting from the observation that during the collapse of the original Tacoma Narrows Bridge the torsional oscillations, that have caused the failure, were associated with the slackening of some hangers, many Authors [1]-[10] have study such phenomenon by considering the effects of the unilateral behavior of the hangers, that react only in tension.

Such papers [1] –[10] focus the attention on the behavior of long span bridges and on the effects of wind loads. In detail in [1]- [5] the Authors have underlined that for taking into account the unilateral behavior of the hangers, the equations of motions have to be rewritten by expressing the hangers restoring forces by means of terms which depends on the sign of the relative displacements between main cables and the deck; consequently, the solution has to be evaluated by means of the numerical integration of the equations of motion.

In detail, in [1]-[3] Mc Kenna et al., due to the difficulties in the numerical integration, have focused their study on the no-node oscillations of the deck, i.e. relative displacements of the same sign on the overall deck. This hypothesis allows to reduce the study of the entire footbridge to an its

single transversal section with a single degree of freedom (the vertical translation of the deck) or two degrees of freedom (vertical and torsional displacements). The same approach has been chosen by other Authors [4][5][7][8] and the activation of large amplitude oscillations have been evaluated for different load conditions and geometrical parameters of the bridge.

However the main limit of this approach is the necessity of a numerical integration of the equations of motion that restricted the effective application of the procedure, for example, a parametric study becomes extremely cumbersome.

In [6][9], the authors have proposed a different approach that substitutes the unilateral behavior of the hangers with a smooth nonlinear one whose parameters are evaluated by minimizing the difference between the variation of the global elastic energy due to a generic deformation associated with the two considered behaviors.

The main advantage of this approach is the possibility of rewriting the equations of motion introducing smooth nonlinear terms which allow the application of analytical integration procedure even if approximated, as the multiple scale method.

Consequently, in [6][9], the solutions of the equations of motion have been analytically evaluated and a parametric study has been performed in order to estimate the geometrical parameters and load conditions which may activate the slackening of hangers.

More recently, some Authors [11]-[13] have underlined the possibility of large amplitude oscillations, due to the nonlinear behavior of the hangers, also into suspended footbridges induced by pedestrian loads.

In fact, as these structures are devoted to static loads smaller than the ones of suspended bridges, and considering the wide spread of innovative materials, it has become possible the realization of suspended footbridges extremely flexible and, as a consequence, more prone to large amplitude oscillations.

In [11] the Authors propose a section model for suspended footbridges which is able to take into account the unilateral behavior of the hangers, and they demonstrate that for a pedestrian load acting along the torsional direction, the model may show large amplitude oscillations associated with the slacking of hangers. In [12] Bruno et al. analyze the 3D finite element model of a suspended footbridge subjected to a torsional load due to pedestrians, in this case the large amplitude oscillations are obtained also for frequency forcing values smaller than the torsional frequency of the model.

In [13] the Authors extend to the suspended footbridges the approach proposed in [6] [9] for suspended long span bridges, evaluate the solution of the equation of motion and plot the oscillation amplitude for different values of the forcing frequency of the pedestrian load.

The present paper analyses the vertical and torsional oscillations of suspended footbridges by considering a simplified continuous model that is able to describe the vertical and torsional relative

displacements between the main deck and the cables. The study investigates the oscillations due to pedestrian loads, which, as well known, may be represented by a n harmonic load acting or in the vertical, or in the vertical and torsional, or only in the torsional direction.

The analysis reveals that, taking into account the nonlinear behavior of the hangers, the footbridges in certain conditions (which are strictly correlated with the geometrical characteristics of the footbridges and with the load conditions) may undergo large amplitude oscillations which cannot be predicted by means of the “classical” models.

2. Suspended footbridge model

The model here presented has the aim of describing the relative oscillations between the main cables and the deck, consequently in order to simplify the equations of motion, the main cables have been considered fixed.

The hangers are assumed to be massless, vertical and able to react only in tension with a linear law, moreover they are modelled as uniformly distributed along the span (i.e. the distance between two consecutive hangers is much lower than the span length $i \ll L$) (Fig.1). The reference equilibrium configuration is characterized by the presence of dead loads, which are assumed to be balanced mainly by the suspension system, as a consequence, the hangers present an initial elongation of w_0 which is considered constant along the span length.

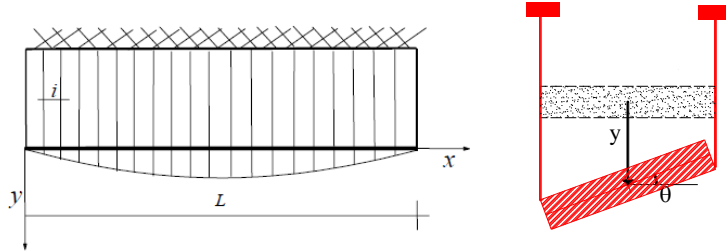


Figure 1. Continuous model of a suspended footbridge: a) longitudinal view, b) cross section.

On the basis of the aforementioned hypothesis, the deformed configuration of the system can be describe by means of a vertical y and a torsional θ displacements, and the equations of motion can be written as follow:

$$m_d \ddot{y} + k_d y^{IV} + C_d \dot{y} + k_p \left[(y + \ell \theta + w_0)^+ + (y - \ell \theta + w_0)^+ \right] - 2k_p w_0 = F_d(x, t) \quad (1)$$

$$I \ddot{\theta} - k_\theta \theta'' + C_\theta \dot{\theta} + k_p \ell \left[(y + \ell \theta + w_0)^+ - (y - \ell \theta + w_0)^+ \right] = F_\theta(x, t) \quad (2)$$

where the prime and the dot symbolize the time and space derivate respectively, m_d and I denote the unit mass and torsional inertia of the deck respectively, while k_d, k_θ the vertical and torsional

geometrical stiffness of the deck per unit length of the bridge; C_d, C_θ are the damping coefficients, F_d, F_θ are the forcing terms, ℓ the deck half-width, the $()^+$ denotes the “positive part” of the function, L the bridge span.

In the present paper the forcing terms are due to pedestrian loads, that are modelled by means of harmonic forces. The equations of motion are treated by substituting the piecewise terms (i.e. the restoring force of the hangers) by an equivalent cubic approximation [6] [9], by rewriting the equations of motion in a non-dimensional form, by expanding the unknown displacements as a linear combination of sinusoidal function with unknown amplitude, and by adopting the multiple scale method [14] to evaluate the analytical solution.

Here for sake of brevity, the application of the aforementioned procedure and the study of stability of the obtained solutions are not reported, while the structural response is plotted for different loading and geometrical parameters. The chosen geometrical parameters are here reported:

$$\omega_0 = \sqrt{\frac{k_d}{m_d L^4}}, \quad \Lambda = \frac{m_d \ell^2}{I}, \quad \lambda_\theta^2 = \frac{m_d L^2 k_\theta}{I k_d}, \quad \xi_d = \frac{C_d}{2m_d \omega_0}, \quad \xi_\theta = \frac{C_\theta}{2I \omega_0} \quad (3)$$

Moreover, it has been introduced the parameter β that represents the ratio between the angular frequency of the first mode of the footbridge and the one of the deck alone, that is the contribution of the suspended system [6] [9].

3. The dynamic response of suspended footbridges

The present paragraph describes the dynamic response of suspended footbridges induced by pedestrian loads; which is modeled by means of a periodic function. To explore all the possible dynamic behavior of the structure, different conditions of external and internal resonances are investigated, varying the geometrical and load parameters.

Firstly, it has been investigated the response in the case of pedestrian load acting along the torsional direction, that Bruno et al. [12] consider as representative of an out- of phase motion of pedestrian walking in opposite directions on the two sides of the deck. In fig. 2 the frequency-response curve of the elongation of the hangers is plotted for the case of a force acting along the torsional direction and resonant with the first torsional mode of the structure and without internal resonant conditions (σ_4 denotes the detuning, i.e. the difference between the forcing frequency and the externally resonant natural frequency of the system). The figure 2 shows that in a range of frequency values there is the coexistence of multiple solutions, one of which is unstable and the other two are stable. Considering the latest two solutions it can be observed that the greatest one, which is associated with the activation of slackening of the hangers, may be also 5-7 times the smaller one. As well known, the effective response of the structure depends on the initial condition of the motion.

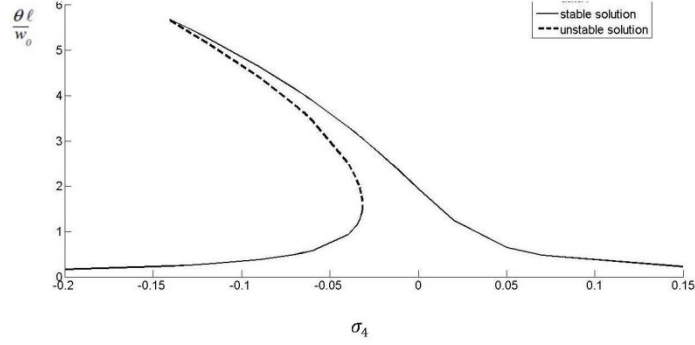


Figure 2. Frequency-response curves of elongation of the hangers: eccentric action on the deck nearly resonant with the relative torsional mode with one halfwaves (frequency $\omega_4(1)$); no internal resonance with vertical modes: $\xi_d = \xi_0 = 0.006$, $\beta = 6$, $\Lambda = 2.71$, $\lambda_0 = 17$, $F_0 = 0.01 m_d g$ 0.6 l, $F_d = 0$

To verify the influence of some parameters on the structural response the aforementioned external conditions have been investigated varying the intensity of the pedestrian load. In figure 3 the frequency- response curve of the elongation of the hangers is plotted considering the torsional pedestrian load acting with an eccentricity equal to 60% of ℓ the deck half-width, and varying the intensity of pedestrian load: in detail two cases are taken into account: a load equal to 1% and to 0.5% of the deck self-weight. The curves demonstrate that also in presence of load with no high intensity, large amplitude oscillations may occur.

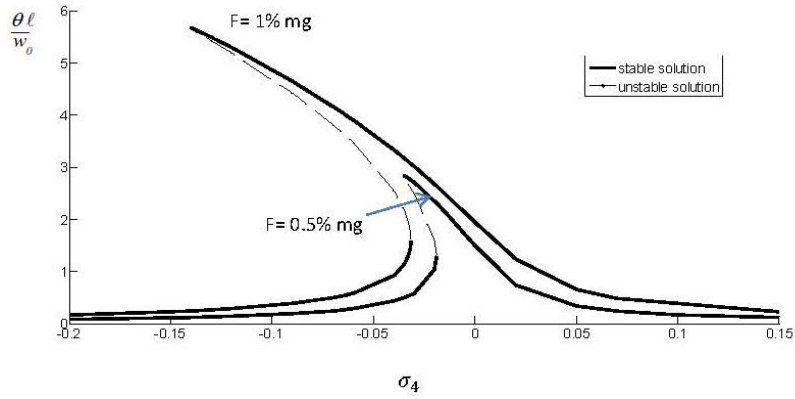


Figure 3. Frequency-response curves of elongation of the hangers: eccentric action on the deck nearly resonant with the relative torsional mode with one halfwaves (frequency $\omega_4(1)$); no internal resonance with vertical modes: $\xi_d = \xi_0 = 0.006$, $\beta = 6$, $\Lambda = 2.71$, $\lambda_0 = 17$, $F_d = 0$, two cases $F_0 = 0.01 m_d g$ 0.6 l and $F_0 = 0.005 m_d g$ 0.6 l

In figure 4 the frequency- response curve of the elongation of the hangers is plotted varying the eccentricity of the pedestrian load, it can be verify that an increase of the eccentricity of 30% of the deck half-width induces an increase of 50% of the amplitude of the maximum amplitude of oscillation, and of 100% of the amplitude of the frequency range in which multiple solutions are possible.

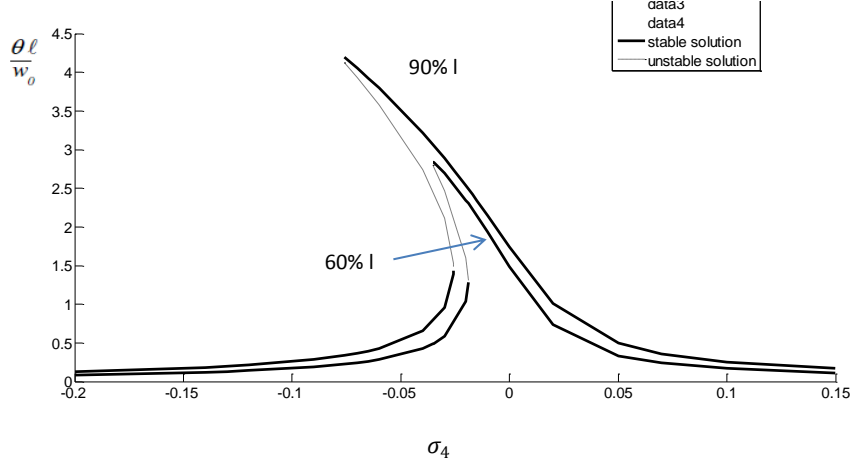


Figure 4. Frequency-response curves of elongation of the hangers: eccentric action on the deck nearly resonant with the relative torsional mode with one halfwaves (frequency $\omega_4(1)$); no internal resonance with vertical modes: $\xi_d=\xi_\theta=0.006$, $\beta=6$, $\Lambda=2.71$, $\lambda_\theta=17$, $F_d=0$, two cases $F_\theta=0.005m_d g$ 0.6 l and $F_\theta=0.005m_d g$ 0.9 l

In figure 5 the solution for a torsional pedestrian load resonant with the first torsional mode of the structure is plotted varying the load frequency; in this case there is also the presence of an internal resonance between the first torsional mode and the third flexural mode of the structure (in figure 5 σ_3 denotes the internal detuning, i.e. the difference between the natural frequency 1:1 internally resonant and the natural frequency externally resonant). Due to this circumstance, the structure manifests the possibility of two kinds of response: one is similar to the ones described in the above reported figures (that is the footbridges shows only torsional oscillations even if there is the coexistence of multiple solutions), while the other is characterized by the activation of oscillations with both torsional and vertical components. As can be seen, there is a frequency range in which 7 different solutions are possible, three of which are unstable.

In this case the structure may show large amplitude vertical oscillations which cannot be estimated by means of the “classical” models.

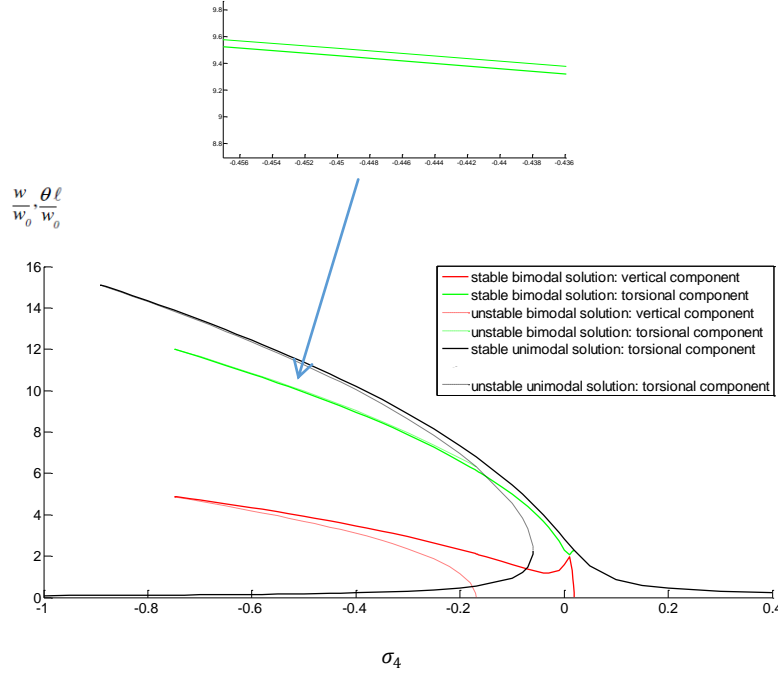


Figure 5. Frequency-response curves of elongation of the hangers: eccentric action on the deck nearly resonant with the relative torsional mode with one halfwaves 1:1 internal resonance with the three half-waves vertical mode: $\xi_d = \xi_\theta = 0.006, \beta = 10, \Lambda = 1.57, \lambda_\theta = 18, \sigma_3 = 0.03$,

$$F_\theta = 0.015 m_d g 0.81, \quad F_d = 0$$

4. Conclusions

This paper studies the nonlinear dynamic response of footbridges due to the unilateral behavior of the hangers. In detail, the equivalent nonlinearization, proposed in [6][9], is here applied to study the response of such structures.

The frequency – response curves of the elongation of the hangers have been plotted for different load and geometrical parameters, showing the possibility of multiple solutions, some of which are characterized by large amplitude and slacking of the hangers.

Moreover, in particular cases in which the geometrical parameters allows the activation of internal resonances, the system may display large amplitude oscillations both in the vertical and in the torsional directions, even if the force has only a torsional component.

The future research will analyze the structural response for a wide range of the geometrical and load parameters, in order to verify the conditions that may inhibit the phenomenon of slackening of the hangers.

Acknowledgments

The author acknowledge the Italian Ministry of Education, Universities and Research (MIUR), PRIN funded program 2010/11 N. 2010MBJK5B titled “Dynamics, Stability and Control of Flexible Structures”.

References

- [1] . McKenna, P.J , Walter, W. Nonlinear Oscillations in a Suspension Bridge, *Archive of Rational Mechanics and Analysis*, 98 (1987) 167-177.
- [2] Glover, A.C. Lazer, J. McKenna, Existence and stability of large scale nonlinear oscillations in suspension bridges, *Journal of Applied Mathematics and Physics (ZAMP)*, 40(1989) 172-200.
- [3] Lazer, A.C., McKenna, P.J. Large-amplitude periodic oscillations in suspension bridges: some new connections with nonlinear analysis. *SIAM Review* 32, (1990), 537-578.
- [4] Jacover, D., Mc Kenna, P.J. Nonlinear torsional flexings in a periodically forced suspended beam. *Journal of Computational and Applied Mathematics* 52, (1994), 241-265.
- [5] McKenna, P. J., Moore, K. S. Multiple periodic solutions to a suspension bridge ordinary differential equation. *Nonlinear Differential Equations*, *Electron. J. Diff. Eqns.* 5, (2000), 183-199.
- [6] Diaferio, M. *Modelli non lineari di strutture elastiche sospese*. PhD Thesis in Structural Engineering (in Italian), University of Firenze, 2000, Supervisors: Prof. P.- Spinelli and V. Sepe.
- [7] Sepe, V., Augusti. G. A deformable section model for the dynamics of suspension bridges. Part I: model and linear response. *Wind and Structures* 4, 1 (2001), 1-18.
- [8] Sepe, V., Diaferio, M., Augusti, G. A deformable section model for the dynamics of suspension bridges. Part II: nonlinear analysis and large amplitude oscillations. *Wind and Structures* 6, 6 (2003), 451-470.
- [9] Diaferio, M., Sepe, V. Smoothed slack cable models for large amplitude oscillations of suspension bridges. *Mechanics Based Design of Structures and Machines* 32, (2004), 363-400.
- [10] Plaut, R.H., Davis F.M. Sudden lateral asymmetry and torsional oscillations of section models of suspension bridges. *Journal of Sound and Vibration* 307, (2007), 894-905.
- [11] Bruno, L. , Venuti, F. , Scotti, A. Limit of hanger linearity in suspension footbridge dynamics: a new section model. *Journal of Sound and Vibration* 330, (2011) 6387–6406.
- [12] Bruno, L. , Venuti, F. , Nascé, V. Pedestrian-induced torsional vibrations of suspended footbridges: Proposal and evaluation of vibration countermeasures. *Engineering Structure* 36, (2012) 228–238.
- [13] Diaferio, M., Sepe, V. Nonlinear oscillations of suspended bridges and footbridges: a regularization technique for non-smooth hangers behavior . *Proceedings of the 9th International Conference on Structural Dynamics, EUROdyn 2014*, Porto, Portugal, 30 June - 2 July 2014, pages 1183-1188.
- [14] A.H. Nayfeh, D.T. Mook, Non linear oscillations. Wiley-Interscience, Eds., New York,1979.

Mariella Diaferio, Assistant Professor: of Politecnico di Bari and Department of Sciences in Civil Engineering and Architetture, via Orabona 4, 70125 Bari, Italy (mariella.diaferio@poliba.it).

Inducing modal interaction during run-up of a magnetically supported rotor (MTR261-15)

Fadi Dohnal, Athanasios Chasalevris

Abstract: In general, introducing a parametric anti-resonance in a vibrating system couples two of the many vibration modes and enables an energy exchange between those two. This feature is employed during the run-up of a JEFFCOTT rotor supported by two active magnetic bearings. The vibration performance at bearing stiffness modulation is compared to the well-known performance at nominal bearing characteristics for a simple run-up at a constant rate. It is shown that by introducing a specific periodic change of the bearing stiffness coefficients, a mode coupling between two selected modes is activated. This coupling impacts the maximum amplitude developed during passage through resonance. At each critical speed transient vibrations of the corresponding mode are excited. Due to the mode coupling, if one mode is excited at a critical speed then energy is transferred to the other mode too. On one hand, the maximum amplitude at the first critical speed is decreased by modulation since some vibration energy is transferred to the highly damped second mode where it is partly dissipated. On the other hand, the maximum amplitude at the second critical speed is increased by modulation since some vibration energy is transferred to the lightly damped first mode. The concept is outlined briefly by numerical studies.

1. Introduction

The beneficial effect of a parametric anti-resonance on self-excited vibration was discovered by TONDL in his pioneering work [15]. This concept was then transferred to general dynamic systems [4], was interpreted physically as an energy transfer between the vibration modes of the original system and was validated experimentally for simple systems including a flexible rotor [7]. A recent summary on this topic can be found in [5]. A parametric anti-resonance is a specific parametric combination resonance which does not lead to a parametric instability but enables an increased dissipation of vibration energy.

Active magnetic bearings as discussed in this paper offer the possibility to apply a desired time-periodic variation of the bearing characteristics with an accuracy that enables a parametric anti-resonance phenomenon. In rotating machines fluid film bearings are commonly used which inspired investigations on applying a variation of the fluid film bearing characteristics via a bearing shell of variable geometry [1–3]. Journal bearings of variable geometry

aim control the fluid film characteristic passively or actively. The recent works on the passive adjustment of the bearing geometry and thus of fluid film characteristics confirmed a displacement reduction during passage through critical speeds. The promising concept of a variable geometry bearing and its physical realisation via a moving bearing shell is followed in very recent studies [10,12] and combined with the concept of parametric anti-resonance. Adjusting bearing properties in a time-periodic manner has several benefits, like increased stability limits that allow a larger operation range and decreased vibration amplitudes when passing through critical speeds.

In the present investigation, a flexible rotor supported by bearings is investigated whose dynamic properties are controlled semi-actively. Such a concept was proposed for active magnetic bearings in [6,9] and validated theoretically and experimentally. It allowed the steady-state operation of active bearings beyond the stability limit of the implemented PID controller. The rotor configuration in [6] is summarised and its run-up characteristic at parametric anti-resonance is discussed briefly.

2. System modelling

Preliminary theoretical investigations [8,16] showed that introducing a periodic change in the bearing stiffness is capable of increasing the rotor speed limit of a simple JEFFCOTT rotor under the influence of a destabilising self-excitation. This approach is followed to enhance the effective damping of an already stable flexible rotor shaft under the action of unbalance and electromagnetic forces [9]. The experimental realisation is shown in Fig. 1: A slender, flexible rotor shaft supported by two active magnetic bearings (AMBs). The shaft is torsionally rigid and isotropic. A rigid disk (D) is attached to the shaft center and two bearing studs (AMB1, AMB2). The disks are unbalanced. The total length of the shaft is 680 mm. The main system parameters are listed in Table 1.

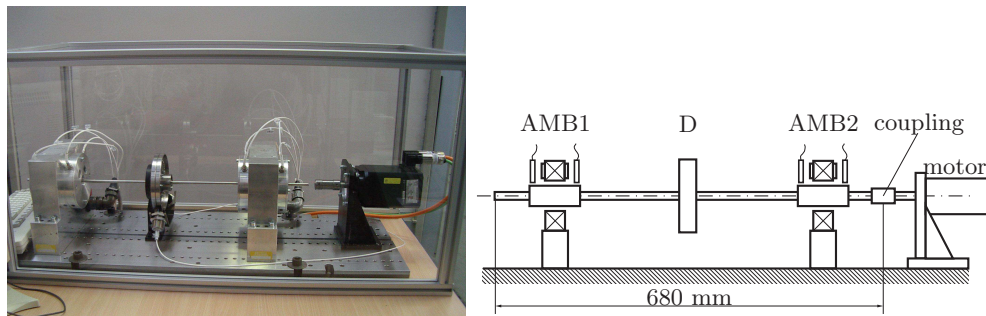


Figure 1. JEFFCOTT rotor supported by two magnetic bearings [6]: (left) experimental test rig, (right) corresponding dynamic model (taken from [6]).

Table 1. Properties of the JEFFCOTT rotor.

bending stiffness of rotor shaft	41.4 Nm
total rotor length and diameter	680 mm, 8 mm
mass and axial moment of inertia of disc	1.20 kg, $1.40 \cdot 10^{-3} \text{ kg m}^2$
mass of studs in AMB1 and AMB2	0.88 kg
radial bearing clearance	0.8 mm
specific load capacity	13 N/cm ²

The electromagnetic forces generated in the AMBs depend on the rotor deflection and the magnetic field. The magnetic field can be changed in a wide range by the current provided to the electromagnets. The actual position of the rotor shaft is measured by inductive sensors (two for each radial direction). These signals are processed by the real-time controller hardware dSPACE which implements decentralised PID controllers to regulate the currents provided by power amplifiers to each of the electromagnets and, hence, to levitate the rotor. The parametric anti-resonance is implemented in parallel to this PID control by an *open-loop control* of the proportional action,

$$k_P(t) = k_P (1 + \varepsilon \sin \nu t). \quad (1)$$

This realises a periodic change in the active bearing stiffness which is implemented in both AMBs in figure 1.

2.1. Nominal operation of an AMB

AMBs consist of pairs of electromagnets that are arranged, in general, in two perpendicular axes enabling to control the rotor position within a plane. Since electromagnets can apply only attracting but no repelling forces, two electromagnets are needed for each direction. A typical arrangement of magnets in a radial magnetic bearing is shown in Figure 2. This geometry has the advantage that the forces in z - and y -direction are (almost) uncoupled and can be calculated separately.

The electromagnetic force generated by the AMB depends on its geometry parameters (cross-section of the pole shoes, size of the air gap) and its electromagnetic properties (number of turns, permeability) and is a strongly nonlinear function of these parameters. In practice, however, the resulting force can be linearised close to a certain operation point. With the rotor displacement from the centre position r and the initial gap width s_0 , the force-current-displacement relationship of the magnetic bearing becomes

$$F_m = F_+ - F_- = k_m \left(\left(\frac{i_+}{s_0 + r} \right)^2 - \left(\frac{i_-}{s_0 - r} \right)^2 \right), \quad (2)$$

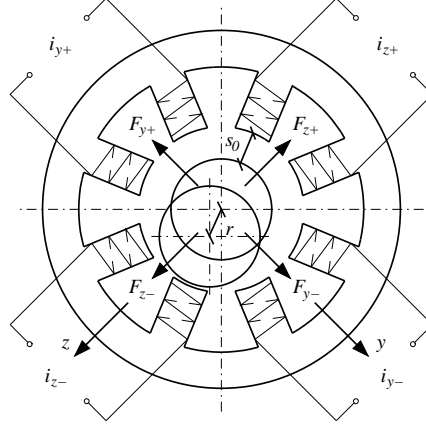


Figure 2. Geometry of the stator and forces in a magnetic bearing.

see [14] for more details. The magnetic bearing constant k_m depends on geometry parameters (cross-section of the pole shoes, size of the air gap) and electromagnetic properties (number of turns, permeability). The nonlinearities of the magnetic force are generally reduced by adding a high bias current i_0 to the control current i_c , so that the actuator currents are given by

$$i_+ = i_0 + i_c \quad \text{and} \quad i_- = i_0 - i_c. \quad (3)$$

It is common to set the bias current to half of the maximally available current (saturation or limitations of the power amplifier) in order to exploit the full operation range. Linearizing the magnetic force about the operation point (i_0, s_0) for small control currents and small displacements results in

$$F_m^{lin} = 4k_m \left(\frac{i_0}{s_0^2} i_s - \frac{i_0^2}{s_0^3} r \right) = k_i i_c - k_s r. \quad (4)$$

Herein, k_i is the current-force constant and $-k_s$ the negative bearing stiffness,

$$k_i = 4k_m \frac{i_0}{s_0^2} \quad \text{and} \quad k_s = 4k_m \frac{i_0^2}{s_0^3}. \quad (5)$$

Assuming a high bias current for pre-magnetisation and small control current i_c and radial rotor deflection r . Herein, k_i is the current-force constant and $-k_s$ the negative bearing stiffness. Cross-coupling parameters are neglected.

The most widely used control concept for an AMB is a PID controller. The proportional (k_P) and the derivative actions (k_D) constitute the stiffness and damping characteristics of

the bearing while the integral action (k_I) assures that the radial rotor deflection r keeps track with a predefined setpoint,

$$i_c = k_P r + k_D \dot{r} + k_I \int r dt. \quad (6)$$

Inserting into eq. (4) leads to

$$F_m^{lin} = c_m r + d_m \dot{r} + k_i k_I \int r dt, \quad c_m = k_i k_P - k_s, \quad d_m = k_i k_D, \quad (7)$$

with the active stiffness and active damping coefficients c_m and d_m . Adjusting the control parameters k_P and k_D determines the dynamic properties of the AMB. Both AMBs are isotropic.

The discrete version of the control law in eq. (6) is realized on the digital real-time hardware dSPACE by a processor board DS1103. Figure 3 shows the control loop of an active magnetic bearing system in block diagram notation. It illustrates that the transfer functions of sensors, filters, AD/DA converters and amplifiers have to be taken into account when analyzing the system. In the most simple case, the transfer functions are all treated as constant and independent of the frequency. This assumption can be made if the bandwidth of the hardware is approximately ten times larger than the highest system frequency of interest, and if the discretisation errors of the AD/DA converters are reasonably small.

The rotor position is measured by four eddy current sensors, two for the z - and two for the y -direction. Collocation of the sensor and actuator is achieved by placing one sensor on each side of the stator. The exact displacement in the centre of the bearing is found by averaging both signals. This improves the control performance significantly. Before the sensor signal reaches the AD converter, it is filtered by a low pass filter with Butterworth characteristic.

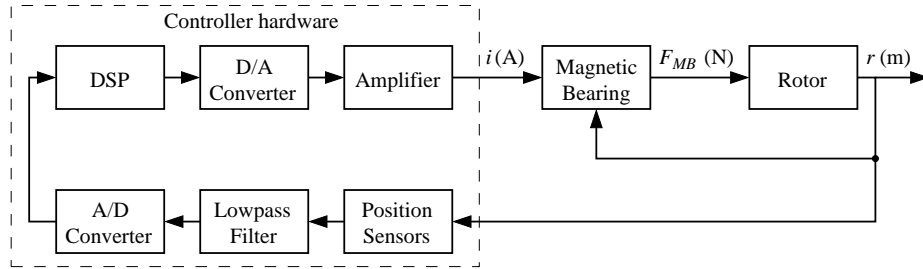


Figure 3. Control loop of an active magnetic bearing system, see [14].

2.2. Equations of motion of a continuous shaft with discrete disks

The flexible, continuous shaft is discretised using finite beam elements. For a finite beam element of length l_i , bending stiffness EI , cross-section A and density ρ , the inertia and

stiffness matrix become [11]

$$\mathbf{M}_{bi}^{z/y} = \frac{\rho A l_i}{420} \begin{bmatrix} 156 & \mp 22l_i & 54 & \pm 13l_i \\ \mp 22l_i & 4l_i^2 & \mp 13l_i & -3l_i^2 \\ 54 & \mp 13l_i & 156 & \pm 22l_i \\ \pm 13l_i & -3l_i^2 & \pm 22l_i & 4l_i^2 \end{bmatrix}, \quad (8)$$

and

$$\mathbf{C}_{bi}^{z/y} = \frac{2EI}{l_i^3} \begin{bmatrix} 6 & \mp 3l_i & -6 & \mp 3l_i \\ \mp 3l_i & 2l_i^2 & \pm 3l_i & l_i^2 \\ -6 & \pm 3l_i & 6 & \pm 3l_i \\ \mp 3l_i & l_i^2 & \pm 3l_i & 2l_i^2 \end{bmatrix} \quad (9)$$

with respect to the element coordinate vector in z -direction and y -direction, respectively,

$$\mathbf{q}_i^z = \begin{bmatrix} z_i & \varphi_{yi} & z_{i+1} & \varphi_{yi+1} \end{bmatrix}^T, \quad \mathbf{q}_i^y = \begin{bmatrix} y_i & \varphi_{zi} & y_{i+1} & \varphi_{zi+1} \end{bmatrix}^T. \quad (10)$$

Rigid disks of mass m_r and moment of inertia Θ_r are attached at discrete positions along the shaft. Their symmetry axis is aligned with the central rotary axis. For rigid disks that are attached to the end points of a finite beam element, the corresponding mass and stiffness matrices have diagonal form and read

$$\mathbf{M}_r = \begin{bmatrix} m_{ri} & & & \\ & \Theta_{ri} & & \\ & & m_{ri+1} & \\ & & & \Theta_{ri+1} \end{bmatrix}. \quad (11)$$

The element matrices in eqs. (8), (9) and (11) are assembled to the global system matrices $\mathbf{M}_b^{z/y}$, $\mathbf{C}_b^{z/y}$ and \mathbf{M}_r with respect to the global coordinate vectors

$$\mathbf{q}^z = \begin{bmatrix} z_1 & \varphi_{y1} & \cdots & z_n & \varphi_{yn} \end{bmatrix}^T, \quad \mathbf{q}^y = \begin{bmatrix} y_1 & \varphi_{z1} & \cdots & y_n & \varphi_{zn} \end{bmatrix}^T. \quad (12)$$

Adjusting the control parameters k_P and k_D determines the dynamic properties of an AMB. With the mechanical properties in eq. (7), the stiffness and damping matrices with respect to the global coordinate vector have diagonal form with entries at the location of the AMBs,

$$\mathbf{C}_m = \begin{bmatrix} \mathbf{0} & & & & \\ & c_{m1} & & & \\ & & \mathbf{0} & & \\ & & & \ddots & \\ & & & & c_{m2} \\ & & & & & \mathbf{0} \end{bmatrix}, \quad \mathbf{D}_m = \begin{bmatrix} \mathbf{0} & & & & \\ & d_{m1} & & & \\ & & \mathbf{0} & & \\ & & & \ddots & \\ & & & & d_{m2} \\ & & & & & \mathbf{0} \end{bmatrix}$$

(13)

The rotor system is excited by unbalance forces originating from eccentricities ε_i of the five rigid disks of mass m_i (including the bearing studs). The unbalance force vectors can be written as

$$\begin{aligned}\mathbf{f}_z &= -(\cos \varphi(t))'' \begin{bmatrix} m_1 \varepsilon_1 & 0 & m_2 \varepsilon_2 & 0 & \dots & m_5 \varepsilon_5 & 0 \end{bmatrix}^T, \\ \mathbf{f}_y &= -(\sin \varphi(t))'' \begin{bmatrix} m_1 \varepsilon_1 & 0 & m_2 \varepsilon_2 & 0 & \dots & m_5 \varepsilon_5 & 0 \end{bmatrix}^T,\end{aligned}\quad (14)$$

where $\varphi(t)$ is the rotary angle of the shaft counted positively in negative x -axis according to the definitions in [13].

The element matrices from eqs. (8), (9) and (11) are assembled to global system matrices with respect to the global coordinate vectors in eq. (12). Together with the global system matrices in eq. (13) describing the electromagnetic actions and the unbalance forces in eq. (14), the equations of motion of the rotor system at constant speed Ω with respect to the global coordinate vector $\mathbf{q} = [\mathbf{q}^{z,T}, \mathbf{q}^{y,T}]^T$ become

$$\mathbf{M} \ddot{\mathbf{q}} + \mathbf{D} \dot{\mathbf{q}} + \mathbf{C} \mathbf{q} = \mathbf{f} \quad (15)$$

with the assembled coefficient matrices and the global force vector

$$\begin{aligned}\mathbf{M} &= \begin{bmatrix} \mathbf{M}_b^z + \mathbf{M}_r & \mathbf{0} \\ \mathbf{0} & \mathbf{M}_b^y + \mathbf{M}_r \end{bmatrix}, \quad \mathbf{D} = \begin{bmatrix} \mathbf{D}_m & -\Omega \mathbf{G}_r \\ \Omega \mathbf{G}_r & \mathbf{D}_m \end{bmatrix}, \\ \mathbf{C} &= \begin{bmatrix} \mathbf{C}_b^z + \mathbf{C}_m & \mathbf{0} \\ \mathbf{0} & \mathbf{C}_b^y + \mathbf{C}_m \end{bmatrix}, \quad \mathbf{f} = \begin{bmatrix} \mathbf{f}^z \\ \mathbf{f}^y \end{bmatrix}.\end{aligned}\quad (16)$$

The only source of damping is the control strategy in the AMBs. The lateral vibrations in y - and z -directions are coupled by gyroscopic effects of the rigid disks, however, within the present investigation, the influence of gyroscopic effects on the first is negligible. For safety reasons, retainer bearings acting at discrete positions along the rotary shaft are applied but these are not in the focus of the present study. The operational deflection of the present rotor is assumed to be sufficiently small such that rotor-stator contacts are excluded and the linearisation of the electromagnetic force in eq. (4) remains valid.

A time-periodic stiffness variation in the rotor system is realised in the AMBs by introducing a time-dependent proportional action $k_P(t)$ in the PID controllers [9]. This control parameter is changed periodically for both AMBs simultaneously according to eq. (1) resulting in the global time-periodic stiffness matrix

$$\mathbf{C}(t) = \mathbf{C}_0 + \varepsilon \mathbf{C}_t \sin \nu t, \quad (17)$$

where \mathbf{C}_0 , \mathbf{C}_t are constant coefficient matrices.

3. Parametric anti-resonance at steady-state operation

Numerical calculations are performed in order to find a proper parametric anti-resonance for this system. The discretised continuous shaft is excited by unbalance forces originating from the rigid disk. The discretised equations are solved by direct numerical integration for different values of the control frequency ν of the time-periodicity introduced in eq. (1).

Initially, the rotor shaft rests at the centre position $\mathbf{q} = \mathbf{0}$. Since unbalance forces \mathbf{f} acts on the rotor system, the rotor shaft is deflected from this initial condition to a new deflection that rotates with the rotor speed Ω . The transition between these two states is described by free vibrations. A sample time history for the radial deflection of the disk D

$$|r_D| = \sqrt{y_D^2 + z_D^2} \quad (18)$$

at constant, nominal AMB characteristics ($\varepsilon = 0$ in eq. (1)) and at a constant rotor speed of $\Omega = 60$ rad/s is shown in Fig. 4. This rotor speed is below the first critical speed. Transient vibrations of the rotor are introduced by an initial deflection of the rotor from the steady-state deflection due to unbalance. The first three natural frequencies obtained from an eigenvalue analysis of the undamped system in eq. (15) at rest are listed in Table 2 together with the resulting parametric anti-resonance and resonance frequencies. Evaluating the analytical predictions in [8] reveals that for the present system, parametric anti-resonance can be only achieved at the difference type $\nu \approx |\omega_k - \omega_l|/n$. Note that the time history in Fig. 4 describes the radial deflection of a disk in a coordinate system that is fixed to the disk. Consequently, the frequency components observed are modulated by the rotor speed.

Now, the periodic open-loop control in the AMBs is switched on following the control law in eq. (1). First, the vibration behaviour is investigated at a control amplitude of $\varepsilon = 0.20$ and a fixed control frequency ν in the range between 0 and 300 rad/s. Numerical integration of the equations of motion in eq. (15) at $\nu = 0$ rad/s results in the time history already shown in Fig. 4. All time histories in the frequency range of interest are summarised in the contour plot in Fig. 5. Light areas depict low values and dark areas high values of the

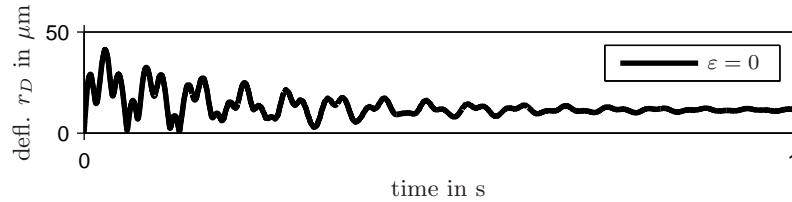


Figure 4. Rotor deflection of disk D under the action of unbalance forces for $\varepsilon = 0$.

disk deflection $|r_D|$. Additionally, frequency lines of parametric resonance and combination resonance frequencies are plotted for the orders $n = 1$ up to $n = 5$ on the right hand side of the figure. Their line thickness is scaled by the order n . The frequencies listed in Table 2 are of order $n = 1$ and are plotted as lines with the largest thickness.

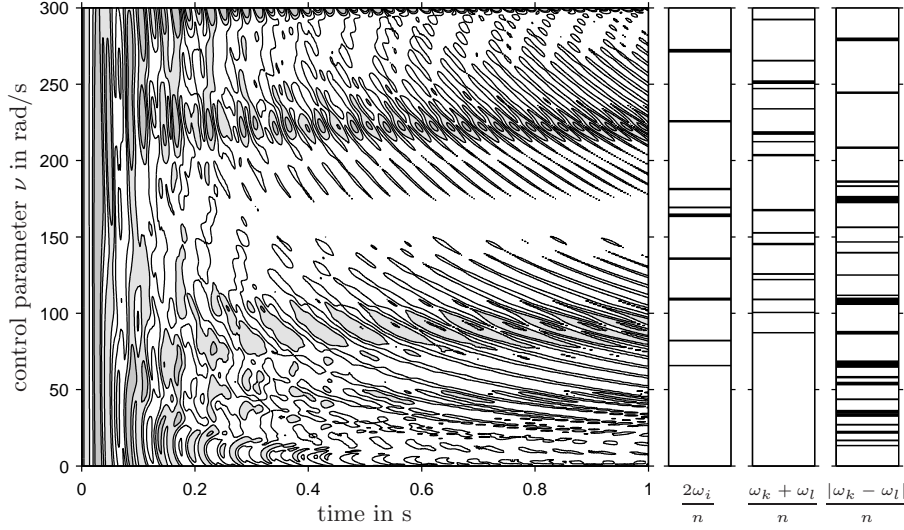


Figure 5. Numerically calculated radial deflection r_D in dependency of the control parameter ν at $\varepsilon = 0.20$ (taken from [6]).

All possible frequency combinations ν_n are divided into three sets corresponding to the three block on the right hand side of the figure: the two sets $2\omega_i/n$ and $(\omega_k + \omega_l)/n$ that correspond to parametric resonances while the set $|\omega_k - \omega_l|/n$ which corresponds to parametric anti-resonances. These frequency lines help encoding the complex distribution of the time series. At each of these frequencies a dense frequency interval exist within which the system vibrations are either excited or damped. If these frequency intervals overlap, it depends which effect dominates. In general, the destabilising effect at frequencies $2\omega_i/n$ dominates over the damping enhancement at parametric anti-resonances.

The transient behaviour of the nominal rotor in Fig. 4 corresponds to $\nu = 0$ in Fig. 5. Switching on the periodic open-loop control of the AMBs following the control law in eq. (1) changes the transient behaviour. Destabilising effects, a decrease in effective damping, are found where the control parameter ν is in the vicinity of the frequencies $(\omega_i + \omega_j)/n$. The corresponding parametric resonance frequencies can be identified by comparison with the frequency lines on the right hand side, e.g. the shaded area at 218 rad/s corresponds to the frequency $(\omega_1 + \omega_2)/2$. Indentations in the distribution towards lower time values in Fig. 5

Table 2. First natural and parametric frequencies of the JEFFCOTT rotor at rest, $\Omega = 0$.

natural frequencies		
$\omega_1 = 164$ rad/s,	$\omega_2 = 272$ rad/s,	$\omega_3 = 339$ rad/s
main parametric resonance frequencies		
$2\omega_1 = 328$ rad/s,	$2\omega_2 = 544$ rad/s	
$\omega_1 + \omega_2 = 436$ rad/s,	$\omega_1 + \omega_3 = 503$ rad/s	
main parametric anti-resonance frequencies		
$ \omega_1 - \omega_2 = 108$ rad/s,	$ \omega_1 - \omega_3 = 174$ rad/s	
$ \omega_2 - \omega_3 = 67$ rad/s		

give hints for a parametric anti-resonance. The main parametric anti-resonance is found at the white region close to the frequency 170 rad/s. This is the optimum control frequency to be chosen for the proposed open-loop control in eq. (1) for this specific rotor system.

4. Parametric anti-resonance during run-up

The run-up characteristics of the JEFFCOTT rotor supported by two active magnetic bearings whose proportional control action is varied periodically are shown in Fig. 6. At constant run-up acceleration, the first critical speed is passed at 2 s showing a major amplitude peak and the second critical speed at 6 s at very small. Activating the optimum parametric anti-resonance $\omega_3 - \omega_1$ identified in the previous section with a strength of $\varepsilon = 0.2$ mode coupling is introduced and energy transfer between the corresponding modes is activated. This coupling leads to an equal distribution of the maximum amplitudes at both critical speeds during run-up. At each critical speed transient vibrations of the corresponding mode are excited. Due to mode coupling, one mode is excited at a critical speed and energy is transferred to the other mode. On one hand, the maximum amplitude at the first critical speed is decreased due the highly damped second mode. On the other hand, the maximum amplitude at the second critical speed is increased due to the lightly damped first mode. Note that the decrease of maximum amplitude is not only achieved at the disc position but also at the stud positions (semi-active concept).

5. Conclusions

During run-up of a rotor, transient vibrations are introduced when passing through critical speeds which excite the corresponding vibration mode. A mode interaction is artificially achieved by employing a parametric anti-resonance via the bearing controller. Due to this mode coupling, if one mode is excited at a critical speed then energy is transferred to the other mode, too. On one hand, the maximum amplitude at the first critical speed is

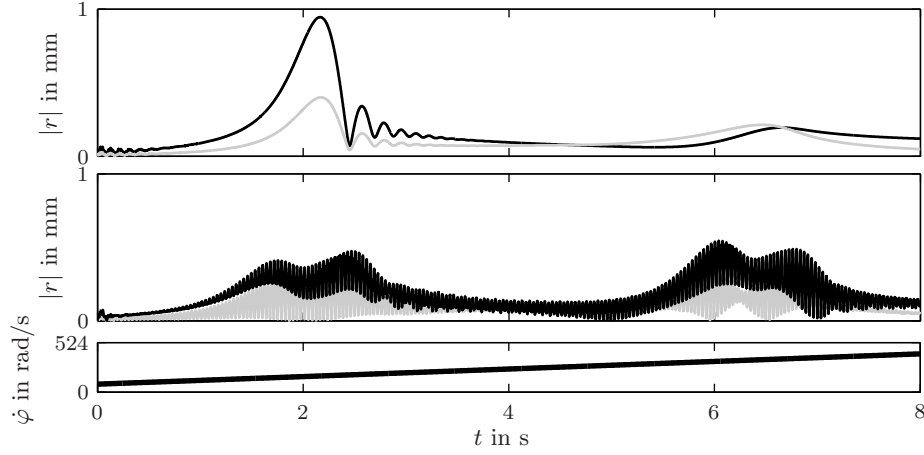


Figure 6. Passage through critical speeds at constant acceleration: (top) speed characteristic, (centre) time histories at nominal, constant bearing characteristic, (bottom) time histories for induced parametric anti-resonance at 170 rad/s and $\varepsilon = 0.2$. Disk deflection (black) and bearing studs (gray) are shown.

decreased by modulation since some vibration energy is transferred to the highly damped second mode where it is partly dissipated. On the other hand, the maximum amplitude at the second critical speed is increased by modulation since some vibration energy is transferred to the lightly damped first mode. It has to be highlighted that the decrease of maximum amplitude is not only achieved at the disc position but also at the journal positions (semi-active concept).

References

- [1] CHASALEVRIS, A., AND DOHNAL, F. A journal bearing with variable geometry for the reduction of the maximum amplitude during passage through resonance. *Journal of Vibration and Acoustics* 134 (2012), 061005: 1–8.
- [2] CHASALEVRIS, A., AND DOHNAL, F. Vibration quenching in a large scale rotor-bearing system using journal bearings with variable geometry. *Journal of Sound and Vibration* 333 (2014), 2087–2099.
- [3] CHASALEVRIS, A., AND DOHNAL, F. A journal bearing with variable geometry for the suppression of vibrations in rotating shafts: Simulation, design, construction and experiment. *Mechanical Systems and Signal Processing* 52-53 (2015), 506–528.
- [4] DOHNAL, F. Damping by parametric stiffness excitation: resonance and anti-resonance. *Journal of Vibration and Control* 14(5) (2008), 669–688.

- [5] DOHNAL, F. *A contribution to the mitigation of transient vibrations, Parametric anti-resonance: theory, experiment and interpretation*. Habilitation thesis, Technische Universität Darmstadt, 2012.
- [6] DOHNAL, F. A magnetically supported Jeffcott rotor at parametric anti-resonance. In *Proceedings of ASME 2012 International Design Engineering Technical Conferences & Computers and Information in Engineering Conference IDETC/CIE* (Chicago, IL, USA, 2012), pp. DETC2012-70962: 1–8.
- [7] DOHNAL, F. Experimental studies on damping by parametric excitation using electromagnets. *Journal of Mechanical Engineering Science* 226(8) (2012), 2015–2027.
- [8] DOHNAL, F., AND MACE, B. Damping of a flexible rotor by time-periodic stiffness and damping variation. In *Proceedings of 9th Int. Conf. on Vibration in Rotating Machinery (VIRM)* (Oxford, U.K., 2008), pp. 1–8.
- [9] DOHNAL, F., AND MARKERT, R. Enhancement of external damping of a flexible rotor in active magnetic bearings by time-periodic stiffness variation. *Journal of System and Dynamics* 5(5) (2011), 856–865.
- [10] F. DOHNAL, B. P., AND CHASALEVRIS, A. Analytical predictions of a flexible rotor in journal bearings with adjustable geometry to suppress bearing induced instabilities. In *Proceedings of the 13th Int. Conf. on Dyn. Syst. Theory and Appl. (DSTA)* (Lodz, Poland, 2015), pp. 1–12.
- [11] GÉRADIN, M., AND RIXEN, D. *Mechanical Vibrations - Theory and Application to Structural Dynamics*. Wiley, 1994.
- [12] PFAU, B., RIEKEN, M., AND MARKERT, R. Numerische Untersuchungen eines verstellbaren Gleitlagers zur Unterdrückung von Instabilitäten mittels Parameter-Antiresonanzen. In *First IFToMM D-A-CH Conference 2015* (Dortmund, 2015).
- [13] R. GASCH, R. NORDMANN, H. P. *Rotordynamik, 2nd edition*. Springer-Verlag, 2001.
- [14] SCHWEITZER, G., AND MASLEN, E. *Magnetic bearings: theory, desing and, applications to rotating machinery*. Springer-Verlag, 2009.
- [15] TONDL, A. To the problem of quenching self-excited vibrations. *Acta Technica CSAV* 43 (1998), 109–116.
- [16] TONDL, A. Self-excited vibration quenching in a rotor system by means of parametric excitation. *Acta Technica CSAV* 45 (2000), 199–211.

Fadi Dohnal, Dr. techn. habil.: Alstom Switzerland Ltd., 5401 Baden, SWITZERLAND (fadi.dohnal@power.alstom.com). The author gave a presentation of this paper during one of the conference sessions.

Athanasios Chasalevris, Ph.D.: Alstom Renewable UK Ltd., Rugby CV21-2NH, U.K. (athanasios.chasalevris@power.alstom.com).

Modelling of mechatronic systems using bond graphs (MTR029-15)

Peter Frankovský, František Trebuňa, Darina Hroncová, Alexander Gmitterko,
Ján Kostka

Abstract: The work shows the use of Bond Graph methodology of modeling electromechanical system consisting of DC motor and gearbox. As an example the electromechanical model is solved by this approach at the level of its physical behavior. This paper introduces a graphical, computer aided modeling methodology that is particularly suited for the concurrent design of multidisciplinary engineering systems with mechanical and electrical components, including interactions of physical effects from various energy domains. In contrast with the classical method, where the equations for individual components are created first and then the simulation scheme is derived on their basis, the described method uses the reverse procedure. In this paper the method of generation of system equations is discussed. From a bond graph diagram of the system, using a step-by-step procedure, system equations may be generated. As a starting point a model of electrical and mechanical is taken. The differential equations describing the dynamics of the system are obtained in terms of the states of the system.

1. Introduction

The methodology of bond graphs and algorithmic progress of creation describing state equations is useful in analyzing dynamic systems with the transformation of various forms of energy (mixed energy systems) occurring in mechatronic systems. Principal advantages of the method are the ability to anticipate formulation properties before writing equations, the availability of a simple check for correctness of the initial system relations, and the specification of a systematic reduction procedure for obtaining state equations in terms of energy variables. Using a multi-energetic approach that allows the modeling of interdisciplinary models, it explores the theory and method to automate the process of the generation of the state equation. This paper explores the bond graph technique as a modeling tool to generate state models. Mechatronic design requires that a mechanical system and its control system be designed as an integrated system. This contribution covers the background and tools for modeling and simulation of physical systems and their controllers, with parameters that are directly related to the real-world system. The theory will be illustrated with example of typical mechatronic system such as electromechanical system. We will discuss a systematic method for deriving bond graphs from electromechanical system in this article. How to enhance bond graph models to generate the model state equations and for analysis is presented. The state equations generation and block diagram expansion of causal bond graphs is treated.

2. Electromechanical system

This chapter describes the procedure for compiling the bond graph, and then power equation of state of an electromechanical system. Electromechanical system (Fig. 1) is composed of a DC motor and gearbox. Formalism of bond graphs and algorithmic approach to generating differential equations describing is just useful in analyzing dynamic systems with the transformation of various forms of energy (mixed systems - mechanical, electrical and other) occurring in mechatronic systems. Furthermore, this analysis electromechanical system using the bond graphs proves it.

The aim of the simulation using Bond Graph is for us to build the model of electromechanical system. The article describes to use graphical formulation of system modeling techniques for engineering systems involving power interactions which in English literature are named Bond Graphs to solve system with electrical and mechanical parts. In various parts of the contributions is given formalism making procedure for establishing performance graph electrical power and mechanical parts of system and subsequently derived an equation of state of the system. Solving electromechanical model consists of a voltage source, motor, gearbox, as shown in Fig. 1.

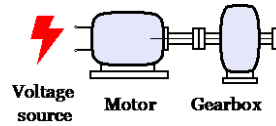


Figure 1. Model of the electromechanical system.

At first the electric part of the model is simulated and secondly the mechanical part of the electromechanical system [1], [3].

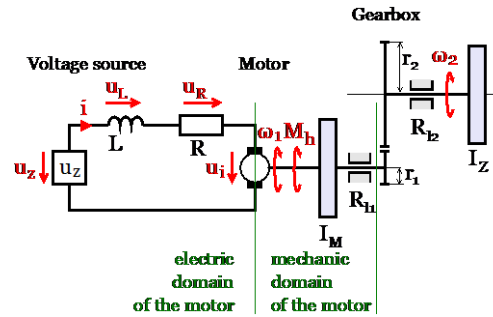


Figure 2. Parameters of the electromechanical system with domain information.

Scheme of model components is illustrated in the following figure (Fig. 2) where: u_z - voltage source, u_i - induced voltage, ω_1 - angular velocity in the motor output, M_h - drive torque at the output of the electric motor, I_M - moment of inertia of the rotor engine, R_{II} - mechanical resistance of the

motor, R_{l2} - gearbox mechanical resistance, ω_2 - angular velocity of the gearbox output, I_z - moment of inertia of the load.

3. Electric domain of the motor

In this subsection is shown the procedure for establishing bond graph from previous task. Description of the flow of current and voltage in the scheme of DC motor and schematic diagram of electric domain of the motor is shown in Fig. 2. The electrical part of the model and the description of voltage and current flow are shown in Fig. 3, [4]. The process of construction of the bond graph and consequently the equation of state is described in the steps below [1]:

Step 1 - We identify the individual components of the system according to the first step of construction of the bond graph. This electrical system contains a source of effort SE with voltage u_z (SE: u_z), inertia element I with inductance L (I:L), the resistance R with resistor R (R:R) and gyrator GY – DC motor as the inverter electrical power to mechanical power of acting rotary motion.

Step 2 – We indicate in the ideal-physical model per domain a reference source – effort voltage u_{ref} (reference voltage with positive direction) in Fig.3. The references are indicated in the ideal physical model: the ideal velocity $u_{ref}=0$.

Step 3 – Identify all other efforts (voltages) and give them unique names u_1, u_2, u_3 (Fig. 3).

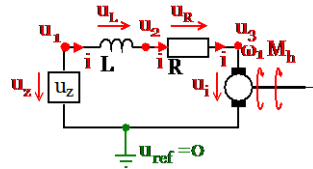


Figure 3. Electrical system – efforts with unique names u_1, u_2, u_3 and reference voltage u_{ref} .

Step 4 – Draw these efforts (electrical: voltages), graphically by 0-junctions (Fig. 4), [5].

Step 5 – Identify all effort differences (electrical: voltage = effort) needed to connect the ports of all elements enumerated in step 1 to the junction structure. When checking all ports of the elements found in step 1 linear voltage differences, u_{12} and u_{23} are identified: $u_1 - u_2 = u_{12}$, $u_2 - u_3 = u_{23}$.

Step 6 – Construct the voltage differences using a 1- junction and draw them such in the graph. We connect 1-junction with 0 - junction. After this step individual elements are connected to this structure. The result is the following bond graph of the electric motor in Fig. 4.

Step 7 – Connect the port of all elements found at step 1 with the 0-junction of the corresponding voltages or voltages differences (Fig. 4).

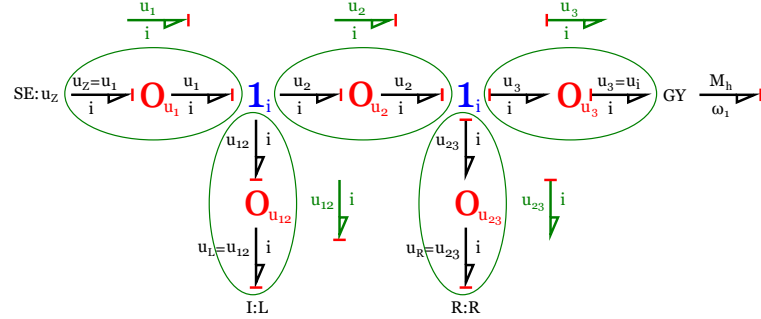


Figure 4. Connecting elements R, I, GY, SE with 0-junction and marking reduction at 0-junction applying the simplification rules.

Step 8 – Simplify the resulting graph by applying the simplification rules (Fig. 4). A junction between two bonds can be left out, if the bonds have a through power direction (one bond incoming, the other outgoing). Two separately constructed identical effort or flow differences can join into one effort or flow difference.

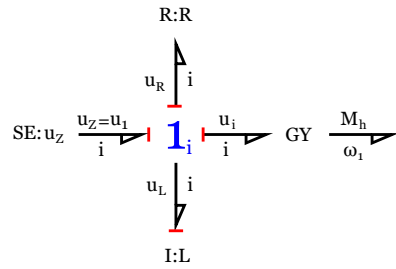


Figure 5. Complete bond graph of the electrical part of motor with signal direction and causality.

Step 9 – Determine the signal direction and causality. Causality establishes the cause and effect relationships between the factors of power. If voltage $u_i = u_R$ then applying the reduction in 1-junction and complete bond graph of the electrical part of motor with signal direction and causality as shown in Fig. 5.

In bond graphs, the inputs and the outputs are characterized by the causal stroke. The causal stroke indicates the direction in which the effort signal is directed (by implication, the end of the bond that does not have a causal stroke is the end towards which the flow signal is directed).

There are two ways of describing an element's behavior (e.g. effort in, flow out vs. flow in, effort out) as different causal forms. Note that the two alternative causal forms may, in general, require quite different mathematical operations. The causal form we use, i.e. which variable we select as input and which we select as output, can make a lot of difference. For example, the required mathematical operations may be well defined in one causal form, but not defined at all in the other.

The causal bond graph of this system can be derived, in which the inputs and the outputs are characterized by the causal stroke. This is the starting point, from which we continue toward the differential equations describing the dynamics of the system.

4. Mechanical part of the motor and gearbox

In this part we consider a model of mechanical part of the motor and gearbox (Fig. 6). Components of model is illustrated in Fig. 6 where: ω_1 - angular velocity of the motor output, M_h - drive torque at the output of the electric motor, I_M – moment of inertia of the rotor engine, R_{l1} - mechanical resistance of the motor, R_{l2} - gearbox mechanical resistance, ω_2 - angular velocity of the gearbox output, I_Z - moment of inertia of the load. Weight of the gearbox is neglected.

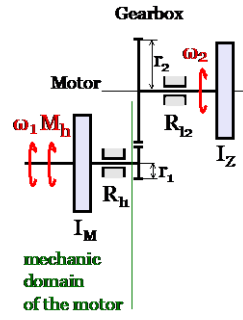


Figure 6. Schematic diagram of the mechanic domain of the motor and gearbox.

This part shows the procedure for establishing bond graphs step-by-step. We identify the individual components of the system according to the first step of construction of the bond graph:

Step 1 - We identify the individual components of the system according to the first step of construction of the bond graph. This electrical system contains a source of effort SE with moment of drive torque at the output of the electric motor M_h (SE: M_h), inductor I with inductance L (I:L), mass m (I:m), moment of inertia of the rotor engine I_M (I: I_M), moment of inertia of the load I_Z (I: I_Z), the resistance R with resistor R_{l1} , R_{l2} (R: R_{l1} , R: R_{l2}), and transformer TF – in the electromechanical system it is gearbox (TF: r_2/r_1).

Step 2 – We mark the reference angular velocity ω_{ref} in rotational movement and the reference velocity v_{ref} in translational motion (Fig. 7). The references are indicated in the ideal physical model: the ideal velocity $\omega_{ref}=0$ and $v_{ref}=0$.

Step 3 – In the model of the mechanical system to identify and select all junctions with different velocity (flows) and give them a unique name. In the solution model to name and mark velocity: ω_1 , ω_2 .

Step 4 – Mark significant points with common speed (the velocity reference is not because it is zero) by the type of junctions. Velocity detected in step 3 draw using 1-junction as

in the mechanical system. The reference velocity is not rendered because it has zero velocity. Velocity marked using 1-junction.

Step 5 – Differences in velocities are identified. These are used to connect the ports. We have no differences velocities in the system.

Step 6 – Mark junction 0 and construct difference velocities using the junction 0. We have no difference velocities in the system and we have not connected 0-junction. Junction structure is now ready and can be connected to individual elements. Connect the transformer to the junction 1. Source of effort, SE: M_h , is connected.

Step 7 – All elements are connected to the appropriate junctions, as shown in Fig. 7.

Step 8 – Bond graph is simplified according to rules of simplification.

Step 9 – Integral causality is marked in simplified bond graph (Fig. 7).

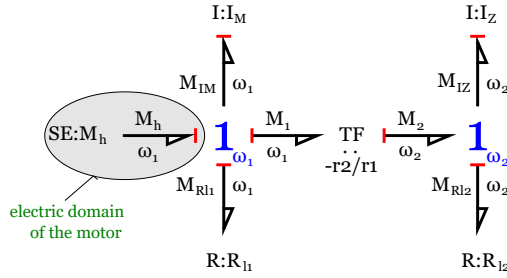


Figure 7. The final bond graph of the electromechanical system with connecting the individual elements to the 1-junction and marked causality.

The inertia characteristics of the load are contained in the moment of inertia I_Z . This section derives the bond graph of reduced mechanical parts. We assemble to the signal diagram and then the state diagram. The results of bond graphs applications are shown in the bond graph diagram of the mechanical part of motor and mechanical part of gearbox (Fig. 7). In formulating the dynamic equations that describe the system, causality defines, for each modeling element, which variable is dependent and which is independent. By propagating the causation graphically from one modeling element to the other, analysis of large-scale models becomes easier.

5. Model of the mechanical part- causality collision

In this part we derive the bond graph of a DC motor and of gearbox, from which we create block scheme. According to the rules for the compilation of bond graph of the electromechanical system designed bond graph marked with integral causality. The resulting graph of motor and a mechanical part of gear box is after editing in the form (Fig. 8).

In this system the load is fixed at the end of a long shaft. At the end of the shaft is the same angular frequency ω_2 as in output from the gearbox. Power bond is connected to junction 1 at the end

of the transformer. Final bond graph of the electromechanical system with conflict of the causality in 1-junction is shown in Fig. 8.

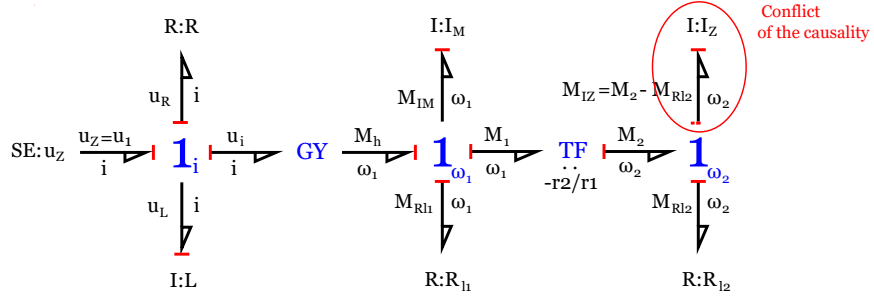


Figure 8. The resulting bond graph of the electromechanical system with designating the conflict of the causality.

There are two ways to resolve this problem of conflict of causality. The first method assumes a certain torsion flexibility of a long shaft to the gearbox output. This is physically justified because it is a perfectly rigid body. The second way is used if we want to have a model with fewer equation of state. In this case we accept a derivative causality by drawing it in the state diagram.

If in the first case of the solution causality collision problem is assumed a certain torsional flexibility of a long shaft gearbox output, then in Fig. 9,

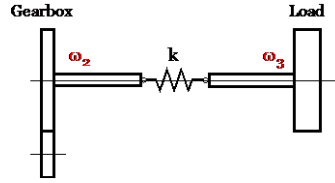


Figure 9. Long shaft with torsion flexibility.

where: k – is constant stiffness of the shaft, ω_2 ω_3 – are the angular velocity of the long shaft.

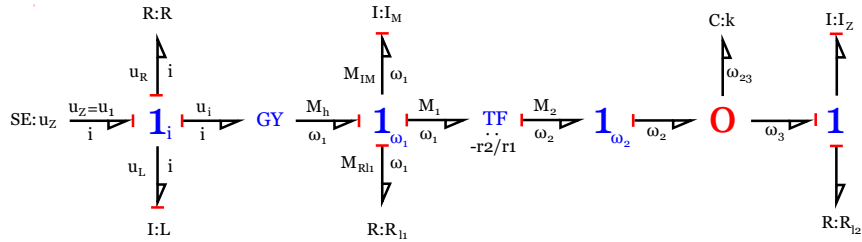


Figure 10. Bond graph of the electromechanical system assuming that we consider compliance torsionally long shaft gearbox output.

In the second method solving the problem of causality accepted the derivative causality, which is plotted in the block diagram. We get the model with fewer equations of state. Bond graph of motor and gear with consideration of the derivative causality in inductor $I: I_Z$ is written in the form (Fig. 11).

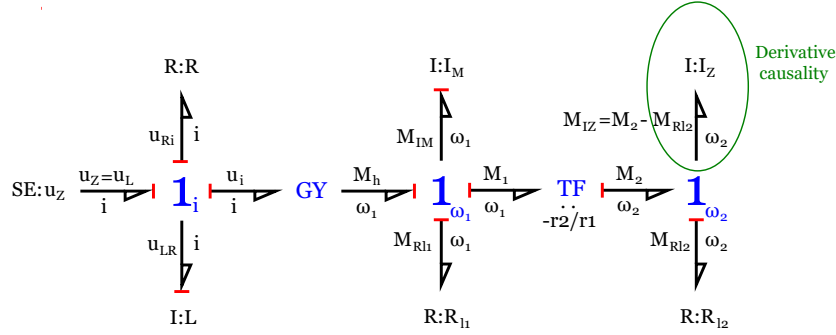


Figure 11. Final bond graph of the electromechanical system with derivative causality.

6. Expansion to block diagrams

The next section describes a three-step transition from the bond graph to the block diagram for the model of the electromechanical system consists only of the motor and gearbox (Fig. 3). Block diagram will be prepared for the bond graph in Fig. 11. We consider the ideal source effort $SE: u_Z$ and derivative causality in integrator $I: I_Z$. All symbols of nodes and elements of the bond graph shall be marked as shown in Fig. 12, [6].

Individual edge bond graph will be replaced by a pair of signal edges and circled symbols nodes shall be connected by these pairs of signal edges (Fig. 12). The orientation signal edge is done in accordance with the marked causality (Fig. 11). Where it is intended that the ideal source of effort is the voltage already is a bond graph with the pair of signal edges in the form shown in Fig. 12.

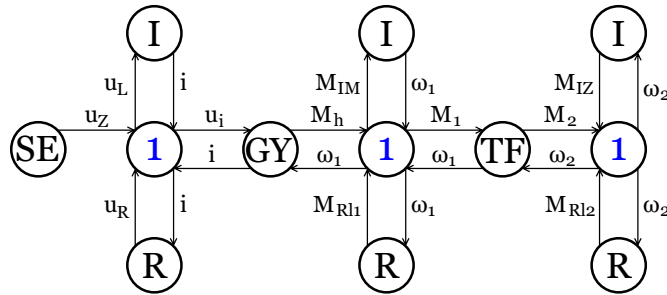


Figure 12. Expansion of bonds to bilateral signal flows of the elevator model.

All nodes are replaced by the block structure. Using the rules set out in the literature will be set up state diagram shown in Fig. 13, which serves as a basis for drawing up the equation of state.

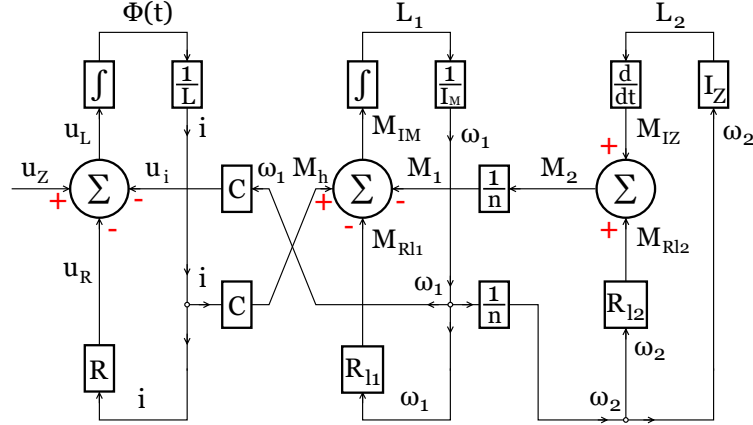


Figure 13. The resulting block diagram of the model in standard form.

Drawing up models of dynamic systems is always based on certain assumptions. Any real system can be complicated. In engineering practice is an effort to assemble the simplest models as possible. But simplification must be to the extent that the model gave us the answer to the problem studied. Therefore, when compiling models it is necessary to decide whether some of inductors, capacitors and resistors can be neglected. Such a simplification, if bad, may lead to such a final model, that might be difficult in next application. In bond graph it shows up as algebraic loops or we cannot avoid using a derivative causality.

Collision of the causality is called situation, it can not be in one or more junctions defined integral causality and must be assigned the derivative causality, which is a non-preferred. This is a sign that the appropriate inductor and capacitor does not represent the state variable. Such elements are also called dependent energy storage as they are in a certain relationship with some algebraic stock positions. An example of such a situation with derivative causality is well designed system Fig.13.

7. Transition from state scheme to state equation

In the state diagram of Fig. 13 has the inductor I_Z differential causality. Energy variable momentum L_2 is not a state variable. State variable for this dynamic system are: inductance Φ and momentum L_1 . Energy variable L_2 is with state variable in algebraic relationship. Therefore, before we write the equation of state, we must see this relationship.

$$\frac{dL_2(t)}{dt} = \frac{I_Z}{n \cdot I_M} \cdot \frac{dL_1(t)}{dt} \quad (5)$$

From block diagram (Fig. 13) for state variables we write (marked $IM=I_M$):

$$\frac{d\Phi(t)}{dt} = u_L, \quad (6)$$

$$\frac{dL_1(t)}{dt} = M_{IM}. \quad (7)$$

We obtain from block diagram:

$$u_L(t) = u_Z(t) - u_R(t) - u_i(t). \quad (8)$$

First state equation is in form:

$$\frac{d\Phi(t)}{dt} = u_Z(t) - \frac{R}{L} \cdot \Phi(t) - \frac{C}{I_M} \cdot L_1(t). \quad (9)$$

From block diagram:

$$M_{IM}(t) = M_h(t) - M_{R1}(t) - M_1(t). \quad (10)$$

Second state equation is in form:

$$\frac{dL_1(t)}{dt} = \frac{C}{LQ} \cdot \Phi(t) - \frac{\left(\frac{R_{l1}}{I_M} + \frac{R_{l2}}{nI_M}\right)}{Q} \cdot L_1(t), \quad (14)$$

$$\text{where: } Q = \left(1 + \frac{I_Z}{n^2 I_M}\right). \quad (15)$$

The equation of state of the electromechanical system are in the matrix form:

$$\begin{bmatrix} \frac{d\Phi(t)}{dt} \\ \frac{dL_1(t)}{dt} \end{bmatrix} = \begin{bmatrix} \frac{R}{L} & -\frac{C}{I_M} \\ \frac{C}{LQ} & -\frac{\frac{R_{l1}}{I_M} + \frac{R_{l2}}{nI_M}}{Q} \end{bmatrix} \cdot \begin{bmatrix} \Phi(t) \\ L_1(t) \end{bmatrix} + \begin{bmatrix} 1 \\ 0 \end{bmatrix} \cdot u(t). \quad (15)$$

The state variables for this dynamic system are the inductance $\Phi(t)$ and the momentum $L_1(t)$ and their another solution may be for example in Matlab/Simulink [2, 7].

8. Conclusions

This article presents techniques for representing elements of combination systems mechanical and electrical in the abstract form of bond graphs instead of the schematic diagrams usually used to show electromechanical system. For some this may seem to be an unnecessary step away from physical reality, but it has useful consequences. Bond graph is a precise way to represent a mathematical model of the dynamic system. Often schematic diagrams are not entirely clear about whether certain effects are to be included or neglected in the model. For many systems involving two or more forms of energy, such as mechanical and electrical, there are no standard schematic diagrams that clearly indicate assumptions made in the modeling process. The methodology of bond graphs and algorithmic progress of creation describing state space equations is useful in analyzing dynamic systems with the transformation of various forms of energy (mixed energy systems) occurring in mechatronic systems [8, 9]. Principal advantages of the method are the ability to anticipate formulation properties before writing equations, the availability of a simple check for correctness of the initial system relations, and the specification of a systematic reduction procedure for obtaining state equations in terms of energy variables. Using a multi-energetic approach that allows the modeling of interdisciplinary models, it explores the theory and method to automate the process of the generation of the state equations. These are typical of mechatronic applications. This paper explores the bond graph technique as a modeling tool to generate state models. The theory will be illustrated with example of typical mechatronic system such as electromechanical system. We present a systematic method for deriving bond graphs from electromechanical system in this article. How to create bond graph models to generate the model state equations and for analysis is presented. The state equations generated from block diagram and causal bond graphs is treated.

Acknowledgments

This work was supported in part by the Ministry of Education of the Slovakia Foundation under grant projects VEGA No. 1/1205/12, VEGA No. 1/0393/14, KEGA 021TUKÉ-4/2013 and KEGA No. 054 TUKÉ – 4/2014.

References

- [1] Broenink, J. F. Introduction to Physical Systems Modelling with Bond Graphs. University of Twente, Dept EE, Netherlands, 1998.
- [2] Merzouki, R., Samantaray, A. K., Pathak, P. M., Bouamama, B. O. Bond Graph Modeling of Mechatronic Systems. In Intelligent Mechatronic Systems, 2013, pp. 15-109.
- [3] Gmíterko, A., Šarga, P., Hroncová, D. Mechatronika 1. 1. vyd. , Košice: SĽ TU, 2012. 304 s. ISBN 978-80-553-0884-5.

- [4] Gmiterko, A., Hroncová, D. Šarga, P. Modeling Mechanical Systems Using Bond Graphs. In.: Modelling of Mechanical and Mechatronical Systems: proceedings of the 4th international conference 2011. Herľany, Košice, Slovakia: Sjf TU, 2011, s. 112-118. ISBN 978-80-553-0731-2.
- [5] Gmiterko, A., Hroncová, D. Šarga, P. Generation of State Equations From a BondGraph Diagram of The Mechanical System. In.: Modelling of Mechanical and Mechatronical Systems: proceedings of the 4th international conference 2011. Herľany, Košice, Slovakia: Sjf TU, 2011, s. 119-123. ISBN 987-80-553-0731-2.
- [6] Karnopp, D. C., Margolis, D. L., Rosenberg, R. C. System dynamics - Modeling and simulation of mechatronic systems. John Willey & Sons, Inc., Hoboken, New Jersey, 2005. ISBN-13-978-0-471-70965-7.
- [7] Moore, H. MATLAB for Engineers. Prentice Hall Press, 2014.
- [8] Borutzky, W. Bond Graph Modelling of Engineering Systems. New York: Springer, 2011.
- [9] Abu-Rub, H., Iqbal, A., Guzinski, J. High performance control of AC drives with MATLAB/Simulink models. John Wiley & Sons, 2012.

Peter Frankovský, Associate Professor: Technical University of Košice, Faculty of Mechanical Engineering, Letná 9, 042 00 Košice, Slovakia (peter.frankovsky@gmail.com).

František Trebuňa, Professor: Technical University of Košice, Faculty of Mechanical Engineering, Letná 9, 042 00 Košice, Slovakia (frantisek.trebuna@tuke.sk).

Darina Hroncová, Ph.D.: Technical University of Košice, Faculty of Mechanical Engineering, Letná 9, 042 00 Košice, Slovakia (darina.hroncova@tuke.sk).

Alexander Gmiterko, Professor: Technical University of Košice, Faculty of Mechanical Engineering, Letná 9, 042 00 Košice, Slovakia (alexander.gmiterko@tuke.sk).

Ján Kostka, Ing. (Ph.D. student): Technical University of Košice, Faculty of Mechanical Engineering, Letná 9, 042 00 Košice, Slovakia (jan.kostka@tuke.sk).

Nonlinear transverse vibrations of a beam under an axial load (VIB106-15)

Paweł Fritzkowski, Krzysztof Magnucki, Szymon Milecki

Abstract: The paper is devoted to transverse in-plane vibrations of a beam which is a part of a symmetrical triangular frame. A mathematical model based on the Hamilton principle, formulated for large deflections of the beam subjected to dynamic axial excitation is presented. A nonlinear ordinary differential equation for the vibration amplitude is derived by means of the Galerkin method. Dynamics of the system is studied numerically for various values of the system parameters, including the excitation amplitude and frequency. The amplitude is taken to be below or above the static critical load. The effect of the parameters on behaviour of the system is analyzed. Several tools are used to specify the vibrations type, e.g. the Poincare maps and the Lyapunov exponents. The regions related to regular and chaotic vibrations are determined in parameter planes. They are compared to the stable and unstable regions of the abbreviated (linear) dynamical system.

1. Introduction

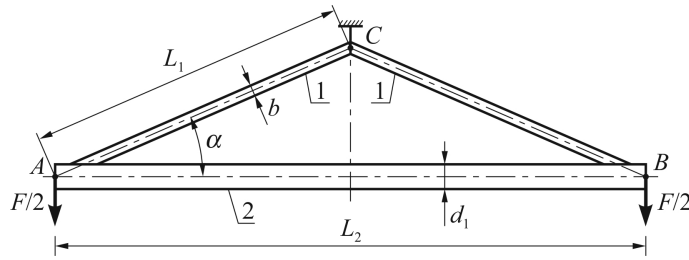
Behaviour of elastic structures like beams/columns under axial loads is a classical problem, studied mainly in the context of static or dynamic stability. Timoshenko and Gere [7] discussed elastic buckling of a wide variety of structural elements, including bars and frames. An extensive review of stability problems was presented by Bažant and Cedolin [1]. Virgin [9] focused attention on the interplay between vibrations and stability in axially loaded structures. Parametrically excited systems of this type, described by linear or nonlinear time-periodic models, were considered by McLachlan [6], Gutowski and Swietlicki [3], and Łuczko [4]. The general theory of dynamic stability of elastic structures and its applications were presented by Bolotin [2].

This paper is devoted to nonlinear vibrations of a beam which is a part of a symmetrical triangular frame. Recently, Magnucki and Milecki [5] studied static buckling of such a system. However, closed planar frames, including the triangular ones, are rarely analyzed in the literature related to the field of dynamics. Moreover, vibrational problems for frame structures are usually solved by using the finite element approach (e.g. see [8, 10]). In what follows, the cross-beam of the triangular frame is appropriately isolated from the system, which simplifies both the model and analysis.

2. Mathematical model

Consider a symmetrical triangular frame (see Fig. 1a) whose arms (1) of length L_1 are connected via a cross-beam (2) of length L_2 . The arms have a rectangular cross-section ($b \times c$), whereas the cross-section of the latter member has the shape of a circular ring: its outer and inner diameters are denoted by d_1 and d_0 , respectively. The vertex C of the frame is fixed while the others, A and B , are simply supported out-of-plane and subjected to in-plane load.

a)



b)

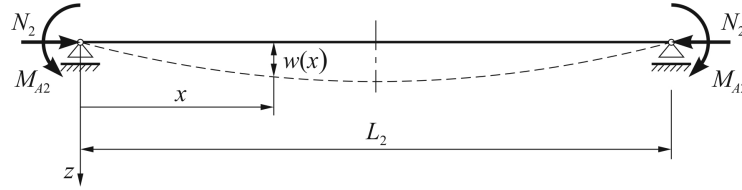


Figure 1. The mechanical system to be considered: a) the full triangular frame, b) the cross-beam isolated from the system

In paper by Magnucki and Milecki [5] one can find, among others, the relations between the load F and the internal forces related to the cross-beam: the axial force N_2 and the bending moment M_2 . Now, in-plane vibrations of the system are considered, i.e. the load is assumed to be a function of time, $F = F(t)$. To simplify dynamic analysis, the beam is isolated from the structure as can be seen in Fig. 1b. The beam is treated as simply supported but subjected to the axial force $N_2(t)$ and opposite end moments $M_{A2}(t)$. For simplicity energy dissipation is neglected.

In case of large deflections $w(x, t)$ the normal strain is given by

$$\varepsilon_x = \frac{\partial u}{\partial x} + \frac{1}{2} \left(\frac{\partial w}{\partial x} \right)^2 \quad \text{with} \quad u(x, z, t) = -z \frac{\partial w}{\partial x}, \quad (1)$$

where u denotes the axial displacement. The elastic strain energy of the system has the form

$$U = \frac{1}{2}E \int_0^{L_2} \int_{A_2} \varepsilon_x^2 dA_2 dx = \frac{1}{2}E \int_0^{L_2} \left[J_{y2} \left(\frac{\partial^2 w}{\partial x^2} \right)^2 + \frac{1}{4} A_2 \left(\frac{\partial w}{\partial x} \right)^4 \right] dx, \quad (2)$$

in which E is Young's modulus and $A_2 = \pi(d_1^2 - d_0^2)/4$, $J_{y2} = \pi(d_1^4 - d_0^4)/64$ are the area of the cross-section and its moment of inertia. Kinetic energy of the beam and the work of the load can be expressed as

$$T = \frac{1}{2} \rho A_2 \int_0^{L_2} \left(\frac{\partial w}{\partial t} \right)^2 dx, \quad W = N_2(t) \int_0^{L_2/2} \left(\frac{\partial w}{\partial x} \right)^2 dx, \quad (3)$$

where ρ denotes the material density. Note that the effect of the moments M_{A2} are not included at this stage. Applying Hamilton's principle

$$\delta \int_{t_1}^{t_2} (T - U + W) dt = 0 \quad (4)$$

leads to the following equation of motion:

$$\rho A_2 \frac{\partial^2 w}{\partial t^2} + E J_{y2} \frac{\partial^4 w}{\partial x^4} - \frac{3}{2} E A_2 \left(\frac{\partial w}{\partial x} \right)^2 \frac{\partial^2 w}{\partial x^2} + N_2(t) \frac{\partial^2 w}{\partial x^2} = 0 \quad (5)$$

We focus on the first mode of vibration and approximate the displacements by

$$w(x, t) = w_a(t) \varphi(x) \quad \text{with} \quad \varphi(x) = \frac{1}{1 + \alpha_0} \left[\sin \left(\frac{\pi x}{L_2} \right) - \alpha_0 \sin \left(\frac{3\pi x}{L_2} \right) \right] \quad (6)$$

where α_0 is a positive constant. Such a mode shape, $\varphi(x)$, allows to incorporate (indirectly) the effect of the end moments M_{A2} into the model. Using the Galerkin method we obtain the approximate equation for the modal amplitude:

$$\ddot{q} + c_1 \left[1 - \tilde{N}_2(t) \right] q + c_3 q^3 = 0, \quad (7)$$

where $q = w_a/d_1$ and \tilde{N}_2 is the relative (dimensionless) axial force. The coefficients c_1 and c_3 are dependent on the beam parameters, and can be determined by considering the static case ($\ddot{q} = 0$) and the relationships given in [5]:

$$c_1 = \frac{1 + 9\alpha_0^2}{1 + \alpha_0^2} \frac{\pi^2}{\rho A_2 L_2^2} N_{2\text{cr}}, \quad c_3 = \frac{3}{8} \frac{1 - 4\alpha_0 + 36\alpha_0^2 + 81\alpha_0^4}{(1 + \alpha_0)^2 (1 + \alpha_0^2)} \frac{\pi^4 E d_1^2}{\rho L_2^4}, \quad (8)$$

where

$$\alpha_0 = \frac{1}{3} \sqrt{\frac{\kappa - 1}{9 - \kappa}}, \quad \kappa = \frac{N_{2\text{cr}}}{N_{2\text{cr}}^E}, \quad N_{2\text{cr}}^E = \frac{\pi^2 E J_{y2}}{L_2^2}. \quad (9)$$

Note that N_{2cr}^E is the Euler critical axial load for a beam/column, while N_{2cr} is the critical force that corresponds to the static critical load F_{cr} calculated for the triangular frame (see [5]). The quantity \tilde{N}_2 in (7) is related just to N_{2cr} , that is, $\tilde{N}_2(t) = N_2(t)/N_{2cr}$.

In the example below we take $\tilde{N}_2(t) = a \sin(\omega t)$. It is convenient to write Eq. (7) for this particular case in the fully non-dimensional form:

$$\ddot{q} + [1 - a \sin(\Omega \tau)] q + \gamma q^3 = 0 \quad (10)$$

in which $\tau = \omega_1 t$, $\Omega = \omega/\omega_1$ where $\omega_1 = \sqrt{c_1}$ is the first natural frequency of a load-free beam and hence $\gamma = c_3/\omega_1^2 = c_3/c_1$. Now obviously, $q = q(\tau)$ and \ddot{q} denotes the derivative with respect to the dimensionless time τ . Without the nonlinear term ($\gamma = 0$) Eq. (10) reduces to the well-known Hill's equation.

3. Vibrations due to a harmonic load

We focus attention on a symmetrical triangular frame with the following parameter values: $L_2 = 1352$ mm, $d_0 = 50$ mm, $d_1 = 60$ mm, $\alpha = \pi/9$, $E = 2 \cdot 10^5$ MPa. The area of the arms' cross-section is constant, $A_1 = 1000$ mm², while the dimension b (and $c = A_1/b$) is altered. This particular set of values is used in the railway industry. We assume that the structure is subjected to harmonic load and the axial force on the cross-beam is $\tilde{N}_2(t) = a \sin(\omega t)$ where $\omega = 2\pi f$. Equation (10) is solved for the initial conditions: $q(0) = 10^{-3}$, $\dot{q}(0) = 0$.

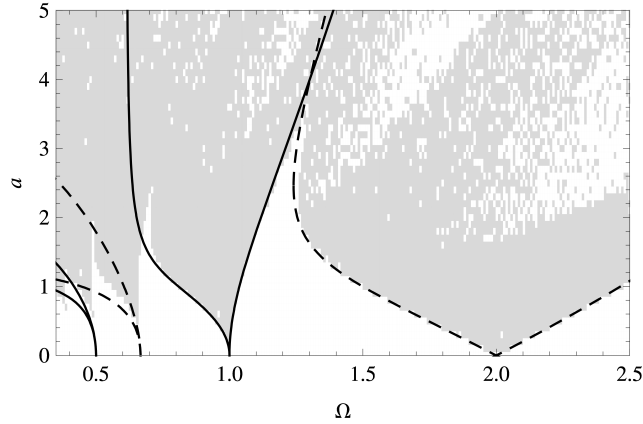


Figure 2. Regions of stable (white) and unstable (grey) motion of the beam ($b = 20$ mm) and the stability boundaries of the linear system

First, the results obtained for $b = 20$ mm are thoroughly presented. Figure 2 shows the parameter plane (Ω, a) with regions of stable and unstable motion of the system. More

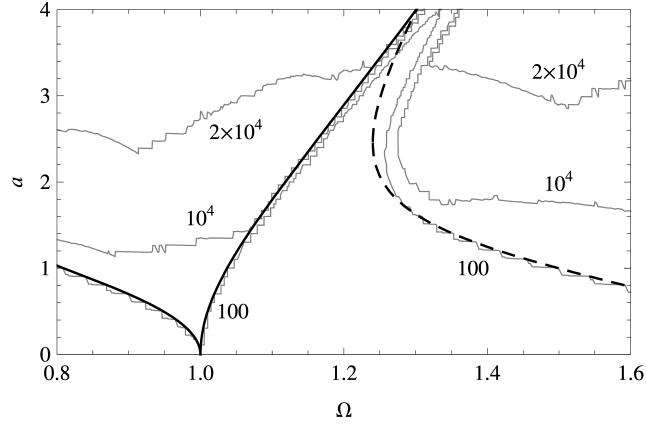


Figure 3. Maximal value of the quantity X_{rel} and the stability boundaries of the linear system

precisely, the areas filled with grey relate to positive values of the maximal Lyapunov exponent (MLE), λ_1 . The map has been computed with steps $\Delta f = 1$ Hz and $\Delta a = 0.1$. The Lyapunov exponents have been evaluated using the Gram-Schmidt orthogonalization procedure and renormalization. Taking into account relatively slow convergence of the numerical computations in the analyzed undamped case, vibrations are classified as chaotic if $\lambda_1 \geq 0.02$.

For comparison purposes, stability boundaries for the abbreviated system ($\gamma = 0$) are shown. The curves correspond to $1T$ -periodic (solid line) and $2T$ -periodic solutions (dashed line) where $T = 1/f$ [2, 3, 6]. Here, the dependencies $a(\Omega)$ have been determined by means of the Rayleigh method, by assuming the solutions in the forms [3]:

$$q(\tau) = B_0 + C_2 \sin(\Omega\tau) + D_2 \cos(\Omega\tau) + C_4 \sin(2\Omega\tau) + D_4 \cos(2\Omega\tau) \quad (11)$$

and

$$q(\tau) = C_1 \sin\left(\frac{\Omega}{2}\tau\right) + D_1 \cos\left(\frac{\Omega}{2}\tau\right) + C_2 \sin\left(\frac{3\Omega}{2}\tau\right) + D_2 \cos\left(\frac{3\Omega}{2}\tau\right) \quad (12)$$

As can be seen, the curves coincide considerably with the numerical results based on the nonlinear model. However, these two cases are not fully comparable. Unstable solutions of the Hill equation (or the Mathieu equation) increase unboundedly with time, while the nonlinear term γq^3 causes amplitude limitation [6]. Thus, deflections of the beam become very large but remain bounded.

This type of behaviour can be detected by analysis of the displacement and velocity amplitudes. Let $\mathbf{X} = [q, \dot{q}]^T$ be the state vector of the system. Character of the system

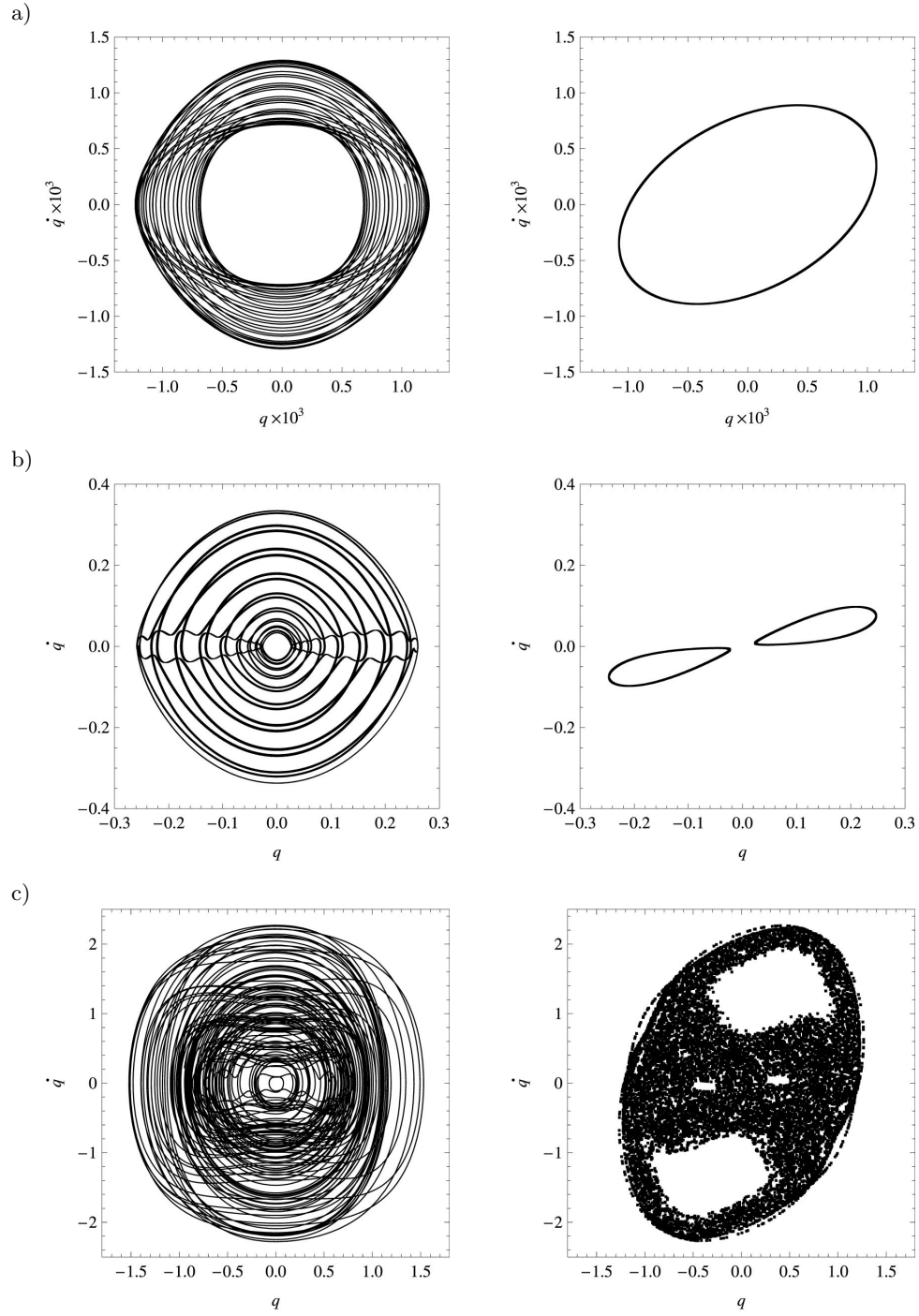


Figure 4. Quasi-periodic and chaotic vibrations of the beam for $f = 160$ Hz: a) $a = 0.5$, b) $a = 1.2$, c) $a = 1.8$

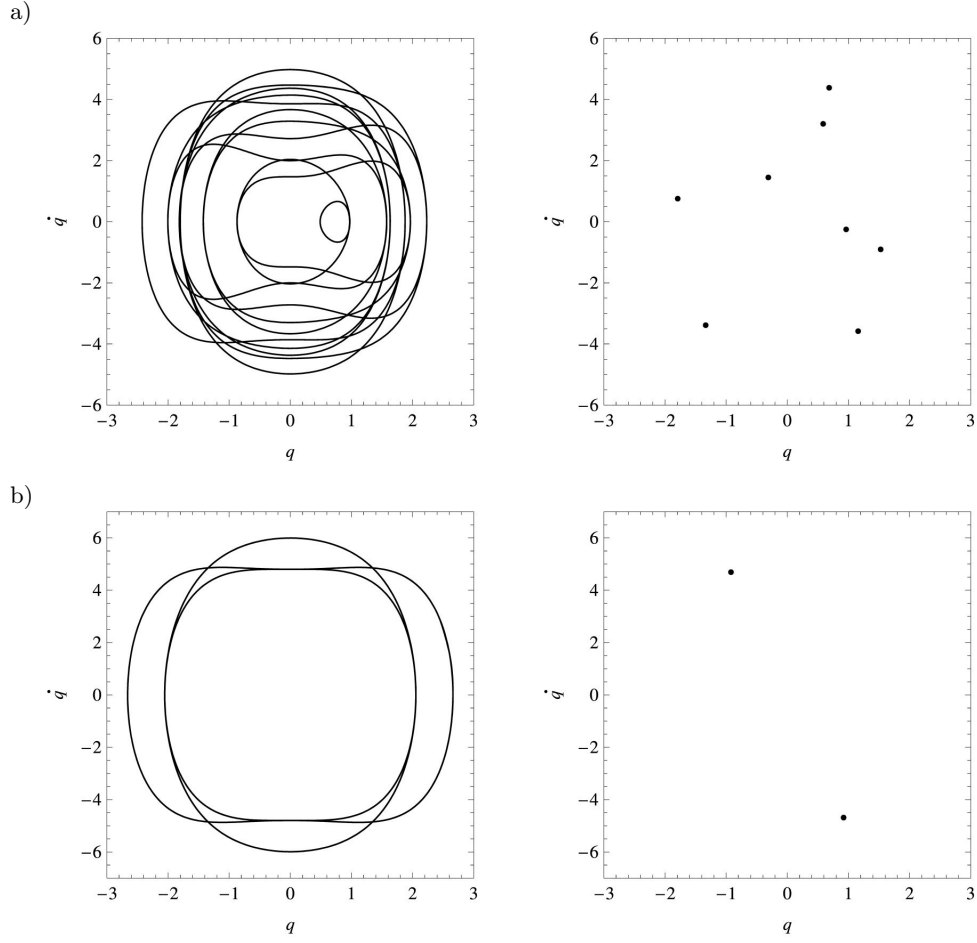


Figure 5. Periodic vibrations of the beam: a) $8T$ -periodic motion ($f = 160$ Hz, $a = 4$), b) $2T$ -periodic motion ($f = 195$ Hz, $a = 4.5$)

evolution can be assessed, for example, by the measure

$$X_{\text{rel}}(\tau) = \frac{\|\mathbf{X}(\tau)\|}{\|\mathbf{X}(0)\|}, \quad (13)$$

where $\|\cdot\|$ denotes the Euclidean norm. The maximal values of $X_{\text{rel}}(\tau)$ found in the range $0 \leq \tau \leq 5 \cdot 10^4$ are plotted in Fig. 3. The contour line corresponding to $X_{\text{rel}} = 100$ fits well with the curves $a(\Omega)$, especially for lower a . As the load amplitude increases, X_{rel} grows significantly but does not exceed $4 \cdot 10^4$.

Naturally, the beam exhibits a rich spectrum of behaviour. Selected responses of the system for $f = 160$ Hz ($\Omega \approx 1.48$) are illustrated in Fig. 4 in the form of phase portraits

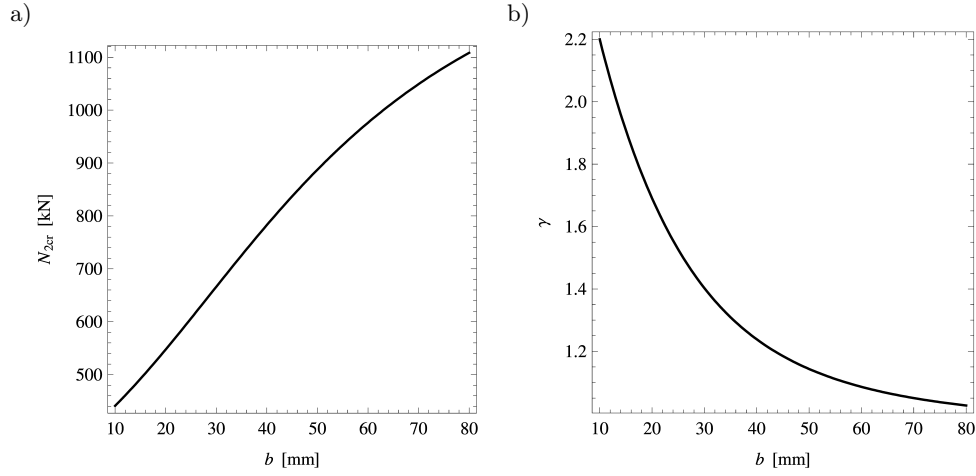


Figure 6. The effect of the dimension b on: a) the critical axial load, b) the coefficient γ

and the Poincaré maps. Similar to the linear case, the stable region is dominated by quasi-periodic vibrations (Fig. 4a). This kind of motion can also be found for larger values of the load amplitude a , however, the displacement and velocity are much higher (Fig. 4b). An example of chaotic solution is depicted in Fig. 4c. Note that $q > 1$ means $w_a > d_1$, i.e. large deflections of the beam, which definitely goes beyond the classical (linear) beam theory.

As results from Fig. 2, there are scattered subregions of regular motion for $a > 1$, above the curves corresponding to the linear system. In fact, subharmonic vibrations can be easily found there. For instance, taking the same frequency as before and $a = 4$, one can obtain quite complex $8T$ -periodic solution (see Fig. 5a). For $f = 195$ Hz ($\Omega \approx 1.8$) and $a = 4.5$, in turn, $2T$ -periodic behaviour arises (Fig. 5b).

In engineering practice the width b of the arms is one of the most important parameters. In the static case, for example, flat buckling of the triangular frame can occur for small values of b (at the given data: $b \leq 18$ mm); otherwise the system undergoes lateral buckling [5]. As presented in Fig. 6, the static critical load of the beam, N_{2cr} , increases with increasing b . At the same time, such a strengthening of the arms in respect of in-plane bending decreases the coefficient of the cubic term, γ . The question is how it affects the dynamics of the beam.

By analogy to Fig. 2, the regions of regular and chaotic motion for $b = 50$ mm are shown in Fig. 7. As in the previous case, the critical value of λ_1 has been set to 0.02. Again the lower boundary is quite well approximated by the curves determined analytically for the linear system. Nevertheless, it seems that an increase of b gradually enlarges the

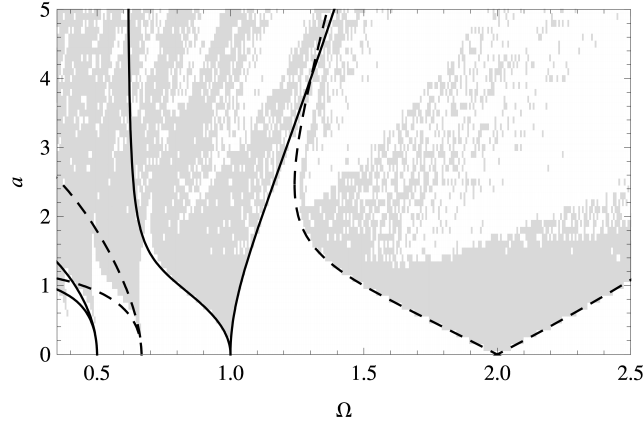


Figure 7. Regions of stable (white) and unstable (grey) motion of the beam ($b = 50$ mm) and the stability boundaries of the linear system

scattered regions indicating regular dynamics, and shifts them towards lower values of both the load amplitude and frequency. More detailed studies of numerical solutions could show an occurrence of harmonic and subharmonic vibrations of large amplitude within these ranges.

4. Conclusions

The problem of dynamics of the symmetrical triangular frame has been reduced to the problem of parametric vibrations of the cross-beam. The mathematical model of the system has been formulated by means of the Hamilton principle and the Galerkin method. The regions of regular and chaotic vibrations have been determined in the 'load frequency – amplitude' plane. The lower boundaries of the chaotic regions are well approximated by the curves specified for the abbreviated dynamical system. Within its stable region the vibration amplitude of the beam increases significantly but remains bounded. Moreover, the scattered regions of regular motion become larger as the width of the frame arms increases.

This kind of analysis, focused on both the vibration type and amplitude growth, is crucial in the formulation of safety conditions for the structure, i.e. certain criteria for the so called technical stability. However, from a practical viewpoint, the dynamic stability problem is associated mainly with behaviour of a system under suddenly applied loads (e.g. an impulse or step load). Since the problem is of great importance in the particular case of brake triangles, it merits special attention in further studies of the mechanical system.

Acknowledgments

The first author have been supported by 02/21/DSPB/3463 Grant.

References

- [1] BAŽANT, Z., AND CEDOLIN, L. *Stability of Structures: Elastic, Inelastic, Fracture and Damage Theories*. World Scientific, London, 2010.
- [2] BOLOTIN, V. *The Dynamic Stability of Elastic Systems*. Holden-Day, San Francisco, 1964.
- [3] GUTOWSKI, R., AND SWIETLICKI, W. *Dynamics and Vibrations of mechanical systems*. PWN (in Polish), Warsaw, 1986.
- [4] ŁUCZKO, J. *Regular and Chaotic Vibrations in Nonlinear Mechanical Systems*. Publishing House of the Crakow University of Technology (in Polish), Cracow, 2008.
- [5] MAGNUCKI, K., AND MILECKI, S. Elastic buckling of a triangular frame subject to in-plane tension. *Journal of Theoretical and Applied Mechanics* 53, 3 (2015), 581–591.
- [6] McLACHLAN, N. *Ordinary Non-Linear Differential Equations in Engineering and Physical Sciences*. Oxford University Press, London, 1950.
- [7] TIMOSHENKO, S., AND GERE, J. *Theory of Elastic Stability*. McGraw-Hill, New York, 1963.
- [8] TRIANTAFYLLOU, S., AND KOUMOUSIS, V. Small and large displacement dynamic analysis of frame structures based on hysteretic beam elements. *Journal of Engineering Mechanics* 138, 1 (2012), 36–49.
- [9] VIRGIN, L. *Vibration of Axially Loaded Structures*. Cambridge University Press, New York, 2007.
- [10] XUE, Q., AND MEEK, J. Dynamic response and instability of frame structures. *Comput. Methods Appl. Mech. Engrg.* 190 (2001), 5233–5242.

Paweł Fritzowski, Ph.D.: Poznan University of Technology, Institute of Applied Mechanics, ul. Jana Pawła II 24, 60-965 Poznań, Poland (pawel.fritzowski@put.poznan.pl). The author gave a presentation of this paper during one of the conference sessions.

Krzysztof Magnucki, Professor: Poznan University of Technology, Institute of Applied Mechanics, ul. Jana Pawła II 24, 60-965 Poznań, Poland (krzysztof.magnucki@put.poznan.pl).

Szymon Milecki, Ph.D.: Institute of Rail Vehicles, ul. Warszawska 181, 61-055 Poznań, Poland (obliczenia@tabor.com.pl).

Mathematical model of a multi-parameter oscillator based on a core-less three-phase linear motor with skewed magnets (MTR070-15)

Jakub Gajek, Radosław Kępiński, Jan Awrejcewicz

Abstract: This paper uses the example of a three-phase core-less linear motor to create a mathematical model of single-dimension multi-parameter oscillator. The studied linear motor consists of: a stator, an U-shaped stationary guide-way with permanent magnets placed askew to the motor's movement's direction; and a forcer, a movable set of three rectangular coils subjected to alternating external electrical voltage. The system's parameters are both mechanical (number of magnets and coils, size of magnets, distances between magnets, size of coils) and electromagnetic (auxiliary magnetic field, permeability, coil's resistance). Lorentz force allows for the transition from electromagnetic parameters to mechanical force and Faraday's law of induction creates a feedback between the forcer's speed and coils voltage. An Ampere's model of permanent magnet is used to determine the simplified function of auxiliary magnetic field distribution throughout the stator. In the model the external voltage applied to each coil serves as the excitation while displacement of the forcer is the output parameter. The solution to the introduced mathematical model of the system is compared with the experimental results showing a good coincidence.

1. Introduction

Over the years linear motors have been taking on bigger and bigger shares in the market for precise positioning systems. They provide a dynamically superior although costly alternative to standard drives such as feed screw conveyors. For a motor to correctly project a desired motion profile a specific close-looped controller should be introduced between the motor and mains. The quality of such system depends on, amongst other things, the precision of motor's model used for building the controller. Most industrial controllers today use simplified models while this paper focuses on construction of a model for a simple core-less motor from scratch.

A lab stand, with HIWIN's coreless linear motor and Copley-Controls' servo-drive, is used as both a physical base for constructing the model and a platform for its validation. The forcer (inductor) is capable of moving at speeds of up to 5 meters per second with a load of 45N. An analogue optical linear encoder can read the forcer's position with a resolution of 0,1 μm and the entire system's positioning error not trailing far behind. Three U-shaped stators with permanent magnets were used to create the motors magnetic guide-way giving the stand a theoretical maximum stroke of 830 mm and an actual stroke of 780 mm. Two high quality linear guide-way provide for a swift and quiet motion. The stand

program allows it to work with both manual input and automatically based on a signal from external devices, [1].

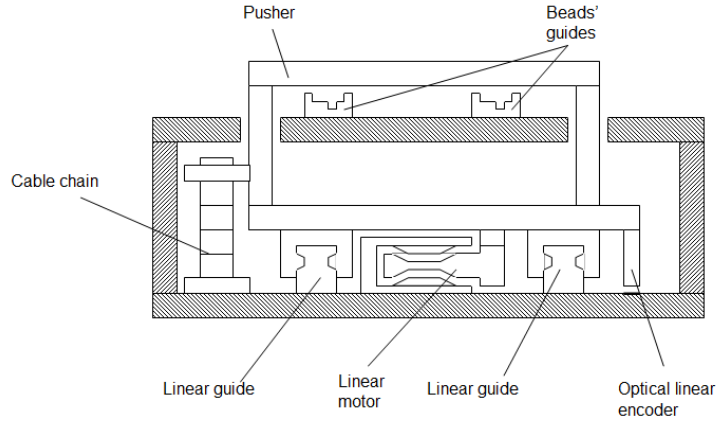


Figure 1. Lab stand's diagram

As the most interesting scientifically only the motor will be modeled in this paper. The stand will serve merely as a validation platform.

2. Model construction

To construct the motor model a simple base model, consisting of a single winding and single magnet, was built first. The force acting on such a coil was calculated with respect to its position and of magnetic field strength. The field's distribution for a single magnet and an infinitely long guide-way was then evaluated using Ampere's model. The entire model for three windings inside the guide-way is then presented and encapsulated to a single ODE.

2.1. Base model

A single motor winding can be modeled as a perfectly rectangular conductor loop, with a certain voltage function U_g applied to it. The means and exact spot of this application is omitted as unimportant for the workings of the model. Let this loop be placed in the vicinity of a C-shaped magnet in a way depicted in Figure 2.

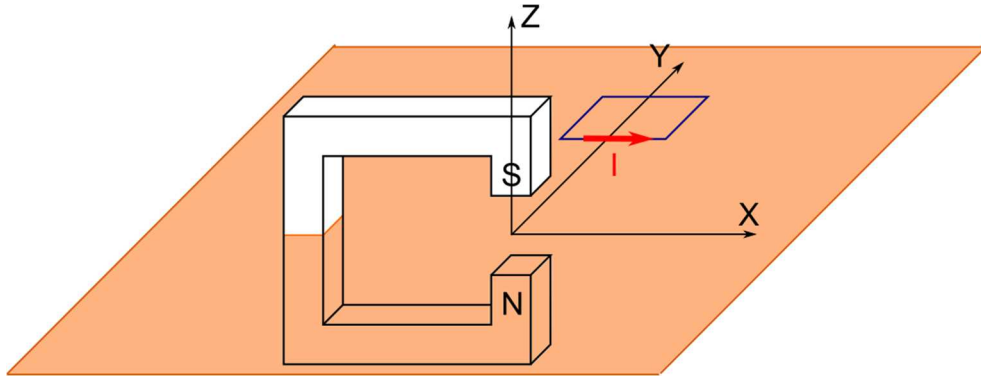


Figure 2. Model of a single winding

Assuming that the loop cannot deform or rotate and can only move along the direction of y-axis it shall always remain a rectangle with a center placed on y-axis and with shorter sides parallel to the direction of motion. Every infinitely small slice of the coil is subjected to Lorentz force acting perpendicularly to its side (see Figure 3).

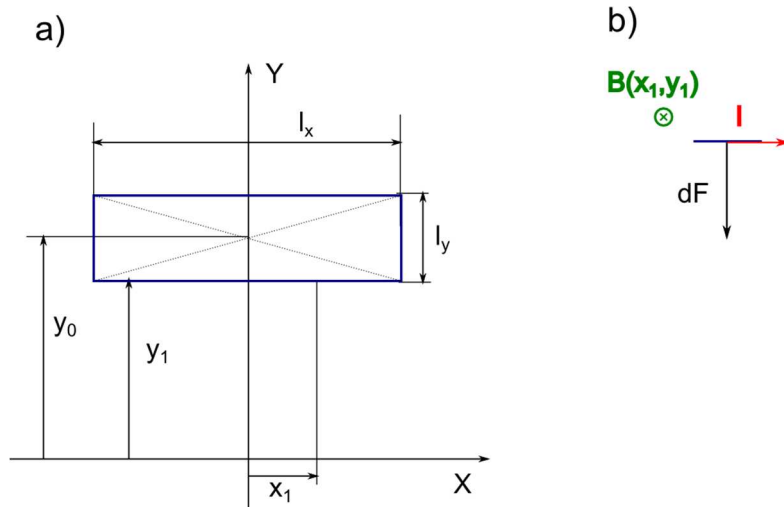


Figure 3. Single loop overview: (a) - coordinate system; (b) - Lorentz force of the elemental slice

The value of that force equals

$$d\vec{F} = \vec{B} \times \vec{l}, \quad (1)$$

$$d\vec{F} = I\vec{B} \times d\vec{l}, \quad (2)$$

where i and B are the vector of electric current and magnetic induction respectively. In every point of a conductor loop the i vector's direction is parallel to the coil while its value can be treated as constant equal to I .

Since the model cannot move in any direction other than along y-axis, the only significant component of the Lorentz force is one parallel to that axis. It is defined as

$$dF' = dF \cos \phi = B' Idl \cos \phi, \quad (3)$$

where ϕ is the angle between dl and the direction of motion. After integration, the equation takes the form

$$F = \oint_L B' I \cos \phi dl. \quad (4)$$

In equation (4) F is the y-component of total force acting on the coil, B' is the z-component of magnetic field acting on dl , and L is the conductor loop's path. The above method can be used for calculating the force working on any other closed loop conductor coils as well. For a specific case of rectangular shape the closed-loop integral can be rewritten as a sum of two definite integrals in the following form

$$F = I \left(\int_{-\frac{l_x}{2}}^{\frac{l_x}{2}} B \left(x, y_0 - \frac{l_y}{2} \right) dx - \int_{-\frac{l_x}{2}}^{\frac{l_x}{2}} B \left(x, y_0 + \frac{l_y}{2} \right) dx \right), \quad (5)$$

where $B(x, y)$ is the function of the magnetic field's z-component distribution, [2].

The electric current I is the result of the external voltage function $U_G(t)$ and the voltage U_I induced in the loop due to Faraday's law of induction. The second component can be calculated as

$$U_I = -\frac{d}{dt} \iint_S B(x, y) dS, \quad (6)$$

where S is the area inside the conductor loop. For a rectangular coil (6) can be recast to the following form

$$U_I = -\frac{d}{dt} \int_{-\frac{l_y}{2}}^{\frac{l_y}{2}} \int_{-\frac{l_x}{2}}^{\frac{l_x}{2}} B(x, y) dx dy. \quad (7)$$

Equation (5) can then be rewritten in the form

$$F = \frac{1}{R_e} \left(U_G(t) - \frac{d}{dt} \int_{-\frac{l_y}{2}}^{\frac{l_y}{2}} \int_{-\frac{l_x}{2}}^{\frac{l_x}{2}} B(x, y) dx dy \right) \left(\int_{-\frac{l_x}{2}}^{\frac{l_x}{2}} B\left(x, y_0 - \frac{l_y}{2}\right) dx - \int_{-\frac{l_x}{2}}^{\frac{l_x}{2}} B\left(x, y_0 + \frac{l_y}{2}\right) dx \right), \quad (8)$$

where R_e is the electric resistance of the coil.

2.2. C-Shape magnets' field distribution

With accordance to [3] the value of magnetic field of a permanent magnet can be approximated by using Ampere's model, that is by assuming that a magnet's magnetic field is the same as that of a perfect, tightly wound solenoid. Then Biot-Savart's law can be applied to calculate the exact value of magnetic field at any point P in the vicinity of the magnet via the following formula

$$\vec{B}(\vec{r}) = \frac{\mu_0}{4\pi} \int_L \frac{d\vec{l} \times \vec{r}'}{|\vec{r}'|^3}, \quad (9)$$

where

$$\vec{r}' = \vec{r} - \vec{l}, \quad (10)$$

and \vec{r} is the distance between point P and the center of the magnet, \vec{l} is the distance between the magnet's center and the infinitely small solenoid length $d\vec{l}$ and μ_0 is the magnetic permeability of the magnet's environment.

In case of a C-shaped magnet the field can be calculated as a resultant fields of two bar magnets placed perpendicular to each other with opposing poles facing each other. For a single bar magnet the field can be then calculated by solving the following integral equation

$$B(x_p, y_p, z_p) = \frac{\mu_0 I}{4\pi} (B_1(x_p, y_p, z_p) + B_2(x_p, y_p, z_p) + B_3(x_p, y_p, z_p) + B_4(x_p, y_p, z_p)), \quad (11)$$

where

$$B_1(x_p, y_p, z_p) = \int_{-\frac{\sigma_z}{2}}^{\frac{\sigma_z}{2}} \int_{-\frac{\sigma_x}{2}}^{\frac{\sigma_x}{2}} \frac{(z - z_p)\hat{y} + \left(y_p - \frac{\sigma_y}{2}\right)\hat{z}}{\sqrt{(x_p - x)^2 + \left(y_p - \frac{\sigma_y}{2}\right)^2 + (z_p - z)^2}^3} dx dz, \quad (12)$$

$$B_2(x_p, y_p, z_p) = - \int_{-\frac{\sigma_z}{2}}^{\frac{\sigma_z}{2}} \int_{-\frac{\sigma_x}{2}}^{\frac{\sigma_x}{2}} \frac{(z - z_p)\hat{y} + \left(y_p + \frac{\sigma_y}{2}\right)\hat{z}}{\sqrt{(x_p - x)^2 + \left(y_p + \frac{\sigma_y}{2}\right)^2 + (z_p - z)^2}^3} dx dz, \quad (13)$$

$$B_3(x_p, y_p, z_p) = \int_{-\frac{\sigma_z}{2}}^{\frac{\sigma_z}{2}} \int_{-\frac{\sigma_y}{2}}^{\frac{\sigma_y}{2}} \frac{(z - z_p)\hat{x} + (x_p - \frac{\sigma_x}{2})\hat{z}}{\sqrt{(x_p - \frac{\sigma_x}{2})^2 + (y_p + y)^2 + (z_p - z)^2}} dydz, \quad (14)$$

$$B_4(x_p, y_p, z_p) = - \int_{-\frac{\sigma_z}{2}}^{\frac{\sigma_z}{2}} \int_{-\frac{\sigma_y}{2}}^{\frac{\sigma_y}{2}} \frac{(z - z_p)\hat{x} + (x_p + \frac{\sigma_x}{2})\hat{z}}{\sqrt{(x_p + \frac{\sigma_x}{2})^2 + (y_p + y)^2 + (z_p - z)^2}} dydz, \quad (15)$$

and (x_p, y_p, z_p) are the coordinates of point P, $\sigma_x, \sigma_y, \sigma_z$ are the bar magnet dimensions in their respective axes, $\hat{x}, \hat{y}, \hat{z}$ are the unit vectors of axes x, y and z and i is the current density over the diameter of wire of the solenoid.

Figures 4-5 show the C-shaped magnet's magnetic field's z-component distribution in a yz-plane calculated with equations (11) - (15) for a sample magnet.

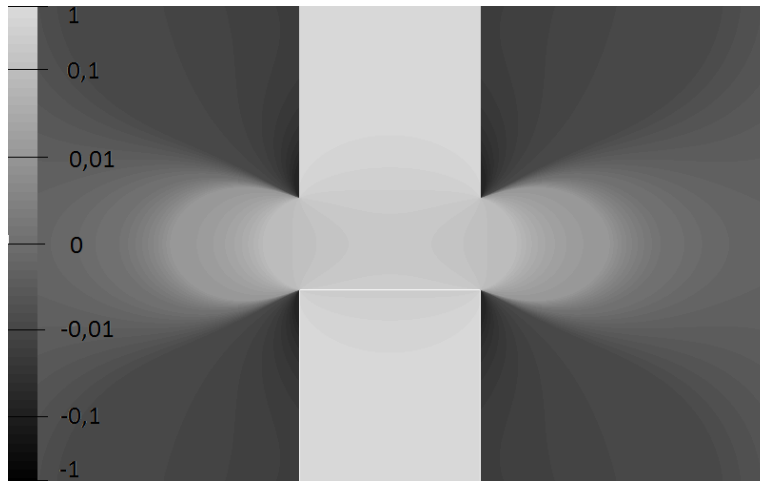


Figure 4. Z-axis coefficient of magnetic field distribution of a C-shaped permanent magnet (in Teslas)

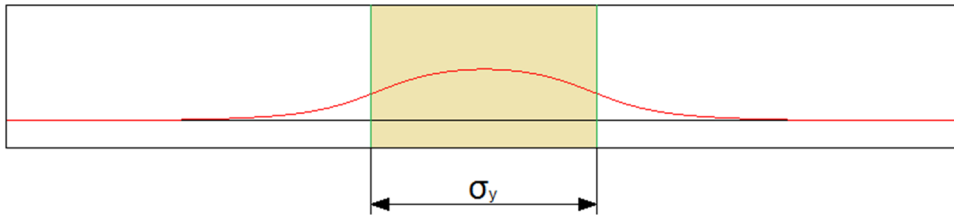


Figure 5. Distribution of C-shaped permanent magnet's magnetic field (z-axis coefficient) on a line ran parallel to y-axis in between the magnet's poles, highlighted part marks the position of magnet's poles

For the ease of use and because of the good coincidence with actual values, the magnetic field's distribution on a xy-plane (coordinate system set as in Figure 3) will be approximated with 2D Gaussian function in the following form

$$B_c(x, y) = B_0 e^{-\left(\frac{x^2}{\sigma_x^2} + \frac{y^2}{\sigma_y^2}\right)}, \quad (16)$$

where B_0 is the given magnet's constant.

2.3. Magnetic guide-way field distribution

An infinitely long magnetic guide-way can be modeled as a set of C-shape magnets placed in equal distance χ_T from one another along the y-axis. All of the magnets are placed askew from the x-axis by the angle ϕ and each two neighboring ones have their poles set oppositely (see Figure 6).

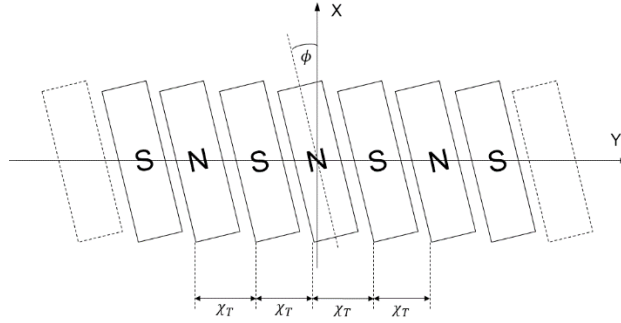


Figure 6. Magnetic guide-way modeled as infinite set of C-shaped magnets

For such a guide-way the magnetic field distribution can be written as

$$B_G(x, y) = B_0 e^{-\left[\frac{x^2}{\sigma_{xs}^2}\right]} \sum_{n=-\infty}^{\infty} (-1)^n e^{-\left[\frac{(y+n\chi_T)^2}{\sigma_{ys}^2} + \frac{x(y+n\chi_T)}{\sigma_{xys}^2}\right]}, \quad (17)$$

where

$$\frac{1}{\sigma_{ys}^2} = \frac{\sigma_y^2 \sin(\phi)^2 + \sigma_x^2 \cos(\phi)^2}{\sigma_y^2 \sigma_x^2}, \quad (18)$$

$$\frac{1}{\sigma_{xs}^2} = \frac{\sigma_y^2 \cos(\phi)^2 + \sigma_x^2 \sin(\phi)^2}{\sigma_y^2 \sigma_x^2}, \quad (19)$$

$$\frac{1}{\sigma_{xys}^2} = \frac{\sin(2\phi) (\sigma_y^2 + \sigma_x^2)}{\sigma_y^2 \sigma_x^2}, \quad (20)$$

are the relative pole sizes for tilted magnets.

After introducing a correlation factor between the relative pole size in y (σ_{ys}) and magnets' displacement (χ_T) in the form

$$k = \frac{\chi_T}{\sigma_{ys}}, \quad (21)$$

the equation (17) can be rewritten in the form

$$B_G = B_{G0} e^{-\left(\frac{x^2}{\sigma^2}\right)} \theta(x, y), \quad (22)$$

where

$$\frac{1}{\sigma^2} = \left(\frac{\sigma_y^2}{4\sigma_{xy}^4} - \frac{1}{\sigma_x^2} \right), \quad B_{G0} = \frac{B_0 \sqrt{\pi}}{2k}, \quad (23)$$

and $\theta(x, y)$ is the sum of two Jacobi theta functions of the third kind ($\vartheta_3(z, \tau)$) in the form

$$\theta(x, y) = \left[\vartheta_3(xz_x + yz_y, \tau_M) - \vartheta_3\left(xz_x + yz_y - \frac{1}{2}, \tau_M\right) \right], \quad (24)$$

where

$$z_x = \frac{\pi \sigma_{ys}}{4\sigma_{xys}^2}, \quad z_y = \frac{\pi}{2k\sigma_{ys}}, \quad \tau_M = e^{-\frac{\pi^2}{4k^2}}. \quad (25)$$

2.4. Three-phase motor model

For a set of three same size, stiffly connected, rectangular conductor loops inside the magnetic guide-way the total force acting on this set can be calculated as a sum of forces acting on each coil. That is

$$F_M = \sum_{j=1}^3 F_j, \quad (26)$$

where F_j is calculated with (8) assuming the filed distribution is equal to (22). This single force can be written as

$$F_j = \frac{B_{G0}}{R_e} (U_{Gj}(t) - U_{ij}) \left(\int_{-\frac{l_x}{2}}^{\frac{l_x}{2}} e^{-\frac{x^2}{\sigma^2}} \left(\theta\left(x, y_j - \frac{l_y}{2}\right) - \theta\left(x, y_j + \frac{l_y}{2}\right) \right) dx \right), \quad (27)$$

where y_j is the position of individual coil and is equal to

$$y_j = y_0 + a(j - 2), \quad (28)$$

and y_0 is the position of the motor's forcer and a is the displacement of coils in the forcer. The induced voltage for j-coil (U_{ij}) is equal to

$$U_{ij} = -B_G z_y \dot{y} \int_{-\frac{l_x}{2}}^{\frac{l_x}{2}} \int_{y_j - \frac{l_y}{2}}^{y_j + \frac{l_y}{2}} e^{-\left(\frac{x^2}{\sigma^2}\right)} \theta'(x, y) dx dy. \quad (29)$$

The $\theta'(x, y)$ is the sum of two Jacobi theta prime functions of the third kind

$$\theta'(x, t) = \left[\vartheta_3'(x z_x + y z_y, \tau_M) - \vartheta_3'\left(x z_x + y z_y - \frac{1}{2}, \tau_M\right) \right]. \quad (30)$$

The complete model's ODE can be written as

$$\ddot{y}_0(t) = \frac{1}{m} \sum_{j=1}^3 F_j, \quad (31)$$

where m is the mass of the forcer. (31) can also be written in developed form

$$\ddot{y}_0(t) = \frac{1}{m R_E} \sum_{j=1}^3 \left[U_{Gj}(t) - B_G z_y \dot{y}_0 \int_{-\frac{l_x}{2}}^{\frac{l_x}{2}} \int_{y_j - \frac{l_y}{2}}^{y_j + \frac{l_y}{2}} e^{-\left(\frac{x^2}{\sigma^2}\right)} \theta'(x, y_0 + a(j-2)) dx dy \right] \quad (32)$$

$$\left[\int_{-\frac{l_x}{2}}^{\frac{l_x}{2}} e^{-\frac{x^2}{\sigma^2}} \left(\theta\left(x, y_0 + a(j-2) - \frac{l_y}{2}\right) - \theta\left(x, y_0 + a(j-2) + \frac{l_y}{2}\right) \right) dx \right]$$

As the integration of Jacobi theta functions $\theta(x, y)$ and Jacobi theta prime functions $\theta'(x, y)$ over x and y are analytically insolvable, it is likewise only possible to solve (32) using numerical methods. The nature of Jacobi theta function makes the equation highly non-linear.

3. Validation

Based on the equation (32) a computer simulation was created and conducted in Wolfram Mathematica. The external voltage functions $U_{Gj}(t)$ were used as excitation while the position of the forcer $y_0(t)$ was the output parameter. The size and displacement of magnets and coils, magnet's skew angle and magnetic field constant and coils' resistance, were treated as constant parameters.

Mathematica gives a wide variety of possible excitation functions to be supplied to the model. Likewise the stand's servo-drive can be set in "maintenance mode" giving, amongst other options, a direct control over the motor from a PC desktop. This function function allows subjecting the coils to a given voltage function. The variety of functions available from the servo-drive manufacturers is scarce but sufficient. All of them have the form of

$$U_{Gj}(t) = U_M(t) \sin\left(\omega t + (j - 1) \frac{2\pi}{3}\right), \quad (33)$$

with $U_M(t)$ (maximum voltage) and ω (angular frequency) changeable in time along a step, a sawtooth or a sinusoidal function. For the purpose of validation a step function of maximum voltage was used. The computer model was supplied with the following set of parameters, taken from the motor's documentation as well as from direct measurement, so that they resemble the actual motor as closely as possible.

Table 1 - Parameters used for the model

Parameter	Symbol	Value
Coils' width	l_x	5,2 [mm]
Coils' length	l_y	49 [mm]
Coils' displacement	a	7,36 [mm]
Magnets' field strength	B_0	1,5 [T]
Magnets' width (x-axis)	σ_x	4,7 [mm]
Magnets' length (y-axis)	σ_y	53 [mm]
Electrical resistance	R_e	6,7 [Ω]
Magnets' displacement correlation	k	2,35 [-]
Forcer's mass	m	0,31 [kg]
Maximum voltage	U_{M0}	1,5 [V]
Voltage frequency	ω	20 [rad/s]
Voltage step function frequency	f	1 [Hz]

Figure 6 displays the function of maximum voltage and the resulting voltage on one of the coils taken from the simulation.

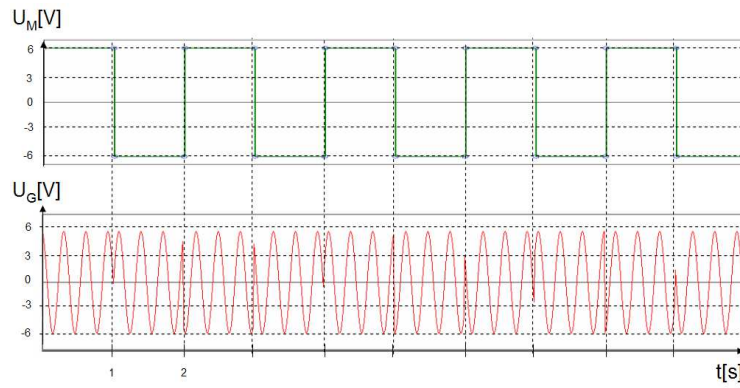


Figure 7. Function of maximum voltage (top most graph) and voltage on the first coil (bottom most graph)

Exactly the same function of voltage was applied to actual motor coils. The result of both the experiment and simulation are presented below.

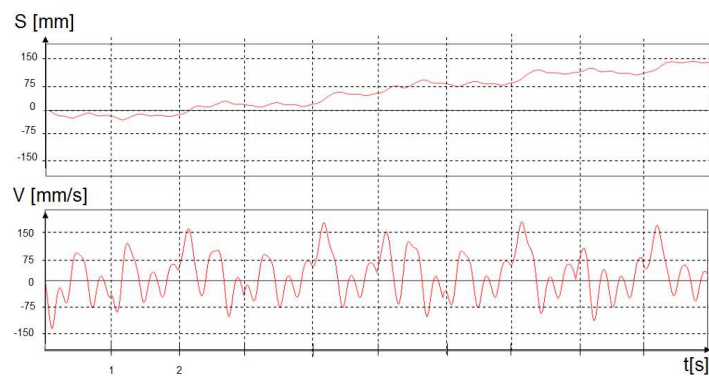


Figure 8. Response of computer simulation: the position and velocity of inductor

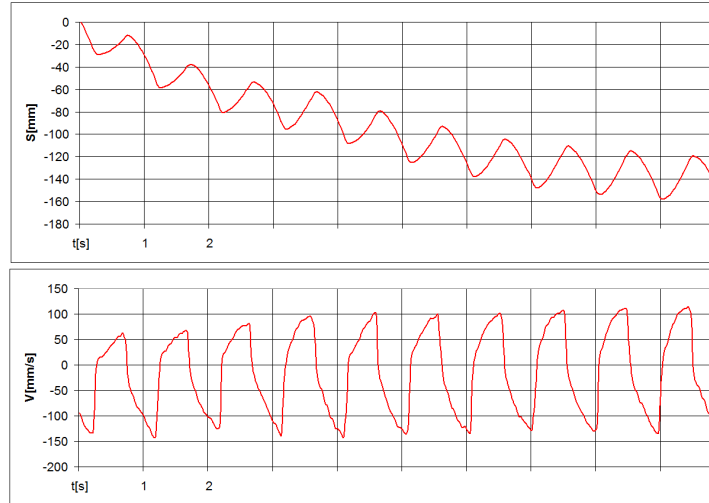


Figure 9. Response of the actual motor

In light of the result above further validation was abandoned.

4. Conclusions

The prepared and studied model does not yet reassemble actual motor with satisfactory precision. Most likely cause of this is the usage of documentation data for parameter identification. Instead the parameters should be identified with numerical methods. The model clearly expresses interesting chaotic behaviors, however the complexity of Jacobi theta functions necessitate a largely time consuming simulations. A further simplification of the model might be required to better study it.

References

- [1] Gajek J.: *Construction of a laboratory stand based on the PVC Glazing beads saw feeder design*, M.Sc. thesis, Lodz University of Technology, 2012, Lewandowski D.
- [2] Chari M. V. K., *Finite elements in electrical and magnetic field problems*, Somerset, John Wiley & Sons, 1980
- [3] DERBY N.; OLBERT S.: Cylindrical magnets and ideal solenoids, *American Journal of Physics*, Volume 78, Issue 3, 2010, pp. 229-235

Jakub Gajek, M.Sc. (Ph.D. student): Lodz University of Technology, 90-924, POLAND (gajek.jakub@gmail.com), the author presented this work at the conference.

Radosław Kępiński, M.Sc. (Ph.D. student): Lodz University of Technology, 90-924, POLAND (radoslaw.kepinski@dokt.p.lodz.pl).

Jan Awrejcewicz, Professor: Lodz University of Technology, 90-924, POLAND (jan.awrejcewicz@p.lodz.pl).

Power consumption analysis of different hexapod robot gaits (MTR308-15)

Dariusz Grzelczyk, Bartosz Stańczyk, Jan Awrejcewicz

Abstract: The paper is focused on the power consumption analysis of different gaits of our constructed hexapod robot controlled by different Central Pattern Generator (CPG) models. There are a lot of gait patterns in the literature constructed either by different CPG models or using a series of oscillations with adjustable phase lag. The mentioned models, as well as those proposed in our previous paper are used and compared from the viewpoint of energy demand. In general, power consumption of the constructed hexapod robot is experimentally analyzed based on the current consumption in the applied servo motors, which drive the robot limbs. For this purpose the suitable drivers allowing a simple measurement of electric energy consumption of servo motors are used. The obtained experimental results show different energy demand for different robot gaits. Because power consumption is one of the main operational restrictions imposed on autonomous walking robots, we show that the performed energy efficiency analysis and the choice of the appropriate robot gaits depending on the actual situation can reduce the energy costs.

1. Introduction

From the point of view of engineering applications various kinds of mobile six-legged robots (hexapod robots) are suitable for exploration of unknown, broken and unstable places [1]. The legged robots can go where it is impossible for the wheeled robots, however they require extra effort for their locomotion control. As the electric power is a limited resource in autonomous systems, the power consumption in autonomous walking robots is one of the main operational restrictions. This is why during the last few decades various types of hexapod walking robots (and other multi-legged machines) have been manufactured, modified and analytically/experimentally investigated in order to reduce their energy demand. Energy costs analysis and power consumption optimization in hexapod robots are analyzed in detail, for instance, in papers [2,3]. In paper [2] authors assume that the energetic cost during locomotion is given by the sum of positive mechanical work and the heat energy loss, which is proportional to the square of joint torque. Next, they examined the optimal locomotor robot gait by the energetic cost using computer simulations of simple dynamical model of the analyzed hexapod robot. In turn, in recent paper [3] an energy efficiency analysis (including the effects of the gait patterns and the mechanical structure of the robot) were performed for a hexapod walking robot to reduce these energy costs. In order to meet the power saving demands of the analyzed robot, the appropriate torque distribution algorithm was established with a formulated

energy-consumption model. The presented in the mentioned paper numerical results show that the proposed method can be applied for reduction of the energy costs during walking of the robot.

There are also numerous other papers devoted to optimization of the energy demand in the walking robot through adjustment other gait parameters [3]. For instance, in order to optimize (minimize) energy demand, in [4] the author optimized the protraction movement trajectory of the robot leg using a modified version of the gradient descent based optimal algorithm of control. Moreover, in this paper the results of optimization were compared with the observations of protraction of stick insects, and it was concluded that a direct biological imitation of protraction is not energy efficient. In papers [2,5] a simulation model of a two-joint six-legged robot is considered. Energy cost analysis is performed with respect to the stride and stance length, the walking velocities, and duty factor of the wave gaits. The paper [6] is focused on the structural parameter analysis, where the foot force distribution for a six-legged walking machine is obtained for minimum energy consumption over a full cycle for regular wave gaits. In addition, in the mentioned paper geometric work loss for a walking machine with articulated legs is minimized by controlling interaction forces at the foot-ground interface. Minimum energy foot forces are also studied for various duty factors, lateral offsets, link proportions, as well as friction between the ground and the robot leg tip. Authors of the paper [7] proposed an energetic model for walking robots based on dynamic and actuator models, which allows the evaluation of the influence of the leg configuration, body weight, or gait parameters on power consumption. The presented in this paper technique is used to find the optimum stride length for the minimum energy expenditure of a biped prototype depending on the speed and payload, taking into account level and slope walking. Various parameters (defining the trajectories of the robot limb tip) aimed on optimizing energy costs of the robot during walking on non-regular terrain are also tested in paper [8]. In turn, the paper [9] is focused on the analysis of the torque contributions of different dynamic components in real leg trajectories taking into account backlash, friction and elasticity effects in the gear reduction system. The authors of this paper propose a new method to derive the dynamics of a robot leg as a function of parameters of the leg-trajectory. The experimentally found simplified equations of motion reflect the reality of the physical system and can be used in a real-time dynamic-control system.

In this paper experimental investigations regarding an energy consumption of our constructed hexapod robot as the sum of the energy consumed in all of the joints are considered. The DC motors of applied servomechanisms in the joint of the leg are used for obtaining the power consumption experimental data from the required voltage and current values. It should be noted that experimental studies of motor mechanisms are especially challenging - they are characterized by a high degree the task of integrating influences from the surrounding environment. Our investigations involve various trajectories of the robot leg generating via different central pattern generator (CPG) signals, namely

Hopf oscillator, van der Pol oscillator, Rayleigh oscillator, and stick-slip induced vibrations. Both direct and inverse kinematics of the robot leg, as well as the mentioned CPGs are considered in detail in our previous paper [10].

The rest of the paper is organized as follows. First biologically inspiration and constructed prototype of the hexapod robot are briefly introduced. Both direct and inverse kinematics of the hexapod robot leg, as well as chosen oscillators as a CPGs signals are presented based on our previous paper [10]. Next, the experimental stand, including the electronic system for measuring energy consumption (taking experimental data from the voltage and current values of the supply) is briefly described. In result, experimental energy consumptions for the mentioned above CPG signals are compared and discussed. The last section contains conclusions of the performed investigations and possible outlook for future investigations.

2. Prototype of the hexapod robot and modeling of the leg tip movements

Construction of the entire body and its six limbs of our hexapod robot was motivated by the morphology scheme of the stick insect presented in Fig. 1. On the basis of the mentioned morphology scheme we consider first a kinematic model (Fig. 2) and finally construct the prototype of the robot (Fig. 3). All six identical limbs are manufactured by aluminum, whereas as the actuators standard servomechanisms are used and applied. The actuators are independently controlled via Pulse Width Modulation (PWM) technique described in [11]. The most important details of the constructed robot legs are presented in Tab. 1.

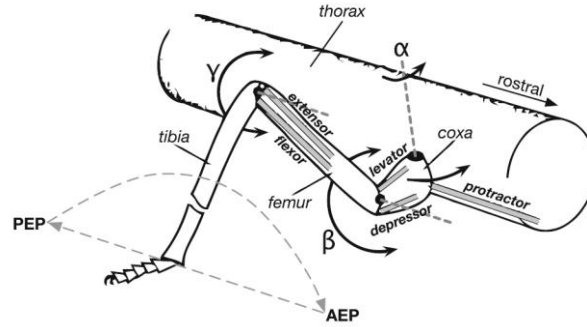


Figure 1. A morphology scheme of a leg of stick insect with coxa (cx), femur (fe) and tibia (ti) as three functional segments. Three mentioned segments are connected through hinge joints: the thorax-coxa joint (α), the coxa-femur joint (β), and femur-tibia joint (γ). The dashed lines denote swing movement and stance movement. PEP (AEP) denotes the posterior (anterior) extreme position, respectively [12].

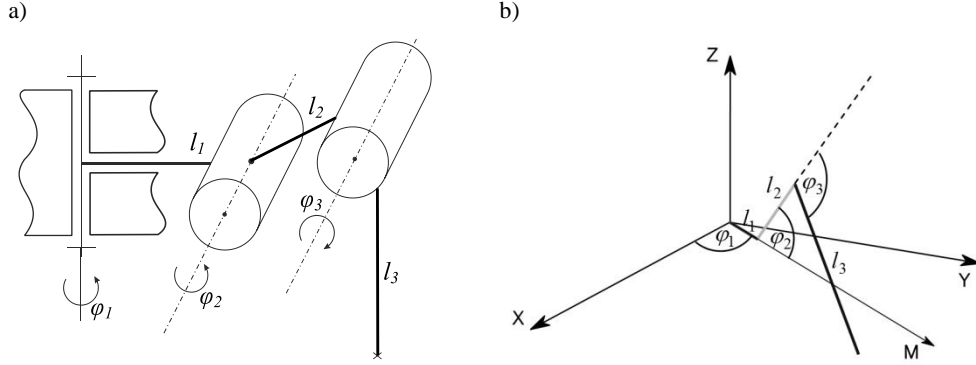


Figure 2. Kinematic structure (a) and location of the hexapod leg in the global base coordinate system (b).

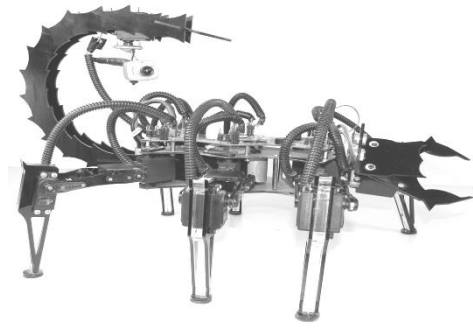


Table 1. Parameters of the hexapod robot legs.

Name	Symbol	Value
coxa	l_1	27 mm
femur	l_2	70 mm
tibia	l_3	120 mm
thorax-coxa joint	φ_1	$0 - \pi$
coxa-trochanterofemur joint	φ_2	$-\pi/2 \dots \pi/2$
femur-tibia	φ_3	$0 \dots 5\pi/6$

Figure 3. Constructed prototype of the hexapod robot.

Direct kinematics of the robot leg can be expressed as follows (see [10])

$$\begin{cases} x = \cos \varphi_1 (l_1 + l_2 \cos \varphi_2 + l_3 \cos \varphi_2 \cos \varphi_3 + l_3 \sin \varphi_2 \sin \varphi_3), \\ y = \sin \varphi_1 (l_1 + l_2 \cos \varphi_2 + l_3 \cos \varphi_2 \cos \varphi_3 + l_3 \sin \varphi_2 \sin \varphi_3), \\ z = l_2 \sin \varphi_2 - l_3 \cos \varphi_2 \sin \varphi_3 + l_3 \sin \varphi_2 \cos \varphi_3, \end{cases} \quad (1)$$

while the inverse kinematics has the form

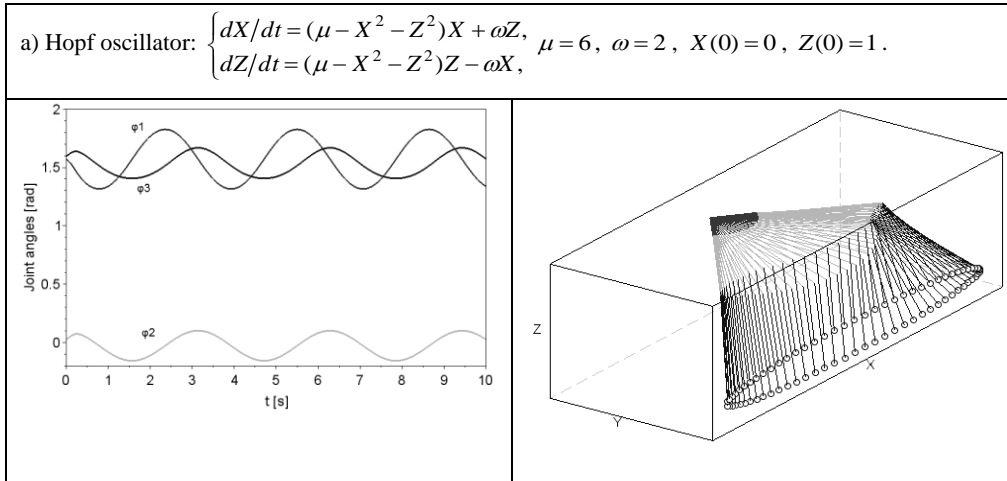
$$\varphi_1 = \begin{cases} \arctan(y/x) & \text{if } x > 0 \\ \pi/2 & \text{if } x = 0, \\ \pi - \arctan(y/(-x)) & \text{if } x < 0 \end{cases}, \quad \varphi_2 = \begin{cases} \alpha + \beta & \text{if } \sqrt{x^2 + y^2} - l_1 \geq 0, \\ \alpha - (\pi - \beta) & \text{if } \sqrt{x^2 + y^2} - l_1 < 0, \end{cases}$$

$$\varphi_3 = \arccos\left(\frac{c^2 - l_2^2 - l_3^2}{2l_2l_3}\right), \quad (2)$$

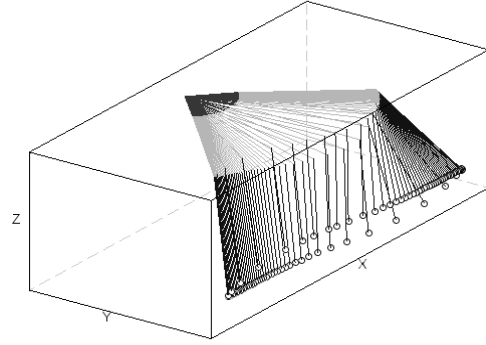
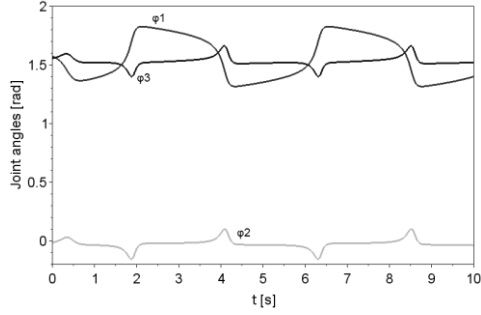
where: $\alpha = \arccos\left(\frac{l_3^2 - l_2^2 - c^2}{-2l_2c}\right)$, $\beta = \arctan\left(\frac{z}{\sqrt{x^2 + y^2} - l_1}\right)$ and $c = \sqrt{z^2 + \left(\sqrt{x^2 + y^2} - l_1\right)^2}$.

In our studies we use the method to control the hexapod robot's leg by planning out the leg tip trajectory and the velocity for transfer phase and support phase. The shape of the trajectory of the robot leg tip is generated by CPG. The appropriate positions of the phase trajectories of individual points are converted into joint space by the inverse kinematics relationships. The corresponding joint angles finally give a predetermined shape of the trajectory of the robot leg tip by employed direct kinematics. There are numerous models to generate the central oscillation presented in the literature [13]. In our investigations we use four different oscillators, namely: Hopf oscillator, van der Pol oscillator, Rayleigh oscillator and stick-slip oscillator. Both equations and system parameters governing the mentioned oscillators are presented in Tab. 2. Moreover, time series of angles in the appropriate leg joints and trajectories of the robot leg tip are presented in Tab. 2. The presented results are used in our experimental investigations in order to comparison different energy demand for various robots gaits.

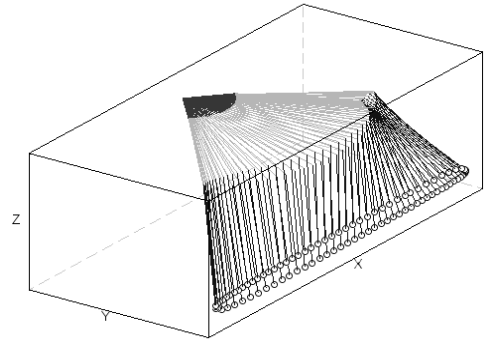
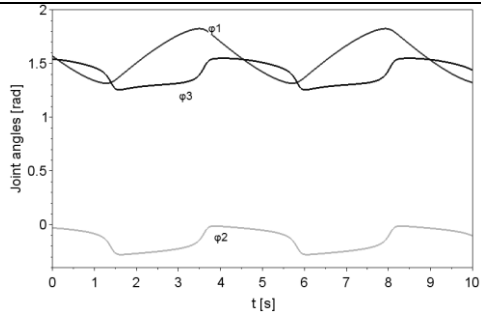
Table 2. CPG models applied to the control of the hexapod leg movements, time series of joint angles and leg configurations with the stable trajectory regarding the leg tip of the robot.



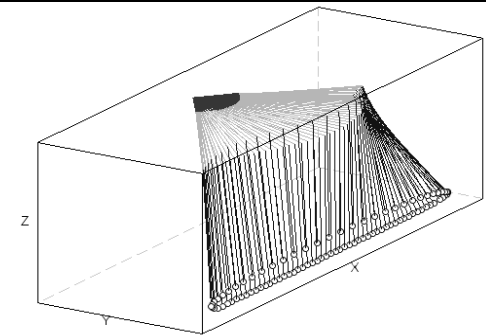
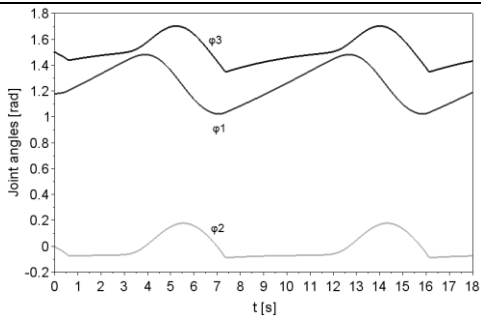
b) van der Pol oscillator: $\begin{cases} dX/dt = Z, \\ dZ/dt = \mu(1 - X^2)Z - \omega^2 X, \end{cases} \mu = 6, \omega = 2, X(0) = 0, Z(0) = 1.$



c) Rayleigh oscillator: $\begin{cases} dX/dt = Z, \\ dZ/dt = \mu(1 - Z^2)Z - \omega^2 X, \end{cases} \mu = 6, \omega = 2, X(0) = 0, Z(0) = 1.$



d) Stick-slip oscillator: $\begin{cases} dX/dt = Z, \\ dZ/dt = -d_c Z - X + F_{fr}(v_r), \end{cases} d_c = 0.01, F_{fr}(v_r) = \frac{F_s}{1 + \delta |v_r|} \tanh\left(\frac{v_r}{\varepsilon}\right),$
 $v_r = v_{dr} - Z, F_s = 1, \delta = 3, v_{dr} = 0.5, \varepsilon = 10^{-2}, X(0) = 0, Z(0) = 0.$



3. Experimental results

Power electric energy demand in servomechanisms of the robot has been performed using computer program created in LabView environment. Figures 4-7 show time series of angular positions and electric power consumption of the appropriate servomechanisms of single hexapod leg. Experimental results are performed for four mentioned earlier different CPG models, namely: Hopf oscillator, van der Pol oscillator, Rayleigh oscillator, as well as stick-slip oscillator. In all cases the stride length of the robot and number of stride lengths are the same. During experimental measurement the obtained total length of the road is 80 cm during time equal 22 s.

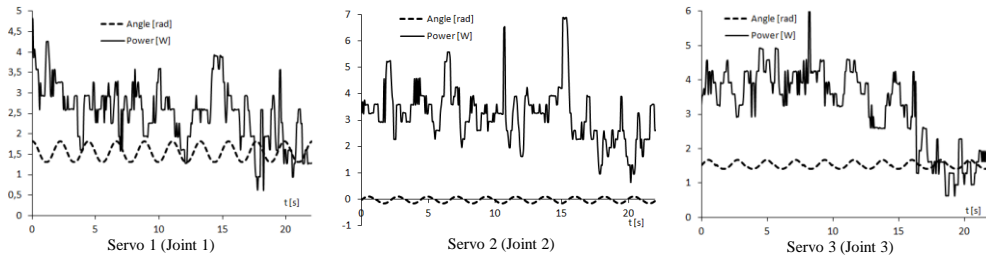


Figure 4. Power consumption analysis of the hexapod movement generated via Hopf oscillator.

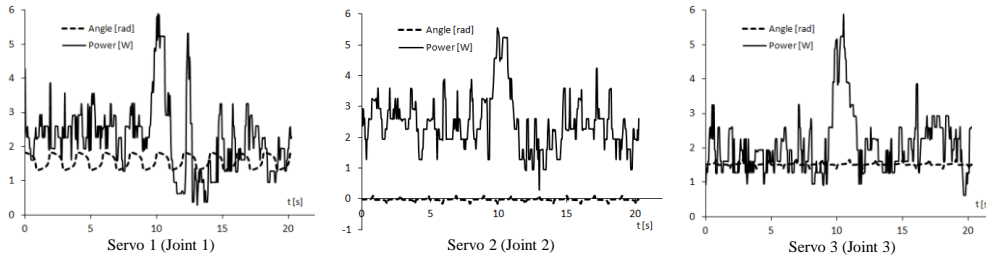


Figure 5. Power consumption analysis of the hexapod movement generated via van der Pol oscillator.

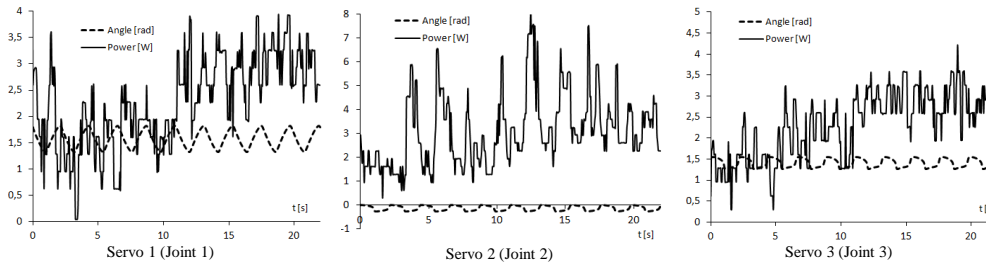


Figure 6. Power consumption analysis of the hexapod movement generated via Rayleigh oscillator.

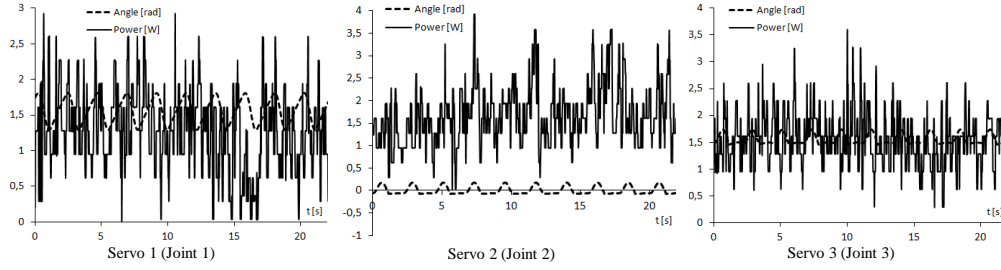


Figure 7. Power consumption analysis of the hexapod movement generated via stick-slip oscillator.

A comparison of the total energy demand of all servomechanisms of the robot, which obtain the same road length in the same time using different CPG models, are presented in Fig. 8.

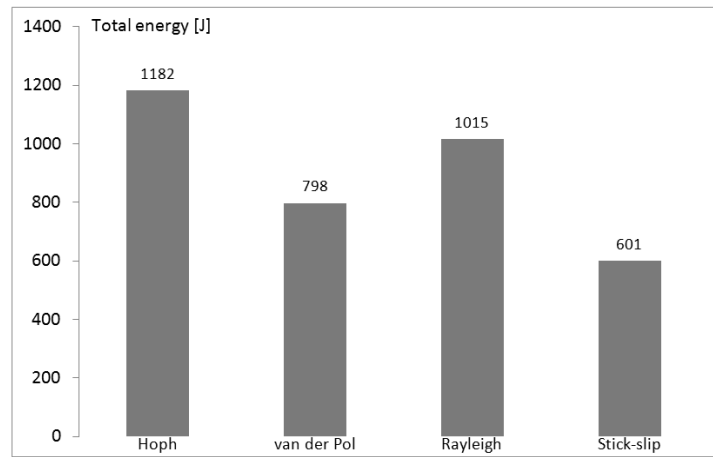


Figure 8. Comparison of the total energy demand of the hexapod robot for different CPG models.

4. Conclusions

In this paper the power consumption analysis of different gaits of our constructed hexapod robot controlled by different CPG models is experimentally investigated. Although there are a lot of gait patterns in the literature constructed via different CPG models, in our investigations we consider three well known CPG models (Hopf, van der Pol and Rayleigh oscillators), as well as proposed in our previous paper CPG model (mechanical stick-slip oscillator). In order to compare electric energy

consumption of the robot for various gaits (based on the electric current consumption in all hexapod servo motors), the appropriate electronic and computer system is proposed and used. The relatively simple experimental measurements of electric power consumption show different energy demand for different robot gaits. Investigations of motor mechanisms are especially challenging because they are characterized by a high degree the task of integrating influences from the environment. As can be seen, from the energy demand point of view the proposed mechanical stick-slip CPG model is more efficient in comparison to other applied CPG models. In this CPG model in the stance movement the distance between the leg tip of the robot and center of the robot coordinate system positioned on the body of the robot at the point of attachment leg is constant. This is a result of keeping the center of gravity of the robot at a constant level, and finally the servo motors placed in leg joints robot do not have to perform extra electric energy, which significantly decreases the energy demand. It should be noted, that the development of multi-legged robots was always restricted by the problem of their high power consumption. This is why the proposed movements of the legs of the hexapod robot can be used to overcome long distances, particularly in the regular terrains in a more efficient way. Power efficiency optimization is this field without improving the power supply unit allow to increase of mission time of the robot.

Acknowledgments

The work has been supported by the National Science Foundation of Poland under the grant MAESTRO 2 No. 2012/04/A/ST8/00738 for years 2012-2016.

References

- [1] Altendorfer, R., Moore, N., Komsuoglu, H., Buehler, M., Brown jr., H.B., McMordie, D., Saranli, U., Full, R., Koditschek, D.E. Hex: a biologically inspired hexapod runner. *Autonomous Robots* 11, 13 (2001), 207-213.
- [2] Nishii, J. Legged insects select the optimal locomotor pattern based on the energetic cost. *Biological Cybernetics* 83, (2000) 435-442.
- [3] Jin, B., Chen, C., Li, W. Power consumption optimization for a hexapod walking robot. *Journal of Intelligent and Robotic Systems* 71, (2013), 195-209.
- [4] Erden, M.S. Optimal protraction of a biologically inspired robot leg, *Journal of Intelligent and Robotic Systems* 64 (3,4), (2011), 301-322.
- [5] Nishii, J. An analytical estimation of the energy cost for legged locomotion, *Journal of Theoretical Biology* 238, (2006), 636-645.
- [6] Kar, D.C., Kurien, I.K., Jayaraman, K. Minimum energy force distribution for a walking robot. *Journal of Robotic Systems* 18(2), (2001), 47-54.
- [7] Guardabrazo, T.A., Gonzalez de Santos, P. Building an energetic model to evaluate and optimize power consumption in walking robots. *Industrial Robot* 31(11), (2004), 201-208.

- [8] Gonzalez de Santos, P., Garcia, E., Ponticelli, R., Armada, M. Minimizing energy consumption in hexapod robots. *Advanced Robotics* 23, (2009), 681-704.
- [9] Garcia, E., Galvez, J.A., Gonzalez de Santos, P. On finding the relevant dynamics for model-based controlling walking robots. *Journal of Intelligent and Robotic Systems* 37, (2003), 375-398.
- [10] Grzelczyk, D., Stańczyk, B., Awrejcewicz, J. On the hexapod leg control with nonlinear stick-slip vibrations. *Applied Mechanics and Materials* 801, (2015), 12-24.
- [11] Stańczyk, B., Grzelczyk, D., Awrejcewicz, J. Control of mobile walking robot (hexapod). *Measurements Automation Robotics* 11, (2012), 157-159.
- [12] Schilling, M., Hoinville, T., Schmitz, J., Cruse, H. Walknet, a bio-inspired controller for hexapod walking. *Biological Cybernetics* 107, (2013), 397-419.
- [13] Ijspeert, A. Central pattern generators for locomotion control in animals and robots: a review. *Neural Networks* 21(4), (2008), 642-653.

Dariusz Grzelczyk, Ph.D.: Lodz University of Technology, Department of Automation, Biomechanics and Mechatronics, 1/15 Stefanowski Str., 90-924 Lodz, Poland (dariusz.grzelczyk@p.lodz.pl).

Bartosz Stańczyk, M.Sc. (Ph.D. student): Lodz University of Technology, Department of Automation, Biomechanics and Mechatronics, 1/15 Stefanowski Str., 90-924 Lodz, Poland (bartosz.stanczyk@dokt.p.lodz.pl). The author gave a presentation of this paper during one of the conference sessions.

Jan Awrejcewicz, Professor: Lodz University of Technology, Department of Automation, Biomechanics and Mechatronics, 1/15 Stefanowski Str., 90-924 Lodz, Poland (jan.awrejcewicz@p.lodz.pl).

Towards the exploitation of local resonances for novel MEMS devices (VIB028-15)

Thomas H. Hanley, Barry Gallacher, Harry Grigg

Abstract: An investigation into potential exploitable behaviour of localised modes and local resonances in linear periodic structures is presented. This behaviour lends itself towards functionalization as the basis for a MEMS transistor or sensor. The particular device described herein operates via excitation of a local resonance. A phenomenon that occurs due to localised forcing of a periodic array at a frequency within the stop band. The resonant region is bordered on one side by an array with tuneable transmission properties. This array couples the forcing region to a sense region. The transmitted wave amplitude through the ‘coupling array’ is used as the output of the system. Methods of operation and functionalization of the device are described in detail. A continuous model of the system is presented and the forced response found. The subsequent insight into the wave dynamics is used to inform device design and assess the potential performance.

1. Introduction

The proposed configuration for investigation consists of two surface acoustic wave (SAW) resonators, separated by an N-period grating. A local resonance is excited by forcing a region of a periodic array at a frequency within its stop band. The resonance is maximised if both the length of the forced cavity and the wavelength of the surrounding arrays are equal to $\frac{\lambda_w}{2}$, where λ_w is the wavelength of the excited wave and n is an integer. N-periods away from the excitation region is a sense IDT, enclosed on one side by the coupling array and on the other side by an enclosing array. The basic arrangement is depicted in figure 1.

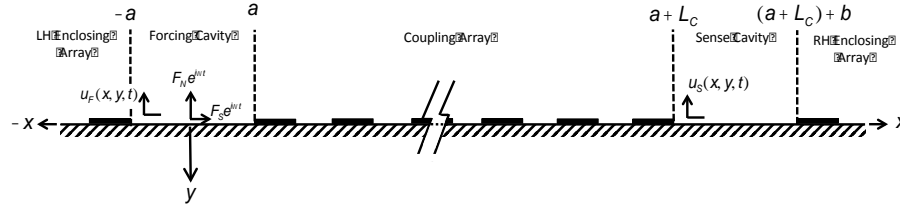


Figure 1. Schematic of the proposed device.

The theory of operation is that the wave-speed within the coupling array is perturbed by some external influence. Therefore, at fixed frequency operation, the wavelength is also perturbed. This

mistunes the coupling array from the Bragg condition, allowing a signal in proportion to the external influence to pass to the sense IDT. In the limit, the array is moved into the pass-band, and the cavity enclosing both IDTs becomes resonant.

Two envisaged exploitation routes are proposed: functionalization as a MEMS transistor, and as a magnetic field sensor. Functionalization depends entirely upon the means in which the wave-speed within the coupling region is perturbed. The transistor will utilise the effect of piezoelectric stiffening to alter the wave-speed. Whereas the magnetometer utilises the change in wave-speed induced by a magnetostrictive thin-film in the presence of a static magnetic field. Both of these effects are known to be small, with reported Rayleigh wave-speed alterations of 1.5% [1] and 0.8% [2] for piezoelectric stiffening and magnetostriction, respectively. It is shown in the sequel that the properties of periodic arrays can be used to enhance the performance of such devices.

2. Mathematical model

Within this section some general expressions will be derived for the ratio of the displacement amplitudes within each cavity, as a function of the device parameters. It can be seen in fig.1 that the device has been divided into five sections. The solutions within each section will be gained separately and then combined using a ray-tracing method. The reflection and transmission properties of each array are all independent of one another with the exception of the coupling array. It is asserted that the proportion of reflection and transmission across the array is not dependent on the direction of wave travel, due to the symmetry of the coupling array.

In order to analyse the performance of the device, the displacement field arising from a localised forcing is required. More specifically, the displacement amplitude within the forcing and sense cavities are sought for varying parameters in the coupling array. The derivation of the model will follow a similar procedure to that conducted in reference [3], with the added complication of the transmission of waves between the two cavities. The forcing and sense cavities will be considered separately to begin with, and their connection through the coupling array modelled using the transfer matrix approach as described in reference [4].

The two-dimensional elastodynamic equations [3-6] (equations 1.1,1.2) govern the wave motion in every section. The differences between each section arise in the boundary conditions, which are defined by the shear, and normal, stresses at the free surface. For the forcing cavity, this incorporates the inhomogeneous equations 1.3 and 1.4. The sense cavity boundary conditions are that of a free surface, given in equations 1.5 and 1.6.

$$(\lambda + 2\mu) \frac{\partial^2 u_1}{\partial x^2} + \mu \frac{\partial^2 u_1}{\partial y^2} + (\lambda + \mu) \frac{\partial^2 u_2}{\partial x \partial y} = \rho \frac{\partial^2 u_1}{\partial t^2} \quad (1.1)$$

$$(\lambda + 2\mu) \frac{\partial^2 u_2}{\partial y^2} + \mu \frac{\partial^2 u_2}{\partial x^2} + (\lambda + \mu) \frac{\partial^2 u_1}{\partial x \partial y} = \rho \frac{\partial^2 u_2}{\partial t^2} \quad (1.2)$$

$$\tau_{xy}^{(f)} = \mu \left(\frac{\partial u_1}{\partial y} + \frac{\partial u_2}{\partial x} \right) = \sqrt{\frac{\mu^3}{\rho \Omega^2}} S \delta(x) e^{-i\Omega t} \quad (1.3)$$

$$\tau_{yy}^{(f)} = \lambda \frac{\partial u_1}{\partial x} + (\lambda + 2\mu) \frac{\partial u_2}{\partial y} = \sqrt{\frac{\mu^3}{\rho \Omega^2}} N \delta(x) e^{-i\Omega t} \quad (1.4)$$

$$\tau_{xy}^{(s)} = \mu \left(\frac{\partial u_1}{\partial y} + \frac{\partial u_2}{\partial x} \right) = 0 \quad (1.5)$$

$$\tau_{yy}^{(s)} = \lambda \frac{\partial u_1}{\partial x} + (\lambda + 2\mu) \frac{\partial u_2}{\partial y} = 0 \quad (1.6)$$

The solutions sought are the steady-state Rayleigh wave solutions, assuming a harmonic solution at the forcing frequency. The forced solution has been presented in references [3] and [5]. The sense cavity does not undergo direct forcing and therefore the free wave solutions are applicable. The free Rayleigh wave solutions are well known, and presented in references [5] and [6]. However, the transfer matrix method applies rigorously only to one-dimensional solutions [7]. As the majority of the displacement field is confined to the surface, a one-dimensional approximate solution, achieved by assuming depth behaviour and relating the two orthogonal displacements by a phase operator, Λ_j , has been shown to provide accurate results [4]. The depth behavior, $\alpha_j(y)$, is found from the free wave solutions in the plated and un-plated substrate. The obvious limitation of this is that bulk waves generated from the forcing, or scattered from the discontinuities, are neglected. However, for plated regions whose thickness is small in comparison to the incident wavelength, the bulk scattering is minimal. The one-dimensional approximation is given in equation 2. Where a single surface displacement variable, $\psi(x)$, is introduced, that will be used in the transfer matrix method.

$$u_j(x, y, t) = \alpha_j(y) \psi(x) e^{-i\Omega t} \quad (2)$$

The displacement fields in the forcing cavity and sense cavity, neglecting reflections, are now defined in equations 3.1-3, where the convention that the physical wave is the real part of the expression is adopted.

$$\psi_F(x)_{x<0} = F_L e^{-i\gamma x} \quad (3.1)$$

$$\psi_F(x)_{x>0} = F_R e^{i\gamma x} \quad (3.2)$$

$$\psi_S(x) = A e^{i\gamma x} + B e^{-i\gamma x} \quad (3.3)$$

It can be seen that the field within the sense and forcing cavities is described by the sum of a leftwards and a rightwards propagating wave. The amplitudes of each, the constants A and B, are to be determined. This is achieved by a ray-tracing method and consideration of the physics of the problem. For brevity a highly condensed version of the method is presented here, highlighting the important steps in the reasoning.

Consider a wave originating at the coupling array boundary. Each route that this wave can take before arriving back at its starting point can be made up of three fundamental paths, depicted in figure 2.

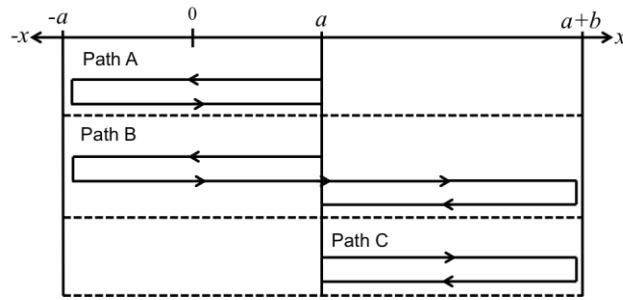


Figure 2. Diagram detailing the routes of the fundamental reflection paths.

Any future wave originating at the coupling boundary is made up of the original wave multiplied by some amount of any, or all, of these paths. Each path is represented mathematically by a phase change due to distance travelled, and an amplitude coefficient due to the partial reflections and transmissions. Note that the phase and amplitude change due to the wave traversing the coupling array is accounted for in the transmission coefficient T_C , to be determined from the transfer matrix solution. The expressions for the paths are given in equations 4.1-3, each path expression will be denoted as χ_α .

$$\text{Path A} = \chi_A = R_{LH}(1 - T_C)e^{i4\gamma a} \quad (4.1)$$

$$\text{Path B} = \chi_B = R_{LH}T_C^2 R_{RH}e^{i\gamma(4a+2b)} \quad (4.2)$$

$$\text{Path C} = \chi_C = R_{RH}(1 - T_C)e^{i2\gamma b} \quad (4.3)$$

Where R_{LH} and R_{RH} are the reflection coefficients for the left- and right-hand enclosing arrays respectively.

Repeating this reasoning for a wave originating at the other boundaries leads to the same conclusion, with identical path expressions. The solution within each cavity can therefore be said to be some product of some initial waves at each boundary and a combination of the path expressions.

The path expression products in the forcing and sense cavities are found to take the forms shown in equations 5.1 and 5.2 respectively.

$$\Gamma_F = \left[\left(\sum_{k=0}^{\infty} \chi_A^k \right) \left(\sum_{k=0}^{\infty} \chi_B^k \right) + \left(\sum_{k=0}^{\infty} \chi_A^k \right) \left(\sum_{k=1}^{\infty} \chi_B^k \right) \left(\sum_{k=1}^{\infty} \chi_C^k \right) \right] \quad (5.1)$$

$$\Gamma_S = \left[\left(\sum_{k=0}^{\infty} \chi_C^k \right) \left(\sum_{k=0}^{\infty} \chi_B^k \right) + \left(\sum_{k=0}^{\infty} \chi_C^k \right) \left(\sum_{k=1}^{\infty} \chi_B^k \right) \left(\sum_{k=1}^{\infty} \chi_A^k \right) \right] \quad (5.2)$$

It is of note that the path expressions have all been placed within an infinite sum. This is due to the fact that, neglecting damping effects, the waves will repeat each reflection and transmission pattern indefinitely. Some simplifications of the expressions can be made to aid with interpretation. As the summations are infinite geometric progressions, it is well known that these can be evaluated as below.

$$\sum_{k=0}^{\infty} r^k = \frac{1}{1-r} \quad (6)$$

Therefore, equations 5.1 and 5.2 simplify to equations 7.1 and 7.2.

$$\Gamma_F = [(1 - \chi_A)^{-1}(1 - \chi_B)^{-1}\{1 + \chi_B\chi_C(1 - \chi_C)^{-1}\}] \quad (7.1)$$

$$\Gamma_S = [(1 - \chi_B)^{-1}(1 - \chi_C)^{-1}\{1 + \chi_A\chi_B(1 - \chi_A)^{-1}\}] \quad (7.2)$$

The path expressions have been derived to represent the cycle a wave undergoes before arriving back at its starting position. The initial waves, however, are defined as the forcing waves, plus the initial reflections that occur before one full cycle of the paths has been completed. These waves can be found to be those given in equations 8.1 and 8.2 for the forcing and sense cavities respectively.

$$\eta_F(x) \quad (8.1)$$

$$= \begin{cases} e^{i\gamma x} (F_R + R_{LH}F_L e^{i2\gamma a}) + e^{-i\gamma x} (R_C F_R e^{i2\gamma a} + T_C^2 R_{RH} F_R e^{i2\gamma(a+b)}); & x > 0 \\ R_{LH}F_L e^{i(x+2\gamma a)} + e^{-i\gamma x} (F_L + R_C F_R e^{i2\gamma a} + T_C^2 R_{RH} F_R e^{i2\gamma(a+b)}); & x < 0 \end{cases}$$

$$\eta_S(x) = T_C \{ e^{i\gamma x} (R_{LH}F_L e^{i2\gamma a}) + e^{-i\gamma x} (R_{RH}F_R e^{i2\gamma(a+b)} + R_{RH}R_{LH}F_L e^{i\gamma(4a+2b)}) \} \quad (8.2)$$

The path expression products and the initial waves can now be combined to provide the displacements within the forcing and sense cavities. These are given by equations 9.1 and 9.2.

$$\psi_F(x) = \Gamma_F \eta_F(x) \quad (9.1)$$

$$\psi_S(x) = \Gamma_S \eta_S(x) \quad (9.2)$$

3. Device design and analysis

In order to use the model derived in the preceding section, the transmission and reflection coefficients of the arrays are required. These have been found from the transfer matrix method presented in references [1] and [4]. The derivation is, however, too extensive to be repeated here. The closed form, non-dimensionalised expression for the transmission amplitude across an N-cell array, \widetilde{T}_N , is however shown in equations 10.1-3.

$$\widetilde{T}_N = \left| \frac{1}{(\widetilde{w}e^{-i\pi\tilde{f}}U_{N-1}(\tilde{\zeta}) - U_{N-2}(\tilde{\zeta}))e^{i\pi N_c\tilde{f}}} \right| \quad (10.1)$$

$$\widetilde{w} = \left(\cos\left(\frac{\pi\mu_c\tilde{f}}{\tilde{v}_c}\right) - i\epsilon_+ \sin\left(\frac{\pi\mu_c\tilde{f}}{\tilde{v}_c}\right) \right) e^{i\pi\mu_c\tilde{f}} \quad (10.2)$$

$$\tilde{\zeta} = \text{Re}(\widetilde{w})\cos(\pi\tilde{f}) + \text{Im}(\widetilde{w})\sin(\pi\tilde{f}) \quad (10.3)$$

$$\epsilon_+ = \frac{1}{2} \left(\tilde{v}_c + \frac{1}{\tilde{v}_c} \right) \quad (10.4)$$

Where $U_N(\tilde{\zeta})$ is the Nth Chebyshev polynomial of the second kind and \widetilde{w} is the non-dimensional form of the upper left component of the single cell transfer matrix. For further detail the reader is encouraged towards the aforementioned references.

The simplest way to find the design parameters, such as operating frequency and dimensions, are to reason them from the transmission amplitude plots of the different arrays and cavities that constitute the devices. There are 5 independent non-dimensional parameters to describe each array, these are listed in table 1 for the example of the coupling array.

Table 1.

Original Parameter	Description and Dimensions	Non-Dimensional Symbol	Relationship
Ω/f	Device operating frequency (rad s ⁻¹ /Hz)	\tilde{f}	$\frac{2s_cf}{v_1}$
v_c	Wave-speed in the perturbed regions within the coupling array (m/s)	\tilde{v}_c	$\frac{v_c}{v_1}$
s_c	Period in the coupling array (m)	\tilde{s}_c	$\frac{s_cf}{v_1}$
$\frac{d_c}{s_c}$	Plating ratio in the coupling array	μ_c	$\frac{d_c}{s_c}$
N_c	Number of periods in the coupling array	N_c	N_c

The device is operated at a fixed frequency and the amplitude ratio is altered by a change in the transmission amplitude across the coupling array, \widetilde{T}_c , due to a change in \widetilde{v}_c by some external stimulus. There are several ways in which the design parameters could be specified. However, it is likely in a SAW device that the starting point will be a known substrate Rayleigh wave velocity and a known perturbed velocity within plated regions. For this reason, the parameters have been normalized to the unperturbed (substrate) wave-speed v_1 . The maximum wave-speed perturbation within the coupling array is set arbitrarily following guideline values from references [1] and [2] at -1%.

The Rayleigh wave-velocity in Y-Z Lithium-Niobate is widely reported [9] and given in eq.11.

$$v_1 = 3488 \text{ m/s} \quad (11)$$

The values of v_c for 200nm thick Aluminium strips on YZ-LiNbO3 is approximately 95% of the free wave velocity [4]. With a wave-speed change of -1% this gives the range of \widetilde{v}_c as shown in eq.12.

$$\widetilde{v}_c = 0.94 - 0.95 \quad (12)$$

It can be seen from equations 10.1-3 that in order to plot the transmission amplitude across the coupling array for a given range of \widetilde{f} , it is necessary to specify the additional parameters μ_c and N_c . These are the plating fraction and number of periods respectively. Initial trial values of these parameters are specified below for all arrays, to be refined with the aid of the transmission plots.

$$\mu_{c(initial)} = \mu_{E(initial)} = 0.5 \quad (13.1)$$

$$N_{c(initial)} = N_{E(initial)} = 25 \quad (13.2)$$

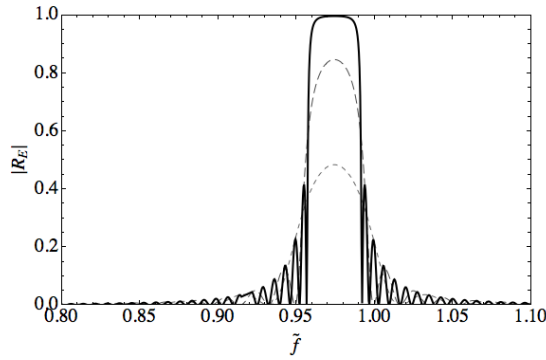


Figure 3. Reflection spectrum plots with initial parameter choices for increasing N_E . Plotted for $N_E = 25$ (light-dashed), $N_E = 50$ (dashed) and $N_E = 125$ (full).

The iterative design adjustments are exemplified in figure 3. These detail the frequency dependence of the reflection amplitude for the enclosing arrays. It is shown that the desired non-dimensional operating frequency is $\tilde{f} = 0.975$, this can be tuned by altering frequency, or period length and therefore can be different in the coupling and enclosing arrays. In addition, sufficiently increasing N_E enforces the reflection coefficient to be equal to unity. This enforces the assumption used in the model derivation that there is zero transmission from the cavity through the enclosing arrays.

It is implicit in the results of the mathematical model and the initial assumptions that the device sensitivity is proportional to the transmission amplitude across the coupling array, \widetilde{T}_c . The final parameters to be found are μ_c and N_c . These parameters will be selected using a plot of transmission across the array for the range of \tilde{v}_c values that will be encountered in operation (fig 4.).

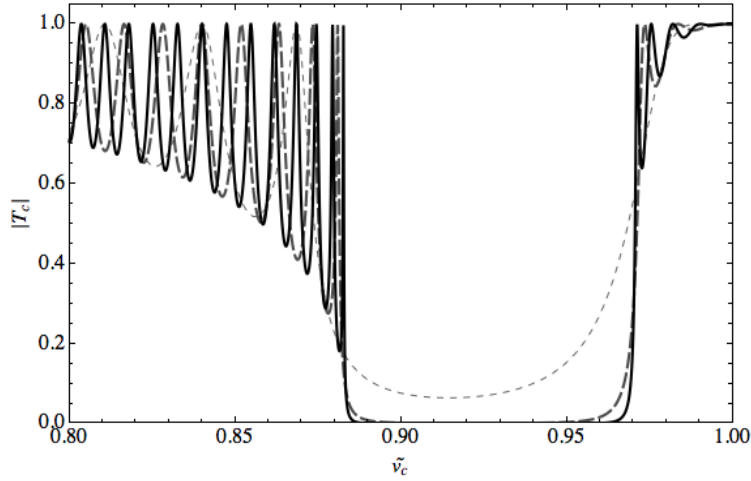


Figure 4. Transmission coefficient plotted against the wave-speed in the plated region expanded around the range of interest. Plotted for $\tilde{f} = 0.975$; $N_c = 50$ (light-dashed), $N_c = 125$ (dashed) and $N_c = 200$ (full).

The proposed operating region is located at an edge of the stop-band seen in fig.4. It can be seen that the upper edge of the stop-band responds more uniformly to an increase in N_c . This plot can be used iteratively to choose the parameters that locate the operating region in the desired location in wave-speed space. It can be seen that increasing the number of periods (N_c), increases the gradient of the transmission coefficient change, and reduces the range of the operating region. The operating region is indicated on the $N_c = 200$ plot in figure 5.

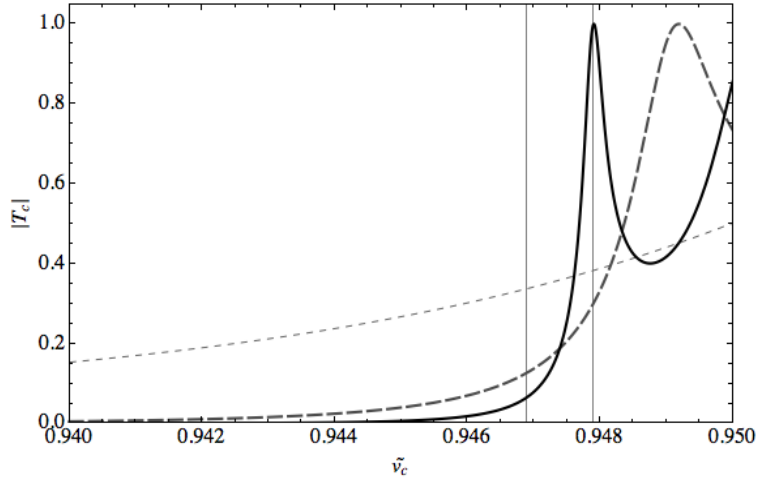


Figure 5. Representation of predicted device operation. The iteratively selected non-dimensional operating frequency is $\tilde{f} = 0.95$. The proposed operating region is shown for the $N_c = 200$ (full-line) case. Values of N_c are displayed as in fig. 4.

4. Conclusions

The design for a novel surface acoustic wave MEMS device has been presented and potential functionalization routes discussed. It has been shown that the number of periods in the coupling array can be used to enhance the sensitivity of the device, at the sacrifice of device range. The analysis has provided dimensions for an initial design to be further explored using numerical, or experimental, methods. In addition, the work provides a reasoned design route that could be applied to find dimensions for different choices of materials, plating thickness or operating frequency.

The effect of bulk wave generation on device operation is not accounted for in the design method. It has been shown in the literature [4] that the effect is negligible if the plating thickness is small in comparison to the wavelength; this constitutes a stipulation on device design. This stipulation necessitates the use of long periodic arrays; the length of these arrays in conjunction with manufacturing tolerances will inevitably determine minimum device size.

References

- [1] Cross, P.S., Haydl, W.H., and Smith, R.S. Design and applications of two-port SAW resonators on YZ-Lithium Niobate. *Proceedings of the IEEE* 64, 5 (1976), 682-685
- [2] Weiyang, L., Dhagat, P., and Jander, A. Surface acoustic wave magnetic sensor using galferol thin film. *IEEE Transactions on Magnetics* 48, 11 (2012), 4100-4102.
- [3] Clarke, N.S., and Burdess, J.S. A Rayleigh resonator. *Wave Motion* 13, (1991), 193-200.

- [4] Sinha, B.K., and Tiersten, H.F. Variational analysis of the reflection of surface waves by arrays of reflection strips. *Journal of Applied Physics* 47, 7 (1976), 2824-2832.
- [5] Graff, K.F. *Wave Motion In Elastic Solids*. Dover Publications, Inc, New York, 1991.
- [6] Achenbach, J.D. *Wave Propagation In Elastic Solids*. North-Holland, Amsterdam, 1973.
- [7] Mead, D.J. Wave propagation in continuous periodic structures: Research contributions from Southampton 1964-1995. *Journal of Sound and Vibration* 190, 3 (1996), 495-524.
- [8] Griffiths, D.J., and Steinke, C.A. Waves in locally periodic media. *American Association of Physics Teachers* 69, 2 (2001), 137-154.
- [9] Kannan, T. *Finite Element Analysis of Surface Acoustic Wave Resonators*. M.Sc. thesis, Department of Electrical Engineering, University of Saskatchewan, 2006, Klymyshyn, D.M.

Thomas Harry Hanley, (Ph.D. student): School of Mechanical and Systems Engineering, Newcastle University, Newcastle Upon Tyne, NE1 7RU, UK (*t.h.hanley@ncl.ac.uk*). The author gave a presentation of this paper during one of the conference sessions.

Barry Gallacher, Ph.D., Reader in Engineering Dynamics: School of Mechanical and Systems Engineering, Newcastle University, Newcastle Upon Tyne, NE1 7RU, UK (*barry.gallacher@ncl.ac.uk*).

Harry Grigg, Ph.D., Lecturer: School of Mechanical and Systems Engineering, Newcastle University, Newcastle Upon Tyne, NE1 7RU, UK (*harry.grigg@ncl.ac.uk*).

Deformation work of Zona Pelucida in process of fertilization (LIF223-15)

Andjelka N. Hedrih, Katica R. (Stevanovic) Hedrih

Abstract: Zona pelucida (ZP) is an extracellular mantel that surrounds mammalian oocytes. This structure is important for fertilization, especially for gamete recognition and integrity of the embryo. ZP is highly sulfated and glycosylated polymer gel that exhibit visco-elastic properties and changing in diameter in different maturation stages. In the process of fertilization numerous spermatozoa impact its external surface giving some energy to the structure. The aim of this paper is to present a possible approximate mechanical model of the ZP in the form of elastic body bound by two concentric spherical surfaces loaded by discrete continuum distribution of spermatozoa impacts in radial directions. Using theory of elasticity for this approximate model, expressions for component stresses and strains are presented, as well as expressions for specific and total deformation work of the model deformation under external constant pressure. On the basis of obtained expressions an analysis of possible stress and strain state and a model of ZP deformation work some conclusions are derived. A specific deformation work as criteria for determination area of possible open put for passing spermatozoa through ZP is proposed.

1. Introduction

Zona pelucida (ZP) is an extracellular, 3D mesh –like structure that surrounds mammalian oocytes. It is highly sulfatated glikoprotein gel 2-6% (w/v) where the glikoproteins are interconnected with non-covalent bounds [1]. The structure is important for fertilization, gamete recognition and integrity of the embryo. It is formed during the process of oocyte maturation [2] and change mechanical and structural properties during oocyte maturation and fertilization process [3]. During these processes it change its diameter. In fully-grown oocyte ZP is the thickest. This structure exists till the early blastocyst stage of an embryo. ZP is mechanically responsive structure [3, 4]. Using atomic force microscope and Arruda–Boyce eight-chain model visco-elastic properties of ZP could be modeled [4]. A computational model of impact of one sperm to the ZP was done in [5]. The ZP can be considered as an oscillatory structure that exhibits transition in oscillatory behavior before and after fertilization [6, 7]. Dissipation of its oscillatory energy occurs when it exhibits visco-elastic properties [7].

1.1. Effect of sperm velocity and its arrangement on mouse ZP oscillatory behavior

During the process of fertilization many spermatozoa will influence the surface of ZP. Spermatozoa are motile cells and in ejaculate there are many spermatozoa (in range of 10^6) with different velocities

and morphological characteristics. Only 10% are functionally capable of fertilizing the oocyte. Number of progressively motile spermatozoa is crucial for fertilization success. "Different distributions of spermatozoa with same/different kinetic parameters result in different distributions of external forces acting on the ZP surface. Each individual spermatozoid generates certain force that acts upon the ZP surface [8] and their joint action will give specific distribution of force on the ZP surface"[9]. Currently valid opinion in science is that distribution of spermatozoa upon ZP surface is stochastic process. The schematic representation of hypothetical sperm distribution upon the ZP surface is presented in figure 1. "A symmetric or asymmetric distribution of forces produced by action of spermatozoa upon ZP surface will cause different oscillatory states of the ZP."[9]. Impact of spermatozoa upon ZP surface is not only mechanical but also involved receptor-recognition mechanism.

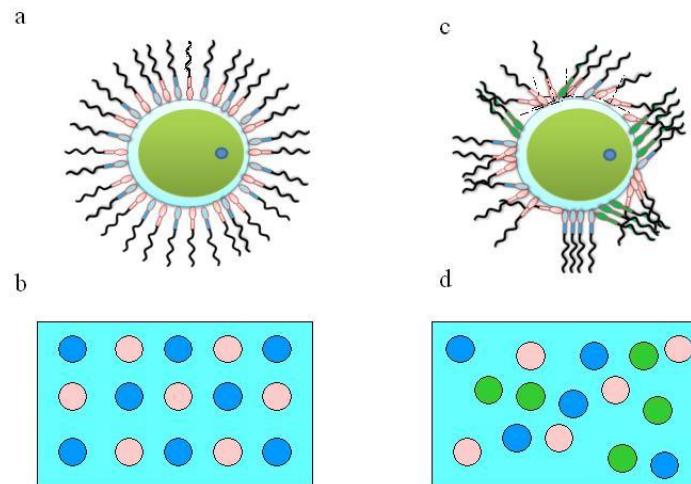


Figure 1. Hypothetical arrangement of spermatozoa on ZP surface. a. Symmetrical arrangement of spermatozoa having two different swimming velocities and same impact angles. b. Symmetrical distribution of areas with same mechano-chemical impact on ZP surface. c. Asymmetrical arrangement of spermatozoa having three different swimming velocities and different impact angles arbitrary arranged. d. Asymmetrical distribution of areas with same mechano-chemical impact on ZP surface. Different colors of spermatozoa (pink, blue or green) on a and c. denote their different swimming velocities. Different colors on b and d denote areas with different mechano-chemical influence of corresponding spermatozoa.

During the external impact of spermatozoa certain amount of kinetic energy is transfer to ZP.

The aim of this paper is to present a possible approximate mechanical model of the ZP in the form of elastic body bound by two concentric spherical surfaces loaded by discrete continuum distribution of spermatozoa impacts in radial directions. Using theory of elasticity for this approximate model, expressions for component stresses and strains are presented, as well as expressions for specific and total deformation work of the model deformation under external constant pressure. On the basis of obtained expressions an analysis of possible stress and strain state as well as model of ZP deformation work some conclusions are derived.

2. Stress and strain in mechanical model of ZP as a elastic body

Determining the Young modulus of mouse oocyte and embryo, using micropipette aspiration technique, Khalilian et al modeled the oocyte as an elastic shell of defined thickness. [10]

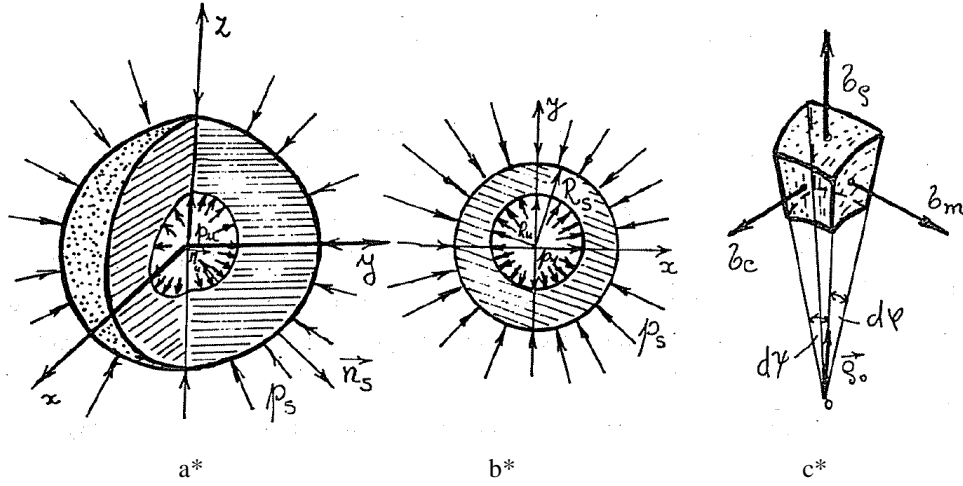


Figure 2. Mechanical model of ZP loaded by central symmetric pressure.

To determine the deformation work of ZP in the state before starting of the process of fertilization with impact of numerous spermatozoa ZP was considered as deformable ideal elastic body, bounded by two spheres with radiuses R_u and R_s with thickness $\delta = R_s - R_u$ in natural and no loaded state.

We made some assumptions of the model: spermatozoa form uniform arrangement on ZP surface. All spermatozoa have same velocities and sperm impact angles, which result in uniform arrangement of external pressure upon the ZP surface. In definite time moment sperm impact is in

form of constant external pressure $\vec{p}_s = -p_s \frac{\vec{r}}{r} = -p_s \vec{r}_0$ in radial direction on the outer surface of

ZP external contour. Pressure on the inner spherical surface of the ZP we can use in the form:

$\vec{p}_u = p_u \frac{\vec{r}}{r} = p_u \vec{r}_0$, (see Figure 2.a* and b*). For special case we can use that this pressure on

other sphere is equal to zero, $p_u = 0$. The thickness of the ZP $\delta = R_s - R_u$ in unperturbed state is uniform. The model and the external discrete continually distributed pressures are centrally symmetric. After deformation the ZP remains symmetric. Displacements of material particles of ZP and on inner and outer ZP surface are central symmetrical and only in radial direction. There is no shearing stress. In this model we take into account only two static configurations: one in natural stationary case before actions of numerous spermatozoa impacts and final deformed configuration of the ZP under static centrally symmetric pressures. Similar model is presented in Figure 2.

Taking into account previous assumptions and determinations the problem could be treated as kvasistatic and according to the model from Theory of elasticity solved in the books [11], [12] as model presented in Figure 2 with an element of the ZP in the form of element in spherical coordinate system, with three main normal stresses in radial circular and meridian directions, we can present there expressions for these elements of stress tensor of stress state in the points of zona pelucida, in the form (see References [11] and [12]):

$$\sigma_r = \frac{1}{1-\psi^3} \left[\psi^3 \left(1 - \frac{R_s^3}{r^3} \right) p_u - \left(1 - \psi^3 \frac{R_s^3}{r^3} \right) p_s \right], \quad (1)$$

$$\sigma_c = \sigma_c = \frac{1}{1-\psi^3} \left[\psi^3 \left(1 + \frac{R_s^3}{r^3} \right) p_u - \left(1 + \psi^3 \frac{R_s^3}{r^3} \right) p_s \right], \quad (2)$$

where $\psi = \frac{R_u}{R_s}$, p_s - pressure on the outer contour surface of the sphere. p_u - pressure of the

inner contour surface of the sphere. Tangential components of the stresses are equal to zero.

For the case when specific shear deformations are equal to zero $\gamma_{rc} = 0, \gamma_{rm} = 0$

and $\gamma_{cm} = 0$, strain-dilatation of line elements in radial, circular and meridian directions are defined by following expressions (see References [11] and [12]):

$$\varepsilon_r = \frac{1}{G(1-\psi^3)} \left[\frac{\psi^3 p_i - p_o}{2(1+3\mu k)} - \psi^3 \frac{p_i - p_o}{2} \frac{R_o^3}{r^3} \right], \quad (3)$$

$$\varepsilon_c = \varepsilon_m = \frac{1}{2G(1-\psi^3)} \left[\frac{\psi^3 p_i - p_o}{(1+3\mu k)} + \psi^3 \frac{p_i - p_o}{2} \frac{R_o^3}{r^3} \right], \quad (4)$$

where G - is shear modulus μ - Poisson ratio of lateral contractions, $k = \frac{1}{1-2\mu}$. Previous

component present approximate elements of the strain tensor of specific deformation line element in the point of the zona pelucida in defined model.

Volume dilatation ε_v of material element around material particles of the ZP on distance r from the center of the sphere is expressed in the form:

$$\varepsilon_v = \varepsilon_r + \varepsilon_c + \varepsilon_m = \frac{3}{2(1+3\mu k)} \frac{\psi^3 p_i - p_o}{1-\psi^3}, \quad (5)$$

Volume of an elementary part of ZP (Figure 2c) in spherical coordinates is with sides: dr , $r \cos \psi d\varphi$ and $rd\psi$ is: $dV = r^2 \cos \psi dr d\varphi d\psi$.

By previous expressions (1)-(2) and (3)-(4)-(5) is possible to analyze quazi static stress and strain around each point inside of ZP including points along the boundary contours inner and outer sphere of the model of ZP in proposed deformed configuration loaded by discrete continuum distribution of spermatozoid impacts.

3. Deformation work of deformed configuration of defined mechanical ZP model

Deformation work of volume unit of ZP could be determined through component stress and component strain. The specific deformation work (elastic potential) of volume element of the defined mechanical model of ZP in deformed configuration should be determined first. It is in the form:

$$\mathbf{A}'_{def} = G \left[(\varepsilon_r^2 + \varepsilon_c^2 + \varepsilon_m^2) + \mu k \varepsilon_r^2 + \frac{1}{2} (\gamma_{rc}^2 + \gamma_{rm}^2 + \gamma_{cm}^2) \right], \quad (6)$$

expressed by elements of strain tensor. Taking into account that for considered case of stress and strain are $\gamma_{rc} = 0$, $\gamma_{rm} = 0$ and $\gamma_{cm} = 0$, specific deformation work is possible present in the form: $A'_{def} = G [(\varepsilon_r^2 + \varepsilon_c^2 + \varepsilon_m^2) + \mu k \varepsilon_r^2]$. If we introduce the following notations:

$$a = \frac{1}{G(1-\psi^3)}, b = \frac{\psi^3 p_i - p_o}{2(1+3\mu k)}, c = \psi^3 \frac{p_i - p_o}{2}, \quad (7)$$

the specific deformation work of defined model of ZP could has the following form:

$$\mathbf{A}'_{def} = G \left[a^2 \left(b - \frac{c}{r^3} \right)^2 + 2 \frac{a^2}{4} \left(2b + \frac{c}{r^3} \right)^2 + \mu k (3ab)^2 \right], \quad (8)$$

and its final form is:

$$\mathbf{A}'_{def} = G \frac{3a^2}{2} \left[(2+3\mu k)b^2 + \frac{c^2}{r^6} \right], \quad (9)$$

Previous expression of specific deformation work of produced under model of ZP up to deformed configuration explicitly expressed by pressures applied along boundary contour surfaces is in the following form:

$$\mathbf{A}'_{def} = \frac{3}{2G(1-\psi^3)^2} \left[\frac{(2+3\mu k)}{4(1+3\mu k)^2} (\psi^3 p_u - p_s)^2 + \psi^6 \frac{(p_u - p_s)^2}{4} \frac{1}{r^6} \right], \quad (10)$$

We can see that specific deformation work - elastic potential of the deformed configuration of the model of ZP is function of radiuses of boundary contour spherical surfaces, inner and outer spherical surfaces; inner and outer continually distributed pressures, with quadratic. Also depend of point position in model depending of distance r from centre of spherical surfaces in opposite proportionality with sixth step r^{-6} . Also with ratio of the radiuses of inner and outer spherical radiuses ψ^6 . Taking into account that this considered model is static, and that real system of ZP dynamic under the action of spermatozoa impacts specific deformation work in the corresponding point can be consider as a elastic potential for rejecting some of next spermatozoa impact or for passing through ZP one of these spermatozoa through zone with point with minimal specific deformation work - elastic potential. One of the aidea in analogy with plastic deformation to introduce hypothesis of minimal or maximal value of specific deformation work for destruction od some zone of ZP for put of passing one spermatozoa after deformation ZP bay invasion of numerous discrete continuum distribution numerous spermatozoa impacts. This is open ida for discussion and evaluations!

To obtain expression for total deformation work for whole mechanical model of ZP the deformation work for all volume units should be summed and present by following volume integral along all volume of the proposed mechanical model in the following form:

$$\mathbf{A}_{def} = \int \int \int_V \mathbf{A}'_{def} dV = \int_{R_i}^{R_o} \int_0^{2\pi} \int_{-\frac{\pi}{2}}^{\frac{\pi}{2}} \mathbf{G} \frac{3a^2}{2} \left[(2 + 3\mu k)b^2 + \frac{c^2}{r^6} \right] r^2 \cos \psi dr d\phi d\psi, \quad (11)$$

and its final form is:

$$\mathbf{A}_{def} = -6\mathbf{G}a^2 \left[(2 + 3\mu k)b^2 R_i^3 \frac{1 - \psi^3}{3} - 3c^2 \frac{\psi^2 - 1}{R_o^2} \right], \quad (12)$$

The total deformation work – elastic potential of the whole model of ZP explicate expressed by all geometrical and material influent parameters, and in the case that model of ZP is loaded by discrete continuum distribute pressures along inner and outer boundary contour spherical surface, is:

$$\mathbf{A}_{def} = -\frac{6}{\mathbf{G}(1 - \psi^3)^2} \left[\frac{(2 + 3\mu k)}{12(1 + 3\mu k)^2} (1 - \psi^3)(\psi^3 p_u - p_s)^2 R_s^3 - \frac{3}{4} \psi^6 (\psi^2 - 1)(p_u - p_s)^2 \frac{1}{R_u^2} \right], \quad (13)$$

The total deformation work – elastic potential of the whole model of ZP explicate expressed by all geometrical and material influent parameters, and in the case that model of ZP is loaded by discrete continuum distributed pressures along only outer boundary contour spherical surface, is:

$$\mathbf{A}_{def} = -\frac{6}{\mathbf{G}(1 - \psi^3)^2} \left[\frac{(2 + 3\mu k)}{12(1 + 3\mu k)^2} (1 - \psi^3)(p_s)^2 R_s^3 - \frac{3}{4} \psi^6 (\psi^2 - 1)(p_s)^2 \frac{1}{R_u^2} \right], \quad (14)$$

4. Dynamical model of ZP

Let consider a oscillatory model of ZP presented in Figure 2, and loaded by continually distributed pressures along boundary contour surfaces, inner and outer surfaces in radial direction in the case that pressures are function of time, it is visible to conclude that mass particle of ZP oscillate central symmetrically in radial direction, Partial differential equation of radial oscillation of mass particle of a model of ZP shell is:

$$\mathbf{G}(\Delta \vec{s} + kgr\text{div}\vec{s}) + \vec{F}_{v'} = \rho \frac{\partial^2 \vec{s}}{\partial t^2}, \quad (15)$$

where $\vec{s}(r, t) = s(r, t) \frac{\vec{r}}{r}$ is displacement in radial direction of material particles of the model of

ZP, \mathbf{G} is shear modulus, \vec{F}_v , specific volume force that could be neglected, $\rho \frac{\partial^2 \vec{s}}{\partial t^2}$ specific force

of inertia of ZP mass, ρ density of ZP biomaterial, $\frac{\partial^2 \vec{s}}{\partial t^2}$ acceleration of mass unit of ZP,

$k = \frac{1}{1-2\mu}$, μ is Poisson ratio, $grad$ -gradient differential vector operator, div - scalar

differential operator, while Δ -Laplace-differential operator in spherical coordinate system has a form differential operator :

$$\Delta = \frac{\partial^2}{\partial r^2} + \frac{1}{r^2 \cos^2 \psi} \frac{\partial^2}{\partial \varphi^2} + \frac{1}{r^2} \frac{\partial^2}{\partial \psi^2} + \frac{2}{r} \frac{\partial}{\partial r} - \frac{tg \psi}{r^2} \frac{\partial}{\partial \psi}, \quad (16)$$

We suppose that displacement of the mass particle of the model of ZP is in the form of product of two functions $\tilde{s}(r)$ and $T(t)$ and that solution of the partial differential equation (15) is possible to suppose in the form:

$$\vec{s}(r, t) = s(r, t) \frac{\vec{r}}{r} = \tilde{s}(r) T(t) \frac{\vec{r}}{r}, \quad (17)$$

and after introducing (17) in (15) we obtain:

$$T(t) \mathbf{G}(1+k) grad div \left[\tilde{s}(r) \frac{\vec{r}}{r} \right] = \rho \ddot{T}(t) \tilde{s}(r) \frac{\vec{r}}{r}, \quad (18)$$

or in the form:

$$\mathbf{G}(1+k) grad div \left[\tilde{s}(r) \frac{\vec{r}}{r} \right] = \rho \frac{\ddot{T}(t)}{T(t)} \tilde{s}(r) \frac{\vec{r}}{r}, \quad (19)$$

or in the form:

$$\frac{\mathbf{G}(1+k)}{\rho} \frac{\frac{d}{dr} \left\langle \tilde{s}(r) + 2 \frac{\tilde{s}(r)}{r} \right\rangle}{\tilde{s}(r)} = \frac{\ddot{T}(t)}{T(t)} = \mp \omega^2, \quad (20)$$

in which we introduce unknown parameter $\mp \omega^2$ which is constant. After introducing that

$$\omega^2 = \lambda^2 \frac{\mathbf{G}(1+k)}{\rho}, \quad (21)$$

from equation (20) we obtain the following two ordinary differential equation, each along only one variable – coordinate and time in the following form:

$$\ddot{T}(t) + \omega^2 T(t) = 0, \quad (22)$$

$$\frac{d}{dr} \left\langle \tilde{s}(r) + 2 \frac{\tilde{s}(r)}{r} \right\rangle + \lambda^2 \tilde{s}(r) = 0, \quad (23)$$

or in the form:

$$\ddot{T}(t) + \omega^2 T(t) = 0, \quad (24)$$

First ordinary differential equation (24) is known and with solution in the form:

$$T(t) = A \cos \omega t + B \sin \omega t, \quad (25)$$

in which ω is eigen circular frequency of free vibrations, and A and B are integral constant defined by initial conditions.

Problem is to solve second, nonlinear differential equation (25). Solution $\tilde{s}(r)$ present eigen amplitude function, which must to satisfy boundary condition on the boundary contour spherical surface. This ordinary differential equation (25) is similar to Bessel differential equation, and it is necessary to find some change of variable if possible to solve this nonlinear differential equation.

At this moment, the question how to solve this differential equation analytically is open or it could be solved by using some numerical method and computer software tools.

5. Conclusions

In conclusion, we can point out, that specific deformation work - elastic potential of the deformed configuration of the model of ZP is function of radiuses of boundary contour spherical surfaces, inner and outer continually distributed pressures, with quadratic, depend of distance r from centre of spherical surfaces with proportion r^{-6} , with ratio of the radiuses of inner and outer spherical radius ψ^6 . The total deformation work of the whole ZP model is inversely proportional to the shear modulus. Taking into account that the considered model is static, specific deformation work of ZP in the corresponding point, during fertilization process, can be consider as an elastic potential for rejecting some of incoming spermatozoa or for penetration through ZP at the point with minimal specific deformation work. The idea is the analogy between plastic deformation and minimal or maximal value of specific deformation work needed for destruction of some zone of ZP. This critical deformation work in certain point of ZP could lead to weakening of the material (ZP) and its plastic flow. It is possible that this local plastic flow of ZP could initiate the process of sperm penetration.

Acknowledgments

This work was supported by the Ministry of Education, Sciences and Technology of the Republic of Serbia through Mathematical Institute SANU, Belgrade and Faculty of Mechanical Engineering, University of Niš, State University of Novi Pazar Grant ON174001.

References

- [1] Green, P.D. Three-dimensional structure of the zona pellucida, *Reviews of Reproduction*, 2, (1997), 147-156.
- [2] Jovine, L., Qi, H., Williams, Z., Litscher, E.S., Wassarman PM. Features that affect secretion and assembly of zona pellucida glycoproteins during mammalian oogenesis. *Society of Reproduction and Fertility Supplement*. 2007, 63: 187-201.
- [3] Murayama, Y., Mizuno, J., Kamakura, H., Fueta, Y., Nakamura, H., Akaishi, K., Anzai, K., Watanabe, A., Inui, H., and Omata, S. Mouse zona pellucida dynamically changes its elasticity during oocyte maturation, fertilization and early embryo development. *Human Cell* 19 (2006), 119–125.
- [4] Boccaccio, A., Lamberti, L., Papi, M., De Spirito, M., Douet, C., Goudet, G., Pappalettere, C. A hybrid characterization framework to determine the visco-hyperelastic properties of a porcine zona pellucida. *Interface Focus* 4, (2014) 20130066.
- [5] Kozlovsky, P., and Gefen, A. Sperm penetration to the zona pellucida of an oocyte: a computational model incorporating acrosome reaction. *Computer Methods in Biomechanics and Biomedical Engineering* 16, 10 (2013) pp.7.
- [6] Hedrih, A. Transition in oscillatory behavior in mouse oocyte and mouse embryo trough oscillatory spherical net model of mouse Zona Pellucida" ch in *Applied Non-Linear Dynamical Systems*, Springer Proceedings in Mathematics & Statistics 93, J. Awrejcewicz (ed.), 93, 295-303. Springer International Publishing Switzerland, 2014.
- [7] Hedrih, N.A., and (Stevanović) Hedrih, R.K. Analysis of energy state of discrete fractional order spherical net of mouse zona pellucida before and after fertilization. *International Journal of Mechanics SI*, 8, (2014), 365-370.
- [8] Hsiao, WW., Liao, HS., Lin, HH., Ding, RF., Huang, KY., and Chang, CS. Motility Measurement of a Mouse Sperm by Atomic Force Microscopy. *Analytical Sciences* 29 (2013), 3-8.
- [9] Hedrih, A., Mitrovic-Jovanovic, A., and Lazarevic, M. Effect of sperm velocity and its arrangement on mouse Zona Pellucida oscillatory behaviour. *to appear*
- [10] Khalilian, M., Navidbakhsh, M., Valojerdi, MR., Chizari, M., Yazdi, PE. Estimating Young's modulus of zona pellucida by micropipette aspiration in combination with theoretical models of ovum. *Journal of the Royal Society Interface*. 7, 45 (2010) 687-94.
- [11] Hedrih (Stevanović), R.K. *Izabrana poglavlja Teorije elastičnosti (Selected Chapter in Theory of Elasticity)*. Masinski fakultet Univerziteta u Nisu, Nis, 1988, pp. 424.
- [12] Rašković D. P., *Teorija elastičnosti (Theory of elasticity)*, Maučma knjiga, Beograd , 1985.

Andjelka Hedrih, M.D. (Ph.D. student): State University of Novi Pazar, 36 300 Novi Pazar, Serbia (handjelka@gmail.com), The author gave a presentation of this paper during one of the conference sessions.

Katica (Stevanovic) Hedrih, Professor: Mathematical institute SANU, 11 000 Belgrade, Serbia, Faculty of Mechanical engineering, University of Nis, 18 000 Nis, Serbia (khedrih@sbb.rs).

Dynamics model of the four-wheeled mobile platform (MTR033-15)

Anna Jaskot, Bogdan Posiadała, Szczepan Śpiewak

Abstract: The dynamics model of the prototype of four-wheeled mobile platform has been presented. The problem has been formulated with consideration of the contact phenomenon between foundation and drive wheels and the possibility of slippage is also included. The model enables to analyze the forced and free motions of the platform with consideration of the changes of drive module positions during the platform motion. The formulated problem has been solved numerically with the use of Runge-Kutta method of the fourth order.

1. Introduction

Analysis of the issue of dynamics of the mobile platforms consists on the motion studies taking into account the forces which are causing this movement and to study the causes and effects of the motion. Considerations about the trajectory tracking and path generation both for kinematics and dynamics of the robots for two-wheeled [3], three-wheeled [1][2][5], or one-sphere [9] are the subject of widely described in the literature. The solutions for the different possible configurations of the wheeled platforms in terms to dynamics is considered and solved in [4].

The aim to know the conditioning of platforms work, the solution of the description of the dynamics of the mobile platform is proposed. The trajectory tracking problem for a 4-wheel differentially driven mobile robot moving on an outdoor terrain is considered in [6]. The design of a four-wheeled mobile platform for a indoor terrain (production halls, factories), which model allows for an analysis of the planar motion, including a progressive and rotational motion of the platform is presented in this paper. A constructional model allows to the change the length between the wheels along the longer side of the platform. Description of the dynamics of the platform in the classical approach ultimately allow to provide the velocity and acceleration, taking into account the cause of the motion and allow to know the position of the platform at a particular point in time.

Solving the problem of the dynamics is based on knowing the relevant motion equations, in the purpose of the studies of the motion trajectory. Knowing the differential equations of motion the simple or inverse task of the dynamics can be solved. Due to the complex form of the equations describing the motion of the system in the inverse task of the dynamics, the solution of it can make a problem. This paper presents a solution to the inverse problem of dynamics. Knowing the differential equations of motion the motion parameters can be determined by using the Eulers

parameters and Kane's method [1], Maggi equations [5], Lagrange method [4][7][9]. In this work, the appropriate calculations were made by using the Runge – Kutta method of the four order. The effect of this is generating and implementing the trajectory of the platforms motion.

The examples of the results of platforms motion simulation due to the driving torque applied to the wheel of the platform and simulation of position changes of the platform while in motion are also presented in this work.

2. Model of the prototype of the platform

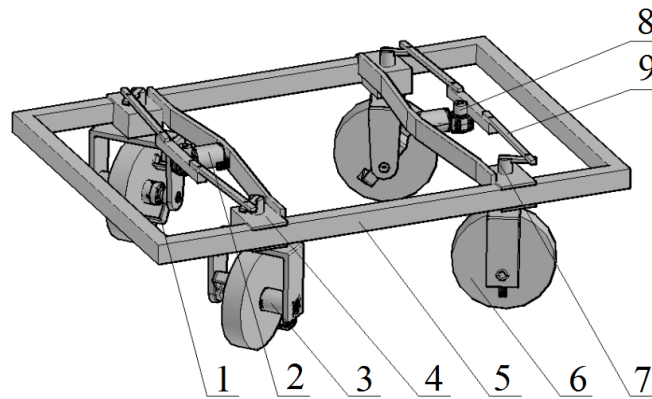


Figure 1. Scheme of the prototype of the mobile platform

The system of the chassis of proposed solution of the mobile platform is pictorially presented in Fig. 1. The modular construction of the design solution has been adopted. Creating configurations of selected positioning of the platform wheels is possible by the using the drive member with electric drive. This allows the realization of the preset trajectories of vehicular transporter.

Body chassis is mounted to the chassis frame. The torsion system of the platform, according to the initial assumption, is dependent in pairs, and is realized through an electric motor conjugated to the worm gear (2), a rod system (9) and a rack and pinion gearing (8). The presented version of a bare chassis of the platform is constructed from a rigid frame (5) on the sides of which the main hitches (4) of stub axle (7) are attached in a clamping method.

Changing the distance between the axis of the driving wheels (6) along the longer side of the frame is possible by the configuration of hitches. Each wheel has an independent drive system constituting the coupling of the electric engine (3) with a planetary gear in co-axial system (3). The symmetry axis of the stub axle (7) passes through the center of gravity of the motor assembly, the planetary gear, driving road wheel, and a driver (1), through which the torque is transmitted.

Additionally, it is possible to embed an independent stub axle drives on hitches (2) in order to study a tracking motion trajectory, when the stub axles are immobilized. The provision of possibility to separate the selected wheel drives has been made. To prepare a model of prototype Autodesk Inventor has been used. The possibility of rotating the wheels of the 360 deg is a big advantage of the system, since it enables the execution of all of the possible maneuvers of the mobile platform.

3. Geometric model of the mobile platform

In this work the description of the dynamics, which includes the determination of the motion equations have been resolved.

In order to describe the dynamics of the mobile platform in a coordinate space the model shown schematically in Fig. 2 is adopted.

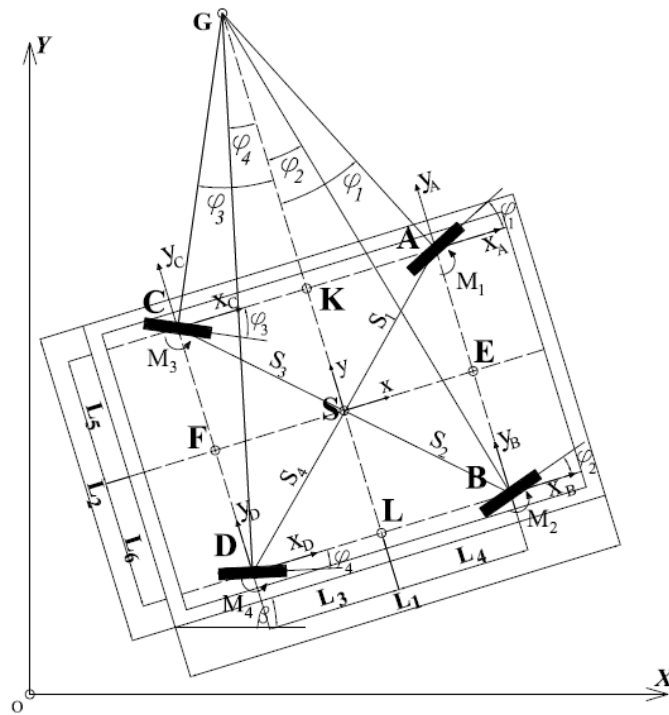


Figure 2. The geometric scheme of the mobile platform

The motion parameters are determined with respect to the global reference frame OXY , according to designations:

A, B, C, D – the points corresponding to a position of the center of rotation for each wheel,

x_i, y_i – coordinates of the i -th point (respectively for points: A, B, C, D),

S – the point corresponding to the centre of gravity and the centre of mass of the platform,

L_i – the lengths of sections from the centre of gravity (point S) to following points A, B, C, D .

β – the platform inclination angle relative to the X axis of the global reference system.

The global and local coordinate systems, and the geometric relations between the position of the respective drive modules are shown in the model scheme.

The motion of the robot occurs in one plane in a planar surface. Instantaneous motion is composed of the progressive motion with the velocity of the centre of the mass and the rotational motion with the velocity around the center of mass of the mobile platform. To determine the sample motion parameters based on the forces that cause the motion the following assumptions have been taken into the account:

- the platform moves on a flat surface,
- during the movement does not occur the phenomenon of detachment of wheels from the ground,
- during motion, the mass of the platform is not changed.

In Fig. 3 the forces occurring in the wheels of platform during the movement are presented. The force N_i , as a reaction on the weight of the platform wheels are considered. In the figure the driving torque M_i which later is a base to determine the active force F_{ci} are also shown.

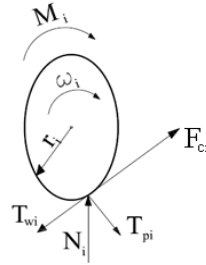


Figure 3. Distribution of forces acting on each wheel of the platform

In Fig. 3 the following forces are presented:

M_i – the drive torque,

F_{ci} – the active driving force,

T_{wi} – the friction force in the longitudinal direction,

T_{pi} – the friction force in the transverse direction,

N_i – the reaction force of the i -th wheel,

ω_i – the angular velocity of the i -th wheel.

4. Description of the dynamics of mobile platform

In determining the forces occurring during the motion there is a need to take into account the drive torque and the friction, which is consequent from the contact of the wheel from the roadway. It is necessary to determine the values of wheel loads on the roadway, W_i force vectors and M_i moments to the points A, B, C, D .

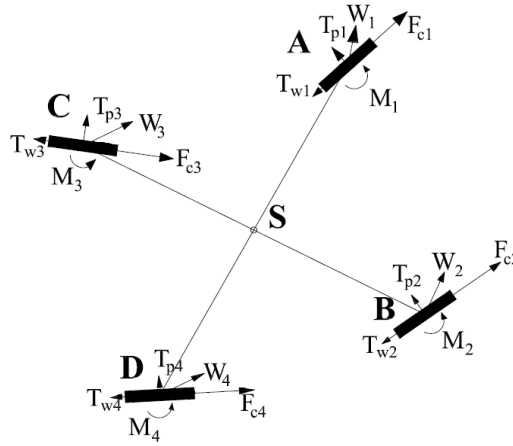


Figure 4. Distribution of forces in the platform wheels

The scheme of the calculation model is presented in Fig. 4. The values of the resultant forces W_i have been calculated as follows:

$$W_1 = F_{c1} + T_{w1} + T_{p1}, \quad (1)$$

$$W_2 = F_{c2} + T_{w2} + T_{p2}, \quad (2)$$

$$W_3 = F_{c3} + T_{w3} + T_{p3}, \quad (3)$$

$$W_4 = F_{c4} + T_{w4} + T_{p4} \quad (4)$$

The active forces acting on each one of the wheel were calculated by the formula:

$$F_{ci} = \frac{M_{ni}}{r} \quad (5)$$

where: M_{ni} – the drive torque of an i -th wheel,

r – radius of a driver wheel.

It is necessary to establish the value of the force N_i , which is a reaction to the weight of the i -th wheel (Figure 3).

In addition to the active forces which cause motion of the system, the passive forces should be determined. The passive forces are the resistance forces such as friction forces T_{wi} in the longitudinal direction, and the friction forces T_{pi} in the transverse direction. The friction force values are different from zero during the platform motion, because the active force F_{ci} is different from zero. The whole values of those forces are described below:

$$T_{wi} = \mu_w \cdot N_i \cdot \text{sign}(v_w) \quad (6)$$

$$T_{pi} = \mu_p \cdot N_i \cdot \text{sign}(v_p) \quad (7)$$

where: μ_w – coefficient of friction for the longitudinal direction,

μ_p – coefficient of friction for the transverse direction.

Considering the formulated formulas (1-7) representing the active and passive forces the translational motion equation can be formulated in the form:

$$ma = \sum_{i=1}^4 W_i \quad (8)$$

where: m – the mass of the whole object,

a – the acceleration of the centre of mass of the platform,

W_i – the i -th resultant force.

This equation enables to determine the motion of the center of mass under the influence of known external forces. The progressive motion of the center of mass is described by Eq. (8) and the rotational motion around the center of mass for the platform should be also described.

The equation of the rotational motion around the center of mass for the platform can be written in the form:

$$\frac{dK}{dt} = \sum_{i=1}^4 s_i \times W_i + \sum_{i=1}^4 M_i \quad (9)$$

where: K – the angular momentum vector of the whole platform,

s_i – the location vector of points: A, B, C, D in the global coordinate system.

By using the derived equations of motion, written in the form of differential equations, the rate of change certain physical quantities (ex. velocity, positioning) can be defined. The dynamic equations of motion can be written in case of the planar motion in the form:

$$m\ddot{X} = W_{ix} \quad (10)$$

$$m\ddot{X} = W_{iy} \quad (11)$$

$$\ddot{\beta} = \frac{\sum_{i=1}^4 (s_{ix} \cdot W_{iy} - s_{iy} \cdot W_{ix})}{I_z} \quad (12)$$

The set of equations (10-12) can be used to formulate the initial problem by adding the initial conditions according to the starting values of the motion parameters. The formulated initial problem has been solved by using the Runge - Kutta method of the fourth order.

5. The exemplary simulation results of platform motion

The description of the dynamics has been drawn up with assumption that the drive torque is given as a trapezoidal function as shown in Fig. 5.

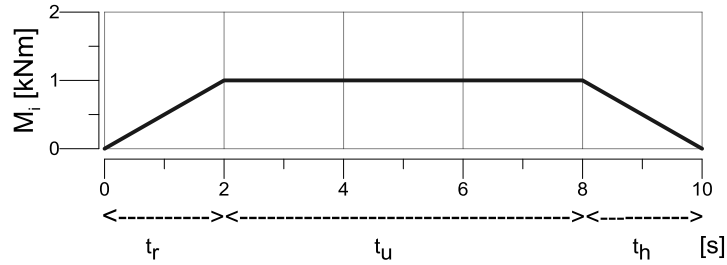


Figure 5. Drive torque as a trapezoidal function ($M_{i_max} = 1$ kNm)

The movement should be considered in three time periods: starting = 2s, established= 6s, braking = 2s.

Solutions for the straight line trajectory according to the principles is presented in Fig. 6. The considered results have been obtained for such values of active forces that no slippage of any wheel has been observed.

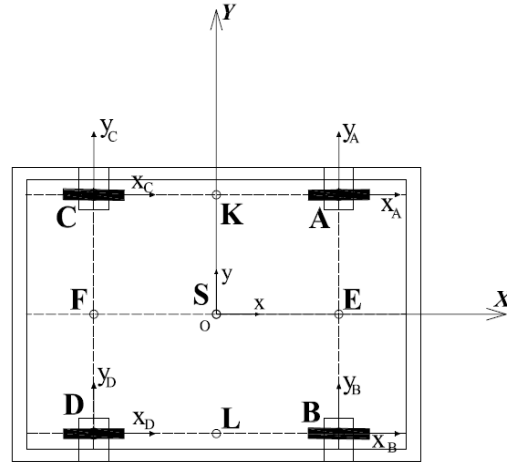


Figure 6. The starting position of the platform in relation to the global coordinate system

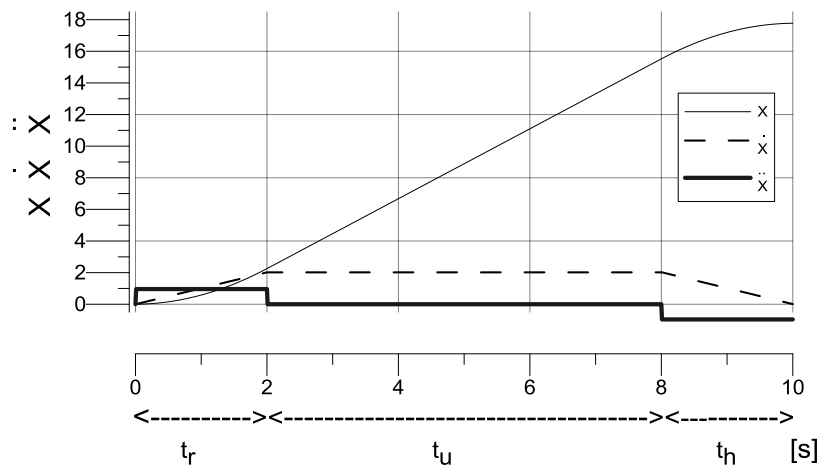


Figure 7. The motion parameters of the centre of the mass of the mobile platform

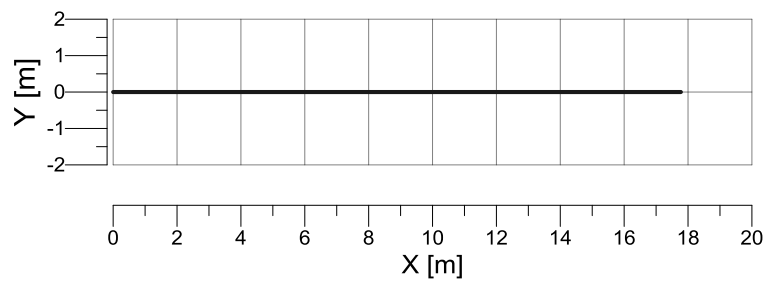


Figure 8. The motion trajectory of the mobile platform

6. Conclusions

The proposed dynamical model of mobile platform motion is useful to examine the different implementation of the active forces and the realization of motion in different configurations of the drive wheels.

Built on the basis of the description of dynamics the calculation model enables understanding of the determinants of platforms work, which in turn allowed the determination of the parameters affecting the movement of both the platform and its components.

The presented in the work the design solution of the mobile platform is designed to enable further research, both experimental and theoretical of the dynamic phenomena that can occur during movement of such facilities, particularly in an effort to investigate the behavior of the platform while slippage and to refrain from falling into the skid.

References

- [1] Azizi M. R., Naderi D.: Dynamic modeling and trajectory planning for a mobile spherical robot with a 3Dof inner mechanism, *Mechanism and Machine Theory* 64, 2013, 251-261.
- [2] Bisse E., Bentounes M., Boukas And E. K.: Optimal Path Generation for Simulated Autonomous Mobile Robot, *Autonomous Robots*, 1995, 11-27.
- [3] Burghardt A.: Sterowanie behawioralne minirobota kołowego, PAK 11/2004, 26-29.
- [4] Campion G., Bastin G., D'Andréa-Novel B.: Structural Properties and Classification of Kinematic and Dynamic Models of Wheeled Mobile Robots, *IEEE Transactions on robotics and automation*, vol. 12, No. 1. Feb. 1996.
- [5] Carelli R., Forte G., Canali L., Mut V., Araguas G., Destefanis E.: Autonomous and teleoperation control of a mobile robot, *Mechatronics* 18, 2008, 187-194.
- [6] Caracciolo L., Luca De A., Iannitti S.: Trajectory Tracking Control of a Four-Wheel Differentially Driven Mobile Robot, *IEEE International Conference on Robotics & Automation* Detroit, 1999, 2632-2638.
- [7] Giergiel, M. i Małka, P.: Modelowanie kinematyki i dynamiki mobilnego mini robota. *Modelowanie Inżynierskie*, 2006, 157-162.
- [8] Kozłowski, K. i Paździerski, D.: Modeling and control of a wheel skid-steering mobile robot. *International Journal of Applied Mathematics and Computer Science*, 14(4), 2004, 477-496.
- [9] Staicu S.: Dynamics equations of a mobile robot provided with caster wheel, *Nonlinear Dyn* 58, 2009, 237-248.

Anna Jaskot, M.Sc. (Ph.D. student): Institute of Mechanics and Machine Design Foundations, Czestochowa University of Technology, ul. Dąbrowskiego 73, 42-201 Częstochowa, Poland, e-mail: (a.jaskot@imipkm.pcz.pl).

Bogdan Posiadała, Professor: Institute of Mechanics and Machine Design Foundations, Czestochowa University of Technology, ul. Dąbrowskiego 73, 42-201 Częstochowa, Poland, e-mail: (b.posiadala@imipkm.pcz.pl).

Szczepan Śpiewak, Ph.D.: Institute of Mechanics and Machine Design Foundations, Czestochowa University of Technology, ul. Dąbrowskiego 73, 42-201 Częstochowa, Poland, e-mail: (*s.spiewak@imipkm.pcz.pl*).

The author gave a presentation of this paper during one of the conference sessions.

Free vibration of cantilever beams of various cross-section (VIB042-15)

Jacek Jaworski, Olga Szlachetka

Abstract: The topic of this study is the first mode of natural transverse vibrations of isotropic, homogeneous and elastic columns (or beams) with clamped bottom and free head. The columns are shaped as tubes with linearly variable wall thickness and with different inclination of lateral faces, from cylinder to cone. The first frequency of free vibrations was determined using the energy method. The deflection line of the column axis during the vibration was assumed in form of the bending line of the column axis subjected to a uniform load. Resulting frequencies (or periods) were compared with these obtained with the use of FEM (ANSYS) and a good compliance of results was observed. As the expression for the energy of an elementary slice of material was integrated over the length of the beam, the formula for the frequency was obtained in form of an integral equation. In the case of a truncated-cone column, an exact solution of integral equation was obtained, however for a tubular column with variable cross-section only a numerical solution was possible.

1. Introduction

The frequencies of subsequent modes of free vibrations of a beam can be obtained by solving the equation of a Bernoulli-Euler beam for specific boundary conditions. The way of proceeding which enables to obtain a numerical solution for a beam having the shape of truncated cone and wedge is presented in [1]. Other methods and further results for bars (beams or posts) with variable cross sections are discussed and presented in [2].

Authors of this paper have set themselves a target to derive, using the Rayleigh method, formulas for the first frequency of natural (transverse) vibrations of cantilever bars having the shape of conical tube, i.e. hollow truncated cone. It has been assumed that the vibration amplitude is small, the material is homogeneous, isotropic and ideally elastic, and the mass is continuously distributed.

In the Rayleigh method, the shape of deflection line of the oscillating bar axis is being assumed. If the shape is assumed in a form of parabola, trigonometric function or a static deflection line being a result of action of an external transversal force applied in its top, the obtained results for cantilever bars with circular cross section are not proper, especially for the bars having the shape close to cone [3]. The results consistent with the FEM calculations and with the solution according to [1] have been obtained with the assumption that the axis of an oscillating post assumes a form of the line of static deflection evoked by a continuous load [4]. The assumption of a continuous mass distribution

sometimes leads to serious difficulties in integration. However, if an exact solution can be found, as it is for example in case of a truncated cone cantilever bar [4], the obtained formula is so simple that a pocket calculator is enough to calculate the first frequency (or period) of free vibrations.

2. Derivation of formulas

2.1. Bar scheme and basic dependences

Free vibrations of a conical tube cantilever bar have been considered. The bar is loaded with a continuous load of a constant value q (Fig. 1). There are introduced the denotations:

$$n = \frac{D}{d}, \quad (1)$$

$$\alpha = \frac{\Delta}{D}, \quad (2)$$

$$\beta = \frac{\delta}{d}. \quad (3)$$

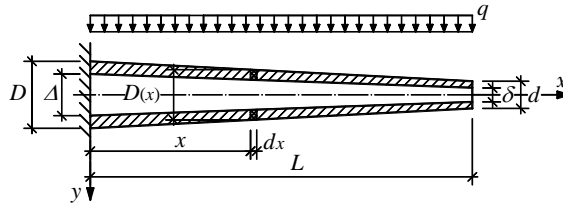


Figure 1. Cantilever beam in form of a uniformly loaded hollow cone tube.

The external and internal diameter of the bar as well as the second area moment in any cross section, given by a coordinate x , are equal respectively:

$$D(x) = D - \frac{D-d}{L}x, \quad (4)$$

$$\Delta(x) = \Delta - \frac{\Delta-\delta}{L}x, \quad (5)$$

$$J(x) = \frac{\pi}{64} [D^4(x) - \Delta^4(x)] \quad (6)$$

where

x, y – coordinate axes,

D, d – bigger and smaller external diameter of the bar,

Δ, δ – bigger and smaller internal diameter of the bar,

n – quotient of the diameters describing a convergence ratio of external walls of the truncated cone,

L – bar length,

J – second area moment of the bar cross section.

2.2. Bar deflection

A deflection has been calculated by integration of the differential equation of bar elastic deflection curve:

$$EJ(x) \frac{d^2 u}{dx^2} = -M(x) = \frac{qL^2}{2} - qLx + \frac{qx^2}{2} \quad (7)$$

where

u – deflection,

E – longitudinal modulus of elasticity,

M – bending moment in the bar section given by a coordinate x ,

q – continuous load of a constant value.

The above equation can be transformed to the form which is convenient to integrate:

$$\frac{2\pi ED^4}{64q} \frac{d^2 u}{dx^2} = \frac{L^2 - 2Lx + x^2}{(ax+b)(cx+e)(fx^2+gx+h)} = \frac{\alpha_1}{ax+b} + \frac{\alpha_2}{cx+e} + \frac{\beta_1 x + \beta_2}{fx^2+gx+h} \quad (8)$$

where a, b, c, e, f, g, h are equal:

$$\begin{aligned} a &= -\frac{n(1-\alpha)-(1-\beta)}{nL}, \\ b &= 1-\alpha, \\ c &= -\frac{n(1+\alpha)-(1+\beta)}{nL}, \\ e &= 1+\alpha, \\ f &= \frac{n^2(1+\alpha^2)-2n(1+\alpha\beta)+(1+\beta^2)}{n^2 L^2}, \\ g &= -\frac{2}{nL} \left[(1+\alpha^2)n - (1+\alpha\beta) \right], \\ h &= 1+\alpha^2. \end{aligned} \quad (9)$$

The symbols $\alpha_1, \alpha_2, \beta_1, \beta_2$ are the quotients of the determinants:

$$\begin{aligned}
\alpha_1 &= \frac{W_{\alpha_1}}{W}, \\
\alpha_2 &= \frac{W_{\alpha_2}}{W}, \\
\beta_1 &= \frac{W_{\beta_1}}{W}, \\
\beta_2 &= \frac{W_{\beta_2}}{W}
\end{aligned} \tag{10}$$

resulting from the application of the Cramer method for the set of linear equations:

$$\begin{aligned}
\alpha_1 cf + \alpha_2 af + \beta_1 ac &= 0, \\
\alpha_1 (ef + cg) + \alpha_2 (bf + ag) + \beta_1 (ae + bc) + \beta_2 ac &= 1, \\
\alpha_1 (eg + ch) + \alpha_2 (bg + ah) + \beta_1 be + \beta_2 (ae + bc) &= -2L, \\
\alpha_1 eh + \alpha_2 bh + \beta_2 be &= L^2.
\end{aligned} \tag{11}$$

After two integrations of Eq. (8), the bar deflection is obtained in the following form:

$$u(x) = \frac{32q}{\pi ED^4} Q(x) \tag{12}$$

where:

$$\begin{aligned}
Q(x) &= C_1 x + C_2 + \frac{\alpha_1}{a^2} (ax + b) [\ln(ax + b) - 1] + \frac{\alpha_2}{c^2} (cx + e) [\ln(cx + e) - 1] + \\
&\quad - \frac{\beta_1 x}{f} + \frac{\beta_1 (fx + g) - \beta_2 f}{2f^2} \ln(fx^2 + gx + h) + \\
&\quad + \left[\frac{\beta_1 \sqrt{4fh - g^2}}{2f^2} + \left(\beta_2 - \frac{\beta_1 g}{2f} \right) \frac{2fx + g}{f \sqrt{4fh - g^2}} \right] \arctan \left(\frac{2fx + g}{\sqrt{4fh - g^2}} \right)
\end{aligned} \tag{13}$$

and the integration constants C_1 and C_2 are equal:

$$\begin{aligned}
C_1 &= -\frac{\alpha_1}{a} \ln(b) - \frac{\alpha_2}{c} \ln(e) - \frac{\beta_1}{2f} \ln(h) - \left(\beta_2 - \frac{\beta_1 g}{2f} \right) \frac{2}{\sqrt{4fh - g^2}} \arctan \left(\frac{g}{\sqrt{4fh - g^2}} \right), \\
C_2 &= -\frac{\alpha_1 b}{a^2} (\ln(b) - 1) - \frac{\alpha_2 e}{c^2} (\ln(e) - 1) - \frac{\beta_1 g - \beta_2 f}{2f^2} \ln(h) + \\
&\quad - \left[\frac{\beta_1 \sqrt{4fh - g^2}}{2f^2} + \left(\beta_2 - \frac{\beta_1 g}{2f} \right) \frac{g}{f \sqrt{4fh - g^2}} \right] \arctan \left(\frac{g}{\sqrt{4fh - g^2}} \right).
\end{aligned} \tag{14}$$

2.3. First natural frequency

With the assumption that the bar axis (Fig. 1) deflected during vibrations has a shape described by (12), the potential energy for the deflected bar and the kinetic energy for the non-deformed bar have been calculated. The potential energy is equal:

$$E_p = \int_0^L \frac{1}{2} q u(x) dx = \frac{1}{2} q \frac{32q}{\pi E D^4} \int_0^L Q(x) dx. \quad (15)$$

If the mass of a material slice with a thickness dx is denoted as $m(x)$, i.e.

$$m(x) = \frac{\rho\pi}{4} [D^2(x) - \Delta^2(x)] dx = \frac{\rho\pi}{4} D^2(ax+b)(cx+e) dx \quad (16)$$

then the kinetic energy of the post is determined as:

$$E_k = \int_0^L \frac{1}{2} \omega^2 u^2(x) m(x) = \frac{1}{2} \omega^2 \frac{\rho\pi}{4} D^2 \left(\frac{32q}{\pi E D^4} \right)^2 \int_0^L (ax+b)(cx+e) Q^2(x) dx. \quad (17)$$

The energy comparison enables to determine the frequency. The period is equal:

$$T = \frac{2\pi}{\omega} = \frac{4\pi}{D} \sqrt{\frac{2\rho}{E} \frac{\int_0^L (ax+b)(cx+e) Q^2(x) dx}{\int_0^L Q(x) dx}} \quad (18)$$

where

T – vibration period,

ω – vibration frequency,

ρ – mass density,

E – longitudinal modulus of elasticity,

D – diameter in the clamp,

L – bar length.

Remaining quantities are described with Eqs. (9), (10) and (13). Expansion of the terms in the integrations in the root in Eq. (18) allows to note that the integrated terms take i.a. the form:

$$\begin{aligned} & x^3 \ln(ax+b) \arctan(cx+e), \\ & x^3 \ln(ex^2 + fx + g) \arctan(cx+e). \end{aligned} \quad (19)$$

These functions are not integrable analytically, therefore the values under the root in Eq. (18) have been calculated numerically using the program MATHEMATICA 9.0. In this aim, the command $\text{NIntegrate}[f, \{x, x_0, x_1\}]$ has been applied, which gives the numerical value of an integral $\int_{x_0}^{x_1} f(x) dx$, [5].

3. Special cases

As the denominators in the Eqs. (8), (10) and (13) cannot be equal zero, the four special cases presented in Fig. 2 must be considered individually. The proper formulas for calculation of the vibration period for them are presented below.

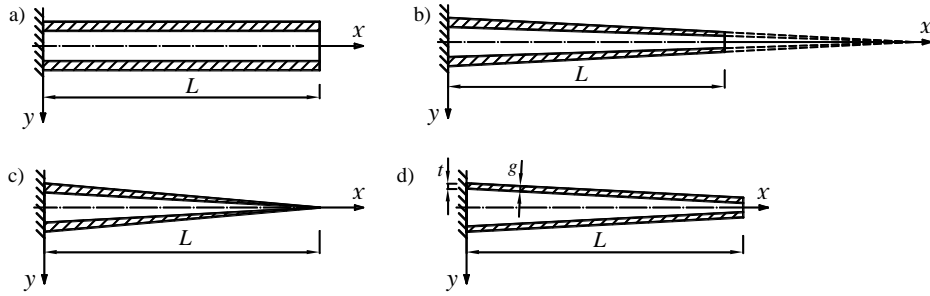


Figure 2. Special cases: a) cylindrical tube, b) conical tube, $\alpha = \beta$, c) hollow cone, d) conical tube with constant wall thickness.

A) Cylindrical tube $d = D$, $\delta = \Delta$ (Fig. 2a). It is a simple case where:

$$T = \frac{4}{9} \frac{\pi L^2}{D} \sqrt{\frac{26\rho}{E(1+\alpha^2)}} \quad (20)$$

B) Conical tube where the generatrices of the internal and external cone cross in the point placed on the longitudinal axis of the bar, $\alpha = \beta$ (Fig. 2b). This case can be described by the vibration period formula for a truncated cone derived in [4]:

$$T_{trunc.cone} = \frac{4\pi L^2}{3D} \frac{n}{(n-1)^2} \sqrt{\frac{\rho}{E}} \sqrt{\frac{F(n)+60G(n)\ln(n)}{10H(n)}} \quad (21)$$

where:

$$\begin{aligned}
F(n) &= 11n^6 - 87n^5 + 375n^4 - 1184n^3 + 3219n^2 - 4281n + 2817 - 1080n^{-1} + 234n^{-2} - 24n^{-3}, \\
G(n) &= 14n^3 - 33n^2 + 15n - 3 - 6n^3 \ln(n), \\
H(n) &= 3n^4 + 10n^3 - 18n^2 + 6n - 1 - 12n^3 \ln(n).
\end{aligned} \tag{22}$$

The vibration period formula is obtained after multiplication of the term (21) by a correcting factor [4], taking into consideration the hollow of such type that $\alpha = \beta$:

$$T = T_{tunc.cone} \cdot \sqrt{\frac{1}{1 + \alpha^2}}. \tag{23}$$

C) The external surface creates a cone, $d = 0$ (Fig. 2c). If this case is considered as a cone [4] with a hole and $\alpha = \beta$, then the vibration period formula takes a form:

$$T = \frac{4\pi L^2}{3D} \sqrt{\frac{1}{30E}} \cdot \sqrt{\frac{1}{1 + \alpha^2}}. \tag{24}$$

D) Conical tube with the constant wall thickness (Fig. 2d). The projection of the wall thickness g on the transversal surface is denoted as t :

$$t = g \frac{\sqrt{4L^2 + (D - d)^2}}{2L}. \tag{25}$$

Further procedure is analogical to that in Section 2. The second area moment is determined as a function of t :

$$J(x) = \frac{\pi}{8} t (D - sx - t) \left[(D - sx)^2 - 2(D - sx)t + 2t^2 \right], \tag{26}$$

$$s = D \frac{n - 1}{nL}. \tag{27}$$

After substitution to the differential equation of bar elastic deflection curve (7) and two integrations, it has been obtained:

$$\begin{aligned}
\frac{\pi Et}{4q} u(x) = R(x) = & C_1 x + C_2 + \frac{D - t - sx}{s^2} \alpha_3 \ln(D - t - sx) + \frac{B\beta_3 + A\beta_3 x - A\gamma}{2A^2} \ln(Ax^2 + Bx + C) \\
& + \frac{A\alpha_3 - s\beta_3}{As} x - \frac{B^2\beta_3 + AB(\beta_3 x - \gamma) - 2A(C\beta_3 + A\gamma x)}{A^2 \sqrt{4AC - B^2}} \arctan\left(\frac{B + 2Ax}{\sqrt{4AC - B^2}}\right)
\end{aligned} \tag{28}$$

where:

$$\begin{aligned}
A &= s^2, \\
B &= -2s(D-t), \\
C &= D^2 - 2Dt + 2t^2, \\
\alpha_3 &= \frac{[sL - (D-t)]^2}{s^2 t^2}, \\
\beta_3 &= \frac{[sL - (D-t)]^2 - t^2}{st^2}, \\
\gamma &= \frac{L^2 s^2 t^2 - [sL - (D-t)]^2 (D^2 - 2Dt + 2t^2)}{s^2 t^2 (D-t)}
\end{aligned} \tag{29}$$

and the integration constants are equal:

$$\begin{aligned}
C_1 &= \frac{\alpha_3}{s} \ln(D-t) - \frac{\beta_3}{2A} \ln(C) - \frac{2A\gamma - \beta_3 B}{A\sqrt{4AC - B^2}} \arctan\left(\frac{B}{\sqrt{4AC - B^2}}\right), \\
C_2 &= -\frac{D-t}{s^2} \alpha_3 \ln(D-t) - \frac{B\beta_3 - A\gamma}{2A^2} \ln(C) + \frac{B^2\beta_3 - AB\gamma - 2AC\beta_3}{A^2\sqrt{4AC - B^2}} \arctan\left(\frac{B}{\sqrt{4AC - B^2}}\right).
\end{aligned} \tag{30}$$

If the mass of a material slice with a thickness dx is determined as:

$$m(x) = \rho \pi t (D - sx - t) dx \tag{31}$$

then the energies can be compared and the dependence is obtained which enables – similarly as from Eq. (18) – to calculate the vibration period in a numerical way:

$$T = 4\pi \sqrt{\frac{\rho}{E}} \sqrt{\frac{\int_0^L (D - sx - t) R^2(x) dx}{\int_0^L R(x) dx}}. \tag{32}$$

4. Examples of calculation and comparison of results

The examples of dependences of vibration period on the geometrical parameters of a cantilever bar with the shape of conical tube are presented in Fig. 3.

The following data have been assumed: $L = 2 \text{ m}$, $D = 0,06 \text{ m}$, $\sqrt{\rho/E} = 7 \cdot 10^{-4} \text{ s} \cdot \text{m}^{-1}$ (plastic).

The convergence ratio of the bar walls varies within the range between the value for a cone ($n = \infty$, $d = 0$) to the value for a cylinder ($n = 1$, $d = D$), the values of the parameters α and β are diversified.

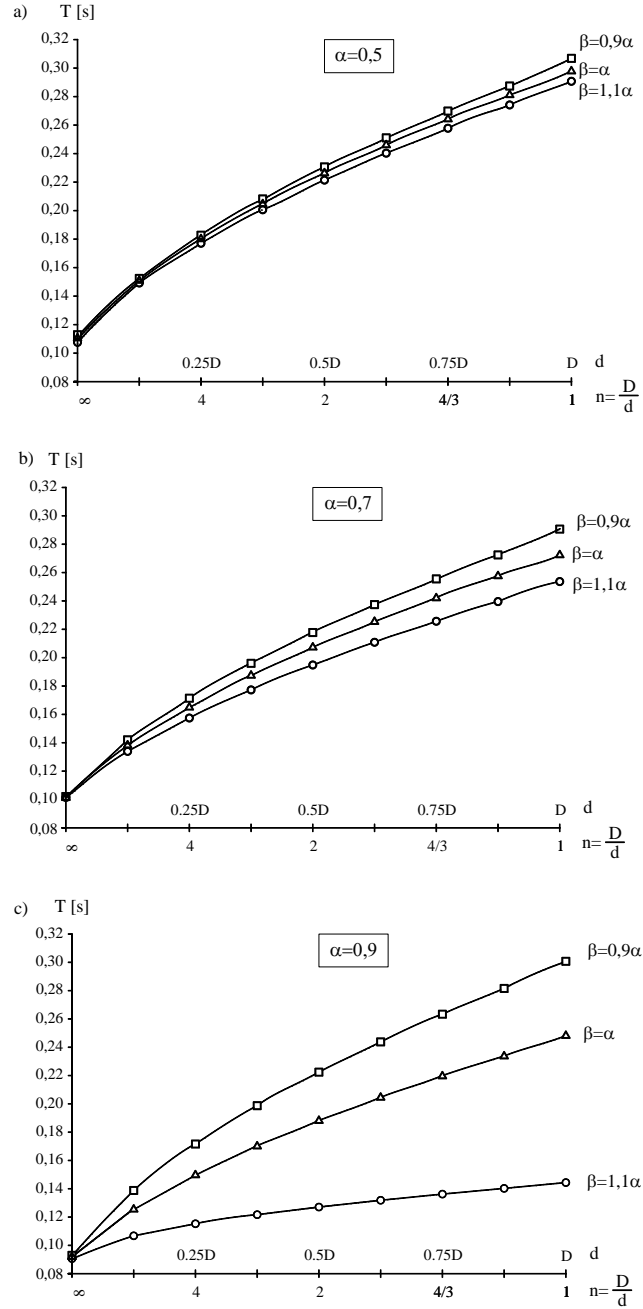


Figure 3. Vibration period for conical tube: a) $\alpha = 0,5$ b) $\alpha = 0,7$ c) $\alpha = 0,9$. The cases are considered for $\beta = 0,9\alpha$, $\beta = 1,0\alpha$, $\beta = 1,1\alpha$.

The curves for $\alpha = \beta$ concern such a conical tube (considered in Section 3) where the generatrices of the internal and external cone cross in the point placed on the longitudinal axis of the bar. The points of these curves have been calculated from the formula (23) which presents the concordance with the results according [1] and with the FEM results what was proved in [4]. It has been also checked that the obtained results exactly correspond to the vibration periods calculated according to Eq. (18) if instead $\beta = \alpha$ it has been taken $\beta = \alpha \pm \theta$, where θ is a quantity much smaller than α . For the tube ($n=1$) and for the cone ($n=\infty$), the values of vibration period have been calculated from the Eqs. (20) and (24), respectively. In this case, the approximated solution can also be obtained from Eq. (18) if there are placed the convergence ratios close to $n=1$ and $n=\infty$, respectively.

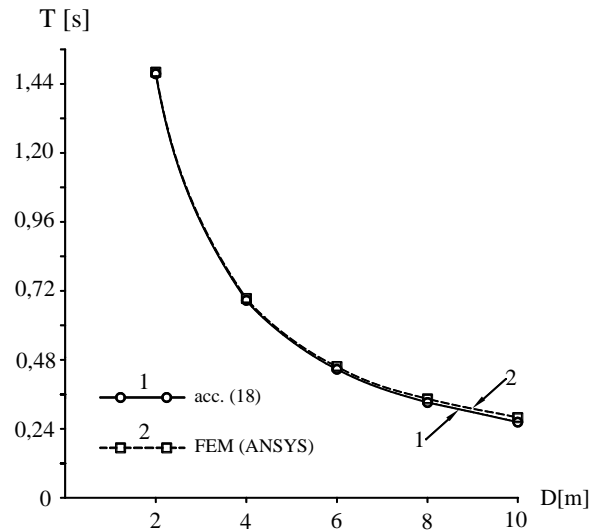


Figure 4. Vibration periods of a ferroconcrete sheet construction calculated: 1 – acc. (18), 2 – with FEM.

Fig. 4 presents the results of calculations of a vibration period of a ferroconcrete stress-skin construction (assumed $\sqrt{\rho/E} = 3,5 \cdot 10^{-4} \text{ s} \cdot \text{m}^{-1}$) with the height $L=48\text{m}$, convergence ratio $n=2$ and wall thickness in the base $0,27\text{m}$ and in the head $0,06\text{m}$. Five diameters in the base have been considered, from $D=2\text{m}$ to $D=10\text{m}$. In this range of diameters, the first natural frequency corresponds to bending vibrations. For the diameters $D \geq 12\text{m}$, the first natural frequency corresponds to other forms of vibrations. The results of calculations according Eq. (18) have been compared to the results obtained with use of FEM (ANSYS). The great concordance of results is visible. For the diameters $D \leq 4\text{m}$ – what corresponds to the slenderness ratio (understood here as

$\lambda = L/D$) greater or equal 12 – the differences between these results are lower than 1%. As the slenderness ratio diminishes, this difference increases and e.g. for $D=10\text{m}$ ($\lambda = 4,8$) is equal 5,6%.

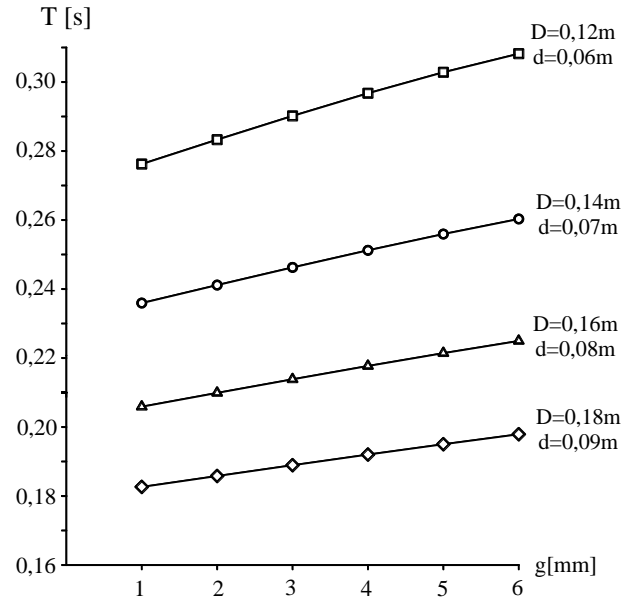


Figure 5. Vibration periods of a steel post with a constant thickness

Fig. 5 presents the results for a post made of steel sheet – such solution is very widely applied in practice. It has been assumed: $\sqrt{\rho/E} = 1,94 \cdot 10^{-4} \text{ s} \cdot \text{m}^{-1}$, height $L = 6 \text{ m}$, diameters by the base D from 0,12 to 0,18m, convergence ratio $n=2$. Various thicknesses g of the sheet have been considered, from 1 to 6 mm. The calculations have been performed using Eq. (32).

5. Conclusions

The formulas for the first natural frequency of bending vibrations of conical tube cantilever bars, derived from the Rayleigh method with the assumption that the axis of the bar deflected during oscillations assumes a shape of a static deflection evoked by a constant continuous load, show high concordance with the FEM solution. Full concordance between the results for a tube having the shape of cone and truncated cone has been also stated.

In the case of truncated cone, an analytical solution of integrals has been found, thus the formula for vibration period (21) is so simple that a pocket calculator is enough for calculations. For the conical tube, the formulas (18) and (34) demand to calculate the integrals in a numerical way.

The scheme of derivation of the formulas for natural frequencies for conical tubes and for hollow regular truncated pyramids is analogical. The analysis of quotients of areas and second area moments of the figures under consideration, which quotients are functions of a diameters or a side length, enables to determine correcting factors which allow to apply the formulas, derived in this paper, for the regular truncated pyramids as well.

Acknowledgments

The authors would like to express their sincere thanks to Jan Grudziński, Ph.D. Eng., for his help in the FEM calculations in the ANSYS.

References

- [1] Conway H.D., Dubil J.F. Vibration Frequencies of Truncated-Cone and Wedge Beams, *Journal of Applied Mechanics (ASME)* 32 (4), 1965, pp. 932-934.
- [2] Ece M.C., Aydogdu M., Taskin V. Vibration of variable cross-section beam, *Mechanics Research Communications (Elsevier)* 34, 2007, pp. 78-84.
- [3] Jaworski J., Szlachetka O. Drgania własne słupów w kształcie ściętego stożka (Free Vibration of Truncated-Cone Columns), *Journal of Civil Engineering, Environment and Architecture*, tom XXXI, zeszyt 61 (nr 2/2014), 2014, pp. 33-42.
- [4] Jaworski J., Szlachetka O., Aguilera-Cortés L.A. Application of Rayleigh's method to calculation of the first natural frequency of cantilever columns with variable cross-section, *to be published*.
- [5] Gliński H., Grzymkowski R., Kapusta A., Słota D. *Mathematica* 8, Wydawnictwo Pracowni Komputerowej Jacka Skalmierskiego, Gliwice, 2012.

Jacek Jaworski, Ph.D., Eng.: Warsaw University of Life Sciences – SGGW/Faculty of Civil and Environmental Engineering/Department of Civil Engineering, Nowoursynowska 166, 02-787 Warsaw, (jacek_jaworski@sggw.pl)

Olga Szlachetka, Ph.D., Eng.: Warsaw University of Life Sciences – SGGW/Faculty of Civil and Environmental Engineering/Department of Civil Engineering, Nowoursynowska 166, 02-787 Warsaw, (olga_szlachetka@sggw.pl)

The dynamics of vertical transportation systems: from deep mine operations to modern high-rise applications

(VIB240-15)

Stefan Kaczmarczyk

Abstract: High speed and high capacity lifting installations move heavy payloads and passengers from depths in excess of 3000 m to heights of nearly 1000 m. This paper discusses mathematical models to predict transient and steady-state resonant vibrations taking place in deep mine and high-rise applications. In these systems long slender continua (LSC) such as steel wire ropes and composite belts play pivotal roles as suspension means and weight-compensation members. The natural frequencies of these systems are slowly varying, rendering them non-stationary. The nonlinear dynamic interactions involve exchanges of energy between various modes of vibration. An adverse situation arises when the host structure is excited near its natural frequency and one of the slowly varying frequencies of LSC approaches the natural frequency of the structure. The models are represented by a system of nonlinear partial differential equations defined in a slowly time-variant space domain. The nature of loads acting upon the lifting systems is often nondeterministic (stochastic) so that the methods of stochastic dynamics need to be employed to predict the dynamic behaviour of the system. The results and conclusions presented in this paper demonstrate that a good understanding and prediction of the dynamic behaviour of vertical transportation systems are essential for developing vibration suppression and control strategies to minimize the effects of adverse dynamic responses so that the installation will operate without compromising the structural integrity and safety standards.

1. Introduction

The design and operation of high-performance systems for passenger transportation in the modern built environment and haulage operations in deep underground mining present many technical challenges due to adverse dynamic responses that often arise due to various sources of excitation present in these systems.

Typically, in deep-mine applications drum winding systems are deployed. The most significant sources of excitation are load due to the winding cycle acceleration/deceleration profile and a mechanism applied on the winder drum surface in order to achieve a uniform coiling pattern. In a deep-mine installation a hoist rope passes from the drum over the headsheave, forming an inclined catenary, to the conveyance forming a vertical (head) rope section. A rope storage mechanism on the drum (normally a Lebus drum liner) imparts a periodic three-dimensional excitation to the system due

to the cross-over motions of the rope on the drum. Often, this results in the catenary whirling motion ('rope whip') which is coupled with the longitudinal and lateral vibrations of the vertical rope and conveyance assembly [1,2].

In the modern high-rise built environment traction drive lift (elevator) systems are used. The underlying causes of vibration in lift systems are varied, including poorly aligned guide rail joints, eccentric pulleys and sheaves, systematic resonance in the electronic control system, and gear and motor generated vibrations [3]. Tall towers and buildings can be substantially affected by adverse environmental phenomena. These include strong wind conditions and earthquakes that cause tall buildings to vibrate (sway) at low frequencies and large amplitudes. When the host (building) structure sways a broad range of resonance phenomena occur in the lift system with large whirling motions of ropes and cables being developed that often result in damage caused by the impact against the lift equipment located in the shaft and/or against the shaft walls [4].

This paper presents an overview of mathematical models developed to predict transient and steady-state resonant vibrations taking place in deep mine and high-rise VT installations. The models are discussed and results of numerical simulation tests are shown and analysed to demonstrate their applications.

2. Vertical transportation systems dynamics

A vertical transport (VT) system may be considered as an assemblage of axially moving elastic one-dimensional long slender continua (LSC) divided into $p = 1, 2, \dots, P$ sections of *slowly* varying length [5,6], constrained by discrete elements such as rigid-body masses and rotating inertia elements. Its response can be described by a system of nonlinear partial differential equations of the following form

$$\rho_s(x_p) \mathbf{U}_{,tt}^p + \mathbf{C}^p[\mathbf{U}_{,t}^p] + \mathbf{L}^p[\mathbf{U}^p] = \mathbf{N}^p[\mathbf{U}] + \mathbf{F}^p(x_p, t, \theta_p), \quad x_p \in \{0 < x_p < L_p(\tau)\}, \quad 0 \leq t < \infty, \quad (1)$$

with the boundary conditions given as

$$\mathbf{B}_1^p(\mathbf{U}^p) = 0 \text{ at } x_p = 0, \quad \mathbf{B}_2^p(\mathbf{U}^p) = 0 \text{ at } x_p = L_p(\tau) \quad (2)$$

where x_p denotes the spatial co-ordinate, $\mathbf{U}^p(x_p, t) = [U_1^p(x_p, t), U_2^p(x_p, t), U_3^p(x_p, t)]$ is a local (component) dynamic displacement vector representing motion of the component p in the lateral and longitudinal directions, $(\cdot)_{,t}$ designates partial derivatives with respect to time t , $\tau = \varepsilon t$ represents the slow time scale, where ε is a small parameter [7], and \mathbf{C}^p and \mathbf{L}^p are local linear operators. Furthermore, \mathbf{N}^p is an operator acting upon the global displacement vector \mathbf{U} , and representing non-linear couplings and inter-component constraints in the system. \mathbf{F}^p is a forcing function with

harmonic terms of frequency $\dot{\theta}_p = \Omega_p$, where the overdot indicates total differentiation with respect to time. The local (component) mass distribution function is defined as

$$\rho_p(x_p) = m_p + \sum_{i=1}^{N_M} M_i \delta(x_p - L_p) \quad (3)$$

In the model given by Eq. 1 the Lagrangian coordinates or Eulerian coordinates may be applied as the spatial coordinate x_p . If the Lagrangian formulation is applied then it is convenient to refer the dynamic elastic deformations of LSC to a moving frame associated with the overall axial transport motion of the system. Otherwise, a fixed (inertial) frame is used to describe the deformations. In order to discretize the continuous slowly varying nonlinear system (1) the following expansion can be used

$$U_k^p(x_p, t) = \sum_{n=1}^{N_p} Y_n^k(x_p; L_p(\tau)) q_n^p(t) \quad (4)$$

where $Y_n^k(x_p; L_p(\tau))$ is the n th eigenfunction of the corresponding linear system and $q_n^p(t)$ represent the n th modal coordinate. This expansion leads to the following first-order ordinary differential equation (ODE) system given as

$$\dot{\mathbf{y}}(t) = \mathbf{A}(t, \tau) \mathbf{y}(t) + \tilde{\mathbf{N}}(\tau, \mathbf{y}) + \tilde{\mathbf{F}}(t, \tau) \quad (5)$$

where \mathbf{y} is the system state vector, \mathbf{A} is a slowly varying linear coefficient matrix, $\tilde{\mathbf{N}}$ is a vector function which represents the non-linear coupling terms, and $\tilde{\mathbf{F}}$ is the external excitation vector. This system cannot be solved exactly. An approximate solution can be sought using asymptotic (perturbation) methods and/or numerical techniques. Alternatively, in some cases, the system of partial differential equations Eq. 1 can be treated directly without discretization and perturbations methods (such as the method of multiple scales) can be applied to investigate the non-stationary behaviour of the system [8,9].

3. Deep mine environment

Figure 1 shows a typical configuration and vibration model of a drum drive hoist system used to carry payloads in deep-mine haulage operations. A LSC member, typically a steel wire cable, of mass per unit length m , modulus of elasticity E and effective cross-sectional area A passes from the drum over the sheave, forming a horizontal or inclined catenary of length L_c , to the conveyance of mass M constrained to move in a vertical shaft, forming the vertical rope of length L_v hanging below the headsheave. The end O_1 of the cable is moving with a prescribed winding velocity $V(t)$ so that the length of the cable coiled onto the drum is given as $l(t) = l(0) \pm \int_0^t V(\xi) d\xi$ where signs \pm

correspond to ascending and descending respectively, and $l(0)$ is the initial length. A cable storage mechanism on the winder drum is applied in order to facilitate a uniform coiling pattern. This system can be treated as an assemblage of two connected, continuous substructures, namely the catenary cable and of the vertical rope, with the sheave acting as a coupling member, and with the winder drum regarded as an ideal energy source. An important feature of this system is that the hoisting cable is of time-varying length. However, the rate of change is small and the length is said to vary slowly. Consequently, the dynamic characteristics of the system vary slowly during the wind, rendering the system nonstationary [1,2].

The mathematical model of the system is developed by applying two frames of reference: a moving frame attached to, and moving with the drum end of the cable, and a stationary inertial system (see the diagram shown in figure 1 [1]). The dynamic response of the system is then described by Eq. 6, in terms of the in-plane and out-of-plane displacements of the catenary cable, denoted as $\bar{v}(s,t)$ and $\bar{w}(s,t)$, respectively, measured relative to the rigid-body cross-over motions at the drum, and the longitudinal displacements $u(s,t)$ of the vertical system comprising the headsheave, vertical rope and conveyance, where s is the Lagrangian coordinate of the cable section in its undeformed configuration.

$$\begin{aligned} m\bar{v}_{tt} - \lambda_1 T_c^i \bar{v}_{sst} + \lambda_2 m\bar{v}_t - T_c^i \bar{v}_{ss} &= EAe(t)\bar{v}_{ss} - m \left[\ddot{v}_l \left(1 - \frac{s-l}{L_c}\right) + 2\dot{v}_l \frac{\dot{l}}{L_c} + v_l \frac{\ddot{l}}{L_c} \right], \\ m\bar{w}_{tt} - \lambda_1 T_c^i \bar{w}_{sst} + \lambda_2 m\bar{w}_t - T_c^i \bar{w}_{ss} &= EAe(t)\bar{w}_{ss} - m \left[\ddot{w}_l \left(1 - \frac{s-l}{L_c}\right) + 2\dot{w}_l \frac{\dot{l}}{L_c} + w_l \frac{\ddot{l}}{L_c} \right], \\ \rho u_{vtt} - \mu_1 EAu_{vss} + \mu_2 \rho u_{vt} - EAu_{vss} &= \rho \ddot{l} + \left\{ k_c [u_l(t) - f_c(t)] - M_s u_{v,sl} \dot{l} \right\} \delta(s - L_1), \end{aligned} \quad (6)$$

In Eq. 6 u_l , v_l and w_l are the boundary excitation time functions, prescribed by the geometry of two diametrically opposed cross-over zones on winder drum circumference. The parameters λ_1 and λ_2 are the coefficients of lateral damping and μ_1 and μ_2 denote the coefficients of longitudinal damping. It is assumed that the catenary cable stretches in a quasi-static manner and $e(t)$ represents the spatially uniform catenary strain. The catenary slowly varying mean tension is denoted by T_c^i , the elastic effects of the catenary on the longitudinal system are represented by the equivalent coefficient of stiffness k_c and function $f_c(l)$, respectively. The mass distribution function in the vertical substructure is given as $\rho = m + M_s \delta(s - L_1) + M \delta(s - L_0)$ where $L_1 = l + L_0$ (see figure 1), M_s denotes the headsheave effective mass, and δ is the Dirac delta function.

Figure 2 shows the slowly varying vertical (longitudinal) and lateral natural frequencies of two catenary-vertical rope systems. The first system (figure 2a) is a double-drum Blair Multi-Rope (BMR) rock winder of maximum depth of winding 2100 m, nominal winding speed 15 m/s, equipped with a

conveyance of total mass (with rated load) $M = 17,600$ kg. The second system (figure 2b) is a single-rope double-drum rock winder of maximum depth of winding 2200 m, nominal winding speed 16 m/s, equipped with a conveyance of total mass $M = 23,650$ kg.

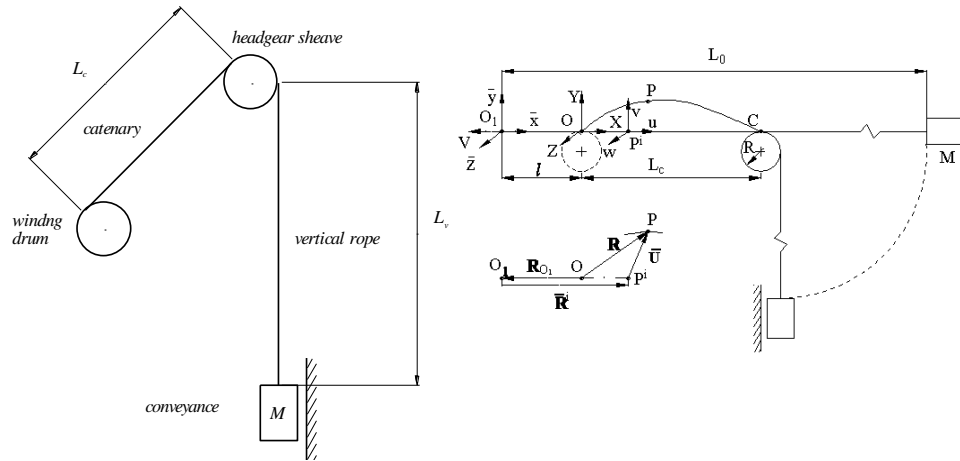


Figure 1. Drum drive hoist system and the catenary – vertical rope model [1].

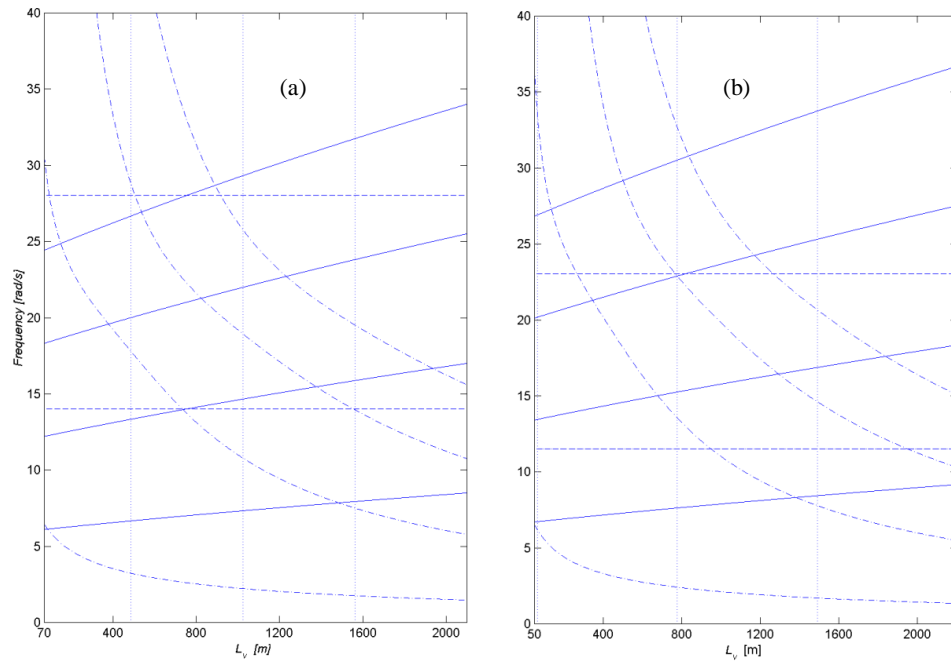


Figure 2. Slowly varying frequencies of the catenary – vertical rope systems: vertical (---) and lateral (—), (a) $V = 15$ m/s $M = 17,600$ kg; (b) $V = 16$ m/s $M = 23,650$ kg.

The first four longitudinal and four lateral natural frequencies of the system are plotted versus the vertical rope length. The horizontal dashed lines denote the first and the second harmonics of the excitation frequency corresponding to the nominal winding velocity and vertical dotted lines indicate the layer change locations. During the ascending cycle the longitudinal frequencies increase, and the lateral frequencies decrease, with the decreasing length of the rope. A number of resonance conditions may arise during the wind. They include resonance phenomena due to the non-linear interactions among different modes of vibration.

The resonance and dynamic interactions are demonstrated by the simulation response plots shown in figure 3 and figure 4, respectively. One-to-one (1:1) lateral internal resonances occur throughout the wind in both systems, since the in- and out-of-plane lateral natural frequencies are the same. It is evident that the large in-plane response is a direct consequence of this autoparametric resonance and of the energy exchange between the lateral modes, with the out-of-plane motion being a parametric excitation for the in-plane motion. One could note that the response plots in figure 3(a) and 3(b) show that the lateral response remains large beyond the 600 m length level, due to cascading energy exchanges among the modes, and consequently a full ballooning motion is developed, which persists till the end of the wind.

Furthermore, upon close examination of the frequency curves for the first system, one can notice that interesting frequency tunings occur in the region $L_v = 900\text{--}700$ m. For example, when the vertical length is about 900 m the fourth longitudinal and the second lateral natural frequencies are in the ratio 2:1, and a two-to-one internal resonance condition takes place. A primary external resonance exists simultaneously with this condition, since at this level the second harmonic of the cross-over motion at the drum directly excites the fourth longitudinal mode. Considering the frequency plots of the second system, they reveal that the second harmonic of the excitation is near the third lateral frequency at approximately $L_v \approx 800$ m. At this depth the third longitudinal frequency is tuned closely to the third lateral frequency, implicating also a one-to-one internal resonance. Also, at the beginning of the wind a passage through the fundamental longitudinal resonance takes place.

The plots shown in figure 3(c) and figure 4(c) demonstrate that the catenary lateral motions result in adverse behavior of the headsheave. However, due to damping in the system the conveyance response, illustrated by plots in figure 3(d) and figure 4(d), respectively, is largely unaffected by the dynamic behavior of the headsheave.

4. Modern built environment

In the modern high-rise built environment high-speed high-capacity traction drive lift systems are used. In these systems the lift car/ counterweight system is driven by tractive forces developed

between the traction shave and the suspension means, such as steel wire ropes (SWR) or composite LSC [3].

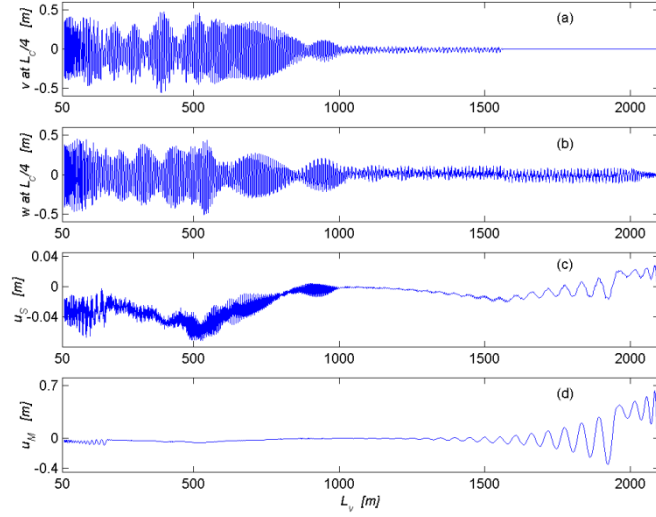


Figure 3. Displacement response $V = 15$ m/s $M = 17,600$ kg: lateral (a) in-plane and (b) out-of-plane motions at the first quarter of the catenary; longitudinal responses (c) at the headsheave and (d) at the conveyance [2].

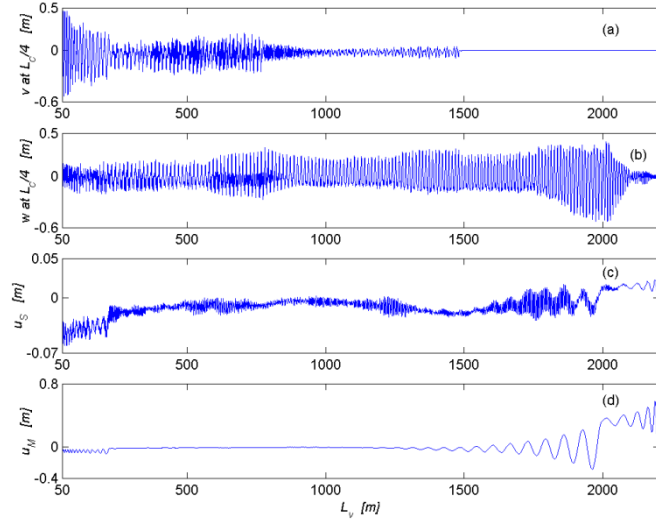


Figure 4. Displacement response $V = 16$ m/s $M = 23,650$ kg: lateral (a) in-plane and (b) out-of-plane motions at the first quarter of the catenary; longitudinal responses (c) at the headsheave and (d) at the conveyance.

SWRs or composite cables/ belts, tensioned by the weight of the compensating sheave, are then used for the compensation of tensile forces over the traction sheave. A schematic diagram of the dynamic model of the lift system is shown in figure 5. The modulus elasticity, cross-sectional metallic area and mass per unit length are denoted as E_1, A_1, m_1 and E_2, A_2, m_2 for the compensating ropes and the suspension ropes, respectively. The compensating ropes are of length L_1 at the car side and the suspension ropes are of length L_2 at the counterweight side, respectively. The length of the suspension rope at the car side and the compensating rope at the counterweight side are denoted as L_3 and L_4 , respectively. The lengths of suspension ropes and compensating cables are slowly varying $L_i = L_i(\tau)$, $i = 1, \dots, 4$ [10,11]. The masses and dynamic displacements of the car, counterweight and the compensating sheave assembly are represented by M_{car} , M_{cwt} and M_{comp} , q_{M1} , q_{M2} and q_{M3} , respectively. The acceleration/ deceleration of the car is denoted by a_{car} .

When the building structure sways at low frequency due environmental phenomena such as strong wind conditions the suspension ropes and compensating cables suffer from large dynamic displacements [4]. Due to the slow variation of their lengths the natural frequencies vary during travel, rendering the system nonstationary. An adverse situation arises when the building is excited by wind near its natural frequency and vibrates periodically. This in turn may result in a passage through external, parametric and internal resonances in the lift system [12]. The nature of loading caused by wind is usually *nondeterministic* (stochastic). The excitation is then represented by a *stochastic process* so that the methods of stochastic dynamics could be employed to predict the dynamic behaviour of the lift system. The motion of the structure can then be expressed as a narrow-band process mean-square equivalent to a harmonic process [10]. However, deterministic models yield results that that can be used to gain an understanding of the behaviour and to predict the fundamental dynamic phenomena that occur in the system.

Eqs (7) represent the mathematical model, based on the diagram in figure 5, with the excitation mechanism expressed by deterministic functions given in terms of the structure deformations due to the tower sway defined in terms of the shape function $\Psi(z/Z_0)$ [13]. Consequently the response of the system is treated as a deterministic. In this model $\bar{v}_i(x_i, t), \bar{w}_i(x_i, t)$, $i = 1, 2, \dots, 4$ represent the dynamic displacements of the ropes and cables, T_b , $i = 1, 2, \dots, 4$, denote the rope quasi-static tension terms, V is the speed of the lift, and a_i , $i = 1, 2, \dots, 4$, are the acceleration / deceleration rates of the car /counterweight. The continuous slowly varying nonlinear system (7) is discretized by using expansion (4) and the resulting ODE set of nonlinear equations is solved numerically.

$$\begin{aligned}
m_i \ddot{v}_{iit} - \left\{ T_i - m_i \left[V^2 + (g - a_i) x_i \right] + E_i A_i e_i \right\} \ddot{v}_{ixx} + m_i g \ddot{v}_{ix} + 2m_i V \ddot{v}_{ixt} &= F_i^v \left[t, L_i(\tau) \right], \quad i = 1, \dots, 4, \\
m_i \ddot{w}_{iit} - \left\{ T_i - m_i \left[V^2 + (g - a_i) x_i \right] + E_i A_i e_i \right\} \ddot{w}_{ixx} + m_i g \ddot{w}_{ix} + 2m_i V \ddot{w}_{ixt} &= F_i^w \left[t, L_i(\tau) \right], \quad i = 1, \dots, 4, \\
M_{car} \ddot{q}_{M1} - E_1 A_1 e_1 + E_2 A_2 e_3 = 0; M_{cwt} \ddot{q}_{M2} - E_1 A_1 e_4 + E_2 A_2 e_2 = 0; M_{comp} \ddot{q}_{M3} + E_1 A_1 e_1 + E_1 A_1 e_4 &= 0, \\
e_1 = \frac{1}{L_1(\tau)} \left[q_{M3}(t) - q_{M1}(t) + \frac{1}{2} \int_0^{L_1} (\bar{v}_{1x}^2 + \bar{w}_{1x}^2) dx_1 + \frac{\Psi_1^2}{2L_1(\tau)} (v_0^2 + w_0^2) \right], \\
e_2 = \frac{1}{L_2(\tau)} \left[q_{M2}(t) + \frac{1}{2} \int_0^{L_2} (\bar{v}_{2x}^2 + \bar{w}_{2x}^2) dx_2 + \frac{(\Psi_h - \Psi_2)^2}{2L_2(\tau)} (v_0^2 + w_0^2) \right], \\
e_3 = \frac{1}{L_3(\tau)} \left[q_{M1}(t) + \frac{1}{2} \int_0^{L_3} (\bar{v}_{3x}^2 + \bar{w}_{3x}^2) dx_3 + \frac{(\Psi_{car} - \Psi_{mach})^2}{2L_3(\tau)} (v_0^2 + w_0^2) \right], \\
e_4 = \frac{1}{L_4(\tau)} \left[q_{M3}(t) - q_{M2}(t) + \frac{1}{2} \int_0^{L_4} (\bar{v}_{4x}^2 + \bar{w}_{4x}^2) dx_4 + \frac{\Psi_{cwt}^2}{2L_4(\tau)} (v_0^2 + w_0^2) \right],
\end{aligned} \tag{7}$$

where $m_3 = m_2$, $m_4 = m_1$, $a_1 = a_{car}$, $a_2 = -a_1$, $a_3 = a_1$, $a_4 = a_2$ and $E_3 A_3 = E_2 A_2$, $E_4 A_4 = E_1 A_1$.

The curves presented in figure 6 (a), (b) shows the variation of the first two natural frequencies (ω_1, ω_2) of the compensating cables at the car side and counterweight side, respectively, in a lift installation servicing a 250 m tall building structure. The frequencies are plotted against the cable length, with the in-plane and out-of-plane excitation frequencies (denoted as Ω_1, Ω_2 , respectively) represented by red horizontal lines. It can be seen that in the length region of about 130 – 170 m passages through the fundamental resonance take place in the system. The displacements of the cables are shown in figures 7 and 8, respectively. The scenario is that the car travels upwards from the bottom level stopping at the highest landing level. It is evident that at the car side the displacements of the cables grow after the passage through resonance, when the cables become fully stretched. On the other hand, the cable displacements at the counterweight side decrease with the shortening length. The lateral responses of the cables are coupled with the vertical motions of the car, counterweight and the compensating sheave assembly. These motions are shown in figure 9 vs time. It is evident that due to autoparametric couplings substantial motions of the vertical masses occur.

5. Conclusions

Dynamic interactions that take place in VT systems deployed in deep-mine hoist systems and high-rise built environment result in adverse behaviour of their components compromising the structural integrity and safety of the entire installation. A VT installation is a slowly varying nonstationary dynamic system. When one of the slowly varying natural frequencies becomes near the frequency of the excitation a passage through resonance takes place.

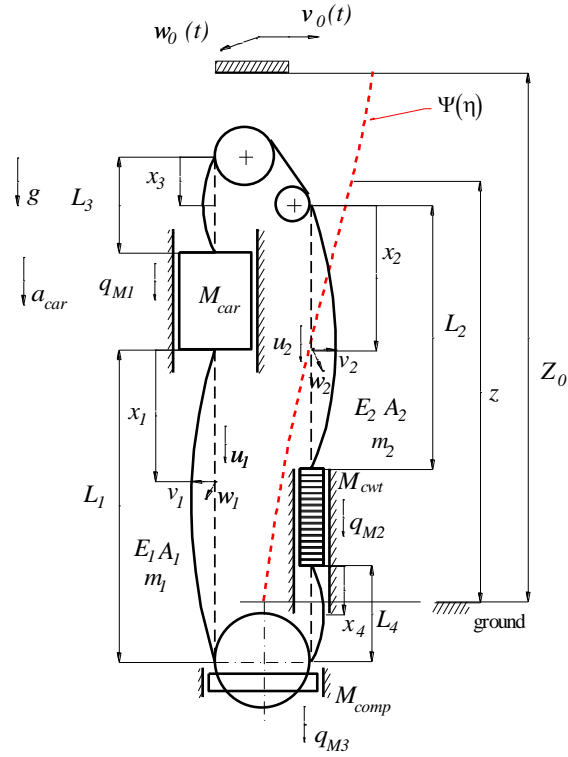


Figure 5. Dynamic model of a lift system.

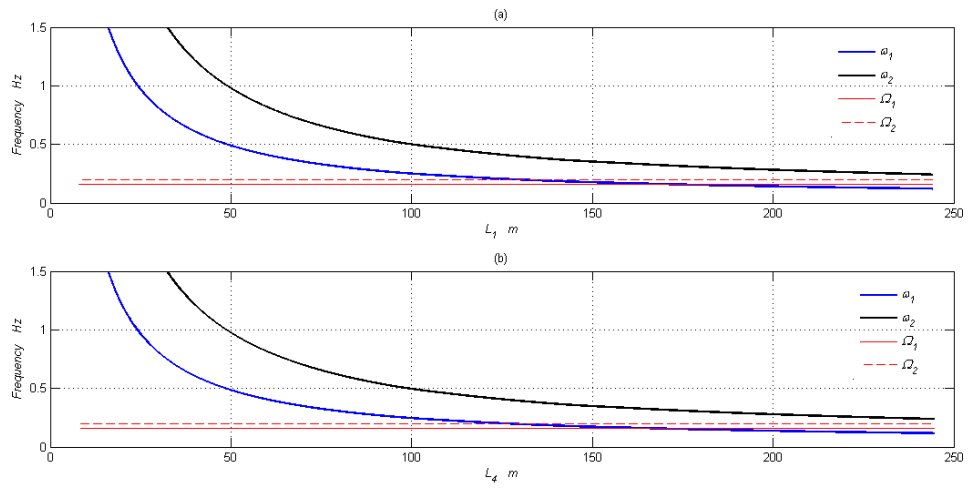


Figure 6. The lateral frequencies of the compensating ropes (a) car side, (b) counterweight side.

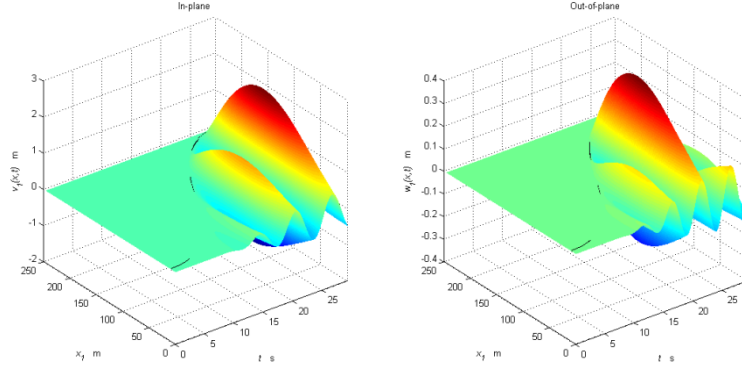


Figure 7. Displacements of the compensating ropes at the car side.

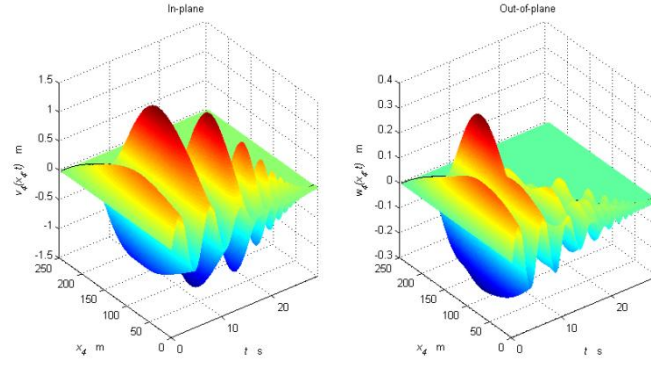


Figure 8. Displacements of the compensating ropes at the counterweight side.

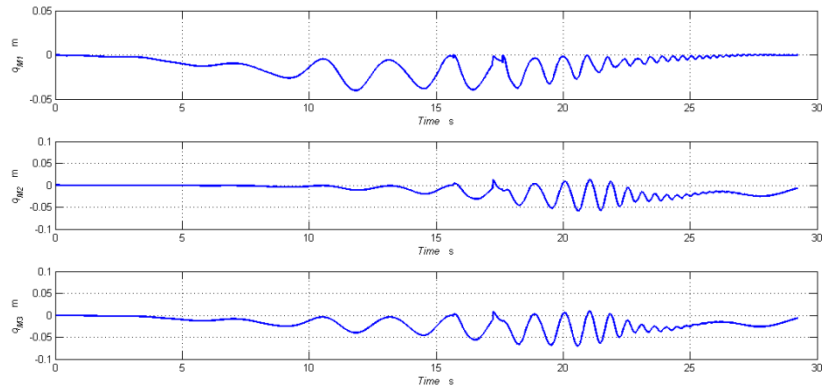


Figure 9. Displacements of the car, counterweight and compensating mass.

Vibration models and simulation techniques can be used to predict a range of dynamic interaction and resonance phenomena. Then, suitable strategies, such as the active stiffness method [14], can be developed to minimize the effects of adverse dynamic responses of the system.

References

- [1] Kaczmarczyk, S. Ostachowicz, W., Transient Vibration Phenomena in Deep Mine Hoisting Cables. Part 1: Mathematical Model. *Journal of Sound and Vibration* 262, 2 (2003), 219 - 244.
 - [2] Kaczmarczyk, S. Ostachowicz, W., Transient Vibration Phenomena in Deep Mine Hoisting Cables. Part 2: Numerical Simulation of the Dynamic Response. *Journal of Sound and Vibration* 262, 2 (2003), 245 - 289.
 - [3] Andrew, J.P. and Kaczmarczyk, S. *Systems Engineering of Elevators*. Elevator World, Inc., Mobile, Alabama (2011).
 - [4] Strakosch, G.R. *The Vertical Transportation Handbook*. John Wiley, New York (1998).
 - [5] Mitropolskii, Y.A. 1965 *Problems of the Asymptotic Theory of Nonstationary Vibrations*. Israel Program for Scientific Translations Ltd., Jerusalem (1965).
 - [6] Goroshko, O.A. and Savin, G.N. *Introduction to Mechanics of One-Dimensional Bodies with Variable Length*. Naukova Dumka, Kiev (1971).
 - [7] Kaczmarczyk, S., The Passage Through Resonance in a Catenary – Vertical Cable Hoisting System with Slowly Varying Length. *Journal of Sound and Vibration* 208, 2 (1997), 243 - 269.
 - [8] Terumichi, Y., Ohtsuka, M., Yoshizawa, M., Fukawa, Y. and Tsujioka, Y. Nonstationary Vibrations of a String with Time Varying Length and a Mass-Spring System at the Lower End. *Nonlinear Dynamics* 12 (1997), 39-55.
 - [9] Sandilo, S.H. and Van Horssen, W.T. On Variable Length Induced Vibrations of a Vertical String. *Journal of Sound and Vibration*, 333, 11 (2013), 2432-2449.
 - [10] Kaczmarczyk, S., Iwankiewicz, R. and Terumichi, Y. The dynamic behaviour of a non-stationary elevator compensating rope system under harmonic and stochastic excitations. *Journal of Physics: Conference Series* 181 (2009), 012047.
 - [11] Kaczmarczyk, S. The Nonstationary, Nonlinear Dynamic Interactions in Slender Continua Deployed in High-rise Vertical Transportation Systems in the Modern Built Environment. *Journal of Physics: Conference Series* 382 (2012), 012037.
 - [12] Salamaliki-Simpson, R., Kaczmarczyk, S., Picton, P. and Turner, S. Non-linear modal interactions in a suspension rope system with time-varying length. *Applied Mechanics and Materials* 5-6 (2006), 217-224.
 - [13] Sánchez Crespo, R., Kaczmarczyk, S., Picton, P. and Su, H. Modelling and Simulation of a high-rise elevator system to predict the dynamic interactions between its components. *Proceedings of the 4th Symposium on Lift and Escalator Technologies*, Northampton, UK, 25-26 September 2014, 175-181.
 - [14] Kaczmarczyk, S. and Picton, P.D. The Prediction of Nonlinear Responses and Active Stiffness Control of Moving Slender Continua Subjected to Dynamic Loadings in Vertical Host Structures. *The International Journal of Acoustics and Vibration* 18, 1 (2013), 39 – 44.
- Stefan Kaczmarczyk, Professor: Department of Engineering and Technology, School of Science and Technology, University of Northampton, St. George's Avenue, Northampton NN2 6JD, UK, (stefan.kaczmarczyk@northampton.ac.uk)

The author gave a presentation of this paper during one of the conference sessions.

**Nonlinear inverted pendulum model with time delay control for postural sway
in humans
(VIB241-15)**

Natalya Kizilova

Abstract A model of human body as multi link inverted pendulum with nonlinear viscoelastic springs in the joints is proposed. The control function is introduced as torque in each joint produced by synergy of groups of flexors and extensors with different time delays provided by neurological diseases or age-related degenerative changes in the neuromuscular coupling. The system of nonlinear ODEs for deflection of each segment of the pendulum from the vertical line is obtained. Its solution is found via non-linear normal modes. The influence of geometry of the pendulum, viscoelastic parameters of the springs, torques in the joints and time delay on the trajectory of the centre of mass of the pendulum is studied. The results are applied for biomechanical explanation of the differences between the postural sway in young healthy volunteers and elderly patients with spine, joint and neurological problems.

1. Introduction

Posturography is widely used in medicine for diagnostics of the locomotory system and balance control. The quantitative assessment of the ability of an individual to produce muscular torques in joints according to the balance control and nervous systems is important for prediction of sudden fall and trauma in elderly. Steady stance is supported by somatosensory, vestibular and visual information relevant for balance control. Improper changes in sensory integration determined by age-related degenerative processes, congenital impairments or diseases lead to the loss of control which might be detected by increased and asymmetric postural sway. Stabilography has gained wide-spread acceptance in rehabilitation of the patients with sclerosis, Parkinson disease, for recovery of the locomotor function and speech after the stroke, for development of the individual training regimes and sport positions of weight-lifters, figure skaters and shooters. Progressive decrease in sway amplitude is observed in the course of training of the sportsmen and the patients with balance impairments on the force platform.

The test is carried out by the force platform that measures the components of the ground reaction forces $\{\vec{R}_i\}_{i=1}^n$ produced by the front and rear parts of the left and right feet. Using the measured ground reaction forces coordinates (x_p, y_p) of the centre of pressure and the centre of mass COM of the body (x_c, y_c) can be calculated. Since the physiological mechanisms with different characteristic times are involved into the balance control, the curves $(x_c(t), y_c(t))$ exhibit quite complex behaviour [1]. The maximal amplitudes of the sway in the sagittal and frontal planes and asymmetries

of the amplitudes are used for primary medical diagnostics. The more detailed studies include tests with different two-leg postures, one-lag balancing, and tests with closed eyes, moving walls, additional support, sudden hits or acute sounds are used for diagnostics of vestibular apparatus, nervous, visual acoustical, tactile and other mechanisms of the balance control [2-8].

In the present paper the mathematical model of the human body as a complex inverted pendulum developed in [7,8] and validated by the posturographic studies [5,6] is modified accounting for nonlinear properties of the muscles and time delay in the physiological functions controlling the posture.

2. Materials and methods

The posturographic studies was carried out on a control group of young healthy volunteers (20 male, 20 female, age=24 ± 3 years, body mass 67.3±19.2 kg, height 1.72±0.2 m) without neuromuscular disorders were asked to keep a quiet vertical stance on the force platform during 30 s (fig.1a). The force platform “Statograph-67” of the laboratory of biomechanics Kharkov institute of spine and joint pathology has been used. The components of the reaction forces $\{\vec{R}_i\}_{i=1}^4$ were measured for each foot and COP trajectories $(x_c(t), y_c(t))$ were automatically computed. The second test were based on the relaxed two-leg stance with transfer of the body weight onto the right and then on the left leg (30 s each). The third test was a step forward off from the force platform on a support of the same thickness starting with left and then with right leg (fig.1b). The same set of tests was repeated after 15 min rest with standard orthopaedic holders was fastened at the knee or/and ankle joints of one of the leg or both. The holders are marked by ‘f’ in fig.1. The presence of the holders allows decrease the number of degrees of freedom (DOF) of the body. Fixation of the joint is a good opportunity to model the pathologies connected with restriction of movement in separate joints. The corresponding database of the patients with different impairments of the low extremities, joint pathology and trauma has been collected and analyzed using the same force platform [5,6].

As an illustration the time series $(x_c(t), y_c(t))$ obtained for one of the volunteers are presented in fig.2. Oscillations of the centre of mass for the normal vertical two-legged stance (fig.2a, central rectangle), for the two-legged stance when the body weight is transferred onto the right (fig.2a, right rectangle) and left leg (fig.2b, left rectangle) and for the step off from the platform (fig.2b) exhibit variations in asymmetry and sway amplitudes in different healthy individuals, but the common feature is location of the centres of the three rectangles almost at the same horizontal line. The sway amplitudes in the frontal and saggital planes were determined as the X and Y dimensions of the corresponding rectangles. Fir instance, in the case presented in fig.1a the sway amplitude in the saggital plane becomes bigger in the relaxed two-leg stays with noticeable asymmetry with bigger oscillations when

the right leg was used as the main support. The sway amplitude in the frontal plane was slightly smaller for the left and right legs, which is normal for young individuals.

Analysis of the results of the same set of tests with holds applied to the joints revealed different types of behaviour. Most volunteers with one leg locked by the holders exhibited significant asymmetry in the COM location (fig.2c). The sway amplitudes in the frontal plane were almost the same as without the holders, but in the saggital plane the sway amplitudes were either noticeable bigger (fig.2c) or smaller. The step off trajectories were asymmetrical and significantly changed when both knee and ankle joints were locked. In the case of the two legs locked the same differences were more clear (fig.3e and 3f accordingly).

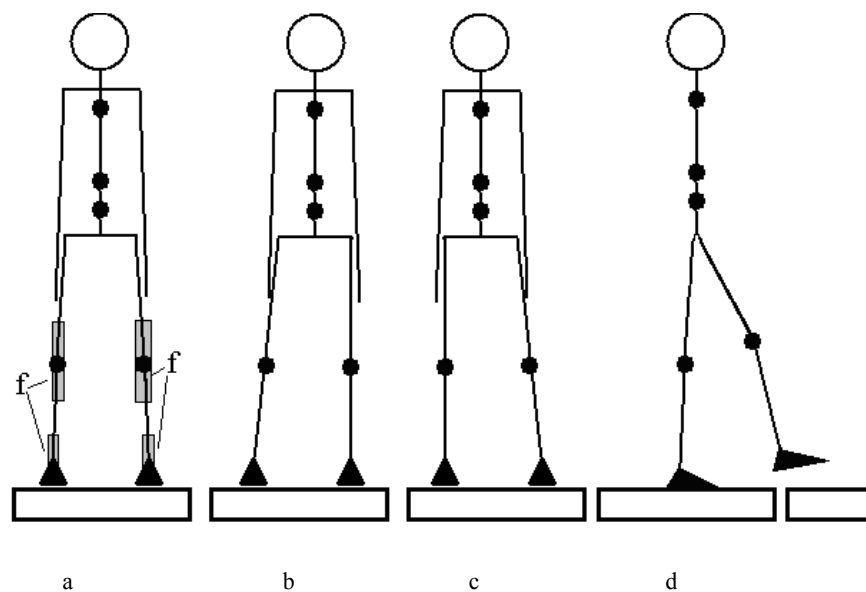


Figure 1. Position of the body during a series of tests: symmetric two-leg (a); two-leg stances with body weight shifted onto the left (b) and right (c) foot; a step forward off from the force platform on the plate of the same thickness (d)

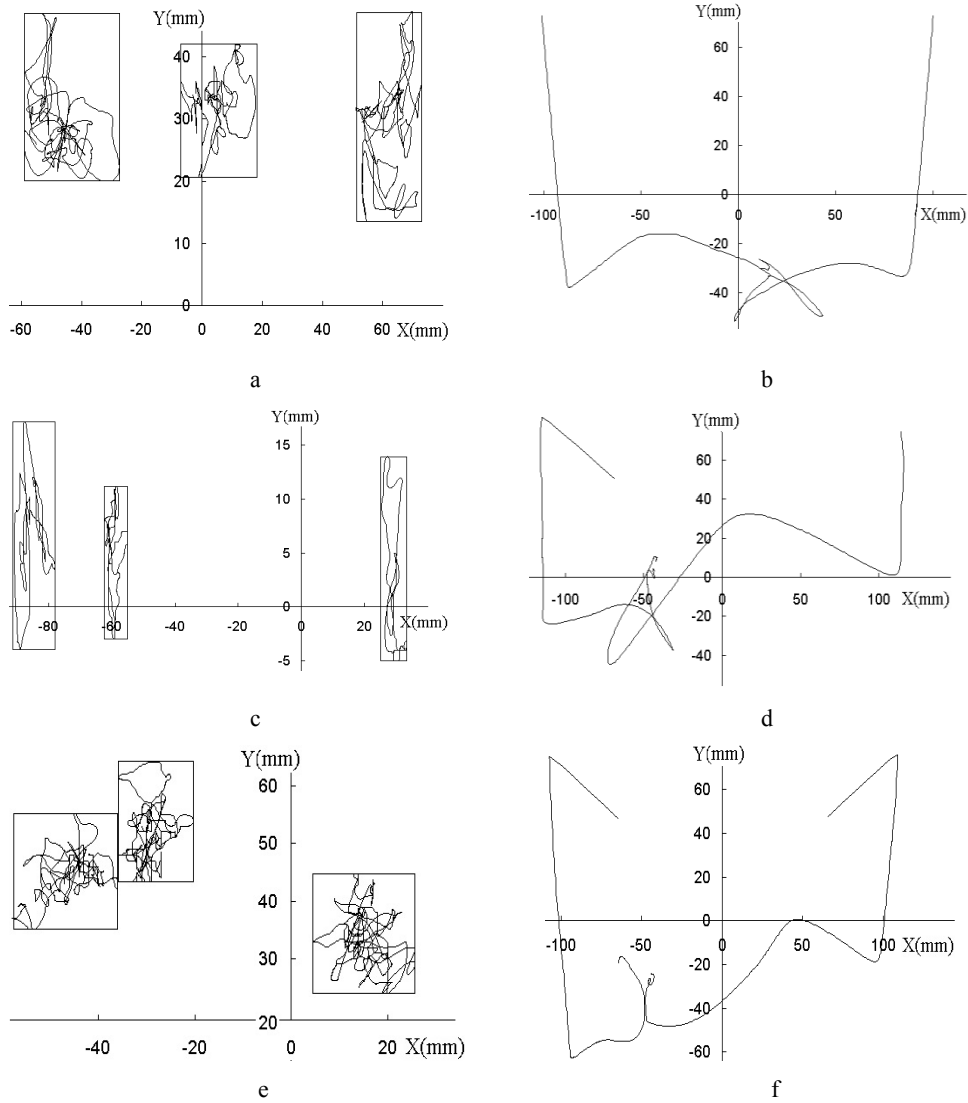


Figure 2. Trajectories of the COM of a healthy person without any holds (a,b), with the hold on the right leg (c,d) and both legs (e,f) joints at 3 two-leg stances (a,c,e) and steps off towards from the force platform (b,d,f)

3. Mathematical model of the inverted pendulum

The is considered as inverted three-link (fig.3a) and 2-link (fig.3b,c) pendulums. The lengths and masses of the segments L_{1-3} и m_{1-3} are known from the measurements on the volunteers. Position

of the centre of mass of segments C_{1-3} is determined by distances d_{1-3} from the beginning of the segment along z-axis. The upper extremities are tightly pressed against the trunk so that the trunk together with the head and extremities may be considered as a single segment with composed mass and inertia parameters. Supposing that the bearing area (feet position) is unchangeable, we describe configuration of the pendulum by angles θ_{1-3} between the segments and the vertical line (z axis). Then the motion of the pendulum is determined by Lagrange's equations of the second kind.

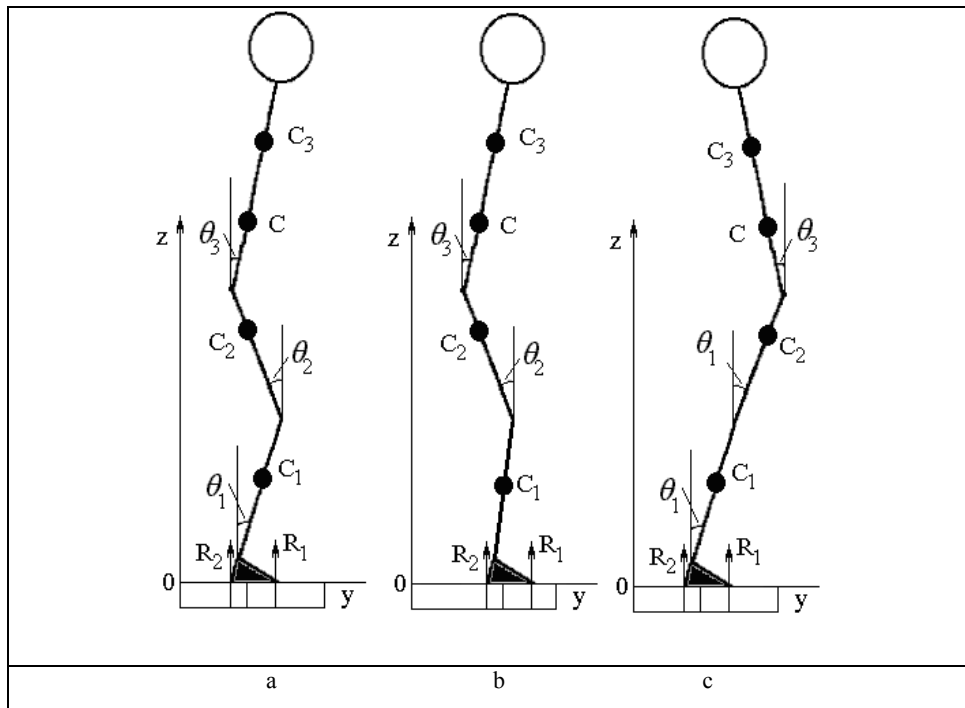


Figure 3. Model of the body sway in the saggital plane for the unlocked joints (a), the ankle (b) and the knee (c) joints with holders.

The first body segment (shank) participates in the rotational motion round the fixed point (ankle-joint). The second (thigh) and third (trunk) segments are involved into the rotational motion round their own centers of mass and transportation motion of the centers of mass caused by motion of the previous segments. For the case expressions for the corresponding energies T_j, Π_j of the separate segments can be written in the form:

$$T_1 = 0.5\dot{\theta}_1^2 (J_1 + m_1 d_1^2), \quad T_{2,3} = 0.5J_{2,3}^c \dot{\theta}_{2,3}^2 + 0.5m_1 V_{2,3}^2,$$

$$\Pi_1 = m_1 g d_1 (1 - \cos \theta_1), \quad \Pi_2 = m_1 g L_1 (1 - \cos \theta_1) + m_2 g d_2 (1 - \cos \theta_2), \quad (1)$$

$$\Pi_3 = m_1 g L_1 (1 - \cos \theta_1) + m_2 g L_2 (1 - \cos \theta_2) + m_3 g d_3 (1 - \cos \theta_3),$$

where J_j is the moment of inertia of the j -th segment, V_j is the velocity of the j -th segment relatively its of mass. The expressions for the velocities may be easily found from geometrical considerations as

$$\begin{aligned} V_2^2 &= L_1^2 \dot{\theta}_1^2 + d_2^2 \dot{\theta}_2^2 + 2L_1 d_2 \dot{\theta}_1 \dot{\theta}_2 \cos(\theta_1 - \theta_2), \\ V_3^2 &= L_1^2 \dot{\theta}_1^2 + L_2^2 \dot{\theta}_2^2 + d_3^2 \dot{\theta}_3^2 + 2L_1 L_2 \dot{\theta}_1 \dot{\theta}_2 \cos(\theta_1 - \theta_2) + \\ &+ 2L_1 d_3 \dot{\theta}_1 \dot{\theta}_3 \cos(\theta_1 - \theta_3) + 2L_2 d_3 \dot{\theta}_2 \dot{\theta}_3 \cos(\theta_2 - \theta_3). \end{aligned} \quad (2)$$

After substitution (1), (2) into Lagrange's equations of the second kind, using power expansions of the trigonometric functions in the small angles θ_i and neglecting the terms smaller than θ_i^2 , we obtain the following system of linear differential equations in the matrix form:

$$M \cdot \frac{d^2}{dt^2} \vec{\theta} + N \cdot \vec{\theta} = 0 \quad (3)$$

where $\vec{\theta}^T = (\theta_1, \theta_2, \theta_3)$, sing T denotes transposition, $M_{11} = J_1 + m_1 d_1^2 + (m_2 + m_3) L_1^2$,
 $M_{22} = J_2 + m_2 d_2^2 + m_3 L_2^2$, $M_{33} = J_3 + m_3 d_3^2$, $M_{12} = m_2 L_1 d_2 + m_3 L_1 L_2$,
 $M_{13} = M_{31} = m_3 L_1 d_3$, $M_{21} = m_2 L_1 d_2 + m_3 L_1 L_3$, $M_{23} = M_{32} = m_3 L_3 d_3$,

$$N = \begin{pmatrix} m_1 g (d_1 + 2L_2) & 0 & 0 \\ 0 & m_2 g (d_2 + L_2) & 0 \\ 0 & 0 & m_3 g d_3 \end{pmatrix}$$

Let us investigate the system (3) and determine the own frequencies of the pendulum substituting $\theta_j = \alpha_j \sin(\omega t + \psi)$ in (3), where α_j, ω, ψ are amplitude, frequency and phase of the oscillations.

Then we obtain the system of linear equations for the frequencies $\vec{\alpha}^T = (\alpha_1, \alpha_2, \alpha_3)$ in the matrix form:

$$(M \omega^2 + N) \cdot \vec{\alpha} = 0. \quad (4)$$

The solvability condition of the system (4) is $\det \left| M \boldsymbol{\omega}^2 + N \right| = 0$ which leads to a polynomial equation for computation of the own frequencies $\boldsymbol{\omega}$. Solution of the equation may be easily obtained by numerical methods when all the parameters of the model are determined.

For the locked joints (fig.3b,c) similar computations give the following results

$$\begin{aligned} T_{2,3} &= 0.5J_{2,3}^c \dot{\boldsymbol{\theta}}_{2,3}^2 + 0.5m_1 V_{2,3}^2, \\ \Pi_2 &= m_1 g (d_1 + d_1 \cos \boldsymbol{\theta}_2 - L_1 \cos \boldsymbol{\theta}_1), \\ \Pi_3 &= m_3 g (L_1 + d_3 - d_3 \cos \boldsymbol{\theta}_3 - L_1 \cos \boldsymbol{\theta}_1), \\ V_2^2 &= L_1^2 \dot{\boldsymbol{\theta}}_1^2 + d_1^2 \dot{\boldsymbol{\theta}}_2^2 + 2L_1 d_1 \cos(\boldsymbol{\theta}_1 + \boldsymbol{\theta}_2) \dot{\boldsymbol{\theta}}_1 \dot{\boldsymbol{\theta}}_2, \\ V_3^2 &= L_1^2 \dot{\boldsymbol{\theta}}_1^2 + d_3^2 \dot{\boldsymbol{\theta}}_3^2 + 2L_1 d_3 \cos(\boldsymbol{\theta}_1 - \boldsymbol{\theta}_3) \dot{\boldsymbol{\theta}}_1 \dot{\boldsymbol{\theta}}_3. \end{aligned} \quad (5)$$

Substituting expressions (5) into Lagrange's equations of the second kind, making power expansions of the trigonometric functions and neglecting the small terms of the same order of magnitude as in the previous case, we obtain the system of differential equations in the form (3) where

$$\begin{aligned} M_{11} &= J_1 + m_1 d_1^2 + (m_1 + m_3) L_1^2, \quad M_{22} = J_2 + m_1 d_1^2, \quad M_{33} = J_3 + m_3 d_3^2, \\ M_{12} &= M_{21} = m_1 L_1 d_1, \quad M_{13} = M_{31} = m_3 L_1 d_3, \quad M_{23} = M_{32} = 0, \\ N &= \begin{pmatrix} m_1 g (d_1 + L_1) + m_3 g L_1 & 0 & 0 \\ 0 & m_1 g d_1 & 0 \\ 0 & 0 & m_3 g d_3 \end{pmatrix} \end{aligned}$$

In the case it is also worth to investigate the free oscillations of the pendulum and compare the results for the one-legged and two-legged stance. Solution of the system can be obtained by the same numerical procedure.

4. Results of numerical computations and discussions

Investigation of the free oscillations of the models has been carried out by numerical methods. The lengths of the segments have been obtained during the measurements on the volunteers and mass, moments of inertia and position of the centre of mass of the segments have been calculated basing on the statistical data [1,7]. Mass and inertia of the segments are considered as an association of the separate segments basing on the of mass theorem and using the measured values of the height and weight of the body of an individual [7,8]. The same calculations have been made for the one-legged stance when the low extremities have been considered as single links consisted of two separate segments. The computational results of the own frequencies are presented in table.1. Comparison of the computed values to the measured posturography data and the data presented in literature has revealed that the calculated own frequencies $f_{1,3}$ correspond to three main oscillation ranges I-III of PSD (fig.4)

that for the averaged posturography data gives $f \in [0.2; 0.4]$ (I), $f \in [0.4; 1]$ (II), and $f \in [1; 1.4]$ (III) for sway in 0y direction, and $f \in [0.2; 0.3]$ (I), $f \in [0.3; 0.9]$ (II), and $f \in [0.9; 1.3]$ (III) for sway in direction of 0x axis. The low frequency component corresponds to mechanical oscillations and the high frequency component corresponds to the physiological tremor [1].

Numerical results for the model of the one-legged stance give the values for the own frequencies which are slightly bigger then the corresponding frequencies for the two-legged stance and relate to the same frequency ranges I-III. The computation results on variations of the own frequencies in the two-legged to the one-legged stance are in agreement with posturography data.

Table.1. Own frequencies of the human body oscillations for the two-legged stance.

N	Height (m)	Weight (kg)	f_1	f_2	f_3
1	1.82	80.75	1.51	1.88	4.95
2	1.56	52.45	1.35	1.83	4.98
3	1.72	60.95	1.38	1.83	4.98
4	1.80	61.1	1.41	1.88	5.63
5	1.69	55.7	1.35	1.91	5.57
6	1.90	84.75	1.51	1.98	6.65
7	1.74	61.5	1.41	1.89	5.65
8	1.82	82.5	1.41	1.81	4.52
9	1.56	50.5	1.34	1.82	4.82
10	1.74	68.9	1.39	1.83	4.88
11	1.83	81.2	1.42	1.86	5.33
12	1.59	54.9	1.55	1.92	5.59
13	1.62	66.5	1.28	1.89	4.92
14	1.90	79.3	1.61	1.92	5.66
15	1.59	58.7	1.65	1.94	5.47
16	1.81	83.5	1.58	1.93	6.65
17	1.73	67.5	1.49	1.88	5.75
18	1.86	81.7	1.54	1.87	4.92
19	1.64	56.5	1.45	1.85	4.94
20	1.79	62.5	1.27	1.89	4.28
Mean value	1.75	65.3	1.42	1.89	5.49

The computed data conforms with the mentioned hypothesis that any decrease in the support area in both longitudinal and transverse directions leads to an increase in instability of the posture [6]. At definite critical values of the supporting area an individual may lose the posture stability. In that case the sway amplitude increases in both sagittal and coronal planes and the low frequency rambling component changes its behaviour, namely the average “free path length” increases that leads to significant increase in maximal sway amplitude. The pattern of the trembling component is changed in a different way.

4. Conclusions

Results of the posturography study of several sorts of two-legged and one-legged stances revealed that the patterns of oscillations of the of mass and the corresponding trajectories $y_c(x)$ are different for different healthy volunteers. Since some relationships in displacement of positions of the of mass for the vertical stance and for the first step off the force platform are the same as have been obtained during the 20 year experience of measurements of posturography data for the patients in the Institute of Spine and Joints Pathology, it implies the state of the even young volunteers (students, schoolchildren) is far from the real healthy and the stealthy spine and joint chronic pathologies have been observed in many cases.

Single-meaning visual interpretation of the posturography data is usually impossible so the mathematical models and biomechanical analysis and interpretation of the data are extremely important in the field. Maximal and mean sway amplitudes may be proposed as separate diagnostic indexes for the two-legged and one-legged vertical stance. Spectral power density is an important characteristic of the own and forced sway frequencies.

Mathematical model of the human body as an inverted pendulum allows computation of the own frequencies and describes correctly the increase in frequency values when an individual transfers from the two-legged to the one-legged stance. The model can be generalized for different joint pathology and for incorporation the feedback control mechanisms.

A comparative study of the posturographic data for the two-legged and one-legged models is a promising way of medical diagnostics, because one-legged stance allows stimulation of the neuromuscular system controlling the body balance that may be significantly changed in entirely different ways at the expense of the age-related and pathological processes.

The obtained results may be useful for biomechanical explanation of the differences between the postural sway in young healthy volunteers and elderly patients with spine, joint and neurological problems.

References

- [1] Latash M.L., Zatsiorsky V.M. *Classics in Movement Sciences*. Human Kinetics, 2001.
- [2] Norr M.E., Forrez G. Posture testing (posturography) in the diagnosis of peripheral vestibular pathology. *Arch. Otorhinolaryngol.*, 243, 1986, 186-189.
- [3] Sologubov E.G., Yavorskii A.B., Kobrin V.I., Nemkova S.A., Sinel'nikova A.N. Use of Computer Stabilography and computer-assisted biomechanical examination of gait for diagnosis of posture and movement disorders in patients with various forms of infantile cerebral paralysis. *Biomed. Eng.*, 34, 2000, 138-143.
- [4] Mochizuki L., Duarte M., Amadio A.C., Zatsiorsky V.M., Latash M.L. Changes in postural sway and its fractions in conditions of postural instability different postural control mechanisms. *J.Appl.Biomech.*, 22, 2006, 51-60.
- [5] Griskevicius J., Jarmaliene E., Sesok A., Daunoraviciene K., Kizilova N. Evaluation of human postural balance in quiet standing by direct measurement of human body center of mass acceleration. *J. Vibroeng.*, 11(3), 2009. 556-561.
- [6] Kizilova N., Karpinsky M., Griskevicius J., Daunoraviciene K. Posturographic study of the human body vibrations for clinical diagnostics of the spine and joint pathology. *Mechanika*, 80(6), 2009, 37-41.
- [7] Kizilova N., Griskevicius J., Karpinsky M., Karpinskaya E. Spectral analysis and mathematical model of human postural sway in sagittal and corollary planes. In: The 10th Intern. Conf. BIOMDLORE2013. Book of abstracts, Technika, Vilnius, 2013, 56-57.
- [8] Kizilova N., Karpinsky M., Karpinska E. Quasi-regular and chaotic dynamics of postural sway in human. *Applied Non-Linear Dynamical Systems*. Jan Awrejcewicz (ed). Springer Proceedings in Mathematics & Statistics, Vol. 93, 2014, 103-114.

Natalya Kizilova, Interdisciplinary Center for Mathematical and Computational Modeling, Warsaw University, ul. Prosta 69, 00-838 Warsaw, Poland, e-mail: kizilova@icm.edu.pl

The subharmonic Melnikov method for a class of planar piecewise-smooth systems

(NON108-15)

Shuangbao Li, Xiaoli Bian

Abstract: In this paper, the well-known Melnikov method of subharmonic orbits for smooth systems is extended to a class of periodic perturbed planar hybrid piecewise-smooth systems. In this class, the switching manifold is a straight line $x = 0$ and divides the plane into two zones, the dynamics in each zone is governed by a smooth system. When a trajectory reaches the switching manifold, then a reset map describing an impacting rule applies instantaneously before entering the trajectory in the other zone. We assume that the unperturbed system is a piecewise-defined Hamiltonian system which possesses two heteroclinic orbits connecting two saddle points on each side of the switching manifold. Furthermore, we assume that the region closed by these heteroclinic orbits is fully covered by a continuum of piecewise-smooth periodic orbits, which cross the switching manifold transversally and whose periods monotonically increase as they approach the heteroclinic orbit. Then, we study the persistence of the continuum of periodic orbits under a nonautonomous periodic perturbation and the reset map. To achieve this objective, we obtain the Melnikov function of subharmonic orbits for the planar hybrid piecewise-smooth systems.

1. Introduction

In recent years, there has been considerable interest in the study of piecewise-smooth dynamical systems. Such systems are widely used in applied science such as switching circuits in power electronics [2], impact and dry frictions in mechanical engineering [8, 9], walking machines [13], relay feedback systems in control theory [7], etc. The study of bifurcations and chaotic dynamics for piecewise-smooth dynamical systems has become very active in recent decades. There is an enormous literature on this subject, in addition to the aforementioned works, see, for example, the monographs [1, 6, 17] and the references therein for more on this issues. The systematic discussion on bifurcations of fixed points and periodic solutions in nonlinear discontinuous systems has been given in [18]. A survey about dynamics and bifurcations of non-smooth systems was presented in [20]. However, there is a large disparity to understand subharmonic bifurcations, homoclinic bifurcations and chaotic dynamics for non-smooth dynamical systems.

For smooth dynamical systems, the Melnikov method is a very powerful tool to study the persistence of periodic orbits and homoclinic orbits for planar regular systems under non-autonomous periodic perturbations [15, 21, 22]. This persistence is studied by the existence of simple zeros of the subharmonic Melnikov function and the Melnikov function, respectively. In recent years, a lot of efforts have been made to extend the Melnikov method to piecewise-smooth dynamical systems, see [3–5, 10–12, 14, 16, 17, 19].

In this paper, we want to study the subharmonic orbits of a class of periodic perturbed planar hybrid piecewise-smooth systems. We assume that the switching manifold is a straight line $x = 0$ which divides the plane into two zones and the dynamics in each zone is governed by a smooth system. When a trajectory reaches the switching manifold, then a reset map describing an impacting rule applies instantaneously before entering the trajectory in the other zone. We assume that the unperturbed system is a piecewise-defined Hamiltonian system, and possesses one saddle point on either side of the switching manifold. Furthermore, we assume that two heteroclinic orbits connect both saddle points and surround a region fully covered by a continuum of piecewise-smooth periodic orbits, which transversally cross the switching manifold and whose periods monotonically increase as they approach the heteroclinic orbit. Under a non-autonomous periodic perturbation and the reset map, the persistence of the periodic orbits can be solved by obtaining the *non-smooth* subharmonic Melnikov function for the planar hybrid piecewise-smooth systems. The key technique in this paper is to choose the switching manifold $x = 0$ as a *Poincaré* section and define an appropriate *Poincaré* impact map. The results presented in the paper are original and interesting for the scientific community.

2. Statement of the problem

We divide the plane into two zones,

$$\begin{aligned} V_- &= \{(x, y) \in \mathbb{R}^2 \mid x < 0\}, \\ V_+ &= \{(x, y) \in \mathbb{R}^2 \mid x > 0\}, \end{aligned} \tag{1}$$

which are separated by the switching manifold

$$\Sigma = \hat{\Sigma}^+ \cup \hat{\Sigma}^- \cup (0, 0), \tag{2}$$

where

$$\begin{aligned} \hat{\Sigma}^+ &= \{(x, y) \in \mathbb{R}^2 \mid x = 0, y > 0\}, \\ \hat{\Sigma}^- &= \{(x, y) \in \mathbb{R}^2 \mid x = 0, y < 0\}. \end{aligned} \tag{3}$$

The normal of Σ is given by

$$\mathbf{n} = (1, 0), \text{ at any } (0, y) \in \Sigma. \tag{4}$$

We consider the planar piecewise-smooth system

$$\begin{pmatrix} \dot{x} \\ \dot{y} \end{pmatrix} = f(x, y) + \epsilon g(x, y, t) = \begin{cases} JDH_-(x, y) + \epsilon g_-(x, y, t), & (x, y) \in V_-, \\ JDH_+(x, y) + \epsilon g_+(x, y, t), & (x, y) \in V_+, \end{cases} \quad (5)$$

where $(x, y) \in \mathbb{R}^2$ and $\epsilon(0 < \epsilon \ll 1)$ is a small parameter. We also assume the Hamiltonian functions $H_\pm : \mathbb{R}^2 \rightarrow \mathbb{R}$ are C^{r+1} and satisfy $H_-(0, y) = H_+(0, y)$ for any $(0, y) \in \Sigma$, and $g_\pm : \mathbb{R}^2 \times \mathbb{R} \rightarrow \mathbb{R}^2$ are C^r with $r \geq 2$ and \hat{T} -periodic in t . We note that $D \equiv (\frac{\partial}{\partial x}, \frac{\partial}{\partial y})$ denotes the gradient operator and the matrix J is the usual symplectic matrix

$$\begin{pmatrix} 0 & 1 \\ -1 & 0 \end{pmatrix}.$$

On the switching manifold Σ , we also consider a reset map to describe an impacting rule on the switching manifold for system (5) given as follows:

$$\begin{aligned} \tilde{\eta} : \Sigma \times \mathbb{R} &\rightarrow \Sigma \\ (0, y, \epsilon) &\mapsto (0, \eta_\epsilon(y)) \end{aligned} \quad (6)$$

satisfying $y \cdot \eta_\epsilon(y) > 0$ for $y \neq 0$ and $0 < \epsilon \ll 1$, $\eta_0(y) = y \in \mathbb{R}$ and $\eta_\epsilon \in C^r(\mathbb{R})$ with $r \geq 1$. We also denote $\tilde{\eta}^{-1}(0, y, \epsilon) = (0, \eta_\epsilon^{-1}(y))$ for any $y \in \mathbb{R}$ and $0 < \epsilon \ll 1$, where $\eta_\epsilon^{-1}(y)$ is the inverse mapping of $\eta_\epsilon(y)$.

Next, we give some notations which will be used in the following analysis. $\Pi_x : \mathbb{R}^2 \rightarrow \mathbb{R}$ is a projection defined by $\Pi_x(x, y) = x$. Similarly, we define $\Pi_y(x, y) = y$. The wedge product of two vectors $\mathbf{a} = (x_1, y_1)$ and $\mathbf{b} = (x_2, y_2)$ is given by $\mathbf{a} \wedge \mathbf{b} = x_1 y_2 - x_2 y_1$.

In the aforementioned description, the switching manifold is a straight line $x = 0$ which divides the plane into two zones, and the dynamics in each zone is governed by a smooth system. We hope that if a trajectory crosses the switching manifold Σ transversally at some point $(0, y)$ at $t = t^*$, then before entering the trajectory in the other zone, the reset map (6) will be applied and the trajectory jumps from $(0, y)$ to $(0, \eta_\epsilon(y))$ instantaneously. We also assume that the trajectories are clockwise oriented without loss of generality. In order to achieve this objective, the following assumption is necessary and presented as follows:

(H1) For any $(0, y) \in \Sigma^+ \cup \Sigma^-$, $[\mathbf{n} \cdot JDH_-(0, y)] \cdot [\mathbf{n} \cdot JDH_+(0, y)] > 0$, and $[\mathbf{n} \cdot JDH_-(0, y)] \cdot y > 0$ for $y \neq 0$.

In this work, we focus on the persistence of subharmonic orbits for the system (5)-(6). It is natural to extend the classical Melnikov method of subharmonic orbits to the planar hybrid piecewise-smooth systems. Hence, we make the assumptions about the unperturbed system of system (5)-(6) as follows:

(H2) For $\epsilon = 0$, Eq.(5) has two hyperbolic equilibria $z^- \equiv (x^-, y^-) \in V_-$ and $z^+ \equiv$

$(x^+, y^+) \in V_+$ of saddle type. There exist a pair of heteroclinic orbits given by $W^u(z^-) = W^s(z^+)$ and $W^u(z^+) = W^s(z^-)$ connecting the equilibria z^- and z^+ on either side of $x = 0$ and belonging to the same energy level

$$\{(x, y) | H_-(x, y) = H_-(z^-) = H_+(x, y) = H_+(z^+) = c_1 > 0\}. \quad (7)$$

(H3) The region enclosed by the pair of heteroclinic orbits is fully filled with a continuous family of periodic orbits given by

$$\Upsilon_c = \{(x, y) | H_-(x, y) = H_+(x, y) = c > 0\} \quad (8)$$

with $0 < c < c_1$, and Υ_c intersects Σ transversally exactly twice.

(H4) The periodic T_c of Υ_c is a regular function of c with strictly positive derivative for $0 < c < c_1$.

The phase portrait of the unperturbed system (5)-(6) is topological equivalent to the one shown in Figure 1

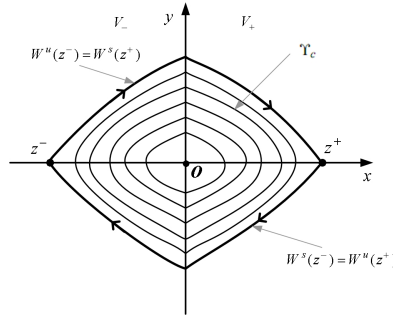


Figure 1. The phase portrait of the system (5)-(6) for $\epsilon = 0$.

We want to determine the persistence of periodic orbits. In the smooth case, the Melnikov method of subharmonic orbits [15] is a classical tool to solve this problem. Hence, it is natural to check whether the classical method is still valid for the planar hybrid piecewise-smooth systems described above and if any changes to the method are necessary.

2.1. Poincaré impact map

We let $q^-(t; t_0, x_0, y_0, \epsilon)$ be the flow associated with system (5) restricted to V_- , and $t_1 > t_0$ is the smallest value of t such that $\Pi_x(q^-(t_1; t_0, x_0, y_0, \epsilon)) = 0$. Similarly, $q^+(t; t_0, x_1, y_1, \epsilon)$ be the flow associated with system (5) restricted to V_+ , and $t_2 > t_0$ is the smallest value of t satisfying the condition $\Pi_x(q^+(t_2; t_0, x_1, y_1, \epsilon)) = 0$. Hence, one can extend the definition of a solution, $q(t; t_0, x_0, y_0, \epsilon)$, of system (5)-(6) for all $t \geq t_0$ by properly concatenating q^+ or

q^- whenever the flow crosses Σ transversally. Depending on the sign of x_0 , one applies either $q^-(t; t_0, x_0, y_0, \epsilon)$ or $q^+(t; t_0, x_0, y_0, \epsilon)$ until the trajectory reaches Σ , and then one applies (6).

In order to describe the dynamics and study the periodic motions of system (5)-(6) more clarity, we need to build the Poincaré impact map of the system (5)-(6). We first consider time as a system variable and add equation $\dot{t} = 1$ to system (5)-(6), and then we choose the sections in the extended phase-space $\mathbb{R}^2 \times \mathbb{R}$ as follows:

$$\Sigma^+ = \{(0, y, t) \in \mathbb{R}^2 \times \mathbb{R} \mid y > 0, 0 < H_+(0, y) < c_1\}, \quad (9)$$

and

$$\Sigma^- = \{(0, y, t) \in \mathbb{R}^2 \times \mathbb{R} \mid y < 0, 0 < H_+(0, y) < c_1\}. \quad (10)$$

Here we note that the first coordinate of points in Σ^+ and Σ^- is always zero, so we will omit its repetition in the following analysis without leading to confusion.

We firstly define a map

$$P_\epsilon^+ : U \subset \Sigma^+ \rightarrow \Sigma^-$$

such that for $(0, y_0, t_0) \in U \subset \Sigma^+$

$$P_\epsilon^+(y_0, t_0) = (\Pi_y(q^+(t_1; t_0, 0, y_0, \epsilon)), t_1) := (y_1, t_1) \in \Sigma^-, \quad (11)$$

where $t_1 > t_0$ is the smallest value of t satisfying the condition $\Pi_x(q^+(t_1; t_0, 0, y_0, \epsilon)) = 0$.

Based on the assumptions aforementioned, we know that a trajectory crossing Σ transversally at the point $(0, y_1)$ will jump from $(0, y_1)$ to $(0, \eta_\epsilon(y_1))$ instantaneously. Hence we can introduce the following map

$$R_\epsilon : \mathbb{R} \times \mathbb{R} \rightarrow \mathbb{R} \times \mathbb{R}$$

such that

$$R_\epsilon(y, t) = (\eta_\epsilon(y), t) \quad (12)$$

with $R_\epsilon^{-1}(y, t) = (\eta_\epsilon^{-1}(y), t)$.

Similarly, we define a map

$$P_\epsilon^- : V \subset \Sigma^- \rightarrow \Sigma^+$$

such that for $(0, y_1, t_1) \in V \subset \Sigma^-$

$$P_\epsilon^-(y_1, t_1) = (\Pi_y(q^-(t_2; t_1, 0, y_1, \epsilon)), t_2) := (y_2, t_2) \in \Sigma^+, \quad (13)$$

where $t_2 > t_1$ is the smallest value of t satisfying the condition $\Pi_x(q^-(t_2; t_1, 0, y_1, \epsilon)) = 0$.

Hence, we choose Σ^+ as the Poincaré section and define the Poincaré map as the composition (see Figure 2)

$$P_\epsilon : U \subset \Sigma^+ \rightarrow \Sigma^+$$

such that

$$P_\epsilon(y_0, t_0) = R_\epsilon \circ P_\epsilon^- \circ R_\epsilon \circ P_\epsilon^+(y_0, t_0). \quad (14)$$

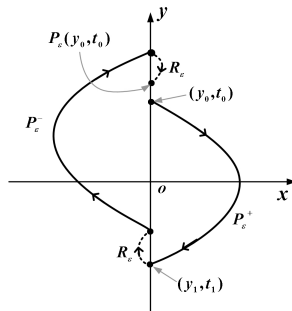


Figure 2. Poincaré impact map (14) represented schematically.

In the unperturbed case, $R_0(y, t) = (y, t)$ and the Poincaré map becomes

$$\begin{aligned} P_0(y_0, t_0) &= P_0^- \circ P_0^+(y_0, t_0) = P_0^-(\hat{y}_0, t_0 + T^+(y_0)) \\ &= (y_0, t_0 + T^+(y_0) + T^-(\hat{y}_0)) = (y_0, t_0 + T_c(y_0)). \end{aligned} \quad (15)$$

where $T^+(y_0)$ is denoted as the time that an orbit of the unperturbed system with initial condition $(0, y_0, t_0)$ spends going from point $(0, y_0)$ to point $(0, \hat{y}_0)$, and $T^-(\hat{y}_0)$ is the time that the orbit spends going from point $(0, \hat{y}_0)$ to point $(0, y_0)$. Let us denote $T_c(y_0)$ as the period of a periodic orbit with the initial condition $(0, y_0, t_0)$ such that $H_+(0, y_0) = c$ with $0 < c < c_1$, i.e.,

$$T_c(y_0) = T^+(y_0) + T^-(\hat{y}_0). \quad (16)$$

Up to now, we have defined the Poincaré impact map of system (5)-(6). We now use solutions of system (5)-(6) with initial conditions $(0, y_0, t_0) \in \Sigma^+$ to define the sequence of impacts $(0, y_\epsilon^i, t_\epsilon^i)$ (see Figure 3), if they exists, as

$$(y_\epsilon^i, t_\epsilon^i) = \begin{cases} R_\epsilon \circ P_\epsilon^+(y_\epsilon^{i-1}, t_\epsilon^{i-1}), & \text{if } y_\epsilon^{i-1} > 0 \\ R_\epsilon \circ P_\epsilon^-(y_\epsilon^{i-1}, t_\epsilon^{i-1}), & \text{if } y_\epsilon^{i-1} < 0 \end{cases}, \quad i \geq 1, \quad (17)$$

where $(y_\epsilon^0, t_\epsilon^0) = (y_0, t_0)$ and P_ϵ^\pm and R_ϵ are defined in (11)-(13), respectively.

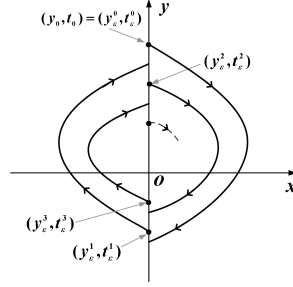


Figure 3. Sequence of impacts defined by the Poincaré for system (5)-(6).

For the unperturbed case, for any point $(0, y_0, t_0) \in \Sigma^+$, the impact sequence (17) becomes

$$(y_0^i, t_0^i) := \begin{cases} (y_0, t_0^{i-1} + T_-(\hat{y}_0)) = (y_0, t_0 + \frac{i}{2}T_c(y_0)), & \text{if } i \geq 2 \text{ even} \\ (\hat{y}_0, t_0^{i-1} + T_+(y_0)) = (\hat{y}_0, t_0 + \frac{i-1}{2}T_c(y_0) + T_+(y_0)), & \text{if } i \geq 1 \text{ odd} \end{cases}, \quad (18)$$

where \hat{y}_0 , $T_-(\hat{y}_0)$ and $T_+(y_0)$ are aforementioned.

Once the impact sequence $(y_\epsilon^i, t_\epsilon^i)$ are defined, the solution of the non-autonomous system (5)-(6) with the initial condition $(0, y_0, t_0) \in \Sigma^+$ is given as

$$q(t; t_0, 0, y_0, \epsilon) = \begin{cases} q^+(t; t_\epsilon^{2i}, 0, y_\epsilon^{2i}, \epsilon), & \text{if } t_\epsilon^{2i} \leq t < t_\epsilon^{2i+1} \\ q^-(t; t_\epsilon^{2i+1}, 0, y_\epsilon^{2i+1}, \epsilon), & \text{if } t_\epsilon^{2i+1} \leq t < t_\epsilon^{2i+2} \end{cases}, i \geq 0. \quad (19)$$

The periodic solution for the unperturbed system of (5)-(6) satisfying the initial condition $(0, y_0, t_0) \in \Sigma^+$ with $H_-(0, y_0) = H_+(0, y_0) = c$ is given as

$$q(t; t_0, 0, y_0, 0) = \begin{cases} q^+(t; t_0^{2i}, 0, y_0^{2i}, 0) := q_c^+(t), & \text{if } t_0^{2i} \leq t < t_0^{2i+1} \\ q^-(t; t_0^{2i+1}, 0, y_0^{2i+1}, 0) := q_c^-(t), & \text{if } t_0^{2i+1} \leq t < t_0^{2i+2} \end{cases}, i \geq 0. \quad (20)$$

2.2. Existence of subharmonic orbits

Next, we will employ the impact map defined in (14) to find periodic orbits. In term of this map, a point in $U \subset \Sigma^+$ will lead to a periodic orbit of period $n\hat{T}$ if it is a solution of the equation

$$P_\epsilon^m(y_0, t_0) = (y_0, t_0 + n\hat{T}) \quad (21)$$

for some m . We take m to be the smallest integer such that (21) is satisfied. In that case, $q(t; t_0, 0, y_0, \epsilon)$ will be a periodic orbit of period $n\hat{T}$, which crosses the switching manifold Σ exactly $2m$ times. This periodic orbit is called an (n, m) -periodic orbit.

In order to study the existence of periodic orbits, we use the Hamiltonian function H_+ to measure the distance between the points $(0, y_\epsilon^{2m})$ and $(0, y_0)$ for $m \geq 1$. We first give a notation which will be used below.

$$\begin{aligned}
& \int_{t_0}^{t_\epsilon^{2m}} f(q(t; t_0, 0, y_0, \epsilon)) \wedge g(q(t; t_0, 0, y_0, \epsilon), t) dt \\
&:= \sum_{i=0}^{m-1} \int_{t_\epsilon^{2i}}^{t_\epsilon^{2i+1}} JDH_+(q^+(t; t_\epsilon^{2i}, 0, y_\epsilon^{2i}, \epsilon)) \wedge g_+(q^+(t; t_\epsilon^{2i}, 0, y_\epsilon^{2i}, \epsilon), t) dt \\
&+ \sum_{i=0}^{m-1} \int_{t_\epsilon^{2i+1}}^{t_\epsilon^{2i+2}} JDH_-(q^-(t; t_\epsilon^{2i+1}, 0, y_\epsilon^{2i+1}, \epsilon)) \wedge g_-(q^-(t; t_\epsilon^{2i+1}, 0, y_\epsilon^{2i+1}, \epsilon), t) dt.
\end{aligned} \tag{22}$$

Hence we have the following lemmas.

Lemma 1. Let $m \geq 1$ and $(0, y_0, t_0) \in \Sigma^+$, and let $(0, y_\epsilon^i, t_\epsilon^i)$, $i = 0, 1, \dots, 2m$, be the associated impact sequence as defined in (17). Then,

$$\begin{aligned}
& H_+(0, y_\epsilon^{2m}) - H_+(0, y_0) \\
&= \epsilon \int_{t_0}^{t_\epsilon^{2m}} f(q(t; t_0, 0, y_0, \epsilon)) \wedge g(q(t; t_0, 0, y_0, \epsilon), t) dt \\
&+ \sum_{i=1}^m [H_+(0, y_\epsilon^{2i}) - H_-(q^-(t_\epsilon^{2i}; t_\epsilon^{2i-1}, 0, y_\epsilon^{2i-1}, \epsilon))] \\
&+ \sum_{i=0}^{m-1} [H_-(0, y_\epsilon^{2i+1}) - H_+(q^+(t_\epsilon^{2i+1}; t_\epsilon^{2i}, 0, y_\epsilon^{2i}, \epsilon))].
\end{aligned} \tag{23}$$

Lemma 2. Let $m \geq 1$ and $(0, y_0, t_0) \in \Sigma^+$, and let $(0, y_\epsilon^i, t_\epsilon^i)$, $i = 0, 1, \dots, 2m$, be the associated impact sequence as defined in (17). Then,

$$\begin{aligned}
& H_+(0, y_\epsilon^{2i}) - H_-(q^-(t_\epsilon^{2i}; t_\epsilon^{2i-1}, 0, y_\epsilon^{2i-1}, \epsilon)) \\
&= \epsilon [\Delta_{2i}^+ - \Delta_{2i}^-] + o(\epsilon), \quad (1 \leq i \leq m),
\end{aligned} \tag{24}$$

$$\begin{aligned}
& H_-(0, y_\epsilon^{2i+1}) - H_+(q^+(t_\epsilon^{2i+1}; t_\epsilon^{2i}, 0, y_\epsilon^{2i}, \epsilon)) \\
&= \epsilon [\Delta_{2i+1}^- - \Delta_{2i+1}^+] + o(\epsilon), \quad (0 \leq i \leq m-1),
\end{aligned} \tag{25}$$

where

$$\begin{aligned}
\Delta_{2i}^+ &= JDH_+(0, y_0) \wedge \frac{\partial \tilde{\eta}(0, y_0, 0)}{\partial \epsilon} \\
&+ \frac{\mathbf{n}(0, y_0) \cdot D^* \tilde{\eta}(0, y_0, 0) JDH_+(0, y_0)}{\mathbf{n}(0, y_0) \cdot JDH_-(0, y_0)} \Delta_{2i}^-, \quad (1 \leq i \leq m),
\end{aligned} \tag{26}$$

$$\begin{aligned}
\Delta_{2i+1}^- &= JDH_-(0, \hat{y}_0) \wedge \frac{\partial \tilde{\eta}(0, \hat{y}_0, 0)}{\partial \epsilon} \\
&+ \frac{\mathbf{n}(0, \hat{y}_0) \cdot D^* \tilde{\eta}(0, \hat{y}_0, 0) JDH_-(0, \hat{y}_0)}{\mathbf{n}(0, \hat{y}_0) \cdot JDH_+(0, \hat{y}_0)} \Delta_{2i+1}^+, \quad (0 \leq i \leq m-1),
\end{aligned} \tag{27}$$

$$\Delta_{2i}^- = \Delta_{2i-1}^- + \int_{(i-1)T_c(y_0)+T^+(y_0)}^{iT_c(y_0)} (JDH_- \wedge g_-)(q_c^-(t), t+t_0)dt, \quad (1 \leq i \leq m), \quad (28)$$

$$\Delta_{2i+1}^+ = \Delta_{2i}^+ + \int_{iT_c(y_0)}^{iT_c(y_0)+T^+(y_0)} (JDH_+ \wedge g_+)(q_c^+(t), t+t_0)dt, \quad (0 \leq i \leq m-1), \quad (29)$$

where $\Delta_0^+ = 0$ and $D^* \tilde{\eta}(0, y, 0)$ denote the adjoint of $D\tilde{\eta}(0, y, 0)$.

Lemma 3. Let $m \geq 1$ and $(0, y_0, t_0) \in \Sigma^+$, and let $(0, y_\epsilon^i, t_\epsilon^i)$, $i = 0, 1, \dots, 2m$, be the associated impact sequence as defined in (17). Then,

$$\begin{aligned} & H_+(0, y_\epsilon^{2m}) - H_+(0, y_0) \\ &= \epsilon \int_{t_0}^{t_0+mT_c(y_0)} f(q(t; t_0, 0, y_0, 0)) \wedge g(q(t; t_0, 0, y_0, 0), t)dt \\ & \quad + \epsilon \left[\sum_{i=1}^m (\Delta_{2i}^+ - \Delta_{2i}^-) + \sum_{i=0}^{m-1} (\Delta_{2i+1}^- - \Delta_{2i+1}^+) \right] + o(\epsilon) \\ &= \epsilon \int_0^{mT_c(y_0)} f(q(t; 0, 0, y_0, 0)) \wedge g(q(t; 0, 0, y_0, 0), t+t_0)dt \\ & \quad + \epsilon \left[\sum_{i=1}^m (\Delta_{2i}^+ - \Delta_{2i}^-) + \sum_{i=0}^{m-1} (\Delta_{2i+1}^- - \Delta_{2i+1}^+) \right] + o(\epsilon) \end{aligned} \quad (30)$$

where Δ_i^\pm , $i = 1, \dots, 2m$ can be obtained by the iterative algorithm presented in (25)-(28).

Next, we will give a simplified form of (29) in a special case.

Lemma 4. Let $m \geq 1$ and $(0, y_0, t_0) \in \Sigma^+$, and let $(0, y_\epsilon^i, t_\epsilon^i)$, $i = 0, 1, \dots, 2m$, be the associated impact sequence as defined in (17). Furthermore, we assume that

$$\frac{\mathbf{n}(0, y_0) \cdot D^* \tilde{\eta}(0, y_0, 0) JDH_+(0, y_0)}{\mathbf{n}(0, y_0) \cdot JDH_-(0, y_0)} = \frac{\mathbf{n}(0, \hat{y}_0) \cdot D^* \tilde{\eta}(0, \hat{y}_0, 0) JDH_-(0, \hat{y}_0)}{\mathbf{n}(0, \hat{y}_0) \cdot JDH_+(0, \hat{y}_0)} = 1, \quad (31)$$

then,

$$\begin{aligned} & H_+(0, y_\epsilon^{2m}) - H_+(0, y_0) \\ &= \epsilon \left\{ \int_0^{mT_c(y_0)} f(q(t; t_0, 0, y_0, 0)) \wedge g(q(t; t_0, 0, y_0, 0), t+t_0)dt \right. \\ & \quad \left. + m(JDH_+(0, y_0) \wedge \frac{\partial \tilde{\eta}(0, y_0, 0)}{\partial \epsilon} + JDH_-(0, \hat{y}_0) \wedge \frac{\partial \tilde{\eta}(0, \hat{y}_0, 0)}{\partial \epsilon}) \right\} + o(\epsilon) \end{aligned} \quad (32)$$

Theorem 1. Consider a system which is defined in (5)-(6) satisfying the assumptions (H1)-(H4), and let $T_c(y_0)$ be the function defined in (16). Assume that the point $(0, \bar{y}_0, \bar{t}_0) \in \Sigma^+$ satisfies

A.1 $T_c(\bar{y}_0) = \frac{n\bar{T}}{m}$, with $n, m \in \mathbb{Z}$ relatively prime,

A.2 $\bar{t}_0 \in [0, \hat{T}]$ is a simple zero of

$$\begin{aligned} M^{n,m}(t_0) := & \int_0^{n\hat{T}} f(q(t; 0, 0, y_0, 0)) \wedge g(q(t; 0, 0, y_0, 0), t + t_0) dt \\ & + [\sum_{i=1}^m (\Delta_{2i}^+ - \Delta_{2i}^-) + \sum_{i=0}^{m-1} (\Delta_{2i+1}^- - \Delta_{2i+1}^+)], \end{aligned} \quad (33)$$

where $q_c(t) = q(t; 0, 0, \bar{y}_0)$ is the periodic orbit such that $T_c(\bar{y}_0) = \frac{n\hat{T}}{m}$ with $c = H_-(0, \bar{y}_0) = H_+(0, \bar{y}_0)$. Then, there exists ϵ_0 such that for every $0 < \epsilon < \epsilon_0$, one can find y_0^* and t_0^* such that $q(t; t_0^*, 0, y_0^*)$ is an (n, m) - periodic orbit.

3. Conclusions

In this paper, we have obtained the Melnikov function for a class of periodic perturbed planar hybrid piecewise-smooth systems. Theorem 1 can be used to study the existence of subharmonic orbits. The Melnikov function defined in (33) has a simple form but with complicated iterative algorithm presented in (25)-(28). So if the condition in Lemma 4

$$\frac{\mathbf{n}(0, y_0) \cdot D^* \tilde{\eta}(0, y_0, 0) JDH_+(0, y_0)}{\mathbf{n}(0, y_0) \cdot JDH_-(0, y_0)} = \frac{\mathbf{n}(0, \hat{y}_0) \cdot D^* \tilde{\eta}(0, \hat{y}_0, 0) JDH_-(0, \hat{y}_0)}{\mathbf{n}(0, \hat{y}_0) \cdot JDH_+(0, \hat{y}_0)} = 1$$

satisfies, then we can obtain a simple form of the Melnikov function

$$\begin{aligned} M(y_0, t_0) := & \int_0^{mT_c(y_0)} f(q(t; t_0, 0, y_0, 0)) \wedge g(q(t; t_0, 0, y_0, 0), t + t_0) dt \\ & + m \left(JDH_+(0, y_0) \wedge \frac{\partial \tilde{\eta}(0, y_0, 0)}{\partial \epsilon} + JDH_-(0, \hat{y}_0) \wedge \frac{\partial \tilde{\eta}(0, \hat{y}_0, 0)}{\partial \epsilon} \right), \end{aligned} \quad (34)$$

which is understood easily with great advantage for calculation and engineering applications. The existence of an (n, m) - periodic orbit can also be given by using the Melnikov function (34).

Acknowledgments

The authors gratefully acknowledge the support of the National Science Foundation of China (NNSFC) through Grant No. 11472298, the Natural Science Foundation of Tianjin City through Grant No.13JCQNJC04400, the Fundamental Research Funds for the Central Universities through Grant No.3122013k005.

References

- [1] AWREJCEWICZ, J. *Smooth and nonsmooth high dimensional chaos and Melnikov-type method*. World Scientific, Singapore, 2007.
- [2] BANERJEE, S., AND VERGHESE, G. *Nonlinear Phenomena in Power Electronics: Attractors, Bifurcations, Chaos and nonlinear control*. Wiley-IEEE Press, New York, 2001.

- [3] BATTELLI, F., AND FECKAN, M. Homoclinic trajectories in discontinuous systems. *J. Dynam. Differential Equations* 20 (2008), 337–376.
- [4] BATTELLI, F., AND FECKAN, M. Bifurcation and chaos near sliding homoclinics. *J. Differ. Equations* 248 (2010), 2227–2262.
- [5] BATTELLI, F., AND FECKAN, M. Nonsmooth homoclinic orbits, melnikov functions and chaos in discontinuous systems. *Physica D* 241 (2012), 1962–1975.
- [6] BERNARDO, M. D., B. C. J. C. A. R., AND KOWALCZYK, P. *Piecewise-smooth dynamical systems: theory and application*. Springer-Verlag, London.
- [7] BERNARDO, M. D., G. L., AND VASCA, F. Bifurcations in piecewise-smooth feedback systems. *Internat. J. Control* 75 (2002), 1243–1259.
- [8] BERNARDO, M. D., K. P., AND NORDMARK, A. B. Sliding bifurcations: a novel mechanism for the sudden onset of chaos in dry friction oscillators. *Int. J. Bifur. Chaos Appl. Sci. Engrg.* 13 (2003), 2935–2948.
- [9] BROGLIATO, B. *Nonsmooth Mechanics*. Springer-Verlag, London, City, 1999.
- [10] CARMONA, V., F.-G. S. F. E., AND TORRES, F. Melnikov theory for a class of planar hybrid systems. *Physica D* 248 (2013), 44–54.
- [11] DU, Z., L.-Y., AND ZHANG, W. Bifurcation of periodic orbits in a class of filippov systems. *Nonlinear Anal.* 69 (2008), 3610–3628.
- [12] DU, Z., AND ZHANG, W. Melnikov method for homoclinic bifurcations in nonlinear impact oscillators. *Comput. Math. Appl.* 50 (2005), 445–458.
- [13] GARCIA, M., C.-A. R. A., AND COLEMAN, M. The simplest walking model: stability, complexity and scaling. *ASME J. Biomech. Eng.* 120 (1998), 281–288.
- [14] GRANADOS, A., H.-S. J., AND SEARA, T. M. The melnikov method and subharmonic orbits in a piecewise-smooth system. *SIAM J. Appl. Dyn. Syst.* 11 (2012), 801–830.
- [15] GUCKENHEIMER, J., AND HOLMES, P. *Nonlinear oscillations, dynamical system and bifurcations of vector fields*. Springer, New York, 1983.
- [16] KUKUCKA, P. Melnikov method for discontinuous planar systems. *Nonlinear Anal.* 66 (2007), 2698–2719.
- [17] KUNZE, M. *Non-smooth dynamical systems*. Springer-Verlag, Berlin, 2000.
- [18] LEINE, R. I., V. C. D. H., AND VAN DE VRANDE, B. L. Bifurcations in nonlinear discontinuous systems. *Nonlinear Dyn.* 23 (2000), 105–164.
- [19] LI, S. B., Z. W., AND HAO, Y. X. Melnikov-type method for a class of discontinuous planar systems and applications. *Int. J. Bifur. and Chaos* 24, 1450022 (2014), 1–18.

- [20] MAKARENKO, O., AND LAMB, J. S. W. Dynamics and bifurcations of nonsmooth systems: A survey. *Physica D* *241* (2012), 1826–1844.
- [21] MELNIKOV, V. K. On the stability of the center for time periodic perturbations. *Tans. Moscow Math. Soc.* *12* (1963), 1–57.
- [22] WIGGINS, S. *Global bifurcations and chaos-analytical methods*. Springer, New York, 1988.

Shuangbao Li, Ph.D.: Civil Aviation University of China/College of Science, Jinbei Road 2898, Dongli District, TianJin City, 300300, CHINA (*shuangbaoli@yeah.net*). The author gave a presentation of this paper during one of the conference sessions.

Xiaoli Bian, M.Sc.: Tianjin University of Technology and Education/School of Science, No.1310, Dagou South Road, Hexi District, Tianjin, 300222, CHINA (*bianxiaoli@yeah.net*).

Switched Reluctance Motor (SRM) mechanical faults and their identification in frequency domain

(MTR297-15)

Jakub Lorencki, Stanisław Radkowski

Abstract: In the paper the authors describe mechanical faults of SRM (rotor imbalance and dynamic eccentricity) that were carried out on the test bench as experiments. The SRM is a brushless electric motor with electronic commutation and due to its qualities it can be applied in locations where reliability is highly important. The measured signals were taken from the motor current sensor and from accelerometers from three different axes. The results of these faults are mainly scrutinized as spectra, however, time domain analysis is also possible. The concept of the research is to capture the exact fault phenomena in the spectrum and its identification and distinction between the eccentricity and load imbalance faults. Subsequently, the impact of these faults onto the overall performance and efficiency of the motor will be observed. The results can be compared to similar measurements taken from another electric motors (as BLDC) and the comprehensive comparison can be made.

1. Introduction

The world economy and environment have experienced significant degradation in recent years. Among those phenomena were global warming and greenhouse effect, depletion and price increase of fossil fuels and strong accumulation of carbon dioxide in the atmosphere[1]. These facts resulted in the idea of return to electric drive in motor vehicles since the 1990s. American and Japanese manufacturers decided to resurrect electric and hybrid electric vehicles for everyday use (e.g. General Motors EV1, Toyota Prius, Nissan Leaf, Tesla Roadster). Until now this technology is being upgraded and every year new models of electric and hybrid electric cars have their own premiere[2][11].

There are many different types of energy sources to supersede diesel oil or gasoline by alternative fuels, however the most applied ones are hybrid electric (i.e. electric motor and engine) and electric drive. For the electric drive almost every type of motor can be used, nevertheless, the most common are induction motor and brushless permanent magnet motor. The induction motor (with inverter) is applied rather for bigger vehicles (e.g. trams and trains). The permanent magnet (BLDC) motors are generally used for electric cars and minor vehicles, but certainly there are higher energy consumption applications for this motor. The BLDC motor has the great advantage of highest energy density because of strong neodymium magnets. This motor has however some drawbacks as well: high cost of magnets, its weight, peril of strong attracting metal force, possible demagnetization (e.g. by high temperature in the close vicinity to combustion engine in hybrid cars). The availability on Earth (especially outside China) of rare earth materials is also somewhat smaller than iron[3][4].

There is however another modern electric motor used for different electric drive applications for vehicles. The motor described in this study is Switched Reluctance Motor (SRM) (Fig.1). Like BLDC motor, the SRM is also brushless and electronically commutated. The difference is that it is entirely built from iron (rotor and stator). It has characteristic salient poles on stator and rotor with windings only on the stator. It has less poles on the rotor than on the stator, the typical configuration of poles ratio (stator to rotor) is 8/6 or 6/4. Because of its characteristic geometry the reluctance of the flux path from a phase winding varies with the position of the rotor.

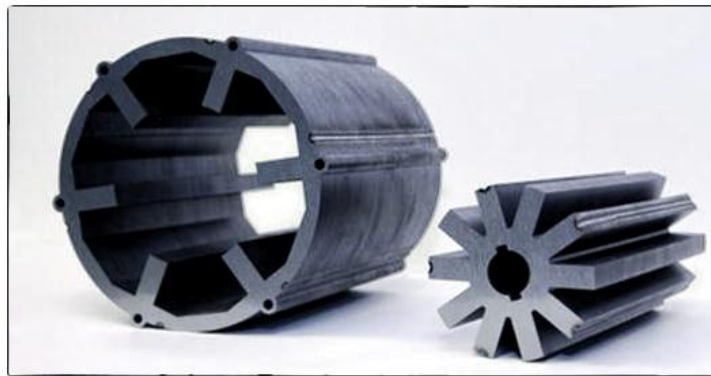


Figure 1. SRM construction [5]

From the scientific point of view it is important to find the influence of the specific faults on the motor's efficiency and on the measurement signals which will be useful for motor diagnosis. Special test bed was designed and built in order to examine the interrelation between those phenomena.

1.1. Purpose of the study

The switched reluctance motor can experience several types of faults during its operating period in the same way as another types of electric motors. There are different motor faults and they are generally divided into electrical and mechanical ones.

From the electrical faults one can distinguish the short-circuit of inter-turn phases due to deterioration of winding insulation which is a severe problem and can occur frequently. The damages of power converter, controller or encoder can certainly also exist but all of these cases are beyond the scope of this study.

The most common mechanical damages that can occur in almost all electric motors are: misalignment, imbalance, looseness, bent shaft, cocked bearing on a shaft and bearing defects[7][8].

The area of this research is the profound study of various aforementioned mechanical faults in the switched reluctance motor. The test bed designed for this study has mechanical elements that will cause these faults.

The purpose of the research is to determine which characteristics of measurement signal can be associated with specific faults. These results can be compared with the similar experiments performed on the permanent magnet motor - another DC motor with electronic commutation. The mechanical faults can have negative effects on the overall efficiency of the electrical drive. Certainly the sooner the problem is detected the better it is for the machinery because its downtime is reduced[8].

The diagnostics of this type of motors is usually made in two ways: by measuring the current signal in the motor's stator or by measurement of vibrations by means of the accelerometer. It is also possible to measure the voltage on stator phases, the speed and angle by means of the encoder and the temperature on the frame of the motor, but these methods are extremely rare and they will be omitted in the scope of this study.

2. SRM mechanical faults

As it was mentioned before the faults that can exist in electric motor generally can be divided into mechanical and electrical ones. The scope of the work are mechanical faults in switched reluctance motor which are: bearing damage, eccentricity/misalignment (static and dynamic) of the air gap, rotor and load imbalance. These are the damages that occur in any type of electric motor and can be found commonly in everyday life of the machines. Each type of electric motor fault cause detrimental symptoms that can be observed as higher vibration and thus noise, stronger torque pulsations, higher losses, unbalanced currents and voltages within the machine circuit[9][10].

2.1 Eccentricity (misalignment)

Eccentricity is a very common mechanical fault that occurs often in all of the types of electrical machines. Basically it causes the non-uniform air-gap between rotor and stator. This phenomenon can be identified in the current spectrum as fault harmonics caused by varying inductances making unbalanced magnetic flux in the air-gap. Should this problem be severe the stator can touch the rotor causing the damage of both of them. There are two types of eccentricity: the static and dynamic (Fig. 2 and 3)

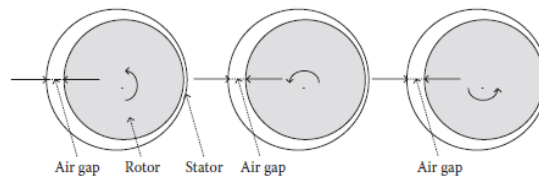


Figure 2. Static eccentricity

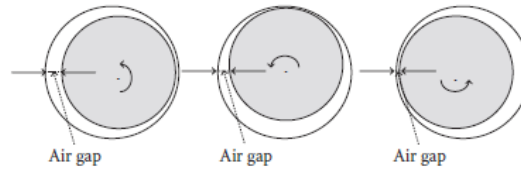


Figure 3. Dynamic eccentricity

In the static eccentricity the centerline of the shaft is at constant offset from the center of the stator, thus non-uniform air-gap is also constant. In the dynamic eccentricity the offset between the shaft's centerline and stator varies in time changing the air-gap length in time. Because of irregularity of the air-gap, magnetic flux changes values there and it results in the unbalanced currents which can be found in the current spectrum. In reality, both static and dynamic eccentricity occur simultaneously. The causes of eccentricity can be numerous as the faults of rotor construction (noncircularity, imbalance), missing or damaged elements in its construction (e.g. bolts), bad mounting or bearing damage.

The eccentricity can be easily detected in the line current spectrum because of its much higher amplitudes in comparison to the signal noise.

2.2 Imbalance

Imbalance is a very common fault. It causes almost half of the machine problems directly or indirectly. When the mass centerline and geometric centerline do not coincide then imbalance takes place. The static, dynamic and coupled imbalance can be distinguished but in real life only coupled imbalance exists with the majority of either static or dynamic imbalance.

The reason of the formation of this kind of failure is similar to the other types of faults, mostly by manufacture defects, debris on the parts of machinery or additional unbalanced shaft fittings.

Because the imbalance produces dynamic loads, the bearing experiences fatigue from excessive stresses.

3. Results

The experiments performed in this study were the dynamic eccentricity and rotor imbalance. The 1st one delivered more sophisticated results, thus is described more thoroughly.

3.1 Eccentricity

Dynamic eccentricity was performed on the test bench. It was possible to test 0.25 mm of misalignment. The other parameters chosen to the studies were load of 1 and 2 Nm and rotational speed 400, 1000 and 1500 rpm.

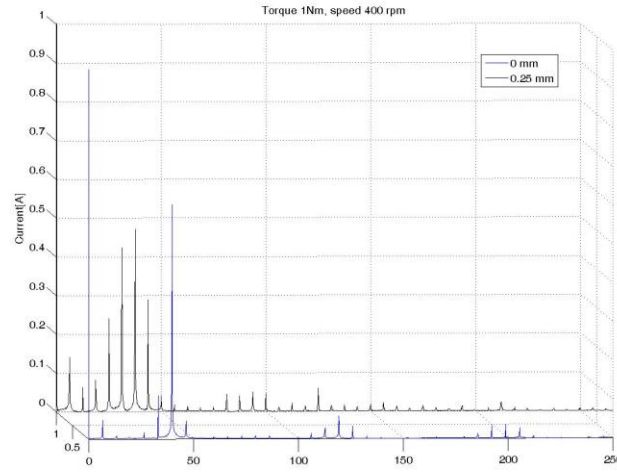


Figure 4. Comparison between the current frequency from healthy motor and with misalignment (with 1 Nm load and 400 rpm).

In fig. 4 we can observe the current in the healthy motor and motor with 0.25 eccentricity. The peculiar thing to these measurements was the highest peak of 40 Hz clearly visible in the healthy motor and the motor with eccentricity results. This is due to fact of the thing that motor has 6 rotor salient poles and the speed frequency of 6.67 Hz, thus $6.67 \times 6 = 40\text{Hz}$. Beside that this frequency is multiplied as odd harmonics, 3th (120Hz), 5th (200Hz) and 7th (280Hz). The motor with eccentricity however, can be clearly characterized with strong 4 and 5th harmonic, with 1st, 2nd and 3rd also visible to some extent. This is due to the fact that in the healthy motor there is only a function of the speed of the salient poles of the rotor. However, in the dynamic eccentricity phenomenon there is a rotor which does another form of rotation that modulates the current output with another variable.

In fig. 5 we can see the similar experiment as in previous figure but here the measurement is the vibration in X-axis. The results are significantly more vague than the data from the current. Because of test bench characteristics there are numerous frequency harmonics with nearly no trend.

In fig. 6 we can see the comparison between different loads from the motor with 0.25 eccentricity. Since the motor has load, the differences between the 1 and 2 Nm are very minor, thus increasing the load (once the motor has some) does not influence the overall output.

In figure 7 we can see the current from three different motor speeds with eccentricity. There are only minor changes. However, increasing speed of the motor has only observable impact between 400 and 1000 rpm. At higher speeds the difference becomes insignificant.

4.2 Rotor imbalance

The latter experiment executed on the test bench was simulation of rotor imbalance. This was done by applying special shield with a screw bolt in one of two holes.

What can be observed from fig. 8 applying the shield has almost none effect of imbalance due to the rigidity of the mechanical collar. The imbalance obviously did not manifest itself as strong as dynamic eccentricity.

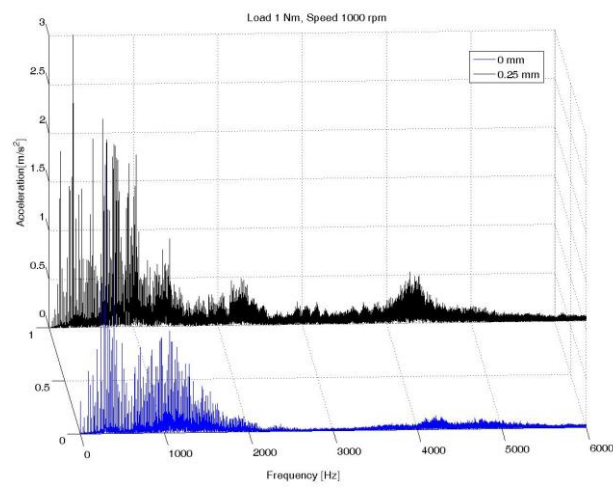


Figure 5. Comparison between the acceleration from healthy motor and with misalignment (with 1 Nm load and 1000 rpm).

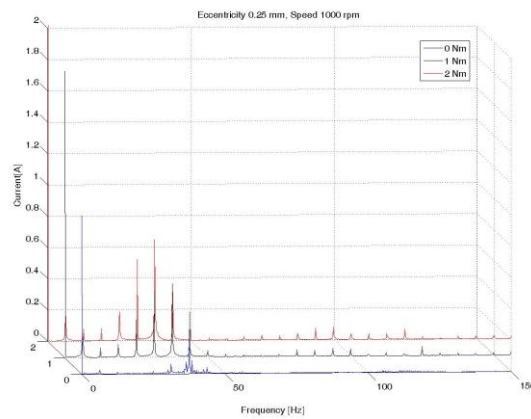


Figure 6. Comparison between the current from 3 different loads from motor with eccentricity with 1000 rpm.

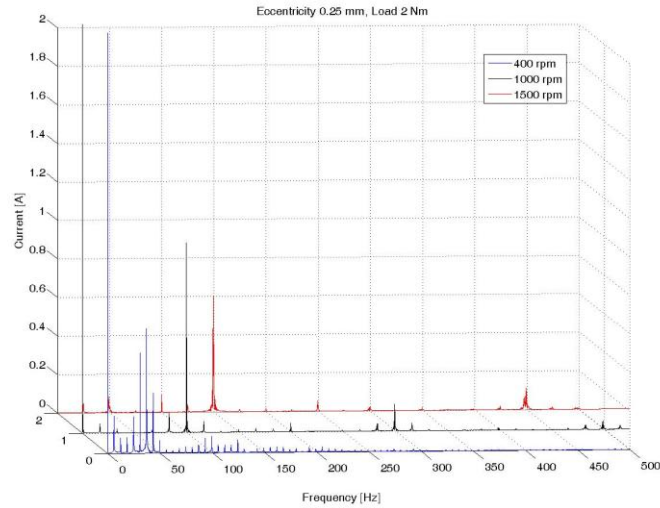


Figure 7. Comparison between the current from 3 different motor speed with eccentricity with 1000 rpm

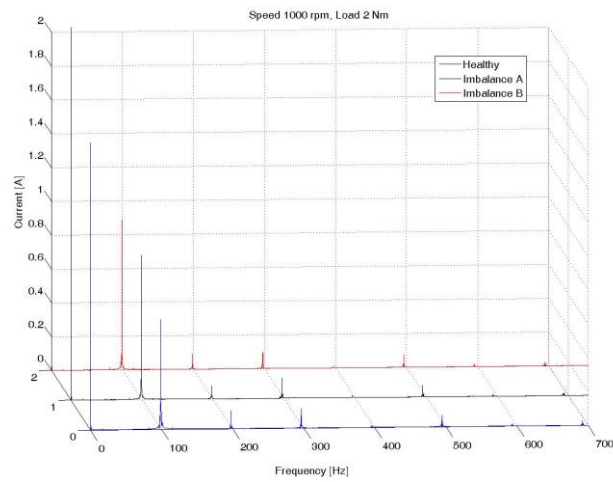


Figure 8. Comparison between the current from 3 different rotor imbalances

4. THE EXPECTED RESULTS AND DISCUSSION

Switched Reluctance Motor might be a reliable candidate for the electric drive for vehicles. It contains of numerous advantages that excel in performance. However, every electric motor has its own disadvantages, they are prone to numerous faults: electrical and mechanical what can

significantly reduce the lifetime of the machine. Fortunately, the modern methods of motor diagnostics can detect the specific fault and alert the machine operator. He can anticipate the downtime of machinery and repair or replace the motor without sudden accidents.

The results from all of the performed tests can be measured in non-invasive way in the line-current signal and by accelerometers. The idea of this research is to compare those signals especially in frequency domain. After that it is possible to determine how these faults affect the motor performance and the efficiency of all drive. Results depict that even minor mechanical faults can have significant effect on overall motor performance.

References.

- [1] Hööka M., Tang X. Depletion of fossil fuels and anthropogenic climate change: a review, Energy Policy, volume 52, January 2013
 - [2] Sperling D., Deborah G, Two billion cars: driving toward sustainability, Oxford University Press 2009
 - [3] Rarity of rare earths prompts a renaissance in motor design <http://www.dpaonthenet.net/article/57042/Rarity-of-rare-earths-prompts-a-renaissance-in-motor-design.aspx>, (Retrieved 15-09-2015)
 - [4] How Beijing Cornered the Rare Earths Market <http://www.foreignaffairs.com/articles/137602/damien-ma/china-digs-it>, (Retrieved 15-09-2015)
 - [5] http://80dr.com/wp-content/uploads/2012/11/HeVT_SRM_Rotor_Stator_Snapseed2.jpg (Retrieved 15-09-2015)
 - [6] Ehsani M., Modern Electric, Hybrid Electric, and Fuel Cell Vehicles: Fundamentals, Theory, and Design, Second Edition (Power Electronics and Applications Series) 2009
 - [7] Toliyat H. Electric Machines: Modeling, Condition Monitoring, and Fault Diagnosis 2012 CRC Press
 - [8] Vibration Diagnostic Guide - SKF Reliability Systems 2000, www.skfrelability.com (Retrieved 15-03-2015)
 - [9] Lorencki J., Radkowski S. - PROCEDURY I ANALIZA USTEREK W SILNIKACH SYNCHRONICZNYCH Z MAGNESAMI TRWAŁYMI, Zeszyty Naukowe Instytutu Pojazdów/Zeszyt 2(98)/2014)
 - [10] Lorencki J., Stanisław Radkowski - ELEKTRYCZNA DIAGNOTYKA ASYMETRII WIRNIKA W POJAZDACH HYBRYDOWYCH, Zeszyty Naukowe Instytutu Pojazdów/Zeszyt 4(95)/2013
 - [11] Jakub LORENCKI, Jerzy TOKARZEWSKI - OSIĄGI POJAZDÓW O NAPĘDZIE NIEKONWENCJONALNYM (Zeszyty Naukowe Instytutu Pojazdów/Zeszyt 5(81)/2010)
- Jakub Lorencki, M.Sc. (Ph.D. student): Warsaw University of Technology, Faculty of Vehicles and Labor Machines, Warszawa, Narbutta 84, 02-524 Poland, (j.lorencki@mechatronika.net.pl). The author gave a presentation of this paper during one of the conference sessions.
- Stanisław Radkowski, Professor: Warsaw University of Technology, Faculty of Vehicles and Labor Machines, Warszawa, Narbutta 84, 02-524 Poland, (ras@simr.pw.edu.pl).

**Parametric study on implementation of viscous dampers
for adjacent buildings
(VIB073-15)**

Elif Cagda Kandemir-Mazanoglu, Kemal Mazanoglu

Abstract: Adjacent buildings are under risk of damages during an earthquake due to structural pounding. Viscous dampers are one of the energy dissipation devices which can be implemented between two buildings to make them coupled or at the same building to reduce interstorey displacements. In this paper, a parametric study is presented by changing storey height of buildings and the parameters of the viscous dampers such as the location and capacity so that the one-sided structural pounding under severe earthquake vanishes. The buildings are considered as lumped mass model whereas the pounding force is assumed as nonlinear elastic spring at the contact point between the colliding structures. The vibration responses are obtained by central difference method. The results are compared to clarify the effective capacity and allocation of viscous dampers.

1. Introduction

The structural pounding due to severe ground motions is one of the major problems of adjacent structures with insufficient gap between them. The impact force occurred on the surfaces of colliding parts can cause serious damages on structures or even collapse of the structure. There are many cases reported in the past that the major failure of structures were due to pounding such as 1985 Mexico City earthquake and 1989 Loma Prieta earthquake [1-4]. The main reason of earthquake-induced structural pounding is different dynamic characteristics of the neighbor buildings showing out-of-phase behavior during an earthquake. To overcome this problem, there are a number of solutions applied in practice and also proposed in the related literature. The coupling of the buildings by linking with the impact preventing devices is one of them. Xu et al. introduces a parametric study about fluid viscous damper application between adjacent buildings with different number of storeys under earthquake excitation. The decrease in responses is identified as the notation for the effectiveness of dampers [5]. Bhaskararao et al. implements friction dampers to reduce seismic responses of adjacent buildings [6]. Raheem uses rubber shock absorber to prevent pounding [7]. Yang et al. performed an experimental seismic study of adjacent buildings with fluid dampers [8]. Basili et al. studied the optimal passive control of adjacent structures interconnected by Bouc-Wen model nonlinear hysteretic devices under seismic excitations of a Gaussian zero mean white noise and a filtered white noise [9]. Kim et al. analyzed the single degree-of-freedom (SDOF) systems connected by

viscoelastic dampers at their seismic joints, subjected to white noise and earthquake ground excitations in order to reduce earthquake-induced structural responses. They also performed dynamic analyses for 5-storey and 25-storey rigid frames connected to braced-frames [10].

In this paper, the 15-storey adjacent buildings with floors in alignment are analyzed through severe ground motion, 1999 Duzce earthquake ($PGA\ 0.754g$), in terms of earthquake-induced structural pounding. The closure of the gap between buildings is concluded with the impact forces between colliding surfaces. The time-domain seismic responses such as displacement time response are obtained by using numerical integration method called central difference method to avoid expensive solution procedure of other methods. The impact forces between adjacent buildings modeled as nonlinear elastic spring are analyzed at first and then a study for prevention of pounding effect is conducted by installation of viscous dampers. The optimum capacity and location of linear viscous dampers are investigated. The capacity and location of viscous dampers are optimized so that required damping ratio is added to the coupled system to vanish impact force between buildings. The command of `fmincon` in Matlab Optimization Toolbox was used for optimization of viscous damper capacity and location. The boundary and equality constraints are constituted according to the supplemental damping ratio formulation proposed by Hwang et al. [11].

2. Formulation

2.1. Viscous Dampers

Viscous dampers are velocity-dependent passive energy dissipation devices which do not possess inherent rigidity. Figure 1 shows a typical viscous damper. The kinetic energy of structure is transformed into heat energy by the viscous fluid inside leading to dissipation of energy. The damper force depends on relative velocity between damper ends as shown in Eq.1 as follows,

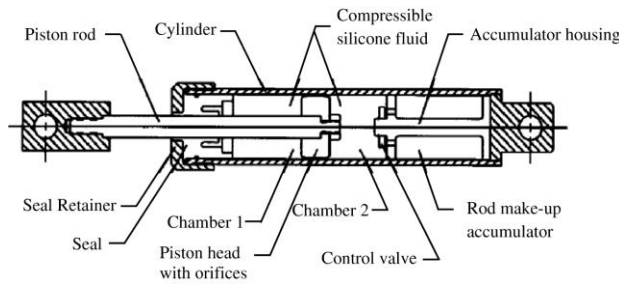


Figure 1. Schematic view of viscous damper (Symans and Constantinou, [12])

$$d = c_{d\alpha} |\dot{x}|^\alpha \operatorname{sgn}(\dot{x}) \quad (1)$$

in which $c_{d\alpha}$ is damping coefficient which depends on the dimensions of damper, α is velocity exponent and takes values between $0 \leq \alpha \leq 1$. This constant value designates the damper type as; for $\alpha = 0$ it is friction damper, for $\alpha = 1$ it is linear viscous damper and for $0 < \alpha < 1$ it is called as nonlinear viscous damper. Linear viscous damper is addressed in this paper as viscous damper without linear term. In equation of motion of a single degree-of-freedom system with viscous damper subjected to ground motion is written as follows,

$$m\ddot{x}(t) + (c + c_{d\alpha})\dot{x}(t) + kx(t) = -m\ddot{x}_g(t) \quad (2)$$

in which m is mass, k is stiffness, c is inherent damping coefficient and \ddot{x}_g is acceleration of ground motion. $x(t)$ is displacement response at time t and overdots symbolize the differentiation with respect to time. The damping ratio added to the system by viscous dampers is given by Eq.3 [11],

$$\xi_d = \frac{T_1 \sum_j c_{d1} \cos^2(\theta_j) (\phi_j - \phi_{j-1})^2}{4\pi \sum_i m_i \phi_i^2} \quad (3)$$

where T_1 is fundamental natural period, θ_j is inclination of damper, ϕ_j is 1st mode modal displacement of j^{th} floor, ϕ_{j-1} is modal displacement of $(j-1)^{th}$ floor, m_i is mass of i^{th} floor, ϕ_i is the modal displacement of i^{th} floor. i , indicates all the floors while j is the floors with the dampers added. As for the adjacent structures linked by dampers, relative modal displacement $(\phi_j - \phi_{j-1})$ should be those where the two ends of dampers are attached. For example, in the case of two adjacent buildings, formulation becomes $(\phi_{j,1} - \phi_{j-1,2})$. In addition to this, the fundamental period of the coupled system is assigned as the largest one among the first natural periods of two buildings.

2.2. Analytical Impact Model

The impact force between adjacent structures can be modeled in various analytical models such as nonlinear elastic model, linear viscoelastic model and nonlinear viscoelastic model. In this paper nonlinear elastic model, i.e. the Hertz model, has been used. This model neglects the plastic deformations during pounding and assumes that the nonlinear elastic spring become active when the gap (a) between buildings is closed. The analytical impact model of adjacent SDOF systems is given in Figure 2.

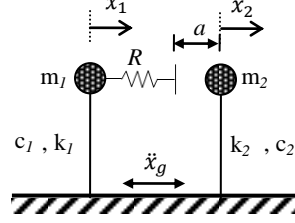


Figure 2. Analytical impact model

The equation of motion is written as in Eq. 4 including the impact force term, F_p . The force is simply calculated as restoring force of the elastic spring with an exponential expression of relative displacement value, δ . R indicates constant stiffness coefficient of the spring. It takes between $40 \text{ kN/mm}^{3/2}$ and $80 \text{ kN/mm}^{3/2}$ ($1.2 \times 10^9 - 2.6 \times 10^9 \text{ N/m}^{3/2}$) according to experimental analyses on concrete surfaces done by Van Mier et al. [13].

$$M\ddot{X} + C\dot{X} + KX + F_p = -M\ddot{X}_g \quad (4)$$

$$p(t) = \begin{cases} R\delta(t)^{3/2} & , \delta(t) \geq 0 \\ 0 & , \delta(t) < 0 \end{cases} \quad (5)$$

$$\delta(t) = x_1(t) - x_2(t) - a \quad (6)$$

M is mass matrix, K is stiffness matrix and C is damping matrix of the coupled structural system. In next section, the constitution of matrices is described in detail.

2.3. Construction of structural matrices

Building 1 and 2 are $(m+n)$ -storey and (n) -storey adjacent buildings, respectively, and connected by viscous dampers at each floor level. Structural properties are given in Figure 1. To conduct time response analysis, the matrices should be constituted. The supplemental damper coefficient matrix in addition to coupled mass, stiffness and inherent damping coefficient matrices are constructed as follows;

$$M_{(m+n, m+n)} = \begin{bmatrix} [M_1] & [0_1] \\ (m, m) & (m, n) \\ [0_2] & [M_2] \\ (n, m) & (n, n) \end{bmatrix} \quad K_{(m+n, m+n)} = \begin{bmatrix} [K_1] & [0_1] \\ (m, m) & (m, n) \\ [0_2] & [K_2] \\ (n, m) & (n, n) \end{bmatrix} \quad (7.1)$$

$$C_{(m+n, m+n)} = \begin{bmatrix} [C_1] & [0_1] \\ (m, m) & (m, n) \\ [0_2] & [C_2] \\ (n, m) & (n, n) \end{bmatrix} \quad Cd_{(m+n, m+n)} = \begin{bmatrix} [A] & [0] & [-A] \\ (n, n) & (n, m-n) & (n, n) \\ [0] & [0] & [0] \\ (m-n, n) & (m-n, m-n) & (m-n, n) \\ [A] & [0] & [-A] \\ (n, n) & (n, m-n) & (n, n) \end{bmatrix} \quad (7.2)$$

In these equations M_1 and M_2 mention the mass matrices of building 1 and building 2, respectively. K_1 and K_2 indicate the stiffness matrices. The damping matrices for inherent damping C_1 and C_2 are coupled in C matrix. The damping matrix provided by viscous dampers can be written in a separate matrix, C_d . In this matrix, $[A] = \text{diag}(cd)$ and $[-A] = \text{diag}(-cd)$ in which c_d is supplemental damper coefficient vector, i.e. $c_d = \{c_{d1} c_{d2} \dots c_{dn}\}$, n is number of storey of building 2. The time response analysis was carried out on Eq.2 with the term of the impact force in Eq.5.

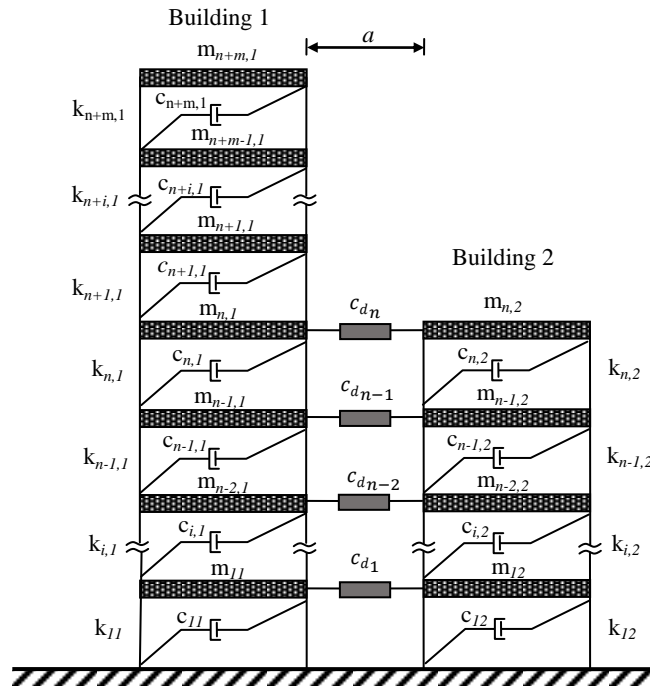


Figure 3. Building models

2.4. Optimization of Viscous Damper Capacity and Location

The important task of installation of viscous dampers is to determine the capacity and location of viscous dampers which can prevent structural pounding. The optimization parameters were arranged to be compatible with the command of “fmincon” in the optimization toolbox in Matlab. In the optimization algorithm the objective function is,

$$\text{Min } f = \sum_{i=1}^n c_{di} \quad (8)$$

where f is the function that minimizes the total damper capacity. i is the floor number. Also the lower and upper bounds should be identified as $lb \leq c_{di} \leq ub$ in which lb , lower bound, is assigned zero to

represent the case of no damper attached between the floors. ub , upper bound, can take various values. Equality constraint is constructed based upon supplemental damping ratio equation (Eq.3) without damper coefficient term;

$$A_{eq(i)} = \frac{T_i}{4\pi \sum_{l=1}^n m_l \phi_i^2} (\phi_i - \phi_{i-1})^2 \quad (9)$$

$$\{A_{eq}\} \times \{c_d\} = \zeta_d \quad (10)$$

$\{A_{eq}\}$ is a vector including n terms in a row whereas $\{c_d\}$ has also n terms in a column. Their multiplication should give ζ_d that is increased gradually in every step of minimization.

In the location optimization, considering the maximum impact forces occurs at the top floor (top floor of the shorter building among adjacent buildings), the dampers should be located starting from top floors. In this sense, the damper coefficients, c_d , put in order from largest to lowest value and located in the correct places in the matrix of $[A]$.

3. Results and discussion

In this paper to carry out analyses, some assumptions have been done. The buildings analyzed are assumed as symmetric in plan. The floors are in alignment and equal in height. The impact forces are assumed to occur on the floor levels. The mass, stiffness and inherent damping coefficient are equally distributed among floors. The buildings are linear multi-degree-of-freedom systems including lumped masses at each floor and stiffness of columns. The plastic deformations during pounding are neglected. Linear dynamic analysis is conducted. Building 1 and 2 are 15-storey buildings. In following sections, however, the number of storey of building 2 is changed in order to observe the effect of different natural periods on the impact force, supplemental damper capacity and location. The damping ratio is taken as $\xi = 0.05$ for both buildings and the gap is assigned as $a = 0.03m$. The spring constant in Hertz model for pounding force is assumed as $80 \text{ kN/mm}^{3/2}$.

3.1. Natural period variation on impact force and supplemental damping ratio

Different vibration characteristics of closely located adjacent buildings result in out-of-phase behavior due to strong ground motions which is the main reason of earthquake-induced structural pounding. The impact force occurs when the gap between the buildings is closed. In this section two cases are investigated in order to observe the effect of natural frequency differences on the impact force. Firstly, natural frequencies obtained by only changing the number of stories of building 2 are analyzed as Case 1. Mass and stiffness values are taken as $m_1 = m_2 = 1 \times 10^5 \text{ kg}$ and $k_1 = k_2 = 6.8 \times 10^7 \text{ N/m}$, respectively. In Case 2, the stiffness of building 2 is altered to $k_2 = 10 \times 10^8 \text{ N/m}$ and the analyses were done again for the various number of storeys. The results were desired to be

given in a comparative scale for two cases. To do so, instead of natural frequency ratio (ω_1/ω_2) which depends on the characteristics of each building, nondimensional frequency parameter (Ω) is defined as follows;

$$\Omega = \omega s^2 \sqrt{\frac{m}{k}} \quad (11)$$

in which ω is natural frequency of building, s is storey number, m and k are mass and stiffness coefficient for one floor. Results are presented by the nondimensional natural frequency ratio, $\Omega_r = \Omega_1/\Omega_2$. Indices 1 and 2 denote two buildings in consideration herein. The decrease in Ω_r indicates that the number of storey of building 2 is reduced. In this sense, $\Omega_r = 1$ indicates that the number of storeys of building 1 and building 2 are equal.

Figure 4(a) shows the maximum impact force variation in accordance with the nondimensional frequency parameter ratio, Ω_r when there is no viscous damper attached to the system, $\xi_d = 0$. Markers on lines can be identified as the floor numbers, i.e. $\Omega_r = 1$ indicates activity at 15th floors of buildings. The floors in which maximum impact force observed are the top floor of building 2 and the same level of building 1. As seen from the figure, the impact force gets maximum value when the buildings are collided at 12th floors in case 1. Equal number of storey of adjacent buildings in case 1 oscillates in-phase which results in no impact force. In case 2, even if the buildings have the same number of storey, the out-of-phase behavior is observed as expected. The maximum impact force occurs at the 13th floors in case 2.

Figure 4(b) demonstrates the necessary supplemental damping ratio added by viscous damper for each nondimensional frequency parameter ratio. Viscous dampers between adjacent buildings reduce the displacement responses of coupled structure by means of increasing total damping ratio. This graph clarifies the required supplemental damping ratio to vanish the earthquake-induced pounding. With this knowledge in hand, the total viscous damper capacity can be found easily by Eq.3. As seen from the figure, for case 1, the largest supplemental damping ratio is needed when the pounding occurs at 10th and 11th floors. For case 2, the maximum impact force occurs at 13th floor also. Figure 4(b) is the reference graph to obtain damper coefficients that shows required supplemental damping ratios which makes the impact force zero. There are various options to put damper between floors as long as the supplemental damping ratio is provided. However, for each option, the damper coefficients are varied. For example, the impact force occurs at 10th floor when the building 2 has 10 storeys. In this case the supplemental damping ratio is 40% to prevent structural pounding. The damper can be implemented to all adjacent floors with the capacity of $1.58 \times 10^5 \text{Ns/m}$ and the total damper capacity becomes $1.58 \times 10^6 \text{Ns/m}$. In another option, the dampers can be installed only to the top floor with the capacity of $7.72 \times 10^5 \text{Ns/m}$. Adding dampers to all floors gives smaller

capacities for each damper however larger total damper capacity. In addition to this, adding only one damper in larger capacity to effective location prevents pounding as well. In the optimization algorithm, the relation between upper bound of damper capacity, total damper capacity and the number of dampers can be stated as: an increase in the upper bound decreases total damper capacity together with the number of dampers and vice versa. The decision about the amount of damper capacity and number should be given by the designer and the manufacturer together in the aspect of economical conditions.

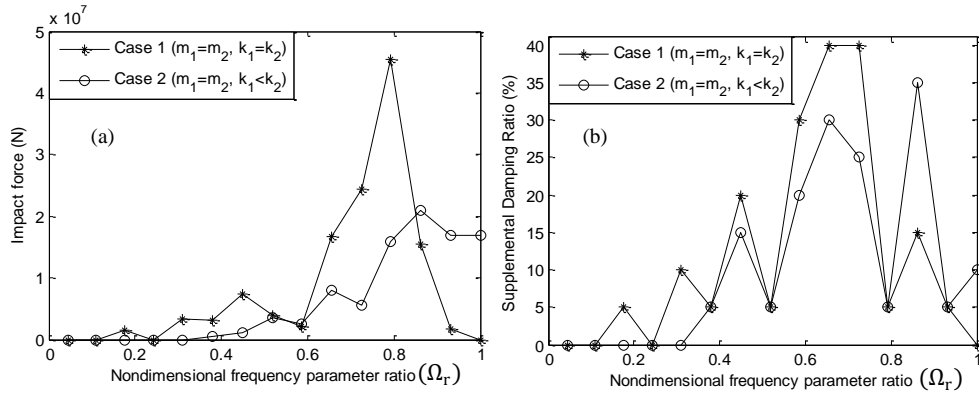


Figure 4. (a) Relation between impact force and Ω_r for $\xi_d = 0$ (b) Relation between supplemental damping ratio and Ω_r for $F_p = 0$

3.2. Installation of viscous dampers

Installation of viscous dampers as a linking element between adjacent structures has advantage in terms of reducing seismic responses of both structures. Figure 5 shows the effect of viscous dampers on the seismic behavior of adjacent structures in terms of reduced displacement responses. Building 2 locates at 0.03m-distance from Building 1. There is no pounding observed when the capacity of viscous damper is $7.72 \times 10^5 \text{Ns/m}$ installed at only 10th floor or each adjacent floors with the capacity of $1.58 \times 10^5 \text{Ns/m}$. This figure also verifies no pounding case since the displacement responses do not intersect with each other. It can be observed that in addition to reduced displacement responses of both buildings, they start to vibrate together after linked by dampers. For case 2, the results are similar with case 1 with different damper capacities. Table 1 tabulates the damper capacities and the locations for different upper bounds of damper capacity for case 1. It is clear that reduction in upper bound gives smaller capacity for each damper; however, placing them to more adjacent floor gives larger total damper capacity. It should be noted that each option providing same supplemental damping ratio results in very close displacement responses. The results observed in case

2, that will not be given inhere, gives smaller damper capacities since the building 2 is stiffer than building 1.

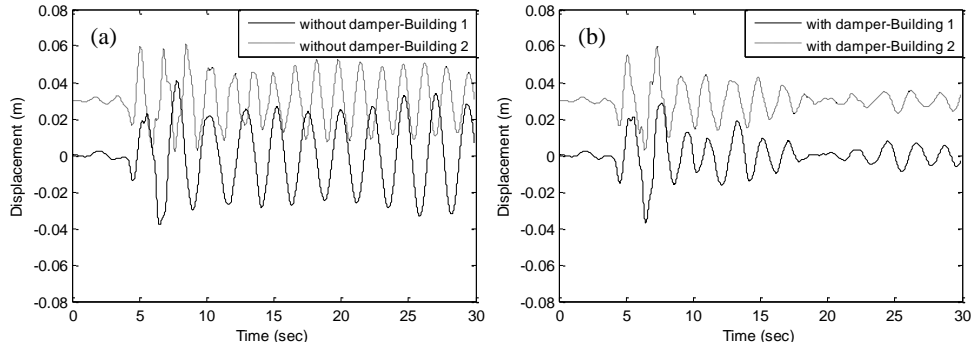


Figure 5. Case 1 - Displacement time responses of building 1 and 2 (a) before (b) after installation of viscous dampers between adjacent 10th floors ($\xi_d = 0.40$, $c_{d10} = 7.72 \times 10^5 \text{Ns/m}$)

Table 1. Damper capacity and locations for different upper bound values of damper capacities

Adjacent floor no.	Upper bound for damper capacity (ub) ($\times 10^5 \text{Ns/m}$)							
	8.00		5.00		2.00		1.00	
	15 & 11 storey	15 & 10 storey	15 & 11 storey	15 & 10 storey	15 & 11 storey	15 & 10 storey	15 & 11 storey	15 & 10 storey
11	7.75	-	5	-	2	-	1.44	-
10	-	7.72	2.95	5	2	2	1.44	1.58
9	-	-	-	2.95	2	2	1.44	1.58
8	-	-	-	-	2	2	1.44	1.58
7	-	-	-	-	1.23	2	1.44	1.58
6	-	-	-	-	-	1.63	1.44	1.58
5	-	-	-	-	-	-	1.44	1.58
4	-	-	-	-	-	-	1.44	1.58
3	-	-	-	-	-	-	1.44	1.58
2	-	-	-	-	-	-	1.44	1.58
1	-	-	-	-	-	-	1.44	1.58
Σ	7.75	7.72	7.95	7.96	9.23	9.63	15.8	15.8

4. Conclusion

The optimization procedure for the damper capacity and location is explained in this paper for adjacent buildings. The estimation of supplemental damping ratio is essential task to control the displacement responses. In the optimization algorithm, the relation between upper bound of damper capacity, total damper capacity and the number of dampers is presented. The upper bound decreases total damper capacity together with the number of dampers and vice versa. For two adjacent buildings which have same mass and stiffness coefficient of each floor, the seismic responses are in-phase in the case of equal number of storeys. On the other hand decreasing floor number and/or changing the structural properties have a trend of increase in impact force until a peak value and then decrease to

zero when no impact force occurs. This means that the structures are in-phase until some threshold of natural frequency ratio. After exceeding this threshold, the out-of-phase behavior starts and continues. The similar trend can be observed in required supplemental damping ratio as well. The threshold values can be investigated in further studies. This paper contributes to related literature in terms of effective solutions for structural pounding problem.

References

- [1] Moustafa A. and Mahmoud S. Damage assessment of adjacent buildings under earthquake loads. *Engineering Structures*, 61 (2014), 153-165.
 - [2] Naserkhaki S., Abdul Aziz F.N.A. and Pourmohammad H. Earthquake induced pounding between adjacent buildings considering soil-structure interaction. *Earthquake Engineering and Engineering Vibration* 11, 3 (2012), 343-358.
 - [3] Rosenblueth E. and Meli R. The 1985 Earthquake: Causes and Effects in Mexico City, *Concrete International*, ACI 8, 5 (1986), 23-36.
 - [4] Kasai K. and Maison B.F. Building Pounding Damage during the 1989 Loma Prieta Earthquake, *Engineering Structures* 19, 3 (1997), 195-207.
 - [5] Xu Y.L., He Q. and Ko J.M. Dynamic response of damper-connected adjacent buildings under earthquake excitation, *Engineering Structures* 21 ((1999), 135-148.
 - [6] Bhaskararao, A.V. and Jangid, R.S. Seismic response of adjacent buildings connected with friction dampers. *Bulletin of Earthquake Engineering* 4 (2006), 43-64.
 - [7] Raheem S.E.A. Mitigation measures for earthquake induced pounding effects on seismic performance of adjacent buildings. *Bulletin of Earthquake Engineering* 12 (2014), 1705-1724.
 - [8] Yang Z., Xu X.L. and Lu X.L. Experimental seismic study of adjacent buildings with fluid dampers. *Journal of Structural Engineering (ASCE)* 129 (2003), 197-205.
 - [9] Basili M. and De Angelis M. Optimal passive control of adjacent structures interconnected with nonlinear hysteretic devices. *Journal of Sound and Vibration* 301 (2007), 106-125.
 - [10] Kim J., Ryu, J., Chung L. Seismic performance of structures connected by viscoelastic dampers. *Engineering Structures* 28 (2006), 183-195.
 - [11] Hwang J.-S., Huang Y.-N., Yi S.-L. and Ho S.-Y. Design formulations for supplemental viscous dampers to building structures. *Journal of Structural Engineering (ASCE)*, 134 (2008), 22-31.
 - [12] Symans, M.D. and Constantinou M.C. Passive Fluid Viscous Damping Systems for Seismic Energy Dissipation. *Journal of Earthquake Technology ISET* 35, 4 (1998), 185-206.
 - [13] Van Mier J.G.M., Puijssers A.F., Reinhardt H.W. and Monnier T. Load-time response of colliding concrete bodies. *Journal of Structural Engineering (ASCE)*, 117 (1991), 354-374.
- Elif Cagda Kandemir-Mazanoglu, Assistant Professor: Usak University, Faculty of Engineering, Civil Engineering Department, 64200 Usak, Turkey (elif.kandemir@usak.edu.tr)
- Kemal Mazanoglu, Assistant Professor: Usak University, Faculty of Engineering, Mechanical Engineering Department, 64200 Usak, Turkey (kemal.mazanoglu@usak.edu.tr)

Rayleigh–Ritz natural frequency analyses for centrifugally stiffened functionally graded and tapered beams (VIB089-15)

Kemal Mazanoglu, Ali Ceylan

Abstract: In this paper, flap wise vibration analyses of centrifugally stiffened tapered and axially functionally graded beams are conducted by the Rayleigh–Ritz method that directly finds a solution using the energy expressions. Euler–Bernoulli beam model is used in calculations. Effects of taper ratio, hub radius and angular velocity are inspected for the beams with several classical boundary conditions. Results given as non-dimensional natural frequencies are compared to the results given in existing literature, and good agreements are obtained. Effects of changes in axial grading function for centrifugally stiffened Euler–Bernoulli beams are also reflected and discussed.

1. Introduction

This paper is on the flexural vibration of tapered and axially functionally graded (AFG) beams rotating around a hub. Beam type elements can rotate around a hub in many applications such as turbine blades, wind turbines, propellers, crank and etc. Design of these components requires taking mechanic, dynamic, aerodynamic and thermal limitations into account to supply the most proper economic conditions and increase the energy efficiency. In order to do this, usage of functionally graded (FG) beams has attracted researchers' attention in recent years. FG components preserve structural integrity by providing appropriate power and weight distributions. Smooth change of material properties removes stress loads, which occur in layered composites, and accordingly eliminates delamination faults. A centrifugally stiffened FG beam may be broken due to dynamic and aerodynamic effects leading resonance although it has sufficient mechanic and thermal resistance. FG beams should have appropriate modal characteristics to avoid resonance. Changes in modal characteristics are easily followed by the natural frequency parameters. Therefore, calculation of natural frequencies plays significant role in achievement of novel designs for rotating FG beams.

Researchers have paid great attention to the flexural vibration of uniform or non-uniform beams rotating around a hub for three decades. Selected papers considering uniform Euler–Bernoulli beam model are presented by Banerjee, Chung and Yoo, Yang et al., Yoo and Shin [1-4]. Beside this, vibration of rotating non-uniform Euler–Bernoulli beams is analysed in some other research works [1,5-8]. Rotating beam vibrations are also studied by the Timoshenko beam model [9-11]. Most of these works use the finite element based analyses to reach approximate solution [2,3,6,8]. In addition,

dynamic stiffness matrix method [1], differential transform method [7], Galerkin's method [9], and Rayleigh–Ritz method [4,10] are some other solution methods used in current literature.

Studies on vibration analysis of FG beams have tremendously increased in recent years. Vibration of AFG beams is inspected in some papers [12-14]. Huang et al. [12] define an additional function to obtain solution using power series method. Huang and Li [13] present a simple procedure to find natural frequencies by the transformation of governing equation with varying coefficients to Fredholm integral equations. Shahba et al. [14] introduce a new element type to reach solution using finite element analysis. There are several papers on vibration analyses of transversely FG beams [15,16]. In referred works, results are obtained by Rayleigh–Ritz method [15] and Navier solution procedure [16].

In current literature, there are a few studies on vibration of rotating beams made of FG materials [17,18]. Rajasekaran [17] compares the differential transform and quadrature methods employed for the flexural vibration analyses of Euler–Bernoulli AFG beams rotating around a hub. Ramesh and Rao [18] consider the vibration of transversely FG rotating beams using the Rayleigh–Ritz method.

To the best of author's knowledge, usage of the Rayleigh–Ritz method for the vibration analysis of AFG beams rotating around a hub is firstly investigated in this paper. Beams are modelled using the Euler–Bernoulli beam theory. The Rayleigh–Ritz solution method is applied using a simple and fast computation technique presented. Simple polynomial shape functions are used in the method. Comparative results are given for tapered and AFG beams rotating around a hub.

2. Theoretical background

In this work, material and/or cross-sectional properties of rotating beam are assumed to vary along the length, L , of beam as shown in Figure 1. Cross-section changes of the tapered beams are expressed by following functions representing height, h , and width, b .

$$h(x) = h_0 \left(1 - c_h \frac{x}{L} \right) \quad (1)$$

$$b(x) = b_0 \left(1 - c_b \frac{x}{L} \right) \quad (2)$$

where h_0 and b_0 symbolize the dimensions at the root of beam. c_h and c_b are the taper ratios for the height and width respectively. Thus, for the rectangular beams, cross-sectional area, $A(x)$, and area moment of inertia, $I(x)$, variations are written as follow:

$$A(x) = b(x)h(x) \quad (3)$$

$$I(x) = b(x)h(x)^3 / 12 \quad (4)$$

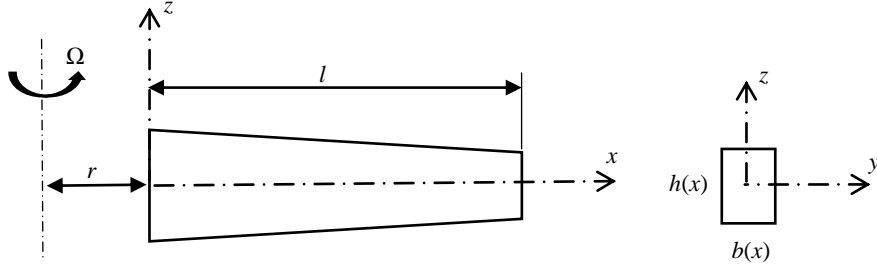


Figure 1. Configuration of rectangular beam rotating around a hub.

Similarly, material parameter, p_m , which may be modulus of elasticity (E) or density (ρ), is assumed to vary as:

$$p_m(x) = (p_{m1} - p_{m2})(x/L)^n + p_{m2} \quad (5)$$

where p_{m1} and p_{m2} denote the parameters of two different materials. n is the material non-homogeneity factor. Within this framework, energy expressions for flap-wise vibration of centrifugally stiffened AFG beams and details of a technique implemented for the Rayleigh–Ritz method are presented in following subsections.

2.1. Energy expressions for centrifugally stiffened beams

In this paper, vibration of centrifugally stiffened AFG and tapered beams is considered in only flap-wise direction. It is assumed that bending-torsion and bending-bending coupling effects are negligible for the beam selected. Since the rotating speed of the hub, Ω , is constant, the beam has no angular acceleration. Hence, there is no tangential inertia force active on the beam. On the other hand, while the beam is rotating around a hub, centrifugal tension force, $F(x)$, at a distance, x , from the origin is given by:

$$F(x) = \int_x^L \rho(x) A(x) \Omega^2 (R + x) dx \quad (6)$$

where R symbolizes the radius of hub. Under this centrifugal force, potential energy, U , is given as follows [11]:

$$U(x) = \frac{1}{2} \int_0^L \{ E(x) I(x) (W''(x))^2 + F(x) (W'(x))^2 \} dx + C_1 \quad (7)$$

W' and W'' stand for the first and second derivatives of flap-wise displacement W with respect to x axis. The first term is the energy expression of the non-rotating Euler–Bernoulli beam and the second term represents the effect of centrifugal stiffening. C_1 is the constant that can be found as,

$$\frac{1}{2} \int_0^L (F(x))^2 / (E(x)A(x)) dx.$$

Kinetic energy (T) of the centrifugally stiffened beams can be expressed as follows [11]:

$$T(x) = \frac{1}{2} \int_0^L \omega^2 \rho(x) A(x) (W(x))^2 dx + C_2 \quad (8)$$

where ω is the natural frequency of flap-wise bending vibration. As is known, the first term is the kinetic energy of non-rotating bending beam. In addition, constant rotation velocity leads constant term as $C_2 = \frac{1}{2} \int_0^L \rho(x) A(x) \Omega^2 (r+x)^2 dx$. Note that the constant terms in Eqs. (7,8) are ineffective on results. In order to obtain results, flexural displacement, W , is represented in the form of function series given as follows:

$$W(x) = \sum_{j=1}^m \kappa_j \lambda_j(x) \quad (9)$$

Here κ denotes the coefficient of terms that indexed by j with total number, m . $\lambda(x)$ is a series of terms that forms an admissible function satisfying the geometric boundaries at least. Table 1 shows general terms of admissible polynomial functions satisfying some classical boundaries and used in solution method detailed in following subsection.

Table 1. General terms of flap-wise displacement polynomials for classical end conditions.

End conditions	$\lambda_j(x)$
Clamped-Clamped	$(x/L)^2 (1-x/L)^{j+1}$
Pinned-Pinned	$(x/L)^1 (1-x/L)^j$
Clamped-Free	$(x/L)^2 (1-x/L)^{j-1}$
Clamped-Pinned	$(x/L)^2 (1-x/L)^j$
Free-Free	$(x/L)^0 (1-x/L)^{j-1}$

2.2. A computation technique for the Rayleigh–Ritz method

The Rayleigh–Ritz method approximately finds modal parameters based upon the conservation of energy law. The energy difference is partially differentiated by the coefficients of shape functions to make the difference minimum.

$$\frac{\partial}{\partial \kappa_j}(U - T) = 0, \quad j = 1, 2, \dots, m \quad (10)$$

The energies are expressed in discretised form as follow:

$$U = \frac{1}{2} \int_R^{L+R} E(x) I(x) \sum_{j=1}^m \kappa_j \lambda''_j \sum_{i=1}^m \kappa_i \lambda''_i dx + \frac{1}{2} \int_R^{L+R} F(x) \sum_{j=1}^m \kappa_j \lambda'_j \sum_{i=1}^m \kappa_i \lambda'_i dx \quad (11)$$

$$T = \frac{1}{2} \omega^2 \int_R^{L+R} \rho(x) A(x) \sum_{j=1}^m \kappa_j \lambda_j \sum_{i=1}^m \kappa_i \lambda_i dx \quad (12)$$

As a simple computation technique suggested in this paper, discretised form of the energy difference expression is partially differentiated with respect to coefficients κ_i and κ_j .

$$d_{i,j} = \frac{\partial^2}{\partial \kappa_j \partial \kappa_i}(U - T) \quad i = 1, 2, \dots, m \quad j = 1, 2, \dots, m \quad (13)$$

This process leads to the elimination of the coefficients in resulting terms, $d_{i,j}$, that are located into the matrix, D , as follows:

$$D = \begin{bmatrix} d_{1,1} & d_{1,2} & \dots & d_{1,n} \\ d_{2,1} & d_{2,2} & \dots & d_{2,n} \\ \vdots & \vdots & \vdots & \vdots \\ d_{n,1} & d_{n,2} & \dots & d_{n,n} \end{bmatrix} \quad (14)$$

Natural frequencies are found as a result of the singularity analysis carried out by equating the determinant of matrix to zero ($\det(D) = 0$). A remarkable point in this computation technique is the use of simple functions that allow one to do integration effortlessly and get results in considerably short duration.

3. Results and discussions

Natural frequencies of centrifugally stiffened tapered and AFG beams are found by the Rayleigh–Ritz method using simple computation technique presented. Results are given using following non-

dimensional parameters expressing the hub radius, hub rotating speed, and beam natural frequencies respectively.

$$\delta = R/L, \quad (15a)$$

$$\alpha = \Omega L^2 ((\rho_0 A_0)/(E_0 I_0))^{0.5}, \quad (15b)$$

$$\mu = \omega L^2 ((\rho_0 A_0)/(E_0 I_0))^{0.5}. \quad (15c)$$

The subscript “0” represent the properties at $x = 0$. AFG beams considered in current literature [17] are inspected to validate success of the method. Material properties of the beams made of Aluminium and Zirconia (ZrO_2) are given as: $E_{al} = 70 \text{ GPa}$, $\rho_{al} = 2702 \text{ kg/m}^3$, $E_z = 200 \text{ GPa}$, $\rho_z = 5700 \text{ kg/m}^3$. Figure 2 shows modulus of elasticity variation for different n values. In following analyses, the Rayleigh–Ritz method is applied using admissible mode shape functions having 8 polynomial terms.

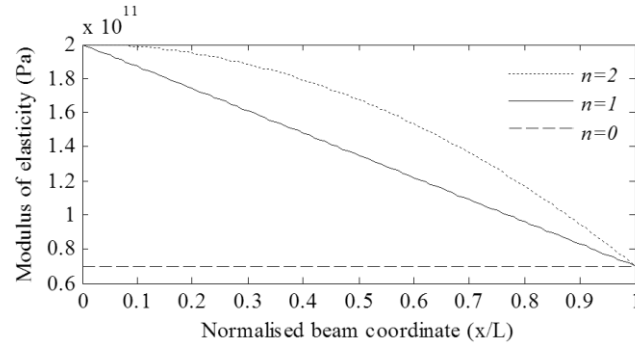


Figure 2. Modulus of elasticity variation for different n values.

Variation of non-dimensional frequency parameters reflecting the effects of non-homogeneity parameter, n , is illustrated in Table 2. Parameters for hub radius, hub rotating speed and cross-section are taken as $\delta = 0$, $\alpha = 5$ and $c_h = c_b = 0$ respectively. It is seen that present results very closely match with the results of Rajasekaran [17] who uses differential transformation and differential quadrature element methods (DQEM). As is known, convergence capability of the Rayleigh–Ritz method decreases as the vibration mode wanted to be obtained increases. Accordingly, negligible error of the method can be easily eliminated by increasing the number of terms in mode shape function. Results also show that the frequency parameters of non-homogeneous beams are lower than those of homogeneous beams ($n = 0$) for pinned-pinned and fixed-fixed boundaries.

Table 2. Effects of non-homogeneity parameter on natural frequency parameters of rotating AFG beam. ($\delta = 0$, $\alpha = 5$, $c_h = c_b = 0$)

Boundary conditions	n	Method	Natural frequency parameters			
			μ_1	μ_2	μ_3	μ_4
Fixed-Free	0	Rayleigh–Ritz	6.4495	25.4461	65.2051	124.7605
		DQEM [17]	6.4494	25.4461	65.2050	124.5664
	1	Rayleigh–Ritz	6.9716	25.6519	63.3087	119.6292
		DQEM [17]	6.9717	25.6522	63.3094	119.5321
	2	Rayleigh–Ritz	6.9289	26.0436	64.6727	122.2474
		DQEM [17]	6.9289	26.0438	64.6733	122.1691
Pinned-Pinned	0	Rayleigh–Ritz	13.0953	43.3513	92.8744	162.2038
		DQEM [17]	13.0953	43.3513	92.8561	162.0019
	1	Rayleigh–Ritz	12.1032	40.6536	87.5369	153.4087
		DQEM [17]	12.1033	40.6541	87.5317	153.0331
	2	Rayleigh–Ritz	12.2333	41.3792	89.2306	156.2901
		DQEM [17]	12.2334	41.3794	89.2251	156.0663
Fixed-Fixed	0	Rayleigh–Ritz	24.5442	64.8012	124.3683	203.5234
		DQEM [17]	24.5442	64.8012	124.3667	203.4994
	1	Rayleigh–Ritz	22.7495	60.6390	116.9549	191.9138
		DQEM [17]	22.7497	60.6397	116.9560	191.8536
	2	Rayleigh–Ritz	22.3541	60.6608	117.9536	194.2948
		DQEM [17]	22.3542	60.6611	117.9543	194.2642

Another analysis is performed to validate Rayleigh–Ritz method for rotating AFG beams with different taper ratios. Table 3 demonstrates good agreement between present results and the results given by Rajasekaran [17]. It is obvious that natural frequency parameters decrease with increasing taper ratio except for the fundamental frequency parameters of cantilever beams.

Success of the method is also investigated for tapered AFG beams with several hub rotating speeds and hub radius. Results shows good harmony with the results of Rajasekaran [17] as illustrated in Table 4. As may be expected, fundamental frequency parameters increase with increasing hub radius and rotating speed due to the augmentation of centrifugal force.

Table 3. Effects of taper ratios on natural frequency parameters of rotating AFG beams ($\delta = 0$, $c_h = c_b = c$, $\alpha = 2$, $n = 2$).

Boundary conditions	μ	Method	Taper ratio (c)			
			0	0.3	0.6	0.9
Fixed-fixed	μ_1	Rayleigh–Ritz	20.8997	17.9485	14.7595	11.3024
		DQEM [17]	20.8998	17.9486	14.7595	11.1558
	μ_2	Rayleigh–Ritz	58.5673	49.8115	40.1356	28.7144
		DQEM [17]	58.5677	49.8119	40.1354	28.1726
	μ_3	Rayleigh–Ritz	115.6538	97.9304	78.1478	54.3656
		DQEM [17]	115.6545	97.9305	78.1470	52.9865
	μ_4	Rayleigh–Ritz	191.8866	162.2092	128.7916	89.1723
		DQEM [17]	191.8569	162.1151	128.7647	85.8165
Fixed-free	μ_1	Rayleigh–Ritz	4.8142	5.3933	6.3690	8.5415
		DQEM [17]	4.8142	5.3933	6.3691	8.5415
	μ_2	Rayleigh–Ritz	23.6961	22.0868	20.4740	19.9850
		DQEM [17]	23.6964	22.0868	20.4739	19.9830
	μ_3	Rayleigh–Ritz	62.2940	54.6112	46.3376	37.7093
		DQEM [17]	62.2946	56.6118	46.3284	37.6610
	μ_4	Rayleigh–Ritz	119.8089	102.9809	84.8333	63.5064
		DQEM [17]	119.7205	102.9720	84.5343	62.8547
Pinned-pinned	μ_1	Rayleigh–Ritz	10.0556	8.3229	6.1982	3.2721
		DQEM [17]	10.0557	8.3230	6.1979	3.2612
	μ_2	Rayleigh–Ritz	38.8038	32.9243	26.6344	19.5282
		DQEM [17]	38.8040	32.9245	26.6332	19.4644
	μ_3	Rayleigh–Ritz	86.5742	73.2563	58.7088	41.3334
		DQEM [17]	86.5673	73.2562	58.7092	41.0533
	μ_4	Rayleigh–Ritz	153.5932	130.2473	103.2995	71.3854
		DQEM [17]	153.3792	129.5636	102.2202	70.3164

4. Conclusion

In this work, natural frequency analyses of rotating tapered AFG Euler–Bernoulli beams are carried out using the Rayleigh–Ritz method with a simple and fast computation technique. The method successfully identifies the effects of changes in boundary conditions, cross-section, functional

grading, hub radius and rotating speed. These effects are clearly stated in the paper. Results can encourage the researchers to apply the method in different analyses of rotating FG beams.

Table 4. Effects of hub rotating speed and hub radius on fundamental frequency parameter of tapered AFG beam. ($c_h = 0.5$, $c_b = 0$, $n = 2$)

α	δ	Method	μ_1 for several boundary conditions		
			Fixed-free	Fixed-fixed	Pinned-pinned
1	0	Rayleigh–Ritz	4.7452	15.4096	6.8560
		DQEM [17]	4.7453	15.4096	6.8560
	0.1	Rayleigh–Ritz	4.7638	15.4219	6.8810
		DQEM [17]	4.7639	15.4220	6.8810
	1	Rayleigh–Ritz	4.9280	15.5323	7.1018
		DQEM [17]	4.9281	15.5324	7.1018
5	0	Rayleigh–Ritz	7.2580	17.1609	9.5239
		DQEM [17]	7.2580	17.1610	9.5239
	0.1	Rayleigh–Ritz	7.5504	17.4305	9.9482
		DQEM [17]	7.5505	17.4305	9.9481
	1	Rayleigh–Ritz	9.7875	19.6626	13.0630
		DQEM [17]	9.7875	19.6627	13.0628
10	0	Rayleigh–Ritz	11.8954	21.5971	14.8935
		DQEM [17]	11.8955	21.5971	14.8930
	0.1	Rayleigh–Ritz	12.5889	22.4077	15.8943
		DQEM [17]	12.5890	22.4077	15.8938
	1	Rayleigh–Ritz	17.6147	28.5078	22.6643
		DQEM [17]	17.6148	28.5077	22.6624

References

- [1] Banerjee, J.R. Free vibration of centrifugally stiffened uniform and tapered beams using the dynamic stiffness method. *Journal of Sound and Vibration* 233, 5 (2000), 857-875.
- [2] Chung, J., Yoo, H.H. Dynamic analysis of a rotating cantilever beam by using the finite element method. *Journal of Sound and Vibration* 249, 1 (2002), 147-164
- [3] Yang, J.B., Jiang, L.J., Chen, D.C.H. Dynamic modelling and control of a rotating Euler–Bernoulli beam. *Journal of Sound and Vibration*, 274 (2004), 863-875.

- [4] Yoo, H.H., Shin, S.H. Vibration analysis of rotating cantilever beams. *Journal of Sound and Vibration*, 212, 5 (1998), 807-828.
- [5] Banerjee, J.R., Su, H., Jackson, D.R. Free vibration of rotating tapered beams using the dynamic stiffness method. *Journal of Sound and Vibration*, 298 (2006), 1034-1054.
- [6] Khulief, Y.A. Vibration frequencies of a rotating tapered beam with end mass. *Journal of Sound and Vibration*, 134, 1 (1989), 87-97.
- [7] Özdemir, Ö., Kaya, M.O. Flapwise bending vibration analysis of a rotating tapered cantilever Bernoulli–Euler beam by differential transform method. *Journal of Sound and Vibration*, 289 (2006) 413-420.
- [8] Shavezipur, M., Hashemi, S.M. Free vibration of triply coupled centrifugally stiffened nonuniform beams, using a refined dynamic finite element method. *Aerospace Science and Technology*, 13, 1 (2009), 59-70.
- [9] Al-Ansary, M.D. Flexural vibrations of rotating beams considering rotary inertia. *Computers and Structures*, 69 (1998), 321-328.
- [10] Zhu, T.L. The vibrations of pretwisted rotating Timoshenko beams by the Rayleigh–Ritz method. *Computational Mechanics*, 47 (2011), 395-408.
- [11] Banerjee, J.R., Sobey, A.J. Energy expressions for rotating tapered Timoshenko beams. *Journal of Sound and Vibration*, 254, 4 (2002), 818-822.
- [12] Huang, Y., Yang, L.-E., Luo, Q.-Z. Free vibration of axially functionally graded Timoshenko beams with non-uniform cross-section. *Composites: Part B*, 45 (2013), 1493-1498.
- [13] Huang, Y., Li, X.-F. A new approach for free vibration of axially functionally graded beams with non-uniform cross-section. *Journal of Sound and Vibration*, 329 (2010), 2291-2303.
- [14] Shahba, A., Attarnejad, R., Marvi, M.T., Hajilar, S. Free vibration and stability analysis of axially functionally graded tapered Timoshenko beams with classical and non-classical boundary conditions. *Composites: Part B*, 42 (2011), 801-808.
- [15] Pradhan, K.K., Chakraverty, S. Free vibration of Euler and Timoshenko functionally graded beams by Rayleigh–Ritz method. *Composites: Part B*, 51 (2013), 175-184.
- [16] Thai, H.-T., Vo, T.P. Bending and free vibration of functionally graded beams using various higher order shear deformation beam theories. *International Journal of Mechanical Sciences*, 62 (2012), 57-66.
- [17] Rajasekaran, S. Differential transformation and differential quadrature methods for centrifugally stiffened axially functionally graded tapered beams. *International Journal of Mechanical Sciences*, 74, 1 (2013), 15-31.
- [18] Ramesh, M.N.V., Mohan Rao, N. Free vibration analysis of rotating functionally-graded cantilever beams. *International Journal of Acoustics and Vibration*, 19, 1 (2014), 31-41.
- Kemal Mazanoglu, Assist. Professor: Usak University, Engineering Faculty, Department of Mechanical Engineering, 1 Eylül Campus, 64200 Usak, Turkey (kemal.mazanoglu@usak.edu.tr).
- Ali Ceylan, (M.Sc. student): Usak University, Institute of Natural and Applied Sciences, 1 Eylül Campus, 64200 Usak, Turkey (e.aliceylan@gmail.com).

Anti-symmetric mode in-plane vibration analyses of several types of frame structures

(VIB075-15)

Kemal Mazanoglu, Elif C. Kandemir-Mazanoglu

Abstract: This paper presents an analytical method for the computation of anti-symmetric mode shapes and corresponding natural frequencies of frame structures. Lumped mass-stiffness model is employed to define the effects of beam on equivalent column system. Equivalent lumped mass and moment of inertia of beam are determined using the principle of kinetic energy conservation. Rotational stiffness of the beam is calculated by the aid of beam element moment equations and the principle of superposition. Equivalent column, which is modelled using Euler–Bernoulli beam theory, is considered by the contribution of compatibility and continuity conditions stated at the beam locations. Applicability of the method is demonstrated on single storey (portal), H type, and double storey frame systems. Results are validated using the outputs of the finite element package and some results given in current literature.

1. Introduction

The vibration characteristics of a frame contain important knowledge about how the structure will behave in vibrating environment such as vehicles, active fault zones, aircrafts and etc. The natural frequency and mode shapes of a frame structure are of importance to provide physical insight into the dynamic behaviour of mechanical and structural components. Especially, vibrations in anti-symmetric modes are crucial in terms of reflecting dynamic behaviour of the systems under the effects of horizontal loading. In view of theoretical aspect, simulating the frame structure into a simple model generally becomes significant process of free vibration analyses. Fundamentals on vibration of structures can be found in related books [1,2].

Numerous methods have been developed by the researchers to identify the natural vibration characteristics and model the frame system in a simple form. Basically, many researchers consider frame structures as multi-degree of freedom systems containing bending, linear or shear components [3,4]. These models allow rough estimation of the modal parameters due to assumptions and simplifications done for computing lumped parameters. It is for this reason that these models are beyond the scope of this work. However, most of the neglected parameters can be taken into consideration using continuous approaches. To the best of author's knowledge, one of the earliest works including continuous approach for the vibration of simple frames is introduced by Bennon [5]. Gladwell [6] presents the use of assumed mode method in the Rayleigh–Ritz analysis for the vibration

of two-storey frame. Laura et al. [7] also use the Rayleigh–Ritz method to obtain fundamental mode planar vibration of single-storey frames carrying concentrated masses. In another work, single-storey frames are considered using differential quadrature element method [8]. Lee and Ng [9] introduce the use of artificial linear and torsional springs together with the Rayleigh–Ritz method in order to analyse in-plane vibrations of portal, T shaped and H shaped frames. These types of frames are also studied using a wave based analytical solution method [10] that is adopted for analysing multi-bay [11] and multi-storey [12] frames. A continuous-discrete model is presented by Zhang and Gargab [13] who consider the beam as shear element. Sakar et al. [14] use the finite element method to carry out vibration and stability analyses of simple and multi-bay frame systems. Finite element based analyses can also be employed to inspect the vibration of damaged frames [15,16]. Some other works include the vibration analysis of frames under the effects of additional rotational springs that supply flexible connection between frame components [17,18].

Following sections of this paper present the analytical solution for the anti-symmetric mode in-plane vibration analysis of frame structures. Continuous solution for columns and lumped mass-stiffness approach for beams have been combined to conduct vibration analysis of frames. Presented model and solution method are validated by using some results in current literature.

2. Theoretical background

2.1. Free vibration of a column

According to Euler–Bernoulli beam theory, following differential equation expresses the bending mode free vibration of a uniform column.

$$EI_c \frac{\partial^4 w(z,t)}{\partial z^4} + \rho A_c \frac{\partial^2 w(z,t)}{\partial t^2} = 0, \quad (1)$$

where, E , I_c , A_c , and ρ represent modulus of elasticity, area moment of inertia, cross-section area, and density of column respectively. Flexural displacement, which is symbolised by w , varies with the axial position z , and the time t . By the separation of the variables z and t , solution form of the mode shape, $W(z)$, is obtained as follows:

$$W(z) = C_1 \cos \beta z + C_2 \sin \beta z + C_3 \cosh \beta z + C_4 \sinh \beta z, \quad (2)$$

where C_1 , C_2 , C_3 , and C_4 are the coefficients of harmonic and hyperbolic terms. Frequency parameter, β , depends upon the natural frequency, ω , as given below:

$$\beta = \sqrt[4]{\frac{\rho A \omega^2}{EI}}. \quad (3)$$

An equation set is formed by using mode shape function and its derivatives satisfying the end conditions of the column. The equations appropriate for some general end conditions are given in Table 1. Singularity analysis for the matrix obtained by the harmonic and hyperbolic terms of functions is needed to find natural frequency parameters.

Table 1. Equations for classical end conditions.

Ends	Equations	
Free	$W''=0$,	$W'''=0$
Fixed	$W=0$,	$W'=0$
Pinned	$W=0$,	$W''=0$

2.2. Lumped mass-stiffness model for frame structures

In this section, vibration of frame structures is explained by lumped mass-stiffness model as shown in Figure 1. First of all, equivalent column is considered to model antisymmetric mode vibrations of frames. Equivalent area, A_e , and inertia moment, I_e , of the columns are taken as follows:

$$A_e = A_L + A_R, \quad I_e = I_L + I_R \quad (4)$$

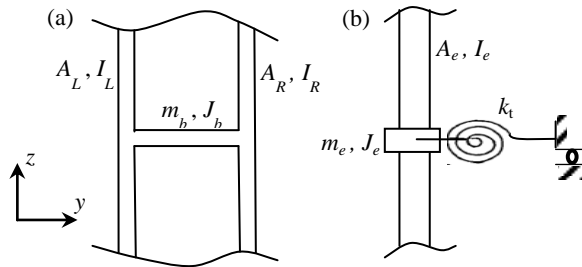


Figure 1. Lumped mass-stiffness model on equivalent column.

Subscripts $_L$ and $_R$ are employed to distinguish the properties of the left and right columns respectively. Note that equivalent column model can be applicable for equal or very close sizes of left and right columns. Mass, inertia and stiffness effects of beam are simulated by adding lumped masses and rotational springs on corresponding locations of the equivalent column. Equivalent mass of the beam can be taken equal to exact mass of the beam since the movement is dominant in horizontal direction.

$$m_e = \rho A_b L_b = m_b \quad (5)$$

where, A_b and L_b symbolise cross-sectional area and length of the beam respectively. Estimation of vertical deformation form is necessary to calculate equivalent mass moment of inertia of the beam. It is intuitively expected that time independent deformation form of the beam, $U(y)$, resembles to one period of a sinusoidal function as follows:

$$U(y) = U_m \sin(2\pi y/L_b) \quad (6)$$

where, U_m denotes the maximum flexural deformation of the beam. It is known that the first derivative with respect to beam's coordinate axis, y , gives the slope of $U(y)$. The maximum slope occurs at $y = 0$, leading unit cosine. Thus, relation between the maximum displacement and the maximum slope is expressed as follows:

$$\theta(0) = \frac{U_m 2\pi}{L_b} \quad (7)$$

Suppose that an equivalent beam having equivalent mass moment of inertia rotates in rigid body mode at the centre ($y = 0$). In this case, expression for equivalent mass moment of inertia, J_e , is found by equating time independent form of kinetic energies as follows:

$$\frac{1}{2} J_e \theta(0)^2 = \frac{1}{2} \int_{-L_b/2}^{L_b/2} \rho A_b U(y)^2 dy \quad (8)$$

Eqs. (6, 7, and 8) results in the following expression for the equivalent mass moment of inertia.

$$J_e = \frac{\rho A_b L_b^3}{4\pi^2} = \frac{3\rho h_b I_{bxy}}{\pi^2} \quad (9)$$

where I_{bxy} is the area moment of inertia for x - y cross-section of the beam ($I_{bxy} = d_b L_b^3 / 12$). h_b and d_b represent the thickness and depth of the beam respectively.

On the other hand, rotational stiffness of the beam is determined by using the moment equations and the superposition principle. In order to apply the principle, it is assumed that while right end of the beam is rotationally fixed, left end is flexible and vice versa. In each case, moments occur as $4EI_{bxz}/L_b$ at flexible side and $2EI_{bxz}/L_b$ at fixed side of the beam ($I_{bxz} = d_b h_b^3 / 12$). Thus, total moment affecting flexible column becomes $6EI_{bxz}/L_b$ [2]. Rotational stiffness can also be taken as $6EI_{bxz}/L_b$ under the assumption of unit angular displacement. When these calculations are repeated

for exchanged position of fixed and flexible ends, equivalent rotational stiffness of a beam, k_t , is found as total stiffness written as follows:

$$k_t = 12EI_{bxz} / L_b \quad (10)$$

As would be expected, longitudinal stiffness has very minor effects on lower vibration modes of frame and thus it can be neglected. All the effects mentioned above are contributed into equivalent column vibration to describe compatibility conditions at beam location. Resulting time independent equations to be satisfied are given as follow:

$$W''(z_b^-) + \lambda W'(z_b) = W''(z_b^+) \quad (11a)$$

$$W'''(z_b^-) + \mu W(z_b) = W'''(z_b^+) \quad (11b)$$

where z_b denotes the location of beam and z_b^{sign} represents the locations just above or below the beam. λ and μ can be defined as follow:

$$\lambda = \frac{J_e \omega^2 - k_t}{EI_e}, \quad (12a)$$

$$\mu = \frac{m_e \omega^2}{EI_e}. \quad (12b)$$

Note that right hand sides of the Eqs. (11a, 11b) become zero if the beam is located at the end of the columns. Besides, continuity conditions should be satisfied by displacements and slopes that are assumed equal at just around the beam location.

$$W(z_b^-) = W(z_b^+), \quad (13a)$$

$$W'(z_b^-) = W'(z_b^+). \quad (13b)$$

In order to analyse the vibration of n sectioned equivalent column separated by the boundary effects of beams, Eq. (2) is rearranged with modified coefficients expressing vibration form of each section, $W_i(z)$.

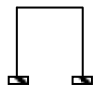
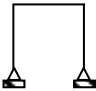
$$W_i(z) = C_{4i-3} \cos \beta z + C_{4i-2} \sin \beta z + C_{4i-1} \cosh \beta z + C_{4i} \sinh \beta z, \quad i = 1, \dots, n \quad (14)$$

3. Results and discussions

In this section, present lumped mass-stiffness model is verified on several frame structures taken into consideration. This model is easily validated by the results given in current literature in terms of anti-symmetric mode shapes and corresponding natural frequencies. In addition, the finite element

package called ANSYS[®] is used for validating the results of double-storey frame. In the program, frame components are modelled as volume using solid meshing element called “Solid95”. Beam and column blocks are attached together by using “vadd” command to shape frame. It is worth noting that solid finite element model allows the area connection of columns and beams in contrast to the continuous model considering beam effects concentrated on a point. Good convergence is provided by using the “smrsize1” command that is the most refined mesh option of the free meshing procedure. Default edge length of the element is taken equal to the half of minimum edge size of the frame. It is set using the “esize” command. At result, natural frequencies are obtained by using “modal analysis” as the analysis type.

Table 2. Non-dimensional natural frequency parameters for the first anti-symmetric in-plane modes of several single-storey frames.

Frame figures	Frame properties			Non-dimensional natural frequency parameter			
	$\frac{EI_c}{EI_b}$	$\frac{\rho A_c}{\rho A_b}$	$\frac{L_c}{L_b}$	$\Omega = \omega L_c^2 (\rho A / EI)^{0.5}$			
				Sakar et al. [14]	Laura et al. [7]	Kolousek [1]	Present work
	0.25	0.25	1.5	2.559	2.5621	2.5614	2.5611
			3	3.327	3.3396	3.3379	3.3382
			6	4.029	4.0791	4.0782	4.0779
	1.5	1.5	1.5	3.933	3.9369	3.9350	3.9334
			3	4.620	4.6299	4.6289	4.6292
			6	5.030	5.0720	5.0719	5.0719
	6	6	1.5	4.043	4.0446	4.0441	4.0416
			3	4.567	4.5713	4.5710	4.5711
			6	4.950	4.9772	4.9769	4.9772
	0.25	0.25	1.5	1.236	1.2378	1.2374	1.2376
			3	1.577	1.5837	1.5833	1.5835
			6	1.867	1.8935	1.8931	1.8933
	1.5	1.5	1.5	1.742	1.7435	1.7432	1.7431
			3	2.047	2.0527	2.0523	2.0526
			6	2.219	2.2446	2.2446	2.2446
	6	6	1.5	1.507	1.5074	1.5072	1.5071
			3	1.845	1.8485	1.8482	1.8485
			6	2.084	2.1033	2.1030	2.1033

Success of presented theoretical model is inspected for following cases of the frames.

Case 1 – Single-storey frame: Fundamental modal characteristics of single-storey frames are reflected with different dimensional properties of beams and columns. Frames with simply supported

and fixed boundaries are both considered. Table 2, which includes the properties of the beams considered, demonstrates the agreement between the fundamental non-dimensional frequency parameters obtained by present method and those given in literature [1,7,14]. Besides, Figure 2 shows equivalent column mode shapes when the column/beam length ratio is $L_c/L_b = 1.5$. Effects of changes in depth of beam and base boundaries can be clearly observed. As would be expected, slope of column mode shape approaches to the slope near the fixed end as the area and inertia moment of beam increase.

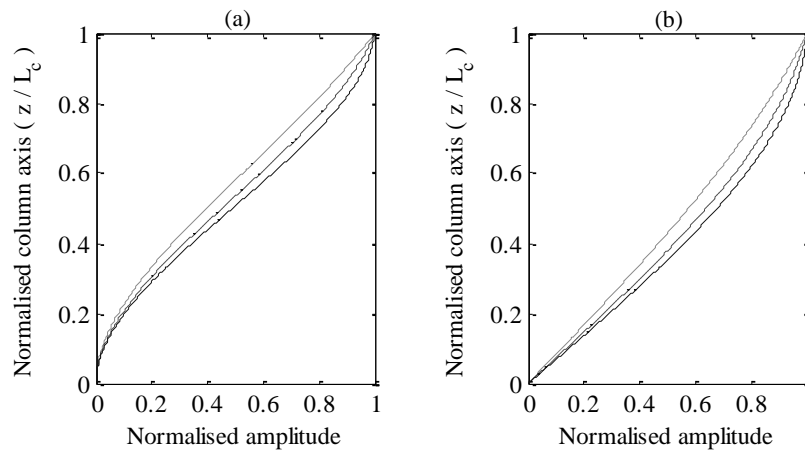


Figure 2. First anti-symmetric mode shapes of equivalent columns for single-storey frames (a) fixed and (b) pinned to the base. $L_c/L_b = 1.5$, A_c/A_b and I_c/I_b ratios: (—) 0.25, (---) 1.5, (- - -) 6.

Case 2 – H shaped frame: In this example, first two anti-symmetric mode natural frequencies and equivalent column mode shapes are found for the H shaped frame considered by Lee and Ng [9] and Mei [10]. The frame is bounded from the base using simple supports. Non-dimensional properties and frequencies of frame are given in Table 3 which exhibits the accuracy of present model. Equivalent column mode shapes are also shown in Figure 3.

Table 3. Non-dimensional natural frequency parameters for the first two anti-symmetric in-plane modes of the H shaped frame.

Frame figure	Frame properties			Non-dimensional natural frequency parameter			
	$\frac{EI_c}{EI_b}$	$\frac{\rho A_c}{\rho A_b}$	$\frac{L_c}{L_b}$	Mode number	$\Omega = \omega(L_c/2)^2 (\rho_c A_c / E_c I_c)^{0.5}$		
					Mei [10]	Lee and Ng. [9]	Present work
	1	1	2	1	0.9	0.92059	0.9122
				2	3.8	3.82212	3.8069

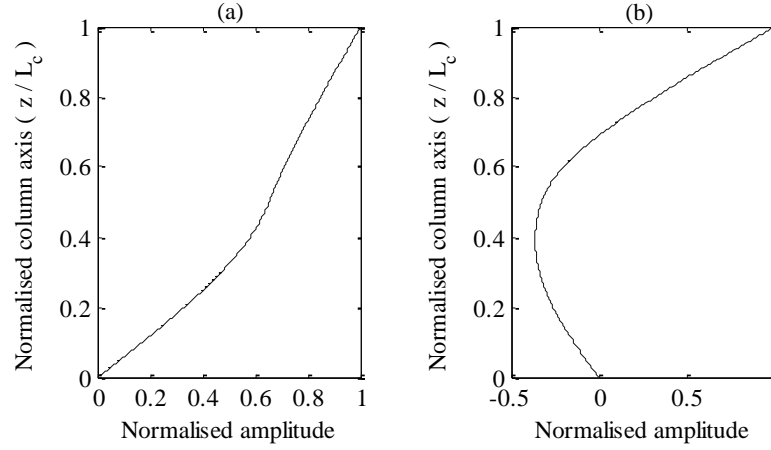
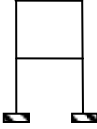


Figure 3. (a) The first and (b) second anti-symmetric in-plane mode shapes of equivalent column for the H shape frame.

Case 3 – Double-storey frame: Present method is also applied for analysing the vibration of double-storey frame fixed to the base. Shape of frame, non-dimensional properties and resulting natural frequencies are seen in Table 4. Results are validated by the natural frequencies obtained by Brasiliano et al.[13] and the finite element package. Material properties are given as the modulus of elasticity $E = 35 \text{ GPa}$ and the density $\rho = 2500 \text{ kg/m}^3$. Columns and beams have the same cross-section as $0.14 \times 0.24 \text{ m}^2$ and their lengths are $L_c = 5.6 \text{ m}$ and $L_b = 2.4 \text{ m}$ respectively. Note that Brasiliano et al. [15] take the shear effects into account with the assumption of Timoshenko beam theory which is not considered in this work. On the other hand, point connection of columns and beams are assumed in theoretical model while solid finite element model takes the area connection into account. These are main reasons of admissible differences seen between the results. Equivalent column mode shapes corresponding to calculated natural frequencies are illustrated in Figure 4.

Table 4. Natural frequencies for the first three anti-symmetric in-plane modes of the double-storey frame.

Frame figure	Frame properties			Natural frequencies (Hz)			
	$\frac{E_c I_c}{E_b I_b}$	$\frac{\rho_c A_c}{\rho_b A_b}$	$\frac{L_c}{L_b}$	Mode number	Brasiliano et al. [15]	Finite element analysis	Present work
	1	1	5.6/2.4	1	8.0633	8.54	8.4053
				2	26.2538	27.7	27.2177
				3	87.6998	92.0	88.5189

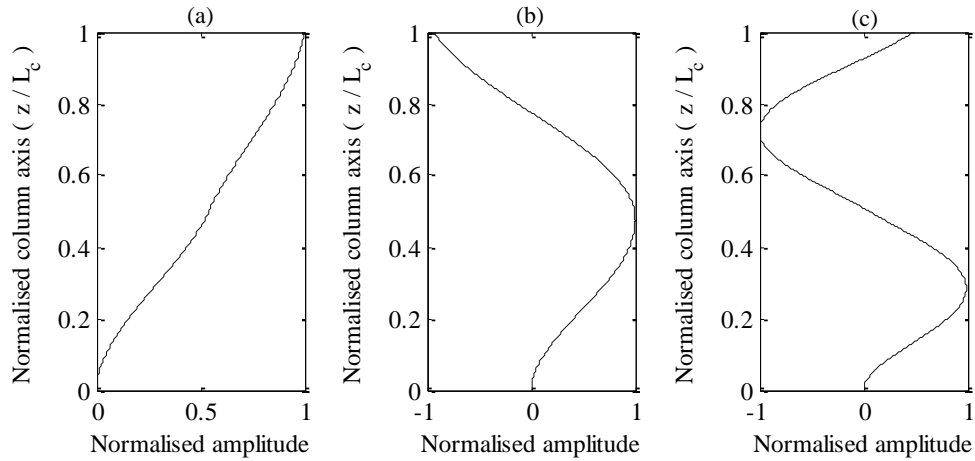


Figure 4. (a) The first (b) second and (c) third anti-symmetric in-plane mode shapes of equivalent column for the double-storey frame.

4. Conclusions

In this paper, analytical solution of frame systems is presented by defining lumped mass-stiffness parameters on equivalent columns. Continuous modelling allows using continuous solution method that is easily applied when the continuity and compatibility conditions are properly stated as represented in this work. Continuous solution presented needs matrices that have relatively small sizes varying with the number of storey. This is a significant advantage resulting in decrease of computational work load and processing duration.

Introduced model and solution method also have some limitations in terms of their applicability. First of all, it should be noted that considered deflection form of the beam is valid only for low anti-symmetric modes of frame structures. Secondly, columns should have close cross-sectional dimensions. Finally, presented model is validated for limited type of frame structures. However, model may be improved in future works by taking different beam deformation shapes into account for obtaining both symmetric and anti-symmetric vibration modes of multi-storey and/or multi-bay frames.

References

- [1] Kolousek, V. *Dynamics in Engineering Structures*. Butterworth and Co., London, 1973.
- [2] Chopra, A.K. *Dynamics of structures*. Prentice Hall, New Jersey, 1995.
- [3] Shepherd R. and Wood J.H. Normal mode properties of multi-storey frameworks. *Journal of Sound and Vibration* 3, 3 (1966), 300-314.

- [4] Dunder C., Mengi Y., and Kiral E. A higher order continuum model for the dynamic shear behaviour of multi-storey frames. *Earthquake Engineering and Structural Dynamics* 12 (1984), 761-775.
- [5] Bennon, S. Natural modes of vibration of simple frames. *Journal of the Franklin Institute* 243, 1 (1947), 13-39.
- [6] Gladwell, G.M.L. The vibration of frames. *Journal of Sound and Vibration* 1, 4 (1964), 402-425.
- [7] Laura, P.A.A., Filipich, C.P., and de Greco, B.H.V. In-plane vibrations of frames carrying concentrated masses. *Journal of Sound and Vibration* 117, 3 (1987), 447-458.
- [8] Wang, X., Wang, Y., and Zhou, Y. Application of a new differential quadrature element method to free vibration analysis of beams and frame structures. *Journal of Sound and Vibration*, 269, (2004), 1133-1141.
- [9] Lee, H.P. and Ng, T.Y. In-plane vibration of planar frame structures. *Journal of Sound and Vibration* 172, 3 (1994), 420-427.
- [10] Mei, C. In-plane vibrations of classical planar frame structures – an exact wave based analytical solution. *Journal of Vibration and Control* 16, 9 (2010), 1265-1285.
- [11] Mei, C. Effects of rotary inertia, shear deformation, and joint model on vibration characteristics of single-storey multi-bay planar frame structures. *Journal of Vibration and Control* 20, 8 (2014), 1224-1238.
- [12] Mei, C. An analytical study of dynamic characteristics of multi-story Timoshenko planar frame structures. *Journal of Dynamic Systems, Measurement and Control* 136 (2014), 1-10 No:DS-11-1365.
- [13] Zhang, R. and Gargab, L. Response features and parametric identification of shear-deformation buildings with continuous-discrete modelling. *Engineering Structures* 59 (2014), 375-385.
- [14] Sakar, G., Ozturk, H., and Sabuncu, M. Dynamic stability of multi-span frames subjected to periodic loading. *Journal of Constructional Steel Research* 70 (2012), 65-70.
- [15] Brasiliano, A., Doz, G.N., and de Brito, J.L.V. Damage identification in continuous beams and frame structures using the residual error method in the movement equation. *Nuclear Engineering and Design* 227 (2004), 1-17.
- [16] Ibrahim A.M., Ozturk, H. and Sabuncu, M. Vibration analysis of cracked frame structures. *Structural Engineering and Mechanics: An International Journal* 45 (2013), 33-52.
- [17] Grossi, R.O. and Albarracin, C.M. Variational approach to vibrations of frames with inclined members. *Applied Acoustics* 74 (2013), 325-334.
- [18] Ratazzi, A.R., Bambill, D.V. and Rossit, C.A. Free vibrations of beam system structures with elastic boundary conditions and an internal elastic hinge. *Chinese Journal of Engineering* 2013 (2013), 1-10 ID 624658.

Kemal Mazanoglu, Assist. Professor: Usak University, Engineering Faculty, Department of Mechanical Engineering, 1 Eylul Campus, 64200 Usak, Turkey (kemal.mazanoglu@usak.edu.tr).

Elif C. Kandemir-Mazanoglu, Assist. Professor: Usak University, Engineering Faculty, Department of Civil Engineering, 1 Eylul Campus, 64200 Usak, Turkey (elif.kandemir@usak.edu.tr).

Numerical simulation of suspension system for autonomous tracked hybrid vehicle (VIB183-15)

Arkadiusz Mężyk, Wojciech Klein, Tomasz Czapla, Gabriel Mura

Abstract: One of the most important components of high speed tracked vehicle is efficient and effective suspension system. The vehicle should be able to operate both in a rough terrain for performing engineering tasks as well as hardened road during high speed operation. This is especially important for autonomous platform with hybrid propulsion system which should not be exposed to severe vibration. In this case critical electronic and electric parts must be protected to ensure the reliability of the vehicle. The paper presents a methodology of determination of dynamical parameters of suspension system of autonomous high speed tracked platform with total weight about 5 tonnes and hybrid propulsion system. As a universal and cost-efficient, torsion-bar system was chosen. One of the most important issues was determining correct track tensioning – in this case an electromechanical system was applied. The selection of system parameters was performed with using numerical model based on multibody dynamic approach. The results of numerical analysis allow estimate the sensitivity of most defined system parameters in view of vibration absorption..

1. Introduction

The suspension system of tracked vehicle is a set of components and mechanisms joining the axis of one or interconnected wheels with a single spring element, the damping element (damper) and a stabilizer (wheel arm) to the hull. The main aim of suspension system is transfer the weight force of the vehicle through wheels or tracks to the ground and isolating the vehicle's components of terrain in order to increase the safety of users, increase the viability of equipment and provide stability of vehicle construction [1].

From the time of establishment of the first tracked vehicle till this day designers developed many variants of the suspension. These can be divided into rigid, semi-rigid and flexible. In high speed track vehicles in particularly military combat machines are used different types of active or semi-active flexible suspension. These systems providing electronically controlled suspension systems which are more and more often also applied in wheeled vehicles [2-5].

Depending on how the wheels are connected to each other and with the hull, the flexible suspension can be divided into individual, locked and mixed. Most modern combat tracked vehicles using variants of the suspension based on the elastic element in the form of the torsion bar or a coil spring with a hydraulic or friction damper or hydro-pneumatic suspension [1].

In the figure 1 is presented a curve of comfort in function of safety, which refers to vehicle transporting people. Although, in this paper is analyzed unmanned vehicle but it is also important to select correct suspension system due to safety of electrical equipment.

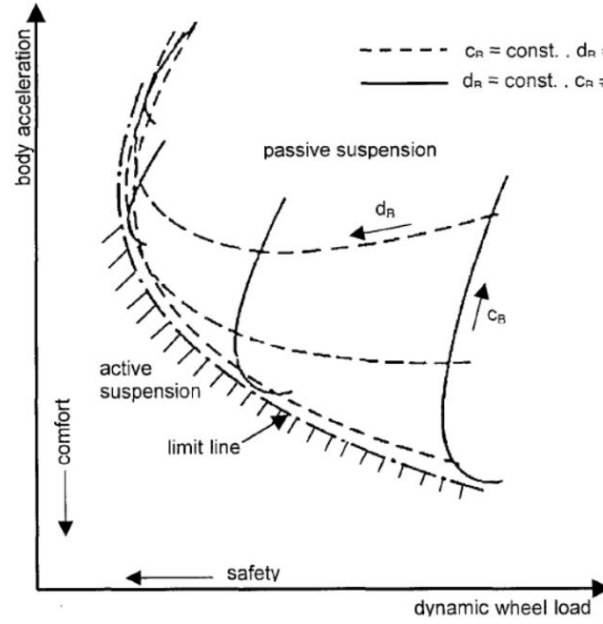


Figure 1. Design conflict between comfort and safety [5].

In aim of multibody dynamics analysis the system was reduced to solving an equations of motion. They are second order ordinary differential equations (ODE), often connected with algebraic equations [6-8]

From the kinematic constrains and driving components it is possible prepared global vector of constraints denoted as Φ , presented below:

$$\Phi(q, t) = 0, \quad (1)$$

where: q is a vector of generalized coordinates and t stands for time.

In the system of parts subject to motion constraints, the bodies are connected together by internal forces of the kinematic. The reaction that act in the joints and are rated to the forces that constrain movements are marked by the vector g^Φ that is the sum of the active and passive forces, marked g that describes all the forces that act on the system and its motion is described Eulerian-Lagrange equation below [6-8]:

$$M \dot{h} = g + g^\Phi, \quad (2)$$

where: M is a global matrix of inertia that comprises masses and an inertia parameter for all the bodies within the system, \dot{h} is the vector of accelerations and g represents the vector of generalized forces.

For a multibody system with constraints that is made up of n bodies, the motion equations for a single body can be repeated n times in order to find out equations for the whole system. It leads to equations of motion for a system with constraints, where the equations are written as [6-8]:

$$M \dot{h} - B^T \lambda = g, \quad (3)$$

The above equation (3) represents a system of n differential equations with $n+m$ unknown variables that correspond to the \dot{h} vector, that represents acceleration, and the vector of Lagrange multipliers. To resolve the system of these equations it is necessary to prepare m additional equations. These additional equations should be obtained from the constraints equations so that in order to ensure that both equations of motion, and kinematic constraints are fulfilled. Unfortunately, in case of this procedure, it is very difficult to find a solution for a multibody system of $n+m$ algebraic and differential equations. That's why the second derivatives of constraints are substituted with equations of constraints on the level of acceleration [6-8]:

$$\ddot{\Phi} = 0 \equiv B \ddot{h} = \gamma^*, \quad (4)$$

The equations (4) are connected with the equations of motions, thus the equations for the constrained multibody system can be presented as a system of differential-algebraic equations (DAE):

$$\begin{bmatrix} M & B^T \\ B & 0 \end{bmatrix} \begin{bmatrix} \dot{h} \\ -\lambda \end{bmatrix} = \begin{bmatrix} g \\ \gamma^* \end{bmatrix}, \quad (5)$$

where: B is the modified matrix of a Jacobian determinant that is expressed by the equation:

$$B = \left[\Phi_{r_1}; \frac{1}{2} \Phi_{p_1} L_1^T; \dots; \Phi_{r_{nb}}; \frac{1}{2} \Phi_{p_{nb}} L_{nb}^T \right], \quad (6)$$

and γ^* is a modified right-hand side of the equation of acceleration. Now, the total number of equations is the same as the total number of unknown variables that correspond to values of acceleration and Lagrange multipliers [4,6,8]. Moreover, λ can be obtained as an explicit function of (q, \dot{q}) and then q is characterized by a second-order ODE. In this way standard ODE software can be applied directly for computing solutions of the DAE [9].

In the market there are many CAE software offering tools to compute multibody dynamics analysis, but authors use only LMS Virtual.Lab to simulate mobility of tracked vehicle.

2. Lay out of numerical model and analysis condition

The model of tracked platform was developed based on the identified mass-geometric parameters. The geometric model of vehicle was divided into elements that do not change their positions relative to the assumed coordinate system in the vehicle movement (hull and cabin), and the elements that change position relative to the hull during motion (wheels, torsion shafts and tracks). Torsion shafts that are linked with the holes in the hull were modelled as revolute joint. The constraints occurring between the individual elements of the suspension system and the characteristics of torsion shafts, modelled as elastic-damping elements (*RSDA*), their torsional stiffness determined on the basis of experimental investigations and estimated material damping were taken into account (see figure 3).

To demonstrate contact forces in the numerical model there was used *Sphere to Extruded surface Contact* function, which is based on simple Hertzian contact. This type of contact was used between wheels and track links, and ground and track links. The representation of rubber track is a group of spheres. In particle each link is represented by 3 spheres and duplicate on rest of the track by module *Discrete Track*, what is shown in figure 3. Discrete Track allows only to simulate track divided to segments, and rubber track can be represented by group of rigid segment with flexible joints. Unfortunately flexible joint between every link increase time of computing of simulations. That's why authors decide to simplify it to simple rotary joint between links, so the tracks in this case is inextensible.

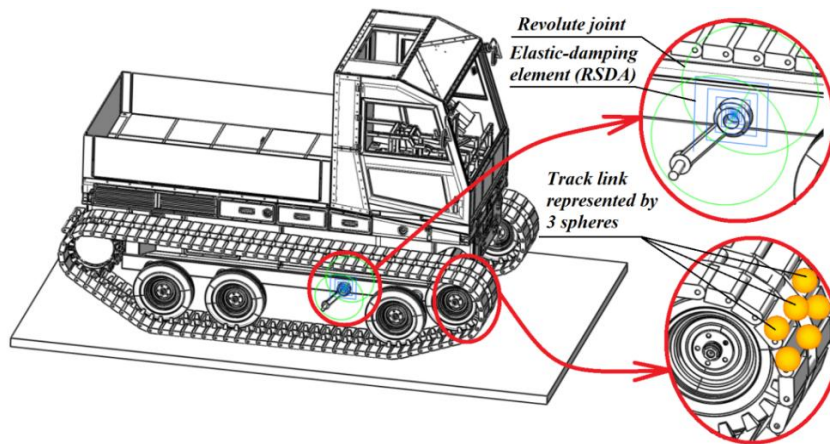


Figure 2. Scheme of layout of numerical model and track link represented by spheres in contact.

Each body from multibody system is based on CAD model of prepared concepts. To each model of wheel, hull or segment of track is assigned material properties (e.g. density). This properties of material conform to material (steel, rubber, concrete) which are established to make from it elements of platform and ground. Based on volume and density of each element was automatically calculated mass and inertia properties, which were used in dynamics analysis.

In each contact force there are defined real value of material properties. The material properties are suitable for material from which contacting parts were made. In the table below it can find contact parameters of all used material and main dynamic and kinematic parameter of multibody simulation of analysed vehicle (see table 1).

Table 1.Parameter of multibody simulation.

Suspension and hull parameter					
Total mass [kg]		Velocity [km/h]		Stiffness of sin-gle node [Nm/rad]	Damping of single node [Nms/rad]
5000		30		9615	200
Contact parameters					
Material	Where was used	Young modulus [Pa]	Poison ratio	Coefficient of restitution	Coefficient of friction
steel	sprocket, hull	2,1E11	0,3	with rubber: 0,5	with rubber: 0,6
rubber	wheels, track	1E8	0,5	with concrete 0,5 with rubber: 0,3 with steel: 0,5	with concrete 0,8 with rubber: 1 with steel: 0,6
concrete	ground	2,7E10	0,2	with rubber: 0,5	with rubber: 0,8

In this paper authors assumed three simulations of mentioned tracked vehicle which passing four triangular obstacle with velocity equal 30 km/h. The arrangement and dimensions of this obstacle is presented in figure 3.

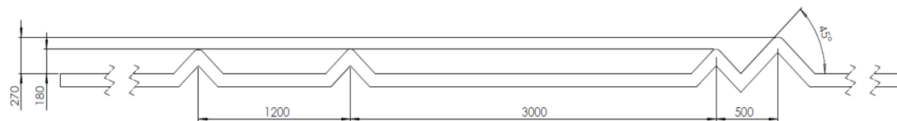


Figure 3. Arrangement and dimensions of triangular obstacles.

3. Results of analyses

In each of three simulations is different tension of track and authors of this paper compared the results to conclude how the tension of track affects on behaviour of tracked vehicle passing obstacle. The tension of track is realized by different position of idler wheel relative to hull of vehicle. Mentioned

three stages of position of idler wheel is 0 mm, 20mm and 50 mm. As a mine parameter which authors used to compare is a displacement and acceleration of centre of mass of the platform or angular displacement of hull. The comparison is shown in the figures 4-6. It is possible to notice that increasing the distance between hull and idler (increasing the tension of track) also increase amplitude of displacement (see figure 4) of hull. It is probably caused by increasing the suspension stiffness. Also curves with acceleration in z axis and angle displacement of hull confirms that the amplitude of vibration is the greater the greater is the tension of the track. This variation of suspension system gives possibilities to apply automatic tensioning system what change simple suspension system to suspension with variable characteristics.

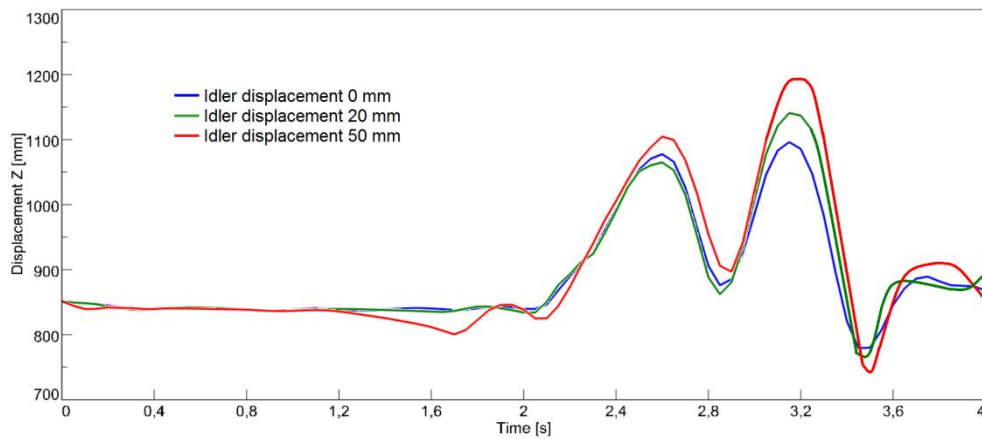


Figure 4. The displacement of tracked vehicle mass centre for different set point of idler wheel.

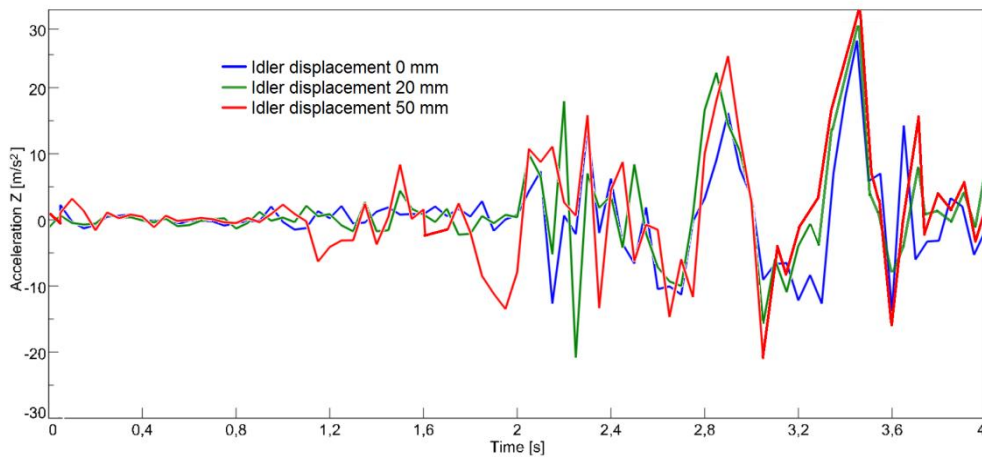


Figure 5. The acceleration of tracked vehicle mass centre for different set point of idler wheel.

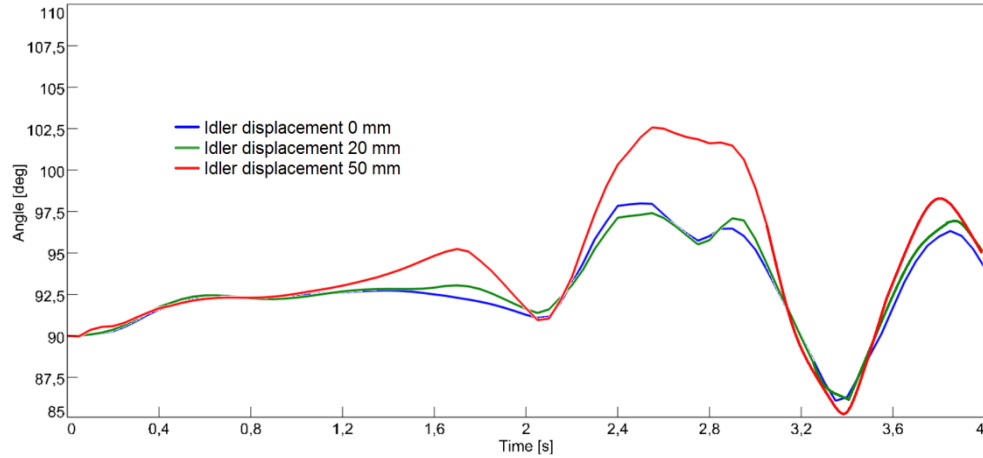


Figure 6. The angle displacement of tracked vehicle hull for different set point of idler wheel.

In the figure 7 is presented a screen shot of animation of results of analysis in the moment of passing the obstacle by the platform. It is possible to notice that platform ride on the first and second obstacle jump over the ground and land on the third and fourth obstacle, then bounce again. The arrangement of obstacle is targeted because authors assumed the most extremely drive of tracked platform.

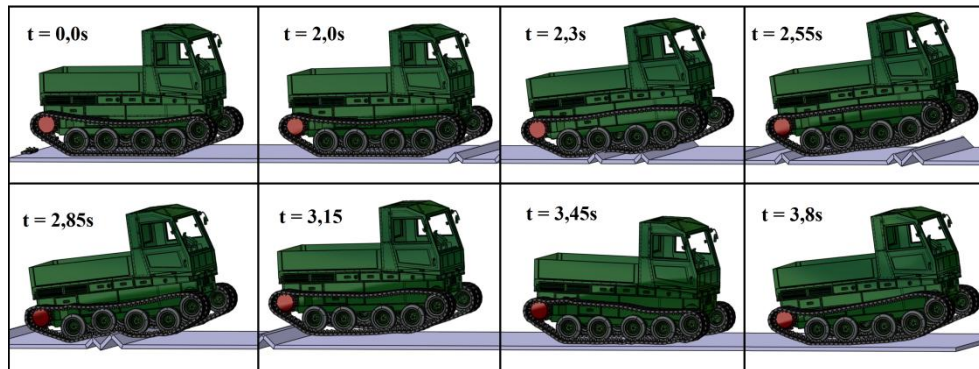


Figure 7. Screenshots of animation of results.

4. Idler wheel

The simulation results indicates need of apply idler mechanism in the aim of the active vibration control systems. In order to achieve active vibration reduction and correct track tension, hydraulic track tensioning system was implemented. Furthermore, hydro-pneumatic accumulators are applied as energy storage and dissipation system in order to protect the track in case of high dynamic loads. Mechanical configuration of hydraulic track tensioning system is shown in figure 8. Hydraulic

cylinder is connected to the idler lever axis and as it extends, pushes the idler forward causing track tension.

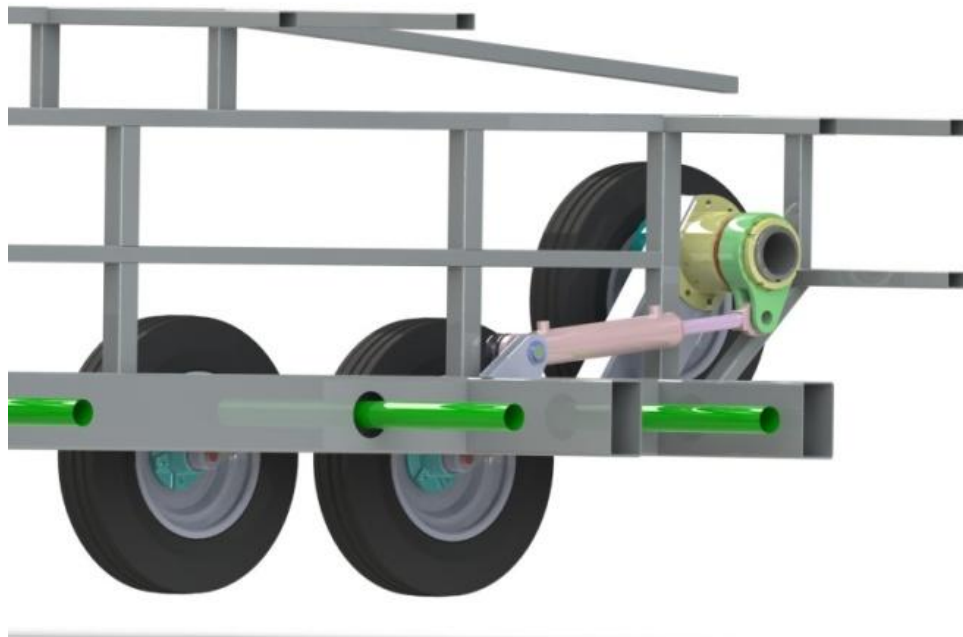


Figure 8. The model of idler mechanism.

Hydraulic connections diagram is shown in figure 9. Hydraulic pump is providing pressure for system operation. Proportional valve is used to generate demanded pressure for hydraulic cylinder responsible for applying the tension force. Another circuit contains hydro-pneumatic accumulator that allows to manage the energy consumed by tensioning system. While the idler absorbs the energy from the track caused by suspension operation, hydraulic cylinder is pressed down and the fluid is transferred via flow control valves to the accumulator. If the load exceeds the certain value, relief valve protects the system from failure.

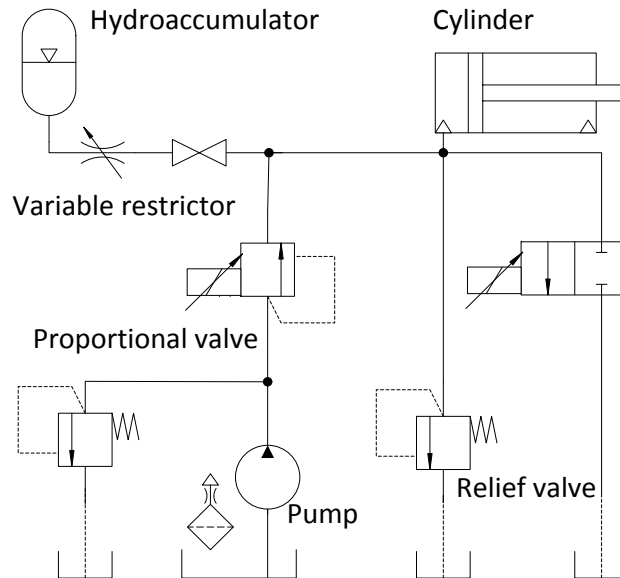


Figure 9. Hydraulic track suspension system – simplified connection diagram.

5. Conclusions

Multibody analysis is very useful to predict behavior of tracked vehicle before building costly prototype. Thanks to the multibody analysis of vehicle or device it can avoid more engineering mistakes than in simple CAD designing.

Increasing the distance between idler wheel and hull, it also increase the total stiffness of vehicle suspension resulting in larger amplitude of displacement of centre of mass of platform during passing obstacle. With lower tension of track it can reach lower hull displacement. Moreover with adjustable idler wheel it is possible to affect to suspension parameter.

Assumed suspension parameter is restrainedly correct in the context of safety of electrical equipment of platform.

It important to remember that in performed simulations were used inextensible rubber track. If becomes an opportunity to perform analysis with extensible track, it is advisable to perform it.

There is a need to perform a research on real vehicle to compare results of numerical analysis and real behavior of platform.

Acknowledgments

This work is carried out in a project agreement No. PBS1/A6/15/2013 (Project Title “Multipurpose engineering hybrid vehicle”).

References

- [1] Ogorkiewicz R. *Technology of Tanks*. Janes Information Group, Virginia, 1991
- [2] Andrzejewski R., Awrejcewicz J. *Nonlinear Dynamics of a Wheeled Vehicle*. Springer Science+Business Media, New York, 2005.
- [3] Sibielski M., Konieczny J., Kowal J., Raczka W., Marszałik D. Optimal Control of Slow-Active Vehicle Suspension-Results of Experimental Data, *Low Frequency Noise, Vibration and Active Control*. 2012, Volumes 32, p. 99–116.
- [4] Mężyk A., Switonski E., Kciuk S., Klein, W. Modelling and investigation of dynamic parameters of tracked vehicles, *Mechanics and Mechanical Engineering*, 2011, 15.4: 115-130.
- [5] Hönlinger, M., Glauch, U.: Mobility analysis of a heavy off-road vehicle using a controlled suspension, *Reduction of Military Vehicle Acquisition Time and Cost through Advanced Modelling and Virtual Simulation*, Paris, 2002.
- [6] Kaliński K., Buchholz C. Mechatronic design of strongly nonlinear systems on a basis of three wheeled mobile platform. *Mechanical Systems and Signal Processing*, 2015, Volumes 52, p. 700-721.
- [7] Gillespie R.B., Colgate J.E.: A survey of multibody dynamics for virtual environments. *Proc. Int. Mechanical Engineering Conf. Exhibition*, 1997.
- [8] Flores P., Ambrósio J.: Revolute joints with clearance in multibody systems, *Computers & Structures*, 2004, Volume 82, pages 1359-1369.
- [9] Ciarlet P.G., Lions J.L. *Handbook of Numerical Analysis Volume VII.*, Elsevier Science B.V., 2002.

Arkadiusz Mężyk, Professor: Silesian University of Technology/ Faculty of Mechanical Engineering/ Department of Theoretical and Applied Mechanics, ul. Konarskiego 18a, 44-100 Gliwice, Poland (arkadiusz.mezyk@polsl.pl).

Wojciech Klein, Ph.D.: Silesian University of Technology/ Faculty of Mechanical Engineering/ Department of Theoretical and Applied Mechanics, ul. Konarskiego 18a, 44-100 Gliwice, Poland (wojciech.klein@polsl.pl).

Tomasz Czapla, Ph.D.: Silesian University of Technology/ Faculty of Mechanical Engineering/ Department of Theoretical and Applied Mechanics, ul. Konarskiego 18a, 44-100 Gliwice, Poland (tomasz.czapla@polsl.pl).

Gabriel Mura, M.Sc (Ph.D. student): Silesian University of Technology/ Faculty of Mechanical Engineering/ Department of Theoretical and Applied Mechanics, ul. Konarskiego 18a, 44-100 Gliwice, Poland (gabriel.mura@polsl.pl).

**Research on vibrations in the train driver's cab in the course
of shunting activity
(LIF274-15)**

Jakub Młyńczak, Rafał Burdzik, Ireneusz Celiński

Abstract: Vibrations occurring in dynamic systems operated by men may exert negative impact on health. When considering means of transport and a man as the driver, the exposure to vibration proves even more important, since vibrations exert direct influence on safety in transport and comfort of passengers. The research on vibration in means of transport must entail many different dynamic forces which may occur while driving. Therefore the paper addresses research on locomotives in the course shunting. The scope of the experiments performed included measurement of vibrations in the SM42 locomotive cabin. The research method included application of proprietary mobile application installed on a mobile device. The acceleration of vibrations in the train driver 's cab was registered. Making use of a GSM mobile phone's GPS module, the vibration characteristics recorded can be correlated with the current geographical position of the locomotive at the station. This enables assessing the impact of vibrations on the driver depending on the activities conducted during the shunting. Furthermore, the system is assessed based on the influence of the subgrade on the vibration characteristics.

1. Introduction

Mechanical vibrations transferred in vibrating systems operated directly by a man may exert negative impact on the latter's organism and, as a rule, it is exactly what happens after prolonged operation. Such a condition is often diagnosed too late. The vibration impact process frequently causes numerous and usually serious somatic disorders in the organism of the person operating the vibrating system [14,15]. The scale of pathological changes, which may be persistent or even irreversible, depends on vibration characteristics, exposure time and the contact area in a man-device system [6-9]. Conditions connected with the negative effect of accelerations are generally referred to as kinetosis [11,12]. One may also speak of vibration stress. It should be noted that these conditions are normal responses of the organism to selected motion stimulants [11].

In this article, the authors have addressed and discussed selected aspects of analysis of the vibration impact on a shunting locomotive driver. In publications concerning this subject, problems of the vibration impact on people are mainly analysed with regard to manually operated machines and devices on account of the scale of the phenomenon. In cases when the phenomenon of vibration impact applies to the entire body, it may primarily cause dysfunctions of the abdominal cavity organs

(especially stomach), whereas it also affects the abdomen in women. Other effects observed in practice in a vibrating system include fatigue, often prolonged, headaches, sleep dysfunctions and the trembling limb symptom, typical of those who operate vibrating equipment. However, in the case discussed, i.e. the whole-body impact of vibrations, this problem may not only concern hands and arms [6-9,11,12].

Prolonged exposure of the human organism to vibrations may trigger a spread of disorders to other internal organs. The fact that effects of vibrations may cause diseases of the cardiovascular, respiratory, digestive as well as musculoskeletal systems has been confirmed [6-9,11,12]. Vibrations affecting the entire body of a machine operator may also lead to changes in the pulse as well as in the vascular and urinary system. Besides the direct hazard to the health and life of a worker exposed to whole-body vibrations, one can also observe reduction of the latter's immunity. Therefore, from the employer's perspective, one which entails maintaining continuity and safety of operation, hazards connected with vibrations occurring in locomotives (or more broadly, in transport) can be divided into short-lasting, which may involve hazard to traffic safety under certain circumstances, and long-lasting, causing deterioration of operating efficiency and loss of highly qualified workers for prolonged periods of time due to sick leaves [6]. In the recent years, absence of highly qualified and experienced drivers and operators has been particularly acute.

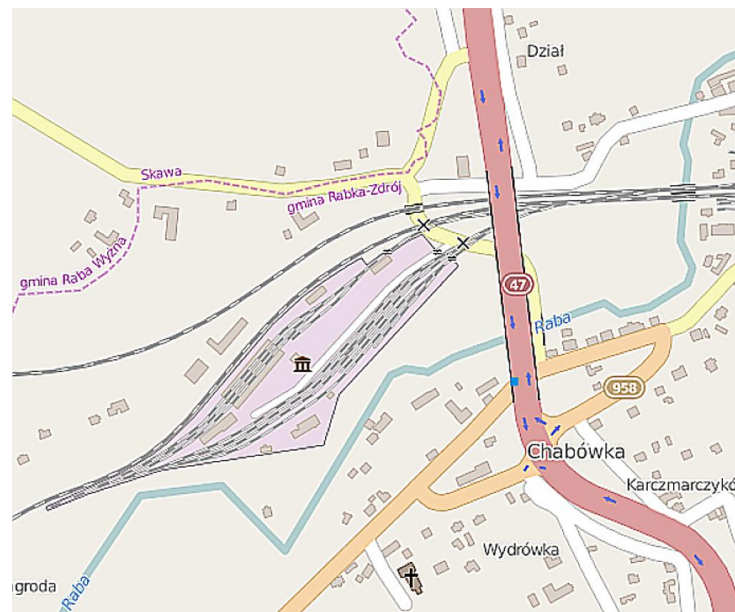


Figure 1. Site plan of the Chabówka (Poland) station where the measurement was conducted. Source: OSM [1,2].

Figure 1 is a site plan of the Chabówka (Poland) station, i.e. the area where the studies in question were undertaken (49.595109N, 19.926443E). Pilot studies were performed using the SM42 series diesel locomotive (Figure 2).



Figure 2. SM42 locomotive used in the studies. Source: authors' photographs.

In this article, the authors have proposed a useful method for measuring vibrations in a rail vehicle using a smartphone application they have developed. In the course of the measurement, a smart phone is placed on a locomotive in order to determine values of linear accelerations affecting the driver's cab. It should be noted that the main difficulty in studying the impact of vibrations on the human body is that all these actions are performed by means of complicated measuring apparatus. Therefore, it is usually impossible to run such tests on a sufficiently large sample (of population) required to establish the correlations functioning in a system comprising the acceleration and biological parameters (health condition of machine operators). On account of simplicity and virtually non-existent financial and organisational expenditure, a method such as the one proposed in the article enables holistic studies to be conducted upon the entire population of interest from the perspective of the observation objective. Moreover, this method allows for the studies to be conducted on a continuous basis, which further makes it possible to correlate the impact of vibrations on the diesel locomotive operators' health in a more reliable manner. When using SMS (Short Message Service) or GPRS (General Packet Radio Service) channels to transfer measurement data, this method may also be used in real time.

2. Methodology

In this article, the authors have focused on validating the simplified method proposed for purposes of vibration measurements in a vibrating system, namely a cabin of the SM42 series diesel locomotive

driver while the latter is performing shunting activity. The simplicity of the method consists in using an unattended mobile application developed by the authors and installed on a mobile phone placed inside the driver's cab. The mobile phone to be used in the measurement should feature a standard accelerometer (MEMS) functionality and a GPS receiver [4,5]. Optionally, the measurement may be conducted using devices such as a tablet or a computer, in which case it does not allow for real-time recording and simultaneous analysis of events according to the holistic approach addressed in the article (since most such devices lack the GSM system).

The method discussed requires virtually no financial or organisational expenditure. The cheap test mobile phone used in the studies, representing the *value end* segment of products, featured an accelerometer system used to record changes occurring in linear accelerations of the driver's cab within a 10-millisecond interval assumed (the interval may vary within a wide range of values). Additionally, using the GPS system installed in the same mobile phone, vibration characteristics may be correlated with the physical position of the locomotive performing the shunting activity within the station's track system (Figure 4). The locomotive trace recorded in the course of the studies has been illustrated in Figure 4. As an outcome of follow-up analyses (not discussed in this article), the locomotive trace measurement enables assessment of the vibration impact on the driver depending on the shunting operations performed.

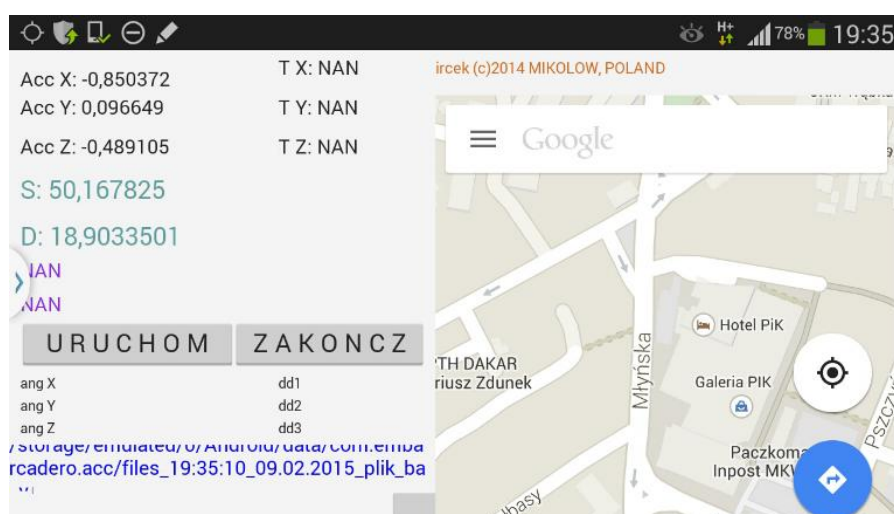


Figure 3. Measuring application. Source: authors' own materials.

As shown in Figure 3, the mobile application installed on the phone measures linear acceleration in three axes (Figure 3). The phone is mounted inside the driver's cab with the upper part of the body oriented towards the driving direction. With such a phone arrangement, the locomotive motion accelerations are designated as ACC_Y, lateral accelerations as ACC_X, and vertical accelerations as

ACC_Z. At the same time, using the GPS receiver installed in the phone, one reads the physical location of the locomotive within the range of the vehicle positions (latitude and longitude). If the mobile phone also features a gyroscope, the application can be used to measure angular accelerations as well (Figure 3). While the application is running in real time, in a window displayed on the left-hand side of the application home page (actually referred to as activities), the measuring system's geographical position is shown. The test application has been developed for the Android platform.

3. Analysis

Another aspect of assessment of the vibration impact on the driver in such a measuring system is the railway track subgrade condition, which may also be correlated with the use of the vehicle position measurement by means of GPS. The observations conducted in the course of the studies were compared with the traction characteristics of the test vehicle, namely the SM42 series diesel locomotive. The studies in question were exclusively aimed at validating the method proposed, and consequently, broad-scale follow-up statistical studies will be undertaken. In a longer time perspective, the authors are planning to conduct extended measurements using dedicated microcontrollers combined with tests of basic biometric parameters of the driver (in order to define biophysical profiles).

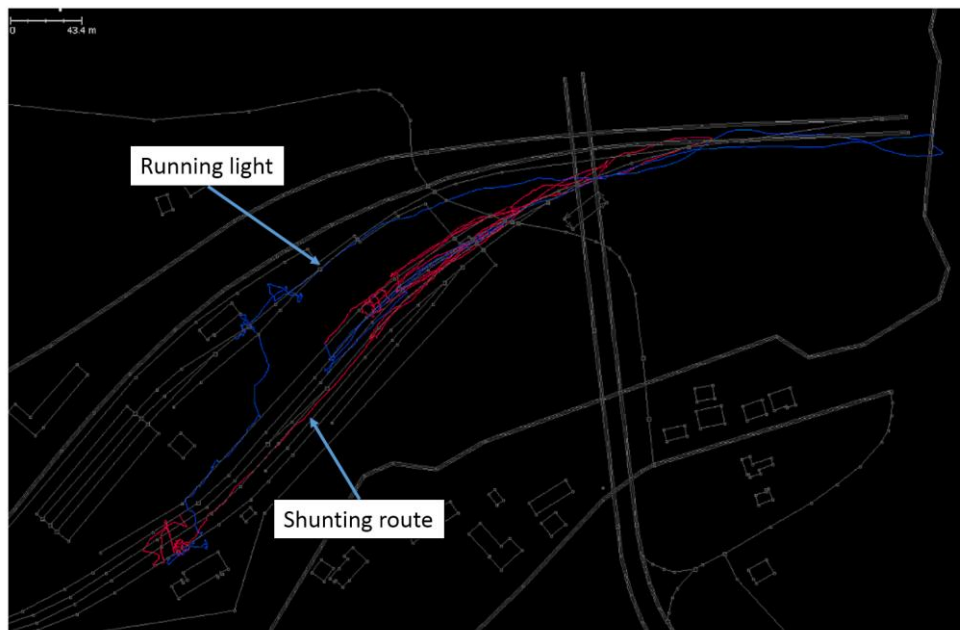


Figure 4. Trace of the SM42 locomotive performing shunting activity at the Chabówka station.

Source: OSM/JSOM [1-3].

Figure 4 illustrates the trace of the SM42 locomotive positions while it was performing shunting activity at the station. The trace of the locomotive performing the said operations has been marked in golden and celadon colours (the division is only due to technical and not subject related reasons). In Figure 4, one can clearly see certain inaccuracies in the GPS signal measurements, namely the deviations between the locomotive positions and those of the track infrastructure elements (ranging up to several metres). However, it is not an obstacle in assigning the locomotive position to major infrastructure elements as the vehicle was performing the shunting activity. In dubious cases, one may correct the relevant positions manually.

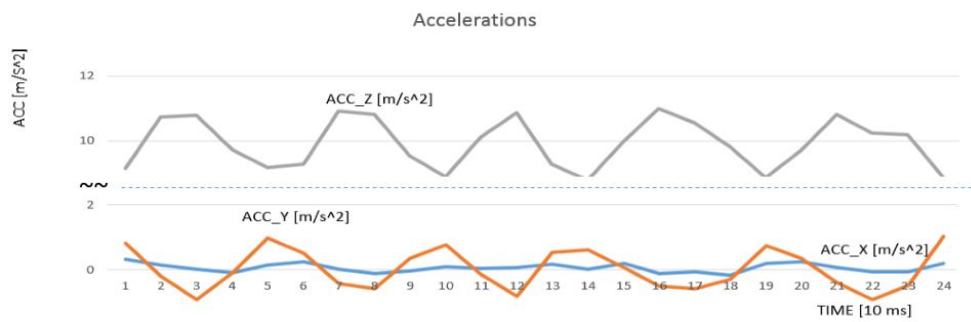


Figure 5. Visualisation of data from the output file containing linear accelerations – sample run in a straight section of the station track. Source: authors' own materials.

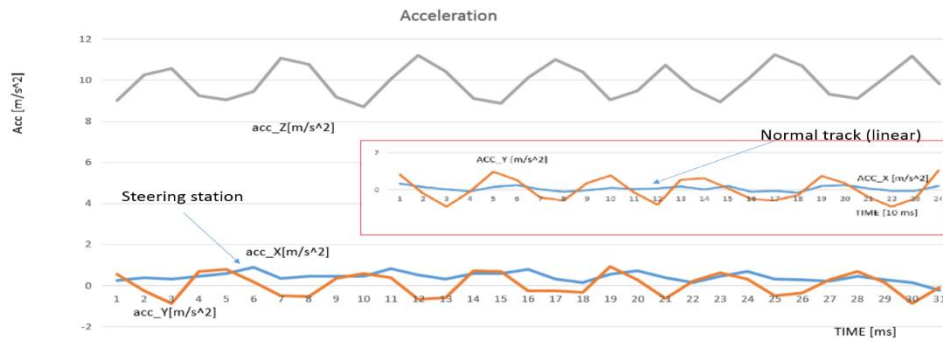


Figure 6. Visualisation of data from the output file containing linear accelerations – sample shunting run in a track section featuring switches. Source: authors' own materials.

Figures 5 and 6 provide a comparison of linear accelerations recorded while running on different track sections at the station in the course of shunting activity. Figure 5 illustrates linear accelerations in a straight section of the station track. Figures 5 and 6 provide a collation of linear accelerations

recorded in a straight track (smaller fragment in the red frame) and in a section with switches. These graphs show how vibrations from different elements of the track infrastructure are reflected in the data recorded by measuring devices. As regards the travel to the railway siding, one can clearly notice that characteristic ACC_X increases across the entire measurement range.

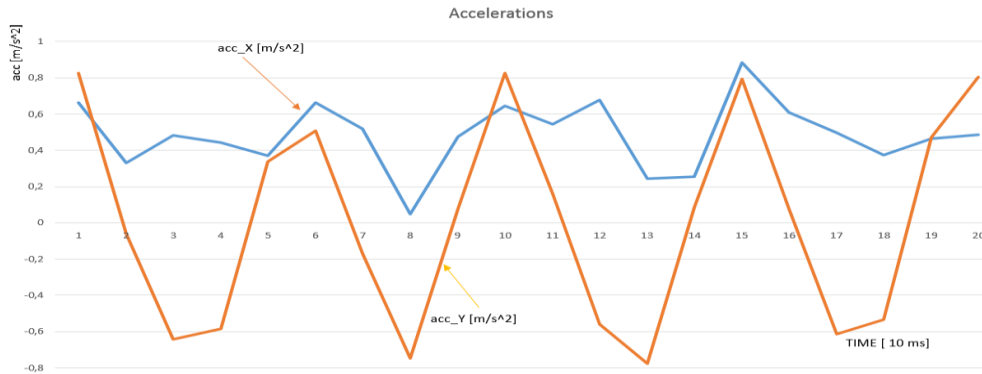


Figure 7. Selected example of strong vibrations experienced in the course of shunting activity at the Chabówka station. Source: authors' own materials.

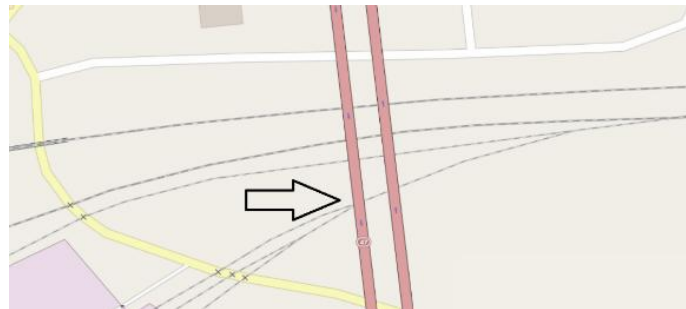


Figure 8. Location of particularly strong vibrations observed in the course of shunting activity at the Chabówka station. Source: authors' own materials.

Figure 7 is a graph illustrating particularly strong vibrations occurring in the longitudinal and the transverse axis of the rail vehicle, as recorded in the course of tests. These vibrations were observed at a turnout located in a direct vicinity of the national road commonly referred to as “Zakopianka” (Figure 8). The figure demonstrates how the vibration frequency increases in a horizontal axis perpendicular to the rail vehicle travel direction.

Table 1. Base statistics

Time [sec]/ parameters	Mean [m/s ²]			Std [-]		
	Acc_x	Acc_y	Acc_z	Acc_x	Acc_y	Acc_z
<0÷1)	0.073694	-0.00331	10.05646	0.134332918	0.571059435	0.761548707
<1÷2)	0.061601	0.013521	10.30152	0.140554178	0.581783612	0.750487929
...
<2,279÷2,280>	0.519932	2.359286	9.746554	0.28375766	0.140438405	0.784827188
All	2.159828	0.138867	7.861463	4.061383536	1.036011861	3.918128238

Source: authors' own elaboration.

Table 1 provides a sample analysis of measurement data obtained based on the accelerometer readouts taken within 38 minutes of the measuring device operation (ca. 200,000 single readouts). The data have been collated with reference to mean values and standard deviation for linear accelerations recorded in individual axes. The data have been computed for individual time intervals and globally for the entire testing period (only four intervals have been provided). The values indicated by the instrument can be compared in terms of the differences between them with reference to the measurement time and the locomotive position. In Table 1, one can clearly notice considerable deviations of individual values in the measurement time (they have been marked with different colours). Based on such an analysis, as demonstrated in Table 1, the shunting activity schedule can be adjusted in order to minimise negative effects occurring in the course of the shunting activity (considerable acceleration deviations observed).

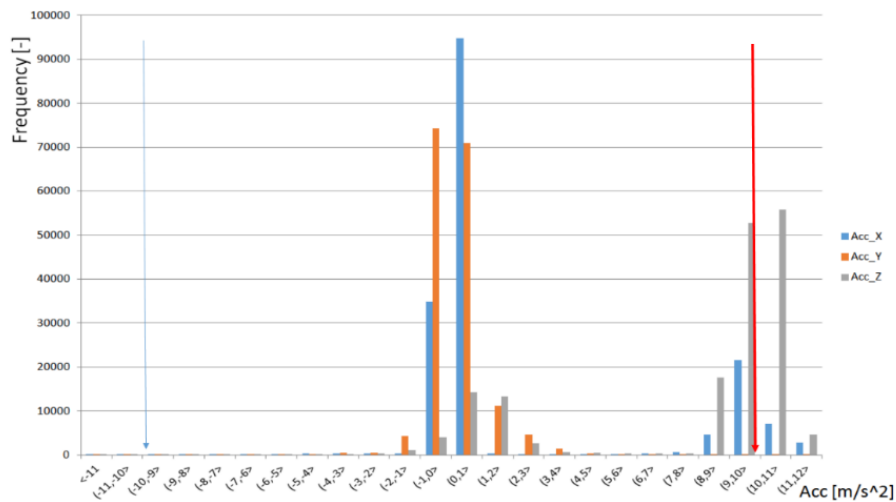


Figure 9. Frequency distribution of linear accelerations. Source: authors' own materials.

Figure 9 shows three frequency distribution graphs for linear accelerations recorded in all axes. The range of variability of each linear acceleration has been divided into twenty four class ranges from -12 [m/s²] to +12 [m/s²]. Such a graph may be referred to as a spectrum of vibrations for a measuring section in which the locomotive conducted the shunting activity. This graph demonstrates the relatively homogeneous characteristic of accelerations in the direction of the locomotive travel (positive aspect). At the same time, one may notice typical abrupt changes to the accelerations occurring in the vertical axis, which may be a consequence of the technical condition of the track subgrade at the given station facility where the measurement was taken. Similar changes are typical of accelerations in the rail vehicle lateral axis.

The methods discussed above are some of the simplest chosen ways to measure the rail vehicle vibrations. The characteristic of the vibrations experienced inside the driver's cab depends on a number of elements, such as the track geometry (longitudinal and transverse slope), the subgrade condition, the rail vehicle suspension condition, atmospheric conditions, the rolling stock load and many more:

$$ACC_i(t) = f(g_1(t), g_2(t), sp(t), sw(t), wa(t), ca, \{\zeta\}...) \quad (1)$$

where:

$ACC_i(t)$ - acceleration in the i^{th} axis [m/s²],

$g_1(t), g_2(t)$ - track geometry parameters,

$p(t), sw(t), wa(t), ca, \{\zeta\}...$ - characteristics of: subgrade condition, suspension condition, atmospheric conditions, rolling stock load and random factors.

It should be noted that one can normalise values of the vibration parameters as far as railway infrastructure elements are concerned. Under such normalisation, it is possible to define an array of permissible vibrations for individual elements of known geometrical parameters and for known means of transport. Such an array may set the range of vibrations being permissible under typical track operating conditions:

$$\Delta ACC_X(t, L); \Delta ACC_Y(t, L); \Delta ACC_Z(t, L) \quad (2)$$

where:

$\Delta ACC_X(t, L)$ - range of correct (permissible) accelerations,

t, L - age of track infrastructure elements,

$L = \{W, LO\}$ - geographical location of infrastructure elements (W - latitude, LO - longitude).

Any anomalies revealed in the course of the measurement in terms of the values envisaged as

standard ones (2) should be considered as a premise for detailed analysis of railway traffic safety. Moreover, the fact of recording vibrations stronger than permissible should lead to reducing the time of locomotive driver shifts worked at track sections diagnosed as above.

4. Conclusions

The intention of the authors of this article was to describe a concept of an extremely simple method enabling holistic studies of the process of vibration impact on drivers with reference to the entire population examined. Having satisfied specific requirements, one may conduct such a study in real time. Consequently, performing such a distributed type of study allows for statistically reliable conclusions to be formulated as regards the impact of the vibrations in question on the health condition of persons operating rail vehicles, and not only of them. Not until the vibration impact is measured based on studies conducted across the entire population (e.g. locomotive drivers) may one correlate linear acceleration characteristics with all health conditions observed (diagnosed) in the population of interest. A problem of secondary nature, yet particularly difficult to solve, is to link these cases with one another. However, it is not a matter of interest for the authors, as it requires advanced medical expertise.

The authors would like to highlight yet another interesting aspect of the method proposed. While conducting studies, one can also measure basic biological parameters, thus making it easier to further correlate health conditions revealed in a group of locomotive drivers and to determine their aetiology (particularly for the conditions arising on grounds related to the vibrations exclusively). Such an examination may not only concern locomotive drivers, but also other members of train personnel, a high considerable of whom – especially in passenger lines – accounts for women. In this respect, one should particularly emphasise the danger of pregnant women being exposed to vibrations. Yet another interesting field of study is a group of railway workers exposed to vibrations and being unable to observe the field in front of the vehicle due to negative aspects of such a location on account of vibration stress.

It should be noted that in cases when optimum efficiency of the train driver is required, e.g. while running in high-speed railways or in trains transporting hazardous substances, the acceleration tolerance of a human organism can be pharmacologically enhanced when one is exposed to vibration stress. In such cases, the golden mean should be sought, namely a compromise between ensuring traffic safety and increasing the driver's resilience to vibration stress (most pharmacological substances, and these include promethazine, scopolamine, meclozine, cinnarizine etc., also cause effects considered adverse from the traffic safety perspective). Therefore, a study such as the one proposed in this article enables administering small and hence safe doses of pharmaceuticals depending on the characteristics of the given route (i.e. of the vibrations observed).

An interesting solution to the problem in question may be designing of locomotive driver seats in a manner ensuring that motion stimulants are minimised. Not only does the foregoing apply to the shock damping solutions currently used in those seats (often incorrectly designed), but also to their physical redesigning in every axis in order to minimise the impact of vibrations on the driver's body. What proves an important aspect of this problem is the positioning of the driver's cab against the locomotive axis (axle base, motor layout etc.).

An important prospective benefit offered by the method proposed will be the capability to conduct the studies in question in real time. As aforementioned, in certain infrequent cases, the impact of vibrations may be translated into traffic safety. It is in those cases that real-time examination of vibrations may increase the safety of train traffic management. Regardless of the foregoing, corrective efforts may be oriented towards upgrading or replacement of track infrastructure elements causing excessive vibrations, and not necessarily should their replacement or upgrading result from scheduled repairs.

As regards the structure of contemporary vehicles (including the rail ones), one may observe a clear trend of engineers striving towards designing virtualised driver's control desks based on LED displays. What is inextricably linked with complicated visual arrangement of rail vehicle control elements is a danger of them being incorrectly operated. A driver's hand trembles at the frequency of 10 up to 20 Hz. The rail vehicle vibrations coincide with these frequencies. It is yet another field of study where the method proposed in this article may find application.

For the sake of validation of the method, the research in question is planned to be extended in the future, and the results obtained owing to the method application compared with those which could be obtained by means of professional measuring sets. Such a set should enable accelerations to be measured directly on the locomotive driver's body. Similar solutions are delivered, for instance, by XSENS [13]. Considering the fact that the driver's cab will inevitably become increasingly saturated with such features as virtualised control panels and HUD projectors, the solutions such as those addressed in the article seem even more important. They are assumed to enable direct measurement of vibrations in individual limbs of the driver's body (including the head) along with determination of their location while professional duties are performed.

Acknowledgments

This article has been developed under externally financed research project DEMONSTRATOR + Supporting scientific research and development works in demonstration scale, the title of the project is Integrated system for support the management of information in passenger railway transportation (no. DEM/1/RT4/2013/0 PASAŻER).

The authors would like to express their gratitude towards the Southern Division of PKP CARGO S.A. based in Katowice for enabling them to conduct the studies discussed.

References

- [1] <http://overpass-turbo.eu/> (10-08-2015)
 - [2] <http://www.openstreetmap.org/#map=17/50.16707/18.91026> (10-08-2015)
 - [3] <https://josm.openstreetmap.de/> (10-08-2015)
 - [4] Parkinson, B.W. *GPS*. American Institute of Aeronautics and Astronautics. 1996
 - [5] Mendizabal, R. and Berenguer, R. and Melendez, J. *GPS and Galileo*. McGraw Hill 2009.
 - [6] Brammer, A. J. *Vibration effects on the hand and arm in industry*, J.Wiley and Sons, NY, 1982.
 - [7] Kákosy, T. Vibration disease. *Baillieres Clin. Rheumatol.* Apr;3(1):25-5,. 1989.
 - [8] Griffin, M. J. *Handbook of Human Vibration*, London Academic Press, 1999.
 - [9] Seidel, H., Blüthner, R., Martin, J. (et all). Effects of isolated and combined exposures to whole-body vibration and noise on auditory-event related brain potentials and psychophysical assessment. *European Journal of Applied Physiology and Occupational Physiology*, No 65., 1992.
 - [10] Atsumia, B., Tokunagab, H., Kanamoria, H. (at all), Evaluation of vehicle motion sickness due to vehicle vibration, *JSAE Review*, Volume 23, Issue 3, July 2002.
 - [11] Benson, A. J. *Motion sickness*. In *Aviation Medicine*, London Butterworths, 1988.
 - [12] Reason, J.T., Brand, J.J. *Motion Sickness*. London Academic Press, 1975.
 - [13] <https://www.xsens.com/tags/motion-capture/> (10-82015)
 - [14] Burdzik, R. *Identification of sources, propagation and structure of vibrations affecting men in means of transport based on the example of automotive vehicles*. JVE International Ltd., Kaunas, 2014.
 - [15] Burdzik, R. Implementation of multidimensional identification of signal characteristics in the analysis of vibration properties of an automotive vehicle's floor panel. *Eksploatacja i Niezawodność – Maintenance and Reliability*, 16 (3) (2014) 439–445.
- 1) Jakub Młyńczak, Ph.D. assistant Professor: Silesian University of Technology, Faculty of Transport, Department of Transport Systems and Traffic Engineering, Krasinskiego Street 8, 40-019 Katowice, Poland (jakub.mlynczak@polsl.pl).
 - 2) Rafał Burdzik, Ph.D. D.Sc. Assistant Professor: Silesian University of Technology, Faculty of Transport, Krasinskiego 8, 40-019 Katowice, Poland (rafal.burdzik@polsl.pl), the author presented this work at the conference.
 - 3) Ireneusz Celiński, M. Sc.: Silesian University of Technology, Faculty of Transport, Department of Transport Systems and Traffic Engineering, Krasinskiego Street 8, 40-019 Katowice, Poland (ireneusz.celinski@polsl.pl).

Numerical simulation of mobility of miners rescue robot (MTR187-15)

Gabriel Mura, Marek Adamczyk, Michał Nocoń

Abstract: Since the beginning of mining industry, miner rescuers must carry out the rescue tasks in underground areas of a coal mines that have been closed due to a catastrophic events such as an explosion of methane or coal dust, a release of carbon dioxide or fire. In this case, the activity of a rescuer is extremely dangerous, and they can enter the hazardous area only if several values of critical parameters, such as methane content and temperature, are fulfilled. Nowadays we can minimize the rescuers' risks by using robots. This paper presents analysis of dynamics and mobility of unmanned, explosion safe, mechatronic platform for virtual teleportation of the rescuer into the areas of a coal mine affected by catastrophic events. In first step there will be presented an area where platform will work, then review of several finished projects of robots for mining and finally there will be shown a comparison of numerical analysis of mobility of platform passing simple obstacle in V-REP and LMS Virtual.Lab software. In the last chapter it will be presented main conclusion of mobility, visibility and steering of platform from numerical analysis of passing whole coal mine tunnel with obstacle like conveyor scraper and longwall system.

1. Introduction

The work of a mine rescuer is extremely dangerous, and often has resulted in deaths. Mine rescuers take a huge risk when they enter in to extremely dangerous environments to check the condition of atmosphere in mine tunnel or longwall system, that is place where the most accident occur. Moreover, human rescuers can enter the restricted area only if several values of critical parameters, such as methane content and temperature, are achieved. Unfortunately, due to the high risk to human life, the rescuers cannot monitor the hazard accurately or perform the rescue operation since they are not allowed to penetrate the hazardous area [1,2]. In this case the best way is to monitor it by mobile robot adapted to hazardous area.

The Central Rescue Mining Station (CRMS) prepare requirements for robots participating in rescue operations in underground coal mines. Beyond the requirements of fulfilling ATEX directive [3], the mine requirement is possibility to pass most of obstacle present in mining tunnel, except tunnel collapse without clearance. Another important requirement is that the robot have to drive through passage in the isolation dam with diameter 800 mm [4]. To pass this requirement the rescue robot needs to have-exceptional mobility, but it is often in conflict with ATEX standards.

2. Review of existing robots

To show difficulties of designing underground mine rescue robots, it is useful to review a few subterranean robots for inspection or rescue. The literature has identified robots such as:

- a) Numbat - is a mine reconnaissance 8-wheeled vehicle (Fig.1a) [5-7],
- b) Remotec Wolverine V-2 - traditional bomb squad tracked robot with a manipulator arm (Fig.1b) [5, 8, 9], but modified for use in coal mines,
- c) Gemini Scout – articulated robot with 4 tracks (Fig.1c) [5, 8, 9],
- d) Unmanned mining robot looks like a digger replacing miner in the mine tunnel (Fig.1d) [10],
- e) Groundhog – 4-wheeled mine reconnaissance vehicle (Fig.1e) [11, 12],
- f) CSIR Mine Safety Platform – tracked robot with 2 stationary and 2 adjustable arms with tracks (Fig.1f) [9,13],
- g) MINBOT-II – tracked robot with 2 stationary and 4 adjustable arms with tracks (Fig.1g) [14],
- h) MPI – 4-whilled articulated robot with ATEX M1 category [3, 16,17] that can work in case of presence of explosive atmosphere (Fig.1h) [15].

All presented robots in figure 1 have increased off-road capability. But based on review of mining robots shown above there are no clearly information which solution is better, wheel or track, for unmanned mining robot. It is hard to predict what kind of obstacles or ground robot will meet, because moving in coal mine tunnel is quite easy, but if it will have to pass tunnel collapse or longwall system, it will cause difficulties. In the last case simple robot with wheel won't be enough, especially that the accident occur most frequently near longwall. This is the main cause for authors why this paper arise.

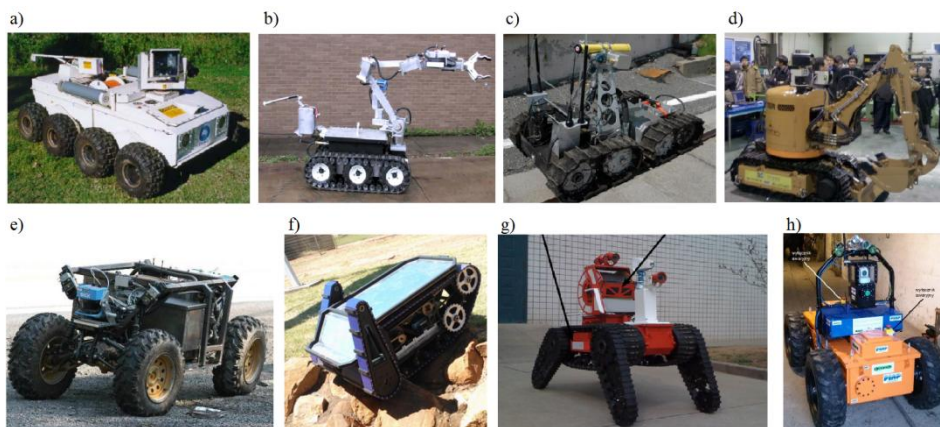


Figure 1. Example of existing robot [5-15]: a) Numbat, b) Remotec Wolverine V-2, c) Gemini Scout, d) Unmanned coal mining robot looks like a digger, e) Groundhog, f) CSIR Mine Safety Platform, g) MINBOT-II, h) MPI.

3. Multibody system

The dynamics and kinematics of multibody systems is a very useful part of Computer Aided Design (CAD) and Computer Aided Engineering (CAE) software. By the definition we can include to multibody systems mechanical systems such as robots, vehicles or other machinery. Mechanisms used in all these devices are normally subjected to large displacements and in this case there is possibility to collide between working parts of mechanism. Its cause kinematic and dynamic problems which must be able to predict and control or eliminate in designing stage. The advantage of numerical simulations performed by CAD and CAE software is that they allow one to predict the kinematic and dynamic behaviour of almost all types of multibody systems from the first concepts to the final product [18]. In the literature we can find many examples where the multi body analysis were used:

- Tracked vehicle with linked tracks or rubber tracks [19-22],
- Wheeled vehicle with 4 or more wheel [19, 23, 24]
- Inspection mobility robots with wheel or tracks [25, 26]

The above review of the usage of multibody simulation to analyze concepts or prototypes mobility during the design phase, gives sufficient proof that these tests are also indicated for the concept of robot to mine rescue.

3.1. Ordinary differential equations in multibody system

Analysis of multibody system dynamics is reduced to solving an equations of motion. They are second order ordinary differential equations (ODE), often connected with algebraic equations. In some modelled system the number of coordinates may be greater than the number of degrees of freedom of this system, so to determine the relationships between the coordinates are additional equations needed [27-29]. Many authors describe detailed ODE, but this is a short overview.

Solving multibody system in very simple case is reduced to solving a system of differential-algebraic equations (DAE):

$$\begin{bmatrix} M & B^T \\ B & 0 \end{bmatrix} \begin{bmatrix} \dot{h} \\ -\lambda \end{bmatrix} = \begin{bmatrix} g \\ \gamma^* \end{bmatrix}, \quad (1)$$

where: B is the modified matrix of a Jacobian determinant that is expressed by the equation:

$$B = \left[\Phi_{r_i}, \frac{1}{2} \Phi_{p_i} L_i^T; \dots; \Phi_{r_{nb}}, \frac{1}{2} \Phi_{p_{nb}} L_{nb}^T \right], \quad (2)$$

and γ^* is a modified right-hand side of the equation of acceleration, \dot{h} is a vector, that represents acceleration, g represents the vector of generalized forces, M is a global matrix of inertia that comprises masses and moment of inertia parameter for all the bodies within the system and λ is a Lagrange multipliers [27-29]. Moreover, λ can be obtained as an explicit function of generalized coordinates is

characterized by a second-order ODE. In this way standard ODE software can be applied directly for computing solutions of the DAE [30].

In the market there are many CAE software offering tools to compute multibody dynamics analysis, but authors use only LMS Virtual.Lab and V-REP to compare different concepts of inspection robot. Each software offer a few different derivative method, which are described below.

3.2. LMS Virtual.Lab integration method

Predict, Evaluate, Correct, Evaluate PECE -is an explicit integration predictor-corrector method elaborated by Adams, Bashforth and Moulton, used in LMS Virtual.Lab. This method uses a differential-geometric approach[31, 32] to solve the DAE. A generalized coordinate partitioning method is used to reduce the DAE to ODE. To solve the reduced ODE variable- step size and variable-order ODE solver is used [31, 33].

Other important thing in building numerical model of multibody mechanism is contact forces. LMS uses Herzian formulations to describe forces between contacting parts. To describe friction it use the Coulomb friction model [31,34].

3.3. V-REP integration method

To compare analysis of concept in different software, authors of this paper prepare also analysis in V-REP software where one of the offered solvers is Open Dynamics Engine. ODE (different than above) is the most popular rigid-body dynamics implementation for robotics simulation. The author of this method is Russell Smith [35, 36, 37] and bellow there is short overview of this method.

Generally multibody dynamic simulators solve the constrained Newton-Euler equation [35]:

$$\ddot{q} = f_{ext} + f_{con} + f_d \quad (3)$$

where f_{ext} is the external applied forces, f_{con} is the constraint forces and f_d is the viscous joint damping forces. ODE makes equation (3) as a linear complementarity problem (LCP) solver in the coordinate system to ensure forces satisfy non-interpenetration and joint-constraints. ODE Quickstep solver uses the projected Gauss-Seidel (PGS) method with Successive Overrelaxation (SOR) [38].

Given that constraints of rigid body are described by a constraint Jacobian J as [35]:

$$Jv = c \quad (4)$$

The following mixed complementarity formulation [35] results:

$$[JM^{-1}J^T]\zeta = \frac{c}{\Delta t} - J \left[\frac{v^n}{\Delta t} + \Delta t^{-1}(f_{ext} + f_d) \right] \quad (5)$$

where $\zeta \geq 0$ and $c \geq 0$ for unilateral contacts.

During an update step of equation 5, the Jacobians J are treated explicitly (held constant). It is possible to write equation (5) as:

$$A\zeta = b, \text{ where:} \quad (6)$$

$$A = [JM^{-1}J^T], \quad \text{and} \quad B = \frac{c}{\Delta t} - J \left[\frac{v^n}{\Delta t} + M^{-1}(f_{ext} + f_d) \right] \quad (7)$$

Solve for the unknowns ζ in (5) using Gauss-Seidel written in delta form:

$$\delta_i = \frac{b_i}{A_{ii}} - \sum_{j=1}^{N_{con}} \frac{A_{ij}}{A_{ii}} \zeta_j, \text{ where } \zeta_i^{n+1} = \delta_i^n + \zeta_i^n \text{ for } i=1, \dots, N_{con} \quad (8)$$

When a relaxation constant ω is introduced with SOR, the update equation of λ becomes [35]:

$$\hat{\zeta}^{n+1} = (1 - \omega)\zeta^n + \omega\zeta^{n+1} \text{ therefore it is possible to written equation (8) as:} \quad (9)$$

$$\delta_i = \omega \left(\frac{b_i}{A_{ii}} - \sum_{j=1}^{N_{con}} \frac{A_{ij}}{A_{ii}} \zeta_j \right) \quad (10)$$

V-REP also use the Coulomb friction model but ODE's friction models are approximations to the friction cone, for reasons of efficiency. There are to choose from currently approximations:

- importance of the friction coefficient is changed so as to specify the maximum friction (tangential) force, which may be present in the contact in each direction tangential friction.
- The friction cone is approximated by a friction pyramid aligned with the first and second friction directions.

4. Lay out of numerical multibody model

Each of mentioned software has similar method of building a dynamically model, but there are some differences, what is described below.

4.1. LMS Virtual.Lab multibody model

To correctly prepare numerical multi-body model of rescue robot in it's necessary to create kinematic joints, where the most popular joint is *Revolute joint* with 1 degree of freedom (1DOF) which can be found between wheel and hull, sprocket and hull, arm and hull or arm and wheel ect.

To demonstrate contact forces in each wheeled model there was used *CAD Contact* function, which is based on simple Hertzian contact. This type of contact was used between wheels and ground or hull and ground. In the picture bellow there are presented a graphical scheme with in different concept model. In the picture 2a we can see the representation of rubber track by group of sphere. In particle there is defined representation only for one pad (segment) of the track. Each pad is represented by 3 spheres and duplicate on rest of the track by module *Discrete Track*.

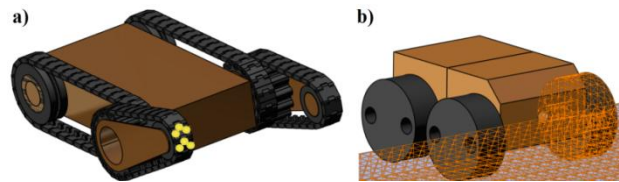


Figure 2. Contact types in different concepts of robot: a) track segment represented by 3 spheres in *Sphere to Extruded surface Contact*, b) discrete wheel and ground in *CAD Contact*.

To each model of wheel, hull or segment of track is assigned material properties (e.g. density). Based on volume and density of each element was automatically calculated mass and inertia properties, which were used in dynamics analysis.

4.2. V-REP multibody model

Models in V-REP are built in the same manner as in other MBS software, but there are some simplification. Vehicle model itself is built from rigid bodies interconnected with joints, in order consistent with its kinematic structure.

Main simplification in V-REP during building model bodies is that rigid bodies should be built from convex primitive shapes as cuboids, cylinders or spheres.

Wheeled platforms chasses are built from cuboids interconnected by revolute joints with spring-damper element. Wheels are connected to chassis with another revolute joints, but every wheel joints acts as independent motor. Motors from one side are driven together from script level. Tracked platform's chassis is one-piece rigid cuboid. Tracks are modelled in simplified way as overlapping wheels. Because of that, contact detection between them is disabled. Every wheel have its own joint in motor mode that is connected to arm body. Arms are attached to chassis also with motorized joints. In the Fig. 3 are shown visual and dynamical model of wheeled and tracked robot in V-REP software

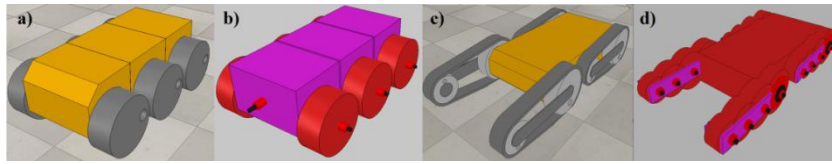


Figure 3. Numerical model in V-REP: a) visual body of wheeled platform, b) dynamic body of wheeled platform, c) visual body of tracked platform, d) dynamic body of tracked platform

5. Simulation condition and compare a results

To compare mobility of different concept, numerical model of each concepts pass two simple obstacles with the same velocity equal 1 m/s. in mentioned software. In the figure 4 is presented dimension and shape of obstacles. Despite large number of concepts, for the purposes of this paper authors reduce number of analyzed concepts of platform to 3 type: 4-wheeled robot with articulated hull, 6-wheeled robot with articulated hull and 4-tracked platform with adjustable arms (Fig.2, Fig.3).

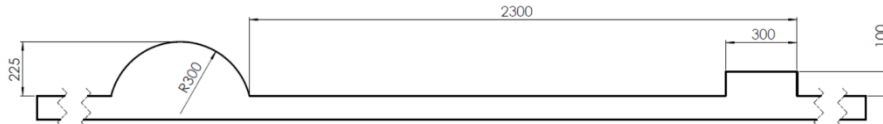


Figure 4. Shape, dimension and arrangement of obstacle

5.1. Results of 4-wheeled platform

In the figure 5 and 6 is presented results of analysis as a curves of displacement of hull in Z axis and torques loading wheels to keep constant rotation velocity. The curves of displacement shows that the both simulations are in line. In LMS simulations there are high picks of the torque in the case when wheel touch edges of obstacle. Moreover there are other differences between simulations in torque curves. Unfortunately in both simulations this concept has no ability to pass semicircle obstacle. In the figure 7 is presented screenshots of animation of results in LMS and V-REP.

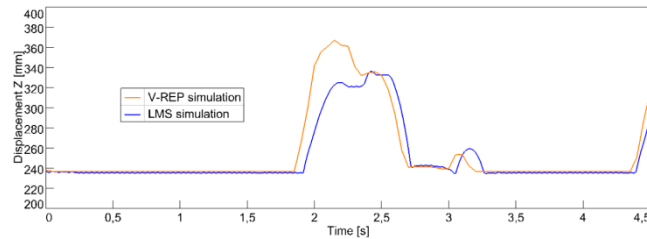


Figure 5. Displacement of hull of 4-wheeled platform in Z axis.

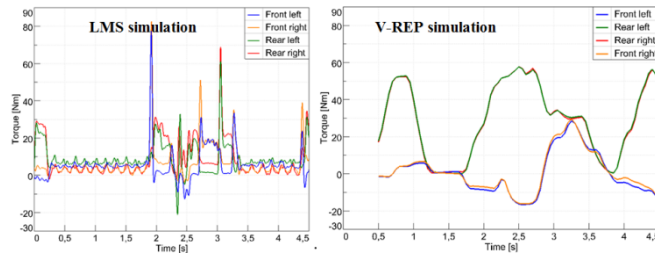


Figure 6. Torque curves loading wheel needed to keep constant velocity in 4-wheeled platform

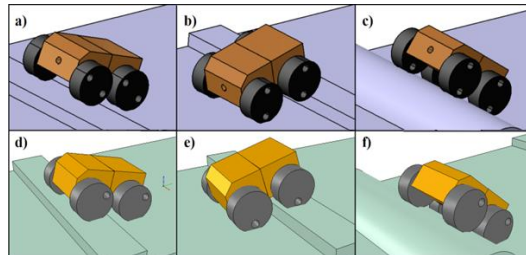


Figure 7. Screenshots of result animation of 4-wheeled platform: a-c – LMS, d-f – V-REP

5.2. Results of 6-wheeled platform

Figure 8 and 9 presents results of analysis as a curves of displacement of hull in Z axis and torques loading wheels to keep constant rotation velocity in 6 wheeled platform. It can be noticed that the order of magnitude of torque is similar in both cases. Also displacements are quite compatible. Unfortunately the curves of torque from V-REP simulation are again more unstable than from LMS.

In this case in both of simulation model of robot pass all obstacles. In the figure 10 is presented screenshots of animation of results in LMS and V-REP.

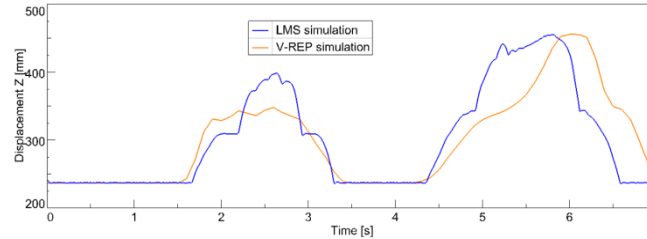


Figure 8. Displacement of hull of 6-wheeled platform in Z axis.

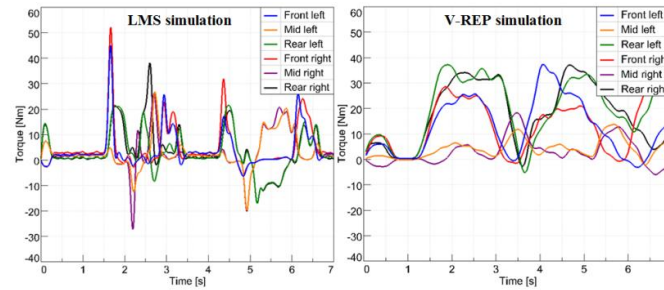


Figure 9. Torque curves loading wheel needed to keep constant velocity in 6-wheeled platform

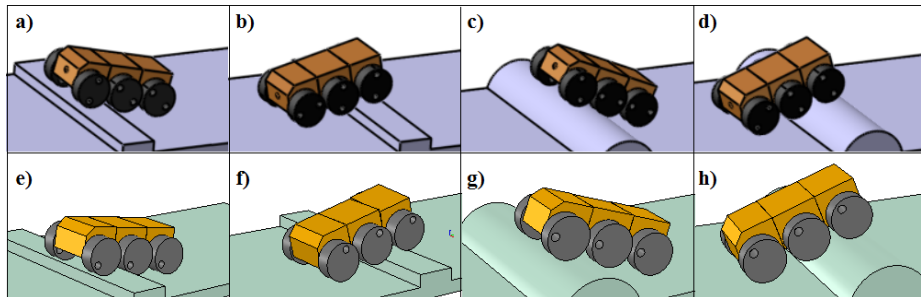


Figure 10. Screenshots of result animation of 6-wheeled platform: a-d – LMS, e-h – V-REP

5.3. Results of platform with 4 adjustable arm with tracks

Figure 11 and 12 presents results of analysis as a curves of displacement of hull in Z axis and torques loading sprocket to keep constant rotation velocity in platform with 4 arms with tracks. It can be noticed that only the order of magnitude of torque is similar in both simulation, but the shape of the curves is different. This differences can be caused because of simplified tracks in V-REP to group of wheel. But behavior of each model in results animation and in displacement of hull is similar what is possible to see in the figures 11 and 13.

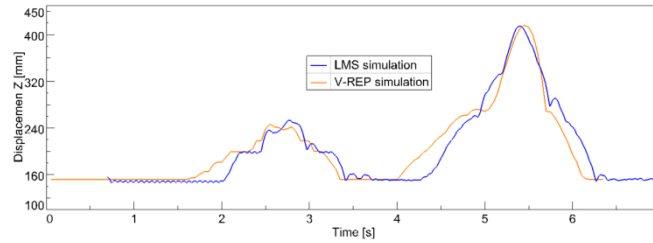


Figure 11. Displacement of hull of tracked platform in Z axis.

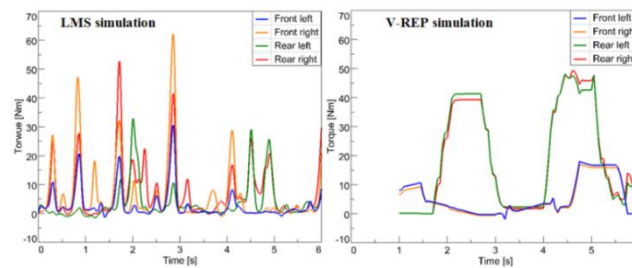


Figure 12. Torque curves loading sprocket needed to keep constant velocity in 4 tracked platform

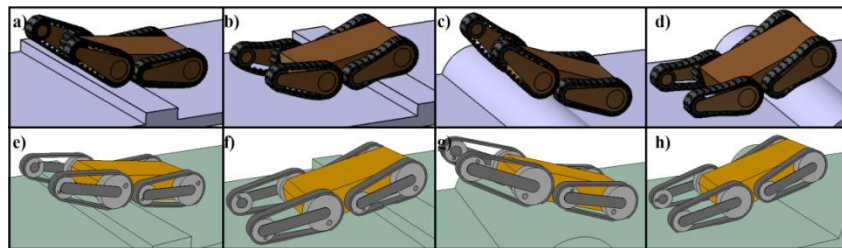


Figure 13. Screenshots of result animation of 4 tracked platform: a-d – LMS, e-h – V-REP

6. Simulation in coal mine environment

Despite differences of curves of torque and difficulties with specifying inertia parameter and contact parameter units V-REP is faster tool to quick predict main functionality and mobility of concepts. Authors of this paper prepare special obstacle field similar to coal mine tunnel and longwall system. Based on simulations above the best possibilities to pass has concept with 4 adjustable arms with tracks, and with this platform was performed the mobility test. The main difficulties of this concept is lateral stability during passing obstacle such a ramp and designers need to find solution of this problem before building prototype. Except this platform pass almost all obstacle. The biggest advantage is that it is possible to perform the simulation in real time. In the Figure 14 is presented screenshots of the simulation.

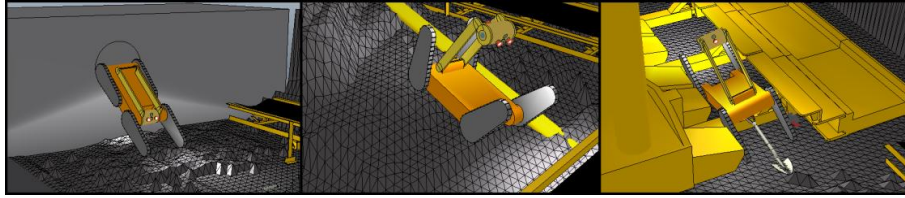


Figure 14. Screenshots of simulation of driving platform with 4 adjustable tracks in coal mine tunnel and longwall system

7. Conclusions

Multibody analysis is very useful to predict behavior of tracked vehicle before building costly prototype. Thanks to the multibody analysis of vehicle or device it can avoid more engineering mistakes than in simple CAD designing.

V-REP is very useful to quick prediction of mobility of vehicle thanks to real-time simulation, but it can gives difficulties in selecting design parameters such as required drivetrain power.

Despite different torque characteristics, both of multibody software gives similar results in displacement of hull and mobility.

Differences between simulations in each multibody software can be caused by different contact type, solver and simplification of track.

Concept of coal mining rescue robot as a platform with 4 adjustable arms with tracks seems to be the best solution for this tasks because of its ability to pass large obstacle.

There is a need to compare results of numerical simulations with real platform in the next stage of the project.

Acknowledgments

This work is carried out in a framework of a programme of the Research Fund for Coal and Steel under the grant No. RFCR-CT-2014-00002 (Project Title: “TeleRescuer”).

References

- [1] Novák P. et al.: Exploration Mobile Robot for Coal Mines. In: Modelling and Simulation for Autonomous Systems: Second International Workshop, MESAS 2015, Prague, Czech Republic, April 29-30, 2015, Revised Selected Papers. Springer, 2015. p. 209.
- [2] Moczulski W., Cyran K., Novak P., Rodriguez A., Januszka M.: TELERESCUER - a concept of a system for teleimmersion of a rescuer to areas of coal mines affected by catastrophes. Proceedings of the Institute of Vehicles No. 2(102)/2015. p. 57-62
- [3] Directive 2014/34/EU of the European Parliament and the Council of 25 February 2014 on the approximation of the laws of the Member States concerning equipment and protective systems intended for use in potentially explosive atmospheres (ATEX)

- [4] Timofiejczuk A., Adamczyk M., Bagiński M., Golicz P.: Requirements for robots participating in rescue operations in underground coal mines Mechanization, Automation and Robotization in Mining Conference 2015, (in Polish)
- [5] Kasprzyczak L., et al: Robot for monitoring hazardous environments as a mechatronic product. *Journal of Automation Mobile Robotics and Intelligent Systems*, 2012, 6: 57-64.
- [6] Hainsworth D. W.: Teleoperation user interfaces for mining robotics. *Autonomous Robots*, 2001, 11.1: 19-28.
- [7] Murphy R., et al. Mobile robots in mine rescue and recovery. *Robotics & Automation Magazine*, IEEE, 2009, 16.2: 91-103
- [8] Reddy A.H., Kalyan B., Murthy C.S.N.: Mine Rescue Robot System—A Review. *Procedia Earth and Planetary Science*, 2015, 11: 457-462.
- [9] Green J.: Mine rescue robots requirements Outcomes from an industry workshop. In: *Robotics and Mechatronics Conference (RobMech)*, 2013 6th. IEEE, 2013. p. 111-116.
- [10] Huh S. et al.: Development of an unmanned coal mining robot and a tele-operation system. In: *Control, Automation and Systems*, 2011 11th Int. Conference on. IEEE, 2011. p. 31-35.
- [11] Ferguson D. et al.: An autonomous robotic system for mapping abandoned mines. In: *Advances in Neural Information Processing Systems*. 2003.
- [12] Thrun S. et al. Autonomous exploration and mapping of abandoned mines. *Robotics & Automation Magazine*, IEEE, 2004, 11.4: 79-91.
- [13] Green J.: Underground mining robot: A CSIR project. In: *Safety, Security, and Rescue Robotics (SSRR)*, 2012 IEEE International Symposium on, On page(s): 1 - 6.
- [14] Wang W., et al. Development of Search-and-rescue Robots for Underground Coal Mine Applications. *Journal of Field Robotics*, 2014, 31.3: 386-407..
- [15] Kasprzyczak L., Szwejkowski S., Nowak D., Cader M.: An analysis of the safety function and the selection of drives for a mining mobile inspection platform. *Electrical Machines - Transaction Journal*, 2/2015, p. 99-106 (in Polish).
- [16] EN 50303 Group I, Category M1 equipment intended to remain functional in atmospheres endangered by firedamp and/or coal dust
- [17] EN 60079-0 Explosive atmospheres - Part 0: Equipment - General requirements.
- [18] De Jalon J.G., Bayo E.: *Kinematic and dynamic simulation of multibody systems: the real-time challenge*. Springer Science & Business Media, 2012.
- [19] Stodola J.: Virtual Approach to Ground Armoured Vehicles Design. *Advances in Military Technology*. Vol. 4, No. 2, 2009, p. 13-25.
- [20] Xingguo M. et al. Modeling and Simulation of Multibody Dynamics for Tracked Vehicle Based on RecurDyn. In: *Intelligent Networks and Intelligent Systems (ICINIS)*, 2010 3rd International Conference on. IEEE, 2010. p. 669-671
- [21] Agapov D., Kovalev R., Pogorelov D.: Real-time model for simulation of tracked vehicles, multibody dynamics 2011, *Eccomas Thematic Conference*, Brussels, Belgium, 4-7 July 2011.
- [22] Madsen J., Heyn T., Negrut D.: *Methods for Tracked Vehicle System Modeling and Simulation*. Technical Report 2010-01. University of Wisconsin, 2010.

- [23] Hönlinger, M., Glauch, U. and Steger G.: Modelling and simulation in the design process of armored vehicles, Paper at the RTO AVT Symposium on "Reduction of Military Vehicle Acquisition Time and Cost through Advanced Modelling and Virtual Simulation", Paris, France, published in RTO – MP – 089, 2002.
- [24] Kading D.: Multibody Dynamic Simulation of Off-Road Vehicles for Load Prediction, Stability, Safety, and Performance. In: ASABE Meeting Presentation. Paper. 2006. p. 1-10.
- [25] Gibbesch A. Schafer B.: Multibody system modelling and simulation of planetary rover mobility on soft terrain. In: 8th International Symposium on Artificial Intelligence, Robotics and Automation in Space (i-SAIRAS 2005), Munich, Germany, September. 2005. p. 5-8.
- [26] Ben-Tzvi P., Goldenberg A.A.; Zu J.W.: Design and analysis of a hybrid mobile robot mechanism with compounded locomotion and manipulation capability. *Journal of Mechanical Design*, 2008, 130.7: 072302.
- [27] Flores P., AMBRÓSIO, Jorge. Revolute joints with clearance in multibody systems. *Computers & structures*, 2004, 82.17: 1359-1369.
- [28] Gillespie R.B., Colgate J.E.: A survey of multibody dynamics for virtual environments. In: ASME Dynamic Systems and Control Division. 1997.
- [29] Mężyk A., Switonski E., Kciuk S., Klein, W.: Modelling and investigation of dynamic parameters of tracked vehicles. *Mechanics and Mechanical Engineering*, 2011, 15.4: 115-130.
- [30] Ciarlet P.G., Lions J.L.: *Solution of Equation in R^n Part 4 Techniques of Scientific Computing Part 4 Numerical Methods for Fluids*, 2002.
- [31] LMS Virtual.Lab Online Help.
- [32] Yen, J., *Numerical Methods for Constrained Equations of Motion in Mechanical System Dynamics*, Ph.D. thesis, May 1990, University of Iowa.
- [33] Shampine, L.F., and Gordon, M.K., *Computer Solution of Ordinary Differential Equations: The Initial Value Problem*, Freeman, San Francisco, 1975.
- [34] Young, W. C. and Budynas R. G., *Roark's Formula for Stress and Strain*, Seventh Edition, McGraw Hill, 2002.
- [35] Drumwright E. et al.: Extending open dynamics engine for robotics simulation. In: *Simulation, Modeling, and Programming for Autonomous Robots*. Springer Berlin, 2010. p. 38-50.
- [36] Smith, R.: *ODE: Open Dynamics Engine*
- [37] Cottle, R.W., et al: *The Linear Complementarity Problem*. Academic Press, Boston, 1992
- [38] Anitescu, M., Tasora, A.: An iterative approach for cone complementarity problems for nonsmooth dynamics. In: *Computational Optimization and Applications*, 2008

Gabriel Mura, M.Sc. (Ph.D. student): Silesian University of Technology, Institute of Fundamentals of Machinery Design, Konarskiego 18A, 44100 Gliwice, Poland (gabriel.mura@polsl.pl).

Marek Edmund Adamczyk, M.Sc. (Ph.D. student): Silesian University of Technology, Institute of Fundamentals of Machinery Design, Konarskiego 18A, 44100 Gliwice, Poland (marek.adamczyk@polsl.pl).

Michał Nocoń, M.Sc.: Silesian University of Technology, Institute of Fundamentals of Machinery Design, Konarskiego 18A, 44100 Gliwice, Poland (michal.nocon@polsl.pl).

The effect of partially embedded inner reinforced core on modal properties of the Euler-Bernoulli beam structures (VIB227-15)

Milan Nadř, Ladislav Rolník, Lenka Čičmancová

Abstract: The beams are considered as fundamental structural elements used in many engineering applications. These beam structures are in the operating regimes very often loaded by the time-dependent forces which cause their undesirable dynamical behavior and the whole system is getting into critical resonance state. It is clear that the reduction of the level of unwanted vibrations or prevention of their occurrence should be one of the important objectives in the design of machine equipment and structures. To achieve these aims, the knowledge of modal properties of beam structures in relation to their internal structure is necessary. The required modification of modal properties of the beam structure (mode shapes, natural frequencies) can be achieved by the partially embedded inner reinforcing core. The dependence of the modal properties of modified beam structure on the geometric parameters and material properties of the embedded reinforcing core is studied in this paper.

1. Introduction

Beams provide a fundamental model for the structural elements of many engineering applications. The recent trends tend to the use of lightweight and more flexible beam structures, and this requirement is vigorously required in various engineering applications. But, the use of lightweight and flexible beam structures has become vulnerable to excessive lateral vibration.

Some of the machining tools (especially cutting tools) can be also classified as a beam structures. During the machining process (turning process), the various excitation effects affect the machine tools. Cutting speeds, cutting forces, chip making, the stiffness of MTW (machine-tool-workpiece) system are the main effects acting on the dynamics of MTW system and also on the machining process (roughness of the machined surface, tool wear, tool or workpiece damage, noise generated by the machining process, etc.). Based on the assessment of subsystems MTW of turning tools are the most critical elements [6]. It can be concluded that many of machining tools (e.g. turning tools, boring tools etc.) have a shape corresponding to beam structure and they are representative structure similar to cantilever beam. During the machining process, these tools are subjected to the various exciting effects. Very serious problems in the machining process occur when the frequencies of periodic changes of the significant effects of machining process are close to the values of the tool natural frequencies. As a result of these operating conditions, the resonant states of machine tool body are

occurring. The technological process carried out when the tool is in or close to resonant state, significantly affects the functionality of the tool and also the quality of the machining process.

The dynamical properties of the tool body depend on its geometrical parameters and material properties. The beam structure representing tool body usually made of homogeneous material, in many cases do not have the required dynamic properties. Therefore, it is necessary to make structural changes of the tool body to meet the requirements to avoid the emergence undesirable dynamic effects. In many cases, it is necessary to eliminate these inconvenient effects by some design or technological treatments. One of the techniques [3] which lead to the change of modal properties (natural frequencies, mode shapes) of beam structure is based on application of reinforcing core inserted into beam body.

2. Formulation of the problem

The considered structure is composite beam having step change of the cross-section caused by insertion of the reinforcing inner core. After inserting the core into the beam, the cross-section of the modified beam consists of a basic beam body and reinforcing core with uniform cross section, which is partially embedded into beam body (Fig. 1). Two concepts [4] for inserting of the reinforcing core are considered. The first approach consists of the insertion reinforcing core into the body of beam and beam structure Type I (Fig. 1a) with two fields is created. Consequently, a length of the inserted core can be in the range from zero to the length of the beam body. The second approach is based on a fixed length core of inserted into beam body (Fig. 1b), which is less than the length beam body. The position of the inserted reinforcing core can be changed and then beam structure Type II has three fields. It is clear that by changing the material properties and geometric parameters of reinforcing core the change in the distribution of mass and stiffness properties of the modified beam structure occurs, which also causes a change in the modal properties. The role of reinforcing inner core is to achieve an appropriate modification of the distribution of mass and stiffness properties of this beam structure.

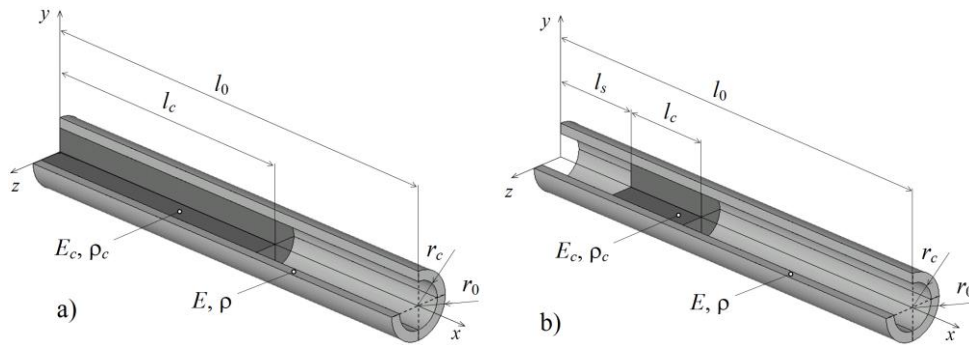


Figure 1. Models of reinforced beam structures (a - Type I, b - Type II)

The computational model describing the studied beam structure will be based on Euler-Bernoulli beam theory. Two underlying assumptions for the Euler-Bernoulli beam analysis are considered. The first assumption is that the beam is long and slender. In practice, the Euler-Bernoulli theoretical approach is valid when the beam length is at a minimum of 10 times its diameter. Within this theory [1], the effect of shear deformation and the rotary inertia is neglected. Next, the Euler-Bernoulli beam theory assumes that the centerline deflection is small and only in the transversal direction.

The other following assumptions to the creation of mathematical model and governing equations of the modified beam structure [2] are considered:

- parts of cross-section of beam structure are lying in plane perpendicular to the neutral axis x ,
- beam cross-section before and during deformation is assumed as planar,
- cross-sections of basic beam profile and core are symmetrical with respect to both axes y, z ,
- isotropic and homogeneous material properties of the parts of beam structure are considered,
- perfect adhesion at the interface of beam structural parts is supposed.

By using Euler-Bernoulli beam theory, the equation of motion for each j^{th} segment of beam, is

$$\frac{\partial^2}{\partial x_j^2} \left[E_j J_j \frac{\partial^2 w_j(x_j, t)}{\partial x_j^2} \right] + \rho_j S_j \frac{\partial^2 w_j(x_j, t)}{\partial t^2} = 0, \quad (1)$$

while in this segment is expected, that the beam bending stiffness $E_j J_j$ and mass $\rho_j S_j$ are constant.

Equation (1) has after introducing the assumed solution $w_j(x_j, t) = W_j(x_j)T(t)$ following form

$$\overline{W}_j^{IV}(\xi_j) - \beta_j^4 \overline{W}_j(\xi_j) = 0 \quad (2)$$

where $\beta_j = \sqrt[4]{\frac{\rho_j S_j}{E_j J_j} \omega_{0m}^2 l_0^4}$ is frequency parameter and ω_{0m} is natural angular frequency and dimensionless parameters are defined as

$$\overline{W}_j(\xi_j) = W_j(x_j)/l_0, \quad \text{and} \quad \xi_j = x_j/l_0, \quad (3)$$

The solution of equation (2) has the following form

$$\overline{W}_j(\xi_j) = A_j S(\beta_j \xi_j) + B_j T(\beta_j \xi_j) + C_j U(\beta_j \xi_j) + D_j V(\beta_j \xi_j), \quad (4)$$

where A_j, B_j, C_j, D_j are integration constants and Krylov's functions are defined as follows

$$\begin{aligned} S(\beta_j \xi_j) &= \frac{\cosh(\beta_j \xi_j) + \cos(\beta_j \xi_j)}{2}, & T(\beta_j \xi_j) &= \frac{\sinh(\beta_j \xi_j) + \sin(\beta_j \xi_j)}{2}, \\ U(\beta_j \xi_j) &= \frac{\cosh(\beta_j \xi_j) - \cos(\beta_j \xi_j)}{2}, & V(\beta_j \xi_j) &= \frac{\sinh(\beta_j \xi_j) - \sin(\beta_j \xi_j)}{2}. \end{aligned} \quad (5)$$

Stepped beam structure (Type I: $j = 1, 2$; Type II: $j = 1, 2, 3$) is fixed on the left edge and on the right edge is free. Boundary conditions [5] are presented in Table 1 and Table 2.

Table 1. Boundary conditions for beam structure Type I (Fig. 1a)

Boundary conditions - beam structure Type I (Fig. 1a)		
$\xi_1 = 0 :$	$\overline{W}_1(0) = 0$	$\overline{W}_1'(0) = 0$
$\xi_1 = \xi_c :$	$\overline{W}_1(\xi_c) = \overline{W}_2(1 - \xi_c)$	$E_1 J_1 \overline{W}_1''(\xi_c) = E_2 J_2 \overline{W}_2''(1 - \xi_c)$
$\xi_2 = 1 - \xi_c :$	$\overline{W}_1'(\xi_c) = -\overline{W}_2'(1 - \xi_c)$	$E_1 J_1 \overline{W}_1'''(\xi_c) = -E_2 J_2 \overline{W}_2'''(1 - \xi_c)$
$\xi_2 = 0 :$	$\overline{W}_2''(0) = 0$	$\overline{W}_2'''(0) = 0$
$E_1 J_1 = E_0 J_0 [1 + \Delta_{EJ}]$ $\rho_1 S_1 = \rho_0 S_0 [1 + \Delta_{\rho S}]$		$E_2 J_2 = E_0 J_0$ $\rho_2 S_2 = \rho_0 S_0$

Table 2. Boundary conditions for beam structure Type II (Fig. 1b)

Boundary conditions - beam structure Type II (Fig. 1b)		
$\xi_1 = 0 :$	$\overline{W}_1(0) = 0$	$\overline{W}_1'(0) = 0$
$\xi_1 = \xi_s :$	$\overline{W}_1(\xi_s) = \overline{W}_2(\xi_s)$	$E_1 J_1 \overline{W}_1''(\xi_s) = E_2 J_2 \overline{W}_2''(\xi_s)$
$\xi_2 = \xi_s :$	$\overline{W}_1'(\xi_s) = -\overline{W}_2'(\xi_s)$	$E_1 J_1 \overline{W}_1'''(\xi_s) = -E_2 J_2 \overline{W}_2'''(\xi_s)$
$\xi_2 = \xi_s + \xi_c :$	$\overline{W}_2(\xi_s + \xi_c) = \overline{W}_3(1 - \xi_s - \xi_c)$	$E_2 J_2 \overline{W}_2''(\xi_s + \xi_c) = E_3 J_3 \overline{W}_3''(1 - \xi_s - \xi_c)$
$\xi_3 = 1 - \xi_s - \xi_c :$	$\overline{W}_2'(\xi_s + \xi_c) = -\overline{W}_3'(1 - \xi_s - \xi_c)$	$E_2 J_2 \overline{W}_2'''(\xi_s + \xi_c) = -E_3 J_3 \overline{W}_3'''(1 - \xi_s - \xi_c)$
$\xi_3 = 0$	$\overline{W}_3''(0) = 0$	$\overline{W}_3'''(0) = 0$
$E_1 J_1 = E_0 J_0$ $\rho_1 S_1 = \rho_0 S_0$	$E_2 J_2 = E_0 J_0 [1 + \Delta_{EJ}]$ $\rho_2 S_2 = \rho_0 S_0 [1 + \Delta_{\rho S}]$	$E_3 J_3 = E_0 J_0$ $\rho_3 S_3 = \rho_0 S_0$

Dimensionless parameters defining position $\xi_s = \frac{l_s}{l_0}$ and length of core $\xi_c = \frac{l_c}{l_0}$.

The parameters Δ_{EJ} and $\Delta_{\rho S}$ mentioned in Table 1 and Table 2 characterize the modification of stiffness and mass properties of the beam. These modification parameters can be expressed [2] as

$$\Delta_{EJ} = \frac{E_c J_c}{E_0 J_0} \quad \text{and} \quad \Delta_{\rho S} = \frac{\rho_c S_c}{\rho_0 S_0}, \quad (6)$$

where E - Young modulus, ρ - density, S - cross-section area and J - second moment of area (subscript 0 is used for the beam and subscript c is used for the core).

Substituting the solution $\bar{W}_j(\xi_j)$ into the boundary conditions (Table 1, Table 2) for beam structures Type I and Type II, the frequency determinants are obtained, i.e.

- beam structure - Type I:

$$\begin{vmatrix} U\left(\frac{\xi_c}{k_1}\beta_2\right) & V\left(\frac{\xi_c}{k_1}\beta_2\right) & -S((1-\xi_c)\beta_2) & -T((1-\xi_c)\beta_2) \\ T\left(\frac{\xi_c}{k_1}\beta_2\right) & U\left(\frac{\xi_c}{k_1}\beta_2\right) & k_1V((1-\xi_c)\beta_2) & k_1S((1-\xi_c)\beta_2) \\ S\left(\frac{\xi_c}{k_1}\beta_2\right) & T\left(\frac{\xi_c}{k_1}\beta_2\right) & -k_2U((1-\xi_c)\beta_2) & -k_2V((1-\xi_c)\beta_2) \\ V\left(\frac{\xi_c}{k_1}\beta_2\right) & S\left(\frac{\xi_c}{k_1}\beta_2\right) & k_3T((1-\xi_c)\beta_2) & k_3U((1-\xi_c)\beta_2) \end{vmatrix} = 0, \quad (7)$$

- beam structure - Type II:

$$\begin{vmatrix} \mathbf{A} & \mathbf{B} & \mathbf{0} \\ \mathbf{0} & \mathbf{C} & \mathbf{D} \end{vmatrix} = 0, \quad (8)$$

$$\mathbf{A} = \begin{bmatrix} U(\xi_s\beta_1) & V(\xi_s\beta_1) \\ T(\xi_s\beta_1) & U(\xi_s\beta_1) \\ S(\xi_s\beta_1) & T(\xi_s\beta_1) \\ V(\xi_s\beta_1) & S(\xi_s\beta_1) \end{bmatrix}, \quad \mathbf{B} = \begin{bmatrix} -S\left(\frac{\xi_s}{k_1}\beta_1\right) & -T\left(\frac{\xi_s}{k_1}\beta_1\right) & -U\left(\frac{\xi_s}{k_1}\beta_1\right) & -V\left(\frac{\xi_s}{k_1}\beta_1\right) \\ -\frac{1}{k_1}V\left(\frac{\xi_s}{k_1}\beta_1\right) & -\frac{1}{k_1}S\left(\frac{\xi_s}{k_1}\beta_1\right) & -\frac{1}{k_1}T\left(\frac{\xi_s}{k_1}\beta_1\right) & -\frac{1}{k_1}U\left(\frac{\xi_s}{k_1}\beta_1\right) \\ -\frac{1}{k_2}U\left(\frac{\xi_s}{k_1}\beta_1\right) & -\frac{1}{k_2}V\left(\frac{\xi_s}{k_1}\beta_1\right) & -\frac{1}{k_2}S\left(\frac{\xi_s}{k_1}\beta_1\right) & -\frac{1}{k_2}T\left(\frac{\xi_s}{k_1}\beta_1\right) \\ -\frac{1}{k_3}T\left(\frac{\xi_s}{k_1}\beta_1\right) & -\frac{1}{k_3}U\left(\frac{\xi_s}{k_1}\beta_1\right) & -\frac{1}{k_3}V\left(\frac{\xi_s}{k_1}\beta_1\right) & -\frac{1}{k_3}S\left(\frac{\xi_s}{k_1}\beta_1\right) \end{bmatrix},$$

$$\mathbf{0} = \begin{bmatrix} 0 & 0 \\ 0 & 0 \\ 0 & 0 \\ 0 & 0 \end{bmatrix}, \quad \mathbf{C} = \begin{bmatrix} S\left(\frac{\xi_s+\xi_c}{k_1}\beta_1\right) & T\left(\frac{\xi_s+\xi_c}{k_1}\beta_1\right) & U\left(\frac{\xi_s+\xi_c}{k_1}\beta_1\right) & V\left(\frac{\xi_s+\xi_c}{k_1}\beta_1\right) \\ V\left(\frac{\xi_s+\xi_c}{k_1}\beta_1\right) & S\left(\frac{\xi_s+\xi_c}{k_1}\beta_1\right) & T\left(\frac{\xi_s+\xi_c}{k_1}\beta_1\right) & U\left(\frac{\xi_s+\xi_c}{k_1}\beta_1\right) \\ U\left(\frac{\xi_s+\xi_c}{k_1}\beta_1\right) & V\left(\frac{\xi_s+\xi_c}{k_1}\beta_1\right) & S\left(\frac{\xi_s+\xi_c}{k_1}\beta_1\right) & T\left(\frac{\xi_s+\xi_c}{k_1}\beta_1\right) \\ T\left(\frac{\xi_s+\xi_c}{k_1}\beta_1\right) & U\left(\frac{\xi_s+\xi_c}{k_1}\beta_1\right) & V\left(\frac{\xi_s+\xi_c}{k_1}\beta_1\right) & S\left(\frac{\xi_s+\xi_c}{k_1}\beta_1\right) \end{bmatrix},$$

$$\mathbf{D} = \begin{bmatrix} -S((1-(\xi_s+\xi_c))\beta_1) & -T((1-(\xi_s+\xi_c))\beta_1) \\ k_1V((1-(\xi_s+\xi_c))\beta_1) & k_1S((1-(\xi_s+\xi_c))\beta_1) \\ -k_2U((1-(\xi_s+\xi_c))\beta_1) & -k_2V((1-(\xi_s+\xi_c))\beta_1) \\ k_3T((1-(\xi_s+\xi_c))\beta_1) & k_3U((1-(\xi_s+\xi_c))\beta_1) \end{bmatrix}.$$

The parameters k_1, k_2, k_3 are expressed by the following relations

$$k_1 = 4\sqrt{\frac{1+\Delta_{EJ}}{1+\Delta_{pS}}}, \quad k_2 = \frac{1}{\sqrt{(1+\Delta_{EJ})(1+\Delta_{pS})}}, \quad k_3 = \frac{1}{\sqrt[4]{(1+\Delta_{EJ})(1+\Delta_{pS})^3}}. \quad (9)$$

3. Numerical analysis and results

The values of the frequency parameters $\beta_{2,i}$ (Type I) and $\beta_{1,i}$ (Type II) for the modified beam structures are obtained by the solution of frequency determinants (7) and (8). Using these frequency

parameters, the modification function for i^{th} natural frequency of vibration the modified beam structure can be expressed. The modification function defined as the ratio of i^{th} natural angular frequency of the modified beam structure to i^{th} unmodified beam structure is expressed in the form:

- beam structure - Type I

$$f_{m,i} = 1 + \Delta f_{m,i}(\Delta_{EJ}, \Delta_{pS}) = \frac{\omega_{0m,i}}{\omega_{0,i}} = \left(\frac{\beta_{2,i}}{\beta_{0,i}} \right)^2, \quad (i = 1, 2, \dots), \quad (10)$$

- beam structure - Type II

$$f_{m,i} = 1 + \Delta f_{m,i}(\Delta_{EJ}, \Delta_{pS}) = \frac{\omega_{0m,i}}{\omega_{0,i}} = \left(\frac{\beta_{1,i}}{\beta_{0,i}} \right)^2, \quad (i = 1, 2, \dots). \quad (11)$$

where $\Delta f_{m,i}(\Delta_{EJ}, \Delta_{pS})$ - increment taking into account the modification of stiffness and mass structure.

The dependence of increment of modification function $\Delta f_{m,i}$ for beam structure Type I on dimensionless length ξ_c for constant values of modification parameters $\Delta_{EJ} = 1.0$, $\Delta_{pS} = 1.0$ is shown in Fig. 2. The modification function is increasing up to 35% for the case of insertion reinforcing core into half length of the beam. The effect of dimensionless length of core ξ_c on the modification functions for additional natural frequencies is less significant. However, the insertion reinforcing core also gives some possibilities for modification higher natural frequencies of modified structure.

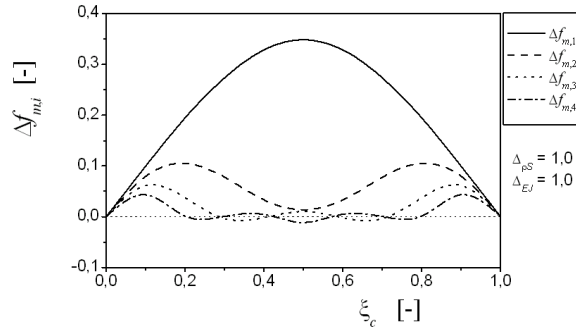


Figure 2. Dependency of $\Delta f_{m,i}$ on ξ_c - Type I ($\Delta_{EJ} = 1.0$, $\Delta_{pS} = 1.0$).

Furthermore, the dependence of increments of modification functions for structure Type I on the dimensionless length of the core for different values Δ_{EJ} , Δ_{pS} are displayed for the first four natural frequencies in the following figures. The largest increase in modification functions when core is inserted is achieved for the first natural frequency. Incremental values of modification functions are considerably dependent on the values of the stiffness modification parameter Δ_{EJ} and mass modification parameter Δ_{pS} (Fig. 3 and Fig.4).

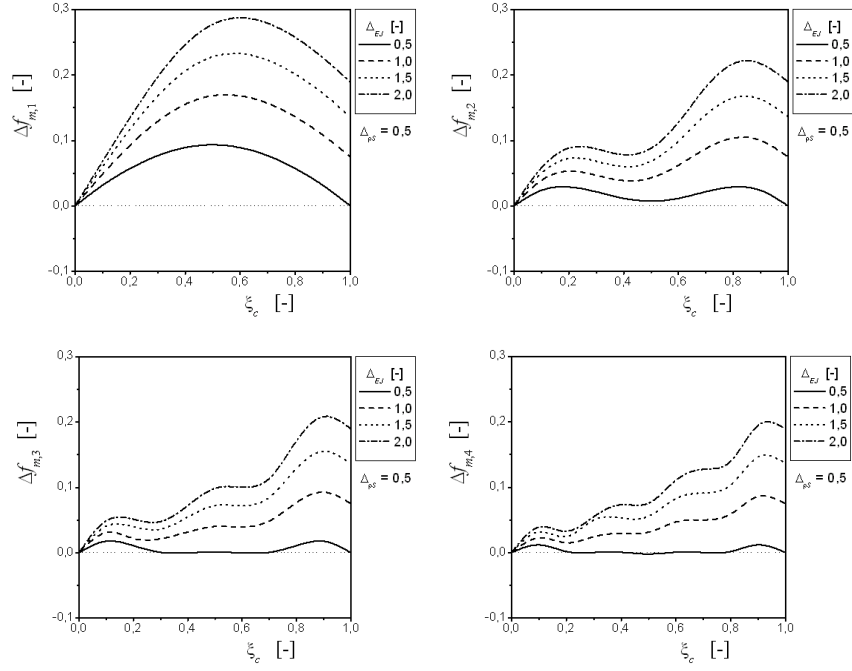


Figure 3. Dependency of $\Delta f_{m,i}$ ($i = 1 \div 4$) on ξ_c - Type I ($\Delta_{EJ} = 0.5 \div 2.0$, $\Delta_{pS} = 0.5$).

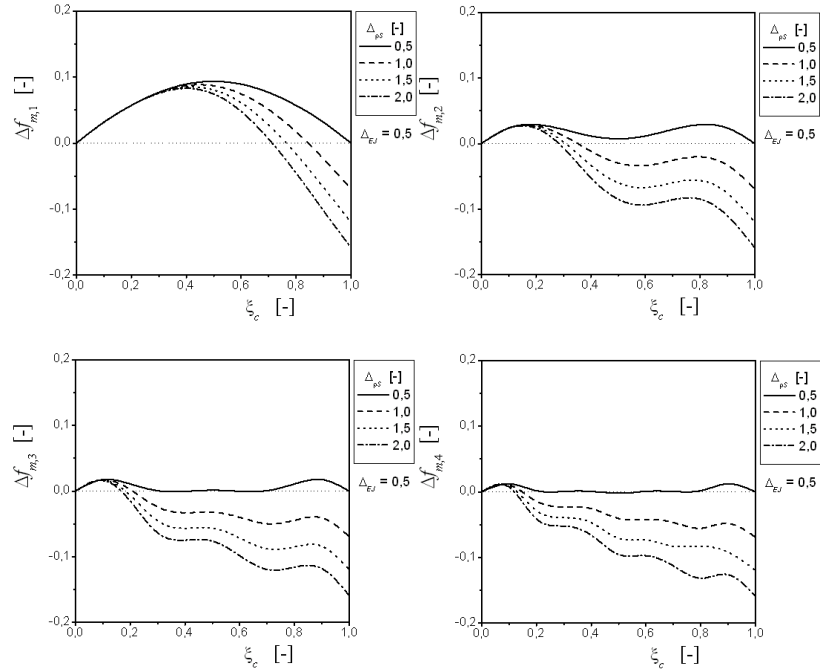


Figure 4. Dependency of $\Delta f_{m,i}$ ($i = 1 \div 4$) on ξ_c - Type I ($\Delta_{EJ} = 0.5$, $\Delta_{pS} = 0.5 \div 2.0$).

The main difference in comparison with modification based on the change of partial insertion of reinforcing core (Type I) is the use of partial reinforcing core (Type II) of constant length l_c (resp. ξ_c) which is less than length of beam. Then the modification of modal properties also depends on the position of reinforcing core l_s (resp. ξ_s) in the beam structure. The dependence of increment of modification function $\Delta f_{m,i}$ ($i = 1 \div 4$) on dimensionless length $\xi_c + \xi_s$, for various values of dimensionless length of core ξ_c and different combinations the stiffness modification parameters Δ_{EJ} and mass modification parameter $\Delta_{\rho S}$ are shown in the following figures (Fig. 5 ÷ Fig. 7). The changes in the considered structural parameters of beam structure Type II have the greatest impact on modification function for the first natural frequency. As it can be seen from Fig.5, the influence of individual considered parameters, especially geometric parameters determining the length and position of reinforcing core on increment of modification function for the second, third and fourth natural frequency seems to be non-significant in regard to the objectives of structural dynamic modification. Similarly as in the case of beam structure Type I, the mutual combination of values of structural modification parameters Δ_{EJ} and $\Delta_{\rho S}$ for Type II have an important role with regard to the value of modification function.

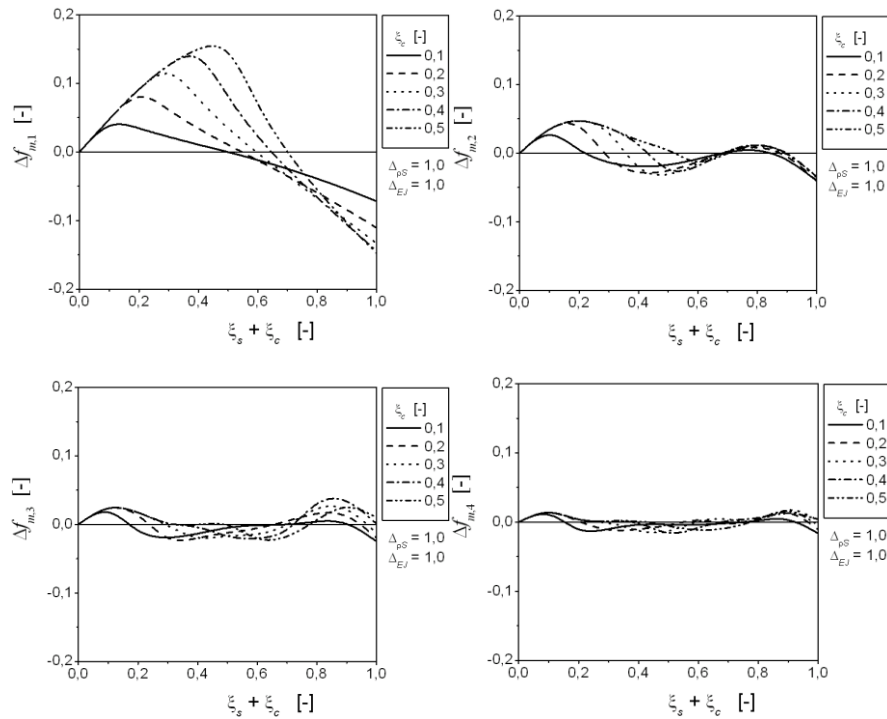


Figure 5. Dependency of $\Delta f_{m,i}$ on $\xi_s + \xi_c$ for different ξ_c - Type II ($\Delta_{EJ} = 1.0$, $\Delta_{\rho S} = 1.0$).

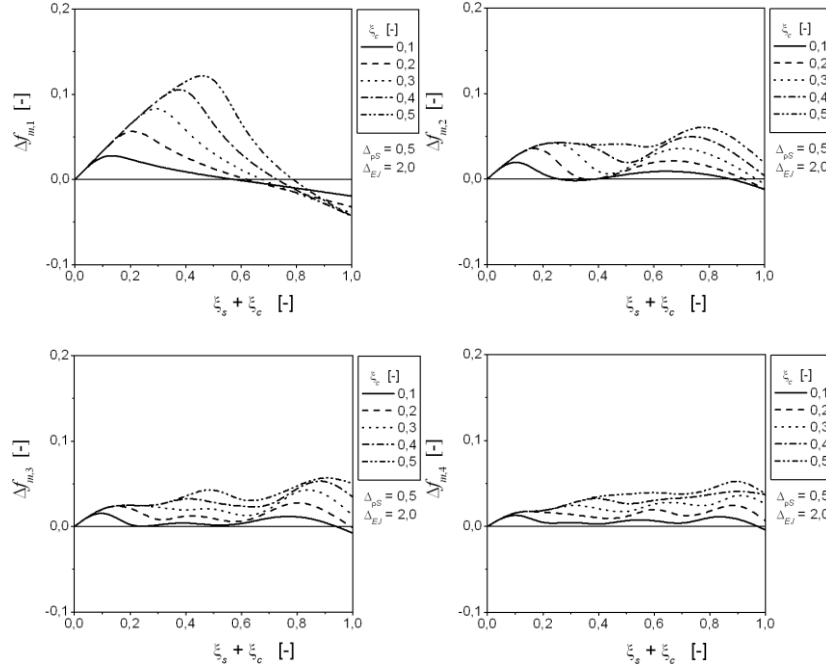


Figure 6. Dependency of $\Delta f_{m,i}$ on $\xi_s + \xi_c$ for different ξ_c - Type II ($\Delta_{EJ} = 2.0$, $\Delta_{pS} = 0.5$).

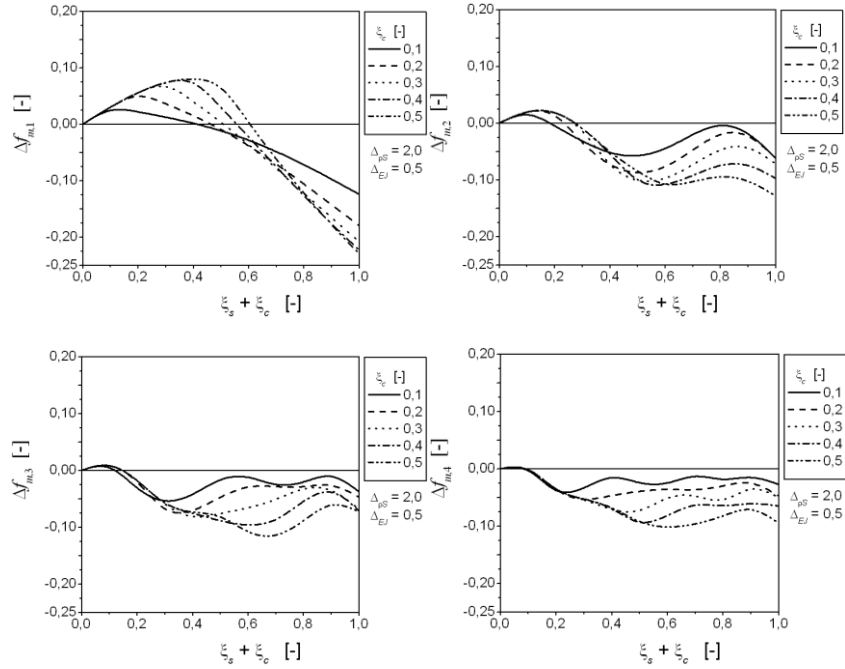


Figure 7. Dependency of $\Delta f_{m,i}$ on $\xi_s + \xi_c$ for different ξ_c - Type II ($\Delta_{EJ} = 0.5$, $\Delta_{pS} = 2.0$).

4. Experimental measurements

Experimental modal analysis of both types of beam structures (Type I, Type II) was performed for verification the results of computational analyses. The material of basic beam body is aluminium alloy EN AW6060 and for reinforcing core the steel threaded rod has been used. The geometrical dimensions and material properties are shown in Table 3. The measurements were carried out using a measuring system PULSE Brüel & Kjær (3560B-120), PULSE LabShop, accelerometer (4508B) and impact hammer (8206-001). Beam structure with attached accelerometer is shown in Fig. 8.

Table 3. Geometrical dimensions and material properties

Part of structure	Material properties			Geometrical parameters [mm]	
	E [GPa]	ρ [kg.m ⁻³]	ν [-]		
basic beam body	53	2709	0.3	$l_0 = 220$	$d_0 = 20$
core - Typ I	163	7805	0.3	$l_c = 0 \div 220$	$d_c = M12$
core - Typ II	163	7805	0.3	$l_c = 40 \text{ and } 80$	$d_c = M12$

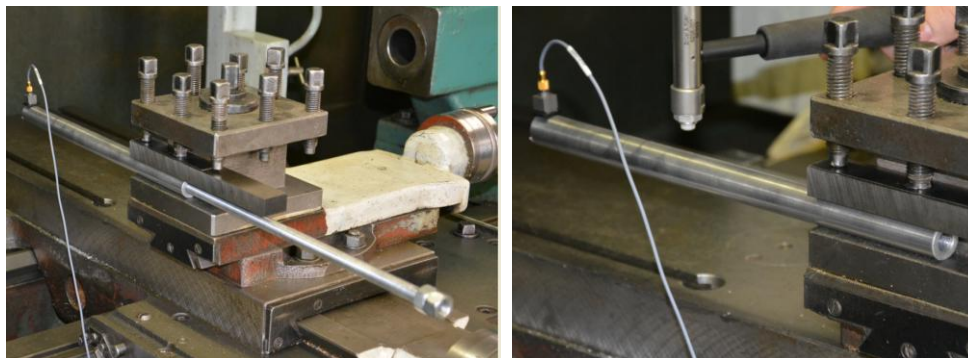


Figure 8. System for the experimental measurements

It can be concluded that the trend of the curves from the above comparison clearly shows the relatively good agreement between the experimental measurement and numerical calculations (Fig.9). In view of the small differences between measured and calculated values it shows that the experimental measurements confirmed the correctness of the results of numerical calculations. The small deviations of the values of natural frequencies can be caused by imperfections in fixing of the beam body or as a result of threaded connection of the core and beam body.

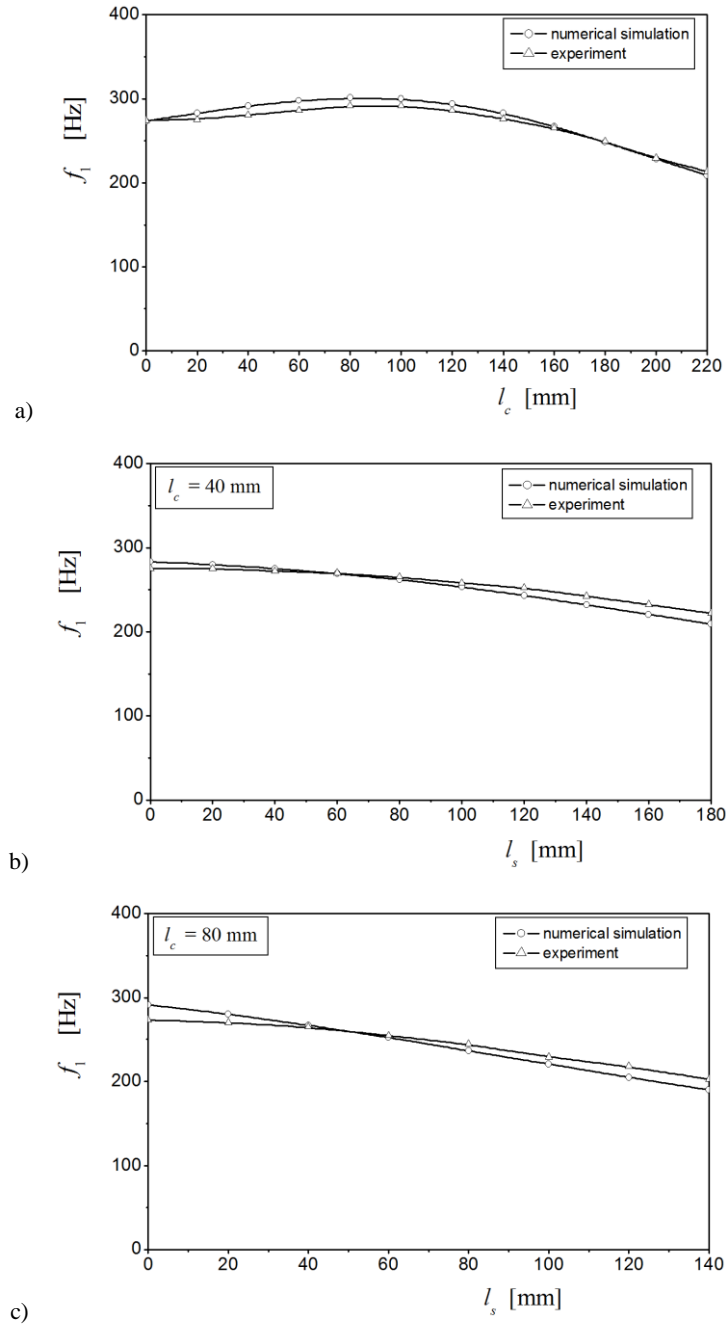


Figure 9. Comparison of measured and calculated values for the first natural frequency f_1
(a - Type I; b - Type II, $l_c = 40$ mm; c - Type II, $l_c = 80$ mm)

5. Conclusions

The modification of dynamical properties of clamped beam structure by reinforcing core is presented in this paper. Structural modification of the beam structure by the length insertion of the reinforcing core with uniform cross-section provides an effective way of the modal properties modification of the beam structures. By changing the core length, inserted into the beam, it is possible to achieve a significant modification of natural frequencies of the beam. The results obtained confirm that this manner of the structural modification of beam offers a very effective tool to the modification of dynamical properties or to the dynamical tuning of the similar beam structures.

Acknowledgments

The support of research project VEGA-1/0356/13 and “Programme to support of young researchers”, project Analysis of dynamical properties of waveguide for application of mechatronical principles in UAM is gratefully acknowledged.

References

- [1] Meirovitch, L. *Analytical methods in vibrations*, McMillan Company, London, 1987.
- [2] Nad', M., Rolník, L., and Steinhauser, J. Vibration analysis of reinforced beam structure using partially inserted longitudinal core. *Applied Mechanics and Materials*, 693 (2014), 311-316.
- [3] Nad', M. Dynamical analysis of machining tool body with reinforced inner core of circular shape. *Applied and Computational Mechanics* 3 (2009), 153–162.
- [4] Rolník, L. *Structural dynamic modification of lathe tool body*. PhD. Thesis, Slovak University of Technology in Bratislava, Faculty of Materials Science and Technology, 2015, supervisor - M. Nad'.
- [5] Thorby, D. *Structural dynamics and vibration in practice - An engineering handbook*, Elsevier Ltd., Oxford, 2008.
- [6] Youssef, A.H., and El-Hofy H. *Machining technology-Machine tools and operations*, CRC Press - Taylor & Francis Group, Boca Raton, 2008.

Milan Nad', Assoc. Professor: Slovak University of Technology in Bratislava, Faculty of Materials Science and Technology in Trnava, Institute of Applied Informatics, Automation and Mechatronics, Department of Applied Mechanics and Mechatronics, Paulínska 16, 917 24 Trnava, Slovak Republic (milan.nad@stuba.sk). “The author gave a presentation of this paper during one of the conference sessions.”

Ladislav Rolník, Ph.D.: Slovak University of Technology in Bratislava, Faculty of Materials Science and Technology in Trnava, Institute of Applied Informatics, Automation and Mechatronics, Department of Applied Mechanics and Mechatronics, Paulínska 16, 917 24 Trnava, Slovak Republic (ladislav.rolnik@stuba.sk).

Čičmancová Lenka, Ph.D.: Slovak University of Technology in Bratislava, Faculty of Materials Science and Technology in Trnava, Institute of Applied Informatics, Automation and Mechatronics, Department of Applied Mechanics and Mechatronics, Paulínska 16, 917 24 Trnava, Slovak Republic (lenka.cicmancova@stuba.sk).

**A hypoid gear pair tribo-dynamic model taking into account the rheological behaviour of fully formulated gear lubricants
(VIB049-15)**

Leonidas Paouris, Stephanos Theodossiades, Ramin Rahmani
Gregory Hunt

Abstract: A fully coupled tribo-dynamic model, capable of predicting the inefficiency and dynamic response of automotive differential hypoid gear pairs, is presented in this study. A gear dynamics solver is coupled with an analytical friction solver, which calculates the viscous shear, as well as the boundary conjunctional friction force. The time varying geometry and contact characteristics of the hypoid gear pair are taken into account by using realistic data available in the literature. The rheological models employed cover a range of two different behaviours: Newtonian and non-Newtonian Eyring (shear thinning). The Chittenden-Dowson equation is used to calculate the central film thickness of the elastohydrodynamic teeth conjunctions. The boundary friction force is calculated using the Greenwood & Tripp model. Finally, the actual surface topography of a run-in hypoid gear is obtained using a stylus profilometer. The results indicate an overestimation of the viscous friction by the Newtonian model, as opposed to the non-Newtonian model, mainly due to shear thinning effects. Comparative studies are performed for different operating conditions, namely close or away from the main resonance, as well as for conditions corresponding to a non-linear sub-harmonic resonance. The frictional damping effect on the dynamic transmission error, which is an indication of the Noise Vibration and Harshness NVH response of the gear pair, is also examined.

Introduction

Hypoid gear pairs are some of the most heavily loaded components of the drivetrains of modern automobiles. They are one of the key components of the differential unit, which is used to transfer the engine torque from the main driveshaft to the wheels of the vehicle. In order to do so, the torque has to be transferred between two perpendicular and non-intersecting shafts. This configuration of the gear pair leads to significant sliding motion between their meshing teeth, which in turn is a major source of conjunctional power losses. An extra amount of power losses is added through the bearing losses, as well as through churning losses in the oil sump of the differential unit [1]. Examining the power losses of hypoid gear pair drives has been a subject of several studies. Xu and Kahraman [2] were among the first to perform such a numerical analysis. They focused on the conjunctional losses of hypoid gear pairs by employing the quasi-static Tooth Contact Analysis (TCA) technique in order to simulate the contact condition within the flanks of the meshing teeth. The friction force calculations were performed by either employing analytical friction coefficient formulae from the published literature, or by solving the one-dimensional Elastohydrodynamic Lubrication (EHL)

problem with known input conditions obtained by the TCA. Nonetheless, the actual dynamic response, prevalent in real life applications of the gear pair, could not be captured since the analysis was quasi-static. Consequently, the influence of non-linear jump phenomena, resonance and tooth separation, which seem to influence the conjunctional power losses [3], were not considered in the results. Additionally, the angled flow component of the entraining velocity of the lubricant has not been taken into account, since the one-dimensional EHL problem has been considered, which also seems to influence the magnitude of the central film thickness [4] and in turn the conjunctional power losses. A more recent study by Karagiannis et al. [5] has also attempted to numerically predict the conjunctional power losses of highly loaded hypoid gear pairs under the influence of dynamic loading. A 2-Degree-of-Freedom (2DoF) torsional gear dynamic model has been employed in order to predict the dynamic response of the gear pair under realistic driving conditions. An analytical EHL friction solver has been used, in conjunction with a boundary friction solver, in order to predict the conjunctional friction. The present study attempts to extend the study of Karagiannis et al. [5] to a 4-Degree-of-Freedom (4DoF) torsional gear dynamics model which takes into account the torsional stiffness of the pinion and the ring gear shafts.

2. Theory and governing equations

2.1 Methodology

A torsional gear dynamics solver is employed to predict the dynamic response of the gear pair under a wide range of input torque. The conjunctional friction force is considered in the equations of motion of the gear pair. An analytical friction solver is employed to calculate the magnitude of the friction force at each time step. The viscous and boundary components of friction between the meshing gear teeth are taken into account. The viscous component of friction is calculated using the Newtonian assumption as well as the non-Newtonian Eyring assumption (shear thinning). The calculation of the component of boundary friction is performed by employing the Greenwood-Tripp model [6]. The Greenwood-Tripp parameters describing the roughness features of the gear teeth surfaces are determined by utilising the surface profile of a run-in pinion tooth and applying the procedure recommended by Arcoumanis et al. [7]. The instantaneous contact geometry and the instantaneous meshing stiffness are determined by employing TCA data that are available in the published literature [8], representing a realistic hypoid gear pair design.

2.2 Gear dynamics

A 4DoF torsional gear dynamics model is used to predict the dynamic response of the gear pair. The degrees of freedom that are considered are the angular displacements of the pinion shaft, the pinion

wheel, the gear wheel and the gear shaft. An additional integration in time domain is performed to calculate the Dynamic Transmission Error (DTE) by considering the time history of its variation. Equations (1) to (4) represent the equations of motion for the 4DoF lumped parameter torsional gear dynamics model employed.

$$\ddot{\phi}_s = \frac{1}{I_s} [-k_{t1}(\phi_s - \phi_p) - c_{t1}(\dot{\phi}_s - \dot{\phi}_p) + T_s] \quad (1)$$

$$\ddot{\phi}_p = \frac{1}{I_p} [-R_p(k_m f + c\dot{x}) + k_{t1}(\phi_s - \phi_p) + c_{t1}(\dot{\phi}_s - \dot{\phi}_p)] \quad (2)$$

$$\ddot{\phi}_g = \frac{1}{I_g} [R_g(k_m f + c\dot{x}) - k_{t2}(\phi_g - \phi_w) - c_{t2}(\dot{\phi}_g - \dot{\phi}_w)] \quad (3)$$

$$\ddot{\phi}_w = \frac{1}{I_w} [k_{t2}(\phi_g - \phi_w) + c_{t2}(\dot{\phi}_g - \dot{\phi}_w) - T_w] \quad (4)$$

The lumped parameter model described by equations (1) to (4) is illustrated in Figure (1).

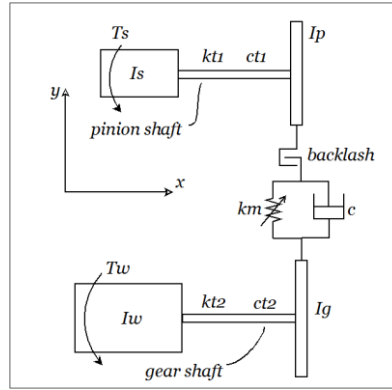


Figure 1. The lumped parameter dynamic model used.

In equations (1) to (4), the backlash function f , the dynamic transmission error x and the resistive torque at the gear shaft are calculated using equations (5) to (7).

$$f = \begin{cases} x - b & \text{when } x \geq b \\ 0 & \text{when } -b < x < b \\ x + b & \text{when } x \leq -b \end{cases} \quad (5)$$

$$x = \int (R_p(t)\dot{\phi}_p - R_g(t)\dot{\phi}_g)dt - e \quad (6)$$

$$T_w = r_w \left(m_v g f_r \cos(a) + m_v g \sin(a) + c_a A_f \frac{\rho}{2} u_v^2 \right) \quad (7)$$

The backlash function used in the present model (equation (5)) is similar to that recommended by Kahraman and Singh [9]. The calculation of the resistive torque on the ring gear shaft (equation (7)) takes into account the rolling resistance between the tire and the road, the resistance due to the

inclination of the road as well as the velocity related aerodynamic drag [10]. Finally, instantaneous values of the contact radii of the pinion and the gear, the meshing stiffness and the static transmission error are calculated by employing equations (8) to (11).

$$g = g_0 + \sum_i g_{si} \sin(iN_g \varphi_g) + \sum_i g_{ci} \cos(iN_g \varphi_g) \quad (8)$$

$$p = p_0 + \sum_i p_{si} \sin(iN_p \varphi_p) + \sum_i p_{ci} \cos(iN_p \varphi_p) \quad (9)$$

$$k_m = k_{m0} + \sum_i k_{msi} \sin(iN_p \varphi_p) + \sum_i k_{mci} \cos(iN_p \varphi_p) \quad (10)$$

$$e = e_0 + \sum_i e_{si} \sin(iN_p \varphi_p) + \sum_i e_{ci} \cos(iN_p \varphi_p) \quad (11)$$

Equations (8) to (11) are expanded until the 8th term. The values of the Fourier coefficients are the same as those used by Mohammadpour et al. [3] and correspond to a hypoid gear pair with the characteristics displayed in Table (1).

Table 1. Geometric features of the hypoid gear pair under study.

Parameter	Pinion	Gear
Teeth Number (-)	13	36
Face Width (mm)	33.851	29.999
Face Angle (°)	29.056	59.653
Pitch Angle (°)	29.056	59.653
Root Angle (°)	29.056	59.653
Spiral Angle (°)	45.989	27.601
Pitch Apex (mm)	-9.085	8.987
Face Apex (mm)	1.368	10.948
Outer Cone Distance (mm)	83.084	95.598
Offset (mm)	24.0	24.0
Sense (hand)	Right	Left

2.3 Elastohydrodynamic Lubrication

The regime of lubrication in highly loaded hypoid gear pairs is predominantly Elastohydrodynamic, as recommended by the results presented in the following sections. In the present study, to reduce the computational cost, the coefficient of the conjunctional viscous friction is calculated in an analytical manner. An EHL friction calculation algorithm is used which is explained in the present section. As soon as the load per flank, the local radii of curvature of the mating teeth and the magnitude of the entraining velocities are known, given the properties of the lubricant in the conjunction, the central and minimum film thickness can be determined analytically using the Chittenden-Dowson equations [11] (equations (12) and (13)).

$$H_{min} = 3.68U_e^{0.68}G^{0.49}W_e^{-0.073} \left[1 - e^{-0.67(R_s/R_e)^{2/3}} \right] \quad (12)$$

$$H_{cen} = 4.31U_e^{0.68}G^{0.49}W_e^{-0.073} \left[1 - e^{-1.23(R_s/R_e)^{2/3}} \right] \quad (13)$$

The low shear dynamic viscosity value of the lubricant used in equations (12) and (13) corresponds to the pressure and temperature of the oil at the inlet meniscus; hence, at atmospheric conditions if the effects of the inlet shear heating and the inlet convectional heating are neglected. The pressure dependence of the low shear dynamic viscosity is calculated according to Roeland's-Houpert equation [12], [13] (equation (14)).

$$\eta = \eta_0 e^{((\ln(\eta_0)+9.67)\{(1+5.1 \cdot 10^{-9}p)^Z-1\})} \quad (14)$$

Coefficient Z is calculated using equation (15), according to Houpert [13].

$$Z = \frac{\alpha}{5.1 \cdot 10^{-9}\{\ln(\eta_0)+9.67\}} \quad (15)$$

After the calculation of the central film thickness, using equation (13) for each pair of teeth in conjunction, its value is used for the calculation of the viscous traction force according to equations (16) and (17). Equation (16) is used when the Newtonian assumption for the lubricant rheological behaviour is considered, whereas equation (17) is employed when Ree-Eyring [14] shear thinning behaviour is assumed.

$$T_{v,N} = (A_{EHL} - A_{asp})\bar{\eta} \frac{|V_s|}{h_c} \quad (16)$$

$$T_{v,RE} = (A_{EHL} - A_{asp})\tau_0 \sinh^{-1} \left(\frac{\bar{\eta}|V_s|}{\tau_0 h_c} \right) \quad (17)$$

In equations (16) and (17) A_{EHL} represents the area of the elliptical contact footprint of the EHL conjunction for each of the meshing teeth. In both of these equations, $\bar{\eta}$ is the low shear dynamic viscosity of the lubricant at a pressure equal to the average Hertzian pressure in the conjunction. Both A_{EHL} and $\bar{\eta}$ are calculated using the theory of dry non-conformal contacts according to Hertz [15]. Finally, A_{asp} represents the contact area where direct inter-asperity contact occurs. The method for determining the value of this area is described in the following section (equation (19)). The gear oil used in the present study exhibits the characteristics listed in Table (2).

Table 2. Gear oil properties.

Property	Value
$\eta_0(Pas)$	0.135
$\alpha(Pa^{-1})$	10^{-8}
$\tau_0(Pa)$	$2 \cdot 10^6$

2.4 Boundary friction

The contribution of boundary friction due to the interaction of asperities is calculated by employing the Greenwood - Tripp model [6]. The underlying assumption is that the peak height distribution of the asperities on the mating surfaces (pinion and gear teeth) follows a Gaussian distribution. This is generally the case for the majority of the metallic engineering surfaces according to Greenwood and Williamson [16]. To calculate the value of the boundary conjunctional friction, equations (18) and (19) are employed yielding the total load carried by the asperities and the total surface area within which inter-asperity contact occurs.

$$W_{asp} = \frac{8\sqrt{2}}{15} \pi A_{EHL} (\eta_G \beta_G \sigma_G)^2 \sqrt{\frac{\sigma_G}{\beta_G}} E_r F_{5/2} \quad (18)$$

$$A_{asp} = \pi^2 A_{EHL} (\eta_G \beta_G \sigma_G)^2 F_2 \quad (19)$$

The Greenwood-Tripp parameters appearing in equations (18) and (19) represent the surface density of the asperity peaks, the average radius of curvature of the asperity summits and the composite r.m.s. surface roughness of the mating surfaces. Greenwood and Tripp [6] suggest that for steel-on-steel contacts $0.03 \leq \eta_G \beta_G \sigma_G \leq 0.05$. For the case of highly loaded run-in hypoid gear pair teeth, where the lubricating oil contains extreme pressure (EP) additives, the lower limit of the recommended range may well be reduced. For that reason, η_G , β_G and σ_G values are calculated individually for a specific run-in hypoid pinion tooth surface, as described in the following section. The value of the statistical functions $F_{5/2}$ and F_2 are calculated according to De la Cruz et al. [17] (equations (20) and (21)).

$$F_2 = -0.0018\lambda_s^5 + 0.0281\lambda_s^4 - 0.1728\lambda_s^3 + 0.5258\lambda_s^2 - 0.8043\lambda_s + 0.5003 \quad (20)$$

$$F_{5/2} = -0.0046\lambda_s^5 + 0.0574\lambda_s^4 - 0.2958\lambda_s^3 + 0.7844\lambda_s^2 - 1.0776\lambda_s + 0.6167 \quad (21)$$

Finally, the magnitude of boundary friction is calculated by employing equation (22).

$$F_b = \tau_0 A_{asp} + \varsigma W_{asp} \quad (22)$$

Equation (22) accounts for two different sources of boundary friction. The product $\tau_0 A_{asp}$ represents the shearing of the tribo-film present at the asperity summits. It is assumed that the shear strength of the tribo-film is equal to the Eyring stress of the lubricant. The second source of boundary friction which is taken into account is the breaking of the cold welds formed between the asperities in contact. Its contribution is accounted for by using the product ςW_{asp} , where ς represents the coefficient of dry sliding friction of steel against steel. Its value is taken to be $\varsigma = 0.17$ according to De la Cruz *et al.* [17].

2.5 Surface topography

In order to take into account the component of boundary conjunctional friction due to the interaction of asperities, the surface profile of a run-in pinion tooth was studied. Two different techniques for determining the surface topography were employed: one optical and one mechanical. The optical technique is based on the principle of focus variation. An Alicona InfiniteFocus® optical microscope was used for that purpose (Figure (2)). A rotational unit was attached on the table of the machine to mount the pinion.

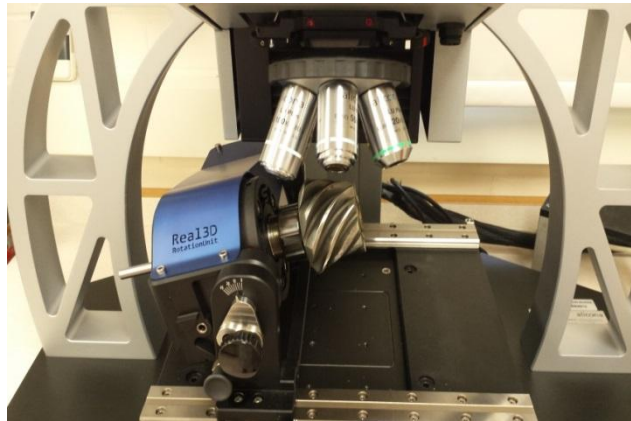


Figure 2. Alicona InfiniteFocus® microscope with the pinion attached on the rotational unit.

The principle of focus variation is explained below. Once the sample (pinion) has been placed on the rotational unit, the microscope is focusing on the region of interest on the tooth. Once it is focused, an upper and a lower focus boundary are set. Cross-sectional images are taken in between those boundaries. The compilation of those images yields the 2D surface topography of the pinion tooth at the point of interest. The mechanical technique of surface profile measurements that was employed is that of stylus profilometry. Six surface profiles along the axial and radial directions of the tooth were obtained: one set of two profiles each on the heel, the middle and the toe of the tooth. It was observed that the surface roughness parameters for each of those three profiles (yellow lines in Figure (3)) were of similar magnitude. Once the surface profiles were obtained, the Greenwood-Tripp parameters were calculated based on the procedure followed by Arcoumanis et al. [7]. The pair of profiles at the middle of the pinion tooth were considered for the present study as illustrated by the yellow lines in Figure (3).

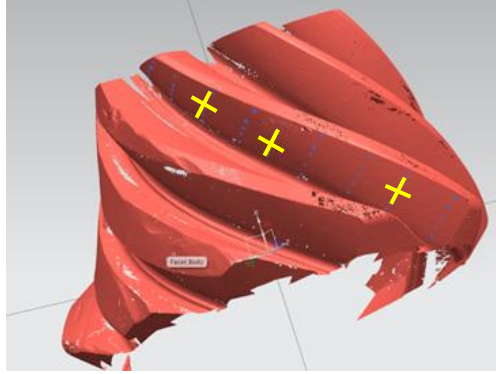


Figure 3. The pinion surface model along with the surface profiles considered (yellow lines).

Three spectral moments can be determined by applying equations (23) to (25) according to McCool [18].

$$m_0 = \overline{z^2(x)} \quad (23)$$

$$m_2 = \overline{\left(\frac{dz(x)}{dx}\right)^2} \quad (24)$$

$$m_4 = \overline{\left(\frac{d^2z(x)}{dx^2}\right)^2} \quad (25)$$

In order to account for the roughness profile along the axial and radial directions of the pinion tooth, the three spectral moments (equations (23)-(25)), are calculated along those directions. The spectral moments are calculated twice for the pinion tooth surface (once along the axial direction and once along the radial direction) and finally twice for the gear surface. In the present study the corresponding gear tooth surface profile has not been determined since it is assumed that it is exactly the same as the pinion tooth surface profile. The choice of the axial and radial directions of the pinion tooth for the determination of the spectral moments was made because the minimum and maximum surface roughness is observed along those directions, respectively. This is due to the fact that the axial direction of the tooth almost coincides with the direction of the polishing wear tracks on it. Equations (26) to (28) are employed to calculate the equivalent isotropic spectral moments of each of the two surfaces (of the pinion and gear) according to Sayles and Thomas [19].

$$m_{0e}^i = 0.5(m_{0a}^i + m_{0r}^i) \quad (26)$$

$$m_{2e}^i = \sqrt{m_{2a}^i + m_{2r}^i} \quad (27)$$

$$m_{4e}^i = \sqrt{m_{4a}^i + m_{4r}^i} \quad (28)$$

In equations (26) to (28), the superscript i refers to either the pinion or the gear tooth surface. The subscripts a and r refer to the axial and radial directions of the tooth surface, respectively. Finally, equation (29) is used to calculate the equivalent isotropic moments for the composite interface.

$$m_{n,ce} = m_{n,e}^p + m_{n,e}^g \quad (29)$$

Where, subscript n represents the spectral moment under determination and superscripts p and g represent the pinion and gear teeth surfaces, respectively. As soon as the equivalent combined isotropic spectral moments are determined, the Greenwood-Trip parameters can be calculated by employing equations (30) to (32) according to Longuet-Higgins [20] and Bush et al. [21].

$$\eta_G = \frac{1}{6\pi\sqrt{3}} \frac{m_{4,ce}}{m_{2,ce}} \quad (30)$$

$$\beta_G = 0.375 \sqrt{\frac{\pi}{m_{4,ce}}} \quad (31)$$

$$\sigma_G = \sqrt{m_{0,ce}} \quad (32)$$

3. Results

The 2D surface topography of the pinion surface (obtained using the focus variation technique) is shown in Figure (4). The same figure also illustrates the 1D profile of the pinion tooth along its axial direction, taken by a stylus profilometer. A cross section along the axial direction of the tooth is taken from the 2D surface topography measurements. The surface roughness parameters calculated using the 2D surface profile measurements and the profile obtained by employing the stylus profilometry come in very good agreement.

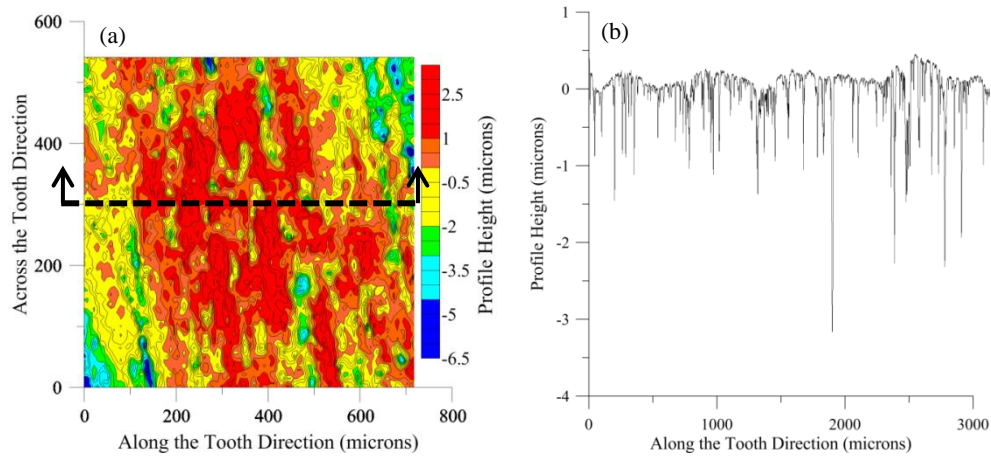


Figure 4. 3D surface topography of the run-in pinion (a) and the corresponding cross section (b).

By applying the Arcoumanis method [7], the Greenwood-Tripp parameters for the run-in hypoid gear pair generate the following values, $\eta_G = 0.0313 \cdot 10^{12} \text{ peaks/m}^2$, $\beta_G = 0.7471 \cdot 10^{-6} \text{ m}$ and $\sigma_G = 0.4462 \cdot 10^{-6} \text{ m}$. The product of those three parameters is 0.0104 which is considerably lower as compared to the typical values recommended by Greenwood and Tripp [6]. This is due to the polishing of the pinion and the ring gear teeth surfaces after some cycles of operation due to the running-in of the gears.

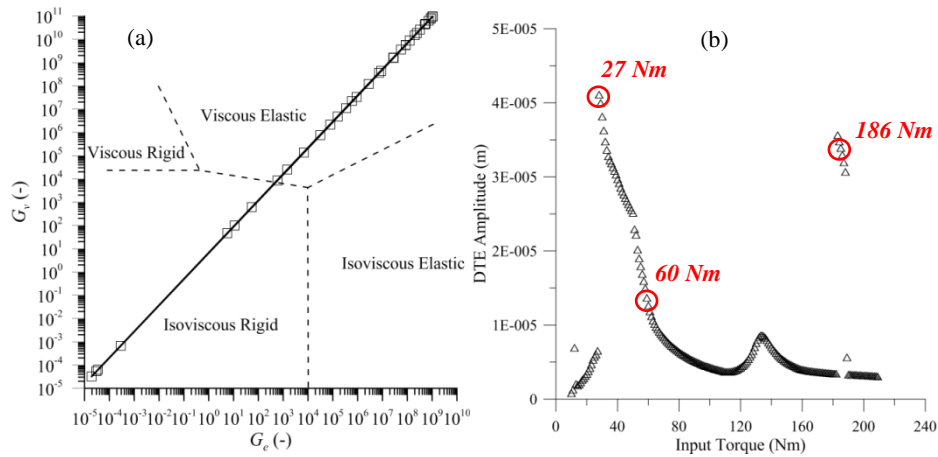


Figure 5. Greenwood chart for 60 Nm input torque (a) and DTE amplitude of the frictionless system (b).

Figure (5) illustrates the Greenwood chart (left) and the DTE response of the gear pair when friction is not taken into account in the integration of the equations of motion (right). An observation of the left part of Figure (5) validates the statement that the regime of lubrication for the greater part of the meshing cycle is that of EHL. Some points of the meshing cycle lie within the isoviscous-rigid regime of lubrication. Those points correspond to the very beginning and the very end of the meshing cycle, where the flank load is extremely reduced. For the present analysis, three different input torque values were chosen in order to investigate the tribo-dynamic response of the system. Those values are illustrated on the right part of Figure (5). The 27 Nm input torque corresponds to the 1st principal resonance frequency where significant tooth separation (due to the presence of backlash) occurs. The 60 Nm input torque corresponds to a vehicle cruising velocity of 80 km/hr while no tooth separation is observed. Finally, the 186 Nm input torque corresponds to a subharmonic resonance frequency. The magnitude of the non-linear jump observed in that region is found to be very sensitive upon the structural damping of the system.

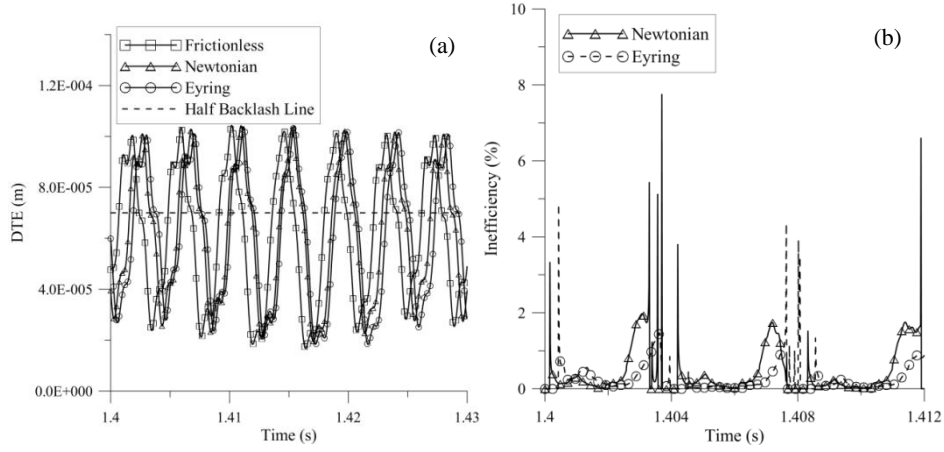


Figure 6. DTE (a) and inefficiency (b) for 27 Nm input torque.

Figures (6) to (8) illustrate the DTE response and inefficiency for the three different values of the input torque discussed above. Comparative curves assuming a frictionless conjunction as well as a lubricated conjunction, with and without the presence of the shear thinning effect, are also plotted. The general trend of those plots indicates that as the effect of the viscous friction becomes more significant, the DTE amplitude is decreased. The effect of viscous dissipation when the Eyring lubricant is considered, is mitigated as compared with the Newtonian lubricant, due to the influence of the shear thinning effect. Consequently, increased viscous dissipation leads to a better NVH response of the dynamic system, since the amplitude of the DTE is reduced. Nonetheless, the inefficiency plots indicate increased conjunctional inefficiency as the effect of viscous dissipation becomes more prevalent.

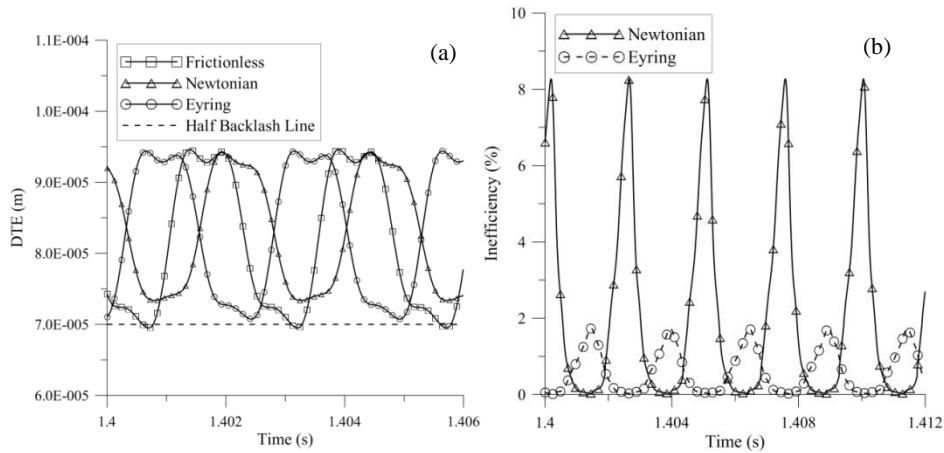


Figure 7. DTE (a) and inefficiency (b) for 60 Nm input torque.

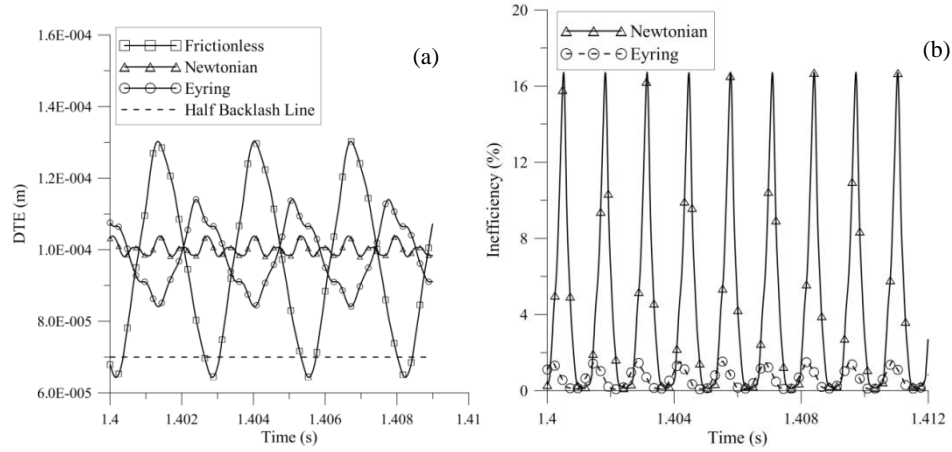


Figure 8. DTE (a) and inefficiency (b) for 186 *Nm* input torque.

The qualitative relationship between the DTE response, the magnitude of viscous dissipation and inefficiency must be carefully examined in order to yield an optimum combination of lubricant, and gear pair design, in terms of the NVH and inefficiency characteristics of the system. Furthermore, by examining Figures (6) to (8) it can be concluded that the inefficiency of the system at 27 *Nm* of input torque (primary resonance) seems to be reduced compared to the rest of the cases examined, despite the fact that the Stribeck parameter variation is within a lower range (Figure (9)), indicating that asperity interaction is more prevalent in that case. The asperity load ratio is also increased as compared to the rest of the cases corresponding to different values of input torque (Figures (9) to (11)). Furthermore, an observation of the inefficiency plots for 60 *Nm* and 186 *Nm* of input torque (Figures (7) and (8)) reveals that the inefficiency when the Newtonian assumption is used is increased for the case of 186 *Nm* of input torque. The opposite occurs when the shear thinning assumption is used. This is due to the fact that in the case of 186 *Nm* the central film thickness is increased, compared to the 60 *Nm*, because of the increased magnitude of the entraining velocity. At the same time, the central film thickness for the Newtonian case and the shear thinning lubricant will be the same for the same input torque, since the value of the low shear dynamic viscosity at the inlet is used for its calculation. However, the shear stress of the shear thinning lubricant will be considerably decreased, as compared to the Newtonian lubricant, when high shear rate is applied, because of the shear thinning effect. This phenomenon, combined with the increased film thickness at high input torque, will lead to a decreased inefficiency for the shear thinning lubricant. Furthermore, Figure (8) reveals that the frequency content of the DTE is changing when the viscous dissipation is taken into account. For the frictionless conjunction, the dominant frequency is half that observed when the

Newtonian lubricant is taken into account. This is because the Newtonian lubricant dissipates more energy from the system, suppressing the magnitude of the subharmonic resonance which is observed in Figure (5) for 186 *Nm* of input torque. The intensity of the shear thinning response of the lubricant strongly depends upon the quantity of the polymer additives (i.e., viscosity modifiers) blended with the base oil. Higher concentration of polymers in the base oil leads to a reduced value of the Eyring stress, and consequently a more intense shear thinning response of the fluid.

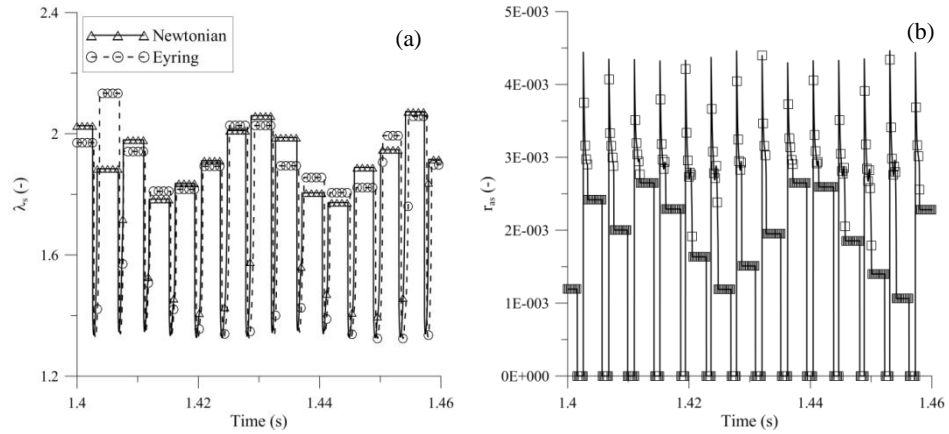


Figure 9. Stribeck parameter (a) and asperity load ratio (b) for 27 *Nm* input torque.

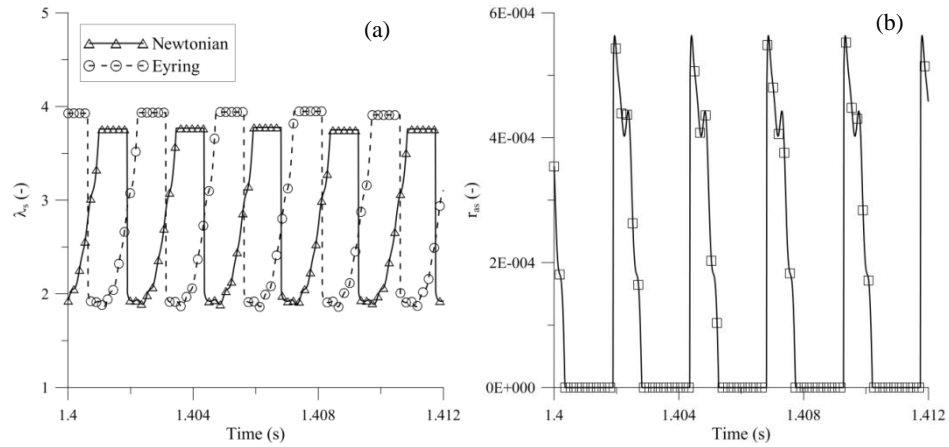


Figure 10. Stribeck parameter (a) and asperity load ratio (b) for 60 *Nm* input torque.

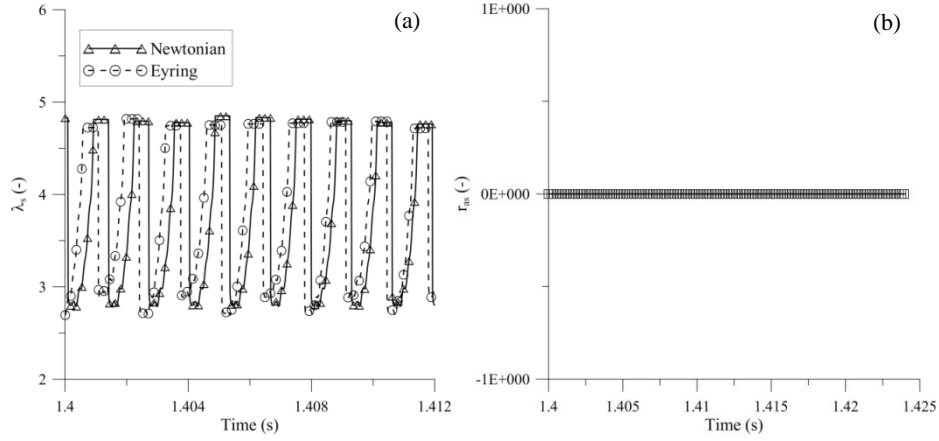


Figure 11. Stribeck parameter (a) and asperity load ratio (b) for 186 *Nm* input torque.

Finally, Figures (9) to (11) reveal the effect of the input torque on the Stribeck parameter and the asperity load ratio r_{as} on the highly loaded flank of the gear pair. Minor differences between the Newtonian and the shear thinning lubricants are observed in terms of those parameters. This is due to the fact that those parameters strongly depend on the magnitude of the central film thickness, which in turn is a function of the low shear characteristics of the lubricant (at the low shear inlet). The load carried by the asperities is in general a very small fraction of the total contact load carried by the flank. This is due to the low surface roughness r.m.s. of the mating teeth, after being polished during the run-in period. Based on the results of Figure (11), no load is carried by the asperities at 186 *Nm* of input torque, mainly due to the increased value of the film thickness which is an outcome of the increased entraining velocity of the lubricant in the conjunction.

4. Conclusions

Summarizing the finding of the present study, the following conclusions can be drawn,

- Increased viscous dissipation leads to improved NVH response of the system, however, the conjuncional inefficiency of the system seems to be increased.
- The conjuncional inefficiency of the system seems to be reduced at the region of the primary resonance, mainly due to teeth separation effects.
- Increased input torque leads to decreased inefficiency when the lubricant exhibits shear thinning behaviour. The opposite occurs when the shear thinning characteristics of the lubricant are not taken into account.
- The load carried by the asperities in run-in hypoid gear pair teeth conjunctions can be significantly lower, as compared to pristine gear teeth, due to the polishing effects taking place during the run-in period.

Acknowledgments

The authors would like to express their gratitude to Lubrizol Ltd. for sponsoring this research.

Nomenclature

a	: road inclination angle (<i>degrees</i>)
A_{asp}	: total area of asperity contact (m^2)
A_{EHL}	: area of the EHL contact ellipse (m^2)
A_f	: frontal area of the vehicle (m^2)
b	: half backlash length (m)
c	: mesh damping coefficient (Ns/m)
c_a	: coefficient of aerodynamic resistance ($-$)
c_{t1}	: torsional damping coefficient of the pinion shaft (Nms/rad)
c_{t2}	: torsional damping coefficient of the gear shaft (Nms/rad)
E_r	: reduced modulus of elasticity of the gear teeth (Pa)
f_r	: coefficient of rolling resistance between the road and the tyre ($-$)
g	: acceleration of gravity (m/s^2)
G	: Chittenden-Dowson material parameter ($-$)
h_c	: central film thickness (m)
H_{cen}	: Chittenden-Dowson dimensionless central film thickness ($-$)
H_{min}	: Chittenden-Dowson dimensionless minimum film thickness ($-$)
I_i	: mass moment of inertia ($i = s, p, g, w$) (kgm^2)
k_t	: torsional stiffness of the supporting shafts (Nm/rad)
m_v	: mass of the vehicle ($-$)
N_g	: ring gear teeth number ($-$)
N_p	: pinion teeth number ($-$)
p	: lubricant pressure (Pa)
r_{as}	: asperity load to total flank load ratio ($-$)
R_e	: radius of curvature along the direction of entraining motion (m)
R_g	: ring gear contact radius (m)
R_p	: pinion contact radius (m)
R_s	: radius of curvature along the side leakage direction (m)
r_w	: radius of the wheel (m)
T_s	: constant input torque at the pinion shaft (Nm)
T_w	: velocity dependent resistive torque at the gear shaft (Nm)

U_e	: Chittenden-Dowson dimensionless speed parameter (–)
u_v	: vehicle cruising speed (m/s)
V_s	: sliding velocity of the mating teeth (m/s)
W_e	: Chittenden-Dowson dimensionless load parameter (–)
α	: pressure-viscosity coefficient (Pa^{-1})
β_G	: asperity summit average radius of curvature (m)
η_0	: lubricant low shear dynamic viscosity at standard temperature and pressure (Pas)
η_G	: asperity summit density per unit area (m^{-2})
λ_s	: Stribeck parameter ($\lambda_s = h_c/\sigma_G$) (–)
ρ	: air density (kg/m^3)
σ_G	: combined r.m.s. surface roughness of the mating teeth (m)
τ_0	: Eyring shear stress of the lubricant (Pa)
φ_i	: rotation angle of the corresponding DoF ($i = s, p, g, w$) (rad)

References

- [1] H. Xu, A. Kahraman, and D. R. Houser, “A Model to Predict Friction Losses of Hypoid Gears,” *AGMA Tech. Pap.*, no. October, pp. 1–15, 2005.
- [2] H. Xu and a Kahraman, “Prediction of friction-related power losses of hypoid gear pairs,” *Proc. Inst. Mech. Eng. Part K J. Multi-body Dyn.*, vol. 221, no. 3, pp. 387–400, Jan. 2007.
- [3] M. Mohammadpour, S. Theodossiades, and H. Rahnejat, “Multiphysics Investigations on the Dynamics of Differential Hypoid Gears,” *J. Vib. Acoust.*, vol. 136, no. 4, p. 041007, Apr. 2014.
- [4] M. Mohammadpour, S. Theodossiades, and H. Rahnejat, “Elastohydrodynamic lubrication of hypoid gear pairs at high loads,” *Proc. Inst. Mech. Eng. Part J J. Eng. Tribol.*, vol. 226, no. 3, pp. 183–198, Jan. 2012.
- [5] I. Karagiannis, S. Theodossiades, and H. Rahnejat, “On the dynamics of lubricated hypoid gears,” *Mech. Mach. Theory*, vol. 48, pp. 94–120, Feb. 2012.
- [6] J. A. Greenwood and J. H. Tripp, “The contact of Two Nominally Flat Rough Surfaces,” *Proc. Inst. Mech. Eng.*, vol. 185, no. 48, pp. 625–633, 1970.
- [7] C. Arcoumanis, P. Ostovar, and R. Mortier, “Mixed Lubrication Modelling of Newtonian and Shear Thinning Liquids in a Piston-Ring Configuration,” *Int. Fall Fuels Lubr. Meet. Expo. Tulsa, Oklahoma, Oct. 13-16*, no. 412, pp. 35–60, 1997.

- [8] M. Mohammadpour, S. Theodossiades, and H. Rahnejat, "Tribo-Dynamics of Differential Hypoid Gears," *Proc. ASME Int. Des. Eng. Tech. Conf. Comput. Inf. Eng. Conf.*, pp. 1–9, 2013.
- [9] A. Kahraman and R. Singh, "Non-Linear Dynamics of a Spur Gear Pair," *J. Sound Vib.*, vol. 142, pp. 49–75, 1990.
- [10] R. Bosch, "Automotive Handbook," *Robert Bosch GmbH*, vol. Postfach, no. Plochingen, p. Germany, 2004.
- [11] R. J. Chittenden, D. Dowson, J. F. Dunn, and C. M. Taylor, "A Theoretical Analysis of the Isothermal Elastohydrodynamic Lubrication of Concentrated Contacts. I. Direction of Lubricant Entrainment Coincident with the Major Axis of the Hertzian Contact Ellipse," *Proc. R. Soc. A Math. Phys. Eng. Sci.*, vol. 397, no. 1813, pp. 245–269, 1985.
- [12] C. Roelands, "Correlational Aspects of the Viscosity-Temperature Pressure Relationship of Lubricating Oils," 1966.
- [13] L. Houpert, "New results of traction force calculations in elastohydrodynamic contacts," *J. Tribol.*, vol. 107, no. 2, pp. 241–248, 1985.
- [14] T. Ree and H. Eyring, "Theory of Non-Newtonian Flow. I. Solid Plastic System," *J. Appl. Phys.*, vol. 26, no. 7, pp. 793–800, 1955.
- [15] H. Hertz, "On the Contact of Elastic Solids," *J. reine angew. Math.*, vol. 92, pp. 156–171, 1881.
- [16] J. A. Greenwood and J. B. P. Williamson, "Contact of Nominally Flat Surfaces," *Proc. R. Soc. A Math. Phys. Eng. Sci.*, pp. 300–319, 1966.
- [17] M. De la Cruz, W. W. F. Chong, M. Teodorescu, S. Theodossiades, and H. Rahnejat, "Transient mixed thermo-elastohydrodynamic lubrication in multi-speed transmissions," *Tribol. Int.*, vol. 49, pp. 17–29, May 2012.
- [18] J. I. McCool, "Comparison of Models for the Contact of Rough Surfaces," *Wear*, vol. 107, pp. 37–60, 1986.
- [19] R. S. Sayles and T. R. Thomas, "Thermal Conductance of a Rough Elastic Contact," *Appl. Energy*, vol. 2, no. 2, pp. 249–267, 1976.
- [20] M. S. Longuet-Higgins, "The Statistical Analysis of a Random, Moving Surface," *Philos. Trans. R. Soc. A Math. Phys. Eng. Sci.*, vol. 249, no. 966, pp. 321–387, 1957.
- [21] A. W. Bush, R. D. Gibson, and T. R. Thomas, "The Elastic Contact of a Rough Surface," *Wear*, vol. 35, pp. 87–111, 1975.

Leonidas Paouris, Dipl. Eng. (Ph.D. student): Dynamics Research Group, Wolfson School of Mechanical & Manufacturing Engineering, Loughborough University, Loughborough, Leicestershire LE11 3TU, United Kingdom (L.Paouris@lboro.ac.uk). The author gave a presentation of this paper during one of the conference sessions.

Stephanos Theodossiades, Professor: Dynamics Research Group, Wolfson School of Mechanical & Manufacturing Engineering, Loughborough University, Loughborough, Leicestershire LE11 3TU, United Kingdom (S.Theodossiades@lboro.ac.uk).

Ramin Rahmani, Lecturer: Dynamics Research Group, Wolfson School of Mechanical & Manufacturing Engineering, Loughborough University, Loughborough, Leicestershire LE11 3TU, United Kingdom (R.Rahmani@lboro.ac.uk).

Gregory Hunt, Ph.D., (Research Chemist): Applied Sciences Department, Lubrizol Ltd., The Knowle, Nether Lane, Hazelwood, Derby, Derbyshire DE56 4AN, United Kingdom (Gregory.Hunt@Lubrizol.com).

Influence of the fibre spring-damper computational models in a mechanical system on the coincidence with the experimental measurement results

(VIB169-15)

Pavel Polach, Michal Hajžman, Miroslav Byrtus, Zbyněk Šika

Abstract: Experimental measurements focused on the investigation of a fibre behaviour are performed on an assembled weigh-fibre-pulley-drive mechanical system. The carbon fibre, which is driven by one drive, is led over a pulley. On its other end there is a prism-shaped steel weight, which moves in a prismatic linkage on an inclined plane. In presented case the position of the weight is symmetric with respect to the plane of a drive-pulley symmetry. Drive excitation signals can be of different shapes with the possibility of variation of a signal rate. Time histories of the weight position and of the force acting in the fibre are measured. The same system is numerically investigated by means of multibody model. The influence of dependences of the fibre spring-damper coefficients on velocity of the weight motion in the computational model on the coincidence of the simulation results and the experimental measurement results is evaluated. The simulations' aim is to create a phenomenological model of a fibre, which will be utilizable in fibre modelling in the case of more complicated mechanical or mechatronic systems.

1. Introduction

The replacement of the chosen rigid elements of manipulators or mechanisms by fibres or cables [1] is advantageous due to the achievement of a lower moving inertia, which can lead to a higher machine speed, and lower production costs. Drawbacks of using the flexible elements like that can be associated with the fact that cables should be only in tension (e.g. [2,3]) in the course of a motion.

Experimental measurements focused on the investigation of the fibre behaviour are performed on an assembled weigh-fibre-pulley-drive system [4-10]. The fibre is driven with one drive, it is led over a pulley and on its other end there is a prism-shaped steel weight, which moves on an inclined plane. The position of the weight can be symmetric (see figure 1) or asymmetric with respect to the plane of a drive-pulley symmetry (note: results with symmetric position of the weight are presented in this paper). It is possible to add an extra mass to the weight. Time histories of the weight position and of the force acting in the fibre are measured. The same system is numerically investigated using multibody models created in the **alaska** simulation tool [11]. The influence of the model parameters on the coincidence of the results of experimental measurements and the simulations results is

evaluated. The simulation aim is to create a phenomenological model of a fibre, which will be utilizable in fibre modelling in the case of more complicated mechanical or mechatronic systems.

The fibre damping coefficient, the fibre stiffness and the friction force acting between the weight and the prismatic linkage were considered to be system parameters of the phenomenological model. The parameters determined at investigating the weight-fibre system [12,13] were applied in the fibre model of the weight-fibre-pulley-drive system. The friction force acting between the weight and the prismatic linkage, as it has been confirmed [4-8], is not the parameter of the phenomenological model. This quantity is dependent on angle α of the inclined plane (see figure 1). At simulating the experimental measurements for “slower” drive motion [4-8] the local extremes of the time histories of the weight displacement and of the force acting in the fibre are independent of the fibre stiffness and the fibre damping coefficient (considered in feasible intervals of values). At simulating the experimental measurements for “quicker” drive motion [4-8] the local extremes of the monitored time histories are dependent on both the phenomenological model parameters (to explain: frequencies of drive motion – i.e. frequencies of input signal – higher than 1 Hz are designated as “quicker” drive motions, frequencies of drive motion lower than 1 Hz are designated as “slower” drive motions). From the obtained results it was evident that these parameters of the fibre phenomenological model must be, in addition, considered dependent on the velocity of the weight motion [9,10,14]. That is why the influence of considering the velocity-dependent stiffness [14] and/or the velocity-dependent damping “coefficient” [9]/[10] in the fibre model on dynamic response of the system was investigated.

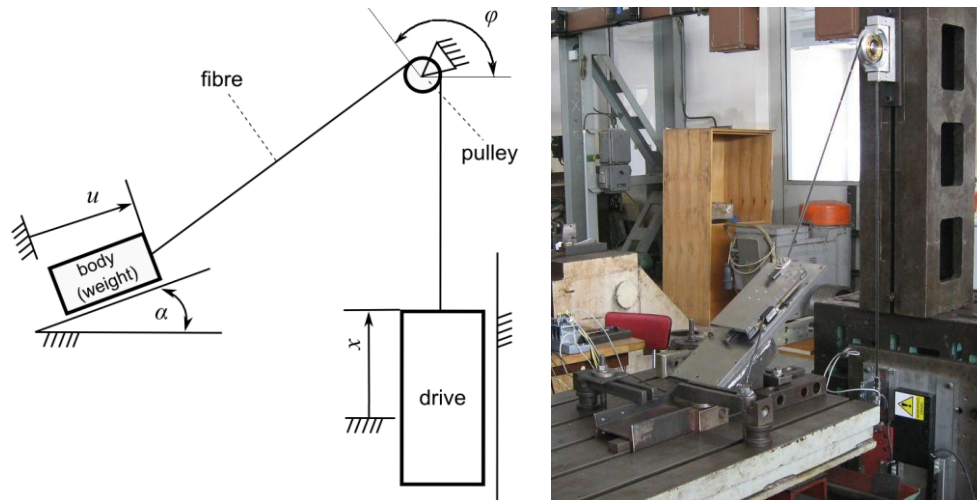


Figure 1. Scheme and a real weight-fibre-pulley-drive mechanical system (symmetric position of the weight).

2. Experimental stand

As it has been already stated experimental measurements focused on the investigation of the fibre behaviour are performed on an assembled weigh-fibre-pulley-drive mechanical system (see figure 1). A carbon fibre with a silicone coating (see e.g. [15]) is driven with one drive and it is led over a pulley. The fibre length is 1.82 meters (fibre weight is 4.95 grams), the pulley diameter is 80 millimetres. The weight position can be symmetric [4,6] (see figure 1) or asymmetric [5,7] with respect to the vertical plane of drive-pulley symmetry (distance of the weight from the vertical plane of drive-pulley symmetry is 280 millimetres in the case of the asymmetric weight position). At the drive the fibre is fixed on a force gauge. In the other end of the fibre there is a prism-shaped steel weight (weight 3.096 kilograms), which moves in a prismatic linkage on an inclined plane. It is possible to add an extra mass (weight 5.035 kilograms) to the weight [6,7]. The angle of inclination of the inclined plane can be changed. In the case of the symmetric weight position the angle is $\alpha = 30$ degrees and the pulley-fibre angle is $\varphi = 150$ degrees (in the case of the asymmetric weight position the angle is $\alpha = 30.6$ degrees and the pulley-fibre angle is $\varphi = 146$ degrees). Drive exciting signals can be of a rectangular, a trapezoidal and a quasi-sinusoidal shape and there is a possibility of variation of a signal rate. The amplitudes of the drive displacements are up to 90 millimetres. Time histories of weight position u (in direction of the inclined plane; measured by means of a dial gauge), of drive position x (in vertical direction) and of the force acting in the fibre (measured by a force gauge at drive) are recorded using a sample rate of 2 kHz.

3. Possibilities of the fibre modelling

The fibre (cable, wire etc.) modelling should be based on considering the fibre flexibility and suitable approaches can be based on the flexible multibody dynamics (see e.g. [16,17]). Flexible multibody dynamics is a rapidly growing branch of computational mechanics and many industrial applications can be solved using newly proposed flexible multibody dynamics approaches. Studied problems are characterized by a general large motion of interconnected rigid and flexible bodies with the possible presence of various nonlinear forces and torques. There are many approaches to the modelling of flexible bodies in the framework of multibody systems [18]. Comprehensive reviews of these approaches can be found in [17] or in [19]. Further development together with other multibody dynamics trends was introduced in [20]. Details of multibody formalisms and means of the creation of equations of motion can be found e.g. in [21] or [22].

The simplest way how to incorporate fibres in equations of motion of a mechanism is the force representation of a fibre (e.g. [23]). It is assumed that the mass of fibres is low to such an extent comparing to the other moving parts that the inertia of fibres is negligible with respect to the other parts. The fibre is represented by the force dependent on the fibre deformation and its stiffness and

damping properties. This way of the fibre modelling is probably the most frequently used one in the cable-driven robot dynamics and control (e.g. [24,25]). The fibre-mass system fulfils all requirements for modelling the fibre using the force representation of the fibre. A more precise approach is based on the representation of the fibre by means of a point-mass model (e.g. [26]). It has the advantage of a lumped point-mass model. The point masses can be connected by forces or constraints.

The massless fibre model is considered in this phase of investigation of the weight-fibre-pulley-drive system. The fibre model is considered to be phenomenological and it is modelled by the forces which comprise e.g. influences of fibre transversal vibration, “jumping” from pulley etc. The multibody models of the weight-fibre-pulley-drive system in the case of considering the symmetric and asymmetric position of the weight with respect to the plane of drive-pulley symmetry slightly differ [4], [5]. In the case of symmetric position the number of degrees of freedom in kinematic joints is 5 (in the case of asymmetric position the number of degrees of freedom in kinematic joints is 6). The weight (with added mass), the pulley and the drive are considered to be rigid bodies. A planar joint between the weight and the base (prismatic linkage), a revolute joint between the pulley and the base and a prismatic joint between the drive and the base (the movement of the drive is kinematically prescribed) are considered. Behaviour of this nonlinear system is investigated using the **alaska** simulation tool [11].

4. Simulation and experimental results

As it has already been stated the simulations aim was to create a phenomenological model of a fibre. When looking for compliance of the results of experimental measurement with the results of simulation influences of the fibre stiffness and the fibre damping coefficient are considered. The friction force acting between the weight and the prismatic linkage in which the weight moves was considered to be phenomenological model parameter in the first phase of investigation [12,13].

Investigation of the (carbon) fibre properties eliminating the influence of the drive and of the pulley was an intermediate stage before the measurement on the stand [12,13]. A phenomenological model dependent on the fibre stiffness, on the fibre damping coefficient and on the friction force acting between the weight and the prismatic linkage was the result of this investigation. When looking for the fibre model [13] that would ensure the similarity of time histories of the weight displacement and time histories of the dynamic force acting in a fibre as high as possible a fibre stiffness and a fibre damping coefficient were considered to be constant in this phase of the fibre behaviour research. The nonlinear friction force course (in dependence on the weight velocity) determined (especially on the basis [27] and [28]) at investigating the weight-fibre mechanical system [12] with the angle of inclination of the inclined plane $\alpha = 30$ degrees is applied in the model of the weight-fibre-pulley-

drive mechanical system [4-8]. Values of fibre stiffness and fibre damping coefficient were calculated on the basis of the values determined in [4] (see table 1).

At simulating the experimental measurements for a “quicker” drive motion [4-8] the local extremes of the time histories of measured and calculated weight displacement were more or less different. From these results it was evident that the parameters of the fibre phenomenological model must be, in addition, considered dependent on the velocity of the weight motion. That is why the influence of considering the velocity-dependent stiffness [14] and/or the velocity-dependent damping “coefficient” [9]/[10] in the fibre model on dynamic response of the system was investigated.

Velocity-dependent stiffness c of the fibre is supposed in the form

$$c = \begin{cases} c_c, & \text{if } v \leq v_{tr} \\ c_c + (v - v_{tr}) \cdot c_2, & \text{if } v > v_{tr}, \end{cases} \quad (1)$$

where c_c is constant fibre stiffness (taken from [4]), c_2 is constant, v is instantaneous velocity of the weight and v_{tr} is threshold value of the velocity of the weight. Optimal (constant) values of constant c_2 and threshold value of weight velocity v_{tr} were found. Threshold value of weight velocity v_{tr} was found in [14] and confirmed in [9] and [10].

Velocity-dependent damping “coefficient” b of the fibre is considered similarly as the velocity-dependent stiffness (see Eq. 1)

$$b = \begin{cases} b_c, & \text{if } v \leq v_{tr} \\ b_c + (v - v_{tr}) \cdot b_2, & \text{if } v > v_{tr}, \end{cases} \quad (2)$$

where b_c is constant fibre damping coefficient (taken from [4]), b_2 is constant. The optimal (constant) value of constant b_2 was found.

The influence of the velocity-dependent stiffness and/or the velocity-dependent damping “coefficient” values on time histories of the weight displacement (and also on time histories of the dynamic force acting in the fibre) was evaluated partly visually and partly on the basis of the value of the correlation coefficient between the records of the experimental measurements and the simulation results. Application of the approach based on the calculation of the statistical quantities that enables to express directly the relation between two time series has appeared to be suitable for comparing two time series in various cases – e.g. [29].

Correlation coefficient $R(\mathbf{p})$ [30] defined for two discrete time series $x^{(1)}$ (the time history recorded at experimental measurement) and $x^{(2)}(\mathbf{p})$ (the time history determined at simulation with the multibody model; function of investigated parameters \mathbf{p}) was calculated

$$R(\mathbf{p}) = \frac{\sum_{i=1}^n (x_i^{(1)} - \mu_1) \cdot [x_i^{(2)}(\mathbf{p}) - \mu_2(\mathbf{p})]}{\sqrt{\sum_{i=1}^n (x_i^{(1)} - \mu_1)^2 \cdot \sum_{i=1}^n [x_i^{(2)}(\mathbf{p}) - \mu_2(\mathbf{p})]^2}}, \quad (3)$$

where μ_1 and $\mu_2(\mathbf{p})$ are mean values of the appropriate time series. The maximum value of the correlation coefficient is 1. The more the compared time series are similar to each other the more the correlation coefficient tends to 1. The advantage of the correlation coefficient is that it quantifies very well the similarity of two time series by scalar value, which is obtained using a simple calculation.

The problem can be put as the problem of the minimization of the objective function in the form

$$\psi(\mathbf{p}) = (1 - R(\mathbf{p}))^2. \quad (4)$$

In table 1 there are given the optimal values of parameters in Eq. 1 and in Eq. 2 of the investigated model of the weight-fibre-pulley-drive mechanical system. From table 2 it is evident that the values of correlation coefficient $R(\mathbf{p})$ are “better” for the determined velocity-dependent coefficients than for the constant coefficients in the fibre model. In the time histories of the dynamic force acting in fibre the correlation coefficient $R(\mathbf{p})$ improvement is not evident very much – see table 3 (the values are of rather informative character). At time histories of dynamic force acting in the fibre during determining the optimum values of velocity-dependent coefficients attention was paid especially to keeping the character of their course and achieving the best possible agreement of extreme values of the measured and the calculated dynamic forces.

Table 1. Values of coefficients of the fibre model.

	Threshold value of the velocity	Stiffness		Damping coefficients	
	[m/s]	[N/m]	[N/s]	[N·s/m]	[N]
	v_{tr}	c_c	c_2	b_c	b_2
Constant coefficients	-	$34 \cdot 10^3$	-	27.5	-
Velocity-dependent stiffness	0.4	$34 \cdot 10^3$	730	27.5	0
Velocity-dependent damping “coefficient”	0.4	$34 \cdot 10^3$	0	27.5	385
Velocity-dependent coefficients	0.4	$34 \cdot 10^3$	850	27.5	3.1

Table 2. Values of correlation coefficient $R(\mathbf{p})$ [-] of the time histories of the weight displacement.

Tested situation	Constant coefficients	Velocity-dependent stiffness	Velocity-dependent damping “coefficient”	Velocity-dependent coefficients
2	0.9929	0.9937	0.9934	0.9954
3c	0.7552	0.9365	0.9190	0.9464
7a	0.9999	0.9999	0.9999	0.9999
10	0.9834	0.9838	0.9838	0.9836
11	0.2187	0.6909	0.6890	0.6534

Table 3. Values of correlation coefficient $R(\mathbf{p})$ [-] of the time histories of dynamic force acting in fibre.

<i>Tested situation</i>	<i>Constant coefficients</i>	<i>Velocity-dependent stiffness</i>	<i>Velocity-dependent damping "coefficient"</i>	<i>Velocity-dependent coefficients</i>
2	0.3904	0.3761	0.3847	0.2868
3c	0.03925	0.0909	0.2084	0.1640
7a	0.5673	0.5743	0.5743	0.5743
10	0.5078	0.5080	0.5142	0.5047
11	0.2323	0.6778	0.1146	0.1462

At “slower” drive motions the time histories of the weight displacement recorded at the experimental measurements and computed at the computer simulations are approximately identical (see [4-10] and figure 6a) and hence it is not desirable to change values of parameters of the fibre phenomenological model (i.e. it is not necessary to consider the parameters of the fibre phenomenological model velocity-dependent). It is evident that it was the reason why the threshold value of velocity v_w of the weight was determined in such a way that the maximum velocity of the weight during “slower” drive motions should be lower than v_w (see table 1).

Results of experimental measurements and simulations of five selected tested situations at weight symmetric position are presented in this paper (see figures 2 to 7). Four tested situations are at a “quicker” drive motion (see time histories of drive motion in figure 2a, figure 3a, figure 4a and figure 5a) and one situation is at a “slower” drive motion (see time history of drive motion in figure 6a).

General pieces of knowledge obtained at investigating the weight-fibre-pulley-drive system, independently of the combination of the position of the weight with respect to the plane of the drive-pulley symmetry (symmetric or asymmetric) [5] and of the mass of the weight (without or with added mass) [9], are similar.

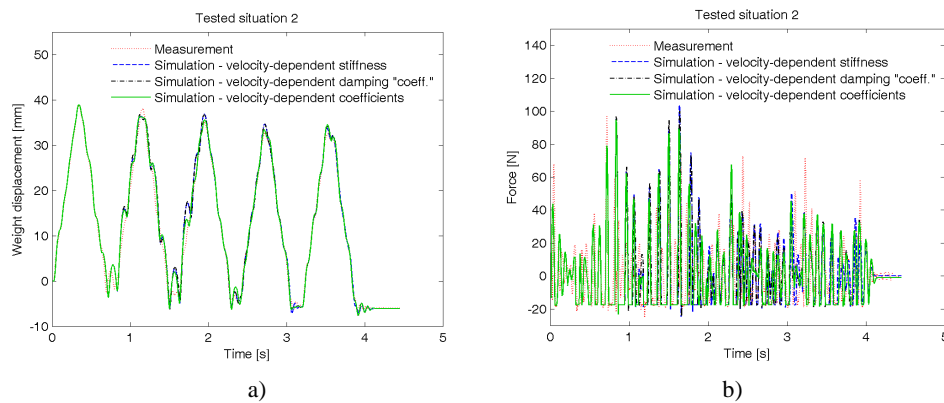


Figure 2. Time histories at a “quicker” tested situation (symmetric position of the weight, the weight without added mass), a) weight displacement, b) dynamic force acting in a fibre.

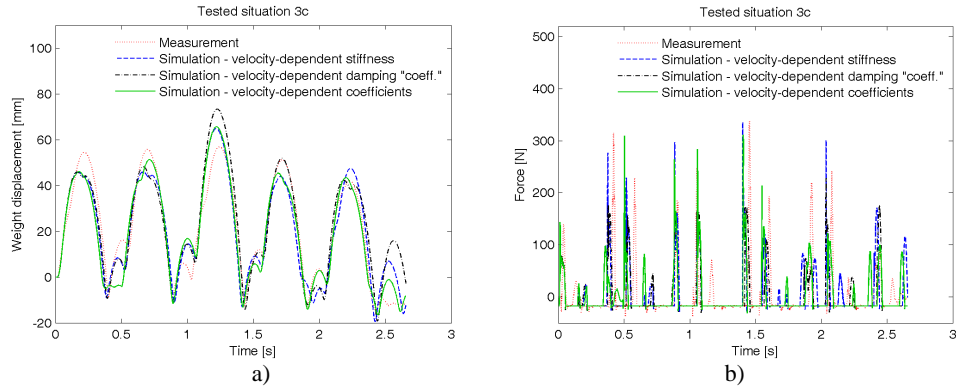


Figure 3. Time histories at a “quicker” tested situation (symmetric position of the weight, the weight without added mass), a) weight displacement, b) dynamic force acting in a fibre.

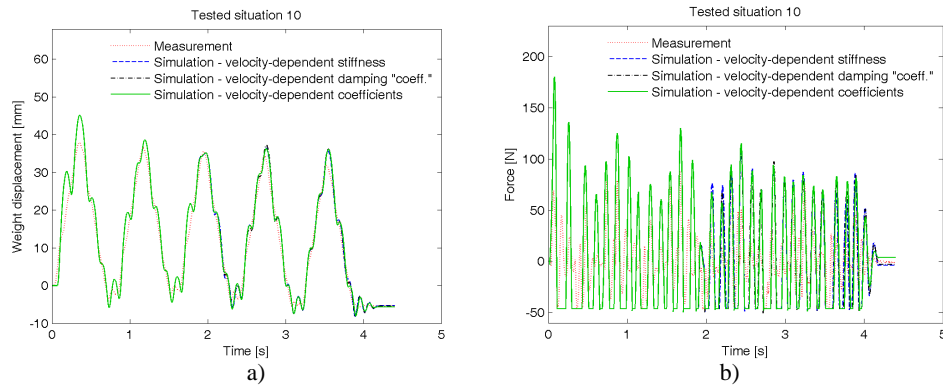


Figure 4. Time histories at a “quicker” tested situation (symmetric position of the weight, the weight with added mass), a) weight displacement, b) dynamic force acting in a fibre.

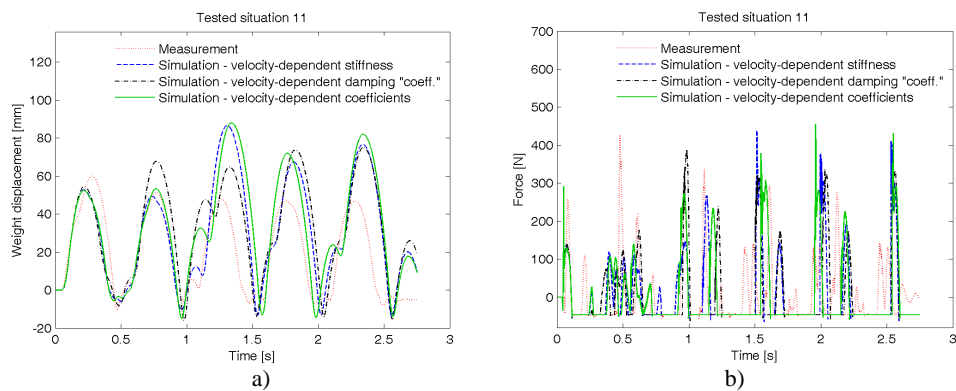


Figure 5. Time histories at a “quicker” tested situation (symmetric position of the weight, the weight with added mass), a) weight displacement, b) dynamic force acting in a fibre.

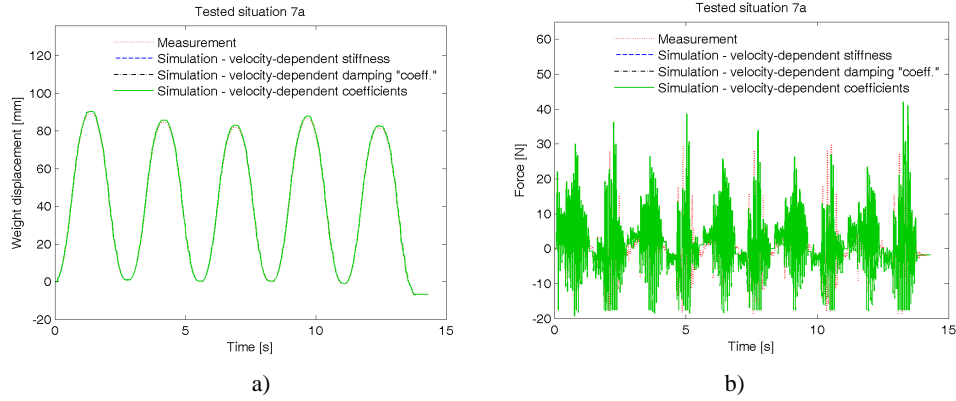


Figure 6. Time histories at a “slower” tested situation (symmetric position of the weight, the weight without added mass), a) weight displacement, b) dynamic force acting in a fibre.

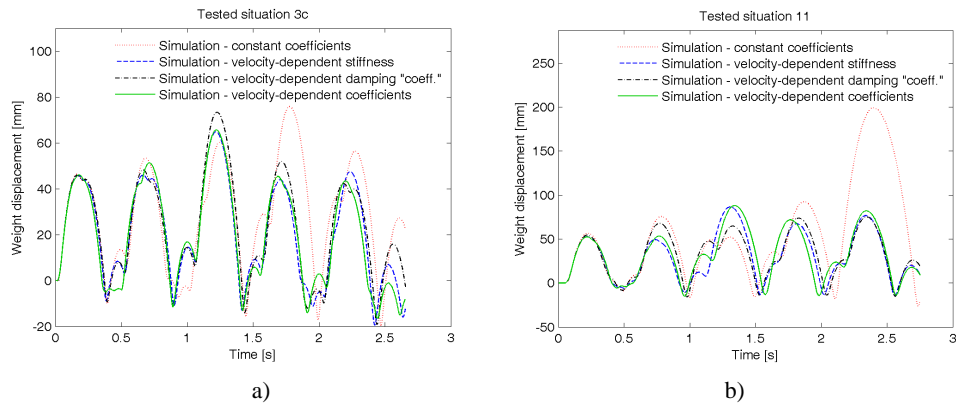


Figure 7. Time histories of the weight displacement at a “quicker” tested situation (symmetric position of the weight), a) the weight without added mass, b) the weight with added mass.

At the “quicker” tested situations the measured and the computed time histories of the weight displacement are of the same character (see figure 2a, figure 3a, figure 4a and figure 5a). On the basis of results it is evident that considering the velocity-dependent stiffness of the fibre in the model (not published), considering the velocity-dependent damping “coefficient” [10] and especially considering both the velocity-dependent stiffness and the velocity-dependent damping “coefficient” [9] have a great contribution to the improvement of agreement of the measured and the computed time histories and the local extremes of the weight displacement (see figure 2a, figure 3a, figure 4a and figure 5a).

As it has already been stated in [4-6,8-10] at all the simulations when changing the computational model parameters the time histories of a dynamic force acting in the fibre are different (more or less) but their character remains the same. From figure 2b, figure 3b, figure 4b, figure 5b and figure 6b it is evident that time histories of dynamic force acting in the fibre are not suitable for

determining the parameters of the fibre phenomenological model. It follows from the fact, that the phenomenological model of a fibre is to cover, as it has been stated, e.g. influences of the fibre transversal vibration, “jumping” from the pulley etc. As it does not include those phenomena physically (but by the change in the already introduced model parameters), it is evident, that the time histories of the dynamic force acting in the fibre cannot be expected to be of the same course.

It is evident that for searching for the parameters of the fibre phenomenological model it is necessary to use the results of experimental measurements with the “quicker” drive motion. The possibility of performing experimental measurements with other time histories of drive motion or with a different geometrical arrangement of the experimental stand will be analysed.

5. Conclusions

The approach to the fibre modelling based on the force representations was utilised for the investigation of the weight motion in the weigh-fibre-pulley-drive mechanical system. The simulation aim is to create a phenomenological model of the fibre, which will be utilizable in fibre modelling in the case of more complicated mechanical or mechatronic systems. The created phenomenological model is assumed to be dependent on the velocity-dependent fibre stiffness and/or the velocity-dependent fibre damping “coefficient”.

Development of the fibre phenomenological model continues. It can be supposed that in a more sophisticated phenomenological model of the fibre more complicated dependencies of the fibre stiffness and of the fibre damping “coefficient” on the weight velocity will be considered.

In addition it must be stated that the model of the fibre-pulley contact appears to be problematic in the computational model.

Acknowledgments

The paper has originated in the framework of institutional support for the long-time conception development of the research institution provided by the Ministry of Industry and Trade of the Czech Republic to Research and Testing Institute Plzeň and solving No. 15-20134S project of the Czech Science Foundation entitled “Multi-level Light Mechanisms with Active Structures”.

References

- [1] Chan, E.H.M. *Design and Implementation of a High-Speed Cable-Based Parallel Manipulator*. PhD Thesis, University of Waterloo, 2005, Supervisor Khajepour, A.
- [2] Valášek, M., and Karásek, M. HexaSphere with Cable Actuation. *Recent Advances in Mechatronics: 2008-2009*. Springer-Verlag, Berlin, 2009, pp. 239-244.
- [3] Gosselin, C., and Grenier, M. On the determination of the force distribution in overconstrained cable-driven parallel mechanisms. *Meccanica* 46, 1 (2011), 3-15.

- [4] Polach, P., Hajžman, M., Václavík, J., Šika, Z., and Svatoš, P. Model parameters influence of a simple mechanical system with fibre and pulley with respect to experimental measurements. *Proceedings of ECCOMAS Thematic Conference Multibody Dynamics 2013*. University of Zagreb, Faculty of Mechanical Engineering and Naval Architecture, Zagreb, 2013, CD-ROM.
- [5] Polach, P., Hajžman, M., Václavík, J., Šika, Z., and Valášek, M. Investigation of a laboratory mechanical system with fibre and pulley. *International Journal of Dynamics and Control* 3, 1 (2015), 78-86.
- [6] Polach, P., and Hajžman, M. Influence of the Mass of the Weight on the Dynamic Response of the Laboratory Fibre-Driven Mechanical System. *Mechanisms and Machine Science 24, New Trends in Mechanism and Machine Science, From Fundamentals to Industrial Applications*. Springer International Publishing Switzerland, 2014, pp. 233-241.
- [7] Polach, P., Hajžman, M., Václavík, J., and Červená, O. Dynamics of the Weight-fibre-pulley-drive Mechanical System: Influence of Mass of Weight at System Asymmetry. *Proceedings of National Colloquium with International Participation Dynamics of Machines 2014*. Institute of Thermomechanics AS CR, Prague, 2014, pp. 115-124.
- [8] Polach, P., and Hajžman, M. Utilizing of a Weight-fibre-pulley-drive Mechanical System for the Investigation of a Fibre Behaviour. *Proceedings of 20th International Conference Engineering Mechanics 2014*. Institute of Solid Mechanics, Mechatronics and Biomechanics, FME, BUT Brno, Svatka, 2014, pp. 500-503.
- [9] Polach, P., and Hajžman, M. Influence of the fibre spring-damper model in a simple laboratory mechanical system on the coincidence with the experimental results. *Proceedings of ECCOMAS Thematic Conference on Multibody Dynamics 2015*. Universitat Politècnica de Catalunya, Barcelona School of Industrial Engineering, Barcelona, 2015, pp. 356-365.
- [10] Polach, P., Hajžman, M., and Dupal, J. Influence of the Fibre Damping Model in a Simple Mechanical System on the Coincidence with the Experimental Measurement Results. *Proceedings of the 8th International Congress of Croatian Society of Mechanics*. Croatian Society of Mechanics, Opatija, 2015, CD-ROM.
- [11] Maißer, P., et al. *alaska, User Manual, Version 2.3*. Institute of Mechatronics, Chemnitz, 1998.
- [12] Polach, P., Hajžman, M., and Václavík, J. Simple fibre-mass model and experimental investigation. *Proceedings of National Colloquium with International Participation Dynamics of Machines 2013*. Institute of Thermomechanics AS CR, Prague, 2013, pp. 79-84.
- [13] Polach, P., Hajžman, M., and Václavík, J. Experimental and Computational Investigation of a Simple Fibre-mass System. *Proceedings of the 19th International Conference Engineering Mechanics 2013*. Institute of Thermomechanics AS CR, Svatka, 2013, CD-ROM.
- [14] Polach, P., Hajžman, M., Šika, Z., and Svatoš, P. Influence of fibre stiffness model in a weight-fibre-pulley-drive mechanical system on coincidence with experimental measurement results. *Proceedings of Extended Abstracts 30th Conference with International Participation Computational Mechanics 2014*. University of West Bohemia in Plzeň, Špičák, 2014, CD-ROM.
- [15] Polach, P., Václavík, J., and Hajžman, M. Load of fibres driving an inverted pendulum system. *Proceedings of the 50th annual international conference on Experimental Stress Analysis*. Czech Technical University in Prague, Faculty of Mechanical Engineering, Tábor, 2012, pp. 337-344.
- [16] Gerstmayr, J., Sugiyama, H., and Mikkola, A. Developments and Future Outlook of the Absolute Nodal Coordinate Formulation. *Proceedings of the 2nd Joint International Conference on Multibody System Dynamics*. University of Stuttgart, Institute of Engineering and Computational Mechanics, Stuttgart, 2012, USB flash drive.

- [17] Shabana, A.A. Flexible Multibody Dynamics: Review of Past and Recent Developments. *Multibody System Dynamics* 1, 2 (1997), 189-222.
- [18] Hajžman, M., and Polach, P. Modelling of flexible bodies in the framework of multibody systems. *Proceedings of the 6th International Conference Dynamics of Rigid and Deformable Bodies 2008*. Faculty of Production Technology and Management, UJEP in Ústí nad Labem, Ústí nad Labem, 2008, pp. 33-42.
- [19] Wasfy, T.M., and Noor, A.K. Computational strategies for flexible multibody systems. *Applied Mechanics Review* 56, 6 (2003), 553-613.
- [20] Schiehlen, W. Research trends in multibody system dynamics. *Multibody System Dynamics* 18, 1 (2007), 3-13.
- [21] Stejskal, V., and Valášek, M. *Kinematics and Dynamics of Machinery*. Marcel Dekker, Inc., New York, 1996.
- [22] Awrejcewicz, J. *Classical Mechanics: Dynamics*. Springer, New York, 2012.
- [23] Diao, X., and Ma, O. Vibration analysis of cable-driven parallel manipulators. *Multibody System Dynamics* 21, 4 (2009), 347-360.
- [24] Zi, B., Duan, B.Y., Du, J.L., and Bao, H. Dynamic modeling and active control of a cable-suspended parallel robot. *Mechatronics* 18, 1 (2008), 1-12.
- [25] Heyden, T., and Woernle, C. Dynamics and flatness-based control of a kinematically undetermined cable suspension manipulator. *Multibody System Dynamics* 16, 2 (2006), 155-177.
- [26] Kamman, J.W., and Huston, R.L. Multibody Dynamics Modeling of Variable Length Cable Systems. *Multibody System Dynamics* 5, 3 (2001), 211-221.
- [27] Půst, L., Pešek, L., and Radolfová, A. Various Types of Dry Friction Characteristics for Vibration Damping. *Engineering Mechanics* 18, 3-4 (2011), 203-224.
- [28] Awrejcewicz, J., and Olejnik, P. Analysis of Dynamic Systems With Various Friction Laws. *Applied Mechanics Review* 58, 6 (2005), 389-411.
- [29] Polach, P., and Hajžman, M. Design of Characteristics of Air-Pressure-Controlled Hydraulic Shock Absorbers in an Intercity Bus. *Multibody System Dynamics* 19, 1-2 (2008), 73-90.
- [30] Rektorys, K., et al. *Survey of applicable mathematics, Vol. II*. Kluwer Academic Publishers, Dordrecht, 1994.
- Pavel Polach, Ph.D.: Research and Testing Institute Plzeň, Materials and Mechanical Engineering Research, Tylova 1581/46, 301 00 Plzeň, Czech Republic (polach@vzuplzen.cz). The author gave a presentation of this paper during one of the conference sessions.
- Michal Hajžman, Ph.D.: University of West Bohemia, New Technologies for the Information Society, European Centre of Excellence, Univerzitní 8, 306 14 Plzeň, Czech Republic (mhajzman@kme.zcu.cz).
- Miroslav Byrtus, Ph.D.: University of West Bohemia, New Technologies for the Information Society, European Centre of Excellence, Univerzitní 8, 306 14 Plzeň, Czech Republic (mbyrtus@kme.zcu.cz).
- Zbyněk Šika, Professor: Czech Technical University in Prague, Department of Mechanics, Biomechanics and Mechatronics, Technická 4, 166 07 Prague, Czech Republic (Zbynek.Sika@fs.cvut.cz).

The influence of piezoelectric actuation on the lateral oscillation of a beam with varying cross section (VIB255-15)

Jacek Przybylski, Krzysztof Kuliński

Abstract: The objects of this studies are the stability and transversal vibrations of a system consisted of a beam with a pair of piezoelectric patches. The system is kinematically loaded as a result of the prescribed axial support displacement. This type of loading not only changes the natural vibration frequencies but it may affect the system's stability. An application of the electric field to the piezo actuators leads to generation of an axial residual force which can enhance the buckling capacity. Such force depends on both the voltage applied to the actuators as well as the geometrical and physical parameters of the system. Taking that into account, different combinations of the length of the piezo patches and their locations have been regarded for four different beam supports preventing the longitudinal displacements. Due to the geometric nonlinearity, Lindstedt-Poincare method has been applied for the solution purposes. A vast number of numerical results shows the effect of the residual piezoforce on the structural instability and non-linear vibration of the system.

1. Introduction

Piezoelectrics are special group of materials which generate voltage under mechanical stress on the basis of direct piezoelectric effect. These materials are widely utilized in airbags, speakers, lighters etc. The generated voltage resulting from a deformation may be also treated as a signal in various types of piezo sensors. A reverse piezoelectric effect, when piezo elements change their dimensions under a driving voltage, is also frequently used in practical engineering. This kind of phenomenon is applicable in control of static and dynamic responses of structures what makes piezo actuators appropriate for micro positioning, structure shaping, various domains of automotive industry, aviation, life and medical sciences etc.. Active control of columns' buckling via piezo actuation has been studied by Thompson and Loughlan [1]. Authors found out that a geometrically imperfect column without active piezoelements is more vulnerable on earlier deformations at lower buckling load, while an application of the controlled voltage to the actuators allows the structure to remain undeflected and overall buckling load capacity is higher. Two significant papers concerning the piezo actuation control were elaborated by Faria [2] and Zehetner and Irschik [3]. Faria [2] proposed a new technique for enhancement of buckling loads of composite beams relied on using stress stiffening to create a non-zero tensile force acting along the beam axis which ultimately permits

the application of higher external compressive forces that lead to traditional buckling instabilities. After application a variational principle it has been demonstrated that the pin-force model must be used with caution when it comes to buckling of composite beams although it can be used to correctly predict the stress stiffening effects. The inconsistency of derivation of the motion equations by other authors for piezo-laminated Euler-Bernoulli beams subjected to an axial compressive load was also announced in [3]. It was demonstrated in that paper that utilization of inadmissible assumptions as an inextensible beam axis and an absence of longitudinal displacement under applied load leads to incorrect conclusions assuming that stability can be modified by piezoelectric axial actuation. On the basis of Faria [2] and Zehetner and Irschik [3] considerations one can state that the stability and vibrations control is only possible for beams or columns with both ends preventing longitudinal displacements where the electric field is applied to bonded piezoceramic elements.

Nonlinear lateral vibration of beams with both ends preventing axial displacement have been the subject of interest by many researchers who have used both classic mathematical approach and finite element method in order to formulate and solve mentioned problems. Semi-analytical approach based on Lagrange principle and the harmonic balance method for the non-linear dynamic response problem of beams with simply supported and clamped ends have been proposed by Azrar et al. [4]. Amplitude-frequency dependence have been determined by means of mathematical formulation concentrated on free and forced vibrations. Moreover a very thorough discussion about methods for increasing the accuracy of the obtained solution have been presented. General model for large vibration amplitudes for straight beams was been elaborated by Benamar et al. [5] who studied the amplitude influence on the mode shape and natural frequency of the systems. The author observed a great increase of beam curvatures near the clamps, causing a highly non-linear increase in bending strain with increasing deflection. Özkaya et al. [6] investigated the non-linear free and forced vibrations of an Euler-Bernoulli beam with different immovable end conditions under concentrated mass. The effect of position, magnitude of the mass and different end conditions on the vibrations has been determined. Application of piezoceramic actuators and their effect on the stability and natural frequency of slender beams were studied by Przybylski [7]. The author considered axially compressed column, divided onto three segments, with both ends sliding in the direction perpendicular to the undeflected axis of the system. The middle segment consisted two piezoelectric actuators colocally and perfectly bonded to the host column. A weakening hinge but strengthened with a spring support between the second and third segments was taken into consideration and von Karman theory was utilised to describe the strain-displacement relation. A broader literature overview and wider area of study of beams with integrated ceramic piezoactuators can be found in [8].

In this paper the influence of induced axial piezoelectric force on static and dynamic response of Euler-Bernoulli beams with varying cross section and different end conditions preventing longitudinal

displacements is discussed. The structure inhomogeneity results from two identical piezoceramic patches perfectly bonded at specified localization at the top and bottom surfaces of the beam. Such prismatic and segmented system is characterized by different axial and bending stiffnesses along its length. That inhomogeneity directly influences the dynamic behaviour of the system and its critical buckling load. In order to control the axial force during lateral vibrations and enhance buckling load capacity, the internal axial compressing or tensile piezo force is induced dependently on the direction of the applied electric field vector. The main purpose of this work is to show the influence of an external axial force on the natural frequency with the stretching or compressing effect caused by piezoelectric force actuation for different lengths of piezo-patches and different beam ends conditions. Moreover the amplitude-frequency relation is investigated.

2. Problem formulation

For the nonlinear lateral vibrations of the beam von Karman theory is used according to which the axial inertia effects can be neglected due to their insignificance regarding the considered type of motion. These assumptions were originally proposed and are continuously applied for elastic plates [9]. The strain-displacement relation which corresponds to small strains and small displacements and the beam's curvature are definite as follows:

$$\varepsilon(x,t) = \frac{\partial U(x,t)}{\partial x} + \frac{1}{2} \left[\frac{\partial W(x,t)}{\partial x} \right]^2 \quad (1)$$

$$\kappa(x,t) = -\frac{\partial^2 W(x,t)}{\partial x^2} \quad (2)$$

where: $\varepsilon(x,t)$ describes mid-plane strain, $U(x,t)$ is the axial displacements, $W(x,t)$ is the transverse displacement, $\kappa(x,t)$ is the beam axis curvature.

In the study four different supports of beam ends preventing longitudinal displacements are taken into consideration: both ends clamped, both ends pinned and mixed ends supports as clamped-pinned and clamped-guided. The analyzed scheme of three-segmented beam with two colocally mounted piezo patches for pinned-pinned supports is shown in figure 1. In the considered model the thickness of adhesive layer is treated as negligibly small. The width of piezo-patches (b) is equal to the width of the host beam. Piezosegment and beam cross sections are rectangular. It is assumed that beam is rectilinear (without geometrical imperfections) and made of a homogeneous elastic isotropic material. The piezoceramic actuators are made of an elastic and transversely isotropic material and are perfectly bonded to the beam along the whole length. The electric field applied is uniform and has a constant value for upper and bottom piezoelement.

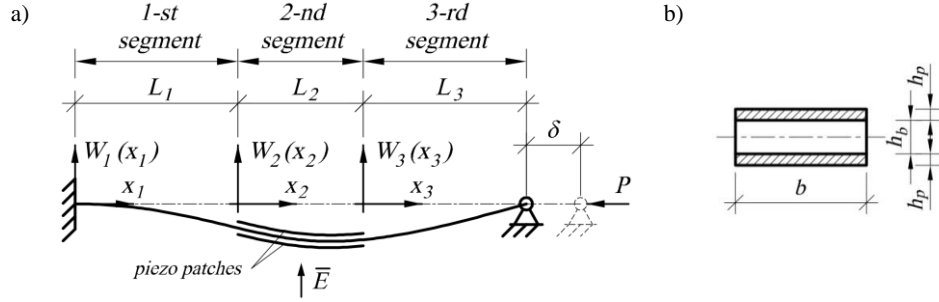


Figure 1. Scheme of the pinned-clamped beam with two piezoelectric patches colocally bounded at its central part (a), cross section of the analyzed beam (b)

The constitutive equation for the piezoelectric material in one-dimensional problem is as follows:

$$\sigma = E_p \varepsilon(x) \pm e_{31} V / h_p \quad (3)$$

where: E_p denotes piezoelectric material Young's modulus, e_{31} is the piezoelectric constant, V is the voltage applied to the piezo-element and h_p is the piezoelectric material thickness. The residual force for the n - sectional beam with both ends preventing axial displacements was derived in [7]. According to these considerations equation describing residual force for three-segmented beam, as in figure 1, takes the form:

$$F_r = F \left[1 + \eta \left(\frac{1}{l_2} - 1 \right) \right]^{-1} \quad (4)$$

where: F is a piezoelectric force induced by the electric field, η is the coefficient identified as a relation of piezosegment axial stiffness to the host beam axial stiffness, l_2 is the non-dimensional length of piezosegment defined as a relation of dimensional length L_2 to the entire beam length L .

Piezoelectric force F depends on piezoelement width b , piezoelectric material constant e_{31} and the applied voltage V [10]. When the force is induced by a single pair of piezoceramic actuators its value is equal to:

$$F = -2be_{31}V \quad (5)$$

The value of piezoelectric force F is limited by the maximal value of voltage allowed to be applied without the risk of depolarization of a piezoelectric material. That threshold value of electric field for standard materials is around 2000 to 3000 [V/mm].

Stretching dynamic force appearing during transversal vibrations of the system shown in figure 1 can be defined on the basis of relation strain-displacement described by Eq. 1 and takes the form:

$$S(t) = E_i A_i \left[\frac{\partial U_i(x_i, t)}{\partial x_i} + \frac{1}{2} \left(\frac{\partial W_i(x_i, t)}{\partial x_i} \right)^2 \right], \quad \text{for } i=1,2,3 \quad (6)$$

After some manipulation of Eq. 6, the axial displacement at the end of each segment is equal to:

$$\Delta U_i(L_i, t) = \frac{S(t)L_i}{E_i A_i} - \frac{1}{2} \int_0^{L_i} \left[\frac{\partial W_i(x_i, t)}{\partial x_i} \right]^2 dx_i, \quad \text{for } i=1,2,3 \quad (7)$$

The imposed natural boundary conditions on the axial displacements of particular segments applicable to the laterally vibrating system, lead to the equality:

$$\sum_{i=1}^3 \Delta U_i(L_i, t) = 0 \quad (8)$$

Introducing non-dimensional quantities and taking into account the initial axial load resulting from prescribed axial displacement and the piezoelectric residual force, the governing equation of transversal beam vibrations can be demonstrated as follows:

$$\frac{\partial^4 w_i(\xi_i, \tau)}{\partial \xi_i^4} \pm \varphi_i p_D^2(\tau) \frac{\partial^2 w_i(\xi_i, \tau)}{\partial \xi_i^2} + \mu_i \omega^2 \frac{\partial^2 w_i(\xi_i, \tau)}{\partial \tau^2} = 0, \quad \text{for } i=1,2,3 \quad (9)$$

in which the axial force parameter has three components: $p_D^2(\tau) = p_u^2 + f_r^2 + s^2(\tau)$, where: p_u^2 is the non-dimensional force parameter resulting from a prescribed support displacement, f_r^2 defines the non-dimensional residual force parameter, and $s^2(\tau)$ is the dynamic force dependent upon the oscillation amplitude on the basis of Eq. (8) according to:

$$s^2(\tau) = \frac{\lambda}{2} \left(\sum_{i=1}^3 \eta^{-\frac{1}{2}(j^{2i+1})} l_i \right)^{-1} \sum_{i=1}^3 \int_0^{l_i} \left[\frac{\partial w_i(\xi_i, \tau)}{\partial \xi_i} \right]^2 d\xi_i, \quad \text{where } \lambda = A_b L^2 / I_b \quad (11)$$

The dimensionless parameters are defined through the substitutions:

$$\begin{aligned} w_i(\xi_i, \tau) &= \frac{W_i(x_i, t)}{L}, \quad \xi_i = \frac{x_i}{L}, \quad l_i = \frac{L_i}{L}, \quad \varphi_i = (1 + r_m)^{\frac{1}{2}(j^{2i+1})}, \quad r_m = \frac{E_p I_p}{E_b I_b}, \quad j = \sqrt{-1}, \\ p_u^2 &= \frac{P_u L^2}{E_b I_b}, \quad f_r^2 = \frac{F_r L^2}{E_b I_b}, \quad \mu_i = \left(\frac{\alpha_1 + (\eta - 1)\alpha_2}{\alpha_1(1 + r_m)} \right)^{\frac{1}{2}(j^{2i+1})}, \quad \alpha_1 = \frac{E_p}{E_b}, \quad \alpha_2 = \frac{\rho_p}{\rho_b}, \\ \eta &= \frac{E_b A_b + E_p A_p}{E_b A_b}, \quad \omega^2 = \Omega^2 L^4 \frac{\rho_b A_b}{E_b I_b}, \quad \tau = \Omega t \end{aligned} \quad (10)$$

and the following notation has been introduced: $E_p I_p$, $E_b I_b$ - the bending stiffness of piezo patches and stiffness of a beam, respectively, ρ_p , ρ_b - the material densities of the actuators and beam, respectively, A_p , A_b - the cross section area of piezopatches and beam, respectively, Ω - the natural frequency of the system, and t is time.

As the solution and analysis of the problem need to cover all types of supports preventing longitudinal displacements of the beam ends, the boundary conditions have been divided into two groups. The first group contains the boundary conditions for all beams. For the clamped-pinned system from figure 1 the boundary conditions are:

$$w_1(\xi_1, \tau)_{\xi_1=0} = w_1'(\xi_1, \tau)_{\xi_1=0} = w_3(\xi_3, \tau)_{\xi_3=l_3} = w_3''(\xi_3, \tau)_{\xi_3=l_3} = 0 \quad (12)$$

where: I and II are the Roman numerals denoting the order of the derivative with respect to the space variable ξ . For a guided support both the slope w' and the shear forces w''' are equal to zero. For a system with mixed type of supports adequate boundary conditions have to be chosen from those described above.

The second group specifies continuity boundary conditions – equality of displacements, slopes, bending moments and shear forces at the ends of particular segments:

$$w_i(\xi_i, \tau)_{\xi_i=l_i} = w_{i+1}(\xi_{i+1}, \tau)_{\xi_{i+1}=0}, \quad w_i'(\xi_i, \tau)_{\xi_i=l_i} = w_{i+1}'(\xi_{i+1}, \tau)_{\xi_{i+1}=0},$$

$$(1 + r_m)^{\frac{1}{2}[j^{2i}+1]} w_i^{Rn}(\xi_i, \tau)_{\xi_i=l_i} = (1 + r_m)^{\frac{1}{2}[j^{2(i+1)}+1]} w_{i+1}^{Rn}(\xi_{i+1}, \tau)_{\xi_{i+1}=0}, \quad \text{for } i = 1, 2, \quad Rn = II, III \quad (13)$$

3. Approximate solutions

In order to solve the stated non-linear boundary problem the Lindsted-Poincare method has been chosen. Lateral displacements, axial dynamic force and vibrations frequency are expanded into an exponential series with respect to the small amplitude parameter ε :

$$w_i(\xi_i, \tau) = \sum_{n=1}^N \varepsilon^{2n-1} w_{i2n-1}(\xi_i, \tau) + O(\varepsilon^{2N+1}) \quad (14)$$

$$s^2(\tau) = \sum_{n=1}^N \varepsilon^{2n} s_{2n}^2(\tau) + O(\varepsilon^{2(N+1)}) \quad (15)$$

$$\omega^2 = \omega_0^2 + \sum_{n=1}^N \varepsilon^{2n} \omega_{2n}^2 + O(\varepsilon^{2(N+1)}) \quad (16)$$

where separation of space ξ and time τ variable is described as:

$$w_{ij}(\xi_i, \tau) = \sum_{k=1}^{b(2k-1)} w_{ij}(\xi_i) \cos(2k-1)\tau, \text{ for } b = \frac{j-1}{2} + 1 \text{ and } j = 1, 3, 5, \dots \quad (17)$$

$$s_j^2(\tau) = \sum_{k=1}^c s_j^2 \cos 2(k-1)\tau, \text{ for } c = \frac{j}{2} + 1 \text{ and } j = 2, 4, 6, \dots \quad (18)$$

Introducing Eq. 14-16 into equations of motion (Eq. 9) and dynamic axial force (Eq. 11) and equating the terms of respective ε exponents to zero, an infinite set of motion and axial force equations is obtained, where the first four are:

$$O(\varepsilon^1): \frac{\partial^4 w_{i1}(\xi_i, \tau)}{\partial \xi_i^4} \pm \varphi_i p_D^2 \frac{\partial^2 w_{i1}(\xi_i, \tau)}{\partial \xi_i^2} + \mu_i \omega_0^2 \frac{\partial^2 w_{i1}(\xi_i, \tau)}{\partial \tau^2} = 0 \quad (19)$$

$$O(\varepsilon^2): s_2^2(\tau) = \frac{\lambda}{2} \left(\sum_{i=1}^3 \eta^{-\frac{1}{2}(j^{2i}+1)} l_i \right)^{-1} \sum_{i=1}^3 \int_0^{l_i} \left[\frac{\partial w_{i1}(\xi_i, \tau)}{\partial \xi_i} \right]^2 d\xi_i \quad (20)$$

$$\begin{aligned} O(\varepsilon^3): & \frac{\partial^4 w_{i3}(\xi_i, \tau)}{\partial \xi_i^4} \pm \varphi_i p_D^2 \frac{\partial^2 w_{i3}(\xi_i, \tau)}{\partial \xi_i^2} + \mu_i \omega_0^2 \frac{\partial^2 w_{i3}(\xi_i, \tau)}{\partial \tau^2} = \\ & = \varphi_i s_2^2(\tau) \frac{\partial^2 w_{i1}(\xi_i, \tau)}{\partial \xi_i^2} - \mu_i \omega_2^2 \frac{\partial^2 w_{i1}(\xi_i, \tau)}{\partial \tau^2} \end{aligned} \quad (21)$$

$$O(\varepsilon^4): s_4^2(\tau) = \lambda \left(\sum_{i=1}^3 \eta^{-\frac{1}{2}(j^{2i}+1)} l_i \right)^{-1} \sum_{i=1}^3 \int_0^{l_i} \frac{\partial w_{i1}(\xi_i, \tau)}{\partial \xi_i} \frac{\partial w_{i3}(\xi_i, \tau)}{\partial \xi_i} d\xi_i \quad i = 1, 2, 3 \quad (22)$$

Equations (19) - (22) are solved sequentially with the use of boundary conditions Eq. 12-13 into which expansions from Eq. 14-16 has been previously introduced. An analytical step-by-step process of solution of those equation has been given in [8]. The solution to Eq. 22 gives the relationship between the load parameter p_D and the first term ω_0 of the natural frequency ω . The second term of the frequency ω_2 is established on the basis of an orthogonality condition applied to Eq. 21 to which the solution of Eq. 20 has been previously introduced. Having computed ω_0 and ω_2 terms, the relationship between the natural frequency ω and the vibration amplitude parameter ε can be determined by using Eq. 16 with a customary restriction up to order of two terms.

4. Numerical results

In figure 2 the relationship between axial force parameter p_u and the natural frequency parameter ω_0 for beams with different ends conditions and different piezosegment length has been sketched. The physical properties of the materials used are given in Table 1.

Table 1. Material properties of the beam and piezosegment

Property	Beam	Piezo-patches
Material model	Aluminium	Piezoceramic P-41
E [GPa]	70.00	83.33
d_{31} [C/N]	-	$1 \cdot 10^{-10}$
h [mm]	3.00	0.50
b [mm]	20.00	20.00
ρ [kg/m ³]	2720	7450
U_{\max} [V/mm]	-	2000

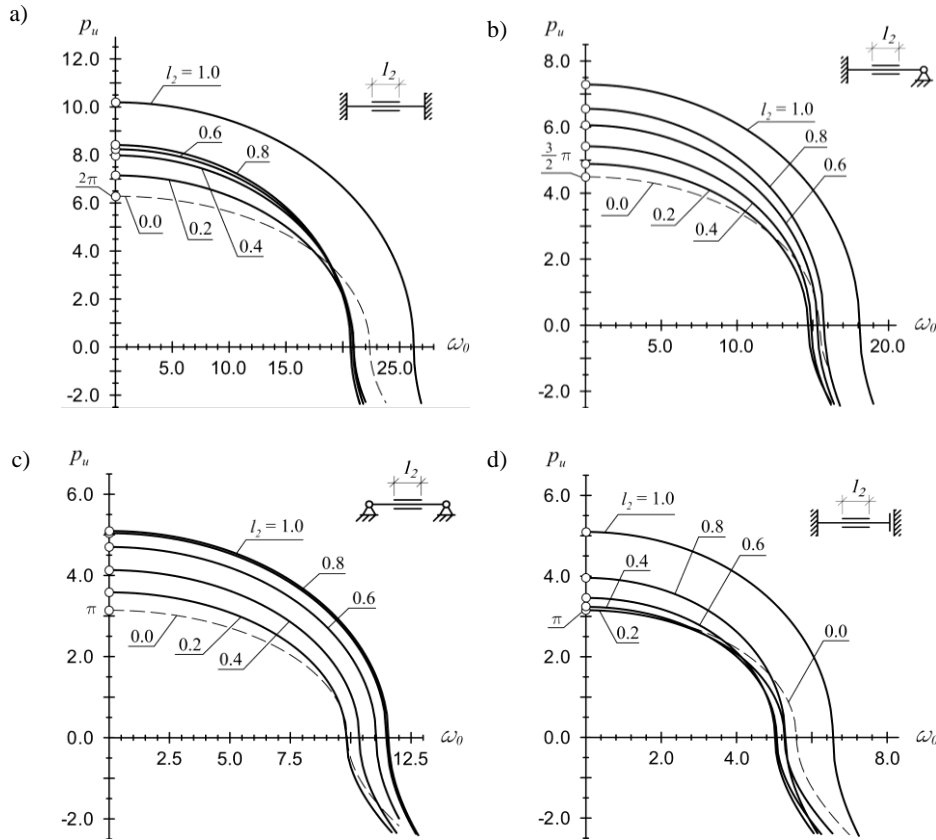


Figure 2. The first natural frequency ω_0 versus non-dimensional load p_u for different lengths of piezosegment and different beam's supports

Small icons included in all figures visualize the way of beam's supporting. The curves sketched with dashed line corresponds to systems without piezopatches, whereas solid lines concern beams with different lengths of piezosegment. The critical forces for each case can be read at points marked with a small circle at the load axis.

The results presented in figure 2 in the form of frequency curves show how courses of those curves and the critical forces are affected when piezo stripes of different lengths are centrally attached to beams of different supports. Comparing the results one can state that for identical piezosegment length the highest value of the critical force is obtained in the following order with respect to the beam ends support: clamped-clamped system (figure 2a), clamped-pinned (figure 2b), pinned-pinned (figure 2c) and clamped-guided (figure 2d). Due to a simultaneous influence of two factors i.e. the bending stiffness and the mass per unit length, the natural frequency at zero external load changes irregularly with an increase of the piezo lengths for different ways of system supporting. Hence one can state that physical and geometrical properties of piezoelements such as their width, length, thickness and type of piezoceramic material determine not only the maximum value of the electric field but also affect the alteration range of both the buckling load and the frequency.

In order to investigate the influence of piezo actuation on the natural vibrations, the non-dimensional value of piezoelectric force f parameter of the value equal to the critical buckling force for a uniform prismatic pinned-pinned beam have been chosen:

$$f = \sqrt{\frac{P_{cr}}{E_b I_b}} L = \pi \quad (23)$$

Despite the fact that all calculations in the study are made in non-dimensional form, an analysis of practical model should also be demonstrated. To verify the applied electric field necessary to generate the piezoelectric force $f = \pi$ the beam of $L = 1.20$ [m] has been selected. The critical buckling load for mentioned beam on the basis of Eq. 23 is equal to 21.59 [N], hence an individual piezoceramic actuator should generate a force equal to 10.80 [N]. To do that, the necessary voltage of the applied electric field should reach the value of:

$$V_{app} = \frac{P_{cr}}{2b_p d_{31} E_p} = 64.77 \text{ [V]} \quad (24)$$

In accordance to the producer recommendation, the maximal applied voltage without risk of depolarisation of piezoceramics should be lower than $V_{max} = U_{max} h_p = 2000$ [V]. Based on this considerations the non-dimensional piezoelectric force $f = \pm \pi$ can be safely treated as a control value for actuation purposes in the considered system. It should be noted here that according to Eq. 4 the

piezoelectric force is equal to the residual force f_r only when the length of piezo stripes (l_2) is identical as the length of the whole beam (l), in other cases $f_r < f$.

An induction of the piezoelectric force can be treated as an introduction of a compressive or tensile axial force to the beam to counteract the stresses that will result from the applied external load. Hence the piezoelectric actuation is a tool for alteration both the critical force and the vibrations frequency. The modification of the natural frequency curves and the buckling loads for beams with different supports and constant piezosegment length ($l_2 = 0.4$) has been demonstrated in figure 3.

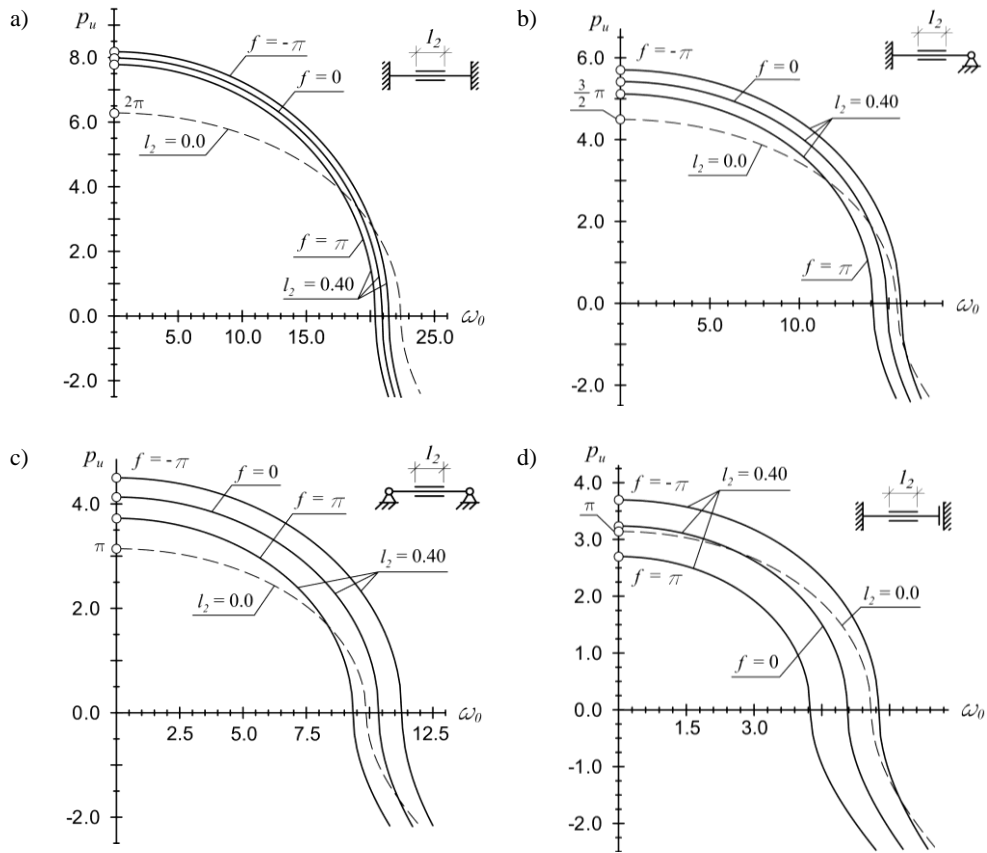


Figure 3. Influence of piezoelectric actuation on the natural vibration frequency of beams with different ends supports

Regardless of the way of beam supporting, an induction of the tensile piezoelectric force results in increasing the vibration frequency in relation to the system without actuation. On the other hand a compressive piezoelectric force reduces system natural frequency and its buckling force. The smallest influence on the stated objectives occurs for a beam with both end clamped. In that case one can

notice 5.01% relative growth in the buckling load for $f = -\pi$ and 2.42% increase in the frequency for $p_u = 0$ at the same level of the piezoelectric force. For the clamped-guided system the relevant changes are: 14.21% growth in the buckling load for $f = -\pi$ and 13.69% increase in the frequency for an externally unloaded system.

An effect of the piezoelectric actuation on the non-linear vibration frequency for amplitude $\varepsilon\sqrt{\lambda} = 3$, two lengths of piezosegment ($l_2 = 0.2, 0.8$) and three different axial force p_u are presented in Table 2.

Table 2. Non-linear to linear frequency for piezo actuated beam

$\frac{\omega}{\omega_0}$						
p_u	$l_2 = 0.2$			$l_2 = 0.8$		
	$f = -\frac{\pi}{\sqrt{2}}$	$f = 0$	$f = \frac{\pi}{\sqrt{2}}$	$f = -\frac{\pi}{\sqrt{2}}$	$f = 0$	$f = \frac{\pi}{\sqrt{2}}$
2	1.37277	1.38673	1.40177	1.25304	1.28019	1.31387
0	1.31633	1.32630	1.33693	1.22929	1.25136	1.27812
-2	1.27477	1.28226	1.29017	1.20961	1.22790	1.24969

The compressing piezoelectric force, which diminishes the frequency ω_0 at each level of the external load, causes an increase in the nonlinear frequency ω , whereas the stretching force acts in an opposite way.

5. Conclusions

The problem of stability and transversal vibrations of the Euler-Bernoulli beam with different ends support conditions and a pair of perfectly bonded piezoelectric patches is discussed. Due to geometric non-linearity, the Lindsted-Poincare method has been applied. The piezoelectric force induced in the system can either enlarge compression or counteract prescribed axial support displacement what depends on the direction of the electric field. In the paper two opposite working operations of the piezoelectric force have been taken into considerations.

The less rigid system the higher influence of the residual force on both the buckling force and transversal vibration frequency has been observed. The geometry of piezo stripes and the type of piezoelectric material has also a crucial effect on the natural vibration frequency and the critical force. It should be noted that geometry of the considered structure is one of possible configurations of the system. A greater number of piezo patches with different localizations and appropriate voltages may be used to directly correct the dynamic features and stability of piezo-beam systems in actuated engineering structures.

References

- [1] Thompson S. and Loughlan J., The active buckling control of some composite column strips using piezoceramic actuators. *Composite Structures*, 1995, 59-67.
- [2] de Faria A. R. and de Almeida S. F., On buckling enhancement of laminated beams with piezoelectric actuators via stress stiffening. *Composite Structures*, 2004, 187-192.
- [3] Zehetner C. and Irschik H., On the static and dynamic stability of beams with an axial piezoelectric actuation, *Smart Structures and Systems*, 2008, 67-84.
- [4] Azrar L., Benamar R. and White R. G., Semi-analytical approach to the non-linear dynamic response problems of S-S and C-C beams at large vibrations amplitudes. Part I: General theory and application to the single mode approach to free and forced vibration analysis. *Journal of Sound and Vibration*, 1999, 183-207.
- [5] Benamar R., Bennouna M. M. K. and White R. G., The effect of large vibration amplitudes on the mode shapes and natural frequencies of thin elastic structures part I: Simply supported and clamped-clamped beams, *Journal of Sound and Vibration*, 1991, 179-195.
- [6] Özkaya E., Pakdemirli M. and Öz H. R., Non-linear vibrations of a beam-mass system under different boundary conditions, *Journal of Sound and Vibration*, 1997, 679-696.
- [7] Przybylski J., Stability of an articulated column with two collocated piezoelectric actuators, *Engineering Structures*, 2008, 3739-3750.
- [8] Przybylski J., *Zagadnienia statyki i dynamiki smukłych układów mechanicznych ze zintegrowanymi elementami piezoelektrycznymi*. Wydawnictwo Politechniki Częstochowskiej, Częstochowa, 2012.
- [9] Malekzadeh P. and Karami G., Large amplitude flexural vibration analysis of tapered plates with edges elastically restrained against rotation using DQM, *Engineering Structures*, 2008, 2850-2858.
- [10] Przybylski J., Non-linear vibrations of a beam with a pair of piezoceramic actuators, *Engineering Structures*, 2009, 2687-2695.

Jacek Przybylski, Professor: Częstochowa University of Technology, Institute of Mechanics and Machine Design Foundations, al. Armii Krajowej 21, 42-200 Częstochowa, Poland (j.przybylski@imipkm.pcz.pl).

Krzysztof Kuliński, M.Sc. (Ph.D. student): Częstochowa University of Technology, Institute of Mechanics and Machine Design Foundations, al. Armii Krajowej 21, 42-200 Częstochowa, Poland (krzysztku@gmail.com). The author gave a presentation of this paper during one of the conference sessions.

**Vibrations of a double-string complex system subjected
to uniformly distributed moving forces
(VIB048-15)**

Jarosław Rusin

Abstract: In this paper the dynamic response of a complex double-string system traversed by uniformly distributed moving load is considered. The conflation is represented by a set of linear springs in Winkler model. The classical solution of the response of complex systems subjected to forces moving with a constant velocity has a form of an infinite series. The main goal of this paper is to show that in the considered case part of the solution can be presented in a closed, analytical form instead of an infinite series. The presented method to search for a solution in a closed, analytical form is based on the observation that the solution of the system of partial differential equations in the form of an infinite series is also a solution of an appropriate system of ordinary differential equations. The dynamic response of complex systems may be used for the analysis the complex models of moving load.

Keywords: vibration complex systems, moving loads, closed-form solutions.

1. Introduction

Complex systems are very important in aeronautical, civil and mechanical engineering as structural members with high strength to weight ratios. This problem occurs in dynamics of bridges, aircrafts, space shuttles, missiles as well as railways and motorways. Dynamics response of complex string systems has been studied by many authors in the recent decades. The problem of a dynamic response of a structure subjected to moving loads is interesting and important whereby various models of moving loads have been assumed Ref. [1,2,12]. A string as a simple model of a one-dimensional continuous system resistant to tension but not to bending is often used in analysis of numerous engineering structures and has been a subject of great scientific interest for a considerable time. This follows from the fact that the vibrations of a string are described by the wave differential equation. This allows one to see the wave effect in a string, contrary to many more complex systems where it might be either not present or not clearly visible. An important technological extension of a single string, beam or plate is that of the double-string, double-beam or string-beam system. Various aspects of vibration of the complex strings and beams has been considered in the papers Ref. [1-3,5-9,11,12-15]. The paper includes the study of a dynamic behavior of a finite, simply supported double-string complex system subject to uniformly distributed moving forces with a constant velocity on the top string. The strings are identical, parallel one upon the other and continuously coupled by a linear

Winkler elastic element. The classical solution has a form of an infinite series. The main goal of the paper is to show that the aperiodic part of the solution can be presented in a closed form instead of an infinite series. In the paper the solutions are derived in a closed form Ref. [10-12]. The presented method to finding a solution in a closed form is based on the observation that the solution of the system of partial differential equations in the form of an infinite series is also a solution of an appropriate system of ordinary differential equations Ref. [3,11-13]. The solution for the dynamic response of the composite strings under moving force is important because it can be used also in order to find the solution for other types of moving loads. The double string connected in parallel by linear elastic elements can be studied as a theoretical model of composite system or prestressed structure in which coupling effects and transverse wave effects are taken into account.

2. Mathematical model and governing equation

Let us consider the vibration of complex system consist of couple strings interface by a linear springs under axial compression N excited by a force $p(x,t)$ moving with a constant velocity v as on Fig.1.

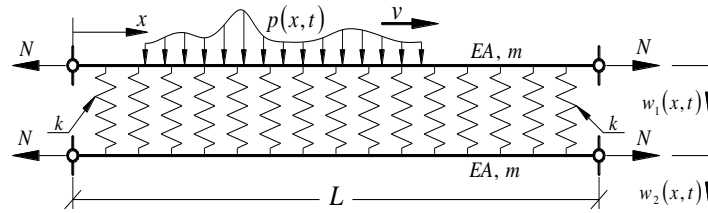


Figure 1. Double-string system under a moving force.

The solution of the system in the classical forms is investigated. It is possible to find the closed forms of the deflection functions $w_i(x,t)$. The letter $i = \{1, 2\}$ denote the first and the second string. The vibration of double-string system is governed by two conjugate partial differential equations:

$$\begin{cases} -N \frac{\partial^2 w_1(x,t)}{\partial x^2} + m \frac{\partial^2 w_1(x,t)}{\partial t^2} + k [w_1(x,t) - w_2(x,t)] = p(x,t), \\ -N \frac{\partial^2 w_2(x,t)}{\partial x^2} + m \frac{\partial^2 w_2(x,t)}{\partial t^2} + k [w_2(x,t) - w_1(x,t)] = 0, \end{cases} \quad (1)$$

where m is the mass spread over the length of the string system, k denotes the stiffness modulus of a Winkler elastic element, and furthermore, EA is the axial stiffness of the strings, E denotes Young's modulus of elasticity and A is the area of the cross-section of the strings. And the boundary conditions:

$$w_i(0,t) = 0, \quad w_i(L,t) = 0, \quad i = \{1, 2\}. \quad (2)$$

The function $p(x,t)$ could occur in four cases as on Fig.2. The entrance on the top of strings system, Fig.2 case (1), can be written as:

$$p(x,t) = q H(vt - x), \quad (3)$$

where q is the intensity of the load and $H(\cdot)$ denotes Heaviside step function. When the load is entirely on the string but its scope is less than the length of the complex system $a < L$, Fig.2 case (2), the load function has the form:

$$p(x,t) = q [H(vt - x) - H(vt - x - a)] \quad (4)$$

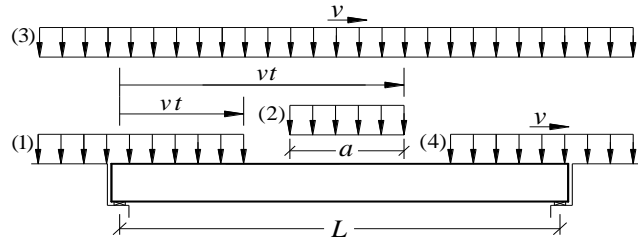


Figure 2. Passage combinations of the moving uniformly distributed load.

In contrast, when the force is entirely on the top of double-string and its range is $a \geq L$, Fig.2 case (3), the load is exactly q . And the last case an exit, Fig.2 case (4), which can be shown as:

$$p(x,t) = q [1 - H(vt - x)] \quad (5)$$

For further consideration we introduce dimensionless variables:

$$\xi = x/L, \quad T = vt/L, \quad \xi \in [0, 1], \quad T \in [0, 1] \quad (6)$$

System of Eq. (1) takes the form:

$$\begin{cases} -w_1''(\xi, T) + \eta^2 \ddot{w}_1(\xi, T) + k_o [w_1(\xi, T) - w_2(\xi, T)] = q_o p(\xi, T), \\ -w_2''(\xi, T) + \eta^2 \ddot{w}_2(\xi, T) + k_o [w_2(\xi, T) - w_1(\xi, T)] = 0, \end{cases} \quad (7)$$

where $p(\xi, T)$ describes the position of the intensity of the load and:

$$v_s = \sqrt{N/m}, \quad \eta = v/v_s, \quad k_o = k L^2 / N, \quad q_o = q L^2 / N. \quad (8)$$

The quantity v_s represents velocity of the transverse wave in the system of double-string. The Roman numerals denote differentiation with respect to the spatial coordinate ξ , and the dots denote differentiation with respect to time T . And the boundary conditions Eq. (2) take the form:

$$w_i(0, T) = 0, \quad w_i(1, T) = 0, \quad i = \{1, 2\}, \quad (9)$$

whereas the initial conditions are the following:

$$w_i(\xi, 0) = 0, \quad \dot{w}_i(\xi, 0) = 0, \quad i = \{1, 2\}. \quad (10)$$

Let us introduce two new functions:

$$w_I(\xi, T) = w_1(\xi, T) + w_2(\xi, T), \quad w_{II}(\xi, T) = w_1(\xi, T) - w_2(\xi, T). \quad (11)$$

From Eq.(8) we obtain two new differential equations for the functions $w_I(\xi, T)$ and $w_{II}(\xi, T)$:

$$-w_I''(\xi, T) + \eta^2 \dot{w}_I(\xi, T) = q_o p(\xi, T), \quad (12)$$

$$-w_{II}''(\xi, T) + \eta^2 \dot{w}_{II}(\xi, T) + 2k_o w_{II}(\xi, T) = q_o p(\xi, T). \quad (13)$$

Eq. (12) describes vibrations of a single string, while Eq. (13) describes vibrations of a single string resting on elastic Winkler support with parameter $2k$ ($2k_o$). From (11) it follows that:

$$w_1(\xi, T) = [w_I(\xi, T) + w_{II}(\xi, T)]/2, \quad w_2(\xi, T) = [w_I(\xi, T) - w_{II}(\xi, T)]/2. \quad (14)$$

The solutions to Eqs. (12) and (13) for boundary conditions (9) are assumed to be in the form of the sine series:

$$w_J(\xi, T) = \sum_{n=1}^{\infty} y_{Jn}(T) \sin n\pi\xi, \quad J = \{I, II\}. \quad (15)$$

By substituting expression (15) into Eqs. (12) and (13) and using the orthogonalization method one obtains the following set of uncoupled ordinary differential equations:

$$\ddot{y}_{Jn}(T) + \omega_{Jn}^2 y_{Jn}(T) = 2q\eta^{-2} \sin n\pi\xi, \quad (16)$$

where for $J=I$, $\omega_{Jn} = \omega_n = n\pi/\eta$, and for $J=II$, $\omega_{Jn} = \omega_{In} = [(n\pi)^2 + 2k_o]^{1/2}/\eta$.

These functions fulfill the initial conditions

$$y_{Jn}(0) = 0, \quad \dot{y}_{Jn}(0) = 0, \quad J = \{I, II\}. \quad (17)$$

The solution to Eq. (18) has the form:

$$y_{Jn}(T) = \frac{2q}{\eta^2 \omega_{Jn}} \int_0^T \sin \omega_{Jn}(T - \tau) \sin n\pi\tau d\tau, \quad \text{for } 0 \leq T \leq 1, \quad (18)$$

$$y_{Jn}(T) = \frac{2q}{\eta^2 \omega_{Jn}} \int_0^1 \sin \omega_{Jn}(T - \tau) \sin n\pi\tau d\tau, \quad \text{for } T > 1. \quad (19)$$

After integrating Eq. (18) we obtain the classical solution for the vibrations of the system of the strings in the form of infinite series. Below we present a method for finding the solution also in a closed analytic form. Let the function $f(\xi, T)$ for $\xi \in [0, 1]$, $T \in [0, 1]$ be given by the series:

$$f(\xi, T) = \sum_{n=1}^{\infty} \frac{b_1(n\pi)^{2r} \sin n\pi T \sin n\pi\xi + b_2(n\pi)^{2s-1} \cos n\pi T \sin n\pi\xi}{a_o(n\pi)^{2k} + a_1(n\pi)^{2(k-1)} + \dots + a_{k-1}(n\pi)^2 + a_k}, \quad (20)$$

where $k, r, s \in \mathbb{N}_0$, quantities a_i ($i = 0, 2, \dots, k$) are real numbers such that $a_o \neq 0$. To function (20) one can associate the following partial differential equation:

$$\begin{aligned} a_o(-1)^k \frac{d^{2k} f(\xi, T)}{d\xi^{2k}} + a_1(-1)^{k-1} \frac{d^{2(k-1)} f(\xi, T)}{d\xi^{2(k-1)}} + \dots + a_{k-1}(-1) \frac{d^2 f(\xi, T)}{d\xi^2} + a_k f(\xi, T) = \\ = b_1(-1)^r \frac{d^{2r} \delta(\xi - T)}{d\xi^{2r}} + b_2(-1)^{s-1} \frac{d^{2s-1} \delta(\xi - T)}{d\xi^{2s-1}}, \end{aligned} \quad (21)$$

where $\delta(\cdot)$ denote the Dirac delta and Eq. (21) has a solution with the boundary conditions:

$$[f(0, T)]^{(2j)} = [f(1, T)]^{(2j)} = 0, \quad (22)$$

wherein $[f(\xi, T)]^{(2j)} = d^{2j} f(\xi, T) / d\xi^{2j}$ and $j = 0, 1, \dots, k-1$.

This can be verified by solving (21) using finite Fourier sine transform. After solving (21) by, for example, Laplace transform and taking into account the boundary conditions (22) we get the function $f(\xi, T)$ in a closed-form.

3. Entrance of moving load

Let us consider vibrations of a double-string complex system of finite length L subjected to an entrance of a load moving with a constant velocity v . The position of the entry force describes $p(\xi, T) = H(T - \xi)$. From Eq. (18) it follows that the solutions Eqs. (12) and (13) for the initial condition (10) are sums of particular integrals $w_I^A(\xi, T)$, $w_{II}^A(\xi, T)$ and general integrals $w_I^S(\xi, T)$, $w_{II}^S(\xi, T)$:

$$\begin{aligned} w_I(\xi, T) &= w_I^A(\xi, T) + w_I^S(\xi, T) = \\ &= \left[2q_o \sum_{n=1}^{\infty} \frac{\sin n\pi\xi}{(n\pi)^3} - \frac{2q_o}{1-\eta^2} \sum_{n=1}^{\infty} \frac{\cos n\pi T \sin n\pi\xi}{(n\pi)^3} \right] + \frac{2\eta^2 q_o}{1-\eta^2} \sum_{n=1}^{\infty} \frac{\cos n\pi\eta^{-1} T \sin n\pi\xi}{(n\pi)^3}, \end{aligned} \quad (23)$$

$$\begin{aligned} w_{II}(\xi, T) &= w_{II}^A(\xi, T) + w_{II}^S(\xi, T) = \left[2q_o \sum_{n=1}^{\infty} \frac{\sin n\pi\xi}{n\pi[(n\pi)^2 + k_o]} + \right. \\ &\quad \left. - 2q_o \sum_{n=1}^{\infty} \frac{\cos n\pi T \sin n\pi\xi}{n\pi[(n\pi)^2(1-\eta^2) + k_o]} \right] + 2\eta^2 q_o \sum_{n=1}^{\infty} \frac{n\pi \cos \left[\left([(n\pi)^2 + k_o] \eta^{-2} \right)^{1/2} T \right] \sin n\pi\xi}{[(n\pi)^2 + k_o][(n\pi)^2(1-\eta^2) + k_o]}. \end{aligned} \quad (24)$$

The functions $w_I^A(\xi, T)$ and $w_{II}^A(\xi, T)$ are aperiodic vibrations and $w_I^S(\xi, T)$ and $w_{II}^S(\xi, T)$ are free vibrations of the strings. Now we will present the aperiodic solutions $w_I^A(\xi, T)$ given by the first series in expression (23) in a closed analytical form. This function consists of two sums, where we assume that a solution first sum is in the form of a polynomial:

$$w_{I1}^A(\xi, T) = a_0 + a_1\xi + a_2\xi^2 + a_3\xi^3, \quad (25)$$

where a_0, \dots, a_3 are certain constants. Then the solution is as follows:

$$w_{I1}^A(\xi, T) = 2q_o \left(\frac{1}{3}\xi - \frac{1}{2}\xi^2 + \frac{1}{6}\xi^3 \right). \quad (26)$$

Let us notice an important fact that a second sum is a solution not only of the partial differential equations (12) but also of the ordinary equation:

$$\left[w_{I2}^A(\xi, T) \right]'' = \frac{q_o}{1-\eta^2} \delta'(\xi - T), \quad (27)$$

for the boundary conditions (9). The variable T in Eq. (27) is the only parameter that describes the location of the moving force on the string. Using the method described by Eqs. (20)–(22) for solving the second sum we can obtain the functions $w_{I2}^A(\xi, T)$ in a closed-form:

$$w_{I2}^A(\xi, T) = \frac{q_o}{1-\eta^2} \left[\left(\frac{1}{3} - T + \frac{1}{2}T^2 \right) \xi + \frac{1}{6}\xi^3 - \frac{1}{2}(\xi - T)^2 H(\xi - T) \right]. \quad (28)$$

Also the function $w_I^S(\xi, T)$ can be presented in the closed-form because. This function is also a solution of the equation:

$$(1-\eta^2) \cdot \left[w_I^S(\xi, T) \right]'' = \eta^2 q_o \cdot \delta'(\xi - T\eta^{-1}) \quad (29)$$

and hence can be presented in the closed-form depending on the parameter η , when $\eta \neq 1$ we obtain:

$$w_I^S(\xi, T) = \frac{-q_o}{1-\eta^2} \left[\left(\frac{T^2}{2}\xi - T\eta\xi + \frac{\eta^2}{3}\xi + \frac{\eta^2}{6}\xi^3 \right) H\left(1 - \frac{T}{\eta}\right) - \frac{1}{2}(T - \eta\xi)^2 H\left(\xi - \frac{T}{\eta}\right) \right]. \quad (30)$$

A part of the aperiodic solution $w_{II}^A(\xi, T)$ given by the first series in the expression (24) is a solution not only of the partial differential equation (13) but also of the ordinary equation:

$$\left[w_{II1}^A(\xi, T) \right]'' - k_o \left[w_{II1}^A(\xi, T) \right]' = -q_o \delta'(\xi - T), \quad \text{for } T = 0, \quad (31)$$

The closed-form of the solution $w_{II1}^A(\xi, T)$ has the form:

$$w_{II}^A(\xi, T) = -\frac{q_o}{k_o} \left[\xi - \text{ctgh} \sqrt{k_o} \sinh \sqrt{k_o} \xi - (1 - \cosh \sqrt{k_o} \xi) H(\xi) \right]. \quad (32)$$

The second series in the expression (24) can be also present in a closed-form depending on the parameter η .

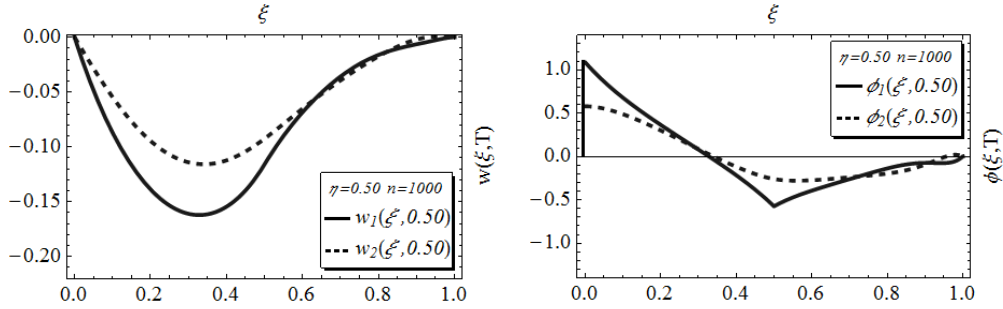


Figure 3. Deflection $w_i(\xi, T)$ and rotation $\phi_i(\xi, T)$ of double-string system under the entrance load.

4. Passage of a uniformly distributed load for $a < L$

Let the moving force be shorter than the length of the strings complex. The position of the passage load describes $p(\xi, T) = H(T - \xi) - H(T - \xi - a_o)$, where $a_o = a/L$. The classic solution $w_I(\xi, T)$ has form:

$$w_I(\xi, T) = w_I^A(\xi, T) + w_I^S(\xi, T) = \frac{2q_o}{1-\eta^2} \sum_{n=1}^{\infty} \frac{\cos[n\pi(a_o - T)] \sin n\pi\xi}{(n\pi)^3} - \frac{2q_o}{1-\eta^2} \sum_{n=1}^{\infty} \frac{\cos n\pi T \sin n\pi\xi}{(n\pi)^3} \quad (33)$$

$$+ \frac{2q_o}{1-\eta^2} \sum_{n=1}^{\infty} \frac{\cos[n\pi T \eta^{-1}] \sin n\pi\xi}{(n\pi)^3} - \frac{2q_o}{1-\eta^2} \sum_{n=1}^{\infty} \frac{\cos[n\pi(a_o - T \eta^{-1})] \sin n\pi\xi}{(n\pi)^3}.$$

For example, the first series Eq. (33) fulfills the following ordinary differential equation:

$$\left[w_{II}^A(\xi, T) \right]^{IV} = -\frac{q_o}{1-\eta^2} \delta'[\xi - (a_o - T)]. \quad (34)$$

The solution of Eq. (34) when $\eta \neq 1$ takes the form:

$$w_{II}^A(\xi, T) = \frac{q_o}{1-\eta^2} \left[\left(\frac{1}{3} - a_o + \frac{1}{2} a_o^2 + (1 - a_o)T + \frac{1}{2} T^2 \right) \xi + \frac{1}{6} \xi^3 + \right. \quad (32)$$

$$\left. - \frac{1}{2} (\xi - a_o + T)^2 H[\xi - (a_o - T)] \right] H(T - a_o).$$

It is known the classic-form solutions a function $w_{II}(\xi, T)$ but it has very extensive form dependent on a number of parameters. According to the procedure from Eqs. (20)–(22) it is easy to find a closed-

form of aperiodic function $w_I^A(\xi, T)$ and $w_{II}^A(\xi, T)$ but for $w_I^S(\xi, T)$ and $w_{II}^S(\xi, T)$ it is possible to obtain only a part free vibration in analytical form.

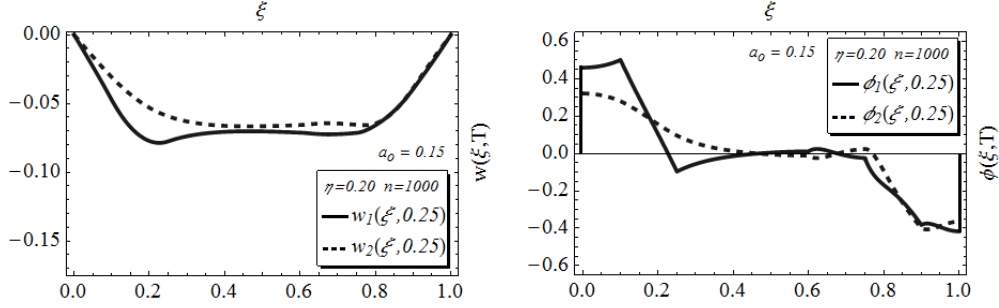


Figure 4. Deflection $w_i(\xi, T)$ and rotation $\phi(\xi, T)$ of double-string system for $a < L$ ($a_0 < 1$).

5. Passage of a uniformly distributed load for $a \geq L$ and exit

We consider a vibration caused by uniformly distributed load when the load is on the whole length of the string system. The function $p(\xi, T) = 1$. The classic solution of $w_I(\xi, T)$ and $w_{II}(\xi, T)$ are known, also closed-forms can be found.

Furthermore, the dynamic component of the tension in the strings is given by:

$$N_i(\xi, T) = EA \frac{\partial w_i(x, t)}{\partial x} = \frac{EA}{L} \frac{\partial w_i(\xi, T)}{\partial \xi}. \quad (33)$$

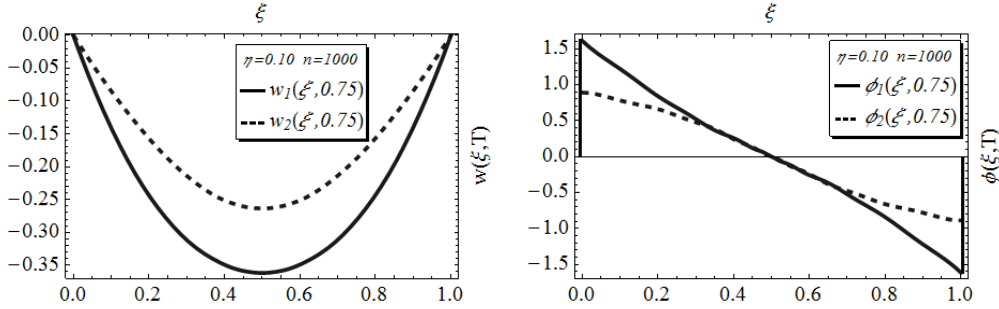


Figure 5. Deflection $w_i(\xi, T)$ and rotation $\phi(\xi, T)$ of double-string system for $a \geq L$ ($a_0 \geq 1$).

Location of the intensity of the load $p(\xi, T)$ during the exit can be written as $1 - H(T - \xi)$. But this is the only difference between the passing for $a \geq L$ ($a_0 \geq 1$) and the entry of load. So both forms solutions are known.

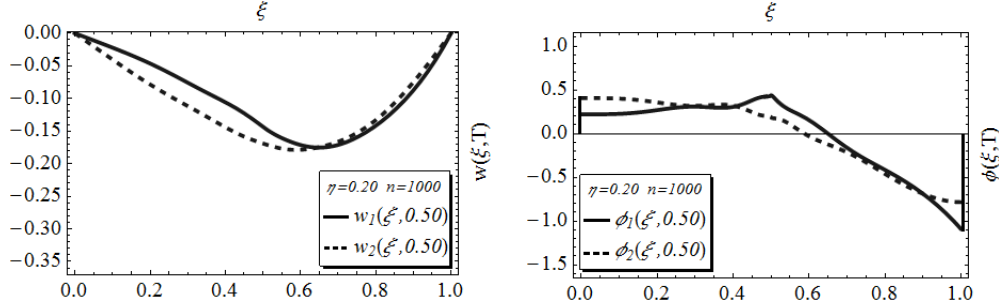


Figure 6. Deflection $w_i(\xi, T)$ and rotation $\phi_i(\xi, T)$ of double-string system under the exit load.

6. Some numerical results

In Figures 3-6, we present deflections $w_i(\xi, T)$ and rotations $\phi_i(\xi, T)$ of double-string complex system under the uniform partially distributed moving load. And the following dimensionless values of the parameters are used in the numerical calculations: $n = 1000$, $k_o = 100$, $q_o = 5$, $a_o = 0.15$, $T = \{0.25, 0.50, 0.75\}$ and $\eta = \{0.1, 0.2, 0.5\}$. The results for different location of the moving force are presented in graphical form in Figs. 3-6. The continuous line represents the functions of loaded string. The dashed line shows functions of the second string for which the load is transferred with the coupling.

7. Conclusions

The dynamics response of an elastically connected double-string complex system loaded by a uniform distributed moving force, in four cases of passing, moving with a constant velocity has been studied. The motion of the system is described by a non-homogeneous conjugate set of two partial differential equations and vibrations can be described by ordinary system equations. The classical solution for transverse displacement function has a form of a sum of two infinite series. It has been shown that aperiodic and a part of free vibrations of strings system of the series can be presented in a closed, analytical form. The closed solutions take different forms depending if the velocity v of a moving force is smaller, equal or larger than the shear wave velocity v_{is} of the strings. This follows from the fact that in string wave phenomena may occur. The presented closed solutions have important meaning in the case when we consider the tension force in the string. The closed solutions improve the preciseness of the classical sine series expansion of the complex system of strings response by considering the vibration as the solution not only to partial of the differential equation but also to appropriate ordinary differential equation. So the closed-form allows analyzing the vibration phenomena due to moving loads without performing numerical calculations. Having determined the closed-form allows us to assess a quantity of necessary function approximation to determine the classical solution.

References

- [1] Dieterman, H. A., Kononov, A. V. Uniform motion of a constant load along a string on an elastically supported membrane. *Journal of Sound and Vibration*, 208 (1997), 575-586.
 - [2] Fryba, L. *Vibration of Solids and Structures under Moving Load*. Telford, London, 1999.
 - [3] Idzikowski, R., Mazij, M., Śniady, P., Śniady P. Vibrations of String due to a Uniform Partially Distributed Moving Load: Closed Solutions. *Mathematical Problems in Engineering*, vol. 2013 (2013), ID 163970, 8 pp.
 - [4] Kączkowski, Z. Vibration of a beam under a moving load. *Proceedings of Vibration Problems*, 4 (4), (1963), 357-373.
 - [5] Kruse, H., Popp, K., Metrikine, A. V. Eigenfrequencies of a two-mass oscillator uniformly moving along a string on a viscoelastic foundation. *Journal of Sound and Vibration*, 218(1998),103-116.
 - [6] Oniszczyk, Z. Transverse vibrations of elastically connected double-strings complex system, Part I: free vibrations. *Journal of Sound and Vibration*, 232 (2) (2000), 355-366.
 - [7] Oniszczyk, Z. Transverse vibrations of elastically connected double-strings complex system, Part II: forced vibrations. *Journal of Sound and Vibration*, 232 (2) (2000), 367-386.
 - [8] Oniszczyk, Z. Damped vibration analysis of an elastically connected complex double-string system. *Journal of Sound and Vibration*, 264 (2003), 253-271.
 - [9] Phylactopoulos, A., Adams, G. G. The response of a non-uniformly tensioned circular string to a moving load. *Journal of Sound and Vibration*, 182 (1995), 415-426.
 - [10] Reipert, Z. Vibration of a beam arbitrarily supported on its edges under moving load. *Proceedings of Vibration Problems*, 2 (10), (1969), 249-260.
 - [11] Rusin, J., Śniady, P. Vibration of a Complex Strings System under a Moving Force, *Proceedings in Applied Mathematics and Mechanics*, 6(1) (2006), pp. 839-840.
 - [12] Rusin, J., Śniady, P., Śniady, P. Vibrations of double-string complex system under moving forces. Closed solutions, *Journal of Sound and Vibration*, 330 (2011), pp. 404-415.
 - [13] Rusin, J. Vibrations of a double-beam complex system subjected to a moving force, *3rd Polish Congress of Mechanics & 21st Computer Methods in Mechanics - PCM-CMM-2015*, short papers vol. 1, pp. 63-64, Gdańsk 2015.
 - [14] Smith, C. S. Motions of a stretched string carrying a moving mass particle. *Journal of Applied Mechanics*, Transactions of the ASME, 31, (1964), 29-37.
 - [15] Szcześniak, W. Vibration of elastic sandwich and elastically connected double-beam system under moving loads. *Scientific Works of Warsaw University of Technology, Civil Engineering*, 132 (1998), 111-151, (in Polish).
- Jarosław Rusin, Ph.D.: University of Zielona Góra, Faculty of Civil Engineering, Architecture and Environmental Engineering, Institute of Civil Engineering, prof. Z. Szafrana 1, 65-516 Zielona Góra, Poland (J.Rusin@ib.uz.zgora.pl). The author gave a presentation of this paper during one of the conference sessions.

On the dynamics of solitary wave solutions supported by the model of mutually penetrating continua (VIB247-15)

Sergii Skurativskyi, Vjacheslav Danylenko

Abstract: The model we deal with is the mathematical model for mutually penetrating continua one of which is the carrying medium obeying the wave equation whereas the other one is the oscillating inclusion described by the equation for oscillators. These equations of motion are closed by the cubic constitutive equation for the carrying medium. Studying the wave solutions we reduce this model to a plane dynamical system of Hamiltonian type. This allows us to derive the relation describing the homoclinic trajectory going through the origin and obtain the solitary wave with infinite support. Moreover, there exist a limiting solitary wave with finite support, i.e. compacton. To model the solitary waves dynamics, we construct the three level finite-difference numerical scheme and study its stability. We are interested in the interaction of the pair of solitary waves. It turns out that the collisions of solitary waves have non-elastic character but the shapes of waves after collisions are preserved.

1. Introduction

Natural geomaterials are highly heterogeneous and interact intensively with the environment. In these conditions the peculiarities of internal medium's structure, namely discreteness and oscillating dynamics [1, 6], can manifest. To incorporate these features of media, the mathematical model for mutually penetrating continua is used [5, 9]. This model consists of the wave equation for carrying medium and equations of motion for oscillating continuum which is regarded as the set of partial oscillators. To generalize the linear counterpart of this model [5, 9], the nonlinearity has been incorporated in the equation of state for carrying medium [2, 3, 7] and in the kinetics for oscillator's equations of motion. We thus are going to treat the following mathematical model

$$\rho \frac{\partial^2 u}{\partial t^2} = \frac{\partial \sigma}{\partial x} - m\rho \frac{\partial^2 w}{\partial t^2}, \quad \frac{\partial^2 w}{\partial t^2} + \Phi(w - u) = 0, \quad (1)$$

where ρ is medium's density, u and w are the displacements of carrying medium and oscillator from the rest state, $m\rho$ is the density of oscillating continuum. To close model (1), we apply the cubic constitutive equation for the carrying medium $\sigma = e_1 u_x + e_3 u_x^3$ and $\Phi(x) = \omega^2 x + \delta x^3$. The novelty of this model lies in the taking into account the cubic terms in the expressions for σ and Φ .

In this report we consider the properties of wave solutions having the following form

$$u = U(s), w = W(s), s = x - Dt, \quad (2)$$

where the parameter D is a constant velocity of the wave front. Inserting (2) into model (1), it easy to see that the functions U and W satisfy the dynamical system

$$D^2 U' = \rho^{-1} \sigma(U') - m D^2 W', \quad W'' + \Omega^2 (W - U) + \delta D^{-1} (W - U)^3 = 0,$$

where $\Omega = \omega D^{-1}$.

This system can be written in the form

$$W' = \alpha_1 R + \alpha_3 R^3, \quad U' = R, \quad (\alpha_1 + 3\alpha_3 R^2) R' + \Omega^2 (W - U) + \delta D^{-2} (W - U)^3 = 0, \quad (3)$$

where $\alpha_1 = \frac{e_1 - D^2 \rho}{m \rho D^2}$, $\alpha_3 = \frac{e_3}{m \rho D^2}$. Through the report we fix $e_1 = 1$, $e_3 = 0.5$, $m = 0.6$, $\omega = 0.9$ in numerical treatments.

1.1. Solitary waves in the model with the linear equation of motion for oscillating inclusions

At first, consider system (3) at $\delta = 0$. Excluding the variable W , system (3) is reduced to the planar system

$$\begin{aligned} (\alpha_1 + 3\alpha_3 R^2)^2 R' &= Z (\alpha_1 + 3\alpha_3 R^2)^2, \\ (\alpha_1 + 3\alpha_3 R^2)^2 Z' &= -[6\alpha_3 R Z^2 + \Omega^2 ((\alpha_1 - 1) R + \alpha_3 R^3)] (\alpha_1 + 3\alpha_3 R^2), \end{aligned} \quad (4)$$

which admits the Hamiltonian

$$H = \frac{1}{2} Z^2 (\alpha_1 + 3\alpha_3 R^2)^2 + \frac{\Omega^2}{2} \left[\alpha_3^2 R^6 + \frac{4\alpha_1 - 3}{2} \alpha_3 R^4 + (\alpha_1^2 - \alpha_1) R^2 \right] = \text{const.}$$

Since solitary waves correspond to homoclinic loops, we thus need to state the conditions when saddle separatrices form a loop. Omitting the detail description [8] of phase plane of dynamical system (4), let us consider the fixed saddle points and their separatrices only. System (4) has the fixed points $O(0;0)$ and $A_{\pm} = \pm \sqrt{(1 - \alpha_1)/\alpha_3}$ if $(1 - \alpha_1)/\alpha_3 > 0$. It easy to see that the origin is a center at $\alpha_1 < 0$, whereas it is a saddle if $0 < \alpha_1 < 1$.

Therefore, we can restrict ourself by the case when $0 < \alpha_1 < 1$ only. So, the homoclinic trajectories that go through the origin satisfy the equation $H = 0$. From this it follows the relation for $Z = Z(R)$ and the expression $s - s_0 = \int dR/Z(R)$ for homoclinic loop which can be written in the explicit form

$$\begin{aligned} s - s_0 &= \frac{3}{2\Omega} \arcsin \left(\frac{4\alpha_3 r - 3 + 4\alpha_1}{\sqrt{9 - 8\alpha_1}} \right) - \frac{1}{2\Omega} \sqrt{\frac{\alpha_1}{1 - \alpha_1}} \times \\ &\ln \left(\frac{1}{r} + \frac{3\alpha_3 - 4\alpha_1 \alpha_3}{4(\alpha_1 - \alpha_1^2)} + \sqrt{\left\{ \frac{1}{r} + \frac{3\alpha_3 - 4\alpha_1 \alpha_3}{4(\alpha_1 - \alpha_1^2)} \right\}^2 - \frac{\alpha_3^2 (9 - 8\alpha_1)}{16(\alpha_1 - \alpha_1^2)^2}} \right) \Bigg|_{r_0}^r, \end{aligned} \quad (5)$$

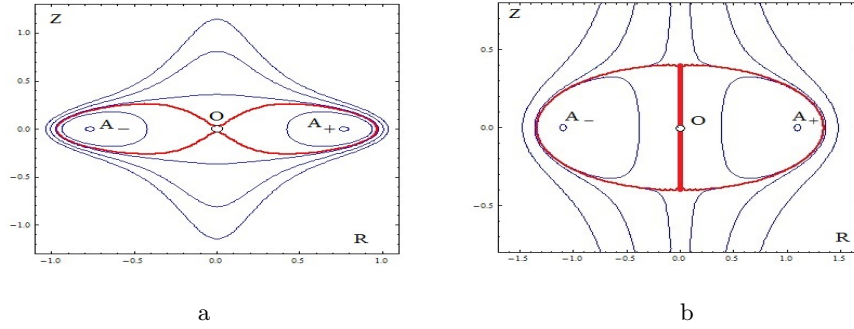


Figure 1. The phase portraits for system (4) at a: $\alpha_1 < 0$ ($D = 0.9$) and b: $\alpha_1 = 0$ ($D = 1$).

where $r = R^2$. The typical phase portrait of dynamical system (4) is depicted in fig. 1a. The pair of homoclinic orbits are drawn with the bold curves. Solution (5) corresponds to the soliton solution with infinite support at $0 < \alpha_1 < 1$.

When α_1 tends to zero, the angles between separatrices of saddle point O are growing. As a result, at $\alpha_1 = 0$ we obtain the degenerate phase portrait presented in fig.1b. The bold lines mark the orbits corresponding to solitary wave solutions with finite support (compacton). These orbits are described by the following expressions

$$R = U'_s = \begin{cases} \sqrt{\frac{3}{2\alpha_3}} \sin\left(\frac{\Omega s}{3}\right), & \frac{\Omega s}{3} \in [0; \pi] \\ 0, & \frac{\Omega s}{3} \notin [0; \pi]. \end{cases}$$

This regime can be thought as a limit state for solution (5) with infinite support.

1.2. Homoclinic loops in the model with cubic nonlinearity in the equation of motion for oscillating inclusions

If $\delta \neq 0$, then system (3) does not reduce to the dynamical system in the plane $(R; R')$. But the first integral for (3) can still be derived in the form

$$I = \Omega^2 (W - U)^2 + \frac{\delta}{2D^2} (W - U)^4 + \alpha_3^2 R^6 + \frac{4\alpha_1 - 3}{2} \alpha_3 R^4 + (\alpha_1^2 - \alpha_1) R^2.$$

Consider the position and the form of homoclinic trajectories when the parameter δ is varied. Since homoclinic loops are described by the level curve $I = 0$, we plot the set of curve $I(\delta) = 0$ (fig.2). Starting from the loop $I(0) = 0$ which coincides with the orbits of fig.1a, we see that increasing δ causes the attenuation of loop's size along vertical axis. If δ decreases, loop's size grows, but at δ_0 the additional heterocycle connecting four new saddle points appears. The bifurcational value δ_0 can be derived via analysing the function $I(\delta)$.

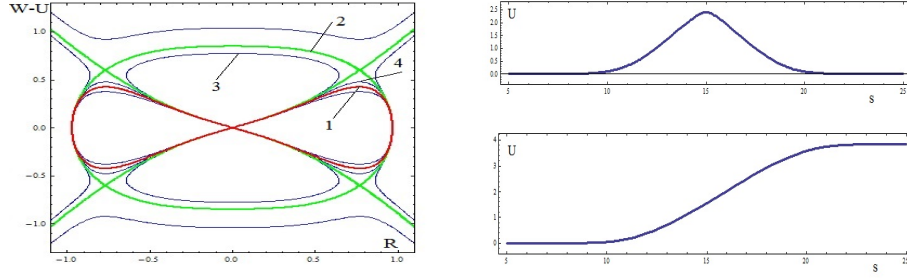


Figure 2. Left: Position of level curves $I(\delta) = 0$ at different values of δ . Curve 1 is plotted at $\delta = 0$, curve 2 at δ_0 , curve 3 at $\delta = -1.5 > \delta_0$, curve 4 at $\delta = -2.7 < \delta_0$. Right: Homoclinic trajectories from the left diagram corresponding to $\delta = -2.7 < \delta_0$ (upper panel) and $\delta = -1.5 > \delta_0$ (lower panel).

Namely, solving the biquadratic equation $I = 0$ with respect to $W - U$, several branches of level curves are obtained. The condition of contact for two branches leads us to a cubic equation with respect to R^2 with zero discriminant. Then $\delta_0 = -\frac{\alpha_3 \Omega^4 D^2}{(\alpha_1 - 1)^2}$ or $\delta_0 = \frac{27\alpha_3 \Omega^4 D^2}{\alpha_1^2(9 - 8\alpha_1)}$.

So, if $D = 0.9$, then $\delta_0 = -2.24732$. From the figure 2 it follows that for $\delta < \delta_0$ the homoclinic loops are placed in the vertical quarters of the phase plane. Note that the profiles of the resulting solitary waves are different (fig.2(right panel)), namely, at $\delta < \delta_0$ the U profile looks like a bell-shape curve, whereas at $\delta > \delta_0$ it is a kink-like regime.

1.3. The numerical scheme for the model (1)

To model the soliton dynamics, we construct the three level finite-difference numerical scheme for model (1) and study its stability.

Let us construct the numerical scheme for model (1) in the region $\Sigma = [0 \leq x \leq L] \times [0 \leq t \leq T]$ with grid lines $x = ih$ and $t = j\tau$, where h, τ are constant, $i = 1 \dots N$. Consider three level numerical scheme. Denote $u = u(t_{j+1})$, $v = u(t_j)$, $q = u(t_{j-1})$, and $K = w(t_{j+1})$, $G = w(t_j)$, $F = w(t_{j-1})$. We use the following difference approximation of derivatives

$$\begin{aligned} \frac{\partial^2 u}{\partial t^2} &\approx \frac{u_i - 2v_i + q_i}{\tau^2}, \quad \frac{\partial^2 u}{\partial x^2} \approx r \frac{u_{i-1} - 2u_i + u_{i+1}}{h^2} + (1-r) \frac{v_{i-1} - 2v_i + v_{i+1}}{h^2}, \\ \frac{\partial u}{\partial x} &\approx \frac{v_{i+1} - v_{i-1}}{2h}, \quad \frac{\partial^2 w}{\partial t^2} \approx \frac{K_i - 2G_i + F_i}{\tau^2}, \quad w - u \approx \frac{3G_i - F_i}{2} - \frac{3v_i - q_i}{2} \equiv \psi_i. \end{aligned}$$

Thus, if $r \neq 0$, then we obtain the three level implicit scheme:

$$A_i u_{i-1} + C_i u_i + B_i u_{i+1} = Y_i, \quad K_i = 2G_i - F_i - \tau^2 \omega^2 \psi_i - \tau^2 \delta \psi_i^3, \quad (6)$$

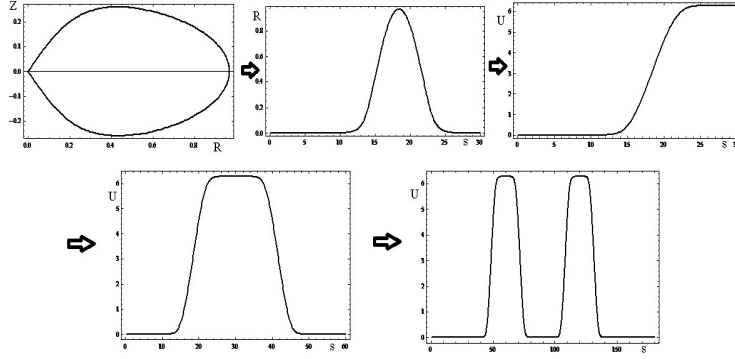


Figure 3. The construction of initial data for numerical scheme.

where $A_i = B_i = \frac{r}{h^2}\varphi$, $C_i = -2\frac{r}{h^2}\varphi - \frac{1}{\tau^2}$, $\varphi = \rho^{-1} \left(e_1 + 3e_3 \left(\frac{v_{i+1} - v_{i-1}}{2h} \right)^2 \right)$,

$$Y_i = - \left(\varphi \frac{v_{i-1} - 2v_i + v_{i+1}}{h^2} (1-r) + m\omega^2\psi_i + m\delta\psi_i^3 + \frac{2v_i - q_i}{\tau^2} \right).$$

System of algebraic equations (6) can be solved by the sweep method. The necessary conditions of the sweep method stability ($|A_i| + |B_i| \leq |C_i|$) are fulfilled. To get the restrictions for spatial and temporal steps, the Fourier stability method, being applied to linearized scheme (6), is used. Let us fix the values of the parameters $e_1 = 1$, $e_3 = 0.5$, $\rho = 1$, $\omega = 0.9$, $m = 0.6$, $D = 0.9$, and the parameters of the numerical scheme $L = 30$, $N = 200$, $r = 0.3$, $h = L/N$, $\tau = 0.05$.

Let us construct the initial data v_i , q_i , G_i , F_i for numerical simulation on the base of solitary waves. To do this, we integrate dynamical system (4) with initial data $R(0) = 10^{-8}$, $Z(0) = 0$, $s \in [0; L]$ and choose the right homoclinic loop in the phase portrait (fig.1). Then the profiles of $W(s)$, $U(s)$, and $R(s)$ can be derived. Joining the proper arrays, we can build the profile in the form of arch:

$$v = U(ih) \cup U(L - ih), \quad q = u(x + \tau D) = [U(ih) + \tau DR(ih)] \cup [U(L - ih) + \tau DR(L - ih)].$$

The arrays G and F are formed in similar manner. Combining two arches and continuing the steady solutions at the ends of graph, we get more complicated profile. The sequence of steps for profile construction is depicted in figure 3 in detail. We apply the fixed boundary conditions, i.e. $u(x = 0, t) = v_1$, $u(x = Kh, t) = v_K$, where K is the length of an array.

Starting from the two-arch initial data, we see (fig.4) that solitary waves move to each other, vanish during approaching, and appear with negative amplitude and shift of phases. After collision in the zones between waves some ripples are revealed. Secondary collision of

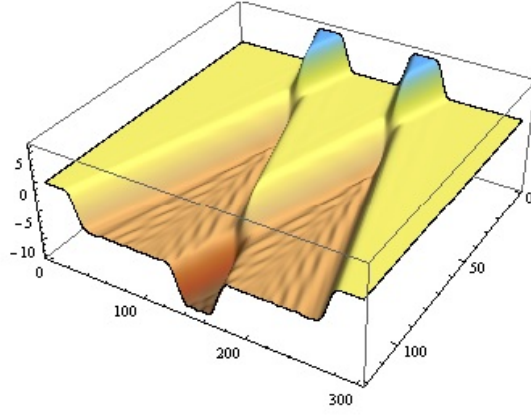


Figure 4. The propagation of solitary waves at $\delta = 0$ starting from the initial profile depicted in the figure 3.

waves are watched also. Note that the simulation of compacton solutions displays similar properties.

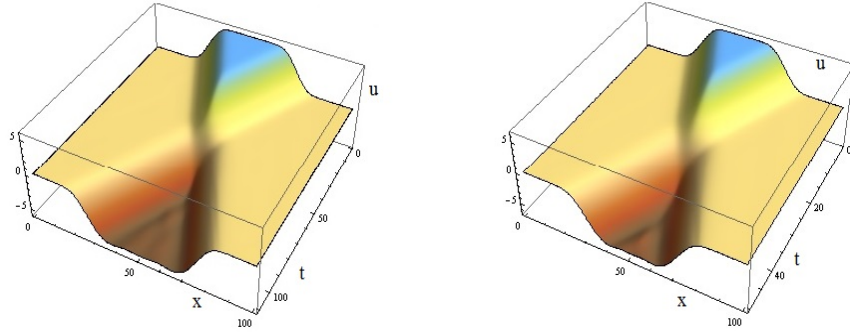


Figure 5. Solitary waves dynamics at $\delta = -0.2$ and $\delta = 1.3$.

Propagation of solitary waves at $\delta \neq 0$ depends on the sign of δ . Analysing the diagrams of figures 5, we see that for $\delta > 0$ the collision of waves is similar to the collision at $\delta = 0$. Behaviour of waves after interaction does not change essentially when $\delta < 0$ and close to zero. But at $\delta = -0.3$ after collision the amplitude of solution is increasing in the place of soliton's intersection (fig.6) and after a while the solution is destroyed.

This suggests that we encounter the unstable interaction of solitary waves or the nu-

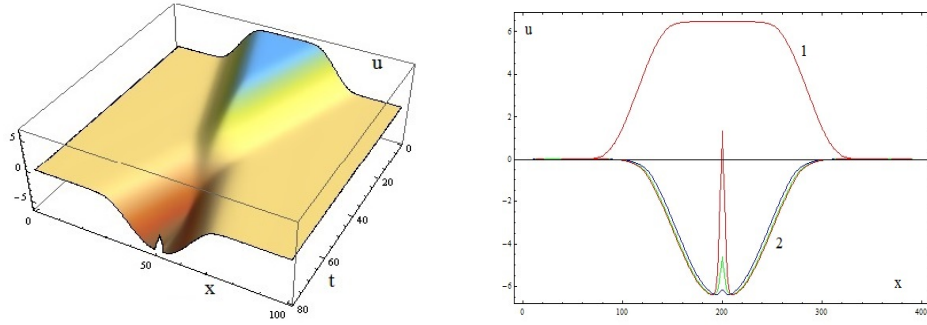


Figure 6. Solitary waves dynamics at $\delta = -0.3$. In the right panel the curve 1 is the initial profile, whereas other curves 2 are the forms of solutions just before blowup.

merical scheme we used possesses spurious solutions. But if we take half spatial step and increase the scheme parameter r up to 0.8, the scenario of solitary waves collision is not changed qualitatively. Therefore, the assertion on the unstable nature of collision is more preferable.

2. Conclusions

So, in this report, we have presented the novel nonlinear generalization of model for media with oscillating inclusions. It is important for application that the new parameters e_3 and δ have clear physical meaning. As it was shown in subsections 1.1 and 1.2, this model possesses the solitary waves of different types including compactons. We have considered the conditions of their existence and bifurcations when the parameters of nonlinearity were varied. The exact solutions describing the solitary waves with both unbounded and compact support were derived. Analysing the expression (5) and Fig. 2a, we should emphasize that the characteristics of solitary waves crucially depend on the dynamics of oscillating inclusions. To study the properties of solitary waves and their interactions, we have proposed the effective numerical scheme based on the finite difference approximation of the continuous model. In particular, we have found out the conditions when the stable propagation of solitons and their collisions are observed. It turned out that the nonlinearity of the oscillating dynamics describing by Φ affects not only the form of solitary waves but their stability properties in collisions (Fig. 6). Finally, there are solitary waves moving without preserving of their selfsimilar shapes. While the numerical results concerning the stable properties of single solitary wave can be confirmed by analytical treatments [10], the studies of wave collisions require mostly the application of improved numerical schemes. The results presented above

can be useful for modelling the behaviour of complex media in vibrational fields, for instance when we deal with the intensification of extracting oil and natural gas [4].

References

- [1] DANYLENKO, V., DANEVYCH, T., MAKARENKO, O., SKURATIVSKYI, S., AND VLADIMIROV, V. *Self-organization in nonlocal non-equilibrium media*. Subbotin in-t of geophysics NAS of Ukraine, Kyiv, 2011.
- [2] DANYLENKO, V., AND SKURATIVSKYI, S. Resonance regimes of the spreading of non-linear wave fields in media with oscillating inclusions. *Reports of NAS of Ukraine*, 11 (2008), 108–112.
- [3] DANYLENKO, V., AND SKURATIVSKYI, S. Travelling wave solutions of nonlocal models for media with oscillating inclusions. *Nonlinear Dynamics and Systems Theory* 4, 12 (2012), 365–374.
- [4] NIKOLAEVSKIY, V. N. Mechanism and dominant frequencies of vibrational enhancement of yield of oil pools. *USSR Acad. Sci., Earth Science Sections*, 307 (1989), 570–575.
- [5] PALMOV, V. A. On a model of medium of complex structure. *Journal of Applied Mathematics and Mechanics*, 4 (1969), 768–773.
- [6] SADOVSKIY, M. A. Self-similarity of geodynamical processes. *Herald of the RAS*, 8 (1986), 3–12.
- [7] SKURATIVSKYI, S. Chaotic wave solutions in a nonlocal model for media with vibrating inclusions. *Journal of Mathematical Sciences*, 198(1) (2014), 54–61.
- [8] SKURATOVSKII, S., AND SKURATOVSKAYA, I. Localized autowave solutions of the non-linear model of complex medium. *Electronic Journal Technical Acoustics*, 6 (2010), [http: ejta.org](http://ejta.org).
- [9] SLEPJAN, L. I. Wave of deformation in a rod with flexible mounted masses. *Mechanics of Solids*, 5 (1967), 34–40.
- [10] VLADIMIROV, V., MACZKA, C., SERGYEYEV, A., AND SKURATIVSKYI, S. Stability and dynamical features of solitary wave solutions for a hydrodynamic type system taking into account nonlocal effects. *Commun. in Nonlinear Science and Num. Simul.*, 19(6) (2014), 1770–1782.

Sergii Skurativskyi, Ph.D.: Subbotin Institute of Geophysics, NAS of Ukraine, Bohdan Khmelnytskyi str. 63-G, Kyiv, UKRAINE (skurserg@gmail.com). The author gave a presentation of this paper during one of the conference sessions.

Vjacheslav Danylenko, Professor: Subbotin Institute of Geophysics, NAS of Ukraine , Bohdan Khmelnytskyi str. 63-G, Kyiv, UKRAINE (vgv-igf@ukr.net).

Simulation results of robot with differential drive moving on circular path (MTR119-15)

Alexandr Štefek, Václav Křivánek, Yves T. Bergeon, Jean Motsch

Abstract: This article discusses basic principles of control of a robot with differential drive and their application to design an circular path. Differentially driven robot moves by use of two motors thus its constant rotation (without any acceleration) can be considered as a constraint. In this case the robot moves on path of a circular arc. It should be noted that circular arc is a function which does not fit all planed paths so some adaptations have to be made. In later chapters two possible adaptation are presented and discussed. The first adaptation is done by modifying known algorithm. The second one is author's own contribution to the problematic. Results are verified in a simulator.

1. Introduction

Path planning is a complex problem, which involves meeting physical constraints of unmanned robot (entity), constraints of operating environment and other operational requirements. For Unmanned Ground Vehicle (UGV) the problem of path planning is mostly reduced to two dimensional space. That is in contrast to Unmanned Aerial Vehicles (UAVs) where path planning is always a three dimensional issue.

The paths can be designed by various techniques based on whether the system has to traverse an area that is known, unknown, or partially known. Physical limitations, operating environment and communication requirements then make the planning more complex. It is essential to have an on-board processor to design and execute paths and trajectories.

Research into path planning is widely documented in fields of ground robotics and manipulation systems [8]. Path planning methods can be divided into several categories, based on criteria like: nature of applications, operation environment, medium of operation and path constraints. These criteria have then resulted in creation of variety of algorithms and techniques. The predominant methods used in ground robotics are (i) the road map method, (ii) the cell decomposition method, (iii) the potential field method.

Purpose of these methods is to generate routes for a robot to move from a start point to a finish point. It is also important to note that these methods rely on accurate definition of the environment. The environment is defined by a map, which contains known and unknown obstacles. Finding a path between two points on the map is simplified by (i) discretization

of the map into small areas or cells or by (ii) converting the map into a continuous field. Hence, path planning can be classified as discrete or continuous. A suitable search algorithm is then used to find a path connecting the start and finish points on this simplified map. The road map and cell decomposition methods transform the environment into a discrete map, while the potential field method transforms the map into a continuous function [9]. These methods, which produce a path for a given map or an environment, are also called *global path planners*. These methods transform the given environment into a searchable database [8].

For the rest of this paper the global path is considered to be known and set of check points to be given. The issue at hand is how to cross from one point on the planned path to another and simultaneously create optimal conditions to reach a third point. Previous experience shows that usage of odometry and inappropriate algorithm can result in missing the check points on the planned path, see figure 7.

The paper deals with description of a new algorithm used to pass through set of given points based on *splines* [6]. The results are then compared with the commonly used method – proportional control. This paper is separated into five sections. Section 2 contains description of differential driven robot control. Section 3 deals with control algorithms alongside with minimum control requirements included the motor motion dynamics. Section 4 describes the simulation results. And finally section 5 contains summarized conclusion of the paper and a plan for the future work in the issue.

For design of general algorithm three types of robot with differential drive were considered, see figure 1. The smallest one is ArduRobot controlled by Arduino. The medium-sized one is DaNI driven by Single Board RIO by National Instruments. And the biggest one is TurtleBot 2 managed by ROS (Robot Operating System). The aim for future work is to apply the proposed algorithm of motion control onto all three platforms and to compare their performance to the simulation results.

2. Robot with differential drive

Differentially driven robot is perhaps the simplest possible design for a ground-contact mobile robot [3, 5]. Differentially driven robot consists of two wheels mounted to a common axis controlled by separate motors, see figure 2. Its movement is done by use of kinematics. Kinematics deals with relationship between control parameters (relative velocity of the two wheels v_r , v_l) and the behavior of system in state space [4].

For the robot to rotate around a point, both left and right wheel have to follow a path that moves around the *Instantaneous center of rotation* (ICC) at the same angular rate ω , at each instant in time, and thus

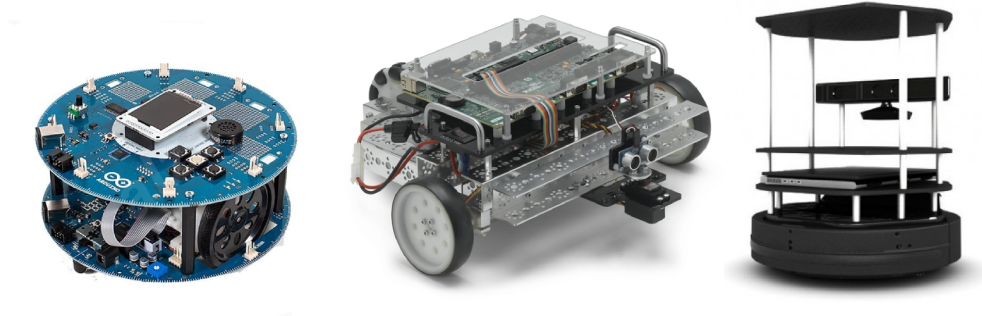


Figure 1. Three types of differentially driven robots. Notes: the pictures are not scaled. From left to right side: (i) ArduRobot; (ii) DaNI; (iii) TurtleBot 2.

$$\omega \left(R + \frac{l}{2} \right) = v_r, \quad \omega \left(R - \frac{l}{2} \right) = v_l. \quad (1)$$

where l is axis distance between the center of the two wheels, v_l is the left wheel's velocity along the ground, v_r is the right wheel's velocity along the ground and R is the distance of ICC to the midpoint between the two wheels [2]. Note that v_l , v_r , ω and R are all functions of time. At any instant in time, solving for R and ω results in

$$R = \frac{l(v_l + v_r)}{2(v_r - v_l)}, \quad \omega = \frac{v_r - v_l}{l}. \quad (2)$$

The equations above are in a standard form which is widely used (as an example see [4]). Nevertheless, for practical implementation, the variable R (radius) becomes problematic, when $v_r = v_l$ (R becomes infinity, see equation 2, and robot is moving on a straight line).

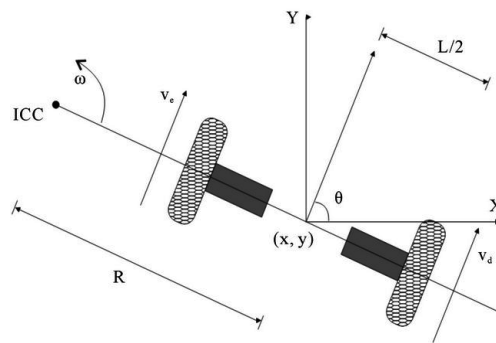


Figure 2. Differentially driven kinematics.

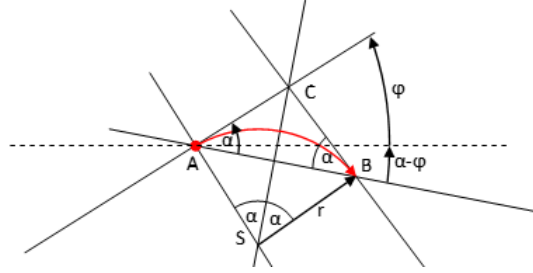


Figure 3. Relationship between two points on the robot path.

As the value of infinity is not usable in computer math implementation this case must be strictly avoided. Thus the equations introduced above can be and have to be changed into different form

$$\begin{pmatrix} \dot{x} \\ \dot{y} \\ \dot{\varphi} \end{pmatrix} = \begin{pmatrix} \cos \varphi & 0 \\ \sin \varphi & 0 \\ 0 & \frac{2}{l} \end{pmatrix} \cdot \begin{pmatrix} v \\ \Delta \end{pmatrix}, \quad (3)$$

where x, y are robot's position coordinates in state space, φ is its orientation, v is its velocity, Δ is half of difference in circumferential velocities of its wheels and l is the distance between the wheels.

$$v = \frac{v_r + v_l}{2}, \quad \Delta = \frac{v_r - v_l}{2}, \quad (4)$$

$$r = \frac{vl}{2\Delta}, \quad (5)$$

$$\omega = \frac{2\Delta}{l}, \quad (6)$$

where r is radius of rotation for planned path and ω is angular velocity of the whole robot. If robot's direction is straightforward then radius r approaches infinity, ω and Δ is zero.

2.1. Traditional approach to control of differentially driven robot

The traditional approach to control differentially driven robot uses difference in angles. Figure 3 depicts this situation. Compare there angles φ , α and $(\alpha - \varphi)$. In this case the differential equation has form

$$\omega = K\alpha, \quad (7)$$

There is also a problem in appropriate setting of the proportional control coefficient K . If the coefficient K is too low then the robot can even miss its goal. This type of differential driven control robot is considered as an etalon for comparison with new approach presented in the next chapters.

3. Derivation of feedback-based control for circular path

Unfortunately, there is an occurrence of delay between estimated and actual time of acceleration and deacceleration(speedups and slowdowns) during the use of classic control method. That results in integration of time errors. If startups and slowdowns occur too often, then the whole dimetric-based measurement systems can show significant deviation. If it could be assured that the angular velocity of both wheels is kept at a constant level during the whole control process(or at least during its significant part), then the resulting trajectory deviation would be kept to a minimum.

If we want to minimize the change in motor speeds during one part of the planned path, then it is necessary to keep these speeds at constant level. Such path, where both motors have constant speed is in shape of a circular arc. To plan adaptive control during the movement of the robot on the circular arc, it is important to define feedback-based control that constantly handles speeds of both motors on each point of the robots path. Taking these requirements into considerations it is possible to reverse-engineer the feedback-based control by the following method.

Two points can be connected by infinite amount of different circular arcs. But given that the robot has a certain starting orientation which is in direction of a tangent line, then there is only one acceptable circular arc to consider, e.g. figure 4.

The figure 3 describes the robot's position and its relation to position of its goal (the starting and the final orientations of the robot are of course also considered). When the robot is moving from point A to point B, the relation between distance of points A and B and radius of rotation can be expressed by equation 8.

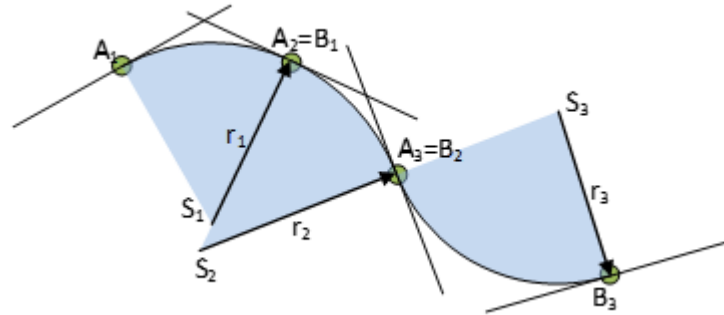


Figure 4. Robot path compounded by circular segments.

$$\begin{aligned} 2 \cdot r \cdot \sin \alpha &= |AB|, \\ \sin \alpha &= \frac{\frac{1}{2}|AB|}{r}. \end{aligned} \quad (8)$$

Considering equation 5 and equation 6

$$\omega = \frac{v}{r} = 2v \frac{\sin \alpha}{|AB|}, \quad (9)$$

the following set of equations can be easily derived with use of trigonometry

$$\begin{aligned} \cos(\alpha - \varphi) &= \frac{ab_x}{|AB|}, \\ \sin(\alpha - \varphi) &= -\frac{ab_y}{|AB|}, \end{aligned} \quad (10)$$

$$\sin(\alpha) = \sin[(\alpha - \varphi) + \varphi] = \cos(\alpha - \varphi) \cdot \sin \varphi + \sin(\alpha - \varphi) \cdot \cos \varphi, \quad (11)$$

$$\sin \alpha = \frac{ab_x \cdot \sin \varphi - ab_y \cdot \cos \varphi}{|AB|}. \quad (12)$$

Combining equation 9 and 12 gives

$$\omega = 2v \frac{ab_x \sin \varphi - ab_y \cos \varphi}{|AB|^2}. \quad (13)$$

Compared to equation 6, the final form of feedback-based control is

$$\omega = \frac{2\Delta}{l} = 2v \frac{ab_x \sin \varphi - ab_y \cos \varphi}{|AB|^2}, \quad (14)$$

thus

$$\Delta = vl \frac{ab_x \sin \varphi - ab_y \cos \varphi}{|AB|^2}. \quad (15)$$

It can be interesting to note that according to equation 3 and equation 14 can be derived

$$\omega = 2 \frac{ab_x \dot{y} - ab_y \dot{x}}{|AB|^2}. \quad (16)$$

Let's be reminded that

$$\vec{AB} = (ab_x; ab_y), |AB| = \sqrt{(ab_x)^2 + (ab_y)^2}. \quad (17)$$

The equations 3, 4 and 15 define the final mathematical form of feedback-based control for robot moving on circular path segments. Derived control has not any option to change robot behavior. Thus K_c coefficient added to equation can play interesting role.

$$\Delta = K_c vl \frac{ab_x \sin \varphi - ab_y \cos \varphi}{|AB|^2}. \quad (18)$$

The equation 18 allows to run multiple experiments / fine-tune a path of a robot on single line segment. In the next chapter two approaches will be compared to each other. One using this form and the other being a classical one (proportional control for ω).

4. Simulation results

This chapter discusses the results of the simulations. To be as close to real results as possible the dynamic of motors was also considered. The comparison in this chapter was done with use of simulation tools. A dynamic model of motor behavior had to be modeled to consider its dynamic characteristic on the robot chassis.

4.1. Motor dynamics

Because two identical motors are used for one robot chassis, only one transfer function will be defined. The common transfer function for single motor is

$$F(s) = \frac{Y(s)}{U(s)} = \frac{1}{a_2 s^2 + a_1 s + 1}, \quad (19)$$

where $a_2 = T_1 \cdot T_2$, $a_1 = T_1 + T_2$, and T_1, T_2 are time constants. Thus from

$$\alpha_2 \ddot{y} + a_1 \dot{y} + y = u, \quad (20)$$

we can obtain state differential equations of both left and right motor

$$\dot{x}_{or} = -\frac{1}{a_2} \cdot v_r + \frac{1}{a_2} \cdot v_{sr}, \quad \dot{v}_r = -\frac{a_1}{a_2} \cdot v_r, \quad (21)$$

$$\dot{x}_{ol} = -\frac{1}{a_2} \cdot v_l + \frac{1}{a_2} \cdot v_{sl}, \quad \dot{v}_l = -\frac{a_1}{a_2} \cdot v_l. \quad (22)$$

In simulations the values T_1 and T_2 were set to 0.03s. The simulation uses this list of equations: 3, 4, 15, 21 and 22. Motor is modeled here as a complex system where input is demanded angular velocity and output is real angular velocity.

4.2. Path comparison

For the purpose of comparison, the parameters have been set to lead to similar trajectories. In figure 5 there are five trajectories based on the same originally planned path that is also shown. Trajectory 'Robot A0' is pure circular path (K_c is equal to 1), 'Robot A1' uses $K_c = 4$, 'Robot A2' uses $K_c = 8$. Two trajectories 'Robot W1' and 'Robot W2' both use the classical approach to motion control but with different increments of coefficient K_c . It is interesting to note that trajectories 'Robot W1' and 'Robot A1' are nearly the same as trajectories 'Robot W2' and 'Robot A2'.

4.3. Limitation of centripetal acceleration

Centripetal acceleration is a very important parameter which has to be observed during robot control. High values can lead to tipping of the robot. For approach presented in this paper it is very easy to limit the centripetal acceleration to a desired interval by use of K_c . That

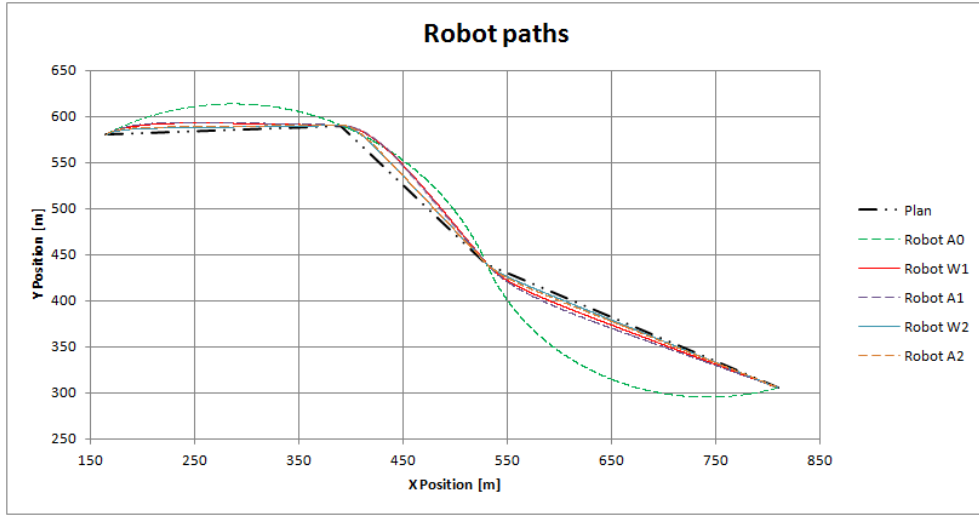


Figure 5. Robots path, overview of all planned paths for different K and K_c .

can be done because the presented algorithm has robust stability (comparatively to figure 7 where the unstable behavior of classical approach is depicted for low value of gain K). Figure 6 shows the centripetal acceleration in time. It should be noted that, for one segment of a path (e.g. from point A to point B), 'Robot A0' has constant centripetal acceleration. The case when centripetal acceleration was strictly in the interval $< -3; 3 >$, was tested. The both paths filtered and unfiltered were compared; difference between both is minimal. In this case centripetal acceleration filtering do not play a significant role. The robot path is nearly the same but the centripetal acceleration is low enough.

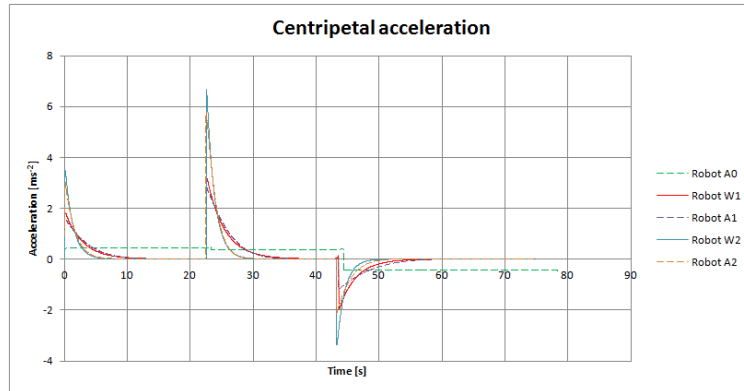


Figure 6. Centripetal acceleration, detailed view.

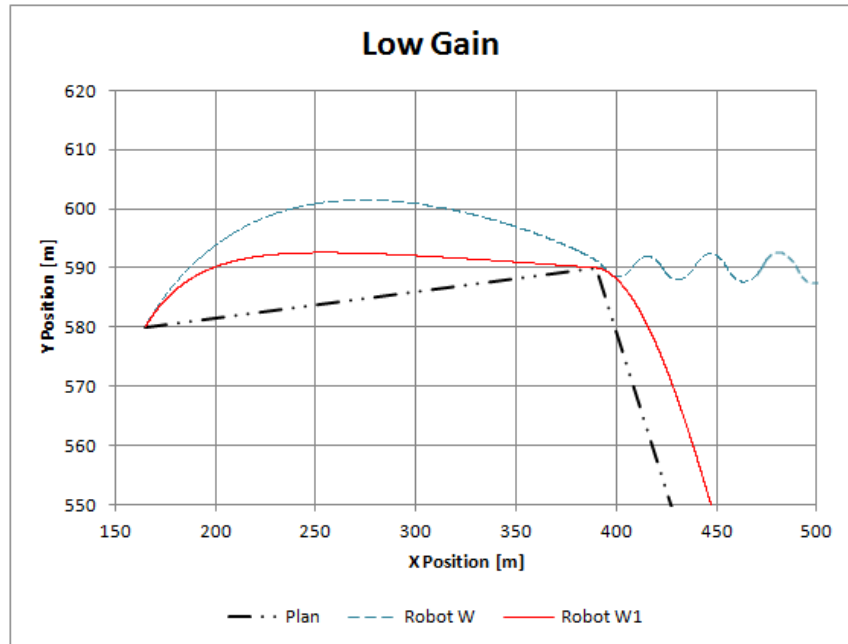


Figure 7. The example of path for both approaches. Classical approach 'Robot W' implies instability around the second check point for low value of gain K .

5. Conclusion

The new approach to differential robot control was derived, presented and compared to classical proportional approach. This approach can help the robot to move on a single segment of its path with minimal changes to both angular velocities of wheels. Moreover the extended version of control with K_c coefficient can play important role in limitation of centripetal acceleration which has a substantial impact on stability of the robot chassis during switching from one path segment to another one.

Possible future work can include on-the-move adaptations of K_c coefficient to find optimal behavior and (sub)optimum of fitness function for given robot (see figure 1). The issue is to compare real path of different approaches made by differential control robots. Very useful appears to construct a portal as a cameras holder to observe the scene with robot. Hence the quality of control process is transform to machine vision problem [1,3].

Proposed algorithm can be used not only for UGVs but also for UAVs as well, which are then going to be able to copy the planned trajectory with minimum of changes caused by dynamic effects of the environment [7]. For the implementation of the algorithm is needed to extend the state space to 3D territory.

Acknowledgments

The work presented in this paper has been supported by the Ministry of Defence of the Czech Republic (Project DZRO K208).

References

- [1] BERGEON, Y. Calculation of the distance covered by a robot thanks to image analysis with a two-robot team. In *International Conference on Military Technologies, ICMT 2011* (2011), University of Defence, pp. 849–854. ISBN 978-80-7231-788-2.
- [2] CHITSAZ, H., LAVALLE, S., BALKCOM, D. J., AND MASON, M. T. Minimum wheel-rotation paths for differential-drive mobile robots. In *Proceedings of International Conference on Robotics and Automation. ICRA 2006* (2006), pp. 1616 – 1623. ISSN 1050-4729.
- [3] DOSKOČL, R., KŘIVÁNEK, V., ŠTEFEK, A., BERGEON, Y., AND MOTSCH, J. Uav assisted landing on moving ugv. In *International Conference on Military Technology* (Brno, 5 2015), V. Křivánek, Ed., pp. 611–615. ISBN 978-80-7231-976-3.
- [4] DUDEK, G., AND JENKIN, M. *Computational principles of mobile robotics*. Computational principles of mobile robotics, 2000. ISBN 0-521-56876-5.
- [5] HELLSTRÖM, T. Kinematics equations for differential drive and articulated steering. Tech. rep., Umeå University, 2011. ISSN 0348-0542.
- [6] PIAZZI, A., BIANCO, C., AND RONANO, M. η^3 - splines for the smooth path generation of wheeled mobile robots. *IEEE Transactions on Robotics* 23, 5 (Oct. 2007), 1089 – 1095. ISSN 1552-3098.
- [7] SALGA, J., AND MATURKANIČ, D. Flight trajectory modelling to increase general aviation safety. *Advance in Military Technology* 6, 1 (June 2011), 107 – 120. ISSN 1802-2308.
- [8] TSOURDOS, A., WHITE, B., AND SHANMUGAVEL, M. *Cooperative Path Planning of Unmanned Aerial Vehicles*. Wiley-Blackwell, nov 2010. ISBN 978-0-470-74129-0.
- [9] ŠEDA, M., AND PICH, V. Planning smooth trajectories in the plane with obstacles. *Cybernetic Letters* (2008), 5. ISSN 1802-3525.

Yves T. Bergeon, Ph.D. D.Sc.: Écoles de Saint-Cyr Coëtquidan, 56381 GUER Cedex, France (yves.bergeon@st-cyr.terre-net.defense.gouv.fr).

Václav Křivánek, Ph.D.: University of Defence, Faculty of Military technology, Kounicova 65, Brno, Czech Republic (vaclav.krivanek@unob.cz).

The author gave a presentation of this paper during one of the conference sessions.

Jean Motsch, Ph.D.: Écoles de Saint-Cyr Coëtquidan, 56381 GUER Cedex, France (jean.motsch@st-cyr.terre-net.defense.gouv.fr).

Alexandr Štefek, Ph.D. D.Sc.: University of Defence, Faculty of Military technology, Kounicova 65, Brno, Czech Republic (alexandr.stefek@unob.cz).

**The influence of pretensioner characteristic of four-point
fastening system on the disabled driver behavior during
frontal crash
(LIF201-15)**

Kamil Sybilski, Jerzy Małachowski

Abstract: In case of disabled driver, task of seat belts (besides limiting longitudinal displacements) is stabilization of his body during maneuvers on the road. In particular it is important, when the driver is deprived of one of the limbs, which is additional support for him. In order to increase stability in most of the cases the four-point fastening systems are used. In best solutions these systems ensure continuous tensioning. The paper presents numerical model development, its sensitivity study and results of multivariate analysis for frontal crash cases of cars being driven by the disabled drivers. The numerical model includes nonlinear interaction between human body-seat belt system and human body response under dynamic conditions. The aim of this work is to estimate the impact of the pretensioner and the seat belts characteristics on biomechanics of the disabled driver body. The simulations were performed using dynamical system integration (explicit). Driver with disabilities was modelled using the modified Dummy Hybrid III 50th model, which was seated using gravity load before simulations. As the result of the performed numerical analysis the charts of dummy's mass centre movement, angle of body rotation, head accelerations, forces between dummy and seat belts are presented. Based on those charts several biomechanical (injury) criteria factors were estimated (e.g. *HIC* and *Nij*).

1. Introduction

Disabled persons are a big part of contemporary societies. In many cases they are well educated and have very unique skills, which are widely sought on working market. Unfortunately very often they could not undertake any kind of activity because of lack of adapted infrastructure which is able to meet their requirements. It concerns especially people who live outside city centres where in many cases their mobility is limited. Therefore if they want to work they have to involve other people to help them get to the workplace or they have to buy car adapted to their disabilities or adapt already bought car in specialist workshop. In Europe and around the world there are a lot of this kind of workshops. Also there is a lot of institutions, which help disabled persons in purchasing of new cars and adaptation equipment. Among many solutions are commonly used four-point seat belts. They are mounted straight to the seat and their main task is increasing stability of driver body. One of their biggest advantages is symmetry and ability to tight fastening. But on the other hand their biggest

disadvantage is a lack of pulling out seat belts during frontal crash. The generated in such situation system of loads acting on the driver can be too high. Therefore authors decided to check impact of the application of pretensioner from three-point seat belts with four-point belts and various characteristics (stiffness) of the seat belts on safety of disabled driver. Investigations were performed based on dynamic analysis using finite element method (FEM) approach.

2. Numerical model – assumptions and brief description

The main aim of the paper was to check impact of an application of pretensioner from three-point seat belts with four-point belts and various characteristics of the their material on disabled driver safety. To meet such very challenging task the FE model was developed. It contained quadrant of C-segment car [1], seat and dummy Hybrid III 50th [2, 3]. During numerical analysis the driver with paralyzed hands was considered. In such cases the driver has to use specialized handle on the steering wheel (Fig. 1). In numerical model it was reflected by the three cylinders fixed to the triangular plate using the 1D rigid connectors. Besides the connectors and sheathing car all elements during analyses were treated as a deformable.

Simulations were performed in two steps. In the first one the subsidence of the dummy on seat and handle under gravity load was carried out. Then four-point seat belts were added to the numerical model (Fig. 1). To properly describe the seat belts operationa the following parts were taken into account: sliprings (in places where the seat belts change direction), pretensioner and retractor. The sliprings allow to change shortening of one 1D seat belt element into elongation of another 1D seat belt element keeping the same tension in both elements. Pretensioner and retractor were placed in bottom of the seat, where can be placed slipring and connector with existing in real car pretensioner and retractor. The pretensioner used in the model represent pyrotechnic device which spins the spool of a retractor and thanks to that the seat belts are reeled in. To control this process a pull-in versus time curve was defined. The retractor was controlled by load curves (pull in/out vs force) for loading and unloading phase respectively. The retractor allow seat belt to be paid out into a 1D belt element. It operates in one of two regimes: unlocked when the belt material is paid out or reeled in under constant tension and locked when assumed force-pullout relationship applies. The retractor is initially unlocked and it pull in belt until triggering of acceleration sensors (set to 2,5g.).

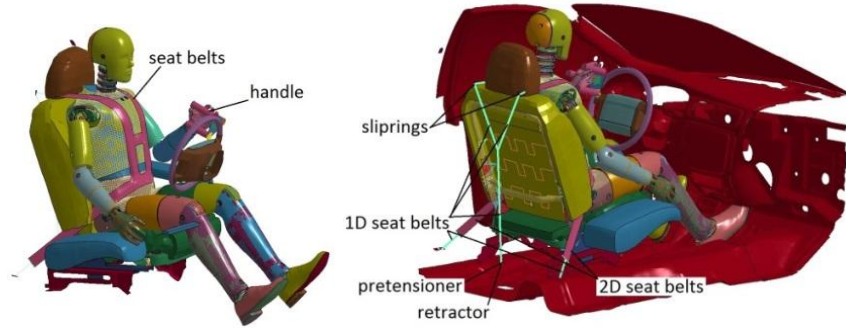


Figure 1. Numerical model used during analysis.

Because of limitation of described elements the seat belts had to be modeled using mix of 1D and 2D elements. The connection between them was modelled with 1D rigid elements on their ends.

The same acceleration sensor (as for the pretensioner) was used to activate airbag placed in steering wheel. In numerical model simple airbag was used, in which pressure is defined by equation [4, 5]:

$$p = \left(\frac{c_p}{c_v} - 1 \right) \cdot \rho \cdot e \quad (1)$$

where: c_p – heat capacity at constant pressure, c_v – heat capacity at constant volume, ρ – density, e – specific internal energy of the gas.

The filling of the airbag was realized by a specifying input mass flow rate.

One of the most important issues of the paper is an accurate numerical description of the two interacting bodies. The presented computational investigations were based on the analytical considerations included in the papers [6, 7, 8]. It was assumed that in the performed analysis the following constitutive relations between contacting bodies are formulated, according to contact normal stress tensor, using penalty method:

$$\bar{t} = \bar{t}_N \bar{n} \quad (1)$$

where $t_N = \varepsilon_N g_N$ and ε_N is the normal penalty factor.

From the finite element formulation, the contact contribution for slave node k is formulated on the following equation:

$$C_c^k = \delta u_c^T F_c = \delta u_c^T K_c \Delta u_c \quad (2)$$

where F_c is the contact force vector, δu_c^T is a displacement vector for the contact elements and K_c is the contact stiffness matrix of the contact element containing the tangent stiffness matrix K_N for the normal contact.

Taking all above into consideration, the final global nonlinear element equation for penalty approach is as follows:

$$M\ddot{U} + [K + K_c]U = F(t) - F_c \quad (3)$$

where: M is the mass matrix, K is the stiffness matrix and vector $F(t)$ describing external force.

It should be concluded that the most challenging problem is the proper contact stiffness assessment which is strongly dependent on many factors. The contact process played a significant role due to its direct influence on the interaction process between contacting/interacting bodies. Thus, it was necessary to simulate the interaction between the segments of collaborating parts as accurately as possible. In explicit software, the interaction between two or more bodies is define using a so called penalty function approach [8]. For elements with different stiffness, the contact stiffness is determined by the following formula:

$$k_{cs}(t) = 0.5 \cdot SLSFAC \cdot \left\{ \begin{array}{c} SFS \\ or \\ SFM \end{array} \right\} \cdot \left(\frac{m_1 m_2}{m_1 + m_2} \right) \cdot \left(\frac{1}{\Delta t_c(t)} \right)^2 \quad (4)$$

where: $SLSFAC$ – scaling factor, SFS and SFM – scaling factor for slave and master side, m_1 and m_2 – masses of master and slave nodes, $\Delta t_c(t)$ – initial time step dependent on the contact procedure (if the solution time step grows, Δt_c is reset to the current time step to prevent unstable behavior of the simulation).

In the above formula, it is possible to observe that the contact stiffness depends, inter alia, on Δt_c , which, in turn, directly influences the solution time step and can be placed in the following formula:

$$\Delta t = C \min(\Delta t_c, \Delta t_{FE}) \quad (4)$$

where: Δt_c – time step size dependent on the contact procedure, Δt_{FE} – time step size based on the discrete element (selected through all elements in the model), C – scale factor related to the CFL stability condition.

The boundary conditions and crash process control were already described in the previous authors' papers [9, 10].

3. Simulation – main stages

During numerical analysis the impact of limiting force for retractor and seat belts characteristic were analysed. In the first case force was changed within the range from 1175 N to infinity (retractor and pretensioner were disabled). In the second case seat belts characteristic (stiffness), both for 1D and 2D elements, was scaled. There was thus obtained a set of characteristics describing force versus engineering strain and stress versus strain (for 1D elements presented in Fig. 2). In the first case seat belt characteristics shown in Figure 2 as a 100% was implemented. In the second stage the limiting force equal to 4 700 N was used.

During all performed simulations can be specify several similar stages. In the first step seat belts were rolled up, what minimized clearances between them and the dummy. Next the car started to slow down sharply, what caused triggering of the sensor and thereby activating pretensioners and filling airbag. In the next stage the dummy started to move on the seat which was accompanied by increasing reaction between the dummy and the seat belts. At the same time the airbag has been filled in and the dummy's chest started pressing it. The filled airbag also rapidly pushed away dummy's hand towards the door. In the last stage the car has changed moving direction and dummy's head hit into the airbag. From that point the body started moving backward.

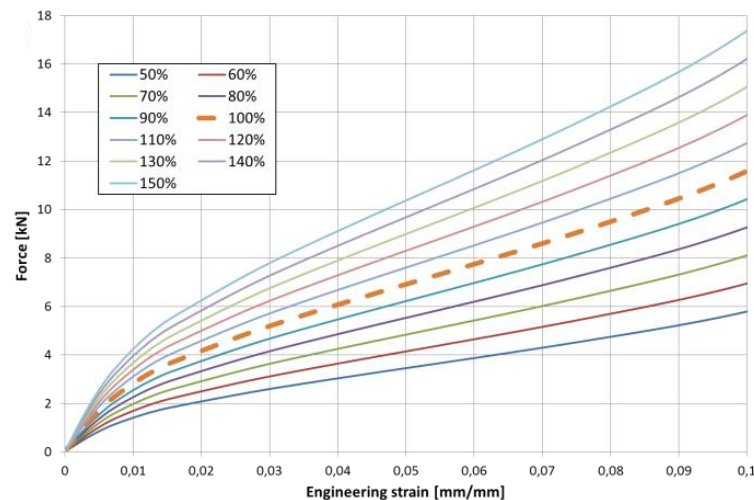


Figure 2. Characteristic force versus engineering strain for 1D seat belts used in analysis.

4. Results – 1st case – limiting force for retractor

In the first case limiting forces in retractor and pretensioner system was changed. It has significant impact on reaction between seat belts and dummy's body (Fig. 3). It can be observed that in the second stage, when the pretensioner acted, the maximum force was obtained for the biggest limit. The lower limit, the lower the maximum force in the second stage was obtained. But in the next

stages this trend is clearly visible only for two groups: the two lowest limiting forces and others. For the first group maximal forces were much lower than in the other cases.

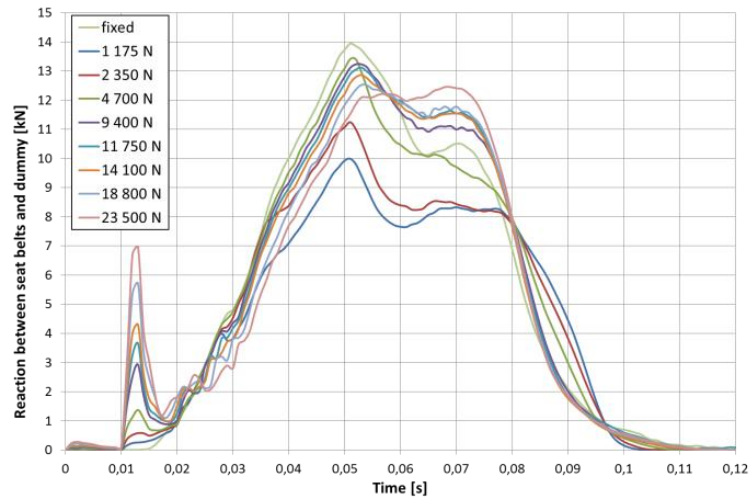


Figure 3. Comparison of reaction between seat belts and dummy.

The limiting force has impact on acceleration of the dummy's head (Fig. 4). The maximal value was obtained for a maximal limiting force. As in the previous case, the results can be divided into two groups. But this time for the first group can be included: disabled retractor and pretensioner, and limiting forces: 1175N, 2350N and 4700N. For these cases, the maximum acceleration was lower by approximately 100 m/s^2 than in the other one.

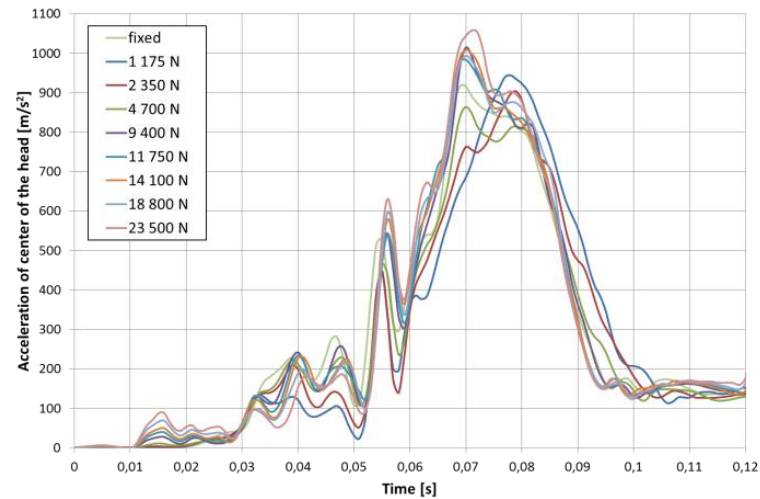


Figure 4. Comparison of acceleration of center of the head.

The course of acceleration had automatically influences the Head Injury Criterion (HIC) (Fig. 5). The lowest value was obtained for limiting force equal to 4700 N (similar to value from three-point seat belts). This indicates that both for three-point and four-point seat belts there is similar optimal limiting force.

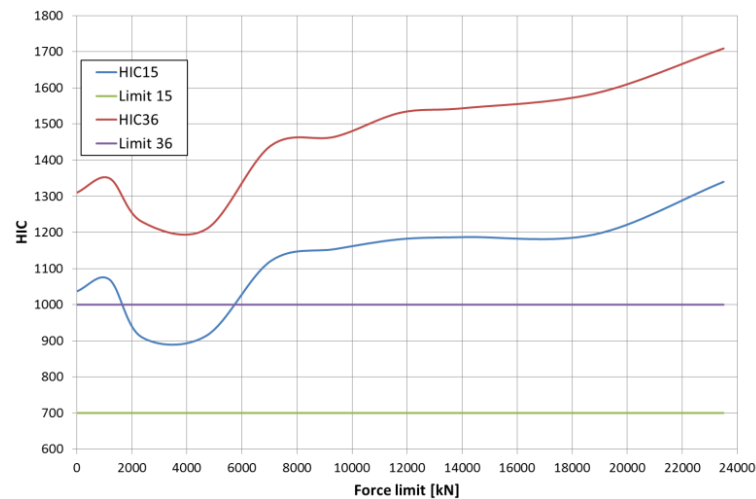


Figure 5. Head Injury Criterion.

The lower value of limiting forces means that the driver is less inhibited during crash by seat belts. It is better for his chest, but on the other hand his velocity is higher during hitting into airbag. Higher kinetic energy, especially head, must be absorbed by airbag.

During the frontal crash the first part of the driver, which was in contact with the air bag, was the trunk. But during this interaction the forces acting between these bodies were very small. Therefore, the biggest part of the energy of the upper drivers body, must absorb belts, which depending on their stiffness and force limiting takes place on a shorter or longer distance. The only part of the body not hampered by external devices was the head. The inhibition resulted from a connection with the torso through the neck and the forces acting in it. At the hitting moment the neck was strongly tensioned and bended. It is visible in the Neck Injury Criterion (N_{ij}) charts. The maximum value of the N_{ij} coincides with the time of full deceleration of the head. The difference between each course of the chart is significant. However none of them approached the limit 1.

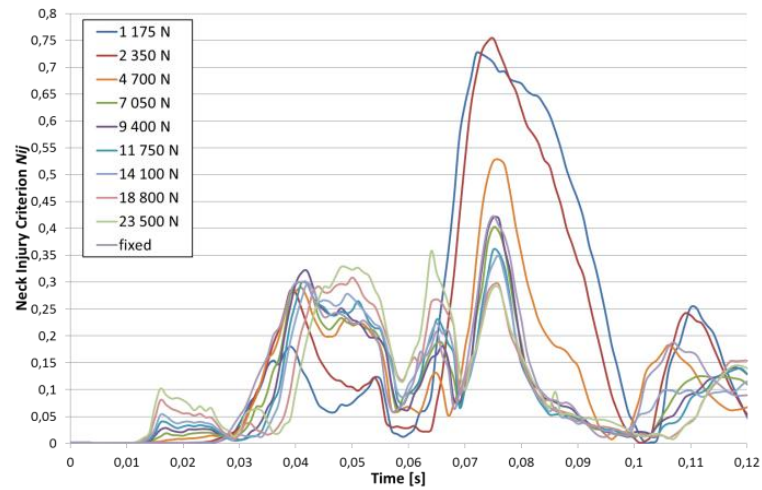


Figure 6. Neck Injury Criterion.

Equipment mounted on steering wheel for drivers with disabilities results in a significant change in the behavior of the body in the crash phase. The reason is a change in body position, which is very asymmetrical relative to a plane passing through the steering wheel. This occurs even when using four-point belts, which are fully symmetrical. In Figure 7 the angle of rotation of the arms for the analyzed cases is shown. The lowest angle (approx. 2 degree) occurs when seat belts are fixed. The biggest angle can be noticed for the smallest limits.

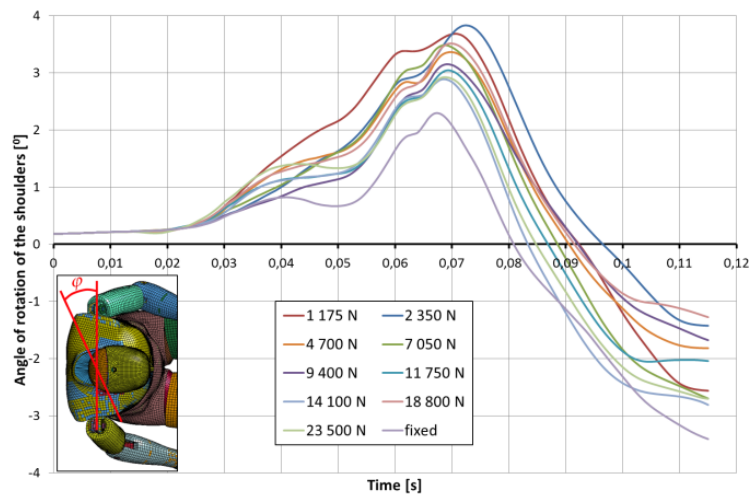


Figure 7. Angle of the shoulders rotation.

5. Results – 2nd case – change of the seat belts characteristic

In the second case characteristic of the seat belts was changed. In Figure 8 the impact of the characteristics of the seat belts on the reaction force between them and the dummy is shown. It can be noticed that the increase of the seat belts stiffness results in the reaction force increase. The maximal obtained value was 15,6 kN and the lowest 9 kN.

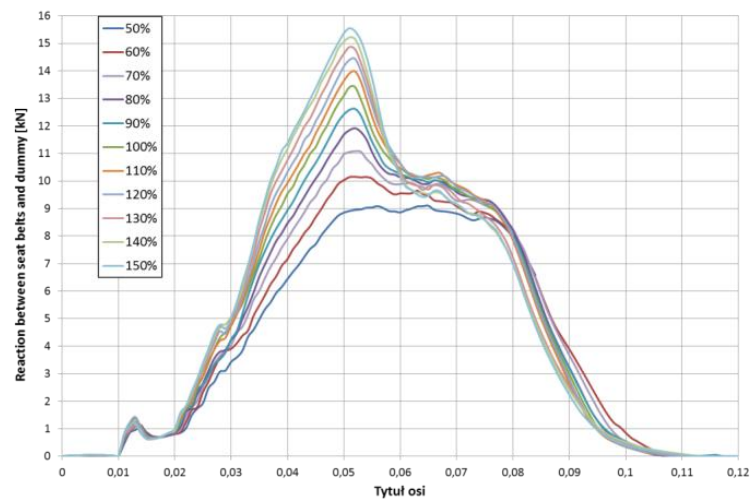


Figure 8. Comparison of reaction between seat belts and dummy.

Seat belts characteristics don't have impact on acceleration of the dummy head (Fig. 9.) The maximal values were similar for each case. Thereby, the Head Injury Criterion also was almost the same for each seat belt stiffness.

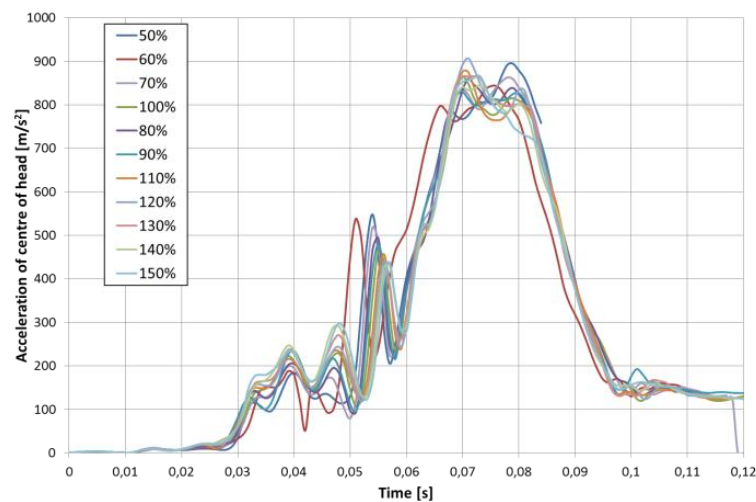


Figure 9. Comparison of acceleration of center of the head.

The same situation appeared in the case of the Neck Injury Criterion (N_{ij}) (Fig. 10). For each of the cases similar courses of the charts were obtained. Additionally, the maximum values were much smaller than the allowable limit.

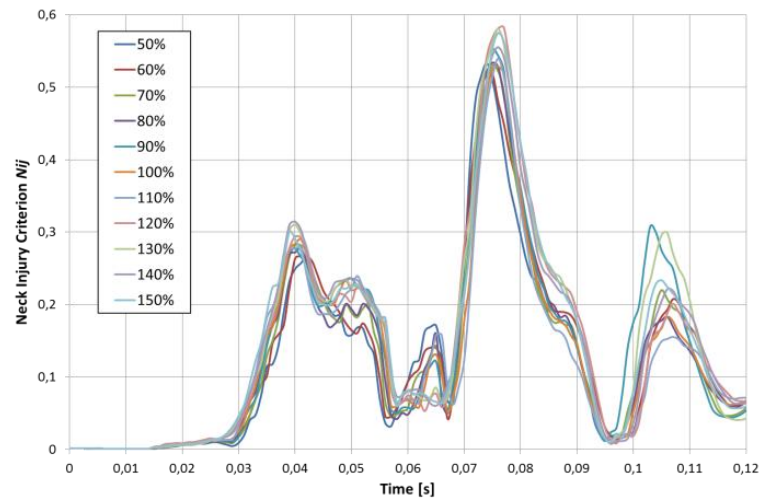


Figure 10. Comparison of acceleration of center of the head.

The stiffness change of the seat belts affected the angle of shoulders rotation (Fig.). The smaller stiffness results in the larger angle of rotation. The change was not such significant. The difference between the extremes values reached 1,5 degree.

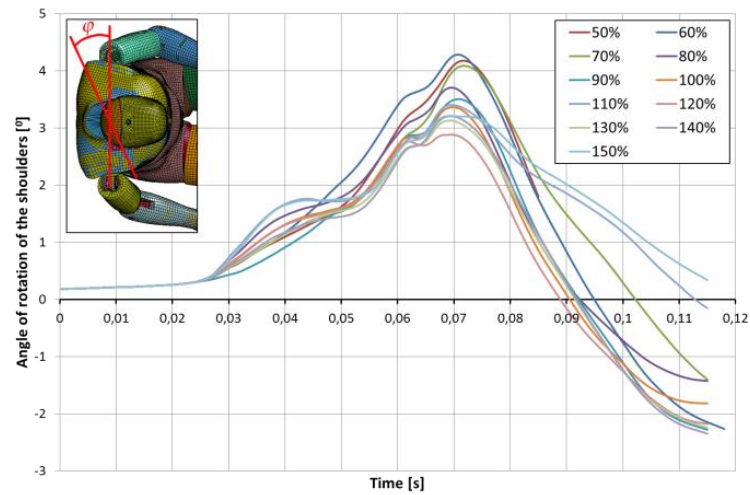


Figure 11. Angle of the shoulders rotation.

6. Summary and conclusions

The paper presents results of research on the two key parameters of seat belts designed for disabled persons. The impact of limiting force and seat belts stiffness on driver safety was analyzed.

Analyzing the obtained results it can be noticed that the limiting force increase affecting higher load on the dummy chest. This effect is strongly is unfavorable phenomenon. Finally, it increases the probability of a critical head injury by a driver. simultaneously the N_{ij} value decrease is observed what is the positive and desirable phenomenon.

Increasing the stiffness of the seat belts also increases the load on the dummy chest. Fortunately, it does not affect the value of the head and neck injury criterion.

Taking into account all above aspects, , the best solution is to use the four-point seat belts with pretensioner and retractor from three-point version..

The next part of the work will be focused on research of connection of left and right side of the four-point seat belts with pretensioner and its impact on disabled driver kinematics.

Acknowledgments

The study is supported by the NCBiR within project INNOTECH-K2/IN2/35/182265/NCBR/13. This support is gratefully acknowledged.

References

- [1] National Crash Analysis Centre: www.ncac.gwu.edu.
- [2] Hybrid-III Male Dummy, Humanetics Innovative Solutions 2013: www.humaneticsatd.com.
- [3] Pradeep M., Chung-Kyu P., Dhafer M., Cing-Dao K., Guha S., Maurath C., Bhalsod D. LSTC/NCAC Dummy Model Development, *11th International LS-Dyna Users Conference*, 2010.
- [4] Hallquist J. *LS-Dyna theory manual*, Livmore Software Technology Corporation, 2006.
- [5] LS-Dyna keyword user's manual, Livmore Software Technology Corporation, 2007.
- [6] Wriggers P., Van T., Stein E. Finite element formulation of large deformation impact-contact problems with friction, *Computers and Structures*, 37, 1990, 319-333.
- [7] Vulovic S., Zivkovic M., Grujovic N., Slavkovic R. Comparative study of contact problems solution based on the penalty and Lagrange multiplier approaches, *J. Serbian Society for Computational Mechanics*, 1, 2007, 174-183.
- [8] Baranowski P., Janiszewski J., Małachowski M. Study on computational methods applied to modeling of pulse shaper in split-Hopkinson bar, *Archives of Mechanics* 11, 2014, 429-452.
- [9] Małachowski J., Sybilski K., Muszyński A., Baranowski P. Problematyka bezpieczeństwa kierowcy wykorzystującego dodatkowe oprzyrządowanie na kierownicy w warunkach zderzenia czołowego, *Logistyka* 3, 2014, 4119-4127.
- [10] Sybilski K., Małachowski J. Wpływ rodzaju pasa bezpieczeństwa na zachowanie kierowcy w trakcie zderzenia czołowego, *Logistyka* 4, 2015, 5889-5897.

Kamil Sybilski, Ph.D.: Military University of Technology, Faculty of Mechanical Engineering, Department of Mechanics and Computer Science, gen. Sylvester Kaliski 2 Street, 00-908 Warsaw, Poland (kamil.sybilski@wat.edu.pl).

Jerzy Małachowski, Associate Professor: Military University of Technology, Faculty of Mechanical Engineering, Department of Mechanics and Computer Science, gen. Sylvester Kaliski 2 street, 00-908 Warsaw, Poland (jerzy.malachowski@wat.edu.pl).

Double pendulum colliding with a rough obstacle (NON254-15)

Grażyna Sypniewska-Kamińska, Roman Starosta, Jan Awrejcewicz

Abstract: The externally excited and damped vibrations of the double pendulum in the vertical plane are considered. The pendulum can collide with a rough obstacle many times during its motion. The pendulum is modeled as a piecewise smooth system. The differential equations govern the motion of the system in the relatively long time between the collisions. When a contact with the obstacle occurs, the pendulum exhibits a discontinuous behaviour. The velocities of both parts of the pendulum and the reaction forces are changing stepwise. An important element of the solving algorithm is aimed on the continuous tracking of the position of the pendulum in order to detect the collision with the unilateral constraints and to determine the state vector of the pendulum at the impact time instant. A single collision is described by the Euler's laws of motion in the integral form. The equations are supplemented by the Poisson's hypothesis and Coulomb's law of friction. The friction law is formulated for the instantaneous values of the reaction forces. The values of their impulses depend on the existence of a slip between the contacting bodies. Furthermore, during the collision the dynamic behaviour may change. Therefore the Coulomb law cannot be generalized for the linear impulses of the forces in a simple way. We have applied the Routh method in order to solve the problem. The method has a simple geometrical interpretation in the impulse space.

1. Introduction

It is well known that in many mechanical engineering systems, a contact between individual elements is not continuous. This may be an intended effect or a result of gradual destruction of the mechanical parts. Regardless of the cause, the collisions between various elements entail significant increase of the dynamic loads what leads to the greater destruction of the colliding elements.

In many papers dealing with collisions in multi-body systems consisting of rigid bodies, the influence of friction forces on the kinematic state of the bodies after impact is omitted. An approach to three-dimensional analysis of the collision of rigid bodies with friction was originally formulated by Routh [1]. In recent years many researchers rediscover the Routh model [2], analysing it in detail [4] and also applying it in modelling of multi-body systems with impacts [5]. On the base of Routh's model some more advanced models have been recently developed [3].

In this paper the collision of a relatively simple system, which is a double pendulum, with a fixed obstacle is investigated. The friction forces accompanying the collision are taken into account and the Routh model is employed.

2. Model of the system

The behaviour of a double pendulum colliding with an obstacle is considered (see Figure 1). The system is constrained to move in a fixed vertical plane. The pendulum, suspended at the point O , consists of two rigid bodies linked by a joint A . One of the bodies is a rod of mass m_1 and length l_1 . The second part of the pendulum is composed of a rod of length l_2 and a disc of radius r . The rod and the disc are fixed connected, and their common mass is equal to m_2 . C_1 and C_2 are the mass centres of the both parts. I_1 and I_2 denote the moments of inertia of the parts with respect to the axes which pass through the points C_1 and C_2 , respectively, and are perpendicular to the plane of motion. There is viscous damping at the both joints with a priori known coefficients c_1 and c_2 . Moreover, two torques $M_1(t) = M_{01}\cos(\Omega_1 t)$ and $M_2(t) = M_{02}\cos(\Omega_2 t)$ are taken into consideration.

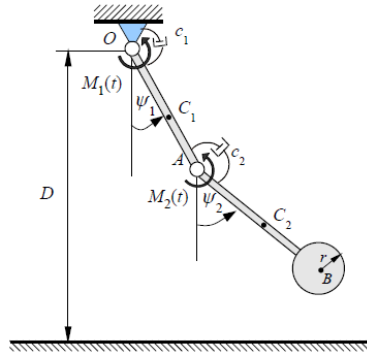


Figure 1. Double pendulum colliding with a rough obstacle.

The angles ψ_1 and ψ_2 are chosen as the general coordinates. The obstacle is motionless, and its surface is plane and rough. We assume that the distance D between the obstacle and the point O fulfils the following conditions

$$l_1 < D < l_1 + l_2 + 2r. \quad (1)$$

So, the motion of the pendulum is constrained by unilateral constraint

$$D - l_1 \cos(\psi_1) - (l_2 + r) \cos(\psi_2) - r \geq 0, \quad (2)$$

and only the disk placed at the end of the pendulum may come into contact with the rough obstacle.

3. Mathematical model

Observe that the unilateral constraint (2) does not act in relatively long intervals. From the point of view of the slow time scale which is suitable to observe the pendulum motion, they become active only in some time instants. When the contact with the obstacle occurs, the pendulum exhibits

discontinuous behaviour. The velocities of both parts of the pendulum as well as the reaction forces at the joints, and in the contact point with the obstacle exhibit stepwise changes. The pendulum, the motion of which is constrained by inequality (2) will be treated as piecewise smooth system. In such an approach, all the intervals in which kinematic and dynamic quantities change continuously are separated from each other by some time instants t_1, t_2, \dots , in which some from them change in stepwise way.

3.1. Motion between collisions

In each relatively long term between the collisions the pendulum motion is determined by differential equations and initial conditions. The equations of motion of the pendulum derived from the Lagrange equations of the second kind and written in matrix notation are as follows

$$\mathbf{A} \cdot \mathbf{\Psi} = \mathbf{Q}, \quad (3)$$

where:

$$\mathbf{A} = \begin{bmatrix} a_{11} & a_{12}(\psi_1, \psi_2) \\ a_{21}(\psi_1, \psi_2) & a_{22} \end{bmatrix}, \quad \mathbf{\Psi} = \begin{bmatrix} \ddot{\psi}_1 \\ \ddot{\psi}_2 \end{bmatrix}, \quad \mathbf{Q} = \begin{bmatrix} q_1(t, \psi_1, \psi_2, \dot{\psi}_1, \dot{\psi}_2) \\ q_2(t, \psi_1, \psi_2, \dot{\psi}_1, \dot{\psi}_2) \end{bmatrix},$$

$$a_{11} = I_1 + l_1^2 \left(\frac{m_1}{4} + m_2 \right), \quad a_{22} = I_2 + l_c^2 m_2, \quad a_{12} = a_{21} = l_1 l_c m_2 \cos(\psi_1 - \psi_2),$$

$$q_1 = M_{01} \cos(\Omega_1 t) - (c_1 + c_2) \dot{\psi}_1 + c_2 \dot{\psi}_2 - l_1 l_c m_2 \sin(\psi_1 - \psi_2) \dot{\psi}_2^2 - \left(\frac{m_1}{2} + m_2 \right) g l_1 \sin \psi_1,$$

$$q_2 = M_{02} \cos(\Omega_2 t) + c_2 (\dot{\psi}_1 - \dot{\psi}_2) + l_1 l_c m_2 \sin(\psi_1 - \psi_2) \dot{\psi}_1^2 - m_2 g l_c \sin \psi_2,$$

where $l_c = A C_2$.

The configuration of the pendulum at time instant t_i and its kinematic state after i -th collision are assumed as the initial values for the motion in $(i+1)$ -th interval. Taking into account also the conditions at $t = 0$, we can write

$$\mathbf{\Psi}(t_i) = \mathbf{\Psi}_{0i}, \quad \dot{\mathbf{\Psi}}(t_i) = \mathbf{\Theta}_{0i} \quad i = 0, 1, 2, \dots \quad (4)$$

The vectors $\mathbf{\Psi}_{00}, \mathbf{\Theta}_{00}$ are known, while both the vectors $\mathbf{\Psi}_{0i}, \mathbf{\Theta}_{0i}$ (for $i > 0$) are determined, using the Routh method, for each of the collision event.

Each of the initial value problems (3) with appropriate initial conditions (4) is solved numerically using the fourth order Runge-Kutta method. Usefulness of the method as well as the choice of the appropriate time step h have been tested numerically.

3.2. Kinematic aspect of the collision

An important element of the algorithm used to solving the initial problem (3)-(4) is the continuous tracking of the position of the pendulum in order to detect the collision with the obstacle. The collision occurs when

$$f(\psi_1, \psi_2) = D - l_1 \cos(\psi_1) - (l_2 + r) \cos(\psi_2) - r = 0. \quad (5)$$

Every time when function f changes its sign the Runge-Kutta algorithm is discontinued. The function f in equation (5) is interpolated linearly in the found interval of length h what allows to determine approximately the instant t_i of starting of i -th collision. Then the configuration of the pendulum as well as all necessary velocities at the instant t_i may be calculated.

3.3. Collision laws

Modelling the collision, we assume commonly used assumptions. All displacements and rotations during the collision are negligible. Impulses of contact forces are bounded, and impulses of all other forces may be neglected. The colliding bodies remain rigid and interact on each other only at one point. In time scale adapted to motion of the pendulum the duration of the collision is very short. However, during the collision velocities, accelerations and forces change, and these changes require to be described in a different time scale. We introduce the fast scale time τ suitable for collision modeling. For each collision, the time τ starts from 0.

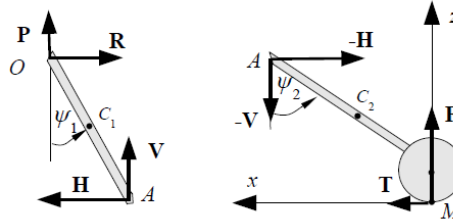


Figure 2. Forces taken into account during collision.

Integrating the Euler laws of motion with respect to time τ , and taking into account only the forces at the contact point M , the internal forces at the joint A , and the reaction forces at the joint O (see Figure 2), we can write

$$m_1(v_{1x}(\tau) - v_{1x}(0)) = \bar{H} - \bar{R}, \quad (6)$$

$$m_1(v_{1z}(\tau) - v_{1z}(0)) = \bar{V} + \bar{P}, \quad (7)$$

$$m_2(v_{2x}(\tau) - v_{2x}(0)) = \bar{T} - \bar{H}, \quad (8)$$

$$m_2(v_{2z}(\tau) - v_{2z}(0)) = \bar{F} - \bar{V}, \quad (9)$$

$$I_1(\omega_{1y}(\tau) - \omega_{1y}(0)) = (\bar{V} - \bar{P}) \frac{l_1}{2} \sin(\psi_1) - (\bar{R} + \bar{H}) \frac{l_1}{2} \cos(\psi_1), \quad (10)$$

$$I_2(\omega_{2y}(\tau) - \omega_{2y}(0)) = (\bar{V}l_c + \bar{F}d) \sin(\psi_2) - (\bar{H}l_c + \bar{T}d) \cos(\psi_2) - \bar{T}r, \quad (11)$$

where: $d = l_2 + r - l_c$, $\bar{F}, \bar{T}, \bar{H}, \bar{V}, \bar{R}, \bar{P}$ are impulses of the components of the forces shown in

Figure 2 (for instance $\bar{F} = \int_0^\tau F(\tilde{\tau}) d\tilde{\tau}$), $v_{1x}, v_{1z}, v_{2x}, v_{2z}$ are components of the velocities \mathbf{v}_1 and \mathbf{v}_2 of

the mass centres C_1 and C_2 , ω_{1y}, ω_{2y} are components of the angular velocities $\boldsymbol{\omega}_1$ and $\boldsymbol{\omega}_2$ of the bodies (perpendicular to the motion plane), whereas $v_{1x}(0), v_{1z}(0), v_{2x}(0), v_{2z}(0)$ and $\omega_{1y}(0), \omega_{2y}(0)$ are known.

Equations (6) - (11) are valid for any instant of time $\tau \in (0, \tau_f)$, whereas τ_f is the time instant in which the collision ends. Due to rigidity of the pendulum, there the following relationships hold

$$\mathbf{v}_1 = \boldsymbol{\omega}_1 \times \overline{OC_1}, \quad (12)$$

$$\mathbf{v}_2 = \boldsymbol{\omega}_1 \times \overline{OA} + \boldsymbol{\omega}_2 \times \overline{AC_2}. \quad (13)$$

Therefore, among the six kinematic quantities in equations (6) - (11), only two are independent, for example $\omega_{1y}(\tau)$ and $\omega_{2y}(\tau)$.

Let us decompose the velocity at the contact point M into two components in directions of the axes of the collision reference frame shown in Figure 2 in the following way

$$\mathbf{v}_M = \mathbf{s} + \mathbf{c} = s\mathbf{i} + c\mathbf{k}, \quad (14)$$

where $\mathbf{s} = s\mathbf{i}$ is called the *sliding velocity*, and $\mathbf{c} = c\mathbf{k}$ is the *closing velocity*. The friction force \mathbf{T} is modeled using the Coulomb law, and hence both the magnitude as well as the direction of the force \mathbf{T} depend on the sliding velocity \mathbf{s} at the contact point M , namely

$$s \neq 0 \Rightarrow T = -\mu F \frac{s}{|s|}, \quad s = 0 \Rightarrow T \leq \mu F, \quad (15)$$

where μ is the friction coefficient, and $T = \mathbf{T} \cdot \mathbf{i}$ is the projection of the vector \mathbf{T} on the common tangent at the contact point.

In accordance with the Poisson hypothesis we distinguish two phases of the collision. They are separated from each other by an instant τ_m in which the magnitude of the normal force \mathbf{F} achieves the maximum, and the closing velocity \mathbf{c} is equal to zero. The impulses of the force \mathbf{F} in the first and in the second phase are coupled as follows

$$\bar{F}_H = k \bar{F}_m, \quad (16)$$

where k is the coefficient of restitution, and $\bar{F}_m = \int_0^{\tau_m} F(\tilde{\tau}) d\tilde{\tau}$, $\bar{F}_H = \int_{\tau_m}^{\tau_f} F(\tilde{\tau}) d\tilde{\tau}$.

Equations (6) - (13), written for time instant τ_f , together with equation (16) and relationships (15) create the set of collision laws. They allow to determine the kinematic state of the pendulum after collision. All of the laws, except the friction laws, have the global nature (in other words they are written in the integral formulation) and concern the whole collision. The law given by (15) is formulated for instantaneous values and it cannot be generalized for the impulses \bar{F} and \bar{T} in a simple way, i.e. by integrating. This is why due to the dual form of the friction law the value of the impulse \bar{T} at the moment τ_f depends on existence of the slip at the contact point M . In what follows we illustrate how to solve this difficulty applying the Routh method.

3.4. Routh's method and collision of double pendulum

It should be emphasized that Routh's method is an exact one. Application of this method requires solving the system of equations (6) - (13) with respect to $\omega_{1y}, \omega_{2y}, \bar{H}, \bar{V}, \bar{R}, \bar{P}$. Then, substituting the solution for ω_{1y} and ω_{2y} into formula

$$\mathbf{v}_M = \boldsymbol{\omega}_1 \times \overline{OA} + \boldsymbol{\omega}_2 \times \overline{AM}, \quad (17)$$

we obtain two equations

$$s(\tau) - s(0) = \alpha \bar{T} + \varepsilon \bar{F}, \quad (18)$$

$$c(\tau) - c(0) = \varepsilon \bar{T} + \gamma \bar{F}, \quad (19)$$

where $\alpha, \varepsilon, \gamma$ are constant dependent on the geometric parameters, the inertia parameters and the configuration of the pendulum at $\tau = 0$. This means that they must be determined for each collision.

The Routh method has a clear geometrical interpretation in the impulse space. In the case of planar motion, this space is two-dimensional. Accordingly to the nature of a normal force \mathbf{F} , its impulse is always non-negative. Therefore, we will say further about the impulse semi-plane.

Assuming that in Eq. (18) $s(\tau) = 0$, one can derive the condition for the collision without slip. A line called the line of sticking corresponds to this condition on the semi-plane. Similarly, supposing $c(\tau) = 0$ in Eq. (19), we obtain the equation of the line of maximum compression. The relationship between impulses \bar{F} and \bar{T} , when $s(\tau) \neq 0$, derived from (15) is as follows

$$\bar{T} = -\mu \bar{F} \frac{s(0)}{|s(0)|}. \quad (20)$$

The line of friction is its image on the impulse semi-plane.

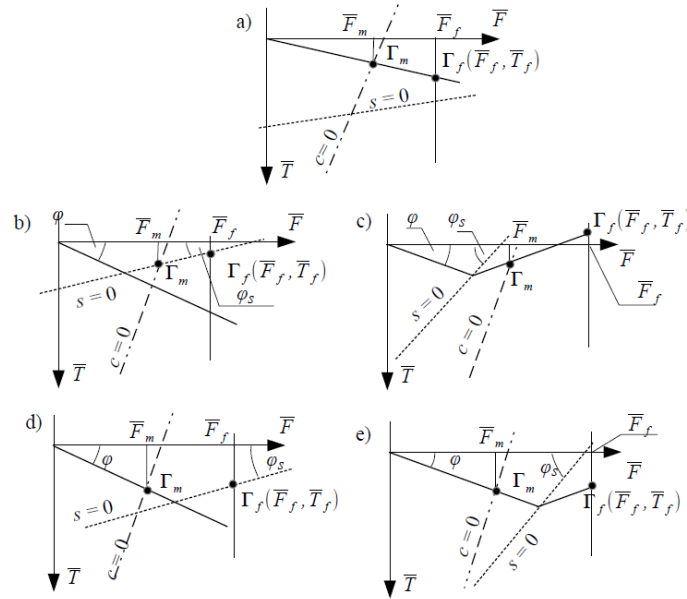


Figure 3. Interpretation of Routh's method on the impulse semi-plane.

It should be noted that all lines are strictly determined by a configuration state of the pendulum as well as the velocity \mathbf{v}_M at the moment in which the collision starts. Mutually location of these lines is of decisive importance for the values of impulses at the end of each collision. There are some possibilities of this arrangement. Five of them are presented in Figure 3. The axes of the coordinate system are scaled in units of impulse. The starting point of the line of friction (depicted by bold solid line) lies always at the origin of the system and represents the beginning of the collision (we assume

that at $\tau = 0$, the slip always appears). On the graph a), the line of friction and the line of sticking (depicted by dotted line) do not cross each other in the first phase of collision (i.e. on the left side of the line of maximum compression $c = 0$). Therefore, the point Γ_m in which the line of friction and the line of maximum compression intersect each other determines the end of the first phase of the collision. In accordance with Eq. (16), the abscissa of the point Γ_m multiplied by $(1+k)$ specifies the line of end of collision (it is always parallel to the vertical axis). The line of friction crosses it at the point Γ_f the coordinates of which are sought values of impulses \bar{F} and \bar{T} at the end of the collision. On the graphs b) and c) the line of friction crosses the line of sticking in the first phase of the collision. That means then the sliding velocity s becomes equal zero. The relation between the angles φ and φ_s is of decisive importance for the possibility of continuation the collision accompanied by the slip. If $\varphi > \varphi_s$, what is shown in Figure 3b), the slip vanishes and the collision without the sliding lasts to the end of the contact with the obstacle. Since that moment, the line of sticking represents the collision and its crossing-points with the lines of maximum compression as well as the line of end of collision determine the point Γ_f . Otherwise, what is shown on the graph c), the friction forces are too small to eliminate the slip. So, the disc having changed the direction still slides on the obstacle. The change of the sign of the vectors s and T causes that on the line of friction appears the discontinuity in slope. Graphs d) and e) concern the situation when the line of friction crosses the line of sticking in the second phase of the collision. For each of the graphs shown in Figure 3 exists its counterpart, that presents an arrangement with the line of friction which is symmetric in respect to the horizontal axis.

4. Results

Let us consider the motion of double pendulum whose parameters are as follows: $m_1 = 3\text{kg}$, $m_2 = 2.4\text{kg}$, $l_1 = 0.5\text{m}$, $l_c = 0.34\text{m}$, $r = 0.04\text{m}$. The moments of inertia due to central principal axis: $I_1 \approx 0.64\text{kgm}^2$, $I_2 \approx 0.94\text{kgm}^2$. During the motion, the pendulum collides with a fixed obstacle that is placed at the distance $D = 0.8\text{m}$ from the point O . The chosen values of the coefficients of friction and restitution are: $\mu = 0.2$, $k = 0.9$. It is assumed that do not act the external torques and there is no damping at the both joints. The values for the initial conditions are as follows: $\psi_1(0) = 130^\circ$, $\psi_2(0) = 90^\circ$, $\dot{\psi}_1(0) = 0.6\text{rad/s}$, $\dot{\psi}_2(0) = 0.5\text{rad/s}$. The numerical simulations have been done using the original software written in Fortran 95.

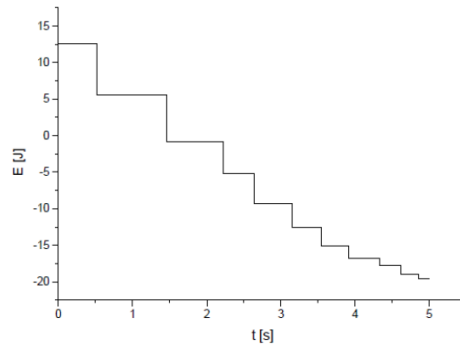


Figure 4. Stepwise changes of mechanical energy of the pendulum.

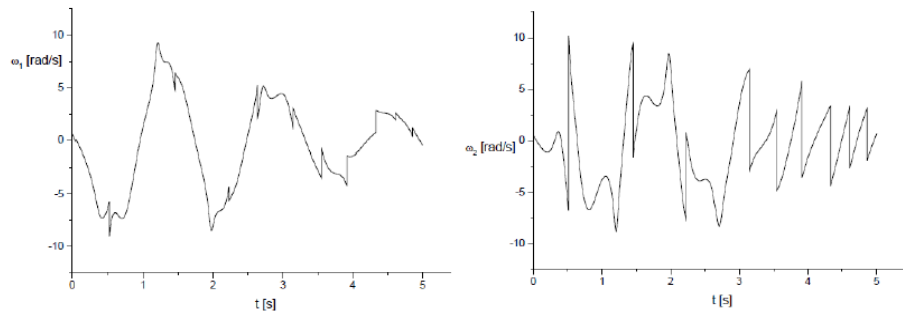


Figure 5. Stepwise changes of angular velocities of the pendulum parts.

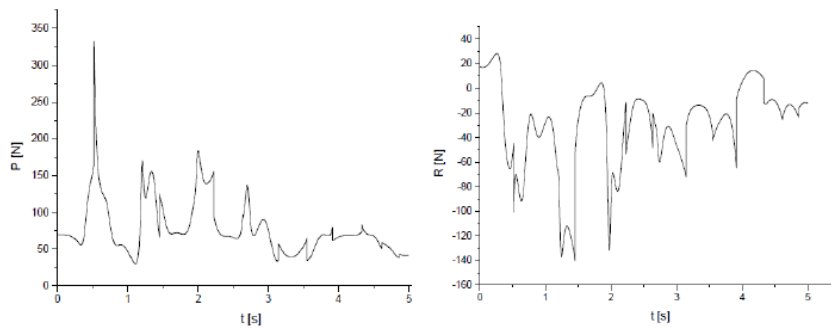


Figure 6. Stepwise changes of reaction forces.

In Figure 4, the loss of mechanical energy versus time of motion is shown. Under the given above assumptions, the system may lose the energy only as a result of collisions. Indeed, between the collisions the total energy is constant. It can be seen that the pendulum collides ten times in time of

simulation. The energy decreases stepwise after each contact with the obstacle (for comparison, the energy of the pendulum at the stable equilibrium position is about of -27.13 J).

In Figure 5, the time histories of the angular velocities of the both part of the pendulum are shown. The observed stepwise changes of their values (in number of ten) are the results of the collisions with the fixed and rough plane. The horizontal and vertical components of the reaction force at the joint O as functions of time are presented in Figure 6.

5. Conclusions

Models of collision phenomena taking into account friction forces at contact are more suitable for real problems. Possibility of the non-sliding type of contact significantly complicates the solving of the problem, even for relatively simple models with only one point of contact. In the paper, the Routh method has been applied to solve the problem concerning the collision of multi-body system. Combination of an exact method with numerical calculations in the framework of the piecewise smooth model allows us to investigate multiple collisions of mechanical systems under consideration.

Acknowledgments

This paper was financially supported by the National Science Centre of Poland under the grant MAESTRO 2, No. 2012/04/A/ST8/00738, for years 2013-2016.

References

- [1] Routh, E.J. *An elementary treatise on the dynamics of a system of rigid bodies*. Macmillan and Co., London, 1887.
- [2] Suslov, G. K. *Theoretical mechanics*. PWN, Warsaw, 1960, in Polish.
- [3] Keller, J.B. Impact with friction. *ASME J. Appl. Mech.* 53, 1986, 1-4.
- [4] Bhatt, V., and Koechling, J. Three-dimensional frictional rigid body impact. *ASME J. Appl. Mech.* 62, 1995, 893-898.
- [5] Sypniewska-Kamińska, G., and Rosiński, Ł. Application of the Routh method in computer simulation of selected problems in collision theory. *Computational Methods in Science and Technology* 14(2), 2008, 123-131.

Grażyna Sypniewska-Kamińska, Ph. D: Poznań University of Technology, Institute of Applied Mechanics, ul. Jana Pawła II 24, 60-965 Poznań, Poland, (grazyna.sypniewska-kaminska@put.poznan.pl). The author gave a presentation of this paper during one of the conference sessions.

Roman Starosta, Ph. D: Poznań University of Technology, Institute of Applied Mechanics, ul. Jana Pawła II 24,, 60-965 Poznań, Poland (roman.starosta@put.poznan.pl).

Jan Awrejcewicz, Professor: Technical University of Łódź, Department of Automatics and Biomechanics, ul. Stefanowskiego 90-924, Łódź, Poland (awrejcew@p.lodz.pl).

Modelling and studies of dynamics of a wheeled mobile robot during longitudinal motion on the soft ground (MTR124-15)

Maciej Trojnacki, Przemysław Dąbek

Abstract: The paper is concerned with the study of longitudinal motion of a four-wheeled mobile robot on the soft ground. Design of the robot and research environment are described. Dynamics model of the robot-ground system taking into account properties of soft ground is presented. Results of simulation research of robot motion and the analogous empirical tests are presented. Actual motion parameters of the robot and the values of longitudinal slip ratio of wheels are determined. The study is focused on influence of the longitudinal robot velocity on longitudinal slip of wheels. The results of simulation and experimental investigations are compared and discussed. The conclusions resulting from performed research are presented.

1. Introduction

Wheeled mobile robots are unmanned vehicles whose motion is primarily a result of interaction of wheels with the ground. An important problem associated with motion of the wheel is the slip phenomenon. Additionally, in case of robot motion on the soft ground deformability of this ground becomes important and its influence on robot motion must be taken into account. Wheel slip phenomena and ground deformability should be considered in the robot dynamics model, which becomes an important tool in the process of robot mechanical design and in the process of synthesis of its motion control algorithms.

The problems of modelling of the tyre-ground system were tackled so far mainly from the point of view of requirements of automotive vehicles, which over the years resulted in development of multiple tyre models with diverse capabilities, both on-road [7] and off-road [1, 11]. However, it turns out that the wheeled mobile robots, especially lightweight robots, differ significantly from automotive vehicles in terms of applications, manoeuvres performed, types of ground, vehicle design and properties of tyres. It seems that there is very little work done so far in the field of modelling of tyre-road interaction for lightweight wheeled robots. Several studies concern wheel-terrain interaction of planetary rovers, where a rigid wheel is considered [6] or a flexible wheel of special design made primarily of metal [3]. Works that study motion of lightweight wheeled robots on deformable ground are not readily available. Therefore a couple of questions arise like: if deformability of both tyres and ground should be included in the tyre-ground model, if the factors affecting the motion of small robotic wheel on deformable ground are similar as in case of the manned vehicles, etc.

The aim of the present work is modelling and studies of dynamics of a lightweight wheeled mobile robot during longitudinal motion on the soft ground. The investigations cover robot motion with various longitudinal velocities on sand. Influence of robot longitudinal velocity on the occurring wheel slips is analysed. Results of the simulation studies are compared and verified against empirical data obtained during experiment at a dedicated test stand.

2. Four-Wheeled Skid-Steered Mobile Robot

The object of the research is a small four-wheeled mobile robot called PIAP GRANITE (Ground Robot for ANalyzes of wheels Interaction with various TERRain). The robot has all wheels driven independently by DC servomotors with gear units and encoders. The current design of the robot is shown in Fig. 1a, and its kinematic structure, in Fig. 1b.

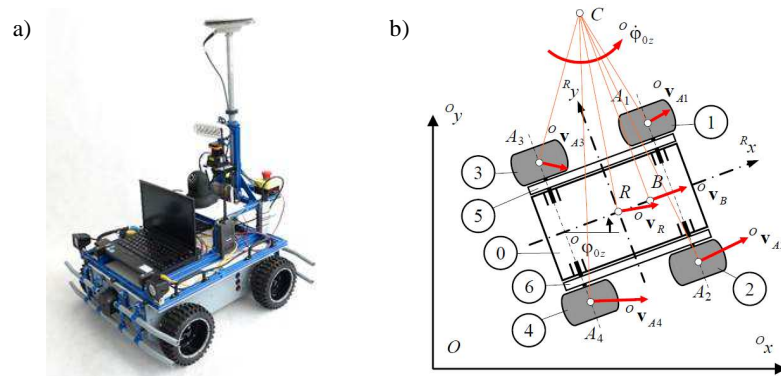


Figure 1. Four-wheeled skid-steered mobile robot PIAP GRANITE:
a – current design, b – kinematic structure.

It is possible to distinguish the following main components of the robot: 0 – body with frame for installation of the research equipment, 1-4 – wheels with toothed belt pulleys, 5-6 – toothed belts. The drive transmission in each drive unit can be decoupled and also toothed belts can be removed which permits obtaining various configurations of the robot drive system. In this paper, the configuration of the robot with independent driving of all 4 wheels is analysed.

The following symbols for the i^{th} wheel have been introduced in the robot model: A_i – geometrical centre, $r_i = r$ – radius, $b_i = b$ – width of tyre tread, θ_i – angle of wheel spin ($i = 1, \dots, 4$).

The robot is equipped with: a laptop computer for control and data acquisition purposes, iNEMO and ADIS inertial measurement units each consisting of 3-axis MEMS accelerometer, gyro and magnetometer, a GNSS receiver and antenna for robot navigation [8], a 2D laser scanner for localization in known environment [5]. The measuring system that allows determination of robot motion parame-

ters in the present work according to the method proposed in [10], consists of inertial measurement units only. The GNSS receiver and antenna are a separate module which can be dismantled. Moreover, in case of robot motion investigations on the soft ground dual tyres are used so that the wheels are subject to less sinkage during motion.

3. Modelling of the Robot

3.1. Robot kinematics

In this paper longitudinal motion of the robot is analyzed. It is assumed that this motion is realized in Oxz plane of the fixed coordinate system $\{O\}$. The moving coordinate system associated with the robot is denoted with symbol $\{R\}$.

In the analyzed case, the desired parameter of robot motion will be velocity of the characteristic point R of the robot (Fig. 1b), that is ${}^O v_{Rd}$. Because the robot is in longitudinal motion, velocities of geometric centres of wheels, that is ${}^O v_{Ai}$, should be equal to ${}^O v_{Rd}$ velocity. In practice, during robot motion wheel slips can occur. The measure of instantaneous longitudinal wheel slip is the longitudinal slip ratio, which can be calculated from the following formula based on [11]:

$$\lambda_i = \begin{cases} 0 & \text{for } v_{oi} = 0, \\ (v_{oi} - {}^R v_{Aix}) / v_{oi} & \text{for other } v_{oi}, \end{cases} \quad (1)$$

where $v_{oi} = \dot{\theta}_i r_i$ and ${}^R v_{Aix}$ are respectively velocity at the wheel circumference and longitudinal component of velocity of wheel geometric centre for i^{th} wheel.

Another measure of the longitudinal slip of wheel, this time for the whole drive system of the robot, can be robot longitudinal slip ratio in the form:

$$\lambda_R = (s_{Rxd} - s_{Rx}) / s_{Rxd}, \quad (2)$$

where: s_{Rx} – actual distance traversed by a robot in longitudinal direction, s_{Rxd} – desired distance equivalent to the distance traversed in case of wheel rolling without slip.

This kind of longitudinal slip measure can be used especially in case of robots moving with small velocities like rover vehicles, which are applied for planetary exploration. This measure can be also used for larger velocities of motion, on condition that only the part of trajectory when the robot is in steady motion will be taken into account.

3.2. Tyre-ground interaction model

Modelling assumptions. As far as conditions of wheel-deformable ground interaction are concerned, in the model the following aspects can be taken into account: the case of not moving tyre, phenomenon of different ground height under and behind the tyre, deformability of tyre, passage of trailing

wheels in the rut created by the leading wheels (multi-pass) and the associated phenomenon of soil compaction, damping in the tyre-ground system, shape of the tyre tread.

In the present work, during determination of the longitudinal slip, based on which the longitudinal wheel force is calculated, the case of not moving wheel is included, which allows determination of forces and moments acting on the robot before motion begins and after it is finished. In the work, the phenomenon of different ground height directly under and just behind the tyre is also taken into account. It is assumed that robot wheels are rigid bodies, which is the assumption usually made by other authors in case of vehicle motion on sand. In the tyre model the multi-pass effect and soil compaction are not included. This phenomenon will take place in case of longitudinal motion and will affect the results obtained from the simulation studies. However, this influence will be negligible if the soil was already compacted (subjected to pressure) before motion and this phenomenon is frequently neglected in models. Tyre-ground interaction damping is included, because otherwise undamped oscillations would occur in the model. In the work the overall tread shape and shape of individual tread blocks is not taken into account. This aspect is taken into account in the advanced tyre-ground models, and it may have significant effect on tyre interaction with deformable ground, therefore it will be the topic of future works of the authors.

Tyre and ground deformation. In Fig. 2 wheel load is schematically illustrated for the case of rigid wheel.

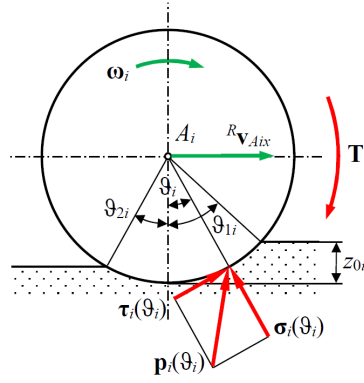


Figure 2. Modelling of load of wheel moving on deformable ground on assumption of the rigid wheel, after [9].

In the figure are shown: driving moment for the wheel T_i , tangential $\tau_i(\vartheta_i)$ and normal $\sigma_i(\vartheta_i)$ stresses and the resultant pressure $p_i(\vartheta_i)$ at a certain point of the wheel-ground contact, that is, for the angle ϑ_i , angular velocity of wheel spin ω_i , longitudinal velocity of geometric centre of wheel R_{Aix} , characteristic angles ϑ_{1i} , ϑ_{2i} and maximum ground deformation z_{0i} .

While the ϑ_{1i} angle and maximum ground deformation z_{0i} can be calculated from geometric relationships, the same is not possible for the ϑ_{2i} angle. In the case when the wheel is stationary one may

assume that the angle ϑ_{2i} is equal to the angle ϑ_{1i} . More difficult is, however, determination of the angle ϑ_{2i} during robot motion, and it has substantial influence on the value of the longitudinal force ${}^R F_{Aix}$.

In the literature sometimes zero value of this angle is assumed, which may lead to undervalued longitudinal force ${}^R F_{Aix}$ as compared to its empirical value. More often models with certain small value of this angle relatively to the angle ϑ_{1i} can be found.

In the present work, the angle ϑ_{2i} is calculated from the relationship:

$$\vartheta_{2i} = k_{\vartheta 2} \vartheta_{1i} \geq \vartheta_{ci}, \quad (3)$$

where the coefficient $k_{\vartheta 2}$ will be chosen as a result of a procedure of fitting the simulation results to empirical results so as to obtain adequate value of the longitudinal force ${}^R F_{Aix}$.

For determination of tangential deformation of the ground in the range $\vartheta_i \in \langle -\vartheta_{2i}, \vartheta_{1i} \rangle$ the following formula will be used [9]:

$$j_i(\vartheta_i) = r_i((\vartheta_{1i} - \vartheta_i) - (1 - \lambda_i)(\sin \vartheta_{1i} - \sin \vartheta_i)), \quad (4)$$

whereas static sinkage will be calculated from the relationship:

$$z_i(\vartheta_i) = \max(z_{0i} - r_i(1 - \cos \vartheta_i), 0). \quad (5)$$

Ground rheological model and stresses. During analysis of robot motion on deformable ground like sand, rheological model of the ground should be taken into account in which important are relations between pressure and sinkage as well as between shear stress and shear displacement.

The pressure-sinkage relation can be described using Bekker formula [1]:

$$p_i(\vartheta_i) = k \left(z_i(\vartheta_i) \right)^n = \left(\frac{k_c}{b_i} + k_\phi \right) \left(z_i(\vartheta_i) \right)^n, \quad (6)$$

where: $p_i(\vartheta_i)$ – pressure, $z_i(\vartheta_i)$ – static sinkage, b_i – width of tyre tread, k_c – cohesive modulus of terrain deformation, k_ϕ – frictional modulus of terrain deformation, n – exponent of terrain deformation.

In the works associated with modelling of tyre-ground interaction usually the implicit assumption is made that normal stresses $\sigma(\vartheta_i)$ acting on tyre at particular points have values close to $p(\vartheta_i)$, that is the following approximation holds true:

$$\sigma_i(\vartheta_i) \approx p_i(\vartheta_i). \quad (7)$$

This assumption is correct in case of small angle $\delta_i(\vartheta_i)$ between directions of the pressure $p_i(\vartheta_i)$ and stress $\sigma_i(\vartheta_i)$ and allows to obtain results of satisfactory accuracy for practical purposes.

Dependency between maximum shear stress $\tau_{imax}(\vartheta_i)$ and normal stress $\sigma_i(\vartheta_i)$ is described by the Coulomb rule in form [1]:

$$\tau_{imax}(\vartheta_i) = c + \sigma_i(\vartheta_i) \tan \phi, \quad (8)$$

where: c – coefficient of cohesion of soil, ϕ – angle of internal friction.

For dry sand, soil cohesion is equal $c = 0$ while for wet clay, $\tan \phi = 0$.

It should be noted that in case when, as a result of tyre-deformable ground interaction, ground shearing is absent but only moving of the tyre surface with respect to the ground takes place, the coefficient of sliding friction μ should be introduced which, depending on velocity of this movement, has different values and it is possible to assume it is contained in the range $\langle \mu_k, \mu_s \rangle$ where μ_k and μ_s are respectively coefficient of kinetic and static friction.

After taking into account what was said above, the maximum shear stress can be determined based on the modified relationship [2]:

$$\tau_{imax}(\vartheta_i) = \min(\mu_s \sigma_i(\vartheta_i), c + \sigma_i(\vartheta_i) \tan \phi), \quad (9)$$

which takes into account both described cases of tyre-ground interaction, and to this relationship coefficient of static friction μ_s is introduced.

Tangential stresses acting on the tyre are determined based on various relationships where normal and tangential stresses in the ground are included.

According to the Janosi-Hanamoto hypothesis [11] tangential stresses are determined based on the relationship:

$$\tau_i(\vartheta_i) = \tau_{imax}(\vartheta_i) \left(1 - \exp\left(\frac{-j_i(\vartheta_i)}{K}\right) \right), \quad (10)$$

where: $j_i(\vartheta_i)$ – soil shear displacement, K – shear deformation parameter.

The present work focuses on investigations of robot longitudinal motion on dry sand. In the further considerations, parameters proposed in the work [4] will be taken into account (Tab. 1).

Table 1. Dry sand characteristic parameters, after [4].

n	k_c	k_ϕ	c	ϕ	K
(–)	(kN/m ⁿ⁺¹)	(kN/m ⁿ⁺²)	(kPa)	(deg)	(m)
1.1	0.90	1 523	1.00	30	0.025

In order to take into account friction phenomenon between tyre and ground, μ_s friction coefficient must be known which for the rubber tyre-dry sand is equal $\mu_s = 0.6$, according to [12].

Forces and moments of force acting on the wheel from the ground. Based on the known tangential and normal stresses acting on the tyre from the ground over the arc described by angle $\vartheta_i \in \langle -\vartheta_{2i}, \vartheta_{1i} \rangle$ and treating the robot wheel as a rigid body, it is possible to calculate resultant forces and moments of force acting on the wheel, that is, respectively static vertical load, motion resistance force, traction force and wheel load torque (sometimes called applied torque) using the following formulas:

$$W_i = b r \int_{-\vartheta_{2i}}^{\vartheta_{1i}} w_i(\vartheta_i) d\vartheta_i = b_i r_i \int_{-\vartheta_{2i}}^{\vartheta_{1i}} (\sigma_i(\vartheta_i) \cos \vartheta_i + \tau_i(\vartheta_i) \sin \vartheta_i) d\vartheta_i, \quad (11)$$

$$R_{ii} = b_i r_i \int_{-\vartheta_{2i}}^{\vartheta_{1i}} r_{ii}(\vartheta_i) d\vartheta_i = b_i r_i \int_{-\vartheta_{2i}}^{\vartheta_{1i}} \sigma_i(\vartheta_i) \sin \vartheta_i d\vartheta_i, \quad (12)$$

$$F_i = b_i r_i \int_{-\vartheta_{2i}}^{\vartheta_{1i}} f_i(\vartheta_i) d\vartheta_i = b_i r_i \int_{-\vartheta_{2i}}^{\vartheta_{1i}} \tau_i(\vartheta_i) \cos \vartheta_i d\vartheta_i, \quad (13)$$

$${}^R M_{Ai\varphi} = M_{\omega i} = -b_i (r_i)^2 \int_{-\vartheta_{2i}}^{\vartheta_{1i}} \tau_i(\vartheta_i) d\vartheta_i. \quad (14)$$

The longitudinal force acting on the tyre in both cases described above is the resultant of the motion resistance and traction force:

$${}^R F_{Tix} = F_i + R_{ii}. \quad (15)$$

In turn, the resultant normal force ${}^R F_{Tiz}$ acting on the tyre should be determined based on the static vertical load after including damping of the tyre-ground system, that is based on the relationship:

$${}^R F_{Tiz} = W_i + c_{ii} \dot{z}_{0i} \operatorname{sgn}(z_{0i}). \quad (16)$$

As mentioned earlier, on the basis of this force and known radial stiffness of the tyre k_r that within certain range can be assumed linear, radial deformation of the tyre Δr_i can be determined from the relationship:

$$\Delta r_i = {}^R F_{Tiz} / k_r. \quad (17)$$

Eventually, forces and moments of force acting on particular wheels and resulting from tyre-ground interaction can be reduced to the wheel geometric centre and written in the following vector form:

$${}^R \mathbf{F}_{Ai} = [{}^R F_{Aix}, 0, {}^R F_{Aiz}]^T = [{}^R F_{Tix}, 0, {}^R F_{Tiz}]^T, \quad {}^R \mathbf{M}_{Ai} = [0, M_{\omega i}, 0]^T. \quad (18)$$

3.3. Multi-body dynamics model

In the present work the dynamics model of the PIAP GRANITE robot will be introduced for the case of longitudinal motion on a horizontal ground.

It is assumed that the robot is under action of the following external forces: ground reaction forces ${}^R\mathbf{F}_{Ti} = [{}^R F_{Tix}, {}^R F_{Tiy}, {}^R F_{Tiz}]^T$ ($i = 1, \dots, 4$) acting on each wheel, gravity force ${}^R\mathbf{G} = m_R {}^R\mathbf{g}$, where m_R denotes total mass of the robot. Above mentioned forces acting on the robot and on the wheel are illustrated in Fig. 3. For particular pairs of wheels the following subscripts are introduced: f – front wheels ($f = 1, 2$), b – back wheels ($b = 3, 4$).

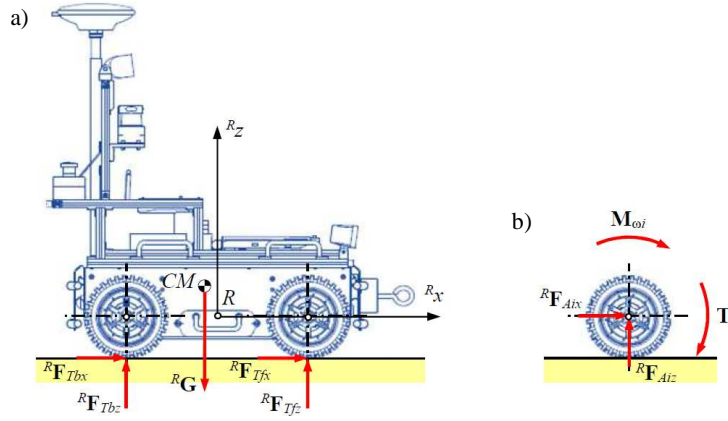


Figure 3. Forces and moments of force in Rxz plane:

a – acting on the PIAP GRANITE robot, b – reduced to the centre of the wheel ($f = 1, 2, b = 3, 4, L = A_f A_b = 2A_f R = 2A_b R$).

Gravity force vector ${}^R\mathbf{G}$ is a function of gravitational acceleration vector ${}^R\mathbf{g} = [{}^R g_x, {}^R g_y, {}^R g_z]^T$ and its application point is at the robot mass centre, whose position is described by the vector ${}^R\mathbf{r}_{CM} = [{}^R x_{CM}, {}^R y_{CM}, {}^R z_{CM}]^T$. Under action of the mentioned forces, according to the Newton's 2nd law, the robot moves with acceleration ${}^R\mathbf{a}_{CM} = [{}^R a_{CMx}, {}^R a_{CMy}, {}^R a_{CMz}]^T$.

Dynamic equations of motion in Oxz plane have the form (Fig. 3):

$$m_R {}^R a_{CMx} = \sum_{i=1}^4 {}^R F_{Aix} + m_R g \sin \Theta = 2 {}^R F_{Afx} + 2 {}^R F_{Abx} + m_R g \sin \Theta, \quad (19)$$

$$m_R {}^R a_{CMz} = \sum_{i=1}^4 {}^R F_{Aiz} - m_R g \cos \Theta = 2 {}^R F_{Afx} + 2 {}^R F_{Abz} - m_R g \cos \Theta, \quad (20)$$

$$\begin{aligned} I_{Ry} \ddot{\Theta} &= -\sum_{i=1}^4 {}^R F_{Aix} {}^R z_{CM} - \sum_{i=1}^4 {}^R F_{Aiz} {}^R x_i = \\ &= -(2 {}^R F_{Afx} + 2 {}^R F_{Abx}) {}^R z_{CM} - 2 {}^R F_{Afx} {}^R x_f - 2 {}^R F_{Abz} {}^R x_b, \end{aligned} \quad (21)$$

where: ${}^R x_f = L/2 - {}^R x_{CM}$, ${}^R x_b = -L/2 - {}^R x_{CM}$, ${}^R x_{CM}$ and ${}^R z_{CM}$ – coordinates of mass centre of the robot in $\{R\}$ coordinate system, I_{Ry} – mass moment of inertia about the axis parallel to ${}^R y$ and passing through the mass centre of the robot, $g = 9.81 \text{ m/s}^2$ – gravity acceleration, Θ – robot body pitch angle (the angle of body rotation about Ry axis).

Moreover, for each of the robot wheels it is then possible to write dynamic equation of motion associated with wheel spin:

$$I_{Wiy} \ddot{\theta}_i = T_i + M_{oi}, \quad (22)$$

where: I_{Wiy} – mass moment of inertia of the wheel about its spin axis, T_i – driving torque, $\epsilon_i = \ddot{\theta}_i$ – angular acceleration of spin of that wheel.

After taking into account the above relationships, it is possible to determine values of linear accelerations in $^R x$ and $^R z$ directions, angular acceleration about $^R y$ axis and angular accelerations of wheel spin for driving torques T_i acting on the driven wheels (forward dynamics problem) based on the following equations:

$$^R a_{CMx} = \sum_{i=1}^4 {}^R F_{Aix} / m_R + g \sin \Theta, \quad ^R a_{CMz} = \sum_{i=1}^4 {}^R F_{Aiz} / m_R - g \cos \Theta, \quad (23)$$

$$\ddot{\Theta} = (-\sum_{i=1}^4 {}^R F_{Aix} {}^R z_{CM} - \sum_{i=1}^4 {}^R F_{Aiz} {}^R x_i) / I_{Ry}, \quad \ddot{\theta}_i = (T_i + M_{oi}) / I_{Wiy}. \quad (24)$$

3.4. Drive units model and controller

The described simplified model of robot dynamics can be also enhanced with the model of its drive units. It is assumed that: each of the robot drive units consists of identical DC motor, encoder, and transmission system, robot drive units are not self-locking, mass moments of inertia of the rotating elements of DC motor, encoder and gear unit are small in comparison to mass moments of inertia of the driven parts of the robot (wheels), that is why they are neglected.

The DC motor model of the i^{th} drive unit is described by relationships:

$$\frac{di_i}{dt} = (u_i - k_e n_d \dot{\theta}_i - R_d i_i) / L_d, \quad T_i = \eta_d n_d k_m i_i, \quad (25)$$

where: u_i – motor voltage input, i_i – rotor current, L_d , R_d – respectively inductance and resistance of the rotor, k_e – electromotive force constant, k_m – motor torque coefficient, n_d – gear ratio of the transmission system, η_d – efficiency factor of the transmission system.

In the present work, robot motion control is conducted by means of a simple linear drive controller. Based on the desired and actual angles and angular velocities of wheel spin, that is, respectively vectors: $\theta_d = [\theta_{1d}, \theta_{2d}, \theta_{3d}, \theta_{4d}]^T$ and $\omega_d = [\omega_{1d}, \omega_{2d}, \omega_{3d}, \omega_{4d}]^T$ as well as $\theta = [\theta_1, \theta_2, \theta_3, \theta_4]^T$ and $\omega = [\omega_1, \omega_2, \omega_3, \omega_4]^T$, controller determines the control vector $\mathbf{u} = [u_1, u_2, u_3, u_4]^T$ for drives of particular wheels.

After assuming that errors of angles and angular velocities of spin for driven wheels are defined as:

$$\mathbf{e}_\theta = \theta_d - \theta, \quad \mathbf{e}_\omega = \omega_d - \omega, \quad (26)$$

the control signal $\mathbf{u} = [u_1, u_2, u_3, u_4]^T$ for motors of driven wheels in (V) can be determined using the control law:

$$\mathbf{u} = \text{sat}(k_p \mathbf{e}_\theta + k_D \mathbf{e}_\omega, \mathbf{u}_{\min}, \mathbf{u}_{\max}), \quad (27)$$

where $\text{sat}()$ – saturation function, k_p, k_D – controller parameters, and $\mathbf{e}_\theta = [e_{\theta 1}, e_{\theta 2}, e_{\theta 3}, e_{\theta 4}]^T$, $\mathbf{e}_\omega = [e_{\omega 1}, e_{\omega 2}, e_{\omega 3}, e_{\omega 4}]^T$, $\mathbf{u}_{\max} = [u_{\max}, u_{\max}, u_{\max}, u_{\max}]^T$, $\mathbf{u}_{\min} = [0, 0, 0, 0]^T$.

4. Simulation Research

Robot motion simulation studies were conducted in the Matlab/Simulink environment. For simulations the Runge-Kutta fixed-step solver was chosen with Δt step size. Convergence of solutions with changes of Δt was investigated, which allowed choice of Δt value as a compromise between results accuracy and computation time.

In the work robot longitudinal motion is analysed, that is, motion in which robot body is by assumption in translational motion, and its wheels are in plane motion. It is assumed that robot motion consists of three phases: accelerating with maximum acceleration a_{Rmax} over the distance l_r , steady motion with constant velocity $v_{Rd} = v_{Ru}$, braking with maximum acceleration (deceleration) a_{Rmax} over the distance l_h . Robot motion is studied for different maximum values of desired linear velocity v_{Ru} , acceleration a_{Rmax} and total distance length L_p . Considered variants of robot motion are summarized in Tab. 2.

Table 2. Parameters of considered cases of robot motion

v_{Ru} (m/s)	0.2	0.3	0.5	0.7	1.0
a_{Rmax} (m/s ²)	0.6	1.2	1.2	2.4	2.4
L_p (m)	1.0	2.0	2.5	3.0	4.0

For the simulation studies the following values of the basic design parameters of the PIAP GRANITE robot are assumed:

- dimensions: $L = 0.425$ m, $W = 0.59$ m (where: $L = A_1A_3 = A_2A_4$, $W = A_1A_2 = A_3A_4$, see Fig. 1b), $r_i = r = 0.0965$ m, $b_i = b = 2 \cdot 0.064$ m,
- masses of the components: $m_0 = 36.54$ kg, $m_i = 1.64$ kg, $m_5 = m_6 = 0.18$ kg,
- robot mass centre coordinates: ${}^R x_{CM} = -0.012$ m, ${}^R y_{CM} \approx 0$ m, ${}^R z_{CM} = 0.06$ m,
- mass moments of inertia: $I_{Wy} = 0.016$ kg m², $I_{Ry} = 0.51$ kg m²,
- tyre parameters: $k_{ri} = k_r = 40\,000$ N/m, $c_{ti} = c_t = 1000$ Ns/m,
- parameters of drive units: $L_d = 0.0823$ mH, $R_d = 0.317$ Ω , $k_e = 0.0301$ Vs/rad, $k_m = 0.0302$ Nm/A, $n_d = 53$, $\eta_d = 0.8$, $u_{max} = 32$ V.

Moreover, tyre-ground contact parameters from Tab. 1 are assumed. The k_{32} angle was chosen empirically as a function of the desired velocity of robot motion so as to obtain agreement of results of

simulation-based and empirical investigations. The acceleration of gravity is assumed $g = 9.81 \text{ m/s}^2$. In simulations the following gains of the drive controller $k_P = 30 \text{ V/rad}$, $k_D = 10 \text{ Vs/rad}$ and fixed-step size $\Delta t = 0.05 \text{ ms}$ are assumed.

5. Experimental investigations

Experimental investigations were conducted in a container with sand dedicated for the research (Fig. 4a). Initially the sand was compacted by compression. During empirical research, similarly as during simulation studies, motion of robot equipped with dual tyres was analyzed (Fig. 4b).

The investigations were conducted for analogous cases of motion as during simulation studies (Tab. 2). For each variant, three repetitions (trials) were performed. Before each trial, the ground was carefully prepared according to procedure which included raking and levelling. During experiment robot motion was recorded using inertial measurement units, according to methodology described in [10].

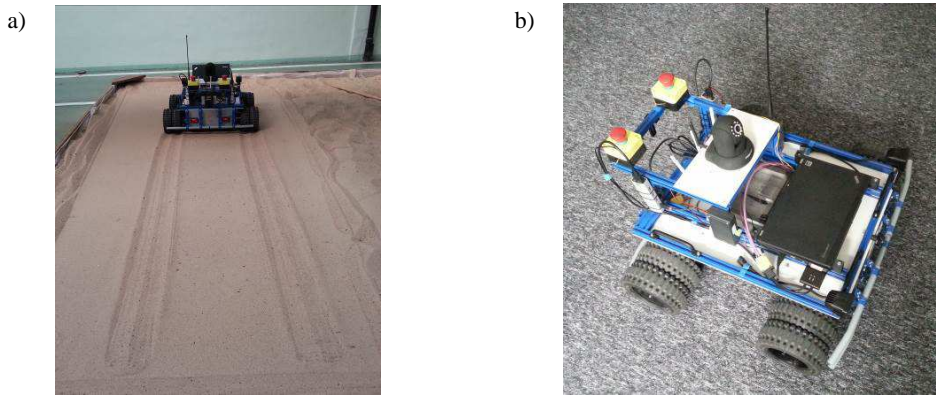


Figure 4. Empirical investigations of robot motion: a – sand container used during experiments, b – the robot in the configuration used during experiments (dual tyres, without GNSS antenna).

6. Simulation vs. experimental research

As a result of simulation and empirical research, the values of longitudinal slip ratio of the robot in analyzed variants of motion shown in Tab. 3 were obtained. In this table also values of the k_{92} coefficient for wheels (Fig. 2) used during simulations are presented – for those values of coefficients the best agreement with results of empirical research was achieved.

Relationship between longitudinal slip ratio and desired linear velocity of the robot obtained as a result of simulation and experimental investigations is illustrated in Fig. 5.

Table 3. Simulation vs. empirical research results – obtained values of longitudinal slip ratio of the robot in analyzed variants of motion.

	v_{Ru} (m/s)	0.2	0.3	0.5	0.7	1.0
Simulation research	λ_R (%)	5.00	8.16	16.6	21.1	26.4
	k_{92} (-)	0.35	0.27	0.13	0.06	0.00
Empirical research	λ_R (%)	5.31	8.35	16.5	22.9	39.8

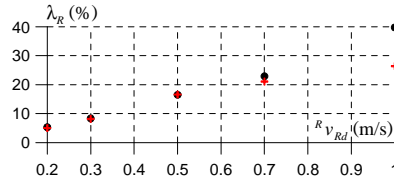


Figure 5. Relationship between longitudinal slip ratio and desired linear velocity of the robot obtained as a result of simulation (●) and empirical investigations (+).

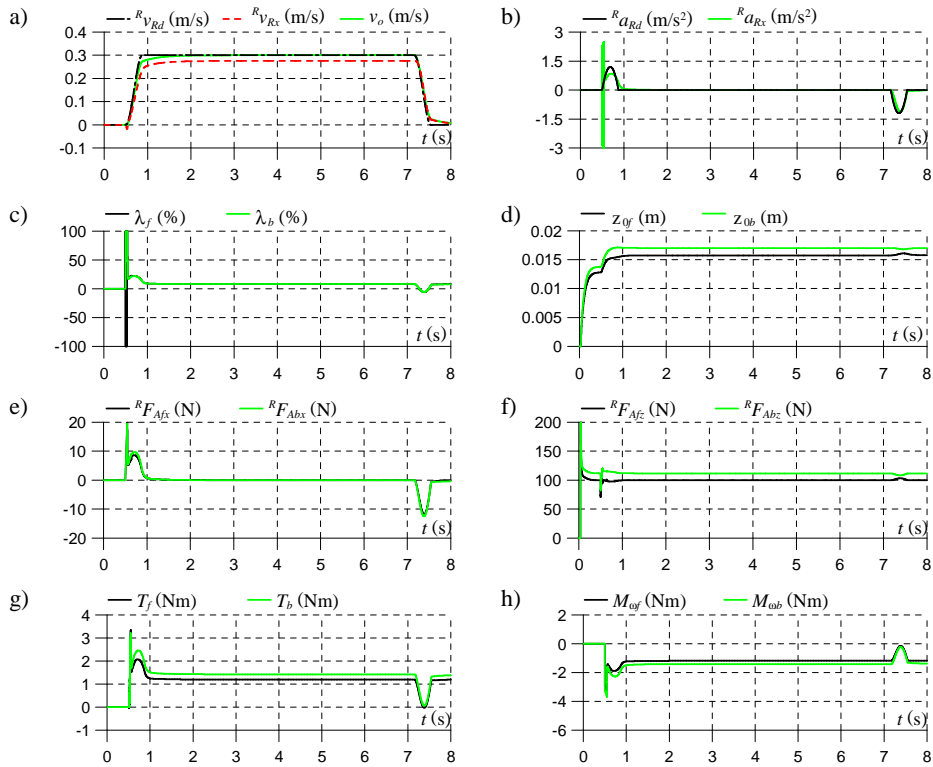


Figure 6. Time histories obtained in simulation research for the case $v_{Ru} = 0.3$ m/s:

- a – desired and actual velocities of the robot as well as circumferential velocity of wheels,
- b – desired and actual accelerations of the robot, c – longitudinal slip ratios for the wheels,
- d – wheels sinkage, e-f – longitudinal and normal components of the ground reaction forces,
- g-h – driving and load torques.

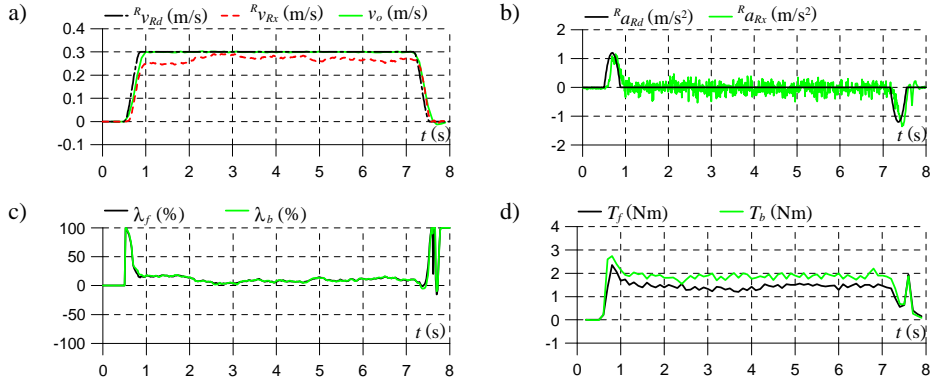


Figure 7. Time histories obtained in experimental research for the case $v_{Ru} = 0.3$ m/s:

- a – desired and actual velocities of the robot as well as circumferential velocity of wheels,
b – desired and actual accelerations of the robot, c – longitudinal slip ratios for the wheels,
d – driving torques calculated on the basis of measured current consumed by the motors.

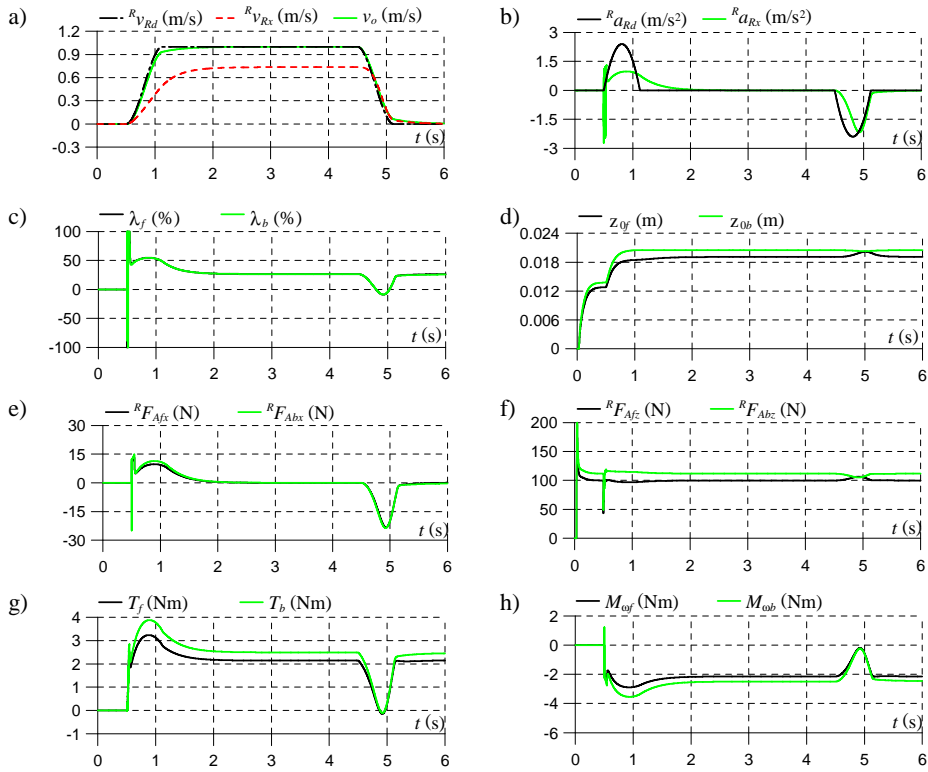


Figure 8. Time histories obtained in simulation research for the case $v_{Ru} = 1$ m/s:

- a – desired and actual velocities of the robot as well as circumferential velocity of wheels,
b – desired and actual accelerations of the robot, c – longitudinal slip ratios for the wheels,
d – wheels sinkage, e-f – longitudinal and normal components of the ground reaction forces,
g-h – driving and load torques.

In the obtained graph very good agreement of simulation and empirical results for the desired linear velocity $^R v_{Rd}$ from range 0.2 – 0.7 m/s is visible. Larger discrepancy is evident for the velocity of 1 m/s.

In Figs. 6-7 time histories of selected quantities describing robot motion with 0.3 m/s velocity obtained respectively from simulation and empirical research are presented.

From comparison of the obtained results, in general their quite good agreement can be noticed. As a result of empirical research larger instantaneous values of longitudinal slip ratio of wheels (Figs. 6c and 7c) were obtained.

In the final phase of motion in the simulation studies occurs slower braking of the robot than in empirical research, and as a result also differences in the time plots of driving torques can be noticed (Figs. 6g and 7d). Driving torques in case of empirical investigations were calculated on the basis of measured current consumed by the motors.

In the empirical investigations also minor differences in rotation of left- and right-hand side wheels were noticed which results in small differences of time histories of driving torques. In Fig. 7 results for left-hand side wheels only are shown.

In two following figures (Figs. 8-9) are presented analogous time histories as previously, but this time for the 1 m/s robot longitudinal velocity.

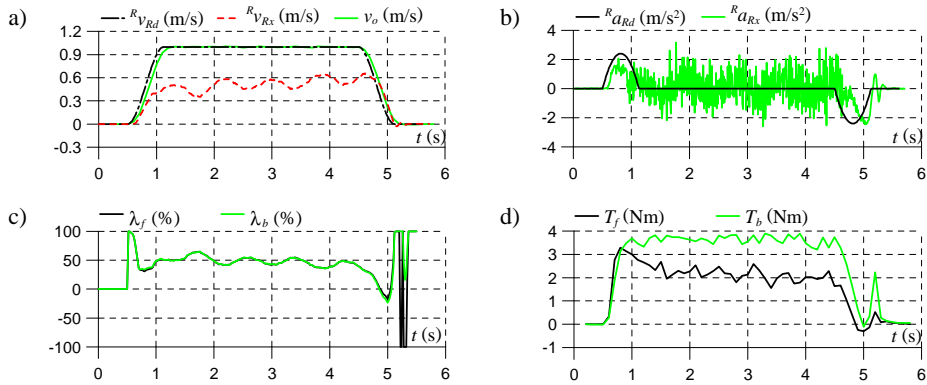


Figure 9. Time histories obtained in experimental research for the case $v_{Ru} = 1$ m/s:

- a – desired and actual velocities of the robot as well as circumferential velocity of wheels,
- b – desired and actual accelerations of the robot, c – longitudinal slip ratios for the wheels,
- d – driving torques calculated on the basis of measured current consumed by the motors.

By comparing the results, one may notice longitudinal velocity oscillations of relatively low frequency occurring for empirical data and not present in the simulation studies (Figs. 8a and 9a). This phenomenon may be associated with operation of the wheel drive unit controller and will be subject to further analyses. Additionally, similarly as previously the differences in wheel slip parameters

during initial and final phase of motion (Figs. 8c and 9c) and in drive torques during final phase of motion (Figs. 8g and 9d) take place.

In general, results agreement is quite good, but worse than in case of 0.3 m/s velocity, because in the simulation studies the wheel slips are slightly too small.

7. Summary and Future Works

In the present work, results of simulation and empirical research for the robot longitudinal motion are presented. The research was conducted for various desired longitudinal velocities of motion.

The most significant conclusions from the research include the following:

- For the given velocities of robot motion in the range 0.2-0.7 m/s good agreement of simulation and empirical results was achieved. For the 1 m/s velocity the presented model seems less adequate, which is evidenced by too small instantaneous values of longitudinal slip ratio for wheels.
- It was noticed that the obtained simulation results are significantly affected by the value of ϑ_2 angle which was calculated based on the ϑ_1 angle by multiplication through assumed k_{ϑ_2} coefficient. In order to obtain better agreement of simulation and empirical results, the k_{ϑ_2} coefficient should change with the velocity of robot motion, specifically it should decrease with this velocity.

Directions of future works will include:

- Simulation studies of robot motion based on the model where deformation of robot tyres, tread shape and multi-pass effect will be taken into account.
- Detailed analysis concerning the ϑ_2 angle, especially influence of robot velocity and longitudinal slip on this angle.
- Simulation and empirical research for some other robot manoeuvres including pivot turn or turning with different turn radii.
- Simulation and empirical research for some other deformable grounds like sandy clay.

Acknowledgements

The work has been realized as a part of the project entitled "Dynamics modelling of four-wheeled mobile robot and tracking control of its motion with limitation of wheels slip". The project is financed from the means of National Science Centre of Poland granted on the basis of decision number DEC-2011/03/B/ST7/02532.

References

- [1] Bekker, M.G. *Off-the-road locomotion. Research and development in terramechanics*. The University of Michigan Press, 1960.
- [2] Harnish, C., Lach, B., Jakobs, R., Troulis, M. and Nehls, O. A new tyre–soil interaction model for vehicle simulation on deformable ground. *Vehicle System Dynamics* 43, supp1. (2005), 384–394.
- [3] Heverly, M., Matthews, J., Lin, J., Fuller, D., Maimone, M., Biesiadecki, J., Leichty, J. Traverse performance characterization for the mars science laboratory rover. *Journal of Field Robotics* 30 (2013), 835–846.
- [4] Iagnemma, K., Dubowsky, S. *Mobile Robots in Rough Terrain. Estimation, Motion Planning, and Control with Application to Planetary Rovers*. Springer-Verlag, Berlin Heidelberg, 2004.
- [5] Jaroszek, P., Trojnecki, M. Localization of the wheeled mobile robot based on multi-sensor data fusion. *Journal of Automation, Mobile Robotics & Intelligent Systems* Vol. 9, No. 3 (2015), 73–84.
- [6] Kobayashi, T., Fujiwara, Y., Yamakawa, J., Yasufuku, N., Omine, K. Mobility performance of a rigid wheel in low gravity environments. *Journal of Terramechanics* 47, (2010), 261–274.
- [7] Pacejka, H.B. *Tire and Vehicle Dynamics*. Elsevier, 2012.
- [8] Perski, A., Wieceński, A., Bożek, K., Kapelko, S., Pawłowski, S. GNSS receivers in engineering practice. Introduction to Global Navigation Satellite Systems. *Pomiary, Automatyka, Robotyka*, Vol. 17, No. 3, (2013), 103–111 (in Polish: “Odbiorniki GNSS w praktyce inżynierskiej. Wprowadzenie do systemów GNSS”).
- [9] Taheri S., Sandu C., Taheri S., Pinto E., Gorsich D, A Technical Survey on Terramechanics Models for Tire-Terrain Interaction Used in Modeling and Simulation of Wheeled Vehicles. *Journal of Terramechanics* 57, (2015), 1–22.
- [10] Trojnecki M., Dąbek P. Determination of Motion Parameters with Inertial Measurement Units. Part 2: Algorithm Verification with a Four-Wheeled Mobile Robot and Low-Cost MEMS Sensors, in: *Mechatronics: Ideas for Industrial Applications*, Springer International Publishing, (2015), 253–267.
- [11] Wong J.Y. *Theory of Ground Vehicles*. Wiley-Interscience, 2001.
- [12] *Tire friction and rolling resistance coefficients*, <http://hpwizard.com/tire-friction-coefficient.html>.

Maciej Trojnecki, Associate Professor: Industrial Research Institute for Automation and Measurements PIAP, Al. Jerozolimskie 202, 02-486 Warsaw, Poland (mtrojnecki@piap.pl). The author gave a presentation of this paper during one of the conference sessions.

Przemysław Dąbek, M.Sc.: Industrial Research Institute for Automation and Measurements PIAP, Al. Jerozolimskie 202, 02-486 Warsaw, Poland (pdabek@piap.pl).

**Dynamics of rigid bodies with multiple frictional contacts:
new faces of Painlevé's paradox
(NON134-15)**

Péter L. Várkonyi

Abstract: the dynamics of finite degree-of-freedom, planar mechanical systems with multiple sliding, unilateral frictional point contacts is investigated. A complete classification of systems with 2 contacts is given. The contact-mode based approach of rigid body mechanics is combined with linear stability analysis using a compliant contact model to find the set of consistent contact modes and their stability in each class. Three new phenomena related to Painlevé's classical non-existence and non-uniqueness 'paradoxes' are described: (i) the stability of an individual contact mode may be unpredictable within the framework of rigid-body theory; (ii) multi-contact systems may undergo spontaneous contact mode transitions; and (iii) having a unique consistent contact mode does not imply the stability of this mode, consequently dynamic phenomena commonly associated with Painlevé's paradoxes also occur in 'non-Painlevé' systems. Preliminary results of an extended analysis focusing on other types of contact dynamics (impact without collision, inverse clattering, sprag-slip oscillations) are briefly discussed.

1. Introduction

Impacts and friction between solids were among the first topics extensively studied in the history of modern physics. Impact laws were already proposed by Isaac Newton whereas the first known laws of dry friction were set up long before Newton's time by Leonardo da Vinci. Nevertheless modelling systems with impacts and friction still poses a challenge because the inherent unreliability of simple impact and friction laws [2], [18], [20]; and the complexity of the dynamics induced by them [20], [22]. The present work addresses Painlevé's paradox, an important source of complexity.

1.1. Painlevé's paradoxes

The piecewise-smooth nature of dry friction suggests that a unilateral, frictional, rigid point contact is in one of 3 possible modes: sliding, sticking or separation (except for those instants when a rigid element hits another). To identify the instantaneous acceleration of a system in the presence of contacts, all combinations of modes for all contacts (briefly: all contact modes of the system) are routinely tested for consistency [11] [21]. A fundamental shortcoming of the contact mode-based approach was already discovered in the late 19th century [9], [16]: the number of consistent solutions may be zero, as well as greater than 1. These observations became known as Painlevé's non-uniqueness and non-existence paradox. For systems with a single contact, all possible types of

indeterminacy and inconsistency have been identified and listed. At the same time the systematic analysis of multiple-contact systems has not been performed yet.

1.2. Contact regularization, and the resolution of non-existence

In addition to identifying all forms of Painlevé’s paradox, much effort has been devoted to the understanding of their physical origin and to their resolution. The paradoxes are consequences of the assumption of rigidity, and thus a common approach of the analysis is contact regularization, i.e. the modelling of contact compliance [1], [8], [10]. The application of this approach to general systems with a single contact [13] as well as to several specific examples (Painlevé’s rod [1], [3], [23], [24]; Painlevé-Klein example [1], [4], [8]; and others [12] [15] [16]) uncovered that the non-existence paradox is resolvable by allowing the possibility of “impact without collision” (IWC), i.e. an impulsive contact force with vanishing pre-impact normal contact velocity. The IWC was also found to be a possible scenario in some cases of the non-uniqueness paradox, but never possible in states free from Painlevé’s paradoxes. Accordingly, it is often assumed that Painlevé’s paradoxes capture those dynamic states where unusual contact dynamics is to be expected.

1.3. Stability analysis and partial resolution of non-uniqueness

The dynamic stability of consistent contact modes can be analysed using contact regularization. The stability analysis of single contact reveals that consistent contact modes may be dynamically unstable [13]. Nevertheless, the stability analysis does not resolve the non-uniqueness paradox due to the possibility of IWCs and multiple stable contact modes. For single-contact systems, the stability properties of each contact mode have been found to be independent of the characteristics of the underlying compliant contact model. Hence, the question of stability is decidable within rigid body theory. The analysis also offers a partial resolution of the non-uniqueness paradox by demonstrating that single-contact systems never undergo spontaneous contact mode transitions: a systems never changes from contact mode M1 to M2 as long as M1 remains consistent. The only remaining ‘paradoxical’ situation is the ambiguity of ‘triggered’ transitions induced by M1 losing its consistency.

1.4. Questions addressed by the current work

As we have seen, most of our knowledge about Painlevé’s paradox comes from the analysis of single-contact planar systems. Many of these properties are believed to be true for more complex systems. The present paper reports on some of the author’s ongoing work of extending the results to general multi-contact systems.

After introducing notations in Sec. 2, a classification of planar systems with two frictional, unilateral, sliding contacts is presented. The classification is based on geometric, and inertial

properties, values of the friction coefficient, and properties of the external loads as inputs. A complete list of consistent contact modes is given for each class in Sec 3. The new classification is the refinement of a coarser scheme by Ivanov [8], who investigated the following question: “which systems are guaranteed to have a unique consistent contact mode regardless of the external forces?” Sec. 4 is devoted to the stability analysis of contact modes, and the paper is closed by a Conclusions section. The analysis allows us to answer the following questions: (i) is the stability of contact modes decidable within rigid body theory? (ii) are spontaneous contact mode transitions impossible in general?; and (iii) is Painlevé’s paradox a necessary criterion of non-stationary, fast contact dynamics (such as impact without collision)?

2. Basic notations

We consider a finite degree-of-freedom mechanical system with two unilateral, sliding point contacts and nonzero initial sliding velocity. Coulomb friction with constant coefficients of friction μ_j is assumed at the two contacts. For simplicity, it is assumed that all internal or external constraint forces of the system other than the contact forces at the two sliding contacts can be expressed explicitly and thus the corresponding constraints can be removed from the equations of motion.

Let \mathbf{q} denote the vector of generalized coordinates of the system and the 2-vector $\mathbf{d}=[d_1 d_2]^T$ contain the gaps between the object and the two contact surfaces. From the Euler-Lagrange equations, one obtains a system of 2 equations of the form:

$$\ddot{\mathbf{d}} = \mathbf{B}(\mathbf{q})\mathbf{f} - \mathbf{a}(\mathbf{q}, \dot{\mathbf{q}}) \quad (1)$$

where dot means derivation with respect to time; $\mathbf{f}=[f_1 f_2]^T$ is a vector of Lagrange multipliers where f_i is the magnitude of the (unknown) normal contact force at the sliding contact i ($i=1$ or 2). The tangential component of the same contact force is $\mu_i f_i$. Vector $\mathbf{a}=[a_1 a_2]^T$ contains minus 1 times the (known) second time derivative of the gap \mathbf{d} in the absence of contact forces. $\mathbf{B}=[b_{ij}]$ is a (known) „local, normal mobility matrix” of size 2 by 2, defined as follows: b_{ij} is the second time derivative of the gap d_i in response to a sliding contact force with normal component 1 and tangential component μ_j at contact j . \mathbf{B} is usually asymmetric due to friction.

We also introduce the following related notations: α for the angle between the vectors \mathbf{a} and $[1 \ 0]^T$ such that $0 \leq \alpha \leq 2\pi$; \mathbf{b}_j for the j^{th} column of \mathbf{B} . \mathbf{b}_j represents the response of both contacts to the contact force at contact j ; β_j for the angle between the vectors \mathbf{b}_j and $[1 \ 0]^T$; and β_j^* for the angle between the vectors $-\mathbf{b}_j$ and $[1 \ 0]^T$;

The primary goal of the contact mode-based approach is to determine stationary values of \mathbf{f} and $\ddot{\mathbf{d}}$, i.e. the contact forces and the instantaneous acceleration of the system.

3. Consistency of contact modes

A closed unilateral contact with zero normal velocity ($\dot{d}_i = \dot{d}_i = 0$) and nonzero tangential sliding velocity in a given direction may remain in sliding mode (S mode) with

$$\ddot{d}_i = 0 \quad (2)$$

$$f_i \geq 0 \quad (3)$$

or it may start free flight (F mode) corresponding to

$$\ddot{d}_i \geq 0 \quad (4)$$

$$f_i = 0 \quad (5)$$

Stick and slip in opposite direction are ruled out by the nonzero initial tangential velocity.

In a system with two contacts, these scenarios determine 4 possible contact modes. To determine the consistency of each contact mode, we combine the equations of motion (1) with the relevant equality constraint (2) or (5) to determine the corresponding value of f_i (sliding) or \ddot{d}_i (free flight). A contact mode is called consistent if the relevant inequality constraint (3) or (4) is satisfied. The consistency of each contact mode depends on the elements of \mathbf{B} and \mathbf{a} ; conditions are summarized in Table 1 (with derivation in Appendix A).

Table 1. consistency conditions of contact modes

name	description	consistency conditions
FF	free flight at both legs	$a_1 < 0$ & $a_2 < 0$
SF	sliding on leg 1, free flight at leg 2	$b_{11}a_1 > 0$ (positive contact force at leg 1) & $b_{21}/b_{11} \cdot a_1 > a_2$ (other leg lifts up)
FS	sliding on leg 2, separation at leg 1	$b_{22}a_2 > 0$ (positive contact force at leg 2) & $b_{12}/b_{22} \cdot a_2 > a_1$ (other leg lifts up)
SS	sliding on both legs	\mathbf{a} is in the cone spanned by vectors \mathbf{b}_1 and \mathbf{b}_2

Using the consistency conditions summarized in Table 1, the consistency of each contact mode can be determined using only the following information:

- the index of the quadrant of \mathcal{R}^2 (real plane) containing \mathbf{b}_1 , or equivalently, the index of β_1 in the ascending ordering of the set $\{\beta_1, \pi/2, \pi, 3\pi/2\}$.
- The index of β_2 in the ascending ordering of the set $\{\beta_1, \beta_1^*, \beta_2, \pi/2, \pi, 3\pi/2\}$
- the index of α in the ascending ordering of the set $\{\alpha, \beta_1, \beta_2, \pi/2, \pi, 3\pi/2\}$

This observation enables us to classify systems by a three digit code ijk where $i \in \{1,2,\dots,4\}$; $j,k \in \{1,2,\dots,6\}$. The first two digits will be used to define a coarse classification (from now: classes), previously described by Ivanov [9]. The last digit will be used as refinement (subclasses). Table 2 presents consistent contact modes for each subclass based on the previously determined conditions (Table 1).

Table 2. classification of systems based on the directions of vectors \mathbf{b}_1 , \mathbf{b}_2 and \mathbf{a} . Column 1 lists classes based on the first two digits of the three-digit labels. A second code in parenthesis indicates the dual of the class obtained by switching the indices of the two contacts. The word ‘same’ indicates a self-dual class. The second columns illustrates the corresponding directions of \mathbf{b}_j (solid arrows), and the directions of the vector \mathbf{a} for every subclass (enumerated dashed arrows). Columns 3-6 contain lists of subclasses associated with each contact mode. A subclass is in the list if the contact mode is consistent. The stability of the contact mode is marked by dark (unstable) hatched (model-dependent) and white (stable) background colors.

classes		contact modes				classes		contact modes			
code	sketch	FF	SS	SF	FS	code	sketch	FF	SS	SF	FS
11 (same)		5	2	1 2 6	2 3 4	24 (36)		4 5	3 4	3 4 5	4
12 (same)		5	2	1 6	3 4	25 (same)		4	3 4 5	3 4	4 5
13 (41)		5	2 3	1 6	4	26 (same)		4	1 2 6	3 4	4 5
14 (31)		4 5	2 3 4	1 6	4	33 (44)		4 5	3 4	5	3
15 (32)		4 5	1 5 6	1 6	4	34 (same)		3 4 5	4	5	3
16 (21)		4	1 6	1 5 6	4 5	35 (same)		3 4 5	4	4 5	3 4
22 (45)		5	3	4 5	3 4	42 (same)		4	1 2 6	5	3
23 (46)		5	3	3 4 5	4	43 (same)		4	3 4 5	5	3

The classification scheme outlined in the paper is not redundant, because there are real mechanical systems in all classes and subclasses. For example, a single planar rigid body with two contacts, and its own weight as external load can belong to any of the subclasses if the positions and directions of contacts as well as the friction coefficients are chosen appropriately.

Inspection of Table 2 reveals many examples of Painlevé's paradoxes. For example, in class 112, three contact modes are consistent, whereas in class 152, none of the contact modes is consistent. These examples of non-uniqueness and non-existence are analogous to previously described examples with a single contact point.

In what follows, a more detailed characterization of contact modes is obtained. A compliant contact model allows the application of linear stability analysis, and uncovers novel phenomena.

4. Contact regularization

In this section we introduce a compliant contact model (Sec. 4.1), and investigate the dynamic stability of the contact modes (Sec. 4.2).

4.1. Contact model

A unilateral, Kelvin-Voigt type, linear, viscoelastic contact model is used with adjustable stiffness. It is assumed that the mechanical system under investigation behaves as a collection of rigid bodies, which are allowed to overlap in small contact areas with each other and with rigid contact surfaces. The signed gap between a pair of objects is denoted by d_i (negative if they overlap). A contact stiffness scaling factor ε is introduced such that $\varepsilon \rightarrow 0$ corresponds to a rigid contact. The normal contact force is a piecewise linear function of the rescaled contact gap $\bar{d}_i = \varepsilon d_i$ and its derivative \bar{d}_i' with respect to rescaled time $\bar{t} = \varepsilon^{-1/2} t$:

$$f_i = \begin{cases} 0 & \text{if } \bar{d}_i > 0 \\ \max \left\{ \begin{matrix} 0 \\ -k_i \bar{d}_i - q_i \bar{d}_i' \end{matrix} \right\} & \text{if } \bar{d}_i \leq 0 \end{cases} \quad (6)$$

The tangential contact force follows Coulomb friction law for sliding. Tangential compliance is not included in the model. The positive scalars k_i and q_i represent rescaled stiffness and damping coefficients of contact i .

The usage of the rescaled variables \bar{d}_i and \bar{d}_i' is motivated by the fact that contacts with $O(\varepsilon^{-1})$ stiffness suffer $O(\varepsilon)$ contact deformations under finite forces, and their contact dynamics has an $O(\varepsilon^{1/2})$ characteristic time-scale. The small deformations and the fast characteristic time scale allow a simplified analysis of contact dynamics, in which the parameters a_i and b_{ij} of (1) can be treated as constants.

4.2. Stability of contact modes

The equation of motion (1) and the compliant contact model (6) together determine the fast dynamics of the contact gaps (\mathbf{d}) and forces (\mathbf{f}). Each contact mode corresponds to a stationary value of \mathbf{f} . The consistency of a contact mode (investigated in Sec. 3) means that this stationary point exists and satisfies the inequality constraint (3) or (4). Nevertheless stationary points of a dynamical system may be dynamically unstable (i.e. repulsive), which means that a system will practically never stay at such a point. Identifying unstable modes offers a partial resolution of the non-uniqueness paradox.

A contact in free-flight (F) state is special in the sense that the vanishing contact force $f_i=0$ is not sensitive to small perturbations of the system. Thus, on the one hand, the FF mode is always stable (provided that it is consistent). On the other hand, in SF mode, the dynamics of contact 1 can be analysed in itself. Equations (2) and (6) determine a second-order ODE for the time-evolution of d_1 , which is rewritten as a system of 2 linear, 1st order ODEs:

$$\mathbf{g}' = \begin{bmatrix} 0 & 1 \\ -b_{11}k_1 & -b_{11}q_1 \end{bmatrix} \mathbf{g} - \begin{bmatrix} 0 \\ a_1 \end{bmatrix} \quad \text{where} \quad \mathbf{g} = \begin{bmatrix} \bar{d}_1 \\ \bar{d}_1' \end{bmatrix} \quad (7)$$

As we show in Appendix B, if b_{11} is negative, then the coefficient matrix in (7) has two real eigenvalues, one positive and one negative. The stationary point of the system is a saddle, i.e. the SF mode is unstable. In the opposite case, the matrix has only negative (real or complex) eigenvalues. Hence the stationary point representing the FS mode is a stable node or a stable focus. Analogously, the FS mode is stable if and only if b_{22} is positive.

For the SS mode, a similar system of ODEs describes the simultaneous dynamics of d_1 and d_2 :

$$\mathbf{g}' = \begin{bmatrix} 0 & 0 & 1 & 0 \\ 0 & 0 & 0 & 1 \\ -\mathbf{BK} & -\mathbf{BQ} \end{bmatrix} \mathbf{g} + \begin{bmatrix} 0 \\ 0 \\ \mathbf{a} \end{bmatrix} \quad (8)$$

where

$$\mathbf{g} = \begin{bmatrix} \bar{d}_1 \\ \bar{d}_2 \\ \bar{d}_1' \\ \bar{d}_2' \end{bmatrix} \quad \mathbf{K} = \begin{bmatrix} k_1 & 0 \\ 0 & k_2 \end{bmatrix} \quad \mathbf{Q} = \begin{bmatrix} q_1 & 0 \\ 0 & q_2 \end{bmatrix}.$$

The stability analysis of this type of system has attracted considerable attention as a minimal model of break squeal [5] [6] [7]. It was found that the stationary point of the dynamics may be destabilized by friction-induced ‘mode coupling’. Our analysis of contact mode stability follows these earlier works.

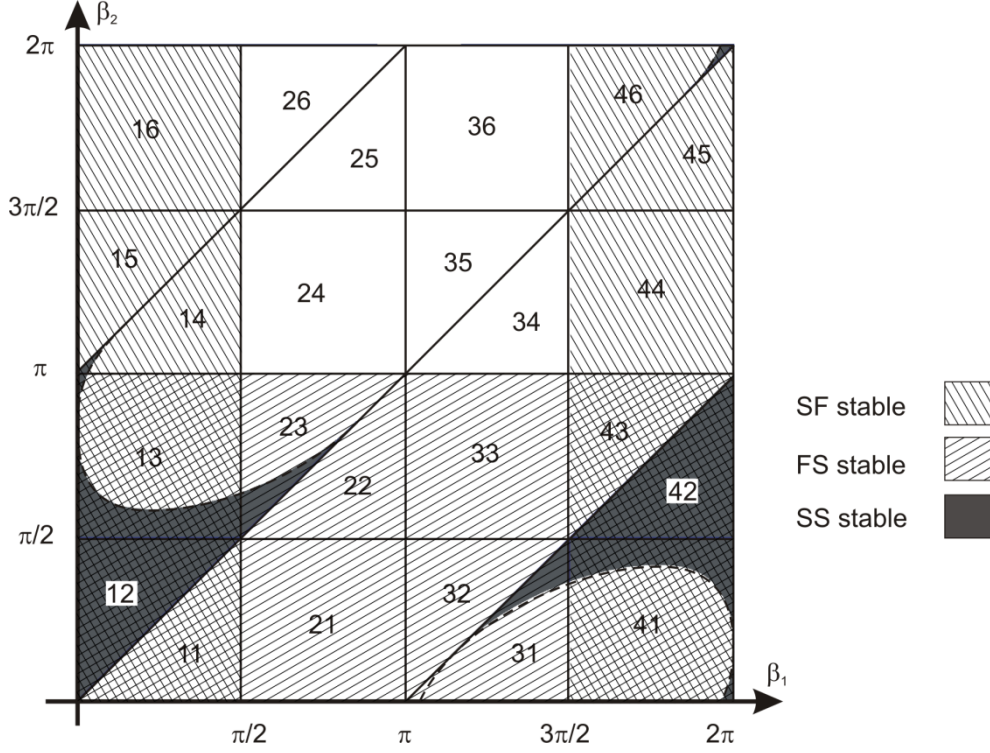


Figure 1. Stability regions of the contact modes (SF, FS, SS) in the β_1 - β_2 plane. The FF mode is always stable (not shown in the figure). The curved boundaries are influenced by $q_1, q_2, k_1, k_2, |\mathbf{b}_1|$ and $|\mathbf{b}_2|$. The curves displayed in the figure emerge if $k_1|\mathbf{b}_1|/k_2|\mathbf{b}_2|=0.5$ and $q_1=q_2=0$. The two-digit numbers are labels of the classes described in Sec. 3.

A stationary point of this system is stable if all eigenvalues of the matrix in (8) have negative real parts. The fulfilment of the stability condition may depend on \mathbf{B}, \mathbf{Q} and \mathbf{K} (but not on \mathbf{a} or ϵ), see Appendix C. There are choices of the angles β_i for which the fulfilment of the condition is decidable based on knowing nothing else but β_i . However there are other intervals of the angles β_i where the stability of the SS mode depends on parameters of the compliant contact model (\mathbf{K} and \mathbf{Q}). The results of the stability analysis of all contact modes are summarized in Table 2 and in Fig. 1. Those values of β_i for which the SS mode is stable are depicted by dark grey shading in Fig. 1. The curved borders of the stability region in classes 13, 14, 23, 31, 41 and 46 depend on the choice of \mathbf{K}, \mathbf{Q} . The straight boundaries of the stability regions at boundaries of classes are however not sensitive to these parameters, as long as the angles β_i are kept constant. Since stability is not affected by \mathbf{a} , each subclass within a class has the same stability properties.

4.3. New properties of contact modes

We have seen that the SS mode has stability boundaries within classes 13, 14, 23, 31, 41 and 46. The shapes of the boundaries depend on several parameters of the compliant contact model. This fact means that the question of stability of the SS mode is often material-dependent, hence undecidable within the framework of rigid body theory. The undecidability of the stability of a contact mode is a new phenomenon, which is not present in systems with a single contact.

We have also demonstrated that the material-dependent stability boundaries lie in the interior of subclasses: variation of the angles β_j within a subclass may push a system through the stability boundary. At the same time, the consistency of a contact mode may only change at the boundaries of subclasses. This property means that a contact mode may become unstable without losing consistency, and thus multi-contact systems may undergo ‘spontaneous’ contact mode transitions. The opposite is known to be true for single-contact systems [13].

Subclasses 261 and 262 display a surprising novel phenomenon. The SS mode is consistent in both subclasses, whereas FF, SF and FS are inconsistent. Hence, these subclasses do not suffer from Painlevé’s paradoxes. At the same time, the SS is robustly unstable in both cases. The result of the stability analysis implies that systems of this type do not follow any contact mode. Instead, they undergo non-stationary fast dynamics. The analysis of the contact dynamics is the subject of ongoing work. Our preliminary results suggest that an impact without collision emerges. This finding is important, because an engineer’s common approach to rigid body dynamics with frictional contacts is to count the number of consistent contact modes. If the number differs from one, unusual dynamic behaviour is to be expected. The converse statement is often believed to be true: the existence and the uniqueness of a consistent contact mode makes it unnecessary to search for other types of behaviour. Nevertheless this implication of existence and uniqueness does not hold in the case of multiple contacts.

5. Discussion

This paper presented the consistency and stability analysis of all contact modes for rigid multi-body systems with two sliding contacts. We adopted the methodology of earlier works, focusing on single-contact systems. The new analysis sheds light on three qualitative differences between single contact systems and general multi-contact systems, including the undecidability of the stability of contact modes within the framework of rigid body theory; the occurrence of spontaneous contact mode transitions; and the possibility of ‘unusual’ contact dynamics despite the uniqueness of a consistent contact mode. The author believes that the last result is an important step towards a deeper understanding of Painlevé’s paradoxes. While the paradoxes are often thought to be the cause of

strange contact dynamics, our results indicate that they are merely members in a large family of peculiar phenomena associated with frictional contacts

Future work to be done includes a systematic investigation of IWCs using the same compliant contact model. The aim of this work will be a description of possible types of IWC (impact at one leg or both legs) and finding conditions under which they occur. Other types of contact dynamics, such as inverse clattering [13] and sprag-slip oscillations [17] may also be analysed in a similar fashion. Important questions addressed by the extended analysis include the following: do IWCs always resolve non-existence? Can we make a finite list of possible patterns of contact dynamics? Efforts to answer these questions are motivated by the need of a complete classification of contact dynamics in rigid multibody systems with frictional contacts, even though such a complete classification will probably never be reached.

Our current investigations and the tasks described above are limited to “instantaneous” phenomena, which are observable within an infinitely short time interval. These include instantaneous accelerations of the system (contact modes), fast contact dynamics (inverse clattering) and singularities of contact dynamics (IWCs). Nevertheless, they do not include singularities of the (much slower) dynamics of sliding motion [3] [15]. Dynamic jamming of multi-contact systems and related phenomena will also be the subject of future work.

Acknowledgments

This work has been supported by the National, Research, Development and Innovation Office of Hungary under grant 104501.

Appendix A: consistency conditions of contact modes

FF mode: in this mode, (5) implies $\mathbf{f}=0$, and $\ddot{\mathbf{d}} = -\mathbf{a}$ by (1). According to the constraint (4), the FF mode is consistent, if $a_1, a_2 < 0$.

SF mode: in this mode, (2) implies $f_2=0$; from (1) and (2) with $i=1$, we have $f_1=a_1/b_{11}$. The constraint (3) for leg 1 is satisfied if $a_1 b_{11} > 0$. Furthermore, $\ddot{d}_2 = -a_2 + b_{21} f_1$, i.e. (4) for leg 2 is satisfied if $-a_2 + a_1 b_{21}/b_{11} > 0$. The consistency condition of FS is analogous.

SS mode: according to (1) and (2) with $i=1$ and 2, $\mathbf{Bf} = \mathbf{a}$. The constraint (3) is satisfied for both legs if \mathbf{a} is in the cone spanned by the two column vectors \mathbf{b}_1 and \mathbf{b}_2 of \mathbf{B} .

Appendix B: eigenvalues of the coefficient matrix in (7)

The determinant of the matrix (i.e. the product of the two eigenvalues) is $b_{11}k_1$; whereas the trace of the matrix (i.e. the sum of the eigenvalues) is $-b_{11}q_1$.

Hence, for $b_{11} > 0$, the determinant is positive and the trace is negative, implying that both eigenvalues have negative real parts. For $b_{11} < 0$, the negative determinant implies two real eigenvalues with opposite signs.

Appendix C: eigenvalues of the coefficient matrix in (8)

The signs of the eigenvalues of matrix

$$\mathbf{M} \stackrel{def}{=} \begin{bmatrix} 0 & 0 & 1 & 0 \\ 0 & 0 & 0 & 1 \\ -\mathbf{BK} & -\mathbf{BQ} \end{bmatrix} \quad (9)$$

are investigated in this part. In the special case of $\mathbf{Q}=0$, the structure of \mathbf{M} implies that its eigenvalues are $\pm\lambda^{1/2}$ and the eigenvectors are $[\mathbf{x}^T \lambda \mathbf{x}^T]^T$ where λ and \mathbf{x} are eigenvalues and eigenvectors of the 2 by 2 matrix $-\mathbf{BK}$. Hence, the problem is reduced to the eigenvalue analysis of a 2 by 2 matrix. \mathbf{M} has an eigenvalue with positive real part if and only if $-\mathbf{BK}$ has a positive eigenvalue, i.e. if either its determinant is negative or its trace is positive. This is impossible in classes 12 and 42; true in some regions within classes 13, 14, 23, 31, 41, 46; and always true in the rest of the classes. Eigenvalues with non-positive real parts are always purely imaginary

In the general case $\mathbf{Q} \neq 0$, the problem is equivalent of a quadratic eigenvalue problem with 2 by 2 matrices. The eigenvalues and eigenvectors can be expressed in closed form, however they appear to have a much more complicated structure than for $\mathbf{Q}=0$. Instead of an analytical calculation, we performed numerical analysis with systematic variations of \mathbf{K} and \mathbf{Q} . The analysis suggests that the answers outlined above for $\mathbf{Q}=0$ remain true except that the eigenvalues with non-positive real parts are no more purely imaginary, but they typically have negative real parts. This is caused by the damping introduced via \mathbf{Q} .

References

- [1] An, L. S.: The Painlevé paradoxes and the law of motion of mechanical systems with Coulomb friction. *J. Appl. Math.Mech.* 54 (1990), 430-438.
- [2] Chatterjee, A., Ruina, A.: A new algebraic rigid-body collision law based on impulse space considerations. *Journal of Applied Mechanics* 65 (1998), 939-951
- [3] Génot, F., Brogliato, B.: New results on Painlevé paradoxes. *Eur. J. Mech. A: Solids* 18 (1999), 653–677
- [4] Grigoryan, S. S.: The solution to the Painleve paradox for dry friction. *Doklady Physics.* 46 (2001), 499–503
- [5] Hervé, B., Sinou, J. J., Mahé, H., Jezequel, L.: Analysis of squeal noise and mode coupling instabilities including damping and gyroscopic effects. *Eur. J. Mech.-A/Solids* 27 (2008), 141-160

- [6] Hoffmann, N., Fischer, M., Allgaier, R., Gaul, L.: A minimal model for studying properties of the mode-coupling type instability in friction induced oscillations. *Mech. Res. Comm.* 29 (2002), 197-205.
- [7] Hultén, J.: Brake Squeal-A Self-Exciting Mechanism with Constant Friction. Proc. SAE Truck and Bus Meeting, Detroit, MI, USA (1993), 932965.
- [8] Ivanov, A. P.: Singularities in the dynamics of systems with non-ideal constraints. *J. Appl. Math Mech.* 67 (2003), 185-192.
- [9] Jellett, J. H.: *A Treatise on the Theory of Friction*. Hodges, Foster, and Co., 1872.
- [10] Lecornu, L.: Sur la loi de Coulomb." *Comptes-rendus Acad. Sci. Paris* 140 (1905), 847-848.
- [11] Leine, R. I., Brogliato, B., Nijmeijer, H.: Periodic motion and bifurcations induced by the Painlevé paradox. *Eur. J. Mech.-A/Solids* 21 (2002), 869-896.
- [12] Liu, C., Zhao, Z., Chen, B.: The bouncing motion appearing in a robotic system with unilateral constraint. *Nonlin. Dyn.* 49 (2007), 217-232.
- [13] Nordmark, A., Dankowicz, H., Champneys, A.: Friction-induced reverse chatter in rigid-body mechanisms with impacts. *IMA J. Appl. Math* 76 (2011), 85-119.
- [14] Or, Y., Rimon, E., 2008: On the hybrid dynamics of planar mechanisms supported by frictional contacts ii: Stability of two-contact rigid body postures. Proc. IEEE Int. Conf. on Robotics and Automation, Pasadena, CA, USA (2008), 1219-1224.
- [15] Or, Y., Rimon, E.: Investigation of Painlevé's paradox and dynamic jamming during mechanism sliding motion. *Nonlin. Dyn.* 67 (2012), 1647-1668
- [16] Painlevé, P.: Sur les lois du frottement de glissement. *Comptes-rendus Acad. Sci. Paris* 141 (1905), 401-405, 546-552.
- [17] Papinniemi, A., Lai, J. C., Zhao, J., Loader, L.: Brake squeal: a literature review. *Applied acoustics*, 63 (2002), 391-400.
- [18] Payr, M., Glocker, C.: Oblique frictional impact of a bar: analysis and comparison of different impact laws. *Nonlin. Dyn.* 41 (2005), 361-383.
- [19] Pfeiffer F., Glocker C.: Multibody dynamics with unilateral contacts. In Wiley Series in Nonlinear Science, New York, 1996.
- [20] Stewart, D. E.: Rigid-body dynamics with friction and impact. *SIAM Rev.* 42 (2000), 3-39.
- [21] Van der Schaft, A. J., Schumacher, J. M.: Complementarity modeling of hybrid systems. *IEEE Tr. Autom. Control*, 43 (1998), 483-490.
- [22] Zhang, J., Johansson, K. H., Lygeros, J., Sastry, S.: Zeno hybrid systems. *Intl. J. Robust and Nonlin. Control* 11 (2001), 435-451
- [23] Zhao, Z., Liu, C., Chen, B., Brogliato, B.: Asymptotic analysis of Painlevé's paradox. *Multibody Syst. Dyn.* (2015), 1-21.
- [24] Zhao, Z., Liu, C., Chen, B.: The Painlevé paradox studied at a 3D slender rod. *Multibody Syst. Dyn.* 19 (2008), 323-343.

Péter L. Várkonyi, associate professor: Budapest University of Technology and Economics, Department of Mechanics, Materials and Structures, Műegyetem rkp. 3, H-1111 Budapest, Hungary (varkonyi@szt.bme.hu). The author gave a presentation of this paper during one of the conference sessions.

Solitary waves in one-dimensional pre-stressed lattice and its continual analog (VIB210-15)

Vsevolod Vladimirov, Sergii Skurativskyi

Abstract: One of the most interesting phenomena occurring in nonlinear media models is the existence of wave patterns, such as kinks, solitons, compactons, peakons and many others. There are known numerous nonlinear evolutionary PDEs, supporting soliton (multi-soliton) and compacton traveling wave (TW) solutions. Unfortunately, the vast majority of the models, with the exception of completely integrable ones, do not enable to analyze the properties of solitary waves interaction using only qualitative methods. Therefore it is instructive, when dealing with the non-integrable PDEs, to combine the qualitative treatment with numerical simulations. In this report we are going to present the results of studying compacton solutions in the continual models for granular pre-stressed chains. The model is shown to possess a pair of compacton TW solutions which are the bright and dark compactons. First we consider the stability properties of the compacton solutions and show that both the bright and the dark compactons pass the stability test. Next we analyze the dynamics of the compactons, simulating numerically the temporal evolution of a single compacton, as well as the intersection of pairs of compactons, including bright-bright, dark-dark and bright-dark pairs. To be able to simulate the evolution of interacting compactons, we have modified the numerical scheme built by J. de Frutos, M. A. Lopez-Marcos, and J. M. Sanz-Serna. Results of simulations are compared with that of evolution of corresponding impulse in the granular pre-stressed chain.

1. Introduction

This paper deals with some nonlinear evolutionary PDEs associated with dynamics of one-dimensional chains of pre-stressed granules. Since Nesterenko's pioneering works, [9–11], propagation of pulses in such media has been a subject of a great number of experimental studies and numerical works. We consider a nonlinear evolutionary PDE associated with an ODE systems describing the interaction of the adjacent elements of the chain with the forces depending on the relative displacement of the centers of mass of the granules. The PDE in question is obtained by means of the passage to the continuum limit, followed by the formal multi-scale decomposition.

We perform in this paper qualitative and numerical study of dark and bright compacton traveling wave solutions, supported by the PDE, paying attention to the stability and dynamical features of the compactons' solutions. The paper is arranged as follows. In section

2 we introduce the continual analog of the granular pre-stressed media with the specific interaction allowing for the propagation of the wave of compression as well as the wave of rarefaction. In section 3 we construct the Hamiltonian representations for the model, and show that the compacton traveling wave solutions, satisfying factorised equations, fulfill necessary conditions of extrema for some Lagrange functionals. Next we perform stability tests for compacton solutions, basing on the approach developed in [2, 6, 7], and show that both the dark and the bright compactons pass the stability test. The results of qualitative analysis are backed and partly supplemented by the numerical study. Numerical simulations show that the compacton solutions completely reestablish their shapes after the mutual collisions. Finally, in section 4 we present the results of numerical simulation of the Cauchy problem for discrete chains and compare the results of the numerical simulation with the analogous simulations performed within the continual analog.

2. Evolutionary PDEs associated with the granular prestressed chains

Unusual features of the solitons associated with the celebrated Korteweg-de Vries (KdV) equation, as well as other completely integrable models [3], are often prescribed to the existence of higher symmetries and (or) infinite set of conservation laws. However, there are known non-integrable equations possessing the localised TW solutions with quite similar features. As a well-known example, the so called $K(m, n)$ hierarchy [4] can be presented:

$$K(m, n) = u_t + (u^m)_x + (u^n)_{xxx} = 0, \quad m \geq 2, \quad n \geq 2. \quad (1)$$

Members of this hierarchy are not completely integrable at least for the generic values of the parameters m, n [14] and yet possess the compactly-supported TW solutions demonstrating the solitonic features [1, 4].

The $K(m, n)$ family was introduced in years 90th of the XX century as a formal generalisation of the KdV hierarchy, without referring to its physical context. Earlier V.F. Nesterenko [9] considered the dynamics of a chain of preloaded granules described by the following ODE system:

$$\ddot{Q}_k(t) = F(Q_{k-1} - Q_k) - F(Q_k - Q_{k+1}), \quad k \in \{0, \pm 1, \pm 2, \dots\} \quad (2)$$

where $Q_k(t)$ is the displacement of granule k centre of mass from its equilibrium position,

$$F(z) = A z^n, \quad n > 1. \quad (3)$$

A passage to the continual analog of the above discrete model is attained by the substitution:

$$Q_k(t) = u(t, k a) \equiv u(t, x), \quad (4)$$

where a is the average distance between granules. Inserting this formula, together with the identities

$$Q_{k\pm 1} = u(t, x \pm a) = e^{\pm a D_x} u(t, x) = \sum_{j=0}^{n+3} \frac{(\pm a)^j}{j!} \frac{\partial^j}{\partial x^j} u(t, x) + O(|a|^{n+4}), \quad (5)$$

into (2) and dropping out terms of the order $O(|a|^{n+4})$ and higher, we get the equation:

$$u_{tt} = -C \left\{ (-u_x)^n + \beta (-u_x)^{\frac{n-1}{2}} \left[(-u_x)^{\frac{n+1}{2}} \right]_{xx} \right\}_x, \quad (6)$$

where

$$C = A a^{n+1}, \quad \beta = \frac{n a^2}{6(n+1)}.$$

Differentiating the above equation with respect to x and employing the new variable $S = (-u_x)$, we obtain the Nesterenko's equation [11]:

$$S_{tt} = C \left\{ S^n + \beta S^{\frac{n-1}{2}} \left[S^{\frac{n+1}{2}} \right]_{xx} \right\}_{xx}. \quad (7)$$

Eq. (7) describes dynamics of strongly preloaded media in which the propagation of acoustic waves is impossible (the effect of "sonic vacuum"). Nesterenko had shown [11] that this equation possesses a one parameter family of compacton TW solutions describing the propagation of the waves of compression. Unfortunately, he did not pay much attention to the investigation of their dynamical features. Our preliminary study show that the compacton solutions supported by Eq. (7) are unstable. This situation is absolutely analogous to that with processing the celebrated Fermi-Pasta-Ulam problem [3] which takes the form of system (2) in which the interaction force has the form $F(z) = A z^2 + B z$ with $|A| = O(|B|)$. Passing to the continual analog by means of the substitution (4) one obtains the Boussinesq equation, possessing unstable soliton-like solutions. The famous KdV equation is extracted from the Boussinesq equation by means the multi-scale decomposition [3].

Our proceedings to the "proper" compacton-supporting equation is following. We start from the discrete system (2) in which the interaction force has the form

$$F(z) = A z^n + B z. \quad (8)$$

In addition, we assume that $B = \gamma a^{n+3}$, $|\gamma| = O(|A|)$. Making in the formula (2) the substitution (4), (5) we get the equation

$$u_{tt} = -C \left\{ (-u_x)^n + \beta (-u_x)^{\frac{n-1}{2}} \left[(-u_x)^{\frac{n+1}{2}} \right]_{xx} \right\}_x + \gamma a^{n+3} (-u_x)_x. \quad (9)$$

Differentiating the above equation with respect to x and introducing the new variable $S = (-u_x)$, we obtain the following equation:

$$S_{tt} = C \left\{ S^n + \beta S^{\frac{n-1}{2}} \left[S^{\frac{n+1}{2}} \right]_{xx} \right\}_{xx} + \gamma a^{n+3} S_{xx}. \quad (10)$$

Now we use a series of scaling transformations. Employment of the scaling $\tau = \sqrt{\gamma a^{n+3}} t$, enables to rewrite the above equation in the form:

$$S_{\tau\tau} = \frac{C}{\gamma a^{n+3}} \left\{ S^n + \beta S^{\frac{n-1}{2}} \left[S^{\frac{n+1}{2}} \right]_{xx} \right\}_{xx} + S_{xx}.$$

Next the transformation $\bar{T} = \frac{1}{2} a^q \tau$, $\xi = a^p (x - \tau)$, $S = a^r W$ is used. If, for example, we make a choice $q = 1$, $p = -1$, $r = 5$, then the higher order coefficient $O(a^2)$ will stand at the term with the second derivative with respect to \bar{T} . So, dropping out the terms proportional to $O(a^2)$, we obtain, after the integration with respect to ξ , the equation:

$$W_{\bar{T}} + \frac{A}{\gamma} \left\{ W^n + \frac{n}{6(n+1)} W^{\frac{n-1}{2}} \left[W^{\frac{n+1}{2}} \right]_{\xi\xi} \right\}_{\xi} = 0.$$

The scaling $T = \frac{A}{\gamma} L \bar{T}$, $X = L \xi$, $L = \sqrt{\frac{6(n+1)}{n}}$ leads us finally to the target equation:

$$W_T + \left\{ W^n + W^{\frac{n-1}{2}} \left[W^{\frac{n+1}{2}} \right]_{XX} \right\}_X = 0. \quad (11)$$

Description of waves of rerefraction in the case $n = 2k$ requires the following modification of the interaction force:

$$F(z) = -Az^{2k} + Bz \quad (12)$$

(for $n = 2k + 1$ the formula (8) describes automatically both wave of compression and rarefaction). Applying the above machinery to the system (2) with the interaction (12), one can get the equation

$$W_T - \left\{ W^n + W^{\frac{n-1}{2}} \left[W^{\frac{n+1}{2}} \right]_{XX} \right\}_X = 0, \quad n = 2k. \quad (13)$$

Thus, for $n = 2k$ the universal equation describing waves of compression and rarefaction can be presented in the form

$$W_T + \text{sgn}(W) \left\{ W^n + W^{\frac{n-1}{2}} \left[W^{\frac{n+1}{2}} \right]_{XX} \right\}_X = 0. \quad (14)$$

Let us note in conclusion that the equations (11) - (14) are obtained by formal employment of the multiscale decomposition method, which cannot be justified in our case because of negativeness of the index p . Nevertheless further investigations of these equations is still of interest because they occur to possess a set of compacton solutions demonstrating interesting dynamical features. As will be shown below, these solutions qualitatively correctly describe propagation of short impulses in the chain of prestressed blocks.

3. Compacton solutions and stability tests

Let us consider the pair of equations (11), (13), which can be expressed in the common form

$$W_T + \epsilon \left\{ W^n + W^{\frac{n-1}{2}} \left[W^{\frac{n+1}{2}} \right]_{XX} \right\}_X = 0, \quad \epsilon = \pm 1. \quad (15)$$

Since we are interested in the TW solutions $W = W(z) \equiv W(X - cT)$, it is instructive to make a passage to the traveling wave coordinates $T \rightarrow T$, $X \rightarrow z = X - cT$. Performing this change, we get:

$$W_T - cW_z + \epsilon \left\{ W^n + W^{\frac{n-1}{2}} \left[W^{\frac{n+1}{2}} \right]_{zz} \right\}_z = 0. \quad (16)$$

Below we formulate several statements, which are easily verified by direct inspection.

Statement 1. *Eq. (16) admits the following representation*

$$\frac{\partial}{\partial T} W = \frac{\partial}{\partial z} \delta (\epsilon H + cQ) / \delta W, \quad (17)$$

where

$$H = \int \left[\frac{n+1}{4} W^{n-1} W_X^2 - \frac{1}{n+1} W^{n+1} \right] dz, \quad Q = \frac{1}{2} \int W^2 dz.$$

Statement 2. *The functionals H, Q are conserved in time.*

Statement 3. *Consider the following functions:*

$$W_c^\epsilon(z) = \epsilon W_c(z) = \begin{cases} \epsilon M \cos^\gamma(Bz), & \text{if } |Kz| < \frac{\pi}{2}, \\ 0 & \text{elsewhere,} \end{cases} \quad (18)$$

where

$$M = \left[\frac{c(n+1)}{2} \right]^{\frac{1}{n-1}}, \quad K = \frac{n-1}{n+1}, \quad \gamma = \frac{2}{n-1}.$$

If $n = 2k + 1$, $k \in \mathbb{N}$, then the functions $W_c^\pm(z)$ are the generalized solutions to the equation

$$\delta (H + cQ) / \delta W|_{W=W_c^\pm} = 0. \quad (19)$$

If $n = 2k$, $k \in \mathbb{N}$, then the function $W_c^\epsilon(z)$ satisfies the equation

$$\delta (\epsilon H + cQ) / \delta W|_{W=W_c^\epsilon} = 0. \quad (20)$$

So, the TW solutions (18) are the critical points of either the Lagrange functional $\Lambda[\beta] = (H + \beta Q)$ (case $n = 2k + 2$) or $\Lambda^\epsilon[\beta] = (\epsilon H + \beta Q)$ (case $n = 2k$) with the common Lagrange multiplier $\beta = c$. A necessary and sufficient condition for $\Lambda[\beta]$ ($\Lambda^\epsilon[\beta]$) to attain the minimum on the compacton solution can be formulated in terms of the positiveness of the second variation of the corresponding functional, which, in turn, guarantees the orbital stability of the TW solution, [5]. Here we do not touch upon the problem of strict estimating the signs of the second variations. Instead of this, we follow the approach suggested in [2,6,7], which enables to test a mere possibility of the local minimum appearance on a selected sets of perturbations of TW solutions.

Let us consider a family of perturbations

$$W_c^\epsilon(z) \rightarrow \lambda^\alpha W_c^\epsilon(\lambda z). \quad (21)$$

By choosing $\alpha = 1/2$ we guarantee that

$$Q[\lambda] = \frac{1}{2} \int_{-\pi/2}^{\pi/2} \left[\lambda^{\frac{1}{2}} W_c^\epsilon(\lambda z) \right]^2 dz = Q[1]. \quad (22)$$

Imposing this condition, we reject the "longitudinal" perturbations, associated with symmetry $T_\gamma[W_c^\epsilon(z)] = W_c^\epsilon(z + \gamma)$. Indeed, since the equations (19), (20) are invariant under the shift $z \rightarrow z + \gamma$, then $T_\gamma W_c^\epsilon(z)$ belongs to the set of solutions as well, while formally the transformation $W_c^\epsilon(z) \rightarrow W_c^\epsilon(z + \gamma)$ can be treated as a perturbation. In order to exclude the perturbations of this sort, the orthogonality condition is posed. Introducing the representation for the perturbed solution

$$W_c^\epsilon(z)[\lambda] = W_c^\epsilon(z)[1] + v(z),$$

and using the condition (22), we get

$$0 = Q[\lambda] - Q[1] = \int_{-\pi/2}^{\pi/2} W_c^\epsilon(z) v(z) dz + O(\|v(z)\|^2).$$

For $\alpha = 1/2$, we get the following functions to be tested:

$$\Lambda^\nu[\lambda] = (\nu H + c Q)[\lambda] = \nu \left\{ \lambda^{\frac{n+3}{2}} I_n^\epsilon - \lambda^{\frac{n-1}{2}} J_n^\epsilon \right\} + c Q, \quad (23)$$

where

$$I_n^\epsilon = \frac{n+1}{4} \int_{-\pi/2}^{\pi/2} [W_c^\epsilon]^{n-1}(\tau) [W_c^\epsilon]_\tau^2(\tau) d\tau, \quad J_n^\epsilon = \frac{1}{n+1} \int_{-\pi/2}^{\pi/2} [W_c^\epsilon]^{n+1}(\tau) d\tau,$$

$$\nu = \epsilon^{n+1} = \begin{cases} +1 & \text{when } n = 2k + 1, \\ \epsilon & \text{when } n = 2k. \end{cases}$$

If the functional $\Lambda^\nu = \nu H + cQ$ attains the extremal value on the compacton solution, then the function $\Lambda^\nu[\lambda]$ has the corresponding extremum in the point $\lambda = 1$. The verification of this property is used as a test.

A necessary condition of the extremum $\left. \frac{d}{d\lambda} \Lambda^\nu[\lambda] \right|_{\lambda=1} = 0$ gives us the equality:

$$I_n^\epsilon = \frac{n-1}{n+3} J_n^\epsilon. \quad (24)$$

Using (24), we can easily get convinced that

$$\left. \frac{d^2}{d\lambda^2} \Lambda^\nu[\lambda] \right|_{\lambda=1} = \nu \frac{n-1}{2} J_n^\epsilon = \epsilon^{2(k+1)} \frac{n-1}{2(n+1)} \int [W_c]^{n+1}(\tau) d\tau > 0$$

for both $n = 2k + 1$ and $n = 2k$.

So the generalized solutions (18) pass the test for stability.

Further information about the properties of the compacton solutions deliver the numerical simulations.

4. Numerical simulations of compactons' dynamics

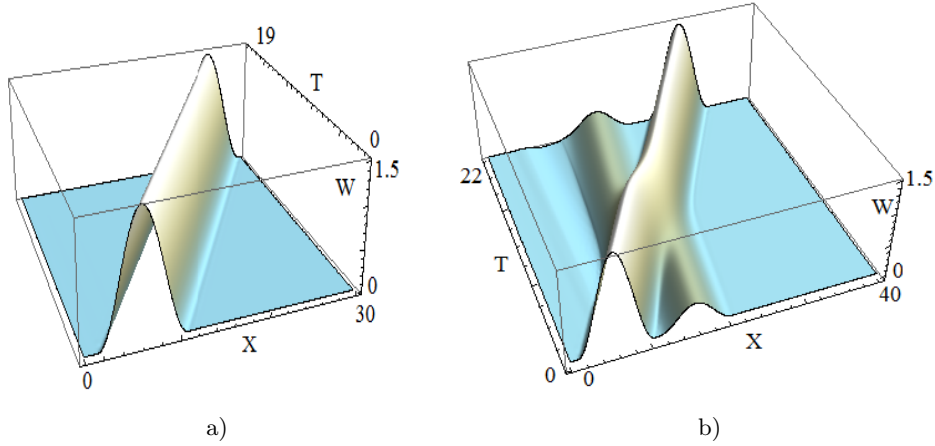


Figure 1. The movement of single compacton with the velocity $D = 1$ to the right (left panel). The movement of two bright compactons with the velocities $D = 1$ and $D = 1/4$, respectively (right panel).

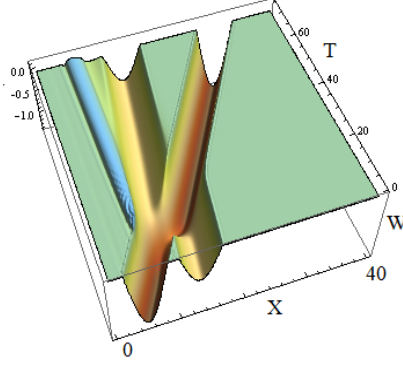


Figure 2. The movement of two dark-compactons with the velocities $D = 1$ and $D = 1/4$, respectively.

The solitary waves' dynamics is studied by means of direct numerical simulation, based on the finite-difference scheme. To derive the finite-difference scheme, e.g., for the model equation (11), we modify the scheme presented in [1]. In accordance with the methodology proposed in this paper, we introduce the artificial viscosity by adding the term εW_{4x} , where ε is a small parameter. Thus, instead of (11) we have in the case $n = 3$ the following equation:

$$W_t + \{W^3\}_x + \{W [W^2]_{xx}\}_x + \varepsilon W_{4x} = 0. \quad (25)$$

Let us approximate the spatial derivatives as follows

$$\begin{aligned} & \frac{1}{120}(\dot{W}_{j-2} + 26\dot{W}_{j-1} + 66\dot{W}_j + 26\dot{W}_{j+1} + \dot{W}_{j+2}) + \\ & + \frac{1}{24h}(-W_{j-2}^3 - 10W_{j-1}^3 + 10W_{j+1}^3 + W_{j+2}^3) + \\ & + \frac{1}{24h}(-L_{j-2} - 10L_{j-1} + 10L_{j+1} + L_{j+2}) + \\ & + \varepsilon \frac{1}{h^4}(W_{j-2} - 4W_{j-1} + 6W_j - 4W_{j+1} + W_{j+2}) = 0, \end{aligned} \quad (26)$$

where $L_j = W_j \frac{W_{j-2}^2 - 2W_j^2 + W_{j+2}^2}{h^2}$.

To integrate the system (26) in time, we use the midpoint method. According to this method, the quantities W_j and \dot{W}_j are presented in the form

$$W_j \rightarrow \frac{W_j^{n+1} + W_j^n}{2}, \dot{W}_j \rightarrow \frac{W_j^{n+1} - W_j^n}{\tau}.$$

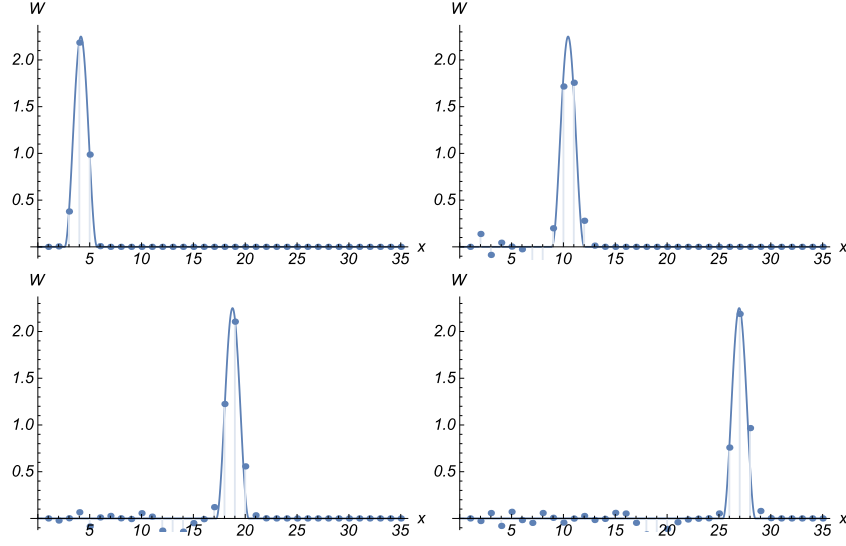


Figure 3. Evolution of the initial perturbation in the granular media (marked with dots) on the background of the corresponding evolution of the compacton (marked with solid lines) upper row: left: $t = 0$ right: $t = 4$; lower row: left: $t = 9$; right: $t = 14$

The resulting nonlinear algebraic system with respect to W_j^{n+1} can be solved by iterative methods.

We test the scheme (26) by considering the movement of a single compacton. Assume that the model's parameters $D_1 = 1$, $s_0 = 5.5$ and scheme's parameters $N = 600$, $h = 30/N$, $\tau = 0.01$, $\varepsilon = 10^{-3}$ are fixed. The application of the scheme (26) gives us the figure 1a.

To study the interaction of two bright compactons, we combine the previous compacton and another one with the lower amplitude taking the velocity $D_2 = D_1/4$ and $s_0 = 15.5$. The result of modelling is presented in fig. 1b. The interaction of two dark compactons has the similar properties and is depicted in fig. 2.

5. Comparison of numerical evolution of compactons with the numerical solution of the granular media, subjected to similar initial conditions

We've performed the comparison of the evolution of compacton solutions with corresponding solutions of the finite (but long enough) discrete system. The discrete analogs to the field $S(t, x) = -\frac{\partial u(t, x)}{\partial x}$ are the "stresses" $R_k = Q_{k-1} - Q_k$, satisfying the system

$$\ddot{R}_1(t) = 0, \quad \ddot{R}_k(t) = A[R_{k-1}^n - 2R_k^n + R_{k+1}^n], \quad \ddot{R}_m(t) = 0$$

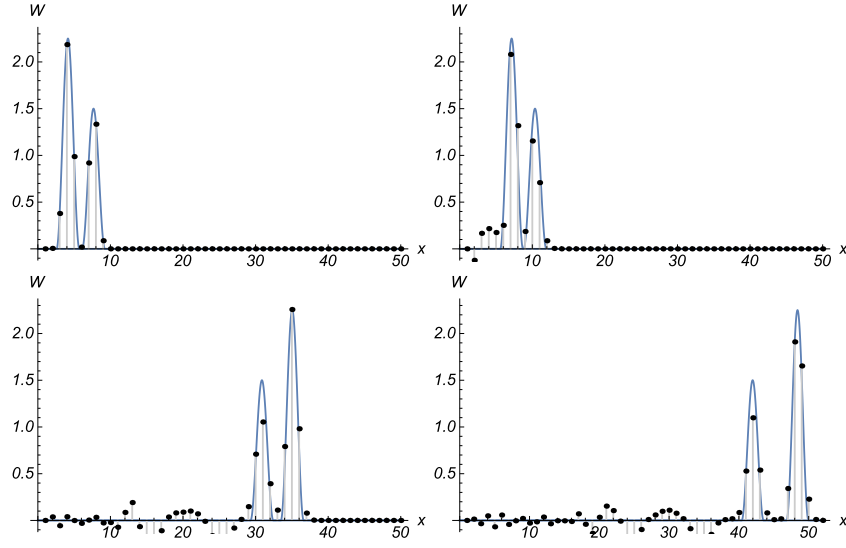


Figure 4. Evolution of two initially separated compacton perturbation in the granular media (marked with dots) on the background of the numerical solution of the continual model with the same initial data (marked with solid lines) upper row: left: $t = 0$ right: $t = 3$; lower row: left: $t = 21.5$; right: $t = 31$

with the initial conditions

$$R_k(0) = \begin{cases} M \cos^\gamma[Bak - I] & \text{if } |Bak - I| < \pi/2 \\ 0 & \text{if otherwise,} \end{cases}$$

and

$$\dot{R}_k(0) = \begin{cases} -Mc\gamma \cos^{\gamma-1}[Bak - I] \sin[Bak - I] & \text{if } |Bak - I| < \pi/2 \\ 0 & \text{if otherwise,} \end{cases}$$

where I is a constant phase, $k = 2, 3, \dots, m - 1$. The result of comparison for a single compacton is shown in fig. 3. In fig. 4 evolution of two initially separated compactons is shown for both continual and discrete models.

6. Conclusion and discussion

In this paper compacton solutions are studied, supported by the continual analogs of the dynamical systems describing one-dimensional chains of prestressed particles. The equation

(10) obtained without resorting to the method of multi-scaled decomposition possesses the compacton solutions which fail to pass the stability test. Numerical experiments show that the compacton solutions are destroyed in a very short time.

Contrary, the equations (11), (13) which are obtained with the help of formal multi scale decomposition, possess families of bright and dark compacton solutions, correspondingly, which occur to be stable. This is backed both by the stability test and results of the numerical simulations.

A characteristic feature of the equation (11) connected with the decomposition used during its derivation is that it describes a processes with the "long" temporal and "short" spatial scales. So it is rather questionable if this equation can adequately describe a localised pulse propagation in a discrete media in which the characteristic sizes of the particles are comparable with compacton's width Δx . In fact, making the backward transformations $X \rightarrow \xi \rightarrow x$ we get the following formula for the width of the compacton solution (18) in the initial coordinate:

$$\Delta x = \pi a \sqrt{\frac{n(n+1)}{6(n-1)^2}}.$$

For $n = 3/2$, corresponding to the Hertzian force between spherical particles, we get $\Delta x \approx 4.96 a$. It is then curious to know that the same results for the particles with the spherical geometry were obtained during the numerical work, and experimental studies [8–10, 12, 13].

Let us remark in conclusion that some of the present results, in particular those concerning the stability study, are only preliminary. The full investigations of stability of compacton solutions supported by (11)-(14) will be published elsewhere.

References

- [1] DE FRUTOS, J., LOPEZ-MARCOS, M. A., AND SANZ-SERNA, J. M. A finite-difference scheme for the $K(2,2)$ compacton equation. *J. Comput. Phys.*, 120 (1995), 248–252.
- [2] DERRICK, G. H. Comments on nonlinear wave equations as models for elementary particles. *J. Math. Phys.*, 5 (1964), 1252.
- [3] DODD, R., EILBECK, J., GIBBON, J. D., AND MORRIS, H. *Solitons and Nonlinear Wave Equations*. Academic Press, London, 1984.
- [4] HYMAN, J., AND ROSENAU, P. Compactons: solitons with finite wavelelngth. *Phys. Rev. Lett.*, 70 (1993), 564.
- [5] KAPITULA, T., AND PROMISLOV, K. *Spectral and Dynamical Stability of Nonlinear Waves*. Springer-Verlag, New York, 2013.

- [6] KARPMAN, V. Stabilization of soliton instabilities by higher order dispersion: KdV-type equations. *Phys. Lett.*, A210 (1996), 77.
- [7] KUZNETSOV, E. A., RUBENCHIK, A. M., AND ZAKHAROV, V. Soliton stability in plasmas and hydrodynamics. *Phys. Rep.*, 142 (1986), 103.
- [8] LAZARIDI, A. N., AND NESTERENKO, V. F. Observation of a new type of solitary waves in a one-dimensional granular medium. *J. Appl. Mech. Techn. Phys.*, 26 (1985), 405.
- [9] NESTERENKO, V. F. Propagation of nonlinear compression pulses in granular media. *J. Appl. Mech. Techn. Phys.*, 5 (1984), 733.
- [10] NESTERENKO, V. F. Solitary waves in discrete media with anomalous compressibility and similar to "sonic vacuum". *J. de Physique IV*, 55 (1994), 729.
- [11] NESTERENKO, V. F. *Dynamics of Heterogeneous Materials*. Springer-Verlag, New York, 2001.
- [12] NESTERENKO, V. F., LAZARIDI, A. N., AND SIBIRYAKOV, E. B. The decay of soliton at the contact of two "acoustic vacuums". *J. Appl. Mech. Techn. Phys.*, 36 (1995), 166.
- [13] VENGROVICH, D. B. private communication.
- [14] VODOVA, J. A complete list of conservation laws for non-integrable compacton equations of $K(n,n)$ type. *Nonlinearity*, 26 (2013), 757, (arXiv:1206.440v1 [nlin.SI]).

Vsevolod Vladimirov, Professor: Faculty of Applied Mathematics, AGH University of Science and Technology, Al. Mickiewicza 30, 30-059 Krakow, POLAND (*vsevolod.vladimirov@gmail.com*). The author gave a presentation of this paper during one of the conference sessions.

Sergii Skurativskiy, Ph.D.: Subbotin Institute of Geophysics, NAS of Ukraine, Bohdan Khmelnytskyi str. 63-G, Kyiv, UKRAINE (*skurserg@gmail.com*). The author gave a presentation of this paper during one of the conference sessions.

Proposed methods of controlling dual fuel CI engine using CAN-BUS information (MTR288-15)

Damian Walczak, Łukasz Zieliński, Krzysztof Szczurowski, Stanisław Radkowski

Abstract: In this article the information concerning proposed methods of controlling the dual fuel engines with compression ignition with an addition of LPG, has been presented. The proposition of the steering method is based on using the copyright controller, originally designed for the test bench and in later solutions – for controlling the work of the LPG fitting system in the commercial passenger vehicle. This method presents the way of utilizing information from the CAN network for controlling the LPG addition into the intake manifold. Two methods of the LPG injector control have been described, and the differences resulting from both methods have been presented. The algorithm calculating the gas injection duration has been described, based on the information obtained from the CAN network, in the first place the information about rotational speed, diesel oil injection dose, or the position of the acceleration pedal. The advantages of the control system using this information have been emphasized, especially that there is no necessity of interference in the analogue signals and thereby in the original factory electric wiring.

1. Introduction

These three pages of the Template should be regarded to as samples. Due to the international scope of the DSTA Conference the contribution should be written in a possibly clear and concise English.

With the introduced increasingly stringent standards of exhaust gases emission [1], and with the shrinking petroleum resources, the new solutions are sought after, enabling reduction of fuel consumption and toxic compounds emission. One of the possible ways to reduce the amount of such compounds is using alternative fuels or their additives. More and more tests are carried out regarding dual fuel engines in which, for example, the basic fuel is diesel oil and the additional fuel – liquefied petroleum gas (LPG), biogas, etc., which are fuels far cheaper than diesel oil and which generate fewer toxic compounds [2].

Development of control systems for the combustion engines allows for attempts of very precise control of dual fuel engines work. LPG is an alternative gaseous fuel, which is a by-product of refining crude oil, consisting basically of propylene, propane, butane, and other light hydrocarbons. A high octane number caused an extensive use of this kind of fuel, mainly in positive ignition engines. As a result of a highly developed distribution network, and the fact that it is easy to store

compared with other gaseous fuels, this fuel can be an essential source of power not only in engines with positive ignition.

Currently, in many research centres the tests are performed, devoted to using gaseous fuels (most frequently LPG and CNG) to fuel the combustion engines with compression ignition. Among the most important directions of research the following should be mentioned:

- fuelling engines with LPG, CNG, LNG (dual fuelling) [3,4,5,6],
- fuelling engines with biogas (by means of the engine modification: changing the compression ratio and installing the additional ignition system) [7],
- fuelling engines with the modified LPG and CNG (using additives enabling self-ignition).

The test results regarding the diesel LPG engines indicate that within the range of certain load and rotational velocity values, combustion of a defined gas additive, causing reduction of toxic compounds, is possible. However, it has also been proved that at smaller load values, poor combustion of LPG takes place, resulting therefore in lowering the engine efficiency and an increase in HC and CO emissions. Analysing the contemporary state of knowledge, it seems reasonable controlling the combustion processes in a way, which uses current engine parameters such as temperature of the exhaust gases, pressure in the combustion chamber, or analysis of the fuel mixture composition [8].

Amount of the added gas should be selected taking into consideration these parameters, and it should be adjusted to the current engine load and participation of gases from the exhaust gas recirculation [9].

In spite of the problems with automating the dual fuel engines, the tendency of increasing popularity of installations enabling addition or replacing LPG can be observed on the European market. It is caused mainly by the possibility of saving resulting from the relatively low price of LPG, at present accounting for approximately 40% of the liquid fuel price. The solutions offered in these installations allow for addition to approximately 30% of propane-butane. This proportion results from the control of the combustion process, especially from the susceptibility to detonation combustion and the tendency of the exhaust gases temperature to rise [10].

In commercial solutions, however, operation of the control system is based on controlling the mixture using the signal from the potentiometer of the accelerator pedal or the signal from the fuel pressure sensor in the container tank [11]. These signals are measured and subsequently the foster signals are generated, which reach the original factory controller. The engine safety is guaranteed by the shut-off of gas flow to the engine in the case of exceeding the temperature difference of exhaust gases in exhaust manifold for dual fuel work, compared to work on diesel oil exclusively, which indicates too heavy load. Such a manner of LPG addition control is relatively easy and reliable, nevertheless, such a low degree of integrity with the manufacturer's system leads to certain

limitations. There is no possibility of influencing such parameters as injection timing, or smooth limitation of LPG addition, which does not support the optimal dual fuel work as far as efficiency and maximal share of LPG are concerned.

Damaging any of the system's elements also results in the control system switching to exclusive diesel oil fuelling. The modification of an engine with compression ignition to LPG fuelling, in case of delivering gas to the intake manifold generates problems, which constitute separate issues [12]. Differences in fuelling can take place depending on the place in which the gas injector is installed. The angle of injector positioning can influence the filling up of the cylinder and possible losses of delivering the mixture to the cylinder. In the case of multi-cylinder engines, the problem consists in the amount of gas delivered to different cylinders because intake manifolds for different cylinders can vary in length. Then, in some cylinders, diesel oil with a smaller addition of LPG gas compared to other cylinders can be combusted.

2. Testing the vehicle's CAN

Taking into consideration the information included in the Introduction section, the authors took up the subject of controlling the dual fuel engine using their own original controller [13], enabling the LPG injection control. The main purpose was lack of interference with the engine's factory wiring and using the CAN network to acquire the information about the engine load.

One of the work stages consisted in finding the frame identifiers [14], in which the information can be sent from the engine controller about the rotational velocity, depressing the accelerator pedal, and diesel fuel dose. After finding the identifiers, the method of computing the data from the CAN frame into real quantities was determined.

Vital information is sent in the High Speed network, this is why the NI USB-8473s card by National Instruments has been used to search the information. The card was connected to the CAN network responsible for the drive system.

Using the chosen card and the software delivered by the manufacturer to test the connected measuring equipment, made it possible finding the frame ID and the byte, in which the information about the accelerator pedal position is sent, together with the method of computing data into real quantities.

The comparative tests on a distance of approximately 60km enabled finding the most interesting information (Fig. 1, Fig. 2). The analyses of the test results showed that the doses registered by the diagnoscope, and read from CAN after proper rescaling do not fully match each other, which is illustrated by the comparative time curve diagram and by the scatter plot.

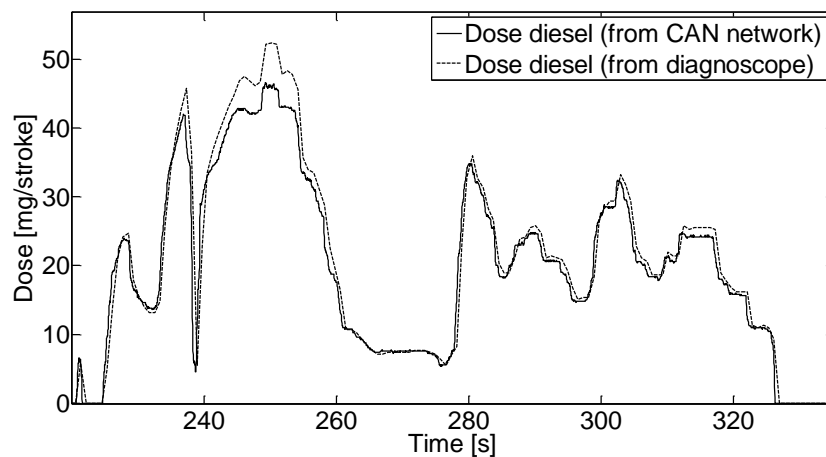


Figure 1. Curve of time for the CAN dose and for the dose registered by the diagnoscope

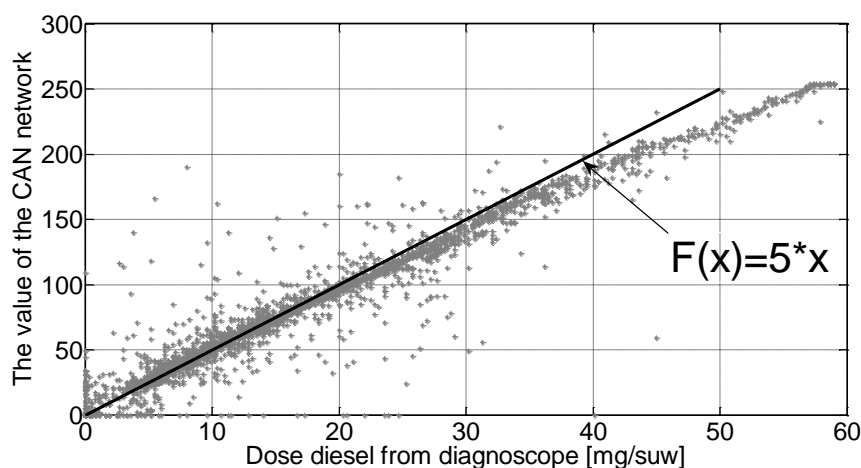


Figure 2. Comparison of the dose with the value from CAN network

As can be observed in the chart (Fig. 2), the linear description is possible only within the limited range (to about 20 mg/stroke). Above this value, a clear discrepancy of the results compared with the linear description can be seen because at normal operation, doses over 20mg/stroke occur relatively rarely; they correspond to heavy loading, this is why the decision was taken to use the linear description in the first step, to fit the needs of the LPG addition installation.

After a thorough analysis of the registered data, an attempt has been made to compare the given value with a different parameter of engine work, which is a calculated torque. It is computed by the engine controller on the basis of the diesel fuel dose.

Figure 3 shows the comparison of the values from the CAN network with the calculated torque registered by the diagnoscope. In this case, the linear description matches the real-life data, which is proved by the earlier proposition of description with the help of a linear model.

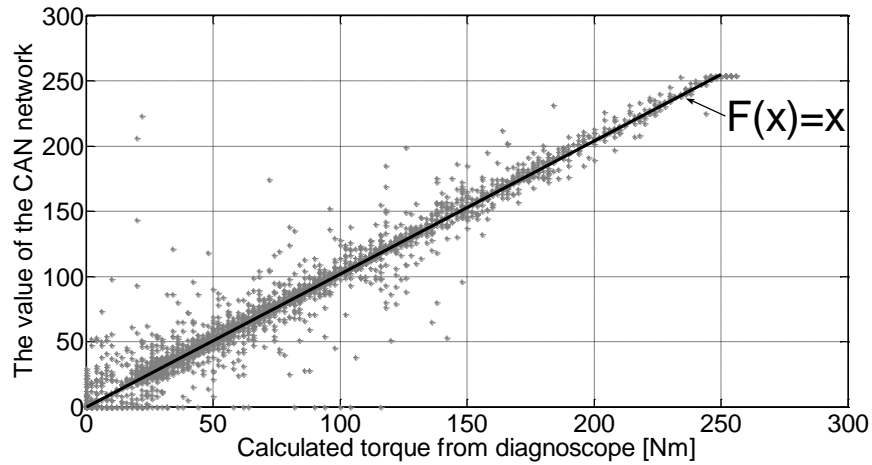


Figure 3. Comparison of the calculated torque with the values from CAN

3. Algorithm of the LPG dose selection

Apart from the information from the CAN network, using additional sensors, dedicated to the LPG fittings, proved necessary:

- integrated LPG pressure sensor,
- exhaust gas temperature (EGT) sensor.

The information from CAN regarding the calculated torque is converted into a diesel fuel dose, and it is used to calculate the LPG base dose. The diesel fuel dose is multiplied by a base dose coefficient, which defines the mass ratio of LPG to diesel oil. It was determined on the basis of the earlier tests and studying the literature of the subject, its value ranges between 0 to 50%, and it is recorded in the controller's memory.

$$q_{LPG_base} = q_{diesel} * m_{mem} \quad (1)$$

Where:

q_{LPG_base} – calculated LPG base dose [mg/stroke]

q_{diesel} – diesel oil dose reading from CAN network [mg/stroke]

m_{mem} – base dose coefficient recorded in the EEPROM memory

The calculated LPG base dose must be corrected because of several reasons, the most important being:

- too big a dose, in given conditions, can lead to detonation combustion which is destructive for the engine;
- injection of too big a dose without sufficient amount of air will cause a decrease in engine efficiency through incomplete fuel combustion, and will result in the growth of hydrocarbon emission.

In the algorithm the following limitations of the dose, applied at different levels, have been implemented:

- limiting the dose coefficient m_{mem}
 - due to the coolant temperature ($m_{max_T_egn}$),
 - due to the position of the accelerator pedal $m_{max_acc_ped}$,
- limiting the dose q_{LPG_base}
 - due to the difference in the current and maximal diesel oil dose for given conditions ($q_{LPG_max_diff_diesel}$),
 - limiting to the maximal dose ($q_{LPG_max_mem}$),
 - due to the exhaust gases temperature (EGT) ($q_{LPG_max_EGT}$).

4. Limitations of the dose coefficient

The first limitation of the dose coefficient is limitation due to the engine temperature. This limitation has a purpose of making the dose smaller when the engine and regulator temperature is still too low to assure the proper functioning, which could lead to an uncontrolled LPG injection. Additionally, the dose coefficient is reduced at high temperature in order to protect the engine from overheating. This limitation is a function consisting of many linear functions and is computed on the basis of the formula presented below. The operating area is illustrated by the diagram (Fig. 4).

$$m_{max_T_egn} = \begin{cases} 0, & T_{eng} < 10^{\circ}C, T_{eng} > 100^{\circ}C \\ (T_{eng} - 10^{\circ}C), & 10^{\circ}C \leq T_{eng} < 40^{\circ}C \\ (T_{eng} - 28^{\circ}C) * 2.5, & 40^{\circ}C \leq T_{eng} < 60^{\circ}C \\ 80, & 60^{\circ}C \leq T_{eng} < 95^{\circ}C \\ (100^{\circ}C - T_{eng}) * 16, & 95^{\circ}C \leq T_{eng} < 100^{\circ}C \end{cases} \quad (2)$$

Where:

$m_{max_T_egn}$ - maximal coefficient of the dose due to the engine temperature [%],

T_{eng} - engine temperature [$^{\circ}C$].

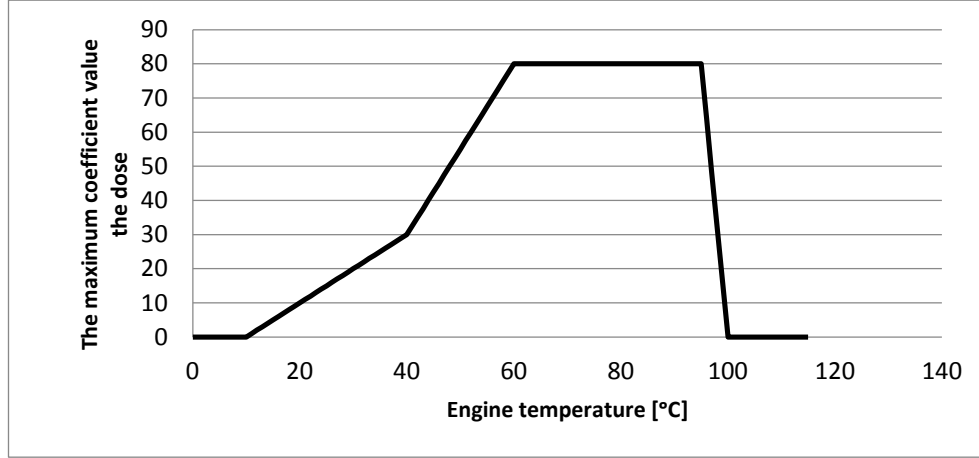


Figure 4. Operating area of the dose coefficient as a function of coolant temperature

The second limitation of the dose coefficient is implemented due to the position of the accelerator pedal, which enables stable engine work with small doses and small movements depressing the accelerator pedal, reducing simultaneously wear of the drive system, due to the smoother increase of the torque. This limitation is calculated on the basis of the following formula:

$$m_{\max_acc_ped} = a * 0,8 \quad (3)$$

Where:

$m_{\max_acc_ped}$ - maximal value of the multiplication factor [%],

a - depressing the accelerator pedal [%].

The calculations made are used for ultimate limitation of the dose coefficient on the basis of the formulae below:

$$m_{final} = \begin{cases} m_{mem}, & m_{mem} < m_{\max_T_egn} \\ m_{\max_T_egn}, & m_{mem} \geq m_{\max_T_egn} \end{cases} \quad (4)$$

$$m_{final} = \begin{cases} m_{final}, & m_{final} < m_{\max_acc_ped} \\ m_{\max_acc_ped}, & m_{final} \geq m_{\max_acc_ped} \end{cases} \quad (5)$$

Where:

m_{final} - ultimate value of dose coefficient [%].

Before approaching the subsequent limitations, the base dose is calculated, after the limitation of the dose coefficient was taken into consideration.

$$q_{LPG_base} = q_{diesel} * m_{final} \quad (6)$$

5. Dose limitations

The first limitation acting directly on the LPG dose is implemented with regard to the difference of the current diesel oil dose and the maximal dose in a given moment. Both values are sent through the factory engine controller through the CAN network. On the basis of this difference, the amount of gas to be totally combusted can be estimated. The value is made bigger by the additional amount of gas in order to improve the engine performance. The dose coefficient for the maximal dose of diesel oil (m_{power}) serves this purpose. Its value was determined experimentally and ranges from 0%, with no performance increase, to 15% for the maximal engine performance.

$$q_{LPG_{max_{diff_{diesel}}} = q_{diesel_{max}} - q_{diesel} + q_{diesel} * m_{power} \quad (7)$$

Where:

- $q_{LPG_{max_{diff_{diesel}}}$ - maximal LPG dose due to diesel oil maximal dose [mg/stroke],
- $q_{diesel_{max}}$ - maximal diesel oil dose in a given moment [mg/stroke],
- m_{power} - diesel oil dose coefficient for maximal diesel oil dose [%].

The second direct limitation of LPG dose ($q_{LPG_{max_{mem}}}$) is a constant value recorded in the controller's EEPROM memory. Its value was experimentally determined at the level of 10 mg/stroke, with the possibility of implementing changes by the user.

The last LPG limitation is implemented due to the exhaust gases temperature (EGT) ($q_{LPG_{max_EGT}}$). This limitation protects the engine from damage caused by too high combustion temperature. This limiter's operation is based on limiting the maximal dose ($q_{LPG_{max_{mem}}}$). The EGT limiter makes the maximal dose smaller, in the temperature range depending on the configured parameters. These parameters define, at which temperature the dose limitation starts ($T_{EGT_{start}}$), how it depends on the temperature (k_{EGT}), and the minimal level of this limiter ($q_{EGT_{min}}$). The method of calculating this limitation is shown in the relationship below.

$$q_{LPG_{max_EGT}} = \begin{cases} q_{LPG_{max_{mem}}}, & T_{EGT} \leq T_{EGT_{start}} \\ q_{LPG_{max_{mem}}} - k_{EGT} * (T_{EGT} - T_{EGT_{start}}), & T_{EGT} > T_{EGT_{start}} \end{cases} \quad (8)$$

$$q_{LPG_{max_EGT}} = \begin{cases} q_{LPG_{max_EGT}}, & q_{LPG_{max_EGT}} \geq q_{EGT_{min}} \\ q_{EGT_{min}}, & q_{LPG_{max_EGT}} < q_{EGT_{min}} \end{cases} \quad (9)$$

Where:

- $q_{LPG_{max_EGT}}$ - maximal LPG dose due to the exhaust gas temperature [mg/stroke],
- T_{EGT} - exhaust gas temperature (EGT) [°C],

- $T_{EGT_{start}}$ - exhaust gas temperature, above which the maximal dose is limited [°C],
- k_{EGT} - współczynnik zmniejszenia dawki ze względu na zwiększenie temperatury [mg/100°C],
- $q_{EGT_{min}}$ - minimalna dawka dla ograniczenia ze względu na temperaturę spalania [mg/suw].

Figure 5 illustrates how the limiter value changes depending on the exhaust gas temperature for different parameters.

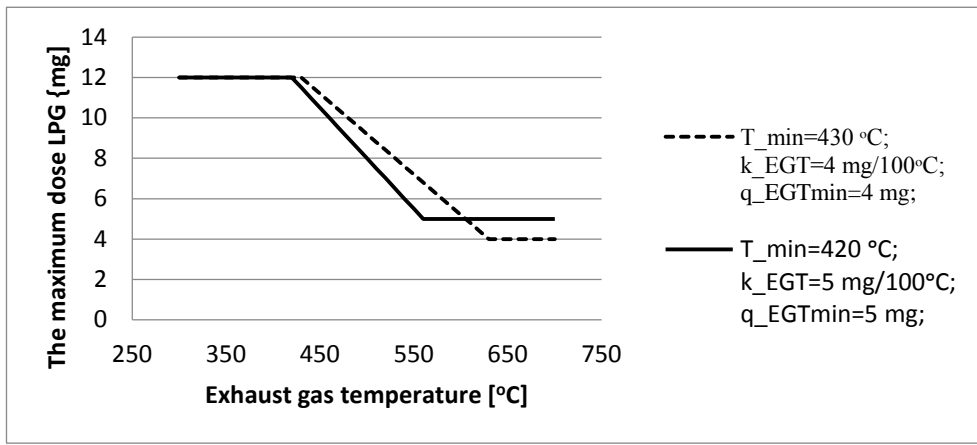


Figure 5. Reducing the amount of gas due to the exhaust gas temperature

The ultimate gas dose is calculated in the following way:

$$q_{LPG_{final}} = \begin{cases} q_{LPG_{base}}, & q_{LPG_{base}} < q_{LPG_{maxdiffdiesel}} \\ q_{LPG_{maxdiffdiesel}}, & q_{LPG_{base}} \geq q_{LPG_{maxdiffdiesel}} \end{cases} \quad (10)$$

$$q_{LPG_{final}} = \begin{cases} q_{LPG_{final}}, & q_{LPG_{final}} < q_{LPG_{max_EGT}} \\ q_{LPG_{max_EGT}}, & q_{LPG_{final}} \geq q_{LPG_{max_EGT}} \end{cases} \quad (11)$$

6. The control algorithm injector

The injector opening time results from the calculated LPG dose, with the assumption of the constant gas pressure behind the regulator, and of the constant pressure in the intake manifold. Because of the changing gas parameters, the coefficient of correction of the injection duration was used in the formula below, calculated on the basis of the LPG pressure and in the intake manifold.

$$inj_{dur} = \frac{q_{LPG_{final}} \cdot C}{q_f} + t_{in} \quad (12)$$

Where:

- inj_{dur} – injection duration [ms]
- q_{LPG} – dose calculated in the previous step [mg/stroke]
- q_f – theoretical injector flow rate [mg/ms]
- t_{in} – injector operation delay, theoretical injection duration, at which injector shows zero flow rate [ms]
- c – correction coefficient resulting from gas pressure, boost pressure and gas temperature

The injector constants are determined experimentally in the process of calibration:

- theoretical injector flow rate $q_f = 0,67 \text{ mg/ms}$,
- injector opening delay $t_{in} = 0,5 \text{ ms}$.

The calibration was performed at the absolute pressure $p_{LPG_0} = 200 \text{ kPa}$ and the temperature $T_{LPG_0} = 20^\circ\text{C}$. The gas changes its mass with changing temperature or pressure, keeping its constant volume in accordance with the ideal gas equation:

$$p * V = m * r * T \quad (13)$$

Where:

- p, V, m, T - variable parameters of gas state: pressure, volume, mass, temperature
- r - individual gas constant

To maintain the constant dose, the constant mass $m = \text{constans}$ was adopted in the formula above, with temperature or pressure change, a different gas volume should be delivered. After simple transformation, the following equation was obtained:

$$\frac{p * V}{T} = \text{constans} \quad (14)$$

$$\frac{p_{LPG_0} * V_{LPG_0}}{T_{LPG_0}} = \frac{p_{LPG} * V_{LPG}}{T_{LPG}} \quad (15)$$

The correction coefficient (c) for the injector opening time determines what gas volume must be delivered proportionally to the volume during performed calibration. The formula below illustrates the method of calculation of the c coefficient.

$$c = \frac{V_{LPG}}{V_{LPG_0}} = \frac{p_{LPG_0} * T_{LPG}}{T_{LPG_0} * p_{LPG}} \quad (16)$$

Where:

- V_{LPG_0} - gas volume during injector calibration [l]
- V_{LPG} - gas volume that must be injected during engine work [l]
- p_{LPG_0} - absolute gas pressure during calibration $p_{LPG_0} = 200 \text{ kPa}$
- T_{LPG_0} - temperature during calibration $T_{LPG_0} = 293 \text{ K } (20^\circ\text{C})$
- p_{LPG} - current gas pressure on the regulator outlet [kPa]
- T_{LPG} - current gas temperature on the regulator outlet [K]

7. Tests

The presented algorithm of the LPG dose selection and of injector automation was recorded as a source code, and subsequently compiled and uploaded into the authors' original controller [13]. The created control system was installed on a Seat Cordoba with the 1.4 TDI engine. A series of tests were conducted, tests of influence of the gas addition on engine performance, among others. The tests were carried out for the maximal engine load, with no diesel oil dose limitation. Figure 6 shows the engine characteristics for powering:

- with diesel oil only
- with diesel oil with 5% LPG addition
- with diesel oil with 10% LPG addition.

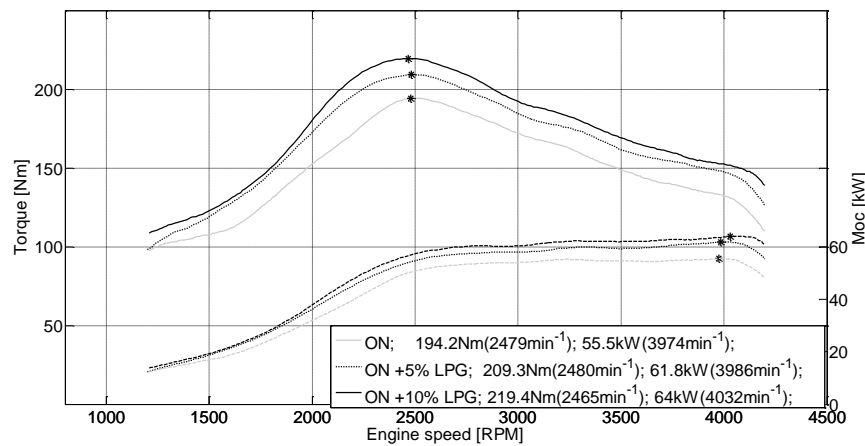


Figure 6. Characteristics of power and torque for different LPG additions

8. Summary

The tests conducted by the authors prove there is a deep sense searching for methods enabling the use of information transferred through the CAN network. This way of obtaining information from the factory installation increases the control system reliability, at the same time allowing for application of a more complex algorithm to calculate the LPG optimal dose.

Modern engines with compression ignition are equipped with turbochargers, the effect of which are the pressure changes in the intake manifold. The injector calibration was performed at idle speed with the constant pressure value. Developing the system, pressure changes in the intake manifold to the correction of injector opening time, are also worth taking into consideration.

References

- [1] Regulation (EC) No 715/2007 of the European Parliament and of the Council of 20 June 2007 on type approval of motor vehicles with respect to emissions from light passenger and commercial vehicles (Euro 5 and Euro 6) and on access to vehicle repair and maintenance information.
- [2] R. Vasu, E. Ramakrishnan, A. Ramesh, B. Nagalingam, K.V. Gopalakrishnan, Measurement and control of particulate emission in four stroke single diesel engine using LPG. Proceedings of the XV National Conference I.C. Engine and Combustion, 199
- [3] S. Ganesan, A. Ramesh, Investigation on the use of Water–Diesel Emulsion in a LPG–Diesel Dual Fuel Engine. SAE 2001-28-0032:2001
- [4] A.M.L.M. Wagemakers, C.A.J. Leermakers, Review on the Effects of Dual-Fuel Operation, Using Diesel and Gaseous Fuels, on Emissions and Performance. SAE 2012-01-0869:2012.
- [5] S. Swami Nathan, G. Nagarajan, An Innovative Application of Isomerisation of LPG by Al₂O₃/Pt Catalyst for Diesel Engine in Dual Fuel Operation. SAE 2003-01-2268:2003.
- [6] Piętak A., Wierzbicki S., Imiołek M., Mikulski M., „Dual-fuel feeding diesel engine behind assistance cng with liquid dose piloting fuel renewable”, Journal of KONES Powertrain and Transport, Vol. 16, No. 3, 2009.
- [7] M.P. Poonia, A. Ramesh, R.R. Gaur, Experimental Investigation of the Factors Affecting the Performance of a LPG – Diesel Dual Fuel Engine. SAE 1999-01-1123:1999.
- [8] Withit Chatlatanagulchai, Shinapat Rhienprayoon, Kittipong Yaovaja, Krisada Wannatong, Air/Fuel Ratio Control in Diesel-Dual-Fuel Engine by Varying Throttle, EGR Valve, and Total Fuel. SAE 2010-01-2200:2010.
- [9] M.P. Poonia, Y.B. Mathur Effect of EGR injection rate and engine load on cyclic variations of an LPG diesel dual fuel engine J. Environ. Res. Dev., 7 (2) (2012)
- [10] Mohsen M. Abdelaal, Basem A. Rabee, Abdelrahman H. Hegab Effect of adding oxygen to the intake air on a dual-fuel engine performance, emissions, and knock tendency Energy, 61 (2013), pp. 612–620
- [11] http://www.elpigaz.com/files/strefa%20B2B/do%20pobrania/materialy%20reklamowe/foldery%20i%20ulotki/Folder_DEGAmix_PL.pdf
- [12] Poonia M.P., Ramesh A., Gaur R.R., Effect of Intake Air Temperature and Pilot Fuel Quantity on the Combustion Characteristics of a LPG Diesel Dual Fuel Engine. SAE 982455:1998.
- [13] Szczurowski K., Walczak D., Zieliński Ł.: „Zastosowanie programowalnego sterownika do wysterowania osprzętu badawczego silnika dwupaliwowego”, Zeszyty Naukowe Instytutu Pojazdów nr 3 (99)/2014, Warszawa, ISSN 1642-347X
- [14] Rokicki K, Szczurowski K.: Methods of Identification of Data Transmitted in the in-Vehicle Can-Bus Networks. Methods and Models in Automation and Robotics - MMAR 2015 Conference, Międzyzdroje, Poland, 24-27th August 2015, IEEE Xplore Digital Library 978-1-4799-8701-6/15/\$31.00 ©2015 IEEE

Stanisław Radkowski, Professor: Institute of Vehicles of Warsaw University of Technology, Narbutta 84, 02-524 Warszawa, Poland (ras@simr.pw.edu.pl)

Krzysztof Szczurowski, Ph.D.: Institute of Vehicles of Warsaw University of Technology, Narbutta 84, 02-524 Warszawa, Poland (kszczur@simr.pw.edu.pl)

Łukasz Zieliński, M.Sc. (Ph.D. student): Institute of Vehicles of Warsaw University of Technology, Narbutta 84, 02-524 Warszawa, Poland (lzielinski@mechatronika.net.pl).

Damian Walczak, M.Sc. (Ph.D. student): Institute of Vehicles of Warsaw University of Technology, Narbutta 84, 02-524 Warszawa, Poland (damian.walczak@outlook.com). The author gave a presentation of this paper during one of the conference sessions.

Nonlinear modal interactions in composite thin-walled beam structures with CAS lay-ups (VIB116-15)

Xiao Wang, Zhanming Qin

Abstract: A second-order geometrically nonlinear theory of anisotropic thin-walled beams is developed to investigate the nonlinear dynamic characteristics of composite aircraft wings in the presence of internal resonance. Some prominent non-classical effects such as of transverse shear strain, warping inhibition, and three-dimensional (3-D) strain are considered. Moreover, Circumferentially Asymmetric Stiffness (CAS) lay-up configuration is adapted to generate the transverse bending-twisting elastic coupling. The governing equations of the dynamic system and the related boundary conditions are derived via Hamilton's Principle. The solution methodology is based on the Extended Galerkin's Method and the method of multiple scales is applied to the system in order to obtain the equations of amplitude and modulation. Steady-state solution and their stability are investigated by means of the eigenvalues of the Jacobian matrix. The peculiarity of the internal resonances and the conditions for saturation and jump phenomenon during the modal interactions are discussed and the commercial code ABAQUS is used to validate the theoretical results we have obtained. Finally, the prominent features of modal interactions in composite thin-walled beam structures are summarized and pertinent suggestions concerning safe design of the wing structures are given.

1. Introduction

Composite materials and structures, due to their vast advantages, have been increasingly used in aerospace industry and other fields of advanced technology. They have even been identified as a major thrust for designing high-performance aerospace structures (see e.g., [4, 5]). Anisotropic composite thin-walled structures are expected to meet the increasingly aggressive missions of the next generation of high-performance flight vehicles. In recent years, some further refinements are conducted to the modeling of open or closed cross-section thin-walled composite beam structures (see e.g., [3, 8, 26, 28]). Among these efforts, Cortinez et al. [3] and Vo and Lee [26] introduced warping shear to try to improve the model's accuracy; and together with a geometrically exact, intrinsic theory of anisotropic beams developed by Hodges [7], the variational-asymptotic beam sectional analysis [28] can be used for arbitrarily large deflections and rotations (see e.g., [19]).

It is well known that nonlinear structures may display manifold nonlinear characteristics such as multiple solutions, limit cycles, sub-harmonic and super-harmonic resonances,

various modal interactions, bifurcations and chaotic motions [16]. Among these behaviors, modal interactions pose a particular concern since as clearly pointed out by [15], it can be dangerous when energy is transferred from low-amplitude high-frequency modes to lower modes with high-amplitude. Although there have been extensive research work on this issue in solid structures, such as solid beam, plate, shell, in the context of aircraft composite wing structures modeled as thin-walled box beams, the issue of modal interactions has not yet been addressed.

In the present paper, based on the theory developed by Bhaskar and Librescu [1], a thin-walled box beam theory with second-order geometrically nonlinear terms is developed. Modal interactions in the presence of combination internal resonance are analytically investigated. Finally, for the purpose of validating the preceding theoretical results, the commercial code ABAQUS [6] is used to simulated the nonlinear vibration responses of the thin-walled box beam subjected to primary-resonance excitation. The fast Fourier transform (FFT) [27] is further used for the frequency-domain analysis.

2. Structural Elements of a Geometrically Nonlinear Theory of Anisotropic Thin-Walled Beams

According to the basic assumptions as proposed in [1,2,11], in the local coordinates (s, y, n) , a material point on the mid-line contour (i.e., $n = 0$) within the walls can also be represented by the global coordinates $(x(s), z(s))$. For arbitrary large rotation ϕ , the 3-D displacements $u(x, y, z, t)$, $v(x, y, z, t)$, $w(x, y, z, t)$ of the beam can be postulated as

$$u = u_0 + (z + n \frac{dz}{ds}) \sin \phi - (x - n \frac{dx}{ds})(1 - \cos \phi), \quad (1a)$$

$$v = v_0 + (x - n \frac{dz}{ds})\theta_z + (z + n \frac{dx}{ds})\theta_x - [F_w + na]\phi', \quad (1b)$$

$$w = w_0 - (x - n \frac{dz}{ds}) \sin \phi - (z + n \frac{dx}{ds})(1 - \cos \phi), \quad (1c)$$

where

$$\theta_x = \gamma_{yz} - w'_0 \cos \phi - u'_0 \sin \phi, \quad \theta_z = \gamma_{xy} - u'_0 \cos \phi + w'_0 \sin \phi, \quad (2a)$$

$$a = -(z \frac{dz}{ds} + x \frac{dx}{ds}), \quad r_n = z \frac{dx}{ds} - x \frac{dz}{ds}. \quad (2b)$$

We note that $u_0(y, t)$, $v_0(y, t)$, $w_0(y, t)$, $\phi(y, t)$, $\theta_x(y, t)$, $\theta_z(y, t)$ represent the 1-D displacement measures, and constitute the basic unknowns of the problem.

The warping function in Eq. (1b) is expressed as

$$F_w = \int_0^s [r_n(s) - \psi(s)] ds, \quad (3)$$

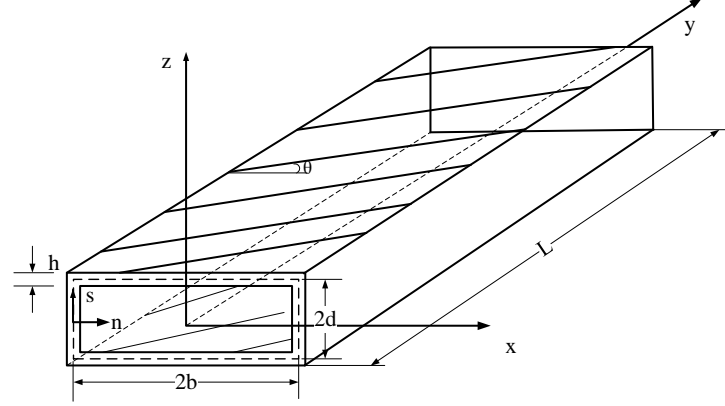


Figure 1. Geometry of an aircraft wing modeled as a thin-walled beam.

here, the torsional function $\psi(s)$ is defined as

$$\psi(s) = \oint_c r_n(s) \, ds \bigg/ \left(h(s) \bar{G}_{sy}(s) \oint_c \frac{ds}{h(s) \bar{G}_{sy}(s)} \right), \quad (4)$$

where $G_{sy}(s)$ is the effective membrane shear stiffness, which is defined as [1]:

$$G_{sy}(s) = \frac{N_{sy}}{h(s) \gamma_{sy}^0(s)}. \quad (5)$$

In order to develop the 2nd-order geometrically nonlinear thin-walled composite beam theory, we truncate up to the quadratic nonlinear terms in the Green strain [1, 11, 22]:

$$\varepsilon_{yy}^0 = [v'_0 + \frac{1}{2}(u'_0)^2 + \frac{1}{2}(w'_0)^2] + x(\theta'_z - w'_0\phi') + z(\theta'_x + u'_0\phi') - F_w\phi'' + \frac{1}{2}(\phi')^2(x^2 + z^2), \quad (6)$$

$$\varepsilon_{yy}^1 = \frac{dx}{ds}(\theta'_x + u'_0\phi') + \frac{dz}{ds}(-\theta'_z + w'_0\phi') - a\phi'' + r_n(\phi')^2, \quad (7)$$

$$\gamma_{ys} = \frac{dx}{ds}(\theta_z + u'_0 - w'_0\phi) + \frac{dz}{ds}(\theta_x + w'_0 + u'_0\phi) + \psi(s)\phi' + 2n\phi', \quad (8)$$

$$\gamma_{ny} = -\frac{dz}{ds}(\theta_z + u'_0 - w'_0\phi) + \frac{dx}{ds}(\theta_x + w'_0 + u'_0\phi). \quad (9)$$

3. Formulation of the Governing System for beams with CAS lay-up

The governing equations with the boundary conditions can be systematically derived from Hamilton's principle [13, pp. 82-86]. Particular lay-ups induce specific types of elastic coupling [20, 23]. In order to generate the transverse bending-twisting elastic coupling that is beneficial for the aeroelastic response behavior of aircraft wings and to apply the tailoring technique, the *circumferentially asymmetric stiffness* (CAS) configuration is adopted [11, 12] in the present case. For beams with the CAS lay-up, there are two types of elastic coupling, viz, extension-transverse shear and bending-twist coupling. Moreover, for the thin-walled CAS beams, the balanced lay-ups on the webs (left and right walls) imply that the stiffness coefficient a_{15} is zero [20], and the coefficient a_{27} is much smaller ($< 2\%$) than a_{37} , a_{22} , a_{55} and a_{77} for all the lay-ups considered, and therefore, can be ignored [20].

Ignoring the 3rd-order and up nonlinear terms, the governing equations for the above CAS lay-up, expressed in terms of the basic unknowns, are:

$$\begin{aligned} \delta u_0 : & \ a_{14}v_0'' + a_{44}(u_0'' + \theta_z') + \underline{a_{14}(u_0'u_0'' + w_0'w_0'') - a_{44}(w_0'\phi)' + a_{48}\phi'\phi''} \\ & + \left[a_{11}v_0'u_0' + a_{14}(u_0' + \theta_z)u_0' + a_{33}\theta_x'\phi' + a_{37}(\phi')^2 + a_{55}(w_0'\phi + \theta_x\phi) \right]' \\ & + p_x - b_1\ddot{u}_0 = 0, \end{aligned} \quad (10a)$$

$$\begin{aligned} \delta v_0 : & \ a_{11}v_0'' + a_{14}(u_0'' + \theta_z') + \underline{a_{11}(u_0'u_0'' + w_0'w_0'') - a_{14}(w_0'\phi)' + a_{18}\phi'\phi''} \\ & + p_y - b_1\ddot{v}_0 = 0, \end{aligned} \quad (10b)$$

$$\begin{aligned} \delta w_0 : & \ a_{55}(w_0'' + \theta_x') + \underline{a_{55}(u_0'\phi)' + a_{58}\phi'\phi''} + [a_{14}(u_0' + \theta_z)w_0' - a_{22}\theta_z'\phi' \\ & - a_{44}(u_0' + \theta_z)\phi + a_{11}v_0'w_0' - a_{14}v_0'\phi]' + p_z - b_1\ddot{w}_0 = 0, \end{aligned} \quad (10c)$$

$$\begin{aligned} \delta \phi : & \ a_{37}\theta_x'' + a_{77}\phi'' - a_{66}\phi^{(iv)} + \underline{a_{37}(u_0'\phi')' + \{[a_{33}\theta_x' + a_{37}\phi']u_0' - a_{22}\theta_z'w_0'\}' } \\ & + a_{55}(w_0' + \theta_x)u_0' + \{[a_{48}(u_0' + \theta_z) + a_{58}(w_0' + \theta_x)]\phi' + a_{18}v_0'\phi'\}' \\ & - a_{44}(u_0' + \theta_z)w_0' - a_{14}v_0'w_0' + m_y + b_w' - (b_4 + b_5)\ddot{\phi} + b_{10}\ddot{\phi}'' = 0, \end{aligned} \quad (10d)$$

$$\begin{aligned} \delta \theta_x : & \ a_{33}\theta_x'' + a_{37}\phi'' - \underline{a_{55}(w_0' + \theta_x) + a_{33}(u_0'\phi')' - a_{55}(u_0'\phi) - a_{58}(\phi')^2/2} \\ & + m_x - b_4\ddot{\theta}_x = 0, \end{aligned} \quad (10e)$$

$$\begin{aligned} \delta \theta_z : & \ a_{22}\theta_z'' - a_{14}v_0' - \underline{a_{44}(u_0' + \theta_z) - a_{22}(w_0'\phi')' - a_{14}[(u_0')^2/2 + (w_0')^2/2]} \\ & + \underline{a_{44}w_0'\phi - a_{48}(\phi')^2/2} + m_z - b_5\ddot{\theta}_z = 0, \end{aligned} \quad (10f)$$

where the inertial coefficients b_1 , b_4 , b_5 , b_{10} , external forces p_x , p_y , p_z , m_y , b_w' , m_y , m_x , m_z and corresponding linear stiffness coefficients $a_{11} \sim a_{77}$ are defined in [12, 20], while $a_{18} \sim a_{88}$ denote the nonlinear stiffness coefficients. Limited by the paper length, we omit the

expressions of $a_{18} \sim a_{88}$ here. The 2nd order nonlinear terms in the governing equations are denoted by underline. We note that the linear part of the governing system (10) can be split into two independent subsystems: one involving extension/lateral bending/lateral transverse shear motions ($u - v - z$ subsystem) and the other involving twist/vertical bending/vertical transverse shear motions ($w - \phi - x$ subsystem) [20, 24].

4. Nonlinear Analysis

In order to solve Eqs. (10a-f) in a general way, the Extended Galerkin Method (EGM) [10, 18] is used. For the thin-walled beams with CAS lay-ups to be investigated here, this method leads to symmetric mass and stiffness matrices [20, 21]. The method of multiple scales [9, 14, 17] is used to solve the governing equation. By considering the possible secular terms with respect to the quadratic nonlinearities, we conclude that when $\omega_p \approx \omega_m + \omega_n$, $\omega_p \approx \omega_m - \omega_n$ and $\omega_p \approx -\omega_m + \omega_n$ extra internal resonance may exist. We introduce the internal and external resonance detuning parameters σ_1 and σ_2 [9, 25]

$$\omega_p = \omega_m + \omega_n + \varepsilon\sigma_1, \quad \Omega = \omega_p + \varepsilon\sigma_2. \quad (11)$$

When the external energy input from the p th mode, i.e. Ω near ω_p , the solvability conditions [14] that governed the amplitude α_p , α_m , α_n and phase β_p , β_m , β_n of the linear system can be obtained as [17]:

$$\dot{\alpha}_p = -N_p \alpha_m^2 \sin \gamma - \mu \alpha_p - F_p \sin \xi, \quad \alpha_p \dot{\beta}_p = N_p \alpha_m^2 \cos \gamma + F_p \cos \xi, \quad (12a)$$

$$\dot{\alpha}_m = N_m \alpha_p \alpha_n \sin \gamma - \mu \alpha_m, \quad \alpha_m \dot{\beta}_m = N_m \alpha_p \alpha_n \cos \gamma, \quad (12b)$$

$$\dot{\alpha}_n = N_n \alpha_p \alpha_m \sin \gamma - \mu \alpha_n, \quad \alpha_n \dot{\beta}_n = N_n \alpha_p \alpha_m \cos \gamma, \quad (12c)$$

where

$$\gamma = \beta_m + \beta_n - \sigma_1 T_1 - \beta_p, \quad \xi = \sigma_2 T_1 - \beta_p, \quad (13)$$

$$N_p = \frac{(\mathbf{N}_{mn}^T + \mathbf{N}_{nm}^T) \mathbf{V}_p}{2\omega_p \mathbf{V}_p^T \mathbf{M}^T \mathbf{V}_p}, \quad N_m = \frac{(\mathbf{N}_{np}^T + \mathbf{N}_{pn}^T) \mathbf{V}_m}{2\omega_m \mathbf{V}_m^T \mathbf{M}^T \mathbf{V}_m}, \quad (14)$$

$$N_n = \frac{(\mathbf{N}_{mp}^T + \mathbf{N}_{pm}^T) \mathbf{V}_n}{2\omega_n \mathbf{V}_n^T \mathbf{M}^T \mathbf{V}_n}, \quad F_p = \frac{\mathbf{Q}^T \mathbf{V}_p}{2\omega_p \mathbf{V}_p^T \mathbf{M}^T \mathbf{V}_p}, \quad (15)$$

in which external force vector \mathbf{Q} , mass matrix \mathbf{M} are defined in [20, 21], while \mathbf{V}_p denotes the eigenvector for the p th mode of the linear system. Matrixes \mathbf{N}_{mn} , \mathbf{N}_{nm} , \mathbf{N}_{mp} , \mathbf{N}_{pm} , \mathbf{N}_{np} and \mathbf{N}_{pn} denote the corresponding 2nd order nonlinear terms. Limited by the paper length, we omit their expressions here.

4.1. Steady-state solution

The steady-state motions occur when $\dot{\alpha}_p = \dot{\alpha}_m = \dot{\alpha}_n = 0$, $\dot{\gamma} = 0$ and $\dot{\xi} = 0$, which correspond to the fixed points solution of Eqs. (12) and (13). It can be found that there are two kinds of fixed points:

(1) $\alpha_p \neq 0$ and $\alpha_m = \alpha_n = 0$,

$$\alpha_p^2 = \frac{F_p^2}{\mu^2 + \sigma_2^2}, \quad (16)$$

(2) $\alpha_p \neq 0$, $\alpha_m \neq 0$ and $\alpha_n \neq 0$,

$$\alpha_p^2 = \frac{(\sigma_1 + \sigma_2)^2 + 4\mu^2}{4N_m N_n}, \quad \alpha_m^2 = \sqrt{\frac{N_m}{N_n}} X, \quad \alpha_n^2 = \sqrt{\frac{N_n}{N_m}} X, \quad (17a)$$

the values of X are determined by the roots of the following quadratic equation

$$N_p^2 X^2 + \frac{N_p}{\sqrt{N_m N_n}} [2\mu^2 - \sigma_2(\sigma_1 + \sigma_2)] X + \alpha_p^2 (\mu^2 + \sigma_2^2) - F_p^2 = 0. \quad (18)$$

For solution (1), the primary (external) resonance plays a dominant role and the internal resonance can be ignored. No energy transfer between modes occur and the response of the system is governed by the directly excited p th mode only. This agrees with the solution of the corresponding linear system. In solution (2), the amplitude of the primary resonance mode α_p is independent of external excitation F_p .

The stability of steady-state solutions can be determined by the eigenvalues of the linearized coefficients matrix of the system (Jacobian matrix) near the corresponding steady-state solution. If the real part of each eigenvalue of the coefficient matrix is not positive, then the corresponding steady-state solution is stable, otherwise is unstable.

5. Example

The material property and geometric specification of the beam used for example are given in Table 1, and the lay-ups are specified in Table 2. From Table 3, a significant relationship for internal resonance can be found: $\omega_3^u \approx \omega_3^w + \omega_4^w$. We make $\omega_p = \omega_3^u$, $\omega_m = \omega_3^w$, $\omega_n = \omega_4^w$, the damping coefficient as $\mu = 0.5$, and external excitation frequency as $\Omega = 195Hz$.

In Figs. 2a and 2b, α_p , α_m and α_n are plotted as functions of external excitation F_p , where stable solutions are indicated in solid lines while unstable solutions in dashed lines. In these two figures, one can clearly see the saturation phenomenon. As the external excitation F_p increases from zero, so does the response of α_p . This agrees with the solution of the corresponding linear system (16). And beyond a critical value, the solution (16) loses stability and another branch of solution determined by (17) dominates. It is clearly seen that the

Table 1. Material property and geometric specification of the thin-walled box beam

Material	Value	Geometric	Value
E_{11}	$206.8 \times 10^9 \text{ N/m}^2$	Width ($2b^a$)	0.254 m
$E_{22} = E_{33}$	$5.17 \times 10^9 \text{ N/m}^2$	Depth ($2d^a$)	0.0681 m
$G_{13} = G_{23}$	$2.55 \times 10^9 \text{ N/m}^2$	Wall thickness (h)	0.0102 m
G_{12}	$3.10 \times 10^9 \text{ N/m}^2$	Number of layers (m_l)	6
$\mu_{12} = \mu_{13} = \mu_{23}$	0.25	Layer thickness	0.0017 m
ρ	$1.528 \times 10^3 \text{ Kg/m}^3$	Length (L)	3.080 m

^a The length is measured on the mid-line contour.

Table 2. Thin-walled box beam with CAS lay-up [unit:deg].

Flanges		Webs	
Top	Bottom	Left	Right
$[45^\circ]_6$	$[45^\circ]_6$	$[45^\circ / -45^\circ]_3$	$[45^\circ / -45^\circ]_3$

Table 3. The natural frequencies of the thin-walled box beam [unit: Hz]

Mode ^{#a}	ω^u	ω^u	Error (%) ^b	ω^w	ω^w	Error (%)
	Theoretical	ABAQUS		Theoretical	ABAQUS	
1st	14.208	14.077	0.93	4.4691	4.4297	0.89
2nd	85.776	85.315	0.54	27.887	27.658	0.83
3rd	194.92	193.45	0.76	77.665	77.164	0.65
4th	228.69	229.81	-0.49	117.20	116.97	0.20

^a ω^u denotes the frequency of the $u - v - z$ subsystem, while ω^w denotes the frequency of the $w - \phi - x$ subsystem.

^b Relative error, $([\text{Analytical}] - [\text{ABAQUS}]) / ([\text{ABAQUS}]) \times 100\%$.

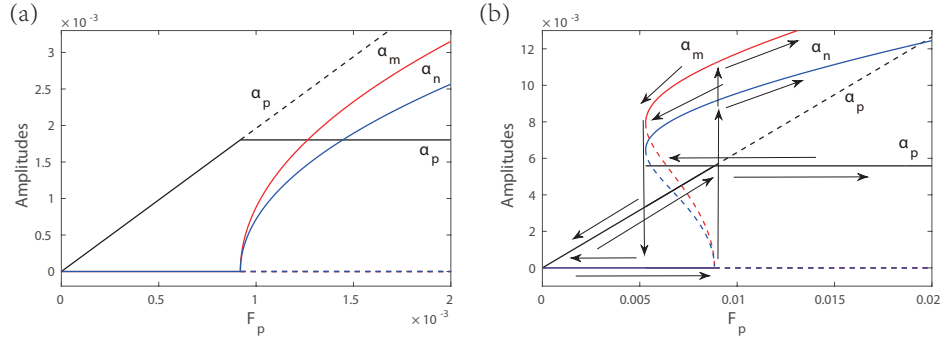


Figure 2. Response amplitudes versus excitation intensity F_p when energy is input from the ω_3^u mode, (a) $\sigma_1 = \sigma_2 = 0.1$, (b) $\sigma_1 = \sigma_2 = 1.5$.

response α_p is independent of external excitation, though the energy is input from the external resonance mode ω_3^u . In Fig. 2b the detunings of the internal and external resonance are both large, a jump phenomenon associated with varying the excitation amplitude F_p occurs. The trend of amplitude responses α_p , α_m and α_n can be traced from two ways, i.e., from $F_p = 0$ to higher values and vice verse. The jump phenomenon can be traced by tracking the arrows.

In Figs. 3a and 3b, α_p , α_m and α_n are plotted as functions of external resonance detuning parameter σ_2 , where stable solutions are indicated in solid lines while unstable solutions in dashed lines. In Fig. 3a, the jump phenomenon associated with varying the frequency Ω of the excitation is indicated by the arrows. The symmetric behavior of the frequency-response curve versus external resonance detuning σ_2 can be seen where the internal resonance detuning σ_1 is zero. The nonzero value of internal resonance detuning parameter σ_1 will cause the unsymmetrical configurations in frequency-response curves which can be seen in Figs. 3b.

6. Validation

In order to test the accuracy of our model and validate our theoretical results on modal interactions, the commercial code ABAQUS [6] is used in simulating the forced nonlinear vibration responses of the box thin-walled beams. A 4-node doubly curved general-purpose shell element type S4 is adopted in the computation. All the responses in validations all come from one node at the tip of the beam. And Fast Fourier Transform (FFT) [27] will be used for the corresponding frequency-domain analysis. Theoretical prediction of the natural frequencies and the results from ABAQUS are compared in Table 3. In all computed modes, an excellent agreement is observed between the theoretical and numerical results.

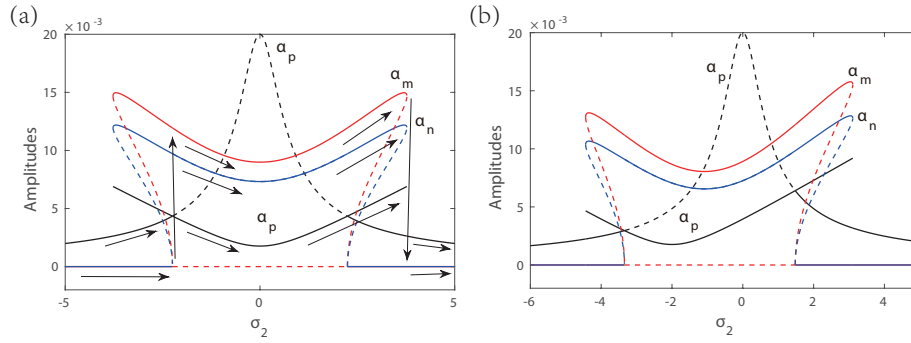


Figure 3. Response amplitudes versus excitation frequency σ_2 when energy is input from the ω_3^u mode, (a) $\sigma_1 = 0$, $F_p = 0.01$, (b) $\sigma_1 = 2$, $F_p = 0.01$.

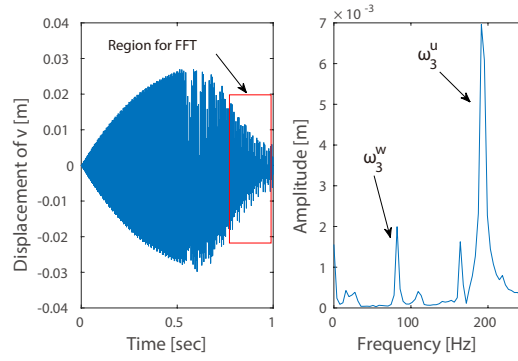


Figure 4. The extension response v and the corresponding frequency-domain analysis when the excitation energy is input from the ω_3^u mode.

The normal uniform shell edge external load distributed on the tip of the beam with magnitude specified as $6000N/m$ and frequency Ω specified as $195Hz$ is considered here. The responses of v , w and ϕ are displayed in Figs. 4, 5a and 5b respectively. It is readily seen that after a transient process about 0.5 second, the vertical bending and twist responses are induced heavily by the extension excitation. And from the results of frequency-domain analysis, it is easy to confirm the induced vertical bending motion mode is ω_3^w , while the induced twist motion mode is ω_4^w . Moreover, the response amplitude of mode ω_3^w and ω_4^w are much larger than that of the response amplitude of mode ω_3^u . Extension excitation induces high-amplitude low-frequency vertical bending and twist response, which agrees with our theoretical prediction.

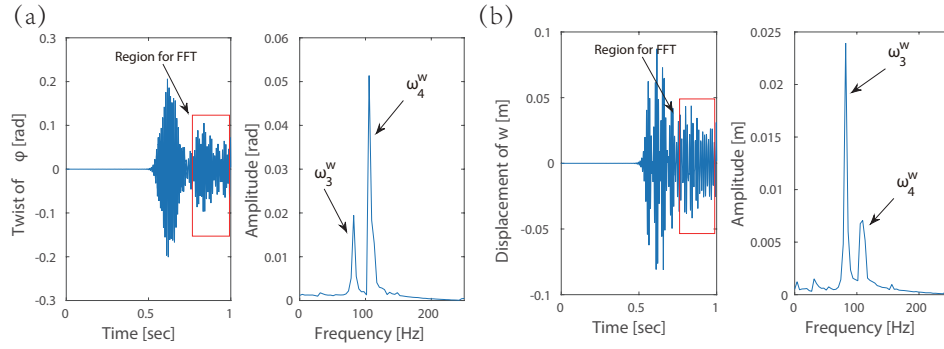


Figure 5. The forced responses of the beam and the corresponding frequency-domain analysis when the excitation energy is input from the ω_3^w mode, (a) twist response ϕ , (b) vertical bending response w .

7. Summary and conclusions

Nonlinear modal interactions of a thin-walled composite beam with CAS lay-ups, due to combination internal resonance and subjected to primary-resonance excitation are investigated. Multiple jump and saturation phenomena in the steady-state response are observed via the parametric analyses. Simulation results by commercial code ABAQUS validates satisfactorily our theoretical predictions. Major conclusions include:

1. Significant modal interactions exist when the thin-walled composite beam with CAS lay-ups exhibits apparent $\omega_p \approx \omega_m + \omega_n$ internal resonance.
2. Due to internal resonance, the independent $u - v - z$ subsystem and $w - \phi - x$ subsystem are coupled again. Energy can transfer between the two subsystems, i.e., lateral bending/extension motions may induce vertical/twist motions and vice versa.
3. Low-amplitude high-frequency motion can induce high-amplitude low-frequency motion due to modal interactions, which should be forbidden in the wing's design.

References

- [1] BHASKAR, K., AND LIBRESCU, L. A geometrically non-linear theory for laminated anisotropic thin-walled beams. *Int. J. Eng. Sci.* 33, 9 (1995), 1331–1344.
- [2] CHANDRA, R., STEMPLE, A. D., AND CHOPRA, I. Thin-walled composite beams under bending torsional and extensional loads. *J. Aircraft* 27, 7 (1990), 619–26.
- [3] CORTINEZ, V., AND PIOVAN, M. Vibration and buckling of composite thin-walled beams with shear deformability. *J. Sound Vib.* 258 (2002), 701–723.

- [4] FORSTER, E., CLAY, S., HOLZWARTH, R., PRATT, D., AND PAUL, D. Flight vehicle composite structures. *The 26th Congress of International Council of the Aeronautical Sciences* (2008). AIAA 2008-8976.
- [5] HARRIS, C., J.H. STARNES, J., AND SHUART, M. Design and manufacturing of aerospace composite structures, state-of-the-art assessment. *J. Aircraft* 39, 4 (Jul.-Aug. 2002), 545–560.
- [6] HIBBITT, KARLSSON, AND SORESENSEN. *ABAQUS/standard user's Manual*, vol. 1. Hibbitt, Karlsson & Sorensen, 2001.
- [7] HODGES, D. Geometrically exact, intrinsic theory for dynamics of curved and twisted anisotropic beams. *AIAA J.* 41, 6 (2003), 1131–1137.
- [8] IBRAHIM, S., CARRERA, E., PETROLO, M., AND ZAPPINO, E. Buckling of composite thin walled beams by refined theory. *Compos. Struct.* 94 (2012), 563–570.
- [9] LEE, C. L., AND PERKINS, N. C. Nonlinear oscillations of suspended cables containing a two-to-one internal resonance. *Nonlinear Dynamics* 3, 6 (1992), 465–490.
- [10] LIBRESCU, L., AND NA, S. Dyanmic response of cantilevered thin-wlled beams to blast and sonic-boom loadings. *Shock. Vib.* 5, 1 (1998), 23–33.
- [11] LIBRESCU, L., AND SONG, O. Behavior of thin-walled beams made of advanced composite materials and incorporating non-classical effects. *Appl. Mech. Rev.* 44, 11 (1991), S174–80.
- [12] LIBRESCU, L., AND SONG, O. *Thin-Walled Composite Beams: Theory and Application*. Springer, New York, 2006. Chap.8, pp. 213-232.
- [13] MEIROVITCH, L. *Principles and Techniques of Vibrations*. Prentice Hall, Upper Saddle River, New Jersey, 1997.
- [14] NAYFEH, A. *Introduction to Perturbation Techniques*. John Wiley & Sons, Inc, N.Y, 1981.
- [15] NAYFEH, A. *Nonlinear interactions: Analytical, computational, and experimental methods*. Wiley Series in Nonlinear Science. John Wiley & Sons, Inc., New York, 2000.
- [16] NAYFEH, A. Nonlinear interactionsanalytical, computational, and experimental methods, 2000.
- [17] NAYFEH, A., AND MOOK, D. *Nonlinear Oscillations*. John Wiley & Sons, Inc, N.Y, 1979.
- [18] PALAZOTTO, A., AND LINNEMANN, P. Vibration and buckling characteristics of composite cylindrical panels incorporating the effects of a higher order shear theory. *Int. J. Solids Struct.* 28, 3 (1991), 341–361.

- [19] PATIL, M., AND HODGES, D. Flight dynamics of highly flexible flying wings. *J. Aircraft* 43, 6 (2006), 1790–1799.
- [20] QIN, Z., AND LIBRESCU, L. On a shear-deformable theory of anisotropic thin-walled beams: further contribution and validation. *Compos. Struct.* 56, 4 (2002), 345–358.
- [21] QIN, Z., AND LIBRESCU, L. Dynamic aeroelastic response of aircraft wings modeled as anisotropic thin-walled beams. *Journal of Aircraft* 40, 3 (2003), 532–543.
- [22] REISMANN, H., AND PAWLIK, P. S. *Elasticity, theory and applications*. Krieger Publishing Company, 1991.
- [23] SMITH, E., AND CHOPRA, I. Formulation and evaluation of an analytical model for composite box-beams. *J. Am. Helicopter Soc.* 36, 3 (1991), 23–35.
- [24] SONG, O., AND LIBRESCU, L. Free vibration of anisotropic composite thin-walled beams of closed cross-section contour. *J. Sound Vib.* 167, 1 (1993), 129–47.
- [25] SRINIL, N., REGA, G., AND CHUCHEEPSAKUL, S. Two-to-one resonant multi-modal dynamics of horizontal/inclined cables. part i: Theoretical formulation and model validation. *Nonlinear Dynamics* 48, 3 (2007), 231–252.
- [26] VO, T. P., AND LEE, J. Flexural-torsional behavior of thin-walled composite box beams using shear-deformable beam theory. *Eng. Struct.* 30 (2008), 1958–1968.
- [27] WELCH, P. D. The use of fast fourier transform for the estimation of power spectra: A method based on time averaging over short, modified periodograms. *IEEE Transactions on audio and electroacoustics* 15, 2 (1967), 70–73.
- [28] YU, W., HODGES, D., AND HO, J. Variational asymptotic beam sectional analysis-an updated version. *Int. J. Eng. Sci.* 59 (2012), 40–64.

Xiao Wang, M.Sc. (Ph.D. student): Politecnico di Milano, Department of Aerospace Science and Technology, Via La Masa, 34, 20156, Milano, Italy (xiao.wang@polimi.it). The author gave a presentation of this paper during one of the conference sessions.

Zhanming Qin, Professor: Xi'an Jiaotong University, School of Aerospace, No.28 West Xianning Road, 710049, Xi'an, P.R. China (zmqin@mail.xjtu.edu.cn).

**Global modal approach for nonlinear dynamical modeling
of an L-shaped beam-mass structure
(VIB150-15)**

Jin Wei, Dengqing Cao, Yang Yang, and Wenhui Huang

Abstract: The purpose of this paper is to formulate a set of mathematically ordinary differential equations of motion describing the nonlinear dynamic of an L-shaped beam structure. Presenting the linear equations of motion for the bending of each beam and associated boundary conditions, the characteristic equation is derived for the whole system. The natural frequencies and global mode shapes of the linear model of the structure are determined, and orthogonality relations of the global mode shapes are established. Then, substituting the global modes into the formula of kinetic energy and potential energy, the nonlinear ordinary differential equations of motion for the structure with multiple-DoF are obtained by using the Lagrange procedure. A comparison between the natural frequencies obtained by the proposed method and those from finite element method is presented to illustrate the validity of governing equation of motion for L-shape structure. The governing equations of motion are expanded to a system with nonlinear terms up to order three to facilitate the study on nonlinear vibration responses by analytical techniques.

1. Introduction

A specific structure composed of multi-flexible-body and of lumped masses is usually used as component in large-scale space structures within the fields of mechanical, aeronautical and civil engineering^[1, 2]. In order to acquire higher precision, reliability and stability, a nonlinear dynamical analysis of such systems is of practical importance for predicting and understanding their behavior under the effect of applied loads.

The nonlinear dynamics of a single beam have been studied in the literature^[3-11]. Comparing with a single beam, the dynamic behavior of the multi-beam structure is more complex due to internal coupling and complex nonlinearities resulting from nonlinear geometry and inertia. In such coupling beam, one subsystem becomes a source of excitation for the other, and it may lead to parametric vibration. This kind of motion analysis is explored in, so-called, L-shaped beam structure in Refs^[12-19]. Haddow et al^[16] present the equation of motion for the structure with only quadratic nonlinearities, taking account of the axial motion of the beam due to bending. In [16], the method of multiple scales is used to determine approximate solution of the resulting equations. Nayfeh et al^[12, 13, 17-19] make a further comprehensive experimental and theoretical study on nonlinear motions of the L-shaped beam

structure, which indicate that a small excitation levels can produce chaotic response under the two-to-one internal resonance. Periodic, quasi-periodic, and chaotic responses predicted by theory are in good agreement with the experimental observations.

Moreover, chaotic vibrations of post-buckled L-shaped beam with an axial constraint are presented in Ref^[20], which are investigated with the Fourier spectra, the Poincare projections, the maximum Lyapunov exponents and Lyapunov dimension. Linear non-planar motion analysis of L-shaped beam structure is presented in Refs^[21-23]. The linear equations of motion for the structure considering rotary inertia effects are derived, and the modal analysis is performed to investigate the influence of rotary inertia terms and shear effects. Meanwhile, another type of an L-shaped beam structure has been addressed in Refs^[24-26]. Due to the essentially different stiffness in two orthogonal directions, the interaction between bending and torsion vibration are different from the model in [21]. Cartmell and Roberts^[25] give the analytical and experimental investigation on the effect of nonlinear coupling between bending modes of vibration, and the results show that a four mode interaction can exhibit non-synchronous large amplitudes of indirectly excited modes and saturation of the directly excited mode. Bux and Roberts^[24] show that violent non-synchronous torsion and bending vibration occur by the existence of quadratic nonlinear coupling and internal resonance effects between three and four modes. Warminski et.al^[26] present a systematic derivation of the differential equations of motion. It is shown that certain modes in the stiff and flexible directions of both beams may interact, and unexpected out-of-plane motion may appear.

It is well known that the multi-beam structures are continuous dynamic models with an infinite numbers of degrees-of-freedom. To suit for the use of numerical and analytical investigations, the approximate methods for the discretization of continuous systems are employed to convert into equivalent discrete systems, which usually represent the solution as a truncated finite series consisting of space-dependent mode functions multiplied by time-dependent generalized coordinates. The accuracy of the dynamic model obtained from the analytical formulation is highly dependent on the adopted mode functions of the beam deflection. Due to the coupling effects between different mode functions, the mode functions of each beam for the multi-beam structure are certainly different from those for a single beam. The present work is devoted towards to obtain an accurate global mode functions for the purpose of developing an explicit set of reduced-order nonlinear differential equations of motion for the multi-beam structures. The nonlinear ordinary differential equations are put into a form which is convenient for the use of analytical techniques to predict nonlinear phenomena exhibited by the structure. Furthermore, the equations developed here are convenient for the design of control laws to the multi-beam structure.

In this article, the natural frequencies and the corresponding global mode shapes of the transverse motion for the system are formulated by the method proposed in Refs^[27, 28]. Consequently, the explicit

orthogonality relationship for vibration modes of the whole system is presented. Then, the Lagrange procedure is employed to establish the reduced-order model that describes the planar nonlinear motion for the L-shaped beam-mass structure. A comparison between the natural frequencies obtained by the proposed method and those from finite element method is given to illustrate the validity of governing equation of motion for L-shape structure. Based on the low-dimension model presented here, the nonlinear analysis of L-shaped beam-mass structure can be conducted easily.

2. Specifications for the deformed configurations

Consider the planar motion of a L-shaped beam structure that consist of two light-weight inextensible beams, which are a horizontal beam with the length l_1 and a vertical beam with the length l_2 , as shown in Figure 1. The L-shaped beam is fixed to the base which is subjected to the horizontal harmonic excitation $\ddot{w}_s = F \cos \Omega t$. A rigid mass m is fixed at the end of the vertical beam. The coordinate system $o_1x_1y_1$ is the fixed inertial frame with origin at the left end of the horizontal beam. The body coordinate system $o_2x_2y_2$ is fixed to the vertical beam with origin at point o_2 , the junction of the horizontal and vertical beam. Its axial and transverse displacements are represented by $u_i(x_i, t)$ and $v_i(x_i, t)$, respectively, which are measured with respect to the coordinate system located at the beginning of the beam. Moreover, assume that the shear deformation and warping is negligible for both the horizontal beam and vertical beam.

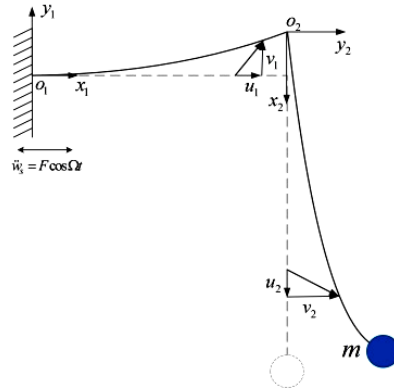


Figure 1. Schematic of L-shaped beam-mass structure.

The kinetic energy is given by

$$T = \frac{1}{2} \int_0^{l_1} \rho \left[(\dot{w}_s + \dot{u}_1)^2 + \dot{v}_1^2 \right] dx_1 + \frac{1}{2} \int_0^{l_2} \rho \left[(\dot{v}_1(l_1, t) + \dot{u}_2)^2 + (\dot{w}_s + \dot{u}_1(l_1, t) + \dot{v}_2)^2 \right] dx_2 \\ + \frac{1}{2} m \left[(\dot{v}_1(l_1, t) + \dot{u}_2(l_2, t))^2 + (\dot{w}_s + \dot{u}_1(l_1, t) + \dot{v}_2(l_2, t))^2 \right], \quad (1)$$

and the potential energy is described as

$$V = \sum_{i=1}^2 \frac{1}{2} \int_0^{l_i} \left[EA \left(u_i' + \frac{1}{2} v_i'^2 \right)^2 + EI v_i''^2 \right] dx_i, \quad (2)$$

where ρ, E, I and A are the density per unit length, Young's modulus, area moment inertia of the cross-section and the cross-sectional area. The superposed dot has the usual meaning of time derivative u_i' , v_i' and v_i'' represent the first and second partial derivatives with respect to x_i , respectively. Moreover, the effect of the weak damping is taken into account and described by the dissipation function

$$D = \frac{1}{2} \int_0^{l_1} c_1 \dot{v}_1^2 dx_1 + \frac{1}{2} c_1 (\rho l_2 + m) \dot{v}_1^2(l_1, t) + \frac{1}{2} \int_0^{l_2} c_2 \dot{v}_2^2 dx_2 + \frac{1}{2} c_2 m \dot{v}_2^2(l_2, t). \quad (3)$$

According to the assumption that the two beams are inextensible, the inextensibility constraint in i -th beam is expressed as

$$[1 + u_i']^2 + [v_i']^2 = 1. \quad (4)$$

Thus, the axial displacements u_i and the transverse displacements v_i are related to each other through the constraint equation (4), and the axial displacements can be expressed as

$$u_i = -\frac{1}{2} \int_0^{x_i} v_i'^2 dx_i. \quad (5)$$

Then, the displacement v_i can be expressed in the following form

$$v_1 = \sum_{j=1}^n \varphi_{1j}(x_1) q_j(t), \quad v_2 = \sum_{j=1}^n \varphi_{2j}(x_2) q_j(t), \quad (6)$$

where $\varphi_{1j}(x_1)$ and $\varphi_{2j}(x_2)$ are the mode shapes of the horizontal and vertical beam for the L-shaped beam-mass structure, respectively, $q_j(t)$ is the generalized coordinate for the whole system. In order to derive the nonlinear equations of motion by using the Lagrange equation, we require the accurate global mode shapes of transverse vibration. Therefore, in next section, the linear equations for the transverse vibration and associated boundary condition for the L-shaped beam-mass structure are presented to obtain the natural frequencies and global mode shapes.

3. Natural frequencies and global mode shapes

Considering the bending moment only on the transverse motion yields the linear dynamical equation of motion of the i -th beam

$$\rho \ddot{v}_i + EI v_i''' = 0 \quad (7)$$

The match conditions and boundary conditions of the L-shaped beam-mass structure are

$$\begin{cases} v_1(0, t) = 0, \quad v_1'(0, t) = 0, \quad v_2(0, t) = 0, \quad v_1'(l_1, t) = v_2'(0, t), \\ EI v_1'''(l_1, t) = (\rho l_2 + m) \ddot{v}_1(l_1, t), \quad EI v_1''(l_1, t) = EI v_2''(0, t), \\ EI v_2'''(l_2, t) = m \ddot{v}_2(l_2, t), \quad EI v_2''(l_2, t) = 0. \end{cases} \quad (8)$$

Let the non-dimensional coordinates $x_i = x$, and assume that the displacement $v_i(x, t)$ are separable in space and time,

$$v_i(x, t) = \varphi_i(x) \sin(\omega t) \quad (9)$$

The eigenvalue problem can be written directly in the form

$$\varphi_i'''(x) - \omega^2 \frac{\rho}{EI} \varphi_i(x) = 0 \quad (10)$$

The boundary conditions in Eq.(8) are reduced to the following forms

$$\begin{cases} \varphi_1(0) = 0, \quad \varphi_1'(0) = 0, \quad EI \varphi_1'''(l_1) = -(\rho l_2 + m) \omega^2 \varphi_1(l_1), \quad EI \varphi_1''(l_1) = EI \varphi_2''(0), \\ \varphi_2(0) = 0, \quad \varphi_2'(0) = \varphi_1'(l_1), \quad EI \varphi_2''(l_2) = 0, \quad EI \varphi_2'''(l_2) = -\omega^2 m \varphi_2(l_2). \end{cases} \quad (11)$$

The solutions of Eq. (10) can be written as

$$\varphi_i(x) = C_1^i \cos(\beta x) + C_2^i \sin(\beta x) + C_3^i \cosh(\beta x) + C_4^i \sinh(\beta x), \quad x \in [0, l_i], \quad (12)$$

where $\beta = \left(\frac{\rho \omega^2}{EI} \right)^{1/4}$. Let

$$\boldsymbol{\Psi} = \begin{bmatrix} C_1^1 & C_2^1 & C_3^1 & C_4^1 & C_1^2 & C_2^2 & C_3^2 & C_4^2 \end{bmatrix}^T. \quad (13)$$

Substituting Eq. (12) into the boundary conditions (11) yields

$$\mathbf{H}(\omega) \boldsymbol{\Psi} = \mathbf{0}, \quad (14)$$

where entries of the matrix $\mathbf{H}(\omega) \in \mathbb{R}^{8 \times 8}$ are given in Appendix A.

The positive roots of the frequency equation $\det(\mathbf{H}(\omega)) = 0$, denoted in ascending order by $\omega_1, \omega_2, \dots$, are the natural frequencies of the L-shaped beam-mass structure. The eigenvector $\boldsymbol{\Psi}^{(r)}$, where $r = 1, 2, \dots$, corresponding to the natural frequency ω_r , can be obtained from Eq.(14). Once the natural frequency ω_r and the corresponding vector $\boldsymbol{\Psi}^{(r)}$ are obtained, the r -th mode shapes for the L-shaped beam-mass structure can be determined from Eq.(12).

Now, let us consider a simple example of the L-shaped beam-mass structure. Assume that the material for both beams is steel with density $\rho=7850\text{ kg/m}^3$, Young's modulus $E=200\text{ GPa}$, Poisson's ratio $\nu=0.31$. The cross section of both beams are $b_1=0.012\text{ m}$, $h_1=0.002\text{ m}$. The length of both beams is $l_1=0.15\text{ m}$. By using the proposed method, the nature frequencies can be calculated and listed in Table 1.

Table 1 Natural frequencies for an L-shaped beam-mass structure.

Mode	Natural frequency (Hz)	Natural frequency (Hz)	Relative difference %
	Propose method	FE method	
1	8.32	8.32	0
2	26.95	26.94	0.3
3	241.78	241.63	0.06
4	417.97	417.41	0.13

Dividing each flexible beam into 20 elements, the natural frequencies are calculated using FE method and listed in Table 1 for validation purpose. The maximum relative error between the natural frequencies from the current and finite element methods, defined by $\frac{\omega_j - \omega_j^{\text{FE}}}{\omega_j^{\text{FE}}}$, is 0.3%. This implies that the natural frequency obtained using the proposed global mode method is a high accurate one. Using the corresponding mode shapes, an accurate set of reduced-order nonlinear differential equations of motion for the multi-beam structures can be obtained by using the proposed method.

4. Orthogonality of the global mode shapes

The global mode shapes associated with the two distinct eigenvalues ω_r and ω_s are denoted by $\phi_r(x)$ and $\phi_s(x)$, respectively, where

$$\phi_r(x) = [\phi_{1r}(x) \quad \phi_{2r}(x)]^T \quad (15)$$

By Eq.(10), one has

$$EI\phi_{1r}'''(x) = \omega_r^2 \rho \phi_{1r}(x), \quad (16)$$

$$EI\phi_{2r}'''(x) = \omega_r^2 \rho \phi_{2r}(x). \quad (17)$$

Now, let us multiply Eqs. (16)~(17) by $\phi_{1s}(x)$ and $\phi_{2s}(x)$, respectively, integrating the resulting equation over the domain $0 \leq x \leq l_1$ for the first beam and domain $0 \leq x \leq l_2$ for the second beam, and add the resulting equations, to get

$$EI \left[\int_0^{l_1} \phi_{1r}'''(x) \phi_{1s}(x) dx + \int_0^{l_2} \phi_{2r}'''(x) \phi_{2s}(x) dx \right] = \omega_r^2 \rho \left[\int_0^{l_1} \phi_{1r}(x) \phi_{1s}(x) dx + \int_0^{l_2} \phi_{2r}(x) \phi_{2s}(x) dx \right]. \quad (18)$$

Integration by parts, yields

$$EI \left[\int_0^{l_1} \phi_{1r}''(x) \phi_{1s}''(x) dx + \int_0^{l_2} \phi_{2r}''(x) \phi_{2s}''(x) dx \right] = \omega_r^2 \rho \int_0^{l_1} \phi_{1r}(x) \phi_{1s}(x) dx + \omega_r^2 \rho \int_0^{l_2} \phi_{2r}(x) \phi_{2s}(x) dx + \omega_r^2 \left[(\rho l_2 + m) \phi_{1r}(l_2) \phi_{1s}(l_2) + m \phi_{2r}(l_2) \phi_{2s}(l_2) \right]. \quad (19)$$

Exchanging the superscripts s and r in Eq.(19), yields

$$EI \left[\int_0^{l_1} \phi_{1s}''(x) \phi_{1r}''(x) dx + \int_0^{l_2} \phi_{2s}''(x) \phi_{2r}''(x) dx \right] = \omega_s^2 \rho \int_0^{l_1} \phi_{1r}(x) \phi_{1s}(x) dx + \omega_s^2 \rho \int_0^{l_2} \phi_{2s}(x) \phi_{2r}(x) dx + \omega_s^2 \left[(\rho l_2 + m) \phi_{1s}(l_2) \phi_{1r}(l_2) + m \phi_{2s}(l_2) \phi_{2r}(l_2) \right] \quad (20)$$

Subtracting Eq. (20) from Eq. (19), the first orthogonality relation can be obtained as

$$(\omega_r^2 - \omega_s^2) \rho \left[\int_0^{l_1} \phi_{1r}(x) \phi_{1s}(x) dx + \int_0^{l_2} \phi_{2r}(x) \phi_{2s}(x) dx \right] + (\omega_r^2 - \omega_s^2) \left[(\rho l_2 + m) \phi_{1r}(l_2) \phi_{1s}(l_2) + m \phi_{2r}(l_2) \phi_{2s}(l_2) \right] = 0, \quad (21)$$

from Eq.(21), the first orthogonality relation can be obtained

$$\rho \left[\int_0^{l_1} \phi_{1r}(x) \phi_{1s}(x) dx + \int_0^{l_2} \phi_{2r}(x) \phi_{2s}(x) dx \right] + \left[(\rho l_2 + m) \phi_{1r}(l_2) \phi_{1s}(l_2) + m \phi_{2r}(l_2) \phi_{2s}(l_2) \right] = M_s \delta_{rs}, \quad (22)$$

where M_s is a positive constant and δ_{rs} is the Kronecker delta. Using of Eqs. (22) and (18), the second orthogonality relation can be obtained as

$$EI \left[\int_0^{l_1} \phi_{1r}''(x) \phi_{1s}''(x) dx + \int_0^{l_2} \phi_{2r}''(x) \phi_{2s}''(x) dx \right] = K_s \delta_{rs}. \quad (23)$$

where K_s is a positive constant.

5. Governing equations of motion

Substituting the global mode shapes obtained by the proposed approach into the expressions (5) and (6), then the kinetic energy and the potential energy expressed in (1) and (2) can be used to obtain the ordinary differential equations of motion for the L-shaped beam-mass structure by following Lagrange procedure, namely,

$$\begin{aligned}
& M_s \ddot{q}_s(t) + K_s q_s(t) + c \dot{q}_s(t) + \sum_{j=1}^n a_1 F \cos \Omega t q_j(t) + \sum_{j=1}^n \sum_{k=1}^n a_2 \ddot{q}_j(t) q_k(t) \\
& + \sum_{j=1}^n \sum_{k=1}^n a_2 \dot{q}_j(t) \dot{q}_k(t) + \sum_{j=1}^n \sum_{k=1}^n \sum_{r=1}^n a_3 \dot{q}_j(t) \dot{q}_k(t) q_r(t) + \sum_{j=1}^n \sum_{k=1}^n \sum_{r=1}^n a_3 \dot{q}_j(t) \ddot{q}_k(t) q_r(t) \\
& + \sum_{j=1}^n \sum_{k=1}^n \sum_{r=1}^n a_3 q_j(t) \dot{q}_k(t) \dot{q}_r(t) + \sum_{j=1}^n \sum_{k=1}^n \sum_{r=1}^n a_4 q_j(t) q_k(t) q_r(t) \\
& = \int_0^{l_2} \rho F \cos \Omega t \varphi_{2s}(x) dx + m F \cos \Omega t \varphi_{2s}(l_2), \quad s = 1, 2, \dots, n.
\end{aligned} \tag{24}$$

where, μ is a damping coefficient, and $a_i (i = 1, 2, 3, 4)$ are constants which can be determined by the global mode shapes.

For generality, we introduce the following dimensionless variables and parameters

$$\begin{cases} \bar{x} = \frac{x}{l_1}, \bar{m} = \frac{m}{\rho l_1}, \bar{\xi} = \frac{E A l_1^2}{EI}, \bar{c} = \frac{c l_1^4}{EI}, \bar{F} = \frac{\rho F l_1^3}{EI}, \\ \chi = \frac{l_2}{l_1}, \beta_0^4 = \frac{\rho \omega_0^2 l_1^4}{EI}, \tau = \omega_0 t, \omega_0 = 1.0 \text{ rad/s}. \end{cases} \tag{25}$$

Then the non-dimensional form of Eq. (24) is

$$\begin{aligned}
& \ddot{q}_s(\tau) + \omega_s^2 q_s(\tau) + \bar{\mu} \dot{q}_s(\tau) + \sum_{j=1}^n \bar{a}_1 \bar{F} \cos \Omega \tau q_j(\tau) + \sum_{j=1}^n \sum_{k=1}^n \bar{a}_2 \ddot{q}_j(\tau) q_k(\tau) + \\
& \sum_{j=1}^n \sum_{k=1}^n \bar{a}_2 \dot{q}_j(\tau) \dot{q}_k(\tau) + \sum_{j=1}^n \sum_{k=1}^n \sum_{r=1}^n \bar{a}_3 \dot{q}_j(\tau) \dot{q}_k(\tau) q_r(\tau) + \sum_{j=1}^n \sum_{k=1}^n \sum_{r=1}^n \bar{a}_3 \dot{q}_j(\tau) \ddot{q}_k(\tau) q_r(\tau) + \\
& \sum_{j=1}^n \sum_{k=1}^n \sum_{r=1}^n \bar{a}_3 q_j(\tau) \dot{q}_k(\tau) \dot{q}_r(\tau) + \sum_{j=1}^n \sum_{k=1}^n \sum_{r=1}^n \bar{a}_4 q_j(\tau) q_k(\tau) q_r(\tau) = f_s \cos \Omega \tau, \quad s = 1, 2, \dots, n.
\end{aligned} \tag{26}$$

where the constants $\bar{\mu}, \bar{a}_i (i = 1, 2, 3, 4)$ and f_s are given in the Appendix B.

6. Conclusions

A set of ordinary differential equations of motion describing the nonlinear dynamic of an L-shaped beam structure have been formulated. The global mode approach was employed to get the natural frequencies and the corresponding global mode shapes for the whole system. A comparison of the natural frequencies obtained by the proposed method with those from FEM has been presented to illustrate the validity of the proposed approach. Moreover, the orthogonality relations of the global mode shapes have been established. Substituting the global modes into the formula of kinetic energy and potential energy, the nonlinear ODEs of motion for the structure with multiple-DoF can be easily obtained by using the Lagrange procedure. Based on the low-dimension model presented here, the nonlinear phenomena of L-shaped beam-mass structure, such as resonant, internal resonant, bifurcation and chaotic motion of the system, can be conducted easily.

Acknowledgments

We gratefully acknowledge the National Natural Science Foundation of China (Grant Nos. 91216106 and 11472089) for the financial support of this work.

Appendix A. Entries of the matrix $\mathbf{H}(\omega)$ in (14)

$$\begin{aligned}
H_{11} &= H_{13} = H_{22} = H_{24} = H_{47} = H_{55} = H_{57} = H_{66} = H_{68} = 1, \quad H_{45} = -1, \\
H_{12} &= H_{14} = H_{15} = H_{16} = H_{17} = H_{18} = H_{21} = H_{23} = H_{25} = H_{26} = H_{27} = H_{28} = 0, \\
H_{35} &= H_{36} = H_{37} = H_{38} = H_{46} = H_{48} = H_{51} = H_{52} = H_{53} = H_{54} = H_{56} = H_{58} = 0, \\
H_{65} &= H_{67} = H_{71} = H_{72} = H_{73} = H_{74} = H_{81} = H_{82} = H_{83} = H_{84} = 0, \\
H_{31} &= \sin(\beta l_1) + \left(\frac{m}{\rho} + l_2\right) \beta \cos(\beta l_1), \quad H_{32} = -\cos(\beta l_1) + \left(\frac{m}{\rho} + l_2\right) \beta \sin(\beta l_1), \\
H_{33} &= \sinh(\beta l_1) + \left(\frac{m}{\rho} + l_2\right) \beta \cosh(\beta l_1), \quad H_{34} = \cosh(\beta l_1) + \left(\frac{m}{\rho} + l_2\right) \beta \sinh(\beta l_1), \\
H_{41} &= -\cos(\beta l_1), \quad H_{42} = -\sin(\beta l_1), \quad H_{43} = \cosh(\beta l_1), \quad H_{44} = \sinh(\beta l_1), \\
H_{61} &= -\sin(\beta l_1), \quad H_{62} = \cos(\beta l_1), \quad H_{63} = \sinh(\beta l_1), \quad H_{64} = \cosh(\beta l_1), \\
H_{75} &= -\cos(\beta l_2), \quad H_{76} = -\sin(\beta l_2), \quad H_{77} = \cosh(\beta l_2), \quad H_{78} = \sinh(\beta l_2), \\
H_{85} &= \sin(\beta l_2) + \frac{m}{\rho} \beta \cos(\beta l_2), \quad H_{86} = -\cos(\beta l_2) + \frac{m}{\rho} \beta \sin(\beta l_2), \\
H_{87} &= \sinh(\beta l_2) + \frac{m}{\rho} \beta \cosh(\beta l_2), \quad H_{88} = \cosh(\beta l_2) + \frac{m}{\rho} \beta \sinh(\beta l_2).
\end{aligned}$$

Appendix B. The constants in Eq. (26)

$$\begin{aligned}
\bar{M}_s &= \beta_0^4 \left[\int_0^1 \varphi_{1r}(x) \varphi_{1s}(x) dx + \int_0^Z \varphi_{2r}(x) \varphi_{2s}(x) dx + (\chi + \bar{m}) \varphi_{1r}(1) \varphi_{1s}(1) + \bar{m} \varphi_{2r}(\chi) \varphi_{2s}(\chi) \right], \\
\bar{\mu} &= \bar{c} / \beta_0^4, \quad f_s = \left[\int_0^Z \varphi_{2s}(x) \bar{F} dx + \bar{m} \bar{F} \varphi_{2s}(1) \right] / \bar{M}_s, \\
\bar{a}_1 &= \left[\int_0^1 \int_0^x \varphi'_{1j}(x) \varphi'_{1s}(x) dx dx + \int_0^Z \int_0^1 \varphi'_{1j}(1) \varphi'_{1s}(1) dx dx + \bar{m} \int_0^1 \varphi'_{1j}(1) \varphi'_{1s}(1) dx \right] / \bar{M}_s, \\
\bar{a}_2 &= [\bar{a}_{21} + \bar{a}_{22} + \bar{a}_{23} + \bar{a}_{24}] / \bar{M}_s, \\
\bar{a}_3 &= [\bar{a}_{31} + \bar{a}_{32} + \bar{a}_{33} + \bar{a}_{34}] / \bar{M}_s, \\
\bar{a}_4 &= [\bar{a}_{41} + \bar{a}_{42} + \bar{a}_{43} + \bar{a}_{44} + \bar{a}_{45} + \bar{a}_{46}] / \bar{M}_s.
\end{aligned}$$

in which,

$$\begin{aligned}
\bar{a}_{21} &= -2\beta_0^4 \int_0^Z \left[\varphi_{1s}(1) \int_0^x \varphi'_{2j}(x) \varphi'_{2k}(x) dx \right] dx, \\
\bar{a}_{22} &= -2\beta_0^4 \int_0^Z \left[\varphi_{2s}(x) \int_0^1 \varphi'_{1j}(1) \varphi'_{1k}(1) dx \right] dx, \\
\bar{a}_{23} &= -2\beta_0^4 \bar{m} \varphi_{1s}(1) \int_0^Z \varphi'_{2j}(1) \varphi'_{2k}(1) dx, \\
\bar{a}_{24} &= -2\beta_0^4 \bar{m} \varphi_{2s}(1) \int_0^1 \varphi'_{1j}(1) \varphi'_{1k}(1) dx, \\
\bar{a}_{31} &= \beta_0^4 \int_0^1 \left(\int_0^x \varphi'_{1s}(x) \varphi'_{1j}(x) dx \right) \left(\int_0^x \varphi'_{1k}(x) \varphi'_{1r}(x) dx \right) dx, \\
\bar{a}_{32} &= \beta_0^4 \int_0^Z \left(\int_0^1 \varphi'_{1s}(1) \varphi'_{1j}(1) dx \right) \left(\int_0^1 \varphi'_{1k}(1) \varphi'_{1r}(1) dx \right) dx, \\
\bar{a}_{33} &= \beta_0^4 \int_0^Z \left(\int_0^x \varphi'_{2s}(x) \varphi'_{2j}(x) dx \right) \left(\int_0^x \varphi'_{2k}(x) \varphi'_{2r}(x) dx \right) dx, \\
\bar{a}_{34} &= \beta_0^4 \bar{m} \int_0^Z \varphi'_{2s}(1) \varphi'_{2j}(1) dx \int_0^Z \varphi'_{2k}(1) \varphi'_{2r}(1) dx, \\
\bar{a}_{41} &= 2\xi \int_0^1 \left(\int_0^x \varphi''_{1s}(x) \varphi'_{1j}(x) dx \right) \left(\int_0^x \varphi''_{1k}(x) \varphi'_{1r}(x) dx \right) dx, \\
\bar{a}_{42} &= 2\xi \int_0^Z \left(\int_0^x \varphi''_{2s}(x) \varphi'_{2j}(x) dx \right) \left(\int_0^x \varphi''_{2k}(x) \varphi'_{2r}(x) dx \right) dx, \\
\bar{a}_{43} &= \frac{1}{2} \xi \int_0^1 \varphi'_{1s}(x) \varphi'_{1j}(x) \varphi'_{1k}(x) \varphi'_{1r}(x) dx, \\
\bar{a}_{44} &= \frac{1}{2} \xi \int_0^Z \varphi'_{2s}(x) \varphi'_{2j}(x) \varphi'_{2k}(x) \varphi'_{2r}(x) dx, \\
\bar{a}_{45} &= -2\xi \int_0^1 \left(\varphi'_{1k}(x) \varphi'_{1r}(x) \int_0^x \varphi''_{1s}(x) \varphi'_{1j}(x) dx \right) dx, \\
\bar{a}_{46} &= -2\xi \int_0^Z \left(\varphi'_{2k}(x) \varphi'_{2r}(x) \int_0^x \varphi''_{2s}(x) \varphi'_{2j}(x) dx \right) dx.
\end{aligned}$$

References

- [1] Erturk A, Renno J M, Inman D J. Modeling of piezoelectric energy harvesting from an L-shaped beam-mass structure with an application to UAVs[J]. Journal of intelligent material systems and structures, 2008,
- [2] Iseki T, Okumura M, Sugawara T, et al. Deflection properties of a MEMS optical scanner with four torsion beams and L-shaped arms[J]. Sensors and Actuators A: Physical, 2012, 178(154-163.
- [3] Abou-Rayan A, Nayfeh A, Mook D, et al. Nonlinear response of a parametrically excited buckled beam[J]. Nonlinear Dynamics, 1993, 4(5): 499-525.
- [4] Ashworth R, Barr A. The resonances of structures with quadratic inertial non-linearity under direct and parametric harmonic excitation[J]. Journal of Sound and Vibration, 1987, 118(1): 47-68.
- [5] Crespo da Silva M, Glynn C. Nonlinear flexural-flexural-torsional dynamics of inextensional beams. I. Equations of motion[J]. Journal of Structural Mechanics, 1978, 6(4): 437-448.

- [6] Crespo da Silva M, Glynn C. Nonlinear flexural-flexural-torsional dynamics of inextensional beams. II. Forced motions[J]. *Journal of Structural Mechanics*, 1978, 6(4): 449-461.
- [7] Da Silva M C, Zaretzky C. Non-linear modal coupling in planar and non-planar responses of inextensional beams[J]. *International Journal of Non-Linear Mechanics*, 1990, 25(2): 227-239.
- [8] Da Silva M C, Zaretzky C. Nonlinear flexural-flexural-torsional interactions in beams including the effect of torsional dynamics. I: Primary resonance[J]. *Nonlinear Dynamics*, 1994, 5(1): 3-23.
- [9] Dwivedy S, Kar R. Non-linear dynamics of a slender beam carrying a lumped mass under principal parametric resonance with three-mode interactions[J]. *International Journal of Non-Linear Mechanics*, 2001, 36(6): 927-945.
- [10] Zaretzky C, da Silva M C. Nonlinear flexural-flexural-torsional interactions in beams including the effect of torsional dynamics. II: Combination resonance[J]. *Nonlinear Dynamics*, 1994, 5(2): 161-180.
- [11] Zavodney L, Nayfeh A. The non-linear response of a slender beam carrying a lumped mass to a principal parametric excitation: theory and experiment[J]. *International Journal of Non-Linear Mechanics*, 1989, 24(2): 105-125.
- [12] Balachandran B, Nayfeh A. Nonlinear motions of beam-mass structure[J]. *Nonlinear Dynamics*, 1990, 1(1): 39-61.
- [13] Balachandran B, Nayfeh A. Observations of modal interactions in resonantly forced beam-mass structures[J]. *Nonlinear Dynamics*, 1991, 2(2): 77-117.
- [14] Cao D-X, Zhang W, Yao M-H. Analytical and experimental studies on nonlinear characteristics of an L-shape beam structure[J]. *Acta Mechanica Sinica*, 2010, 26(6): 967-976.
- [15] El-Bassiouny A. Modal interaction of resonantly forced oscillations of two-degree-of-freedom structure[J]. *Applied mathematics and computation*, 2003, 134(2): 217-242.
- [16] Haddow A, Barr A, Mook D. Theoretical and experimental study of modal interaction in a two-degree-of-freedom structure[J]. *Journal of Sound and Vibration*, 1984, 97(3): 451-473.
- [17] Nayfeh A, Balachandran B. Experimental investigation of resonantly forced oscillations of a two-degree-of-freedom structure[J]. *International Journal of Non-Linear Mechanics*, 1990, 25(2): 199-209.
- [18] Nayfeh A, Balachandran B, Colbert M, et al. An experimental investigation of complicated responses of a two-degree-of-freedom structure[J]. *Journal of Applied Mechanics*, 1989, 56(4): 960-967.
- [19] Nayfeh A, Zavodney L. Experimental observation of amplitude-and phase-modulated responses of two internally coupled oscillators to a harmonic excitation[J]. *Journal of Applied Mechanics*, 1988, 55(3): 706-710.
- [20] Onozato N, Nagai K-i, Maruyama S, et al. Chaotic vibrations of a post-buckled L-shaped beam with an axial constraint[J]. *Nonlinear Dynamics*, 2012, 67(4): 2363-2379.
- [21] Georgiades F, Warminski J, Cartmell M P. Linear Modal Analysis of L-shaped Beam Structures–Parametric Studies[C]. *Proceedings of the Journal of Physics: Conference Series*, IOP Publishing, 2012: 012006.

- [22] Georgiades F, Warminski J, Cartmell M P. Linear modal analysis of L-shaped beam structures[J]. *Mechanical Systems and Signal Processing*, 2013, 38(2): 312-332.
- [23] Georgiades F, Warminski J, Cartmell M P. Towards linear modal analysis for an L-shaped beam: Equations of motion[J]. *Mechanics Research Communications*, 2013, 47(50-60).
- [24] Bux S, Roberts J. Non-linear vibratory interactions in systems of coupled beams[J]. *Journal of Sound and Vibration*, 1986, 104(3): 497-520.
- [25] Cartmell M, Roberts J. Simultaneous combination resonances in an autoparametrically resonant system[J]. *Journal of Sound and Vibration*, 1988, 123(1): 81-101.
- [26] Warminski J, Cartmell M, Bochenski M, et al. Analytical and experimental investigations of an autoparametric beam structure[J]. *Journal of Sound and Vibration*, 2008, 315(3): 486-508.
- [27] Cao D, Song M, Zhu W, et al. Modeling and analysis of the in-plane vibration of a complex cable-stayed bridge[J]. *Journal of Sound and Vibration*, 2012, 331(26): 5685-5714.
- [28] Song M, Cao D, Zhu W. Dynamic analysis of a micro-resonator driven by electrostatic combs[J]. *Communications in Nonlinear Science and Numerical Simulation*, 2011, 16(8): 3425-3442.

Jin Wei, M.Sc. (Ph.D. student): Harbin Institute of Technology/ School of Astronautics/ Division of Dynamics and Control, Harbin Institute of Technology, West Dazhi Street No.92, Nangang District, Harbin 150001, China. (weijin@hit.edu.cn). The author gave a presentation of this paper during one of the conference sessions.

Dengqing Cao, professor: Harbin Institute of Technology/ School of Astronautics/ Division of Dynamics and Control, Harbin Institute of Technology, West Dazhi Street No.92, Nangang District, Harbin 150001, China. (dqcao@hit.edu.cn).

Yang Yang, M.Sc. (Ph.D. student): Harbin Institute of Technology/ School of Astronautics/ Division of Dynamics and Control, Harbin Institute of Technology, West Dazhi Street No.92, Nangang District, Harbin 150001, China. (181042yy@163.com).

Wenhu Huang, professor: Harbin Institute of Technology/ School of Astronautics/ Division of Dynamics and Control, Harbin Institute of Technology, West Dazhi Street No.92, Nangang District, Harbin 150001, China. (whhuang@hit.edu.cn)

Optimization of micro-jet dynamical systems cooling after steel welding (MTR259-15)

Tomasz Węgrzyn, Jan Piwnik, Aleksander Borek, Wojciech Tarasiuk

Abstract: The paper focuses on low alloy steel after an innovative welding method with micro-jet cooling. Weld metal deposit (WMD) was carried out for standard MIG process with micro-jet cooling. This method is very promising mainly due to the high amount of acicular ferrite in WMD. That structure corresponds to good mechanical properties, and has a high impact on the toughness of welds. Dynamical systems of micro-jet cooling just after welding can find application in automotive industry.

1. Introduction

Micro-jet technology gives the chance to obtain weld that corresponds to a much better impact toughness of WMD compared to actual welding processes [1-5]. Good mechanical properties of weld correspond to low-nitrogen and low-oxygen processes. The amount of nitrogen and oxygen has a strong influence on the metallographic structure because of the influence on the acicular ferrite (AF) formation. The amount of AF must be treated as the most beneficial structure in low alloy steel WMD that directly corresponds with high impact toughness of weld [6-8]. Acicular ferrite is formed with non-metallic inclusion contact (nitride and oxide inclusions of welds). Even having the optimal inclusion parameters it is only possible to get maximum 50 % of AF in weld [9, 10]. Micro-jet cooling just after welding gives a new chance to increase the amount of AF in weld and consequently micro-jet cooling has an effect on the impact toughness of weld [11-15]. The micro-jet cooling was tested for low alloy steel with various micro-jet gases: argon, helium and nitrogen. First, gas mixtures of argon with carbon dioxide were tested for dynamic micro-jet cooling.

2. Aim and plan of the research

The present paper aims to outline the micro-jet innovations in MIG welding process which represent steps ahead to achieve the following objective:

- a high amount of acicular ferrite in WMD,
- an increase of the impact toughness of WMD.

The weld metal deposit was prepared by welding with micro-jet cooling, with varied gases, and mixtures for MIG welding and dynamic micro-jet cooling process to obtain various amounts

of acicular ferrite in the weld, a welding process with a micro-jet injector was installed. The main parameters of micro-jet cooling were slightly varied:

- cooling steam diameter was varied twice (40 μm and 50 μm),
- number of cooling jets was varied twice (1 and 2),
- gas pressure was varied twice (0.4 MPa until 0.5 MPa),
- micro-jet gases were varied (argon, nitrogen, helium, a gas mixture of 79% Ar and 21% CO_2 gas mixture of 90% Ar and 10% CO_2).

Figure 1 illustrates the assembly of the welding head with the micro-jet injector.

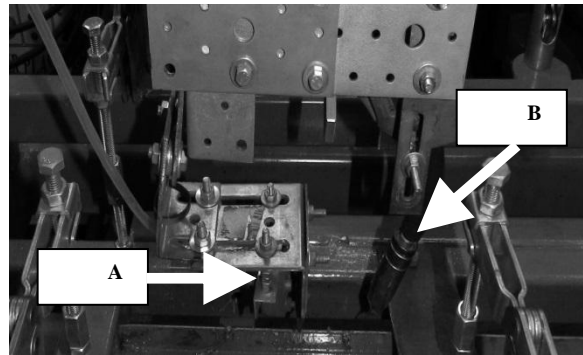


Figure 1. Montage of welding head (B) and micro-jet injector (A).

3. Materials to research

The basic materials to research were S355J2G3 steel. A typical weld metal deposit has rather similar chemical composition in all tested cases, except oxygen amount (table 1). Argon was chosen as the shielded gas for MIG welding in all the cases.

Table 1. Chemical composition of WMD without micro-jet cooling.

Element	Amount
C	0.08%
Mn	0.79%
Si	0.39%
P	0.017%
S	0.018%
O	380 ppm
N	50 ppm

4. Research and discussion

Various welds of standard MIG welding process with and without micro-jet cooling were compared. Micro-jet gas has an influence on the intensive dynamic cooling conditions, but it does not have serious influence on chemical WMD composition. The oxygen amount in the WMD was counted only for the main micro-jet parameters:

- Diameter of micro-stream (40 μm),
- Number of jets (1),
- Gas pressure (0.4 MPa).

A typical weld metal deposit had rather similar chemical composition in all the tested cases, except oxygen amount (Table 2).

Table 2. Oxygen and nitrogen in WMD after MIG welding with micro-jet cooling.

Welding process	Diameter of micro-stream [μm]	Gas pressure [MPa]	Number of jets	Oxygen amount
without micro-jet cooling	-	-	0	380 ppm
He as micro-jet gas	40	0.4	1	375 ppm
Ar as micro-jet gas	40	0.4	1	375 ppm
N ₂ as micro-jet gas	40	0.4	1	385 ppm
Gas mixture of (79% Ar and 21% CO ₂),	40	0.4	1	530 ppm
Gas mixture of (90% Ar and 10% CO ₂),	40	0.4	1	465 ppm

For standard MIG welding, various amount of oxygen in WMD were observed. It is easy to deduce that micro-jet cooling with gas mixtures after welding has a strong influence on the oxygen amount in WMD. After chemical analyses the metallographic structure analysis was carried out. The various amounts of acicular ferrite are shown in Table 3

Table 3. Acicular ferrite in WMD after welding with various micro-jet cooling.

Micro-jet gas	Micro-jet gas pressure [MPa]	Micro-jet diameter [μm]	Ferrite AF
-	-	-	55%
He	0.4	40	60%
He	0.4	50	61%
He	0.5	40	61%
He	0.5	50	59%
Ar	0.4	40	71%
Ar	0.4	50	73%
Ar	0.5	40	73%
Ar	0.5	50	72%
N ₂	0.4	40	53%
N ₂	0.4	50	51%
N ₂	0.5	40	50%
N ₂	0.5	50	49%
79% Ar and 21% CO ₂	0.4	40	64%
79% Ar and 21% CO ₂	0.4	50	69%
79% Ar and 21% CO ₂	0.5	40	68%
79% Ar and 21% CO ₂	0.5	50	66%
90% Ar and 10% CO ₂	0.4	40	68%
90% Ar and 10% CO ₂	0.4	50	70%
90% Ar and 10% CO ₂	0.5	40	71%
90% Ar and 10% CO ₂	0.5	50	68%

Tables 3 shows that in all cases argon is the most beneficial micro-jet gas. Also, the experiment with a gas mixture of 90% Ar and 10% CO₂ can be conducted to be a good choice. Helium must be treated as an intensive cooling gas. Nitrogen as micro-jet gas could be treated as a wrong choice (perhaps because of the higher amount of N in WMD that was not measured). In standard MIG welding process (i.e., without micro-jet cooling) there are higher amounts of grain boundary ferrite (GBF); there are also usually observed and site plate ferrite (SPF) fraction meanwhile after welding with micro-jet cooling both GBF and SPF structures were not so dominant. In all tested cases, MAC (self-tempered martensite, retained austenite, carbide) phases on the level of 3% were also observed. Acicular ferrite with percentage above 70% could be obtained only in two cases: after MIG welding with argon micro-jet cooling and after MIG welding with argon gas mixture (90% Ar and 10% CO₂) micro-jet cooling (shown in Figure 2 and in Table 3).

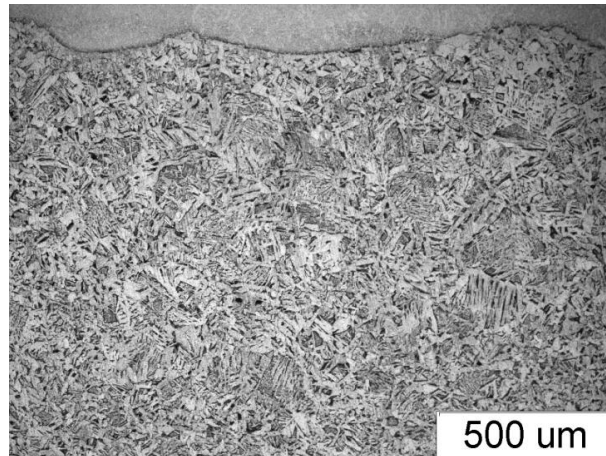


Fig. 2. High amount of acicular ferrite in weld (73%) after an Ar micro-jet cooling.

After the microstructure studies, the Charpy V impact toughness test of the deposited metal were carried out (5 specimens). The Charpy tests were only carried out at temperatures of - 40° C and +20° C. The impact toughness of WMD was determined only for the same micro-jet parameters:

- Diameter: 40 μm,
- Number of jet: only one,
- Gas pressure: only 0.4 MPa.

The impact toughness results are given in Table 4.

Table 4. The impact toughness of WMD after welding with various micro-jet cooling.

Welding method	Micro-jet gases	Impact toughness KCV, J (at - 40° C)	Impact toughness KCV, J (at -20° C)	Impact toughness KCV, J (at +20° C)
MIG	-	43	65	181
MIG with micro-jet	Ar	59	81	195
MIG with micro-jet	He	51	64	182
MIG with micro-jet	N ₂	below 40	46	155
MIG with micro-jet	79% Ar and 21% CO ₂	53	76	191
MIG with micro-jet	90% Ar and 10% CO ₂	56	79	193

It is possible to deduce that impact toughness at ambient and negative temperature (-20° C and -40° C) of weld metal deposit is apparently affected by different types of micro-jet cooling. Micro-jet technology always has a strong effect on the impact toughness of WMD. Argon and gas mixture of 90% Ar and 10% CO₂ might be treated as proper micro-jet gases.

5. Conclusion

The results confirm that for low alloy steel welding there are two general types of tests performed: impact toughness and microstructure. Acicular ferrite and MAC phases (self-tempered martensite, upper and lower bainite, retained austenite, carbides) were fully analysed and counted for each weld metal deposit. The innovative micro-jet technology was firstly recognized successfully for MIG welding. In paper dynamic micro-jet cooling technology was also precisely described and tested for MIG welding process with various micro-jet gases: argon, helium, nitrogen, and various gas mixtures of argon and carbon dioxide. On the basis of investigation it is possible to deduce that micro-jet technology could be important complement of both welding methods: MIG and MAG. An important part of this article was to analyse impact toughness of welds after various dynamic micro-jet cooling. Final conclusions:

- micro-jet cooling could be treated as an important element of MIG welding processes,

- b) micro-jet cooling after welding can prove a significant amount of ferrite AF, the most beneficial phase in low alloy steel WMD,
- c) argon or gas mixture of argon and carbon dioxide could be conducted to be the optional micro-jet gases for low alloy steel welding processes for MIG process,
- d) helium and nitrogen could not be treated as a good choice for low alloy steel micro-jet welding; however micro-jet helium cooling gives better results than simple MIG/MAG welding without micro-jet cooling.

References

- [1] Węgrzyn T., Piwnik J., Wieszała J., Hadryś D.: Control over the steel welding structure parameters by micro-jet cooling, *Archives of Metallurgy and Materials*, ISS 1, Vol 57, 2012, no 3, pp. 679-685.
- [2] Piwnik J., Hadryś D., Skorulski G.: Plastic properties of weld after micro-jet cooling ; *Journal of Achievements in Material and Manufacturing Engineering*, Vol 59, 2013, No 1, pp. 20-25.
- [3] Węgrzyn T.: The Classification of Metal Weld Deposits in Terms of the Amount of Oxygen. *PROC OF ISOPE 1999*,Cupertino – California – USA IV,1999, pp. 212 – 216.
- [4] Węgrzyn T.: The Classification of Metal Weld Deposits in Terms of the Amount of Nitrogen. *PROCEEDINGS of ISOPE'2000*, Seattle, USA, 2000, pp. 130 – 134.
- [5] Szczucka-Lasota B., Formanek B., Hernas A., Szymański K.: Oxidation models of the growth of corrosion products on the intermetallic coatings strengthened by a fine dispersive Al₂O₃, *Journal of Materials Processing Technology*, Volumes 164-165, 2005, pp. 935-939.
- [6] Formanek B., Józwiak S., Szczucka-Lasota B., Dolata-Grosz A., Bojar Z., Intermetallic alloys with ceramic particles and technological concept for high loaded materials, *Journal of Materials Processing Technology*, Volumes 164-165, 2005, pp. 850-855.
- [7] Formanek B., Szymański K., Szczucka-Lasota B.: New generation of protective coatings intended for the power industry, *Journal of Materials Processing Technology*, Volumes 164-165, 2005, pp. 850-855.
- [8] Słania J.: "Influence of phase transformations in the temperature ranges of 1250-1000°C and 650-350°C on the ferrite content in austenitic welds made with T 23 12 LRM3 tubular electrode", *Metallurgy and Materials*, Vol 3/2005.
- [9] Burdzik R., Folega P., Łazarz B., Stanik Z., Warczek J.: Analysis of the impact of surface layer parameters on wear intensity of friction pairs, *Archives of Metallurgy and Materials*, Vol. 57, 2012, No 4, pp. 987– 993.
- [10] Burdzik R.: Research on the influence of engine rotational speed to the vibration penetration into the driver via feet - multidimensional analysis, *Journal of Vibroengineering*, Vol. 15 , 2013, No 4, pp. 2114 – 2123.

- [11] Lukaszewicz K., Kriz A., Sondor J.: "Structure and adhesion of thin coatings deposited by PVD technology on the X6CrNiMoTi17-12-2 and X40 CrMoV5-1 steel substrates", *Materials Science and Engineering*, Vol. 51, pp. 40-47.
- [12] Yoshifumi A., Hozumi G.: Friction and wear of carbon steel near T1-transition under dry sliding, *Tribology International*, Vol. 39, 2006, pp. 756 – 762.
- [13] Lisiecki A.: Diode laser welding of high yield steel. Proc. of SPIE Vol. 8703, *Laser Technology 2012: Applications of Lasers*, 87030S (January 22, 2013), DOI: 10.1117/12.2013429.
- [14] Lisiecki A.: Welding of titanium alloy by Disk laser. Proc. of SPIE Vol. 8703, *Laser Technology 2012: Applications of Lasers*, 87030T (January 22, 2013), DOI: 10.1117/12.2013431.
- [15] Tarasiuk W., Szczucka-Lasota B., Piwnik J., Majewski W.: Tribological Properties of Super Field Weld with Micro-Jet Process, *Advanced Materials Research* 1036, 452-457 (2014), DOI:10.4028/www.scientific.net/AMR.1036.452.

Tomasz Węgrzyn, dr hab. inż., TECHNICAL UNIVERSITY OF SILESIA, Transport Department, PL, (tomasz.wegrzyn@polsl.pl)
The author gave a presentation of this paper during one of the conference sessions.

Jan Piwnik, Professor, BIALYSTOK UNIVERSITY OF TECHNOLOGY, Mechanical Faculty, PL, (j.piwnik@pb.edu.pl)

Aleksander Borek, PLASMA-SYSTEM, PL, (borek@systems.pl)

Wojciech Tarasiuk, Ph.D., BIALYSTOK UNIVERSITY OF TECHNOLOGY, Mechanical Faculty, PL, (w.tarasiuk@pb.edu.pl)

Mathematical model for two-dimensional dry friction modified by dither (NON052-15)

Adam Wijata, Jan Awrejcewicz, Jan Matej, Michał Makowski

Abstract: A new dynamic two-dimensional friction model is developed which is based on the bristle theory. Actually it is the Reset Integrator Model converted into a two-dimensional space. Usually two-dimensional friction models are indeed one-dimensional models which are rotated into the slip velocity direction. However, this often used approach cannot be applied to the bristle model. That is why an idea of a two-dimensional bristle is presented. Bristle's deformation is described using polar coordinates. The carried out numerical simulation of a planar oscillator has proved that the new model correctly captures the mechanism of smoothing dry friction by dither applied via perpendicular and co-linear way regarding the body velocity. Furthermore, the introduced mathematical model captures two-dimensional stick-slip behaviour. The Cartesian slip velocity components are the only inputs to the model. In addition, our proposed model allows to describe a friction anisotropy using the bristle parameters. The paper contains results of an experimental verification of the new friction model conducted on the special laboratory rig being used to investigate the two-dimensional motion in the presence of dither as well as to validate our numerical results.

1. Introduction

Although friction belongs to natural and common phenomena, it is still difficult to find a general mathematical model for friction force being valid in various regimes of contact dynamics of machine elements. Fundamental problem in friction modelling is discontinuity in transition from sticking to slipping phase of motion. Even in sticking phase some microscopic motion occurs, which is called pre-sliding displacement. A force needed to initiate macroscopic motion is called break-away force. It was experimentally proven, that this force changes with a rate of increase of external force applied to contacting bodies. During motion a friction force is referred as kinetic friction. There are static effects applied to kinetic friction like Stribeck or viscous friction effects. On the other hand and from dynamical point of view there exists a hysteresis effect called frictional lag which applies to kinetic friction [1].

Over the years any general theory of friction, which explains all frictional effects has not been developed yet. On the other hand numerous mathematical models were created. In general friction models can be divided into two classes: static and dynamic models. Static models are those which describe friction phenomenon only as a function of a slip velocity. This category includes classical models, the Karnopp model and Armstrong's model. In many cases internal state variables and the appropriate differential equations are used as the attributes of dynamic friction models. Examples of

dynamic models are the Dahl model, the bristle model, the reset integrator model and the LuGre model [2,3,4].

2. Smoothing dry friction by dither

Dither is a word for intentionally introduced vibrations or noise. In mechanical systems with friction, vibrations of one of contacting bodies can be understood as dither. Dither may influence friction characteristic essentially. In general it plays an important role since it smoothes transition from stick to slip regimes. In addition, dither can be used to quench or even eliminate a harmful stick-slip behaviour. Noticeable effect of introducing dither into mechanical system is realised via change of system's damping character. It is a well-known that oscillatory motion damped only with dry-friction decays with straight-line envelopes. After introducing dither, envelopes change into exponential shapes. It means that dither changes dry friction damping into viscous damping. Furthermore, this effect possesses a directional property. Namely, the motion co-linear with dither is lightly damped in comparison to the motion perpendicular to it. However, the mechanism of modification for dither perpendicular to and co-linear with the body velocity is different. A role of the crucial parameter which influences the friction damping plays an amplitude of dither velocity.

For dither co-linear with body velocity the resultant slip velocity can be described as a difference between body velocity and dither velocity. Assuming friction described by simple Coulomb model, friction force reaches the value $\pm F_C$ depending on a slip velocity sign, where F_C denotes here the Coulomb friction force.

Dither perpendicular to body velocity actually makes friction two-dimensional. Friction force is directed opposite to resultant slip velocity. Components of friction force are proportional to components of slip velocity, i.e. dither and body velocity. It means that, the friction force component co-linear with body velocity is modulated by both body and dither velocity. The so far given brief description can be treated as an introduction to the detailed analysis on the mechanism of smoothing dry friction by dither presented in reference [5].

3. The new model of two-dimensional dry friction and numerical experiments

The developed friction model is a two-dimensional interpretation of the reset integrator model, presented by Haessing and Friedland in 1991 [3]. Bristle theory introduced and developed in reference [3] concerns frictions as effect of contact and deformation of irregularities of contacting surfaces. In the reset integrator model this effect is approximated by a single bristle. Strain of the bristle (z) is the internal state variable of the model. Strain is increasing till limiting value z_0 is reached, which can be interpreted as the stiction range. After reaching this value, strain is kept on a constant level, what in-

deed represents a slipping phase of the studied motion. An idea of bristle's strain and generation of friction force is presented in Fig. 3.1, where the variable z is governed by the following equation:

$$\frac{dz}{dt} = \begin{cases} 0 & \text{if } v_s > 0 \text{ and } z \geq z_0 \\ 0 & \text{if } v_s < 0 \text{ and } z \leq z_0 \\ v_s & \text{otherwise} \end{cases} \quad (3.1)$$

Friction force is divided into static and kinetic friction, whereas bristle's strain z plays the role of a switching variable:

$$F_F = \begin{cases} \sigma_0(1+a)z + \sigma_1 \frac{dz}{dt} & \text{if } |z| < z_0 \\ \sigma_0 z & \text{if } |z| \geq z_0 \end{cases} \quad (3.2)$$

In equation (3.2) σ_0 is the bristle stiffness, a is the stiction gradient and σ_1 stands for the damping parameter.

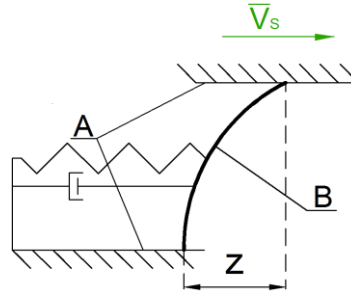


Figure 3.1. Bristle deformation: (A) contacting bodies, (B) bristle, (Z) – bristle's strain

In reference [6] two-dimensional model for investigation of stick-slip motion is presented. Components of friction force are calculated on the basis of *friction direction angle* concept, which is defined by both slip velocity and applied force. On the other hand the friction model presented in [5] allows for introducing anisotropy into friction force description. Friction force angle is chosen using the principle of maximum energy dissipation. Both models can be considered as one-dimensional models which are rotated with respect to the vector of the slip velocity. However, this approach cannot be applied to converting dynamic friction models into two-dimensional space. It is especially useless as far as interpretation of internal state variable is based on the bristle theory. Simple rotating of such a model results in loss of capturing spring-like behaviour before gross sliding occurs. It could even lead to not detecting transition between sticking and slipping phase of the studied motion. Frictional lag phenomenon is also lost. In conclusion, majority of advantages of these models is lost. That is why a different approach is highly required with respect to transformation of bristle models into a two-dimensional space.

A role of the basic parameter of every bristle model plays a stiction range. In the case of planar motion, stiction range should be described by the following planar set:

$$\Theta_z = \{ \mathbf{Z} \in \mathbb{R}^2, \Phi_z(\mathbf{Z}) \leq 0 \}. \quad (3.3)$$

In our further investigation $\Phi_z(\mathbf{Z})$ is governed by a circle formula with a radius being equal to the required pre-sliding displacement. In other words, it means that the isotropic stiction range has been assumed.

In order to obtain an appropriate physical character of the bristle model, its two-dimensional interpretation must ensure deforming bristle in two directions and hold resultant deformation during slipping phase of motion. During a planar motion the slip velocity can change its direction without obtaining value equal to zero or even without changing this value at all. It means that in the slipping phase, deformation of bristle must be hold at the same level, while its components may change. One may say that the bristle “rotates to the direction of a slip”. The so far carried out consideration leads to division of the bristle deformation into two components, i.e. rotation and strain. This division gives motivation to choose polar coordinates as the appropriate one for description of the bristle deformation:

$$\mathbf{Z} = \begin{bmatrix} z_r \\ z_\varphi \end{bmatrix}. \quad (3.4)$$

This choice has its consequences in description of the internal state variable \mathbf{Z} . Slip velocity is distributed into two components: rotational v_φ and radial one v_r , which is co-linear with the deformed bristle. Mechanism of this division is shown in Fig. 3.2 Rotational component v_φ forces the bristle to rotate into current slip velocity direction, whereas radial component v_r is responsible for regulation of bristle’s strain.

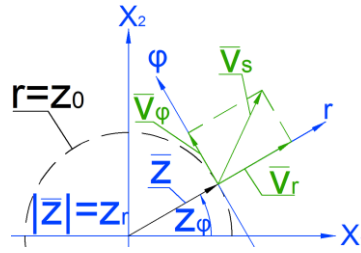


Figure 3.2. Mechanism of dividing slip velocity

Resulting description of variable \mathbf{Z} dynamic is described by the following equations:

$$\frac{dz_r}{dt} = \begin{cases} 0 & \text{if } v_r > 0 \text{ and } z_r \geq z_0 \\ 0 & \text{if } v_r < 0 \text{ and } z_r \leq z_0 \\ v_r & \text{otherwise} \end{cases}, \quad (3.5)$$

$$\frac{dz_\phi}{dt} = \frac{v_\phi}{z_r}.$$

The friction force originates from the bending of the bristle. The scheme shown in Fig. 3.3 illustrates an idea of generating two-dimensional vector of the friction force. Although the bristle deformation is described by polar coordinates, the resulting friction force is given in Cartesian coordinates. In order to make our model more application oriented, the transition into polar coordinates is carried out inside the model. It means that both input and output of the model are presented in Cartesian coordinates. Like in the reset integrator model (RIM), two different components of the sticking and slipping phase while describing the friction force are introduced:

$$\mathbf{F}_F = \begin{bmatrix} F_{F1} \\ F_{F2} \end{bmatrix} = \begin{cases} \begin{bmatrix} \sigma_{01}(1+a_1)z_1 + \sigma_{11}\dot{x}_1 \\ \sigma_{02}(1+a_2)z_2 + \sigma_{12}\dot{x}_2 \end{bmatrix} & \text{if } z_r < z_0 \\ \begin{bmatrix} \sigma_{01}z_1 \\ \sigma_{01}z_2 \end{bmatrix} & \text{if } z_r \geq z_0 \end{cases} \quad (3.6)$$

Description of the friction force by equation (3.6) makes it possible to use hints from paper [3] regarding a selection of parameters of the model. Even though stiction range is assumed to be isotropic, anisotropy of friction can be introduced in description of each friction force component separately. Actually there are three parameters for both directions introduced, which can be set independently.

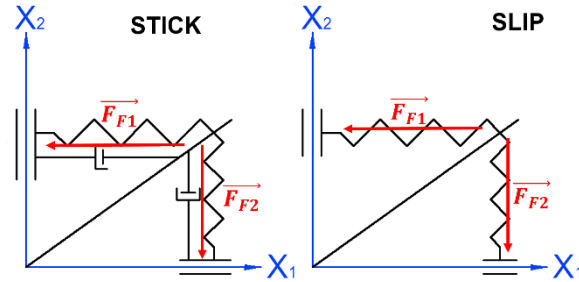


Figure 3.3. Idea of generating two-dimensional friction force

A few numerical experiments concerning application of the new friction model exhibiting the introduced damping parameters σ_{11} and σ_{12} as velocity dependent has been carried out. Actually they decrease with velocity increasing, owing to the following formula [1]:

$$\sigma_i(v_s) = \sigma_i \exp \left[- \left(\frac{v_s}{a_v} \right)^2 \right], \quad (3.7)$$

where the parameter a_v is small (for instance of order 10^{-2}).

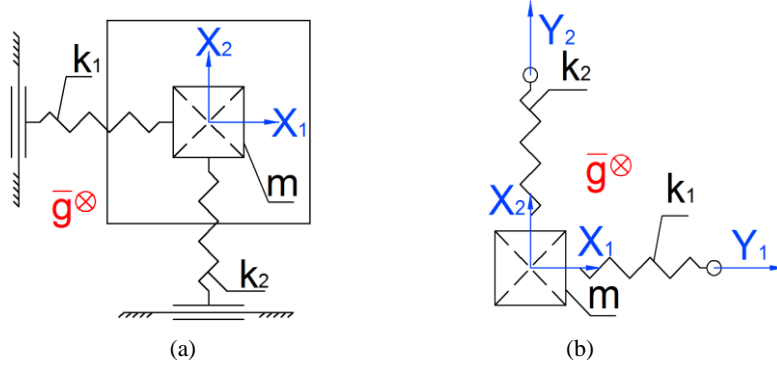


Figure 3.4. Planar oscillator (a) and spring-mass system for stick-slip investigation (b)

In order to validate numerical computation, a simple planar oscillator (Fig. 3.4(a)) has been studied with following fixed parameters and initial conditions:

- (i) friction parameters: $\sigma_{01} = \sigma_{02} = 10^2 [\text{N m}^{-1}]$, $\sigma_{11} = \sigma_{12} = 74,15 [\text{N s m}^{-1}]$, $a = 0,1 [-]$, $z_0 = 10^{-2} [\text{m}]$;
- (ii) oscillator parameters: $m = 1 [\text{kg}]$, $k_1 = k_2 = 100 [\text{N m}^{-1}]$;
- (iii) initial conditions: $x_1(t_0) = x_2(t_0) = 0,08 [\text{m}]$, $v_1(t_0) = -0,8 [\text{m s}^{-1}]$,
 $v_2(t_0) = 0,8 [\text{m s}^{-1}]$, $z_r(t_0) = 10^{-4} [\text{m}]$, $z_\phi(t_0) = 135 [^\circ]$.

Displacement of the body in two, perpendicular directions is shown in Fig. 3.5. Observe that both x_1 and x_2 displacements are decaying with straight-line envelopes, what is characteristic feature for motion damped by dry friction. Fig. 3.6 shows polar diagram of radial and rotational components of the internal state variable z . Actually, this diagram shows trajectory of bristle deformation during the simulated motion. As can be seen, components of two-dimensional friction force are proportional to bristle's deformation, except the place where sticking phase begins, what has to be expected.

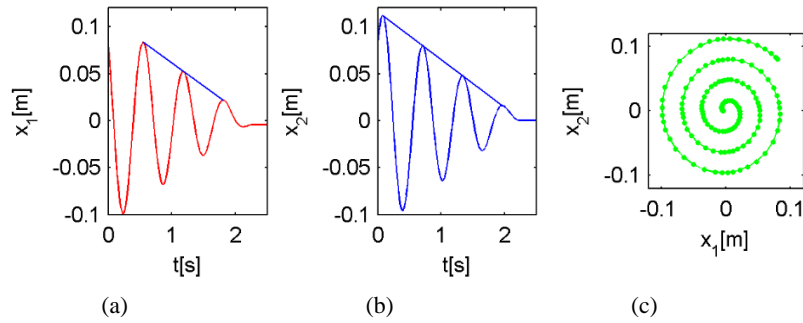


Figure 3.5. Simulation results: displacements $x_1(t)$ (a) and $x_2(t)$ (b) versus time and trajectory (c)

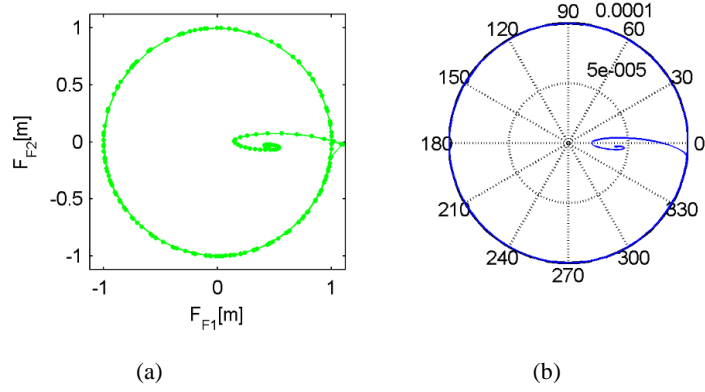


Figure 3.6. Simulation results: two-dimensional friction force (a) and bristle trajectory (b)

Next, experiment concerning two-dimensional stick-slip behaviour has been conducted regarding the system shown in Fig. 3.4 (b) for the following fixed parameters: $x_1(t_0) = x_2(t_0) = 0[\text{m}]$, $v_1(t_0) = v_2(t_0) = 0[\text{m s}^{-1}]$, $z_r(t_0) = 10^{-4}[\text{m}]$, $z_\varphi(t_0) = 135[^\circ]$, $v_{y1} = 0,01[\text{m s}^{-1}]$, $v_{y2} = 0,005[\text{m s}^{-1}]$, $v_{y1} = v_{y2} = \text{const}$. Friction and system parameters are the same as in the previous simulation.

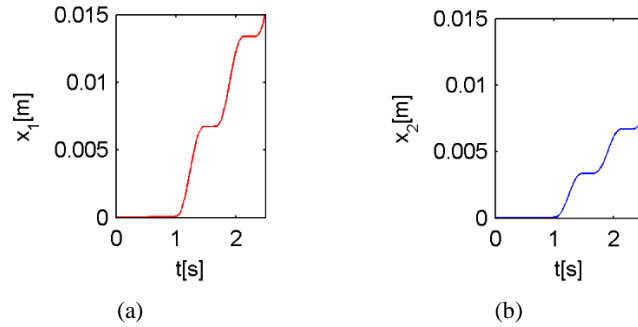


Figure 3.7. Time histories of the stick-slip behavior: (a) $x_1(t)$, (b) $x_2(t)$

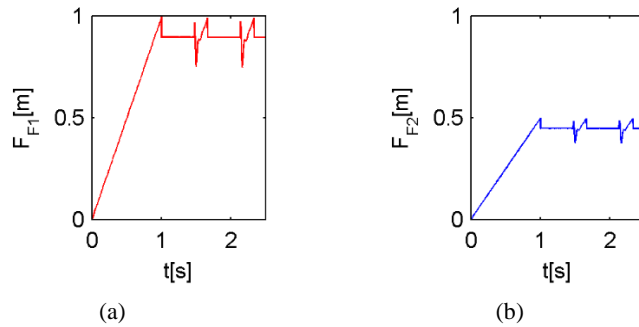


Figure 3.8. Time histories of the friction force: (a) $F_{F1}(t)$, (b) $F_{F2}(t)$

Fig. 3.7 and Fig. 3.8 present simulation results, which capture two-dimensional stick-slip behaviour.

5. Conclusions

The new model of two-dimensional friction has been proposed and validated numerically and experimentally. The proposed model is two-dimensional interpretation of the Reset Integrator Model presented by Haessing and Friedland in reference [3] as more computational efficiency version of the bristle model (presented in the same paper). One-dimensional model was converted into two-dimensional space with usage of original two-dimensional bristle concept. The developed by us model allows introducing anisotropy of friction in bristle parameters. It has been tested numerically regarding capturing two-dimensional stick-slip effect and mechanism of smoothing friction by dither. Furthermore the experimental verification has been carried out using special laboratory rig. The carried out laboratory experiments dealt with 2D friction modified and not by dither. Results obtained from the experiment and numerical simulation have shown good agreement, which validates our 2d friction model.

Acknowledgements

The work has been supported by the Polish National Science Centre, MAESTRO 2, No. 2012/04/A/ST8/00738.

References

- [1] K. Canudas de Wit C. Gafvert M. Lischinsky P. Olson, H. Astrom. Friction models and friction compensation. *European Journal of Control*, 4(1998):176–195, 1998.
- [2] Dahl P. R. A solid friction model. The Aerospace Corporation, California, 1968.
- [3] Friedland B. Haessig, Jr. D.A. On the modeling and simulation of friction. *Journal of Dynamic Systems, Measurements, and Control*, 113:354–362, 1991.
- [4] C.C. De Wit, H. Olsson, K.J. Astrom, and P. Lischinsky. A new model for control of systems with friction. *Automatic Control, IEEE Transactions on*, 40(3):419–425, Mar 1995.
- [5] J. Piotrowski. Smoothing dry friction damping by dither generated in rolling contact of wheel and rail and its influence on ride dynamics of freight wagons. *International Journal of Vehicle Mechanics and Mobility*, 48(6):675–703, 2010.
- [6] F. Xia. Modelling of a two-dimensional coulomb friction oscillator. *Journal of Sound and Vibration*, 265(2003):1063–1074, 2002.

Jan Awrejcewicz, Professor: Lodz University of Technology, Department of Automation, Biomechanics and Mechatronics, 1/15 Stefanowski Str., 90-924 Lodz, Poland (jan.awrejcewicz@p.lodz.pl).

Jan Matej, Ph.D/ D.Sc.: Warsaw University of Technology, Department of Vehicles, 84 Narbutta Str., 02-524 Warsaw, Poland (jmt@simr.pw.edu.pl)

Michał Makowski, Ph.D.: Warsaw University of Technology, Department of Vehicles, 84 Narbutta Str., 02-524 Warsaw, Poland (michal.makowski@simr.pw.edu.pl)

Adam Wijata, Ph.D. student: Lodz University of Technology, Department of Automation, Biomechanics and Mechatronics, 1/15 Stefanowski Str., 90-924 Lodz, Poland (wijataadam@gmail.com).

Mathematical model of pennate muscle (LIF043-15)

Wiktoria Wojnicz, Bartłomiej Zagrodny, Michał Ludwicki,
Jan Awrejcewicz, Edmund Wittbrodt

Abstract: The purpose of this study is to create a new mathematical model of pennate striated skeletal muscle. This new model describes behaviour of isolated flat pennate muscle in two dimensions (2D) by taking into account that rheological properties of muscle fibres depend on their planar arrangement. A new mathematical model is implemented in two types: 1) numerical model of unipennate muscle (unipennate model); 2) numerical model of bipennate muscle (bipennate model). Applying similar boundary conditions and similar load, proposed numerical models had been tested. Obtained results were compared with results of numerical researches by applying a Hill-Zajac muscle model (this is a Hill type muscle model, in which the angle of pennation is taken into consideration) and a fusiform muscle model (a muscle is treated as a structure composed of serially linked different mechanical properties parts).

1. Introduction

The human movement system consists of striated skeletal muscles that have different architectures. Among these muscles are fusiform muscles and pennate muscles (unipennate muscles, bipennate muscles and multipennate muscles) [7]. The fusiform muscle fibers run generally parallel to the muscle axis (it is line connecting the origin tendon and the insertion tendon). The unipennate muscle fibers run parallel to each other but at the pennation angle to the muscle axis [6]. The bipennate muscle consists of two unipennate muscles that run in two distinct directions (i.e. different pennation angles). The multipennate muscle is composed of a few bundles of fibers that run in distinct directions.

From the physiology point of view the unipennate muscle consists of three parts: the muscle insertion ('muscle – insertion tendon' connection), the belly (muscle fibers), and the muscle origin ('muscle – origin tendon' connection). It is assumed that during contraction the belly maintains the isovolume, each tendon moves only along its axis and muscle fibers become more pennated (the pennation angle is increased) [12].

The spatial arrangement of pennate muscle fibres determines the muscle fibres length, the lengths of tendons and mechanical properties of muscle. That is why the contractile characteristic (i.e. force-generating capacity) depends on the pennation angle [6]. Moreover, one should take into consideration that a real pennate muscle is a non-homogenous structure: the distal muscle fascicles

tend to contract more (i.e. they act at greater pennation angles) than the more proximal muscle fascicles.

Applying an imaging techniques, such as nuclear magnetic resonance (MRI) and ultrasonography (US), with a motion analysis techniques, one might perform *in vivo* non-invasive measurements to estimate volumes of muscles, muscle fibres lengths and pennation angles [6]. However, one should perform invasive measurements to obtain [1]: 1) mechanical properties values (by applying tensile tests and sonomicrometry); 2) muscle morphology and architecture evaluated at the microscopic level (by using a muscle biopsy); 3) muscle static characteristic (length-force dependence); 4) muscle dynamic characteristic (velocity-force dependence); 5) muscle-tendon parameters used in the Hill-type muscle model. That is why a very limited amount of data describing mechanical properties of pennation muscles can be found in literature.

To model behaviour of pennate muscle one should take into consideration that spatial arrangement of muscle fibers influence mechanical properties and contractile properties of this muscle. Nowadays, to describe pennate muscle function in muscle biomechanics there are applied rheological models: Hill-type muscle models and Hill-Zajac muscle models [4,12]. However, application of these models is very limited due to problems related to the obtainment of model parameters.

The purpose of this study is to create a new mathematical model of pennate striated skeletal muscle that describes behaviour of isolated flat pennate muscle in two dimensions (2D) by taking into account that rheological properties of muscle fibres depend on their planar arrangement. A new mathematical model is implemented in two types: 1) numerical model of unipennate muscle (unipennate model); 2) numerical model of bipennate muscle (bipennate model).

2. Pennate muscle modelling

2.1 Principles of modelling

The mathematical models of unipennate muscle and bipennate muscle were created on the base of a deformation schema of unipennate muscle shown in the Figure 1. According to this deformation schema, the muscle contraction occurs in the plane (two-dimension space) along muscle fibers directed at the pennation angle α_p towards the line connecting the muscle insertion (it is a movable part with one degree of freedom) and the muscle origin (it is a non-movable part). It is assumed that during muscle contraction the muscle width tt is constant (according to [5]) and muscle fibers generate a contractile muscle force F_m , which causes the displacement of muscle insertion x and counterbalances an external force F_{ext} :

$$F_{ext} = F_m \cdot \cos \alpha_p . \quad (1)$$

During contraction the muscle fibers are shortening and the muscle insertion is translated from the point B to the point B' (the distance BB' is equal to x). It causes the change of pennation angle: the initial value of pennation angle α_{po} (at the length of muscle equals AB), is changed to the value α_p (at the length of muscle equals AB'). Analyzing the deformation schema of unipennate muscle, the following relation can be derived:

$$tt = AB \cdot \cos \alpha_{po} = AB' \cdot \cos \alpha_p. \quad (2)$$

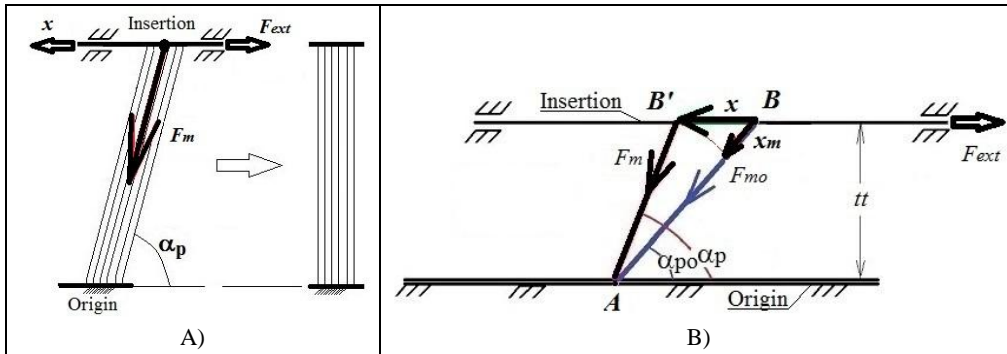


Figure 1. Deformation schema of unipennate muscle:

A) directions of acting of external force F_{ext} and contractile muscle force F_m towards the muscle insertion displacement x ; B) schema of deformation of unipennate muscle (AB – the initial length of muscle (before contraction); AB' – the finish length of muscle (after contraction); F_{mo} – initial contractile muscle force at the length of muscle equals AB ; F_m – finish contractile muscle force at the length of muscle equals AB' ; α_{po} – the pennation angle before contraction (at the length of muscle equals AB); α_p – the pennation angle after contraction (at the length of muscle equals AB'); x_m – change of muscle length that is equal to the difference of the length AB and the length AB').

Taking into consideration a deformation schema of unipennate muscle, five rheological models were created:

- 1) Unipennate muscle model WW (the author is Wiktoria Wojnicz) (part 2.2);
- 2) Unipennate muscle model BZ (the author is Bałomiej Zagrodny) (part 2.3);
- 3) Hill-Zajac unipennate muscle model (part 2.4);
- 4) The bipennate muscle model WW (the author is Wiktoria Wojnicz) (part 2.5);
- 5) The bipennate muscle model BZ (the author is Bałomiej Zagrodny) (part 2.6).

Assuming that the time variable is t , proposed models can be applied to solve the dynamics task formulated in three following problems:

- 1) Input variables are the insertion displacement $x(t)$ and the external force $F_{ext}(t)$; output variables are the internal force $P^w(t)$ (this force is generated by the contractile elements of muscle model and it causes an appearing of contractile muscle force $F_m(t)$), the pennation angle $\alpha_p(t)$ and deformations of muscle model parts (for chosen muscle models);

- 2) Input variables are the insertion displacement $x(t)$ and the internal force $P^w(t)$; output variables are the external force $F_{ext}(t)$, the pennation angle $\alpha_p(t)$ and deformations of muscle model parts (for chosen muscle models);
- 3) Input variables are the external force $F_{ext}(t)$ and the internal force $P^w(t)$; output variables are the insertion displacement $x(t)$, the pennation angle $\alpha_p(t)$ and deformations of muscle model parts (for chosen muscle models).

2.2. Unipennate muscle model WW

The unipennate muscle model WW describes behaviour of unipennate muscle with the pennation angle equals α_p (Figure 2). This muscle behaviour is described by the rheological model created on the base of the rheological model of fusiform muscle published in [10,11]. The rheological model of unipennate muscle model WW is composed of serially linked three fragments (two passive (non-contractile) fragments and one active (contractile) fragment) that describe different mechanical properties of muscle parts. Each fragment is composed of mass element, elastic element and viscous element. Active fragment has additionally a contractile element that models an ability of muscle to contract. Two lateral fragments model the passive muscle parts (muscle-tendon connections of the muscle insertion and the muscle origin). One middle fragment models the active muscle part (i.e. muscle belly). This model has three degrees of freedom. According to this model: 1) the difference of displacements $(x_0 - x_1)$ describes the change of upper passive muscle fragment; 2) the difference of displacements $(x_1 - x_2)$ describes the change of middle active muscle fragment; 3) the displacement x_2 describes the change of lower passive muscle fragment.

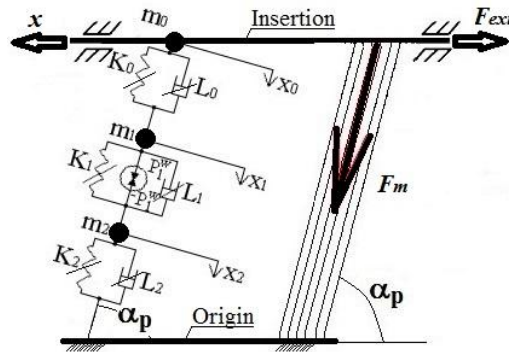


Figure 2. Unipennate muscle model WW (rheological model).

The mathematical model of the unipennate muscle model WW is described by the system of three differential equations:

$$\begin{aligned}
m_0 \cdot \ddot{x} + L_0 \cdot (\dot{x}_0 - \dot{x}_1) \cdot \cos \alpha_p + K_0 \cdot (x_0 - x_1) \cdot \cos \alpha_p &= -F_{ext}(t) \\
m_1 \cdot \ddot{x}_1 + L_0 \cdot (\dot{x}_1 - \dot{x}_0) + K_0 \cdot (x_1 - x_0) + L_1 \cdot (\dot{x}_1 - \dot{x}_2) + K_1 \cdot (x_1 - x_2) &= P_1^w(t) \\
m_2 \cdot \ddot{x}_2 + L_1 \cdot (\dot{x}_2 - \dot{x}_1) + K_1 \cdot (x_2 - x_1) + L_2 \cdot \dot{x}_2 + K_2 \cdot x_2 &= -P_1^w(t)
\end{aligned} \tag{3}$$

and following geometrical relations:

$$\alpha_p = \arcsin\left(\frac{l_0 \cdot \sin \alpha_{po}}{l_0 - x_0}\right), \tag{4A}$$

$$x_0 = l_0 + \frac{x \cdot \cos \alpha_{po} - l_0}{\cos(\alpha_p - \alpha_{po})}, \tag{4B}$$

$$\dot{x}_0 = \frac{dx_0}{dt} = \frac{\dot{x} \cdot \cos \alpha_{po}}{\cos(\alpha_p - \alpha_{po}) - A(x_0) \cdot \sin(\alpha_p - \alpha_{po}) \cdot (x_0 - l_0)}, \tag{4C}$$

$$A(x_0) = \frac{l_0 \cdot \sin \alpha_{po}}{(l_0 - x_0)^2} \cdot \frac{1}{\sqrt{1 - \left(\frac{l_0 \cdot \sin \alpha_{po}}{l_0 - x_0}\right)^2}}, \tag{4D}$$

where: m_j – mass of the j -th element; K_j – stiffness coefficient of the j -th elastic element; L_j – damping coefficient of the j -th viscous element; $P_1^w(t)$ – internal force of the contractile element; l_0 – initial length of muscle model; α_{po} – initial pennation angle when the length of muscle model is equals to l_0 .

2.3. Unipennate muscle model BZ

The unipennate muscle model BZ describes behaviour of unipennate muscle with the pennation angle equals α_p (Figure 3). This model is similar to the unipennate muscle model WW (part 2.2). The unipennate muscle model BZ takes into consideration that stiffness and dumping characteristics of skeletal muscle is described by a nonlinear relationship according to [2,9]:

- 1) $K_j = k_j \cdot x_j^2, j = w, z, 1, 2$, where k_j is a correction factor of stiffness;
- 2) $C_j = c_j \cdot \dot{x}_j^2, j = w, z, 1, 2$, where c_j is a correction factor of damping.

Applying the geometrical relations (4A – 4D), the mathematical model of unipennate muscle model BZ is described by the system of two following equations:

$$\begin{aligned}
m_w \cdot \ddot{x}_w + C_w \cdot \dot{x}_w + K_w \cdot x_w - \frac{C_z \cdot (\dot{x}_z - \dot{x}_1) + K_z \cdot (x_z - x_1)}{\cos \alpha_p} &= P_w(t) \\
m_z \cdot \ddot{x}_z - C_z \cdot (\dot{x}_z - \dot{x}_1) - K_z \cdot (x_z - x_1) &= -F_{ext}(t)
\end{aligned} \tag{5}$$

where: $x_1 = x_w \cdot \cos \alpha_p$; x_w – displacement of mass m_w ; x_z – displacement of mass m_z .

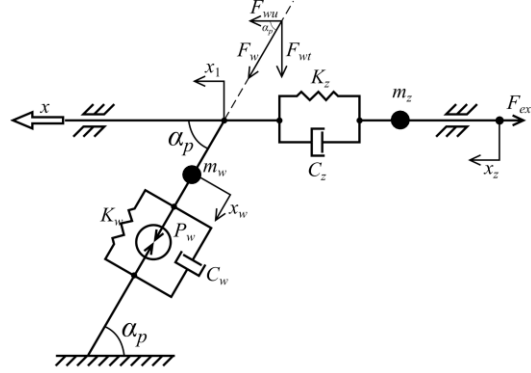


Figure 3. Unipennate muscle model BZ.

2.4. Hill-Zajac unipennate muscle model

The Hill-Zajac unipennate muscle model describes behaviour of unipennate muscle by using the Hill-type muscle model and Zajac muscle model (this is a Hill type muscle model, in which the angle of pinnation α_p is taken into consideration). There are a lot of modifications of these models [4,12]. In this paper it was assumed that Hill-Zajac unipennate muscle model has a rheological structure shown in the Figure 4. In this model the muscle length is the sum of belly length $L_m/\cos(\alpha_p)$ and tendon length L_t . Mechanical properties of muscle are described by using a mass element M (this is a muscle mass reduced to a point) and parallel linking of three elements: a contractile element that generates a force F_{CE} (it depends on the actual muscle length l , velocity of muscle fibers contraction and activation Act that originate from a nervous system), a parallel elastic element described by a stiffness coefficient equals K_{PE} and a viscous element described by a damping coefficient equals L . Tendon behaviour is modelled by using an elastic element and its force depends on the tendon stiffness coefficient K_t and the tendon elongation described by a difference of displacements $(x_t - x)$.

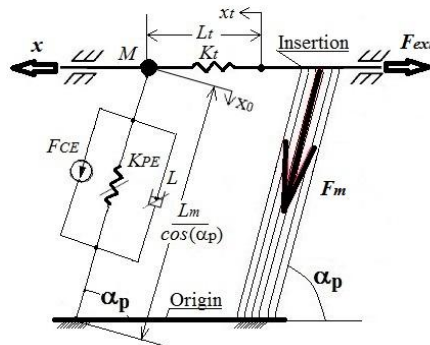


Figure 4. Hill-Zajac unipennate muscle model (rheological model).

The mathematical model of Hill-Zajaca unipennate muscle model is described by the system of two equations:

$$\begin{aligned} F_{ext} + K_t \cdot (x - x_t) &= 0 \\ M \cdot \ddot{x} + K_t \cdot (x - x_t) &= F_m \cdot \cos \alpha_p \end{aligned} \quad (6)$$

where the contractile muscle force is equals to:

$$F_m = F_{CE} - K_{PE} \cdot x_0 - L \cdot \dot{x}_0 \quad (7)$$

It was assumed that force of contractile element F_{CE} depends on the muscle activation Act , the muscle length l and difference between the active component of static muscle characteristic F_m^{act} and the passive component of static muscle characteristic F_m^{pas} :

$$F_{CE} = Act \cdot (F_m^{act}(l) - F_m^{pas}(l)) \quad (8)$$

To implement the Hill-Zajac unipennate muscle model there were used: 1) a static muscle characteristic (length-force relationship) proposed in [5]; 2) a static tendon characteristic (elongation-force relationship) proposed in [12]; 3) a dynamic muscle characteristic (velocity-force relationship) published in [12]; 4) data described musculotendon properties (the maximum isometric muscle force, the optimal muscle fiber length, the tendon slack length) according with [5].

2.5. Bipennate muscle model WW

The bipennate muscle model WW described behaviour of bipennate muscle composed of two parts directed at the pennation angle α_{p1} (left part with a constant muscle width tt_1) and the pennation angle α_{p2} (right part with a constant muscle width tt_2) towards the muscle insertion (it is movable part) and muscle origins (there are non-movable parts) (Figure 5). Each muscle part behaviour is modelled as a rheological model of the unipennate muscle WW described in the part 2.2 (i.e. each muscle part is composed of two passive fragments and one active fragment). The bipennate muscle model WW has six degrees of freedom. According to this model: 1) difference of displacements ($x_{01} - x_{11}$) describes the length change of upper passive fragment of muscle left part; 2) difference of displacements ($x_{11} - x_{21}$) describes the length change of middle active fragment of muscle left part; 3) displacement x_{21} describes the length change of lower passive fragment of muscle left part; 4) difference of displacements ($x_{02} - x_{12}$) describes the length change of upper passive fragment of muscle right part; 5) difference of displacements ($x_{12} - x_{22}$) describes the length change of middle active fragment of muscle right part; 6) displacement x_{22} describes the length change of lower passive fragment of muscle right part.

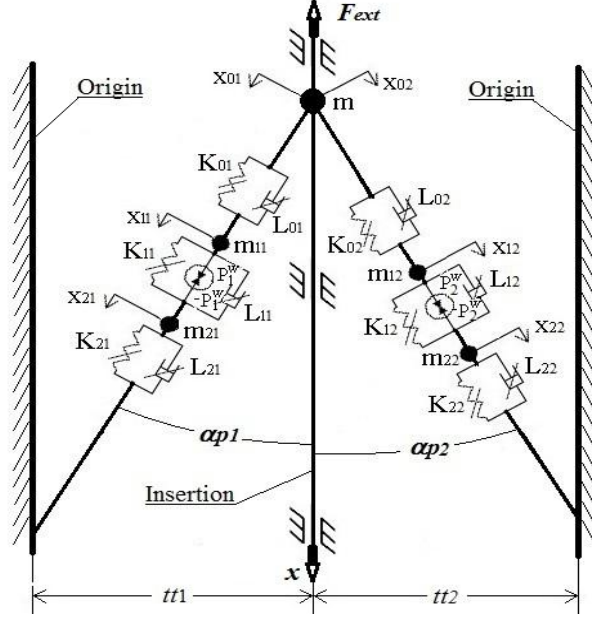


Figure 5. Bipennate muscle model WW (rheological model).

The mathematical model of bipennate muscle model WW is described by the system of five differential equations:

$$\begin{aligned}
 & m \cdot \ddot{x} + L_{01} \cdot (\dot{x}_{01} - \dot{x}_{11}) \cdot \cos \alpha_{p1} + K_{01} \cdot (x_{01} - x_{11}) \cdot \cos \alpha_{p1} + \\
 & + L_{02} \cdot (\dot{x}_{02} - \dot{x}_{12}) \cdot \cos \alpha_{p2} + K_{02} \cdot (x_{02} - x_{12}) \cdot \cos \alpha_{p2} = -F_{ext}(t) \\
 & m_{11} \cdot \ddot{x}_{11} + L_{01} \cdot (\dot{x}_{11} - \dot{x}_{01}) + K_{01} \cdot (x_{11} - x_{01}) + L_{11} \cdot (\dot{x}_{11} - \dot{x}_{21}) + K_{11} \cdot (x_{11} - x_{21}) = P_1^w(t) \\
 & m_{21} \cdot \ddot{x}_{21} + L_{11} \cdot (\dot{x}_{21} - \dot{x}_{11}) + K_{11} \cdot (x_{21} - x_{11}) + L_{21} \cdot \dot{x}_{21} + K_{21} \cdot x_{21} = -P_1^w(t) \\
 & m_{12} \cdot \ddot{x}_{12} + L_{02} \cdot (\dot{x}_{12} - \dot{x}_{02}) + K_{02} \cdot (x_{12} - x_{02}) + L_{12} \cdot (\dot{x}_{12} - \dot{x}_{22}) + K_{12} \cdot (x_{12} - x_{22}) = P_2^w(t) \\
 & m_{22} \cdot \ddot{x}_{22} + L_{12} \cdot (\dot{x}_{22} - \dot{x}_{12}) + K_{12} \cdot (x_{22} - x_{12}) + L_{22} \cdot \dot{x}_{22} + K_{22} \cdot x_{22} = -P_2^w(t)
 \end{aligned} \tag{9}$$

and following geometrical relations:

$$\alpha_{p1} = \arcsin \left(\frac{l_{01} \cdot \sin \alpha_{p1}}{l_{01} - x_{01}} \right), \quad \alpha_{p2} = \arcsin \left(\frac{l_{02} \cdot \sin \alpha_{p2}}{l_{02} - x_{02}} \right), \tag{10A}$$

$$x_{01} = l_{01} + \frac{x \cdot \cos \alpha_{p1} - l_{01}}{\cos(\alpha_{p1} - \alpha_{p01})}, \quad x_{02} = l_{02} + \frac{x \cdot \cos \alpha_{p2} - l_{02}}{\cos(\alpha_{p2} - \alpha_{p02})}, \tag{10B}$$

$$\begin{aligned}
 \dot{x}_{01} &= \frac{dx_{01}}{dt} = \frac{\dot{x} \cdot \cos \alpha_{p1}}{\cos(\alpha_{p1} - \alpha_{p01}) - A(x_{01}) \cdot \sin(\alpha_{p1} - \alpha_{p01}) \cdot (x_{01} - l_{01})}, \\
 \dot{x}_{02} &= \frac{dx_{02}}{dt} = \frac{\dot{x} \cdot \cos \alpha_{p2}}{\cos(\alpha_{p2} - \alpha_{p02}) - A(x_{02}) \cdot \sin(\alpha_{p2} - \alpha_{p02}) \cdot (x_{02} - l_{02})},
 \end{aligned} \tag{10C}$$

$$\begin{aligned}
A(x_{01}) &= \frac{l_{01} \cdot \sin \alpha_{p1}}{(l_{01} - x_{01})^2} \cdot \frac{1}{\sqrt{1 - \left(\frac{l_{01} \cdot \sin \alpha_{p1}}{l_{01} - x_{01}} \right)^2}}, \\
A(x_{02}) &= \frac{l_{02} \cdot \sin \alpha_{p2}}{(l_{02} - x_{02})^2} \cdot \frac{1}{\sqrt{1 - \left(\frac{l_{02} \cdot \sin \alpha_{p2}}{l_{02} - x_{02}} \right)^2}},
\end{aligned} \tag{10D}$$

where: m_{ji} – mass of the j -th element of i -th muscle part; m – mass of the element m_{01} and the element m_{02} ; K_{ji} – stiffness coefficient of the j -th elastic element of i -th muscle part; L_{ji} – damping coefficient of the j -th viscous element of i -th muscle part; $P_1^w(t)$ – internal force of the contractile element of left muscle part; $P_2^w(t)$ – internal force of the contractile element of right muscle part; l_{01} – initial length of left part of muscle model; l_{02} – initial length of right part of muscle model; α_{p01} – initial pennation angle when the length of left part of muscle model is equal to l_{01} ; α_{p02} – initial pennation angle when the length of right part of muscle model is equal to l_{02} .

2.6. Bipennate muscle model BZ

The bipennate muscle model BZ described behaviour of bipennate muscle directed at the pennation angle α (left part) and the pennation angle β (right part) towards the muscle insertion (it is movable part) and muscle origins (there are non-movable parts) (Figure 6).

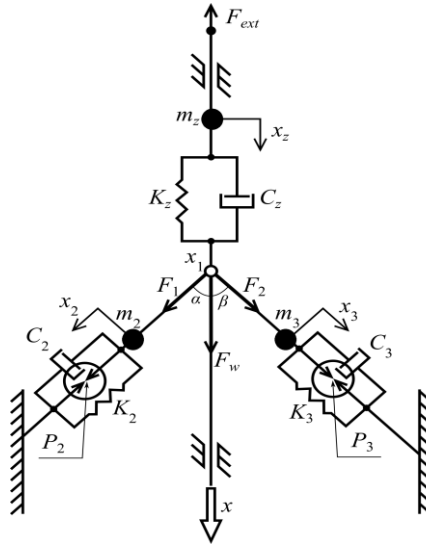


Figure 6. Bipennate muscle model BZ.

The bipennate muscle model BZ is similar to the bipennate muscle model WW (part 2.5) but it takes into consideration that stiffness and dumping characteristics of skeletal muscle are nonlinear (part 2.3). Applying the geometrical relationships (10A – 10D), the mathematical model of bipennate muscle model BZ is described by the system of four following equations:

$$\begin{aligned} m_z \cdot \ddot{x}_z + C_z \cdot (\dot{x}_z - \dot{x}_1) + K_z \cdot (x_z - x_1) &= -F_{ext}(t) \\ m_2 \cdot \ddot{x}_2 + C_2 \cdot \dot{x}_2 + K_2 \cdot x_2 &= P_2(t) + F_1(t) \\ m_3 \cdot \ddot{x}_3 + C_3 \cdot \dot{x}_3 + K_3 \cdot x_3 &= P_3(t) + F_2(t) \\ F_1(t) \cdot \cos \alpha + F_2(t) \cdot \cos \beta &= C_z \cdot (\dot{x}_z - \dot{x}_1) + K_z \cdot (x_z - x_1), \end{aligned} \quad (11)$$

where: $x_1 = x_2 \cdot \cos \alpha = x_3 \cdot \cos \beta$.

3. Numerical simulation results

Numerical models of unipennate muscle and bipennate muscle were created on the base of proposed mathematical models. To perform numerical researches there were used data describing a lateral head of triceps brachii published in [5]. Applying similar boundary conditions and similar load, proposed numerical models had been tested. Numerical model of unipennate muscle model WW (described in part 2.2) was applied to solve three problems of the dynamics task described in part 2.1. Chosen results obtained from numerical solving of the third problem are shown at the Figure 7.

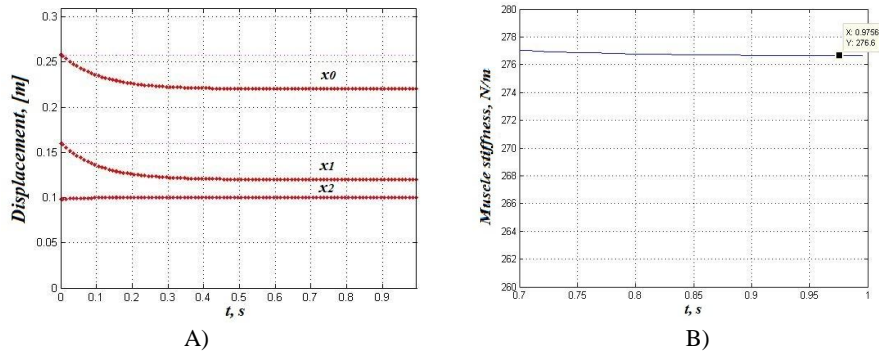


Figure 7. Numerical simulation results of the unipennate muscle model WW: A) displacement of muscle points; B) stiffness of muscle.

Numerical model of Hill-Zajac unipennate muscle model (described in part 2.4) was applied to solve a dynamics task formulated in the following problem: input variables are the insertion displacement $x(t)$, the pennation angle $\alpha_p(t)$ and the external force $F_{ext}(t)$; output variables are the force of contractile element F_{CE} and muscle activation Act . Chosen results obtained from numerical solving of this problem are shown at the Figure 8.

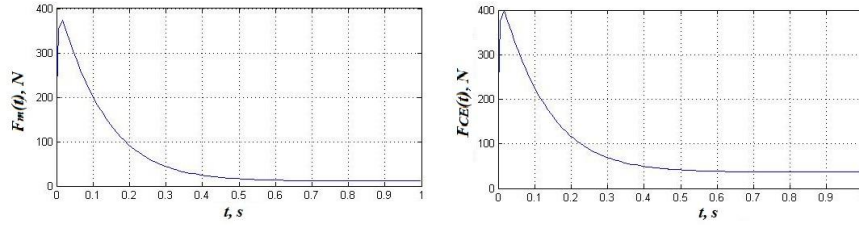


Figure 8. Numerical simulation results of the Hill-Zajac unipennate muscle model: contractile muscle force F_m and force of contractile element F_{CE} .

Numerical model of bipennate muscle model WW (described in part 2.5) was applied to solve the third problem of the dynamics task (described in part 2.1). Chosen results obtained from numerical solving of the third problem are shown in the Figure 9.

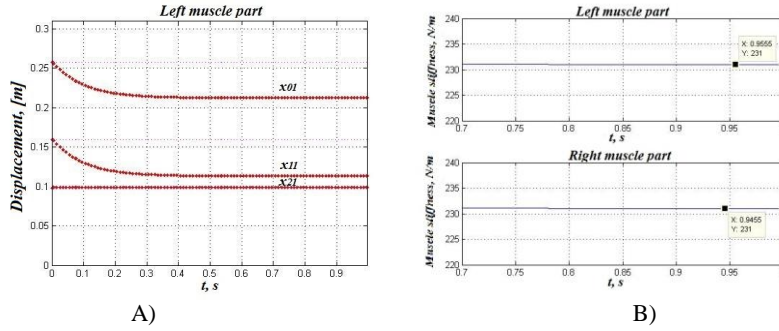


Figure 9. Numerical simulation results of the bipennate muscle model WW: A) displacement of left muscle part points; B) stiffness of muscle left and right part.

Numerical model of unipennate muscle model BZ (described in part 2.3) and bipennate muscle model BZ (described in part 2.6) were applied to solve the third problem of the dynamics task (described in part 2.1). Chosen results obtained from numerical solving of the third problem are shown in the Figure 10.

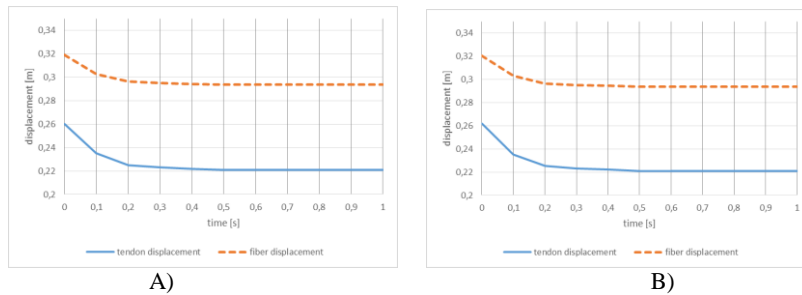


Figure 10. Numerical simulation results of: A) the unipennate muscle model BZ (displacement of the tendon x_z and muscle fiber x_w ; B) the bipennate muscle model BZ (displacement of the tendon x_z and muscle fibers $x_2 = x_3$ in the case of $\alpha = \beta$).

To compare the influence of planar arrangement of muscle fibers the numerical model of fusiform muscle model published in [11] was applied to solve the third problem of the dynamics task (chosen results are shown in the Figure 11).

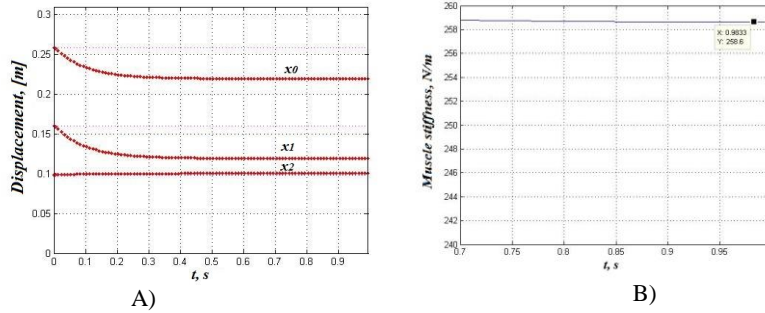


Figure 11. Numerical simulation results of the fusiform muscle model: A) displacement of muscle points; B) stiffness of muscle.

4. Method of verification

To prove models proposed in this paper a method of verification was elaborated. According to this method, a first step consists in applying a non-invasive image analysis and a second step consists in performing experiments by using the prototype of pennate muscle. An image analysis (US or MRI) allows us to perform static image analysis (for a single image) and dynamical image analysis (for a multiple images or a single movie). It is worth noticing that an image analysis requires that an image has high resolution to precisely distinguish muscle fibers [3,8]. Single image of muscle section allows to measure a pennation angle α_p , a muscle diameter and a muscle length (Figure 12).



Figure 12. Muscle geometrical parameters in visual analysis: pennation angle α_p , muscle diameter d and muscle length l .

The prototype of pennate muscle is composed of four artificial pneumatic muscles (Figure 13). Each artificial muscle is a linear McKibben actuator. This prototype allows us to form four initial pennation angles: 9° , 14° , 18° and 24° . Chosen experiments results and numerical simulation results are shown in the Figure 14. Analysing these results, we may conclude that greater pennation angle causes the drop of force measured along a long axis of the muscle (each pneumatic actuator produces the same maximal force, which is independent of the pennation angle).



Figure 13. A prototype of pennate muscle (a prototype is composed of four artificial pneumatic muscles)

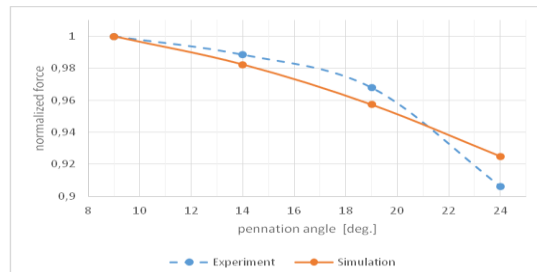


Figure 14. Normalized force as a function of pennation angle.

5. Conclusions

The aim of this study was to create mathematical models of unipennate striated skeletal muscle and bipennate striated skeletal muscle. New models were created in the form of rheological models by taking into consideration that muscle contraction occurs in two-dimension space and the arrangement of muscle fibers influence mechanical properties and contractile properties of this muscle. Moreover, at this stage of modelling we assumed that slow and fast muscle tissues have identical mechanical properties.

Analysing results of numerical simulations we concluded that:

- 1) efficiency of fusiform muscle (it is a quotient the external force to the contractile muscle force) is more than the efficiency of unipennate muscle (because a unipennate muscle works in a plane and a part of its contractile force is devoted to spatial arrangement of muscle fibers);
- 2) the efficiency of bipennate muscle is more that the efficiency of unipennate muscle;
- 3) to model a behaviour of pennate muscle one should precisely describe the geometrical relations occurring between pennate muscle fibers (i.e. geometrical constrains) and the force-length relations depended on the time variable (i.e. dynamics equations of motion).

Acknowledgments

The numerical simulations had been performed using computers of “Centrum Informatyczne Trójmiejskiej Akademickiej Sieci Komputerowej” in Gdansk, Poland.

References

- [1] Aagaard P., Andersen J.L., Poulsen P.D., Leffers A.M., Wagner A., Magnussin S.P., Kristensen J.H., Simonsen E.B. A mechanism for increased contractile strength of human pennate muscle

in response to strength training: changes in muscle architecture. *Journal of Physiology* 534.2, 2001, pp.613-623

- [2] Awrejcewicz J., Kudra G., Zagrodny B. Nonlinearity of muscle stiffness. *Theoretical and Applied Mechanics Letters* 2(5), 2012, pp. 1-3
- [3] Csapo R., Malis V., Hodgson J., Sinha S. Age-related greater Achilles tendon compliance is not associated with larger plantar flexor muscle fascicle strains in senior women. *Journal of Applied Physiology* 116 (8), 2014, pp. 961–969
- [4] Delp S.L. *Surgery simulation – a computer graphics system to analyze and design musculoskeletal reconstructions of the lower limb*. PhD. thesis, Stanford University Press, 1990, Stanford, Zajac F.
- [5] Garner B.A., Pandy M.G. Estimation of musculotendon properties in the human upper limb. *Annals of Biomedical Engineering* 31, 2003, pp. 207-220
- [6] Narici M. Human skeletal muscle architecture studied in vivo by non-invasive imaging techniques: functional significance and applications. *Journal of Electromyography and Kinesiology* 9, 1999, pp. 97-103
- [7] Nigg B.M., Herzog W. *Biomechanics of the musculoskeletal system*. John Wiley & Sons, 1994, Chichester
- [8] Noorkoiv M., Stavnsbo A., Aagaard P., Blazevich A.J. In vivo assessment of muscle fascicle length by extended field-of-view ultrasonography, *Journal of Applied Physiology* 109 (6), 2010, pp. 1974–1979.
- [9] Soderberg G.L. *Kinesiology: Application to pathological motion*, Baltimore, Williams & Wilkins, 1986.
- [10] Wojnicz W., Wittbrodt E. Analysis of muscles' behaviour. Part I. The computational model of muscle. *Acta of Bioengineering and Biomechanics* 11, 2009, pp. 15-21
- [11] Wojnicz W., Wittbrodt E. Application of muscle model to the musculoskeletal modeling. *Acta of Bioengineering and Biomechanics* 14, 2012, pp. 29-39
- [12] Zajac F. Muscle and tendon: properties, models, scaling and application to biomechanics and motor control. *Critical Reviews in Biomedical Engineering* 17, 1989, pp. 359-410

Wiktoria Wojnicz, Ph.D.: Gdansk University of Technology, str. G. Narutowicza 11/12, 80-233 Gdansk, POLAND (wiktoria.wojnicz@pg.gda.pl). The author gave a presentation of this paper during one of the conference sessions.

Bartłomiej Zagrodny, Ph.D.: Lodz University of Technology, str. Stefanowskiego 1/15 , 90-924 Lodz, POLAND (bartlomiej.zagrodny@p.lodz.pl).

Michał Ludwicki, Ph.D.: Lodz University of Technology, str. Stefanowskiego 1/15 , 90-924 Lodz, POLAND (michal.ludwicki@p.lodz.pl).

Jan Awrejcewicz, Professor: Lodz University of Technology, str. Stefanowskiego 1/15 , 90-924 Lodz, POLAND (jan.awrejcewicz@p.lodz.pl).

Edmund Wittbrodt, Professor: Gdansk University of Technology, str. G. Narutowicza 11/12, 80-233 Gdansk, POLAND (e.wittbrodt@pg.gda.pl).

**Dynamics of vibrating machines with unbalanced drive in case
of flat vibrations of bearing body
(VIB018-15)**

Nikolay Yaroshevich, Ivan Zabrodets, Tatyana Yaroshevich

Abstract: Expressions for vibration moments (additional dynamic loading caused by the vibrations of bearing body) during the passage of resonant zone by vibration machines with the flat vibrations of bearing body both with one arbitrarily located vibration exciter and with two self-synchronization vibration exciters for the different modes of starting are got in an analytical form by method of direct division of motions. Using approaches of vibration mechanics of I.I. Blekhman possibilities of improvement of process of running approach of vibration machines with unbalanced vibration exciters are demonstrated by using of methods the "double" (in case of one vibration exciter) and "separate" starting of electric motors (in case of two vibration exciters). It is shown that the first method is based on using semislow vibrations arising in the resonant zone. The necessary condition of the successful using of this method is motion on the rotor of exciter in the moment of the repeated including of engine of rotary-type vibration moment. The conditions when the separate starting is effective are shown. Conclusions and practical recommendations that allow to facilitate starting of vibration machines with an unbalanced drive are pointed.

1. Introduction

Posing the problem and its connection with the main scientific tasks. Solutions of problems of run-up and run-down of vibrational systems with inertial drive is of considerable interest for vibrational technical devices. When inertial vibroexciter passes the zone of natural frequencies an onset of resonance vibrations is possible which cause both a sufficient rise of dynamic loads on the rotor of electric motor, on elements of machine bearing construction and additional losses of power in the system. So, the start of vibration machine with unbalanced drive needs the power of the drive with sufficiently exceed the power needed for operating in stationary mode (2-5 times as large by some data). In addition to that, in case of large machines with the drive from electric motors of asynchronous type the striking starting current exerts negatively upon the feeding electrical network.

In order to lower the level of vibrations when passing the resonance zone various means are used – from vibroexciters with automatically regulated static moment of unbalance mass to algorithms with feedback. No doubt, to successful realization of the lasts it is important to have more thorough conception of dynamics of the occurring processes.

Analysis of the latest investigations.

The survey of investigations, concerning the passing of the resonance zone by inertial vibroexciter one may find in [1-3]. In the last years a number of tasks are solved on the basis of vibrational mechanics approaches, in particular, by using the method of direct separation of motions. In [3] it is shown by the example of the simplest system with linear vibrations of the bearing body and one unbalanced exciter that the important merit of such approach is its comparative simplicity and physical integration of the results.

In work [1] attention is paid to the peculiarity of the motion of the system nearby the resonance – the availability of the so called inner pendulum and its “semislow” motions, which are physical base of the efficiency of some methods of controlling the starting of vibration machines with inertial exciting of vibration.

A great number of works are dedicated to the use of the phenomenon of selfsynchronization in vibration machines and devices, they are shown in [1, 3], and the latest ones in [4-6]. However, no attention was paid to the dynamics of starting of such vibrations machines. The presented paper is dedicated to generalization and development of the results of works [2, 7, 8].

Statement of the task. The majority of vibration machines with unbalanced drive may be idealized in the form of a system, consisting with a single lifting rigid body, which may execute plane-parallel motion and is connected with stationary base with elastic and damping elements (fig. 1). As exciters of vibrations of lifting body mostly unbalanced vibroexciters (disbalanced rotors) driven by the electric motors of asynchronous type are used. Motion equations of such system may be written down in the following form (see, for instance, [1-3]):

$$\begin{aligned} M\ddot{x} + \beta_x \dot{x} + \tilde{n}_x x &= m_i \varepsilon_i \sum_{i=1}^s (\ddot{\varphi}_i \sin \varphi_i + \dot{\varphi}_i^2 \cos \varphi_i), \\ M\ddot{y} + \beta_y \dot{y} + \tilde{n}_y y &= m_i \varepsilon_i \sum_{i=1}^s (\ddot{\varphi}_i \cos \varphi_i - \dot{\varphi}_i^2 \sin \varphi_i), \\ J\ddot{\varphi} + \beta_\varphi \dot{\varphi} + \tilde{n}_\varphi \varphi &= \sum_{i=1}^s m_i \varepsilon_i r_i (\ddot{\varphi}_i \cos(\varphi_i + \delta_i) - \dot{\varphi}_i^2 \sin(\varphi_i + \delta_i)), \quad s = 1 \dots n \end{aligned} \quad (1)$$

$$I_i \ddot{\varphi}_i = L_i(\dot{\varphi}_i) - R_i(\dot{\varphi}_i) + m_i \varepsilon_i [\ddot{x} \sin \varphi_i + \ddot{y} \cos \varphi_i + r_i \ddot{\varphi} \cos(\varphi_i + \delta_i) + g \cos \varphi_i], \quad (2)$$

where M , J – are correspondingly, mass and moment of inertia of the lifting body as to the axis which passes through its center of gravity; x , y , φ – are coordinates, determining the position of the lifting body; φ_i – are the angles of rotation of vibroexciter; r_i and δ_i – are polar coordinates of axes of vibroexciters; m, ε – are, correspondingly, mass and accentricity of the exciter; I_i – is

applied to the shaft of the vibroexciter moment of inertia of the rotating parts of the drive; c_x, c_y, c_φ – are horizontal, vertical and rotational rigidity of the elastic elements; $\beta_x, \beta_y, \beta_\varphi$ – are coefficients of viscous resistance; $L_i(\dot{\varphi}_i), R_i(\dot{\varphi}_i)$ – is the torque of the electric motor and moment of forces of resistance to rotation; g – is a free-fall acceleration.

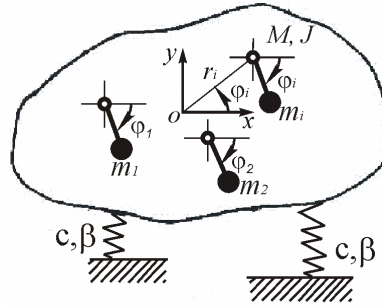


Figure 1. General diagram of vibrational system with unbalanced vibroexciters

Exposition of the basic material. To solve the set of equations (1), (2) we use the method of direct separation of motions [1, 3]. Set us accept as a zero-order approximation $\varphi_i = \omega t$, $q_i = P_i \sin \omega t + Q_i \cos \omega t$ where $\omega = \omega(t)$ – are slowly and $q_i = x, y, \varphi$ – fast changing time functions. Then it is not complicated to come from the original system of equations of vibroexciters rotors motion (2) to the equations of their rotation in the resonance zone in the form, obtained in [3]

$$I_i \dot{\omega} = L_i(\omega) - R_i(\omega) + V_i(\omega), \quad (3)$$

where $V_i(\omega) = m_i \varepsilon_i \langle \ddot{x} \sin \varphi_i + \ddot{y} \cos \varphi_i + r_i \ddot{\varphi} \cos(\varphi_i + \delta_i) \rangle$.

French quotes in (3) point out at averaging for the $T = 2\pi$ by fast time $\tau = \omega t$.

It should be noted that equation (3) differs from classic equation of machine assembly by presence of item $V_i(\omega)$ – vibrational moment which defines the peculiarity of vibrational system conduct. Presence of vibrational moment explains both Zommerfield's effect and selfsynchronization of vibroexciters. Determination of the vibrational moment is of main interest.

It should be noted that equation (3) keeps its form, obtained for the system with linear vibrations of the lifting body [3] for the examined more general case as well. Only expression for vibrational moment has more complicated structure, algorithm of its obtaining remains previous, only computing difficulties grow up.

Vibrational systems with one vibroexciter Zommerfield's effect. Certain part of operating at present machines has one unbalanced vibroexciter. It is not complicated to obtain expressions of

vibrational moment in the resonance zone for the case of vibroexciter, placed arbitrarily as to centre of masses of the lifting body in plane vibration in the form

$$V(\omega) = -\frac{(m\varepsilon\omega)^2}{M} \left[\frac{n_x}{B_x^2} + \frac{n_y}{B_y^2} + \frac{Mr^2}{J} \frac{n_\varphi}{B_\varphi^2} \right], \quad (4)$$

$$B_q = \sqrt{(1 - \lambda_q^2)^2 + 4n_q^2}; \quad \lambda_q = \frac{p_q}{\omega}; \quad n_q = \frac{\beta_q}{2M_q\omega},$$

where p_q – are the frequencies of the natural vibration of the system.

Here, if $q = x, y$, then $M_q = M$, if $q = \varphi$, then $M_q = M \frac{p^2}{h^2}$; in addition to that, $n_\varphi = \frac{\beta_\varphi}{2J\omega}$.

One can see that all items in formula (4) are negative. Hence, vibrational moment is always braking one, that is, it is an additional dynamic load upon the rotor of the engine, its dependence from frequency is of resonance character and, therefore, an essential braking exertion is manifested in comparatively narrow range of natural frequencies. In addition to that, rapid growth of value $V(\omega)$ at approaching to resonance just explains the possible “sticking” of frequency in the process of starting (Zommerfeld’s effect) and, as consequence, the necessity of overrated (from starting conditions) power of the drive of postresonance vibromachines. Such conclusion follows from diagramic presentation of dependences $L(\omega)$ and $M_{sum} = R(\omega) - V(\omega)$ (fig. 2), abscissas of intersection points correspond to possible stationary modes (curves L describe statical characteristics of electric engines. Stability of motions is easily determined geometrically by the sign and values of slope angles tangent to curves $L(\omega)$ and M_{sum} . It is evident that right slopes of resonance curve cannot be realized. According to the figure, the presence of several resonance peaks of the curve of vibrational moment may lead to the emergence (as compared with the system of linear vibration of the lifting body) points of curves intersection. So, there exists a possibility of several stationary modes of motions, having different angular velocities (up to seven, four of them may be stable). However, there are only two, different in lessence modes of motion: “sticking” (curves 1) of the system with engine of deficient power in the resonance zone (motor) on having come in the process of running to this mode, would not be able to overcome the resonance peak and far postresonance mode with frequency of electric motor. If the motor power is sufficient, then, as a rule, after some breaking in the resonance zone, the system rapidly (upsetting) passes to far postresonance modes of motion (curves 2).

So, to reach by the exciter the working frequency, the moment of the motor should overcome vibrational moment $V(\omega)$ during its running. According to (4), maximal (peak) value of moment $V(\omega)$ is as much large as a damping of n_q becomes less and higher of the own vibrations of system p_q . Hence, it is important not to overrate the value of rigidity of elastic elements; the use of elastic

suspension may be effective; it is possible to lower resonance peak values of vibrations as well as the power of the drive by installation of dampers of maximal vibrations. Expression (3) may be presented in the form of the sum of “partial” vibration movements v_q , which characterize the impact of vibrations, corresponding to each of the generalized coordinates: $V(\omega) = \sum_{q=x,y,\theta} v_q$, where

$$v_q = \frac{1}{2} F a_q \sin \gamma_q; \quad \sin \gamma_q = -\frac{2n_q}{B_q}; \quad a_q = \frac{m\varepsilon}{M_q B_q}; \quad F = m\varepsilon \omega^2.$$

It is natural that maximal breaking exertion is effected by “partial” vibrational moment which corresponds to the highest natural frequency of vibrations p_q , so it is often enough to use damper of only such vibrations.

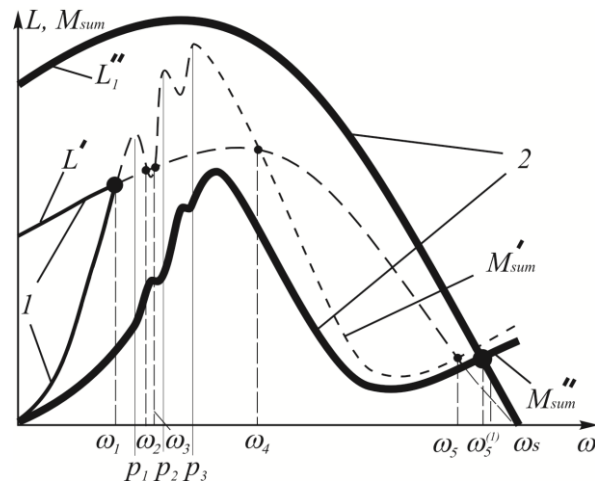


Figure 2. Stationary modes of rotation of vibroexciter: 1 – “sticking” in resonance zone, 2 – far postresonance mode

It is clear from formula (4) that start of vibromachine at the absence of working load is more complicated than at its presence; that to make the start easier it is advisable to install vibroexciter in the centre of masses of the system or as close to it, as possible. So, the breaking vibrational moment, resonance vibrations and, correspondingly, the necessary power of the motor are sufficiently less for centre-drilled system (fig. 3, a) than, for instance, for the diagram shown in fig. 3, b (in the first case the last component in formula of vibrational moment (4) disappears). It should also be noted that “rapid” (with frequency 2ω) vibrations of vibrational moment do not take place in such system in the steady mode, which is favorable for the durability of the system

On the other hand, taking into account the fact that the value of the vibrational moment depends, first of all, on the velocity of running of the rotor of vibroexciter, to make easier the start, engines with higher starting moment are recommended (it facilitates, also, the solution of the problem of

lifting the unbalanced mass at first half-turn). At prescribed static moment unbalance mass should be designed with minimal moment of inertia. So, constructions of vibroexciters with laid on unbalanced mass are more preferable for changing the amplitude of vibrations, then those, having regulated static moment. In addition to this, it is recommended to exclude from the construction (if they are available) synchronizers, mechanical transmissions and so on, using the phenomena of selfsynchronization, employing controlled electric drive.

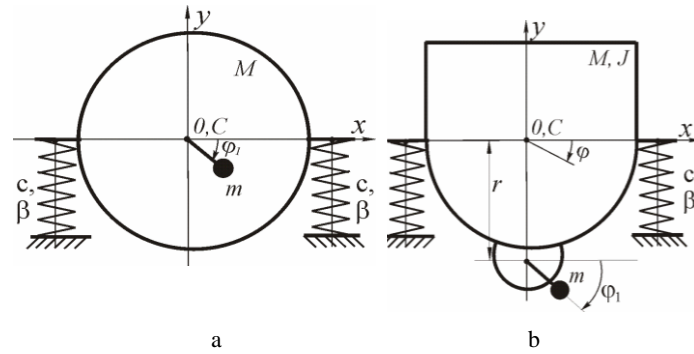


Figure 3. Diagrams of vibromachines: a) with centrally installed vibroexciter; b) with shifted vibroexciter

Manifestation of Zommerfield's effect during the run-up of vibromachine is visually demonstrated by the results of numerical modelling, obtained for vibrational system (fig. 3, a) with parameter $M = 330 \text{ kg}$; $J = 8,02 \text{ kg} \cdot \text{m}^2$; $\tilde{n}_y = \tilde{n}_o = 4,5 \cdot 10^5 \text{ N/m}$; $\tilde{n}_\varphi = 2,8 \cdot 10^4 \text{ N} \cdot \text{m}$; $m = 40 \text{ kg}$; $\varepsilon = 0,036m$, electric engine – asynchronous, with frequency of rotation $n_c = 1500 \text{ rot/min}$, of power $P = 1,5 \text{ kW}$. According to fig. 4, at passing the natural frequencies zone ($t = 0,15 - 0,42 \text{ s}$) dynamic load upon the rotor of electric engine grows sufficiently (curve 1); one can see that the value of vibrational moment is larger, than in stationary mode several times as much and its maximal vibrations are compatible with starting moment of the engine.

Correspondingly, the velocity of running of the rotor of exciter shows down intensively up to short-term stabilization of the frequency of rotation (curve 2), in addition to that, maximal resonance vibration of the lifting body are excited. Just after passing the resonance the value of vibrational moment decreases sufficiently fast and its vibrations cover positive zone, that is it becomes rotating in some moments of time. Then their damping takes place as to small negative level (determined by resistance to the vibrations of the lifting body); the amplitude of vibrations of lifting body decreases as fast and the value of rotating moment of the engine changes from starting to nominal value (curve 3).

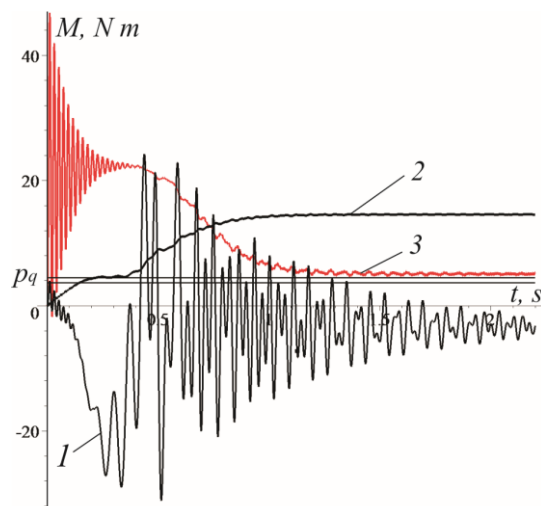


Figure 4. Changing in time: 1 – of engine moment; 2 – of vibrational moment; 3 – of vibroexciter velocity

As it follows from the diagrams of velocity of rotation of vibroexciter for cases of different powers of driving electric motor (fig. 5) at replacing motor of power $P = 1,5kW$ with motor of power $P = 2,2kW$, slowing down of velocity of exciter in resonance zone is practically absent (curve 3) while its steady postresonance mode of operating becomes impossible (curve 2 – “sticking” of angular velocity in postresonance zone).

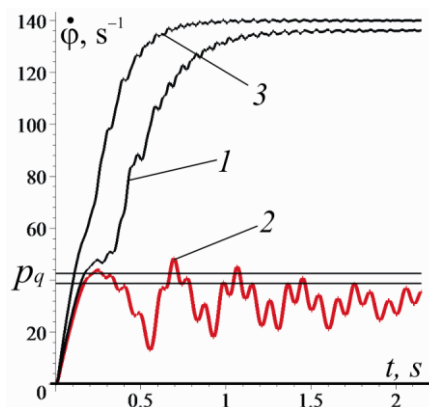


Figure 5. Changing in time the vibroexciter velocity: 1 – $P = 1,5kW$; 2 – $P = 1,1kW$ (“sticking” of velocity); 3 – $P = 2,2kW$

Double start of vibrational machines with unbalanced drive. In practical use of such machines the so called method of “double starting” is applied for lowering the level of vibrations during passing the resonance frequencies. Its technical realization is rather simple. Method consists in switching-off and next switching-on the electric motor in the resonance zone in predetermined moment of time. Theoretical grounding of the method with account of standpoints of vibrational mechanics facilitates its wider use. The basis of the method lies in two existing appropriatenesses of motion of the system close to the region of manifestation of Zommerfeld’s effect: the first one – at switching-off the motor in the resonance zone vibrational moment effecting the rotor of vibroexciter becomes positive, that is, rotating (it follows from the basic equation of vibrational mechanics (3), written down for the case of stationary mode); the second one – availability of so called inner pendulum and its “semislow” motions. So, using the method of direct separation of motions and accepting as the first approximation $\varphi_1 = \varphi_1^{(1)} = \omega t + \psi$, $q = q^{(0)} + q^{(1)}$, for general system (fig. 1) in case of one vibroexciter it is not complicated to obtain equation of “semislow” vibrations in the form [2]

$$\ddot{\Psi} + 2n_1 \dot{\Psi} + B \sin \Psi - P \sin^2 \frac{\Psi}{2} = 0, \quad (5)$$

for the system under consideration $B = \sum_{q=x,y,\varphi} b_q$; $b_q = \frac{(m\varepsilon\omega^2)^2}{2MI} \frac{p_q^2 - \omega^2}{(p_q^2 - \omega^2)^2 + 4n_q^2\omega^4}$; $P = \sum_{q=x,y,\varphi} \rho_q^2$;

$$\rho_q = \frac{(m\varepsilon\omega^2)^2}{MI} \frac{2n_q\omega^2}{(p_q^2 - \omega^2)^2 + 4n_q^2\omega^4}; \quad 2n_1 = k / I; \quad k - \text{is a coefficient of damping.}$$

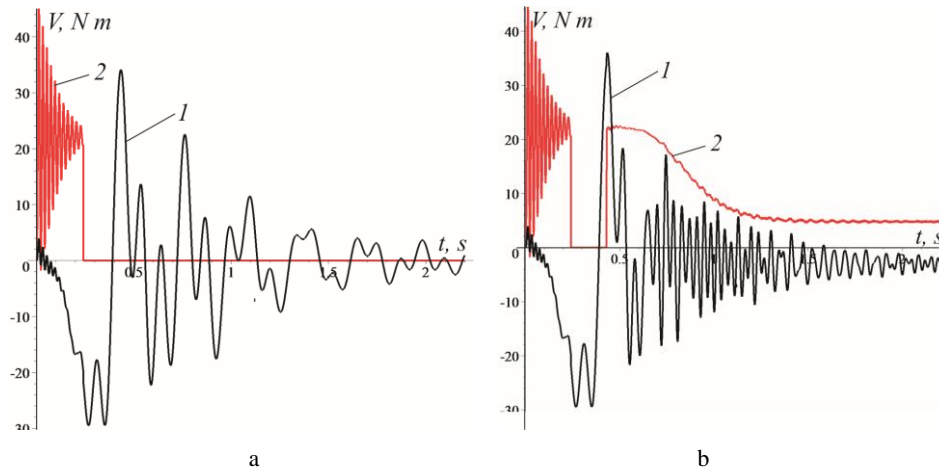


Figure 6. Changing in time: 1 – of vibrational moment; 2 – of motor moment ($P = 1,1kW$):

- a) switching-off of the motor in the resonance zone, $t_{sw.-off} = 0,3$ s;
- b) double starting of the engine, $t_{sw.-off} = 0,3$ s, $t_{rep. sw.-on} = 0,48$ s

The value $q = \sqrt{|B|}$ is frequency of small free vibrations of the inner pendulum on condition of slow changing of the frequency of rotation of rotor ω [2]. The effect of appearance of semislow vibrations in the resonance zone may be observed in the fig. 5-7. In addition to that, according to fig. 6, a (curve 1) semislow (with frequency $2q$) vibrations of vibrational moment take place after switching-off of the motor with regard to the shifted to the positive side level.

Fig. 6, b and fig.7 demonstrate the possibility of realization of running ang coming to the mode of rotation with frequency, close to nominal of the motor of “unsufficient” power ($P = 1,1kW$) with the help of method of double starting as one can see, the necessary condition of successful use of the method is, first of all, effect upon the rotor of vibroexciter in the moment of repeated switching-on of the motor (in figures $t_{rep. sw.-on} = 0,48 s$) of rotating vibrational moment commensurable with its starting moment. The abovementioned condition is not complicated to realize with the help of modern means of controlling the electric motors. Applied recommendations to switch off the motor in the moment of growing of intensive resonance vibrations of the lifting body and at once (in a period of time of semiperiod of semislow vibrations $t = 2 / q$) switch it on again.

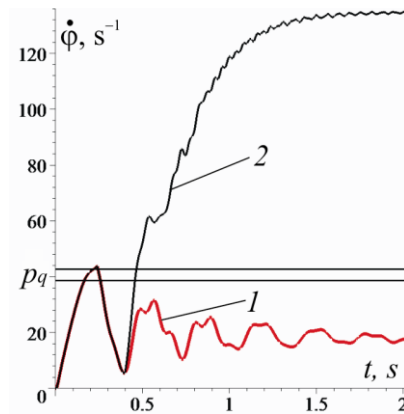


Figure 7. Changing in time of the velocity of vibroexciter ($P = 1,1kW$): 1 – switching-on the motor

in the resonance zone, $t_{sw.-off} = 0,3 s$; 2 – double start of the motor, $t_{sw.-off} = 0,3 s$,

$$t_{rep. sw.-on} = 0,48 s$$

Vibrational systems with two selfsynchronizing exciters. Separate starting. Many modern vibrational machines, in particular, screens and platforms with directed vertical (horizontal) vibrations are realized by the diagram, shown in fig. 8. Expressions for vibrational moments influencing in resonance zone upon the rotors of exciters rotating in opposite directions are presented in the form

$$V_i(\omega) = -\frac{1}{2} \frac{(m\varepsilon\omega)^2}{M} \frac{n_y}{B_y^2}. \quad (6)$$

Vibrational machines with selfsynchronizing exciters permit the possibility of separate (in turns) start of electric motors, however, it is not applied in practice. Using the approach under consideration, it is possible to demonstrate possibility advantages of such start.

It is not complicated to establish that vibrational moment in case of running only one of vibroexciters will equal $V_{separ}(\omega) = \frac{1}{4}V(\omega)$, where $V(\omega)$ is determined by formula (4). It follows from analysis (4) that if natural frequencies of vibrational system p_q differ sufficiently enough (it may always be reached by the choice of elastic elements), then with the grows of frequency ω in the process of running each item (except the one corresponding to $\omega \approx p_q$) will be disregarded small.

Taking into account the fact that ratio Mr^2/J is for the dynamic system in consideration, sufficiently less than unity it is possible to come to the following estimation of the value of vibrational moment, functioning in the resonance zone in case of separate start of its electric motors:

$V_{separ}(\omega) \approx \frac{1}{2}V_i(\omega)$. So, by corresponding choice of the parameters of the system at separate start of motors it is possible to attain the decrease of resonance vibrational moments and, as a result, to attain all connected with this possible of improvement of dynamic and power characteristics of vibromachines.

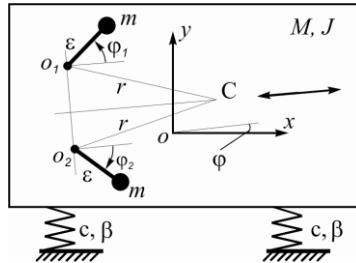


Figure 8. Diagram of vibrational machine with selfsynchronizing exciters

In favor of decrease of vibrational moments at separate start of selfsynchronizing vibroexciters are the facts that, owing to the differences between their phases, some “collateral” vibrations of the lifting body occur and that it is necessary at more precise determination of vibrational moment of the exciter under consideration, to take account of the effect of other exciters. That is, at calculation of vibrational moment it should be presented in the form of the sum of two items, one of which (being determined above) represents additional load, caused by losses of power at vibrations, and the second (noticeably less in the resonance zone, as a rule) is caused by the influence of other vibroexciters. It

should be noted, that the second item represents redistribution of power between the vibroexciters. Formulas for determination of its value for many of vibrational systems may be found in specialize literature [1, 3]. The positive effect may be magnified by installation of damper of vertical vibrations. Besides, in case of using separate start of motoes, the decrease (almost twice as much) of starting currents is rather important.

It should be noted that somewhat excessive power of electric drive is recommended for easing the start in case of vibromachines with two selfsynchronizing exciters. In addition to that, effect of vibrational support of rotation of unbalanced exciter in steady state should be used, working with one switched off motor. Especially as mode of vibrational support of rotation is the most stable for the dynamic system under consideration. It follows from comparison (4) and (6) that dynamic load upon the rotors of electric motors and, correspondingly, the necessary total power of electric drive in case of vertical vibrations of the working part of vibromachine will be sufficiently less than at elliptic trajectory.

Results of simulation confirm the advantages of separate start. Thus, for instance, according to fig. 9 ($Mr^2 / J = 0,52$), in case of such start resonance amplitudes of vibration of masses centre of the lifting body are sufficiently less than those at synchronous start of the motors. In addition to that amplitudes of horizontal and turning resonance vibrations grow. However, their amplitudes are far from maximal values of amplitudes of vertical vibrations.

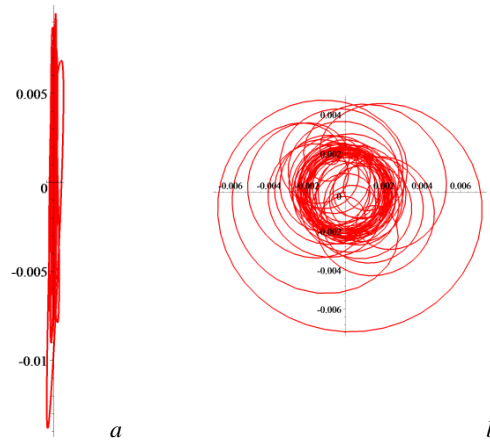


Figure 9. Trajectories of the centre of masses of lifting body: *a)* synchronous (ordinary) start of motors; *b)* start of one motor (separate start)

Findings. Thus, the majority of mechanisms of behavior of inertial vibroexciters and vibrational system in general at passing the resonance zone may be explained on the basis of approaches of vibrational mechanics. On this ground practical conclusions and recommendations improving

dynamic and power characteristics of vibromachines with unbalanced drive may be obtained. Methods of double and separated start are effective for easing the start of postresonance vibromachines with unbalanced drive.

References

- [1] Blekhman I.I. (2013), Theory of vibration processes and devices. *Vibration mechanics and vibration technology. The Publishing House "Ore and Metals"*. – 640 p.
 - [2] Blekhman I.I. Indeitsev D.A., Fradkov A.L. (2008), Slow motions in systems with inertial excitation of vibrations, *Journal of Machinery Manufacture and Reliability*, no 1, pp. 21-27.
 - [3] Blekhman I.I. (2000), *Vibrational Mechanics*, World Scientific, Singapore.
 - [4] Li Y., Li H., Wei X., Wen B. (2014), Self-synchronization theory of a vibrating system with a two-stage vibration isolation frame driven by two motors Zhendong yu Chongji, Dongbei Daxue Xuebao, *Journal of Northeastern University*. – Vol. 35, pp. 836-840.
 - [5] Zhang X., Wen B., Zhao C. (2014), Vibratory synchronization and coupling dynamic characteristics of multiple unbalanced rotors on a mass-spring rigid base, *Journal of Mechanical Science and Technology*. – Vol. 28, pp. 249-258.
 - [6] Franchuk V.P., Savluk N.V. (2004), Applying of self-synchronisation in mountain vibration machines, *Vibrations in technics and technology*. – no 1(33). – pp. 12-14.
 - [7] *Nonlinear problems of theory of oscillation and theory of control Vibrational Mechanics. IMEP of RAS (2009)* / under redact. V. Beletskiy, D. Indeitsev, A. Fradkov. – SPb.: Nauka, 528p.
 - [8] Yaroshevich N.P., Sylyvonuk A.V. (2013), About some features of dynamic acceleration of vibration mashines with self-synchronisation inertia vibroexciters, *Scientific Bullietin of National Mining University*, no 4 (136), pp.70-75.
- Nikolay Yaroshevich, Professor, Lutsk National Technical University, Lvivska Str., 75, Lutsk, 43018, Ukraine, E-mail m_yaroshevich@mail.ru
- Ivan Zabrodets, student, Lutsk National Technical University, Lvivska Str., 75, Lutsk, 43018, Ukraine, E-mail m_yaroshevich@mail.ru
- Tatyana Yaroshevich, Ph.D., Lutsk National Technical University, Lvivska Str., 75, Lutsk, 43018, Ukraine, E-mail m_yaroshevich@mail.ru

INDEX OF AUTHORS

Adamczyk Marek	365
Andrianov Igor V.....	11
Awrejcewicz Jan.....	11, 23, 65, 185, 197, 261, 295, 407, 483, 493, 587, 595
Baier Andrzej	77
Bąkowski Henryk	37
Bencsik Laszlo	47
Bergeon Yves	57, 461
Bian Xiaoli	283
Biesiacki Paweł	65
Borek Aleksander	579
Buchacz Andrzej.....	77, 89
Bučinskas Vytautas	99
Bulín Radek	111
Burdzik Rafał.....	353
Burghardt Andrzej	121
Byrtus Miroslav.....	419
Cao Dengqing	567
Celiński Ireneusz	353
Ceylan Ali	333
Chasalevris Athanasios	151
Chigarev Anatoli	131
Czapla Tomasz	343
Čičmancová Lenka	377
Danylenko Vjacheslav.....	453
Dąbek Przemysław	503
Diaferio Mariella.....	143
Dohnal Fadi	151
Frankovský Peter	163
Fritzkowski Paweł	175
Dzedzickis Andrius	99
Gajek Jakub.....	185, 261
Gallacher Barry	207
Gałęziowski Damian	89
Gierlak Piotr	121

Gmiterko Alexander	163
Grigg Harry.....	207
Grzelczyk Dariusz	197
Hajžman Michal	111, 419
Hanley Thomas H.....	207
Hedrih Andjelka	217
Hedrih Katica	217
Herbuś Krzysztof.....	77
Hroncová Darina	163
Huang Wenhua	567
Hunt Gregory	389
Iljin Igor	99
Jaskot Anna.....	227
Jaworski Jacek.....	237
Kaczmarczyk Stefan	249
Kazickij Artur.....	99
Kępiński Radosław	185, 261
Kizilova Natalya	273
Klein Wojciech	343
Kostka Ján	163
Krivanek Vaclav	57, 461
Kuliński Krzysztof.....	431
Kurc Krzysztof	121
Lewandowski Donat	493
Li Shuangbao.....	283
Lipa Sebastian	295
Lorencki Jakub	305
Ludwicki Michał.....	595
Magnucki Krzysztof.....	175
Majzner Michał.....	77
Makowski Michał.....	587
Małachowski Jerzy.....	471
Markert Bernd	11
Matej Jan	587

Mazanoglu Elif Cagda Kandemir	313, 323
Mazanoglu Kemal	313, 323, 333
Mężyk Arkadiusz	343
Milecki Szymon	175
Młyńczak Jakub	353
Motsch Jean	57, 461
Mrozowski Jerzy	65, 295
Mura Gabriel	343, 365
Muszyńska Magdalena	121
Nad' Milan	377
Nocoń Michał	365
Ociepka Piotr	77
Olejniki Paweł	23
Paouris Leonidas	389
Parandyk Wiktor	407
Piwnik Jan	579
Polach Pavel	111, 419
Polenov Victor	131
Posiadała Bogdan	227
Przybylski Jacek	431
Qin Zhanming	555
Radkowski Stanisław	305, 543
Rahmani Ramin	389
Rolník Ladislav	377
Rusin Jarosław	443
Shirvel Pavel	131
Skurativskyi Sergii	453, 531
Stańczyk Bartosz	197
Starosta Roman	483
Starushenko Galina A.	11
Stefek Alexandr	57, 461
Sybilski Kamil	471
Sypniewska-Kamińska Grażyna	483
Szczurowski Krzysztof	543

Szlachetka Olga.....	237
Szybicki Dariusz.....	121
Szymanowska Olga.....	493
Szymkiewicz Gabriel.....	493
Śpiewak Szczepan.....	227
Šešok Nikolaj.....	99
Šika Zbyněk.....	419
Šutinys Ernestas.....	99
Tarasiuk Wojciech.....	579
Theodossiades Stephanos.....	389
Trebuňa František.....	163
Trojnacki Maciej.....	503
Varkonyi Peter.....	519
Vladimirov Vsevolod.....	531
Walczak Damian.....	543
Wang Xiao.....	555
Wei Jin.....	567
Węgrzyn Tomasz.....	579
Wijata Adam.....	587
Wittbrodt Edmund.....	595
Wojnicz Wiktoria.....	595
Yang Yang.....	567
Yaroshevich Nikolai.....	609
Yaroshevich Tetiana.....	609
Zabrodets Ivan.....	609
Zagrodny Bartłomiej.....	595
Zelei Ambrus.....	47
Zieliński Łukasz.....	543

ISBN 978-83-7283-707-3